

is Copy

**REPORT ON RESEARCH ACTIVITIES  
FOR CALENDAR YEAR 1990**

Prepared for  
**Nuclear Regulatory Commission  
Contract NRC-02-88-005**

Prepared by  
**Center for Nuclear Waste Regulatory Analyses  
San Antonio, Texas**

**February 1991**

# **REPORT ON RESEARCH ACTIVITIES FOR CALENDAR YEAR 1990**

*Prepared for*

**Nuclear Regulatory Commission  
Contract NRC-02-88-005**

*Edited by*

**Wesley C. Patrick**

**Center for Nuclear Waste Regulatory Analyses  
San Antonio, Texas**

**February 1991**

## ABSTRACT

This is an annual status report on the results of research conducted on behalf of the NRC by the Center for Nuclear Waste Regulatory Analyses in support of activities under the Nuclear Waste Policy Act, as Amended. Eight specific projects are underway. The Geochemistry project is using laboratory methods and computer calculations to assess key geochemical constraints and to evaluate sorptive properties of zeolites present at the proposed repository site. The Thermohydrology project has as its focus improved understanding of heat and fluid flow in unsaturated media. Laboratory, field, and calculational studies are combined in the Seismic Rock Mechanics project to examine the effects of repeated seismic loadings on the rock-mechanical and hydrological responses of rock masses. The Integrated Waste Package Experiments have been initiated to evaluate degradation modes of candidate waste container alloys. Three-dimensional computer analysis techniques are being used to investigate spatial variability of flow and transport in variably saturated fractured porous media in the Stochastic Flow and Transport project. The recently initiated Geochemical Analogs project seeks to investigate the role of such analogs in the licensing process, and is currently focused on locating and evaluating a potential site for investigation. The Performance Assessment project is directed toward developing and evaluating methodologies for evaluation of the long-term performance of the proposed repository.

# TABLE OF CONTENTS

ABSTRACT .....	iii
LIST OF FIGURES .....	xiv
LIST OF TABLES .....	xxii
ACKNOWLEDGMENTS .....	xxv
1. EXECUTIVE SUMMARY .....	1-1
1.1 INTRODUCTION .....	1-1
1.2 GEOCHEMISTRY .....	1-1
1.3 THERMOHYDROLOGY .....	1-3
1.4 SEISMIC ROCK MECHANICS .....	1-4
1.5 INTEGRATED WASTE PACKAGE EXPERIMENTS .....	1-6
1.6 STOCHASTIC ANALYSIS OF FLOW AND TRANSPORT .....	1-7
1.7 GEOCHEMICAL ANALOGS .....	1-8
1.8 PERFORMANCE ASSESSMENT RESEARCH .....	1-9
1.8.1 Multi-phase Flow and Transport .....	1-9
1.8.2 Evaluation of Sandia National Laboratory Technology .....	1-9
2. UNSATURATED MASS TRANSPORT (GEOCHEMISTRY) <i>by Roberto T. Pabalan and William M. Murphy</i> .....	2-1
2.1 EXPERIMENTAL STUDIES .....	2-1
2.1.1 Technical Objectives .....	2-1
2.1.2 Thermodynamics of Ion Exchange .....	2-2
2.1.3 Experimental .....	2-5
2.1.3.1 <i>Characterization of Clinoptilolite Samples</i> .....	2-5
2.1.3.2 <i>Preparation and Chemical Analysis of                     Clinoptilolite Material</i> .....	2-11
2.1.3.3 <i>Ion Exchange Kinetic Experiments</i> .....	2-14
2.1.3.4 <i>Ion Exchange Isotherms</i> .....	2-15
2.1.4 Results and Discussion .....	2-20
2.1.5 Conclusions .....	2-23
2.2 GEOCHEMICAL MODELING .....	2-24
2.2.1 Technical Objectives .....	2-24
2.2.2 Reaction-Path Modeling of Gas-Water-Rock Interactions .....	2-24

TABLE OF CONTENTS (Cont'd)

2.2.2.1 *Groundwater and Mineral Chemistry at Yucca Mountain* . . . . . 2-25

2.2.2.2 *Near-field Modeling: Nonisothermal Kinetics and Gas Fractionation* . . . . . 2-34

2.2.2.3 *Reaction-Path Modeling for Analcime-Clinoptilolite Phase Equilibrium Experimental Design* . . . . . 2-41

2.2.2.4 *Thermodynamic Analysis of Aqueous Solution Chemistry in Localized Corrosion Experiments* . . . . . 2-46

2.2.3 Status of EQ3/6 Modeling and Capabilities . . . . . 2-49

2.3 REFERENCES . . . . . 2-50

3. THERMOHYDROLOGY *by Ronald T. Green and Franklin T. Dodge* . . . . . 3-1

3.1 INTRODUCTION . . . . . 3-1

3.2 TECHNICAL OBJECTIVES . . . . . 3-2

3.3 ASSESSMENT OF THE STATE-OF-KNOWLEDGE OF THERMOHYDROLOGY IN UNSATURATED MEDIA . . . . . 3-3

3.4 DESIGN AND EXECUTION OF PRELIMINARY SEPARATE-EFFECTS EXPERIMENTS . . . . . 3-3

3.4.1 Separate Effects Experimental Apparatus . . . . . 3-4

3.4.1.1 *Large-Test Chamber Construction* . . . . . 3-4

3.4.1.2 *Small-Test Chamber Construction* . . . . . 3-5

3.4.2 Support Equipment . . . . . 3-9

3.4.2.1 *Selection and Description* . . . . . 3-9

3.4.2.2 *Instrumentation Modifications* . . . . . 3-10

3.4.3 Experimental Media Characteristics . . . . . 3-12

3.4.3.1 *Bead Size Calculations* . . . . . 3-12

3.4.3.2 *Porosity Measurements* . . . . . 3-12

3.4.3.3 *Hydraulic Conductivity Calculations* . . . . . 3-14

3.4.4 Separate Effects Experiments . . . . . 3-14

3.4.4.1 *Experiment Test 1* . . . . . 3-18

3.4.4.2 *Experiment Test 2* . . . . . 3-18

## TABLE OF CONTENTS (Cont'd)

3.4.4.3	<i>Experiment Test 3</i>	3-18
3.4.4.4	<i>Experiment Test 4</i>	3-19
3.4.4.5	<i>Experiment Test 5</i>	3-19
3.4.4.6	<i>Experiment Test 6</i>	3-19
3.4.5	Separate Effects Experiments Results	3-20
3.4.5.1	<i>Experiment Test 1</i>	3-20
3.4.5.2	<i>Experiment Test 2</i>	3-21
3.4.5.3	<i>Experiment Test 3</i>	3-21
3.4.5.4	<i>Experiment Test 4</i>	3-21
3.4.5.5	<i>Experiment Test 5</i>	3-22
3.5	DIMENSIONAL ANALYSIS OF THERMOHYDROLOGIC EQUATIONS FOR POROUS, VARIABLY SATURATED, FRACTURED MEDIA	3-22
3.5.1	Conservation Equations, Constitutive Equations and Boundary and Initial Conditions	3-25
3.5.1.1	<i>Conservation of Water</i>	3-25
3.5.1.2	<i>Conservation of Air</i>	3-27
3.5.1.3	<i>Conservation of Energy</i>	3-28
3.5.1.4	<i>Constitutive Equations and Initial Boundary Conditions</i>	3-29
3.5.2	Nondimensional Equations	3-29
3.5.3	Nondimensional Parameters	3-31
3.5.4	Discussion of the pi Terms	3-32
3.6	SIMULATION ANALYSIS AND RESULTS	3-33
3.7	SUMMARY AND DISCUSSION OF RESULTS	3-36
3.8	SYMBOLS AND TYPICAL DIMENSIONAL UNITS	3-42
3.9	REFERENCES	3-45
4.	SEISMIC ROCK MECHANICS <i>by Simon M. Hsiung and Asadul H. Chowdhury</i>	4-1
4.1	TECHNICAL OBJECTIVES	4-1
4.2	EVALUATION OF ROCK-JOINT MODELS AND COMPUTER CODES	4-2

## TABLE OF CONTENTS (Cont'd)

4.2.1	Cyclic Loading of a Specimen with a Slipping Joint . . . . .	4-3
4.2.2	Circular Excavation Intersected by a Joint . . . . .	4-3
4.2.3	Slip in a Jointed Body Induced by a Harmonic Shear Wave . . . . .	4-5
4.2.4	Line Source in an Elastic Medium with a Slip-Prone Joint . . . . .	4-6
4.2.5	Summary of Results . . . . .	4-7
4.3	PRETEST ANALYSIS FOR THE ROCK-JOINT DYNAMIC SHEAR TEST . . . . .	4-7
4.3.1	3DEC Models of the Dynamic Shear Test . . . . .	4-8
4.3.2	Simulation of the Demonstration Test on a Concrete-Joint Specimen . . . . .	4-8
4.3.3	Preliminary Numerical Simulations of Tuff Joints . . . . .	4-10
4.3.3.1	<i>Monotonic Loading</i> . . . . .	4-12
4.3.3.2	<i>Load Reversal</i> . . . . .	4-12
4.3.3.3	<i>Harmonic Loading</i> . . . . .	4-13
4.3.3.4	<i>Earthquake Loading</i> . . . . .	4-13
4.3.4	Influence of Test Conditions . . . . .	4-13
4.3.4.1	<i>3DEC Full-Shear Box Model</i> . . . . .	4-17
4.3.4.2	<i>Dynamic Analysis</i> . . . . .	4-17
4.3.5	Summary and Recommendations . . . . .	4-18
4.4	LABORATORY INVESTIGATION OF ROCK-JOINT BEHAVIOR . . . . .	4-19
4.4.1	Development of Laboratory Test Apparatus . . . . .	4-19
4.4.1.1	<i>Normal Load System</i> . . . . .	4-22
4.4.1.2	<i>Horizontal Load System</i> . . . . .	4-22
4.4.1.3	<i>Instrumentation and Control</i> . . . . .	4-22
4.4.1.4	<i>Data Acquisition and Processing</i> . . . . .	4-23
4.4.1.5	<i>Pseudostatic Demonstration Tests</i> . . . . .	4-23
4.4.1.6	<i>Preliminary Dynamic Tests for Earthquake Simulation with an Artificial Joint</i> . . . . .	4-25
4.4.1.7	<i>Conclusions</i> . . . . .	4-31
4.4.2	Sample Collection and Preparation Activities . . . . .	4-32
4.4.2.1	<i>Site Selection for Sample Collection</i> . . . . .	4-32

## TABLE OF CONTENTS (Cont'd)

4.4.2.2	<i>Important Considerations for Sample Collection</i>	4-33
4.4.2.3	<i>Techniques for Sample Collection</i>	4-34
4.4.2.4	<i>Discussion for Sample Collection</i>	4-35
4.4.2.5	<i>Summary of Results</i>	4-38
4.4.3	Specimen Preparation/Testing Activities	4-39
4.4.3.1	<i>Direct Shear Specimen Preparation</i>	4-40
4.4.3.2	<i>Uniaxial and Triaxial Compression Specimens</i>	4-40
4.4.3.3	<i>Brazilian Disk Tension Specimens</i>	4-40
4.4.3.4	<i>Problems for Direct Shear Specimen Preparation</i>	4-41
4.4.3.5	<i>Development of Rock Profiler</i>	4-41
4.5	NEVADA TEST SITE (NTS) DATA COLLECTION ON GROUND-SHOCK EXCITATION	4-48
4.5.1	Site Geometry	4-52
4.5.2	Material Properties	4-52
4.5.3	Tectonic Stress	4-53
4.5.4	Block Motion Data	4-53
4.6	FIELD SITE INVESTIGATION	4-66
4.6.1	Field Site Evaluation and Selection	4-67
4.6.2	General Description and Site Geology	4-68
4.6.3	Mine-Wide Seismic Activity Monitoring System	4-68
4.6.4	Instrumentation	4-68
4.6.4.1	<i>Excavation Response</i>	4-69
4.6.4.2	<i>Pore Water-Pressure Measurement</i>	4-71
4.6.5	Data Acquisition	4-74
4.6.6	Instrument Calibration	4-74
4.6.6.1	<i>Five-Anchor Extensometer Calibration</i>	4-74
4.6.6.2	<i>Triaxial Velocity-Gauge Calibration</i>	4-77
4.6.6.3	<i>Vibrating-Wire Piezometer Calibration</i>	4-81
4.6.7	Discussion and Summary	4-83
4.7	SUMMARY	4-85

## TABLE OF CONTENTS (Cont'd)

4.8 REFERENCES .....	4-87
5. INTEGRATED WASTE PACKAGE EXPERIMENTS	
<i>by Gustavo Cragnolino and Narasi Sridhar</i> .....	5-1
5.1 TECHNICAL OBJECTIVES .....	5-1
5.2 CORROSION OF CONTAINER MATERIALS .....	5-2
5.2.1 Review of Experimental Results Related to Localized Corrosion .....	5-2
5.2.2 Characterization of Container Materials in the Initial Condition .....	5-7
5.2.2.1 <i>Metallography</i> .....	5-7
5.2.2.2 <i>SEM-EDX Analysis of Surfaces and Bulk</i> .....	5-9
5.2.2.3 <i>Corrosion Tests in Standard Solutions</i> .....	5-9
5.2.3 Pitting Variability Tests on Alloy 825 .....	5-12
5.2.4 Effect of Environmental Variables on Localized Corrosion of Alloy 825 .....	5-17
5.2.4.1 <i>Factorial Design</i> .....	5-17
5.2.4.2 <i>Electrochemical Observations</i> .....	5-20
5.2.4.3 <i>Visual and SEM Examination</i> .....	5-20
5.2.4.4 <i>Localized Corrosion Index (LCI)</i> .....	5-20
5.2.5 Effect of Temperature on Localized Corrosion of Alloy 825 .....	5-29
5.2.6 Effect of Si on Localized Corrosion of Alloy 825 .....	5-30
5.2.7 Effect of Mg <sup>2+</sup> on Localized Corrosion .....	5-32
5.2.8 Effect of Nitrite .....	5-32
5.2.9 Effect of Aeration and H <sub>2</sub> O <sub>2</sub> .....	5-32
5.3 SUMMARY OF RESULTS .....	5-35
5.4 REFERENCES .....	5-37
6. STOCHASTIC ANALYSIS OF UNSATURATED FLOW AND TRANSPORT <i>by Rachid Ababou</i> .....	6-1
6.1 INTRODUCTION .....	6-1
6.2 IDENTIFICATION OF SITE-SPECIFIC HYDROGEOLOGIC ISSUES ...	6-2
6.2.1 Regulatory Background .....	6-2

## TABLE OF CONTENTS (Cont'd)

6.2.2	Specific Technical Issues	6-3
6.3	CONCEPTUAL APPROACHES TO FIELD-SCALE FLOW MODELING	6-6
6.4	NUMERICAL HYDRODYNAMICS	6-8
6.4.1	Numerical Analysis of Nonlinear Unsaturated Flow	6-8
6.4.2	Algebraic System Solvers	6-9
6.5	DIRECT HIGH-RESOLUTION SIMULATIONS	6-9
6.5.1	Background	6-9
6.5.2	Simulation Results and Analysis	6-9
6.6	EFFECTIVE AND SUB-SCALE HYDRODYNAMIC MODELS	6-10
6.7	SUMMARY	6-12
6.8	REFERENCES	6-12
7.	GEOCHEMICAL NATURAL ANALOGS <i>by English C. Percy and William M. Murphy</i>	7-1
7.1	TECHNICAL OBJECTIVES	7-1
7.2	RESEARCH RESULTS FROM TASK 1	7-1
7.2.1	Limitations of Natural Analog Studies	7-2
7.2.2	Contributions of Natural Analog Studies	7-2
7.2.3	Natural Analog Studies	7-3
7.2.4	Processes and Events Likely to Control Contaminant Transport at Yucca Mountain	7-4
7.2.4.1	<i>Processes Important to Contaminant Transport at Any Geologic HLW Repository</i>	7-4
7.2.4.2	<i>Processes and Events Peculiar to Contaminant Transport at Yucca Mountain</i>	7-5
7.2.5	Geochemical Processes Amenable to Natural Analog Study	7-5
7.2.6	Criteria for the Successful Use of Natural Analogs	7-6
7.2.7	Potential Sites for a Natural Analog Study	7-7
7.2.8	Conclusions	7-7
7.3	REFERENCES	7-8

## TABLE OF CONTENTS (Cont'd)

8. PERFORMANCE ASSESSMENT RESEARCH <i>by Budhi Sagar and A. Berge Gureghian</i> . . . . .	8-1
8.1 REVIEW OF EQUATIONS FOR MULTI-PHASE MULTI-SPECIES FLOW AND TRANSPORT IN FRACTURED POROUS MEDIA . . . . .	8-1
8.1.1 Task Objectives . . . . .	8-1
8.1.2 Introduction . . . . .	8-1
8.1.3 Conceptual Framework . . . . .	8-2
8.1.4 Balance Laws of Continuum Mechanics . . . . .	8-2
8.1.4.1 <i>Balance Laws For a Simple Continuum</i> . . . . .	8-2
8.1.4.2 <i>Balance Equations For Mixtures</i> . . . . .	8-5
8.1.5 Momentum Equation . . . . .	8-10
8.1.6 Energy Equation . . . . .	8-11
8.1.7 Treatment of Fractures . . . . .	8-11
8.1.8 Review of Existing Multiphase Codes used in the HLW Program . . . . .	8-13
8.1.8.1 <i>TOUGH Computer Code</i> . . . . .	8-13
8.1.8.2 <i>NORIA Computer Code</i> . . . . .	8-14
8.1.8.3 <i>PETROS Computer Code</i> . . . . .	8-16
8.1.8.4 <i>Model by Forsyth</i> . . . . .	8-16
8.1.9 Summary and Conclusions . . . . .	8-18
8.2 EVALUATION OF DCM3D - A DUAL CONTINUUM, 3-D GROUND-WATER FLOW CODE FOR UNSATURATED, FRACTURED, POROUS MEDIA . . . . .	8-20
8.2.1 Technical Objectives of Task . . . . .	8-20
8.2.2 Introduction . . . . .	8-20
8.2.3 Approaches for Modeling Flow in Fractured Geologic Media . . . . .	8-21
8.2.3.1 <i>Analysis Needs</i> . . . . .	8-21
8.2.3.2 <i>Modeling Approaches</i> . . . . .	8-22
8.2.3.3 <i>Fluid Motion in Geologic Media</i> . . . . .	8-32

TABLE OF CONTENTS (Cont'd)

8.2.3.4 <i>Review of DCM3D</i> . . . . .	8-38
8.2.3.5 <i>Preliminary Conclusions</i> . . . . .	8-40
8.3 REFERENCES . . . . .	8-41

## LIST OF FIGURES

<u>Figure</u>	<u>Title</u>	<u>Page</u>
2-1	Scanning electron microscope images of clinoptilolite from Death Valley Junction, California . . . . .	2-7
2-2	X-ray diffraction pattern of clinoptilolite-rich tuff from Death Valley Junction, California: (a) before and (b) after heating overnight at 450°C. Cl=clinoptilolite; Q=quartz . . . . .	2-8
2-3	X-ray diffraction pattern of heulandite from Poona, Maharashtra State, India: (a) before and (b) after heating overnight at 450°C. . . . .	2-10
2-4	X-ray diffraction pattern of clinoptilolite-rich tuff from Death Valley Junction, California, after heavy liquid separation: . . . . .	2-12
2-5	Aqueous concentration of K <sup>+</sup> as a function of time in the KCl-NaCl solution equilibrating with initially homoionic Na-clinoptilolite . . . . .	2-16
2-6	Aqueous concentration of Na <sup>+</sup> as a function of time in the KCl solution equilibrating with initially homoionic Na-clinoptilolite . . . . .	2-17
2-7	Aqueous concentration of Ca <sup>2+</sup> as a function of time in the CaCl <sub>2</sub> -NaCl solution equilibrating with initially homoionic Na-clinoptilolite . . . . .	2-18
2-8	Aqueous concentration of Na <sup>+</sup> as a function of time in the CaCl <sub>2</sub> -NaCl solution equilibrating with initially homoionic Na-clinoptilolite . . . . .	2-19
2-9	Isotherms at 25°C for the K <sup>+</sup> -Na <sup>+</sup> binary system at total solution concentrations of: A) 0.05 N and B) 0.50 N. . . . .	2-21
2-10	Isotherms at 25°C for the Ca <sup>2+</sup> -Na <sup>+</sup> binary system at total solution concentrations of: A) 0.05 N and B) 0.50 N. . . . .	2-22
2-11	Values of $g^{\alpha}$ (cal/mol) vs. the cationic mole fraction of Na <sup>+</sup> , $X_{Na}$ , in the zeolite for the K <sup>+</sup> -Na <sup>+</sup> binary systems. . . . .	2-24
2-12	Comparison of aqueous solution compositions calculated in an isothermal (25°C) reaction-path model (curves) to measured water compositions from the tuffaceous aquifer at Yucca Mountain (open circles) . . . . .	2-31

## LIST OF FIGURES (Cont'd)

<u>Figure</u>	<u>Title</u>	<u>Page</u>
2-13	Comparison of aqueous solution compositions calculated in an isothermal (25°C) reaction-path model (curves) to measured water compositions from the tuffaceous aquifer at Yucca Mountain (open circles) . . . . .	2-32
2-14	Changes in solution composition and moles of calcite precipitated as a function of temperature (°C) along a nonisothermal reaction path with buffered CO <sub>2</sub> . . . . .	2-37
2-15	Rates of mineral dissolution and growth and changes in solution compositions as a function of temperature (°C) along a nonisothermal reaction path with buffered CO <sub>2</sub> . . . . .	2-38
2-16	Variation of clinoptilolite composition, moles of calcite and K-feldspar precipitated and changes in solution composition as a function of temperature (°C) along a nonisothermal reaction path with buffered CO <sub>2</sub> . . . . .	2-39
2-17	Changes in solution composition, moles of K-feldspar and calcite precipitated and clinoptilolite compositions as a function of temperature (°C) along a nonisothermal reaction path with open-system CO <sub>2</sub> volatilization . . . . .	2-42
2-18	Reaction paths (represented by dashed arrows) for clinoptilolite-analcime equilibration studies, plotted in a thermodynamic activity diagram representing fields of mineral stability as a function of aqueous solution composition at 25°C . . . . .	2-45
3-1	Test chamber - Front view . . . . .	3-5
3-2	Configuration of sensors in larger test chamber . . . . .	3-6
3-3	Design details of the smaller test chamber used in test 5 with densitometer measurement locations . . . . .	3-7
3-4	Design details of the smaller chamber used in test 6 with tensiometer and densitometer measurement locations . . . . .	3-8
3-5	Schematic of the tensiometer . . . . .	3-10

## LIST OF FIGURES (Cont'd)

<u>Figure</u>	<u>Title</u>	<u>Page</u>
3-6	Moisture release curve for No.s 1420 and 2740 glass-bead mixture . . . . .	3-15
3-7	Calculated hydraulic conductivity curve for No. 1420/No. 2740 glass bead mixture . . . . .	3-16
3-8	Photograph of test chamber at day 7 of test 5 . . . . .	3-23
3-9	Photograph of test chamber at day 14 of test 5 . . . . .	3-23
3-10	Photograph of test chamber at day 23 of test 5 . . . . .	3-23
3-11	Schematic of finite difference grid used in numerical simulations . . . . .	3-34
3-12	Moisture release curves for different sets of van Genuchten parameters . . . . .	3-37
3-13	Temperature distribution - Simulation 1 . . . . .	3-38
3-14	Capillary pressure (Pascals) - Simulation 1 . . . . .	3-38
3-15	Liquid saturation content - Simulation 1 . . . . .	3-39
3-16	Gas saturation content - Simulation 1 . . . . .	3-39
3-17	Temperature distribution - Simulation 2 . . . . .	3-40
3-18	Capillary pressure (Pascals) - Simulation 2 . . . . .	3-40
3-19	Liquid saturation content - Simulation 2 . . . . .	3-41
3-20	Gas saturation content - Simulation 2 . . . . .	3-41
4-1	Four benchmark analytical problems: (a) Cyclic loading of a specimen with a slipping joint, (b) Joint intersecting a circular excavation, (c) Slip in a jointed body induced by a harmonic shear wave, and (d) Line source in an elastic medium with a slip-prone joint . . . . .	4-4
4-2	Comparison of dimensionless slip at point P with Coulomb joint-model dimensionless slip = $(4 h p \delta^2 / m_0) \delta u$ , dimensionless time = $t \delta / h$ . . . . .	4-8

## LIST OF FIGURES (Cont'd)

<u>Figure</u>	<u>Title</u>	<u>Page</u>
4-3	3DEC simple base model of a jointed tuff specimen . . . . .	4-9
4-4	3DEC full model consisting of a jointed tuff specimen inside the shear box . . . . .	4-9
4-5	Comparison of 3DEC model to laboratory test results for joint closure variation with pseudostatic normal stress . . . . .	4-11
4-6	Comparison of 3DEC model to laboratory test results for joint stress variation with joint shear displacement at normal stress = 4.36 MPa . . . . .	4-11
4-7	Shear stress displacement curve for monotonic loading with Coulomb friction model and continuously yielding model cases 1 and 2 . . . . .	4-13
4-8	Shear displacement path for load reversal . . . . .	4-14
4-9	Shear stress displacement curve for load reversal with Coulomb friction model . . . . .	4-14
4-10	Shear stress displacement curve for load reversal with continuously yielding model, case 1 . . . . .	4-15
4-11	Shear stress displacement curve for harmonic loading with continuously yielding model, case 2 . . . . .	4-15
4-12	Shear stress displacement curve for earthquake loading with Coulomb friction model . . . . .	4-16
4-13	Shear stress displacement curve for earthquake loading with continuously yielding model, case 2 . . . . .	4-16
4-14	Vertical section through 3DEC full shear box model . . . . .	4-18
4-15	Horizontal and vertical displacement histories for 500 Hz input frequency . . . . .	4-19
4-16	Horizontal and vertical displacement histories for 50 HZ input frequency . . . . .	4-20
4-17	Assembly and instrumentation diagram . . . . .	4-21

## LIST OF FIGURES (Cont'd)

<u>Figure</u>	<u>Title</u>	<u>Page</u>
4-18	Joint closure variation with pseudostatic normal stress for the concrete joint . . . . .	4-26
4-19	Joint closure variation with pseudostatic normal stress for the natural rock joint . . . . .	4-26
4-20	Influence of shear displacement on joint normal displacement for the concrete joint under combined pseudostatic load . . . . .	4-27
4-21	Influence of shear displacement on joint normal displacement for the natural rock joint under combined pseudostatic load . . . . .	4-27
4-22	Shear stress versus shear displacement relationship for the concrete joint under combined pseudostatic load . . . . .	4-28
4-23	Shear stress versus shear displacement relationship for the natural rock joint under combined pseudostatic load . . . . .	4-28
4-24	Frictional characteristics of both the concrete and natural rock joints under combined pseudostatic load . . . . .	4-29
4-25	Unfiltered acceleration response spectrum at upper specimen block . . . . .	4-29
4-26	Filtered acceleration response spectrum at upper specimen block . . . . .	4-31
4-27	Truck-mounted Joy 22 drill rig . . . . .	4-40
4-28	Location of drilled holes for sample collection at the Apache Leap Site . . . . .	4-37
4-29	18-inch diameter core with a smooth joint interface . . . . .	4-39
4-30	Core drilled at the field site shown set up for laboratory coring . . . . .	4-41
4-31	Direct shear specimen shown in the cutting process using a slab saw . . . . .	4-42
4-32	Three prepared direct shear specimens . . . . .	4-42
4-33	Two Brazilian disk tension specimens and one compression specimen in the preparation process . . . . .	4-46

## LIST OF FIGURES (Cont'd)

<u>Figure</u>	<u>Title</u>	<u>Page</u>
4-34	Profilometer for joint surface profile measurement . . . . .	4-48
4-35	Plan view of the Lucky Friday orebody showing fault structures . . . . .	4-69
4-36	Ramp system at the 5210 level at the Lucky Friday Mine . . . . .	4-71
4-37	Instrumentation array for cross sections of the 5210 level (a) LFM95 - C1 site (b) LFM95 - C2 site . . . . .	4-72
4-38	Geologic mapping of extensometer hole no. 5 at LFM95-C1 site . . . . .	4-73
4-39	Lucky Friday silver shaft cross section of the drill hole for piezometer installation (view looking N74°E) . . . . .	4-73
4-40	Schematic drawing of piezometer installation showing straddle packers . . . . .	4-75
4-41	Schematic diagram of extensometer and piezometer data acquisition system . . . . .	4-75
4-42	Schematic of seismic data acquisition system . . . . .	4-76
4-43	Five-anchor extensometer . . . . .	4-78
4-44	Field data acquisition system . . . . .	4-79
4-45	Extensometer calibration curve for MPBX No. B, position 3 . . . . .	4-81
4-46	Calibration of electrolab triaxial velocity transducers . . . . .	4-82
4-47	Output voltage in the principal excitation direction (X-Axis for this plot) versus frequency . . . . .	4-83
5-1	SEM-EDX analysis of polished and etched CDA-613 alloy . . . . .	5-10
5-2	Surface Cr depletion . . . . .	5-11
5-3	ASTM A-262 B test results . . . . .	5-13

## LIST OF FIGURES (Cont'd)

<u>Figure</u>	<u>Title</u>	<u>Page</u>
5-4	Sample curve from a cyclic polarization test . . . . .	5-16
5-5	Effect of chloride in simulated J-13 water on pitting of Alloy 825 P=pit, C=crevice attack . . . . .	5-18
5-6	Effect of chloride in simulated J-13 water on pitting of 304L stainless steel pits . . . . .	5-19
5-7	Typical cyclic polarization curves for alloy 825 at 95°C indicating the effect of nitrate at a chloride concentration of 1000 ppm . . . . .	5-21
5-8	Typical cyclic polarization curves for alloy 825 at 60°C indicating the effect of fluoride at a chloride concentration of 6 ppm . . . . .	5-22
5-9	$E_p - E_{rp}$ vs. visual rating of alloy 825 specimens indicating a lack of correlation between these two parameters . . . . .	5-24
5-10	The coefficients in eqn. (2) plotted for various factors along with their 95 percent confidence intervals . . . . .	5-27
5-11	Effect of temperature and chloride concentration on $E_p$ and $E_{rp}$ of alloy 825 . . . . .	5-31
6-1	Idealized moisture flow system through the east-west section at Yucca Mountain (modified from Montazer and Wilson, 1986, and DOE Site Characterization Plan, 1988) . . . . .	6-4
6-2	Idealized moisture flow system through the east-west section at Yucca Mountain (from Peters and Klavetter, 1988) . . . . .	6-5
6-3	Front view of a peeled-off three-dimensional moisture plume from stochastic flow simulations . . . . .	6-11
6-4	Back view of a three-dimensional moisture pattern from stochastic flow simulations; the cut-off moisture plume is visible in purple and blue . . . . .	6-11
8-1	Conceptual picture of multiphase flow through fractured porous media . . . . .	8-3

## LIST OF FIGURES (Cont'd)

<u>Figure</u>	<u>Title</u>	<u>Page</u>
8-2	Macroscopic control volume for continuum balance equations . . . . .	8-6
8-3	Schematic representation of: (a) fractured medium, (b) double-porosity medium, (c) discrete-fractured medium, (d) heterogeneous medium (Streltsova, 1976) . . . . .	8-23
8-4	Statistical definition of permeability and representative elementary volume (REV) . . . . .	8-24
8-5	Conductivity curve for unit CHnz (Klavetter and Peters, 1986) . . . . .	8-26
8-6	Idealization of naturally fractured porous medium . . . . .	8-29
8-7	Example of a discrete-fracture network generated with two orthogonal fracture sets (Schwartz and Smith, 1985) . . . . .	8-30
8-8	Example of (a) a three-dimensional fracture network of disk shaped orthogonal fractures and (b) cubic region isolated from the network shown in (a) . . . . .	8-31
8-9	Soil characteristic curves (Updegraff and Lee, 1990) . . . . .	8-36

## LIST OF TABLES

<u>Table</u>	<u>Title</u>	<u>Page</u>
2-1	Petrographic Analysis of Sample CDV. . . . .	2-9
2-2	Mineralogic Composition of Clinoptilolite Samples . . . . .	2-13
2-3	Clinoptilolite Chemical Analyses . . . . .	2-14
2-4	Comparison of K <sup>+</sup> or Ca <sup>2+</sup> Equivalents Removed from Solution with Na <sup>+</sup> Released into Solution . . . . .	2-20
2-5	Bulk Composition (Weight Percent) of Topopah Springs Tuff (TST) Represented as Feldspar Plus Cristobalite, and Model Mineral Chemistry . . . . .	2-28
2-6	Kinetic Data . . . . .	2-30
2-7	Computed Water Chemistry Data for Localized Corrosion Studies . . . . .	2-47
3-1	Glass Beads Population and Volume Distribution Statistics . . . . .	3-13
3-2	Summary to the Separate Effects Experiments . . . . .	3-17
3-3	van Genuchten Parameters used in the Numerical Simulation Analyses . . . . .	3-36
4-1	Comparison of 3DEC Results with Conceptual Model and UDEC for a Block with a Slipping Crack Under Cyclic Loading . . . . .	4-5
4-2	Assumed Tuff-Joint Model Parameters . . . . .	4-12
4-3	Assumed Properties for 3DEC Full Shear Box Model . . . . .	4-17
4-4	Instrumentation Channel Identification . . . . .	4-24
4-5	Uniaxial Compressive Strength, Young's Modulus, and Poisson's Ratio of Apache Leap Tuff . . . . .	4-43
4-6	Triaxial Compressive Strength for Apache Leap Tuff . . . . .	4-45

**LIST OF TABLES (Cont'd)**

<u>Table</u>	<u>Title</u>	<u>Page</u>
4-7	Results of Brazilian Disk Tension Test of Apache Leap Tuff . . . . .	4-47
4-8	Field Tests for Block Motion Database . . . . .	4-51
4-9	Summary of Rock-Mass and Joint Properties for HANDEC II and ROCKTEST II Sites . . . . .	4-54
4-10	Summary of Rock-Mass and Joint Properties for STARMET Site . . . . .	4-55
4-11	Rock-Mass Deformation Properties for Stratigraphic Units at MIGHTY EPIC/DIABLO HAWK Site . . . . .	4-56
4-12	Summary of Assumed Intact Rock-Strength Properties for Stratigraphic Units at MIGHTY EPIC/DIABLO HAWK Site . . . . .	4-56
4-13	Summary of Assumed Joint Strength Properties for MIGHTY EPIC/ DIABLO HAWK Site . . . . .	4-57
4-14	Summary of Tectonic Stress Data for MIGHTY EPIC/DIABLO HAWK Site . .	4-57
4-15	HANDEC II, ROCKTEST II and STARMET Data Summary . . . . .	4-58
4-16	MIGHTY EPIC and DIABLO HAWK Data Summary . . . . .	4-59
4-17	Extensometer Calibration Data Chart for MPBX No.B . . . . .	4-80
4-18	Transducer Serial No. 12785 Reading Chart . . . . .	4-84
4-19	Comparison of Calibration Factors . . . . .	4-85
5-1	Chemical Composition Ranges of J-13 Wellwater (Glassley, 1990) . . . . .	5-4
5-2	Heat Numbers and Chemical Compositions of the Candidate Container Materials in the IWPE Program . . . . .	5-8
5-3	Results of Cyclic Polarization Tests on Incoloy Alloy 825 in Simulated J-13 Solutions Modified to Various Chloride Levels . . . . .	5-15

## LIST OF TABLES (Cont'd)

<u>Table</u>	<u>Title</u>	<u>Page</u>
5-4	Rating of Localized Corrosion by Visual and SEM-EDX Examination . . . . .	5-23
5-5	Effect of Si on Localized Corrosion of Alloy 825 in a Cyclic Polarization Test . . . . .	5-33
5-6	Effect of $Mg^{2+}$ on Localized Corrosion of Alloy 825 . . . . .	5-33
5-7	Effect of $NO_2^-$ on Localized Corrosion of Alloy 825 . . . . .	5-34
5-8	Effect of Aeration of $H_2O_2$ Addition on Open-circuit Potentials (mV vs. SCE) of Alloy 825 and Pt Simulated J-13 Solutions at $95^\circ C$ . . . . .	5-34

## ACKNOWLEDGMENTS

This report was prepared to document work performed by the Center for Nuclear Waste Regulatory Analyses (CNWRA) for the U. S. Nuclear Regulatory Commission under Contract No. NRC-02-88-005. The research activities reported here were performed on behalf of the NRC Office of Nuclear Regulatory Research, Division of Engineering. The report is an independent product of the CNWRA and does not necessarily reflect the views or regulatory position of the NRC.

Each chapter of this report acknowledges those investigators who, although not specifically involved in writing the report, made significant contributions to the research projects. In addition, the authors gratefully acknowledge the technical support and technical reviews conducted by other members of the CNWRA and Institute staffs. Appreciation is particularly due Bonnie Garcia, Mary Ann Gruhlke, and Deanna Bump, who prepared input to the individual chapters of the report, and to Yolanda Lozano and Pamela Smith, who prepared the final text of this document and the preceding *Quarterly Reports* upon which it builds. We also acknowledge the able assistance of Curtis Gray, who provided graphical assistance, and Dr. Shirley Heller, who provided a full range of expert editorial services in the preparation of the final document.

## **NOTICE TO ACCOMPANY THE DISSEMINATION OF EXPORT-CONTROLLED TECHNICAL DATA**

If you print or display an abstract of any unclassified report marked EXPORT CONTROL, the following notice applies.

1. Export of information contained herein, which includes, in some circumstances, release to foreign nationals within the United States, without first obtaining approval or license from the Department of State for items controlled by the International Traffic in Arms Regulations (ITAR), or the Department of Commerce for items controlled by the Export Administration Regulations (EAR), may constitute a violation of law.

2. Under 22 U.S.C. 2778 the penalty for unlawful export of items or information controlled under the ITAR is up to 2 years imprisonment, or a fine of \$100,000, or both. Under 50 U.S.C., Appendix 2410, the penalty for unlawful export of items or information controlled under the EAR is a fine of up to \$1,000,000, or five times the value of the exports, whichever is greater; or for an individual, imprisonment of up to 10 years, or a fine of up to \$250,000, or both.

3. In accordance with your certification that established you as a "qualified U.S. contractor," unauthorized dissemination of this information is prohibited and may result in disqualification as a qualified U.S. contractor, and may be considered in determining your eligibility for future contracts with the Department of Defense.

4. The U.S. Government assumes no liability for direct patent infringement, or contributory patent infringement or misuse of technical data.

5. The U.S. Government does not warrant the adequacy, accuracy, currency, or completeness of the technical data.

6. The U.S. Government assumes no liability for loss, damage, or injury resulting from manufacture or use for any purpose of any product, article, system, or material involving reliance upon any or all technical data furnished in response to the request for technical data.

7. If the technical data furnished by the Government will be used for commercial manufacturing or other profit potential, a license for such use may be necessary. Any payments made in support of the request for data does not include or involve any license rights.

8. A copy of this notice shall be provided with any partial or complete reproduction of these data that are provided to qualified U.S. contractors.

10 U.S.C. 140c [(DoD Directive 5230.25 (Encl 5))]

# 1. EXECUTIVE SUMMARY

## 1.1. INTRODUCTION

This is the first in a series of research annual reports that document and make available to the technical community work undertaken by the Center for Nuclear Waste Regulatory Analyses (CNWRA) as part of its contract with the U.S. Nuclear Regulatory Commission (NRC). Reports are also prepared each calendar quarter and published as CNWRA documents. The fourth such report each year constitutes the annual progress report and is published as a NUREG/CR.

Each of the research projects discussed here is conducted in accordance with approved Research Project Plans, which were developed in response to research needs identified by the NRC and the CNWRA. These Plans are the vehicle for the established objectives, technical approach, justification, and funding for each of the studies. They also describe the interrelationships among the various projects which provide a sound basis for integrating research results. As the Plans address primarily planning and management matters, they are not discussed in this project (with the exception of objectives).

Because several of the projects have only recently been approved, they have relatively little work to report at this time. In such cases, this report provides basic information on the objectives of the new projects as well as early activities such as literature assessments. Other projects begun earlier have significant technical progress in laboratory, calculational, or field studies to report.

This document provides, first, an Executive Summary that covers in capsule form the progress of each research project over the past year. The Executive Summary is followed by Chapters 2 through 8 representing each of the seven currently active research projects, respectively. Project objectives and a report of research activities and results (as appropriate) to date are given in each chapter.

## 1.2. GEOCHEMISTRY

A major geologic feature potentially affecting the suitability of Yucca Mountain, Nevada as a repository site for high-level nuclear wastes (HLW) is the presence of thick, laterally extensive zones of zeolitic tuff. Because of their sorptive properties, zeolites could provide important geologic barriers to migration of radionuclides from the repository to the accessible environment. For example, sorption of elements such as cesium, strontium, and barium on Yucca Mountain tuffs correlates well with the amount of zeolites present in the rocks. The sorption of these elements onto zeolitized tuffs has been interpreted to be due to ion exchange processes. Ion exchange between zeolites and aqueous solutions depends on factors including compositions of the aqueous and zeolite phases and solution concentration. In addition, the thermodynamic stability of zeolite minerals and their susceptibility to diagenetic alteration also

depend on aqueous and solid phase compositions. Therefore, spatial variations in zeolite compositions, which have been observed at Yucca Mountain, as well as natural or repository-induced changes in groundwater chemistry may result in variations in the effectiveness of the zeolite minerals as retardation agents.

To support NRC's HLW program, the CNWRA is conducting experimental studies on the thermodynamic and ion exchange properties of zeolites under Task 3 of the Geochemistry Research Project. The studies conducted during the past year were designed to evaluate the use of thermodynamic models to describe and predict the solid solution and ion exchange properties of the zeolite mineral clinoptilolite, and to provide a quantitative basis for understanding the effects of zeolites in the retardation of radionuclides in the Yucca Mountain system. Ion exchange experiments were conducted between well-characterized specimens of clinoptilolite and aqueous solutions of alkali and alkaline earth elements. The experiments were done to obtain isotherm data and to evaluate the use of thermodynamic models in describing and predicting the solid solution and ion exchange properties of clinoptilolite. The experimental data were interpreted using excess Gibbs energy models for the aqueous solution and zeolite phases to account for nonideality in the system. The results indicate that the thermodynamic models allow predictions of clinoptilolite ion exchange behavior at ionic strengths and relative concentrations for which data are absent, and provide a foundation for the interpretation of ion exchange equilibria in multicomponent geochemical systems.

Under Task 2 of the Geochemistry Research Project, theoretical reaction-path modeling of gas-water-rock interactions has been applied to the interpretation of natural and experimental systems pertinent to ambient and repository geochemical conditions at Yucca Mountain, Nevada. The results of four applications are summarized. In the first exercise, the evolution of idealized water and mineral chemistry is simulated for the ambient system at Yucca Mountain. Comparison of the model results to water and mineral data collected at Yucca Mountain show that many important geochemical features are reasonably represented. A water and mineral phase assemblage generated in this ambient system model is used to set initial conditions for reaction-path computations of the geochemical consequences of near-field heating in the second application. Modeling of geochemical processes as a function of temperature and time shows that significant variations in water and mineral chemistry are possible on time scales that are short relative to the period of repository heating. Two alternate models are explored for nonisothermal gas-water-rock relations, the first using CO<sub>2</sub> gas pressure buffering, and the second employing equilibrium, open-system gas fractionation.

Two additional applications of reaction-path modeling are made to experimental systems. A set of reactions is designed theoretically to determine the reversed phase equilibrium between analcime and clinoptilolite in support of the experimental program of the Geochemistry Research Project. Testing conditions are identified that should minimize ambiguity in the interpretation of the experimental results and maximize their utility. A second application is to the interpretation of aqueous solution chemistry in localized corrosion studies conducted in the Integrated Waste Package Experiments (IWPE) Research Project. Computations of equilibrium aqueous speciations in experimental solutions and the evolution of solution chemistry on minor

vaporization at elevated temperatures provide an explanation for the observed evolution of pH and identify aqueous species of potential importance.

### 1.3. THERMOHYDROLOGY

Technical issues and uncertainties for the Yucca Mountain HLW repository site indicate a need for research on thermohydrological phenomena, i.e. phenomena associated with heat and fluid flow, to provide information relevant to performance assessment and design criteria. The class of thermohydrological phenomena examined in the thermohydrology research project includes phenomena driven by heat emanating from HLW emplaced in a geologic repository. Information derived principally from research is used to establish a knowledge base of thermohydrologic phenomena which will be used to assess models of processes used in performance assessments.

The specific objectives of the thermohydrology research project are summarized as follows: to perform a critical assessment of the state-of-knowledge of thermohydrology in unsaturated fractured media; to perform a detailed dynamic similarity or similitude analysis on the governing equations relevant to unsaturated flow; to design and perform a series of separate effects experiments in order to identify and understand the role of the coupled processes involved in thermohydrologic phenomena; to develop the laboratory facilities, experimental methods, measurement techniques and associated analytic skills to design and perform comprehensive experiments whose results will continue to identify key dependent and independent parameters and their relationships to each other in the context of thermohydrologic issues; to examine and correlate laboratory results with field data and to aid in the design of future field experiments.

The research project has been separated into five tasks for the purpose of accomplishing these objectives. Two of these tasks are active at this time: Task 1, Assessment of the State-of-Knowledge of Thermohydrology in Unsaturated Media; and Task 2, Design and Execution of Preliminary Separate Effects Experiments.

The Thermohydrology Research Project has progressed in three areas during the past year: experimentally, numerically and analytically. The first four separate effects experiments (Tests 1 to 4) were designed and executed for scoping purposes. Test 5 provided interesting insights into thermohydrological phenomena but did not provide sufficiently quantified results. Separate effects experiment Test 6 has been designed and is currently being performed. The objective of Test 6 is to perform an experiment similar to Test 5 but with a higher level of control so as to provide more meaningful data for analysis and comparison with analytical results and numerical simulations.

Preliminary results of the numerical simulations performed using a modified version of the TOUGH code have been evaluated. The objective of these numerical exercises is to evaluate the capabilities of TOUGH to simulate the two significant flow patterns observed in Test 5, the apparent formation of a convection cell and the reluctance to flow across a simulated fracture under less-than-saturated conditions. Preliminary analysis of the numerical simulation of the

Test 5 case has provided results that have been interpreted to suggest that fractures proximal to heat-generating waste may respond differently than those in an isothermal medium. The presence of a fracture within the regime of a heat pipe could arrest the return flow of liquid water resulting in the collapse of the heat pipe. Temperatures at the heat source boundary then could be expected to rise significantly above 100°C. The effect of a fracture in this nonisothermal environment is different from the predicted effect of a fracture in an isothermal environment where liquid-water flow would not be significantly affected.

Dimensional analyses have yielded a set of three dimensionless equations and twenty-seven dimensionless terms that may provide a means to apply dynamic similitude analysis to the problem of using laboratory-scale experiments to understand thermohydrologic phenomena at field-scale. The analyses can not be reasonably performed until the processes observed at the laboratory scale have been sufficiently understood. Foremost remaining in the characterization of the laboratory-scale experiments is the highly nonlinear fracture-matrix relationship.

#### 1.4. SEISMIC ROCK MECHANICS

A state-of-the-art literature review reveals that the seismic-effects calculations performed to date on underground structures have not been subjected to an adequate level of experimental and field investigations. The experimental support for most of the programs has focused on soils rather than on structurally complex rock formations. Computer programs are currently available to model dynamic events of underground structures in rock formations. However, these programs have not been validated with well-planned and rigorous experimental and field protocols. The Seismic Rock Mechanics Research Project is aimed at developing a better understanding of the key parameters affecting the repository under seismic loadings and, consequently, validation of computer programs for use in seismic assessment of underground structures in tuffaceous media.

Activities performed for the Seismic Rock Mechanics Project during the past year included computer code qualification studies, laboratory test-apparatus development, sample collection and preparation, pre-test analysis for rock-joint dynamic test, pseudostatic rock-joint shear tests, testing of cylindrical specimens for tuff characterization, development of rock-joint profile measurement capability, Nevada Test Site (NTS) data collection on ground-shock excitation, calibration of field instruments used at Lucky Friday Mine, and instrumented field studies. Substantial progress for the project was made in this past year.

For qualification studies on the UDEC and HONDO II codes, four benchmark analytical problems were exercised. The results indicate that UDEC performs valid simulations of jointed rock, to the extent that the mechanics of these media may be represented by the conceptual models expressed in the problems, while HONDO II has a limited capability. Some of HONDO II's deficiencies are related to the treatment of static and dynamic boundary loads in the code.

Three of the four benchmark analytical problems were analyzed for the qualification study on the 3DEC computer code. A special version of 3DEC (3DECSP) was used for the

analysis of the problem identified as slip in a jointed body induced by a harmonic shear wave. This version includes the capability of simulating nonzero cohesion and tension when discontinuity shear and/or tensile strength is exceeded. The results of the analyses indicate that 3DEC provides satisfactory correspondence with the conceptual models expressed in the three benchmark problems. The result also indicates that the effect of the nonreflecting boundary condition as implemented in the 3DEC for dynamic analysis depends on the size of the domain used in the analysis.

A dynamic direct shear test apparatus was developed which includes a 90,000-lb (0.4 MN) vertical and 50,000-lb (0.222 MN) horizontal loading capacity and is designed to house a specimen with maximum size of 12 x 8 x 4 in. (30.5 x 20.5 x 10.2 cm) for the lower specimen and 8 x 8 x 4 in. (20.3 x 20.3 x 10.2 cm) for the upper specimen. The test apparatus is designed in a flexible manner such that specimens with larger dimensions can be accommodated with minor modifications. Demonstration shake-down tests of the apparatus indicate that it is capable of accomplishing the tasks in the Seismic Rock Mechanics Project.

The Apache Leap site in Arizona was selected for sample collection. The welded tuff at Apache Leap has several characteristics similar to those at the repository horizon at Yucca Mountain. From this site about 50 potentially usable joint specimens were collected.

Preparation of direct shear-test specimens and cylindrical specimens for material characterization tests is currently underway. Twenty-five direct shear specimens were prepared. Water was used as a cutting fluid for the preparation of shear test specimens to minimize the potential of altering fracture-surface mechanical characteristics. However, use of water reduces cooling and cutting effectiveness, and contributes to blade wear. Tests were conducted on 45 uniaxial compression specimens, 5 triaxial compression specimens, and 27 Brazilian disk tension specimens. The average strength was 23,373 psi (161 MPa) in uniaxial compression. The average strengths in triaxial compression are 29,225 psi (202 MPa) with a confining pressure of 500 psi (3.45 MPa), 34,944 psi (241 MPa) with a confining pressure of 1,000 psi (6.9 MPa), and 40,720 psi (281 MPa) with a confining pressure of 1,500 psi (10.3 MPa). Average values for Young's modulus and Poisson's ratio of the Apache Leap tuff are  $5.83 \times 10^6$  psi ( $4.02 \times 10^4$  MPa) and 0.2, respectively.

Pre-test analysis was performed to provide guidance to assist in evaluating the effects of shear-test apparatus on dynamic response of the tuff joint specimen. A series of numerical calculations were performed with the 3DEC to simulate the apparatus and dynamic shear test of a naturally jointed tuff specimen. The results of the calculations for the typical range of frequencies of earthquake loadings (i.e., less than 50 Hz) showed that the response of the shear-test apparatus, given the assumed properties, did not influence joint response significantly.

Development and assemblage were completed of a rock profilometer for profile measurement of rock-joint surfaces. A custom computer program written in Borland's TurboC was developed to perform profile measurements, and to format and store the measured data to a

PC/AT data file. The measured profile data will be processed to calculate the corresponding joint roughness coefficient to be used for analyzing the Barton-Bandis rock-joint model.

Vast amounts of data on ground motion under impulsive loading have been generated in the course of underground nuclear explosions at the Nevada Test Site, and during other field tests related to weapons performance. An important component of this information is a block-motion study for which velocity and displacement data along major discontinuities forming geologic blocks are recorded. Five field test cases for which some of the most complete data sets have been collected were selected, and data were summarized. A database has been constructed that contains test information and results regarding the five tests. A detailed report regarding the data-collection activity was prepared.

The Lucky Friday Mine at Mullan, Idaho, has been selected for the instrumented field studies on mechanical and geohydrologic responses to seismic activities. This mine is seismically active with 10 to 20 seismic events per year with magnitudes greater than Richter 2.0. Other features of the mine are: (1) it is well characterized geologically and structurally, (2) it has a macro-seismic monitoring system with 16 channels in place, (3) extensive rock-mechanics studies conducted in the past on the mine are readily available for use, and (4) mine technical personnel are cooperative and interested in this project. Installation of a field-instrumentation network to monitor the short- and long-term response of excavations to repeated seismic events as a result of seismic loading was completed. Data collection is underway. This instrumentation network is coupled with the mine-wide, macro-seismic network of the U.S. Bureau of Mines.

### **1.5. INTEGRATED WASTE PACKAGE EXPERIMENTS**

The objectives of the Integrated Waste Package Experiments (IWPE) Research Project are to critically evaluate the current material degradation data and to determine parameters affecting long-term container performance. Following extensive peer review and a thorough assessment of recently available information, a new program plan for this project (IWPE, Revision 2) was completed and sent to NRC staff for review on May 23, 1990. Revision 2 of the plan was approved with some required changes, which were made and submitted as Revision 3 on December 20, 1990. This report follows the task classifications in Revision 2 of the IWPE program plan. The program plan is organized according to six tasks: Task 1. Corrosion, Task 2. Stress Corrosion Cracking, Task 3. Materials Stability, Task 4. Microbiologically Influenced Corrosion, Task 5. Other Degradation Modes, and Task 6. General Reporting. The present report focuses on the accomplishments in Task 1, under the subtask of localized corrosion.

A critical review of literature on localized corrosion of candidate alloys is being conducted with specific focus on experimental approaches. A brief summary of the review is given in this report along with recommendations for future studies.

During this reporting period, the experimental work was concentrated initially in the characterization of the microstructures of the candidate alloys: 304L and 316L stainless steels,

alloy 825, CDA 102 (oxygen free copper), CDA-715 (Cu-30%Ni), and CDA 613 (Cu-7% Al). The CNWRA reference alloy, alloy C-22, was also examined. Surface analyses indicated that the Ni-based alloys, alloys 825 and C-22, as-received, exhibited significant chromium depletion on the surface. Tests in standard ASTM solutions resulted in higher corrosion of the depleted surfaces of these alloys compared to the surfaces without Cr depletion. This finding may be important in the eventual performance of container materials in the field.

The corrosion studies concentrated on the effects of environmental variables on the localized corrosion of alloy 825. A two-level, full factorial design was used to examine the main effects and interactions of chloride, sulfate, nitrate, fluoride, and temperature. These four anions, together with bicarbonate, maintained at a constant initial concentration in all the tests, are the predominant anionic species in J-13 well water, the reference water for the experimental work in the Yucca Mountain Project (YMP). Additionally, the effects of chloride concentration and temperature were examined in detail.

Cyclic, potentiodynamic polarization tests were used to determine the susceptibility of the alloy to localized corrosion. The electrochemical parameters measured in these tests (pitting potential, repassivation potential, and the difference between them) were not accurate indicators of the extent of localized corrosion observed visually. Therefore, visual observation of the specimens using a low magnification microscope, expressed in terms of a rating number, was combined with the electrochemical parameters in a localized corrosion index (LCI). This index was used to quantify the extent of localized corrosion and the effect of the environmental factors. Chloride and sulfate were found to be promoters of localized corrosion, whereas nitrate and fluoride acted as inhibitors. Temperature had no effect in the 60 to 95°C range. Localized corrosion in alloy 825 in simulated J-13 water at 95°C occurred with increasing probability starting at a chloride concentration of about 20 ppm. The electrochemical parameters indicating localized corrosion were independent of temperature up to a chloride concentration of about 1000 ppm. Only at very high chloride concentrations (10,000 ppm) was a pronounced effect of temperature on the pitting and repassivation potentials observed.

The effects of other environmental species, including nitrite, silicon (added as metasilicate), hydrogen peroxide, oxygen, and magnesium, were examined separately.

## **1.6. STOCHASTIC ANALYSIS OF FLOW AND TRANSPORT**

A quantitative characterization of large-scale flow and radionuclide transport through the heterogeneous unsaturated fractured rock of Yucca Mountain will be necessary to evaluate compliance with the siting criteria and performance objectives associated with the proposed Yucca Mountain HLW repository (10 CFR 60.112 and 60.113). Realistic modeling of the complex, heterogeneous flow and transport processes at Yucca Mountain will require incorporating the effects of relatively small-scale as well as large-scale space-time variability in modeling unsaturated flow and radionuclide transport. Examples of geologic features that can have significant effects on flow and transport are faults and fractures, finer fissures, and stratification leading to anisotropic behavior.

The specific objectives of the project are to: perform a review of the literature and assess available models and data relevant to the subject site, select a global approach to model large-scale flow and transport in unsaturated fractured rock, develop submodels for incorporation into the global model, and perform large-scale simulations and participate in the validation of flow/transport models for the Yucca Mountain repository. The project is divided in three tasks. The currently active task is Task 1: "Review, Analysis, and Development of a Modeling Approach," including Subtask 1, "Literature Review of Modeling Approaches"; Subtask 2, "Data Review and Assessment"; and Subtask 3, "Selection and Initial Development of a Global Modeling Approach." The effective starting date of the project was February 2, 1990. Work accomplished during this fiscal year is described in Section 6. The main accomplishments so far are as follows: development of a conceptual framework for large-scale flow modeling in the presence of heterogeneities (Section 6.3) progress in numerical analyses and algorithms towards efficient equation solvers (Section 6.4) analysis and visualization of anisotropic flow phenomena involving fully three-dimensional simulation datasets (Section 6.5) and initial development of auxiliary model of unsaturated hydrodynamic properties (Section 6.6). The complete results of literature review, initial data assessment, model selection, and first stages of model development will be presented in the final Technical Report for Task 1, due May 1, 1991.

## 1.7. GEOCHEMICAL ANALOGS

The Geochemical Analog Project is designed to provide knowledge of the state of the art in natural analog studies applied to contaminant transport and to conduct investigations of a specific site or sites. The project began in February 1990; Task 1 of the project, "Literature Review," has been completed, and Task 2, "Identification of Site and Development of Workplan," is presently underway. Objectives of Task 1 included: compilation and evaluation of research conducted on natural analogs relevant to contaminant transport at the candidate HLW repository at Yucca Mountain; review of literature on potential sites for a natural analog study to be undertaken; and evaluation of these sites with respect to the degree of relevance to understanding contaminant transport at Yucca Mountain, the possibility of constraining initial and boundary conditions, the feasibility of research at the sites, and the potential usefulness for unsaturated-zone contaminant-transport model validation. The Task 1 summary report entitled *Geochemical Natural Analogs Literature Review* (CNWRA 90-008) was submitted on October 30, 1990.

Task 1 resulted in the identification of a wide variety of material occurrences and processes which have been studied as natural analogs. Though many sites could be considered as comparable to some aspect of a HLW repository, it is necessary to select sites for analog study that most closely match the important characteristics of the system of interest while bearing in mind the limitations inherent in analog studies. These limitations include the incompleteness of the geologic record, difficulty of quantifying important effects, presence at a given site of only a subset of the processes which will occur in a repository, and existence at natural sites of materials which are only approximations of the materials to be used in a repository. Because of these limitations, it may be that a given model cannot be validated (in a strict sense) through the use of natural analogs. Nevertheless, natural analogs provide the only means of testing

models of long-term, large-scale processes for pertinence; of assessing the relative importance of various processes; and of determining the effects of the coupling of processes.

Other results of Task 1 include identification of sites to be evaluated for possible analog study relevant to the proposed HLW repository at Yucca Mountain, Nevada. The uranium ore deposits at Peña Blanca, Mexico, and McDermitt Caldera, Nevada-Oregon, and the archaeological site at Santorini, Greece, offer good analogs of processes that would be expected to occur in the geologic setting of the proposed repository at Yucca Mountain. All of these sites occur in the hydrologically unsaturated zone of siliceous tuff sequences and have climates similar to that of southern Nevada. The past and present oxidation of uraninite at Peña Blanca and at McDermitt constitutes an analog for the alteration of spent nuclear fuel. The processes of  $UO_2$  alteration and migration of uranium and other elements from sites of initial mineralization under unsaturated oxidizing conditions are analogous to those that would occur in the Yucca Mountain repository. Studies using buried artifacts at the Santorini archaeological site as analogs of contaminant sources would permit analyses of the rates and mechanisms of trace elemental migration in a geologic environment similar to that of Yucca Mountain.

## **1.8. PERFORMANCE ASSESSMENT RESEARCH**

### **1.8.1. Multi-phase Flow and Transport**

The objective of the multi-phase flow and transport task within the Performance Assessment (PA) Research Project is to enhance the PORFLO3 computer code to enable it to perform phase transfer and deal with a mixture of gases. The existing PORFLO3 is designed to perform flow and mass transport in variably saturated media. It treats the gas phase as passive except for capillary actions. The modified code will treat the gas phase as mobile. In addition, liquid-gas phase changes will be accommodated in the modified code.

Preparatory to modification, equations for multi-species flow and transport equations under nonisothermal conditions in fractured porous media are being reviewed. The review is limited to continuum equations where each phase is assumed, in an average sense, to be a continuum. Interaction between boundaries of different phases are treated through constitutive equations that relate phase saturations to capillary pressures and phase mobilities.

### **1.8.2. Evaluation of Sandia National Laboratory Technology**

Task 3 in the PA Research Project has its objective evaluation of the PA technology developed by the Sandia National Laboratory (SNL) for the NRC. Work performed under this task is discussed two parts. The first presents a review of the state-of-the-art of modeling groundwater flow in fractured geologic media; and the second a preliminary evaluation of the DCM3D finite-difference code developed by SNL. Five conceptual modeling approaches are presented; the equivalent continuous porous-medium model, the discrete fracture-network model, the discrete fracture-equilibrium model, the discrete fracture nonequilibrium model, and the double-porosity model implemented in the DCM3D code. In particular, the difficulty in

estimating the transfer coefficient term, which determines the rate of fluid transfer between fracture and matrix blocks, is highlighted. Advantages and disadvantages of each of these modeling concepts as well as the current state of the DCM3D's review process are also reported.

## 2. UNSATURATED MASS TRANSPORT (GEOCHEMISTRY)

*by Roberto T. Pabalan and William M. Murphy*

*Investigators: William M. Murphy (CNWRA), Roberto T. Pabalan (CNWRA), Paul Bertetti (CNWRA) and Ronald Martin (CNWRA)*

### 2.1. EXPERIMENTAL STUDIES by Roberto T. Pabalan

#### 2.1.1. Technical Objectives

A major geologic feature potentially affecting the suitability of Yucca Mountain, Nevada, as a repository site for HLWs is the presence of thick, laterally-extensive zones of zeolitic tuff. Because of their sorptive properties, zeolites could provide important geologic barriers to migration of radionuclides from the repository to the accessible environment. For example, sorption of elements such as cesium, strontium, and barium on Yucca Mountain tuffs correlates well with the amount of zeolites present in the rocks (Daniels et al., 1982; Meyer et al., 1987). The sorption of these elements onto zeolitized tuffs has been interpreted to be due to ion exchange processes (Meyer et al., 1987).

Published geochemical studies on zeolite minerals at Yucca Mountain indicate lateral and vertical variations in zeolite compositions. For instance, Broxton et al. (1986) show that on the western side of Yucca Mountain the zeolite mineral clinoptilolite is Na-K-bearing and becomes Na-rich with depth, while on the eastern side it is Ca-K-bearing and becomes Ca-rich with depth. Ion-exchange behavior of zeolites depends on several factors, including solid and aqueous phase compositions as well as aqueous solution concentrations (Barrer, 1978). Therefore, spatial variations in zeolite composition, and natural or repository-induced changes in groundwater chemistry, may result in variations in the effectiveness of zeolite minerals as retardation agents.

The thermodynamic stability of zeolites, hence their susceptibility to diagenetic alteration, also shows dependence on their composition. For example, thermodynamic calculations by Bowers and Burns (1990) indicate that in the Yucca Mountain environment, the thermodynamic stability field of clinoptilolite broadens with increasing atomic substitution of Ca for Na, and K for Ca. Calculations such as these, which are designed to predict the relative stability of zeolites under varying geochemical conditions, depend on thermodynamic data for a range of zeolite solid solution compositions.

To support NRC's HLW program, the CNWRA is conducting experimental studies on the thermodynamic and ion-exchange properties of zeolites under Task 3 of the Geochemistry Research Project. The studies conducted during the past year were designed to evaluate the use of thermodynamic models to describe and predict the solid solution and ion-exchange properties of the zeolite mineral clinoptilolite, and to provide a quantitative basis for understanding the effects of zeolites in the retardation of radionuclides in the Yucca Mountain system. Although isotherm data on ion exchange between aqueous solutions and clinoptilolite

are available for some binary systems (Ames, 1964a,b; Cheleshev et al., 1973; Semmens and Seyfarth, 1978; Townsend and Loizidou, 1984; Jama and Yucel, 1990), these experiments were conducted at a single concentration only. In addition, because adequate amounts of macroscopic crystals of clinoptilolite are not readily available, reported ion exchange studies have used clinoptilolite-rich zeolitized tuff specimens. These contain variable amounts of mineral impurities that complicate comparisons of results from different studies.

Ion-exchange experiments were conducted between well-characterized specimens of clinoptilolite and aqueous solutions containing alkali and alkaline earth cations. The experiments investigated the effects on the exchange equilibrium of changes in total concentration of the aqueous solution and the relative concentrations of the different exchangeable ions initially found in solution. The experimental data were interpreted using excess Gibbs energy models for the aqueous and zeolite phases to account for nonideality in the system. The data were also used to test model predictions of isotherm shapes and selectivities at other total solution concentrations based on a single measured isotherm.

### 2.1.2. Thermodynamics of Ion Exchange

The theoretical treatment of zeolite ion-exchange equilibria has been discussed in a number of publications (Helferrich, 1962; Barrer and Klinowski, 1974; Breck, 1976; Barrer, 1978; Dyer et al., 1981). For a binary exchange reaction involving ions  $A^{z_A+}$  and  $B^{z_B+}$  initially in solution and zeolite, respectively, the basic reaction may be written as



where  $z_A$  and  $z_B$  are the valences of the respective ions and  $L$  is defined as a portion of zeolite framework holding unit negative charge (Vanselow, 1932; Townsend, 1986). The thermodynamic equilibrium constant,  $K$ , is given by

$$K = (\bar{a}_A)^{z_B} (a_B)^{z_A} / (a_A)^{z_B} (\bar{a}_B)^{z_A} \quad (2)$$

where  $a$  represents activities of the aqueous species and  $\bar{a}$  represents activities of the zeolite components, which are defined here as homoionic A- or homoionic B-zeolites  $AL_{z_A}$  and  $BL_{z_B}$ , respectively. Equation (2) may be expanded to give

$$K = [(\bar{X}_A)^{z_B} (m_B)^{z_A} / (\bar{X}_B)^{z_A} (m_A)^{z_B}] [(f_A)^{z_B} / (f_B)^{z_A}] [(\gamma_B)^{z_A} / (\gamma_A)^{z_B}] \quad (3)$$

or

$$K = K_v [(f_A)^{z_B} / (f_B)^{z_A}]; \quad K_v = [(\bar{X}_A)^{z_B} (m_B)^{z_A} / (\bar{X}_B)^{z_A} (m_A)^{z_B}] [(\gamma_B)^{z_A} / (\gamma_A)^{z_B}] \quad (4)$$

where  $K_v$  is the Vanselow corrected selectivity coefficient (Vanselow, 1932; Townsend, 1986) and  $m_A$  and  $m_B$  are the molalities of  $A^{z_A+}$  and  $B^{z_B+}$  in the aqueous phase.  $\bar{X}_A$  and  $\bar{X}_B$  are cationic mole fractions in the zeolite phase and are defined by

$$\bar{X}_A = n_{ALz_A} / (n_{ALz_A} + n_{BLz_B}); \quad \bar{X}_B = n_{BLz_B} / (n_{ALz_A} + n_{BLz_B}) \quad (5)$$

where the  $n$  terms are the number of moles of the appropriate components.

A convenient standard state for each solid-phase component is the appropriate homoionic zeolite component in equilibrium with an infinitely dilute solution of the same cation (Gaines and Thomas, 1953; Sposito, 1981). Then the criterion for ideal behavior in the zeolite solid solution is that  $\bar{a}_i = \bar{X}_i$  for all  $\bar{X}_i$ . For the aqueous electrolyte solution, the usual standard state of a hypothetical one-molal solution referenced to infinite dilution is used.

The quantities  $\gamma_A$  and  $\gamma_B$  are single-ion activity coefficients for the aqueous species, and  $f_A$  and  $f_B$  are rational activity coefficients for the solid components. The ratio  $[(\gamma_B)^{z_A} / (\gamma_A)^{z_B}]$  is a nonideality correction for the aqueous solution phase, while  $[(f_A)^{z_B} / (f_B)^{z_A}]$  is a correction for nonideal behavior in the zeolite phase.

The evaluation of  $K$ ,  $f_A$ , and  $f_B$  from experimental data results from an appropriate integration of the Gibbs-Duhem relation (Argersinger et al., 1950). Together with Eqn. (4), the Gibbs-Duhem equation gives the following expressions for calculating the zeolite phase activity coefficients and the value of  $K$ :

$$\ln K = \int_0^1 \ln K_v d(\bar{E}_A), \quad (6)$$

$$\ln f_A^{z_B} = -\bar{E}_B \ln K_v + \int_{\bar{E}_A}^1 \ln K_v d(\bar{E}_A), \quad (7)$$

and

$$\ln f_B^{z_A} = \bar{E}_A \ln K_v - \int_0^{\bar{E}_A} \ln K_v d(\bar{E}_A) \quad (8)$$

where  $\bar{E}_A$  and  $\bar{E}_B$  are cationic equivalent mole fractions defined as

$$\bar{E}_A = z_A n_{ALz_A} / (z_A n_{ALz_A} + z_B n_{BLz_B}); \quad \bar{E}_B = z_B n_{BLz_B} / (z_A n_{ALz_A} + z_B n_{BLz_B}). \quad (9)$$

The standard free energy of the exchange reaction is given by

$$\Delta G^\circ = -RT \ln K; \quad (10)$$

and per equivalent of exchange, the standard free energy is

$$\Delta G^\ominus = \Delta G^\circ / (z_A z_B). \quad (11)$$

The above thermodynamic formulations are valid under conditions where imbibition of neutral electrolyte is negligible, which for zeolites is at solution concentrations <0.5 m (Barrer and Walker, 1964), and where the effects of water activity changes are insignificant.

Equations (6) through (8) enable calculation of the equilibrium constant and zeolite phase activity coefficients from isotherm data to which the aqueous activity coefficient corrections have been applied.  $K$ ,  $f_A$ , and  $f_B$  may be determined by graphical integration of the plot of  $\ln K$ , vs  $\bar{E}_A$ , or by integration of an analytical function fit to the data.

It is apparent from Eqns. (4) through (11) that equilibrium constants, Gibbs energies of exchange reactions, and zeolite phase activity coefficients evaluated from isotherm data depend on the values used for aqueous phase activity coefficients. Ion exchange studies by Fletcher and Townsend (1985) demonstrated the importance of correctly evaluating aqueous solution activity coefficients for accurate interpretation of exchange equilibria, particularly on studies with mixed background anions. In principle  $\gamma_i$ 's, which account for nonideal behavior in the aqueous solution, can be calculated from well-established electrolyte solution theories (Guggenheim, 1935; Glueckauf, 1949; Scatchard, 1968; Pitzer, 1973, 1979, 1987). In the examples given here, the Pitzer equations (Pitzer, 1973, 1979, 1987) were used to calculate activity coefficients of the aqueous species. This model has the advantage of having a large database of parameters at 25°C and above, and demonstrated success in applications to multicomponent systems over wide ranges of solution compositions and concentrations.

Nonideal behavior in the zeolite phase is reflected in the activity coefficients  $f_A$  and  $f_B$ . However, no activity-coefficient model has been generally accepted for exchangeable ions or solid solutions. Commonly used models are based on general equations for the molar-excess Gibbs energy ( $g^{ex}$ ) of mixtures (Grant and Sparks, 1989), which may be defined as

$$g^{ex}/RT = \sum_{i=1}^n \bar{X}_i \ln f_i \quad (12)$$

where  $R$  is the gas constant and  $T$  is temperature (K). Values of  $g^{ex}/RT$  can be calculated from isotherm data through Eqns. (7) and (8).

A thermodynamic model that has been found useful for both solid and liquid solutions is the Margules formulation. For a two-component system the Margules model [also referred to as subregular solution model (Ganguly and Saxena, 1987)] describes  $g^{ex}$  as

$$g^{ex}/RT = \bar{X}_A \bar{X}_B [\bar{X}_B W_A + \bar{X}_A W_B] \quad (13)$$

where  $W_A$  and  $W_B$  are empirical parameters which are functions only of temperature and pressure. These parameters can be derived by fitting Eqn. (13) to  $g^{ex}$  values derived from isotherm data using Eqns. (7), (8), and (12).

Representation of solid-phase nonideality in terms of a  $g^{ex}$  model such as Eqn. (13) makes convenient the calculation of zeolite solid solution and ion-exchange properties over the

whole range of zeolite composition. Using the Gibbs-Duhem equation and Eqns. (12) and (13),  $\ln f_A$  and  $\ln f_B$  can be expressed in terms of  $W_A$  and  $W_B$  by

$$\ln f_A = \bar{X}_B^2[W_A + 2\bar{X}_A(W_B - W_A)]; \quad \ln f_B = \bar{X}_A^2[W_B + 2\bar{X}_B(W_A - W_B)]. \quad (14)$$

Similar expressions can be derived for systems with three or more components (Ganguly and Saxena, 1987; Grant and Sparks, 1989). The Vanselow selectivity coefficient,  $K_v$ , for the reaction represented by Eqn. (1) can then be calculated from

$$\ln K_v = \ln K + z_A \bar{X}_A^2[W_B + 2\bar{X}_B(W_A - W_B)] - z_B \bar{X}_B^2[W_A + 2\bar{X}_A(W_B - W_A)]. \quad (15)$$

$K$  in Eqn. (15) can be derived either from Eqn. (6) or from nonlinear regression of Eqn. (15) to isotherm data (Grant and Sparks, 1989). If the zeolite phase behaves ideally,  $f_A = f_B = 1$  and  $g^{\alpha}/RT$  is zero for all values of  $\bar{X}_A$ , and  $K = K_v$ .

It is possible to predict the exchange equilibria at constant temperature over a range of phase compositions and total solution concentrations using Eqns. (4) and (15) (Barrer and Klinowski, 1974; Townsend, 1986). These predictions rest on the assumption that the ratio of activity coefficients for the zeolite components varies little as the total concentration of the aqueous phase changes. It is also assumed that the effects of water-activity changes and salt imbibition are negligible. If these are true, then the Vanselow selectivity coefficient,  $K_v$ , will be invariant with changes in total solution concentration. Thus isotherm shapes and selectivities for a particular exchange reaction can be predicted for variable aqueous solution concentrations and zeolite compositions based on a single experimentally determined exchange isotherm (Barrer and Klinowski, 1974; Townsend et al., 1984; Townsend, 1986). The only requirement is that aqueous solution activity coefficients can be calculated by some thermodynamic means.

To evaluate the application of the above thermodynamic models to the zeolite mineral clinoptilolite, ion-exchange experiments were conducted as discussed below.

### 2.1.3. Experimental

#### 2.1.3.1. Characterization of Clinoptilolite Samples

Published experimental data on ion-exchange between clinoptilolite and aqueous solutions show that ion-exchange behavior and the resultant thermodynamic quantities derived from them are sensitive to the nature of the materials used in the experiments (Pabalan and Murphy, 1990). Most ion-exchange studies have used specimens of zeolitized volcanic tuff because sufficient amounts of macroscopic crystals of clinoptilolite are not readily available. These tuff samples commonly contain mineral impurities such as quartz, feldspar, iron oxides, clays, and volcanic glass. The detailed mineralogy of samples from different localities are different, and samples from different outcrops within the same locality may show variations in mineralogical composition. Because mineralogical and chemical composition can influence the results of ion-exchange and phase-equilibrium studies, the clinoptilolite materials to be used for the experiments must be characterized. Mineralogic characterization of the

samples is necessary to: (1) identify the best specimens to use, (2) identify procedures that can be used to eliminate mineral impurities, and (3) aid in the interpretation of experimental results.

In connection with the Center's experimental studies on clinoptilolite, specimens of zeolitized tuff from the following localities were obtained: (1) Hector, California; (2) Barstow, California; (3) Death Valley Junction, California; (4) Castle Creek, Idaho; (5) Buckhorn, Grant County, New Mexico; and (6) Tilden, Texas. The samples from the first four localities were obtained from Minerals Research (P.O. Box 591, Clarkson, New York 14430), and the samples from the latter two localities were obtained from Zeotech Corporation (3224 Candelaria N.E., Albuquerque, New Mexico 87107).

Characterization of these samples was done using X-ray diffraction (XRD) analysis, petrographic (thin section) analysis, and scanning electron microscopy coupled with energy-dispersive X-ray spectrometry. The mineralogy of the bulk samples was identified by petrographic analysis of thin sections and by XRD analysis of finely ground (-325 mesh) material. The X-ray diffraction pattern and detailed petrographic description for each tuff sample were reported previously (Pabalan and Murphy, 1990). The analyses indicated that the samples contain mostly well-crystallized clinoptilolite, which has replaced the glass in the poorly welded tuffs. The clinoptilolite, however, is very fine grained (micron-size); and well-formed crystals occur only in vugs or in voids previously occupied by glass shards. In addition to clinoptilolite, other phases identified in the samples were mordenite, erionite, quartz, smectite, illite, plagioclase, K-feldspar, gypsum, dolomite, calcite, halite, and unaltered volcanic glass.

The samples from Death Valley Junction, California (sample name CDV) contained the least impurities, and were therefore selected as the materials for the ion exchange experiments. The typical morphology of clinoptilolite in the Death Valley Junction samples is shown in the scanning electron micrographs of Figure 2-1. The more distinctive 'coffin-shaped' morphology is exhibited by clinoptilolite crystals in the samples from Hector, California (Pabalan and Murphy, 1990). The XRD pattern of CDV is given in Figure 2-2(a). Table 2-1 gives the petrographic description of the CDV sample, and Table 2-2 gives its approximate mineralogic composition.

The mineral clinoptilolite is isostructural with heulandite, differing principally in the cation composition and Al/Si ratio (Gottardi and Galli, 1985). Clinoptilolite is the name given to the alkali- and Si-rich end-member, and heulandite is the alkaline earth- and Al-rich variety. Clinoptilolite is substantially more stable with respect to short-term heating in the laboratory than is heulandite. Indeed, Mumpton (1960) suggested differentiation of the two on the basis of an overnight heating test at 450°C: clinoptilolite retains its crystalline structure, whereas heulandite becomes X-ray amorphous. Heating tests at 450°C were performed on the zeolitized tuff samples that were characterized previously. The XRD pattern of heat-treated Death Valley Junction sample is shown on Figure 2-2(b). For comparison purposes, the XRD patterns of heulandite (source locality: Poona, Maharashtra State, India) before and after heating are shown on Figure 2-3(a) and 2-3(b), respectively. The clinoptilolite XRD pattern changed very little after heating, while heulandite became X-ray amorphous.

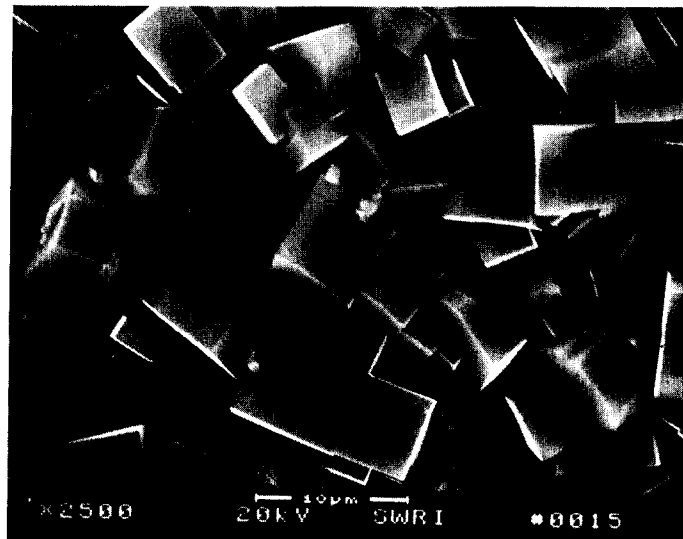
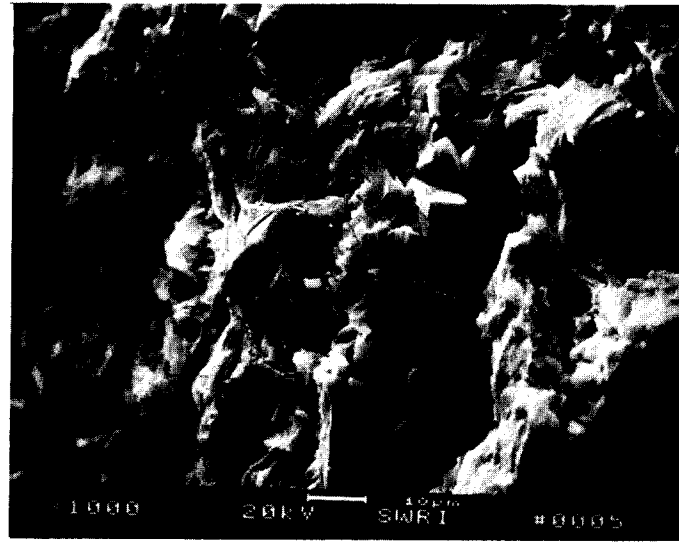


Figure 2-1. Scanning electron microscope images of clinoptilolite from Death Valley Junction, California

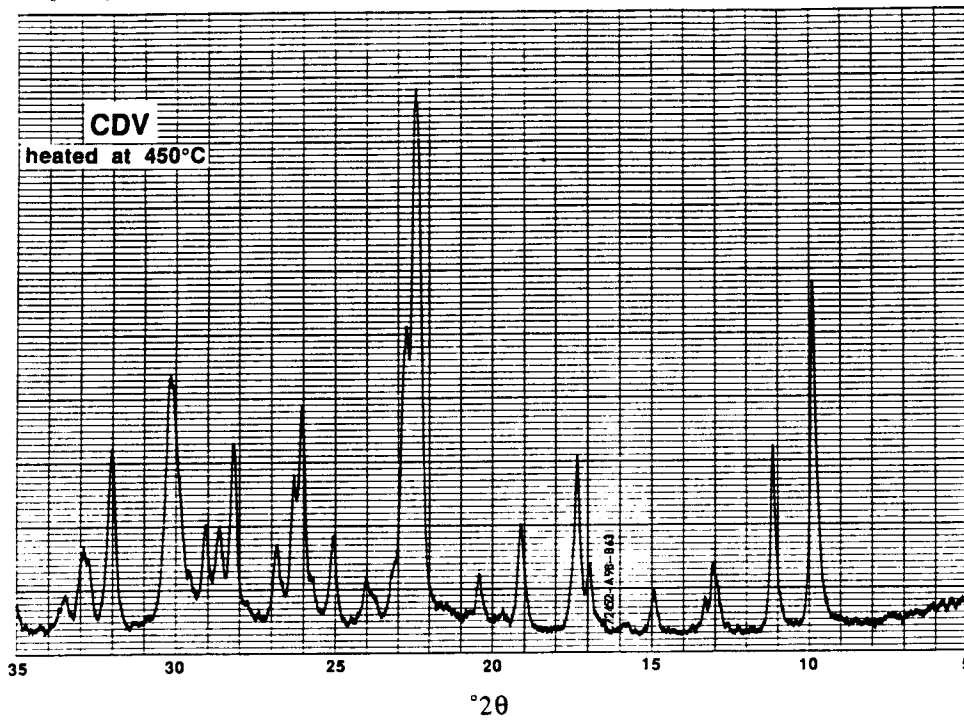
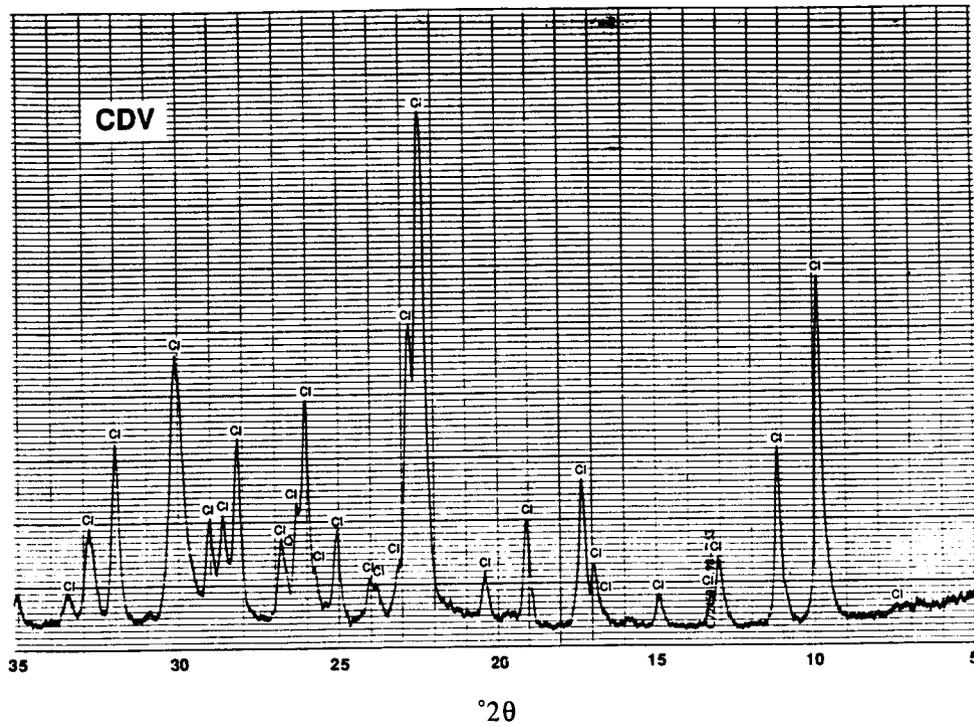


Figure 2-2. X-ray diffraction pattern of clinoptilolite-rich tuff from Death Valley Junction, California: (a) before and (b) after heating overnight at 450°C. Cl=clinoptilolite; Q=quartz.

**Table 2-1. PETROGRAPHIC ANALYSIS OF SAMPLE CDV**

**LOCALITY:** Death Valley Junction, California

**TYPE OF ROCK:** Quartz Latite/Dacite Tuff

**MATRIX:** 95%

Zeolitized glass shards (50-90%)

Non descript opaque (5-10%)

Many shards of formerly vesicular glass

Brownish opaque mineral around shards

**GRAINS:** 5%

**Phenocrysts:**

Quartz and feldspars (2-5%)

Biotite (1-2%)

Clinopyroxene (trace)

**Lithoclasts:**

A few glassy lithic fragments with plagioclase microlites

Some detrital iron-titanium oxide

**TEXTURE:**

Poorly welded, no compaction or deformation of shards.

Abundant shards, bordered with a highly birefringent mineral (possibly sericite), and rimmed and replaced by zeolites.

Relatively large-grained shards and phenocrysts, many around 500 microns or larger.

**ALTERATION/MINERALIZATION:**

Many of the plagioclase phenocrysts are altered to sericite.

Many of relict shards appear to be rimmed; it appears that the shards were dissolved out and then infilled with zeolites. Many of the shard borders are outlined with a high birefringent mineral.

**DEPOSITIONAL ORIGIN:** Fallout tuff or possibly surge deposit

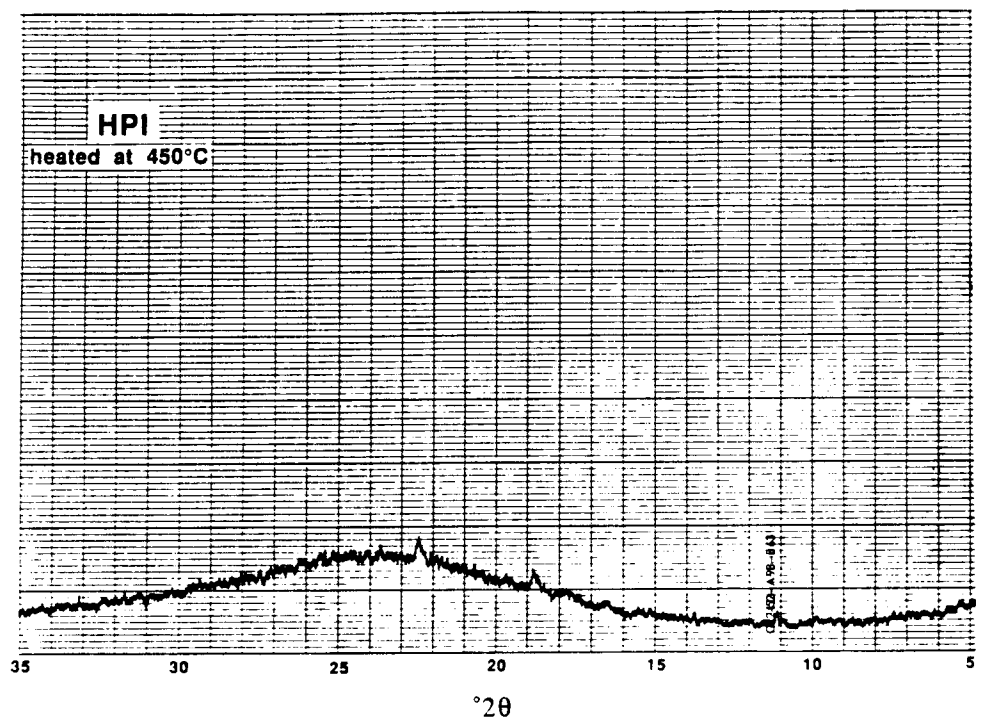
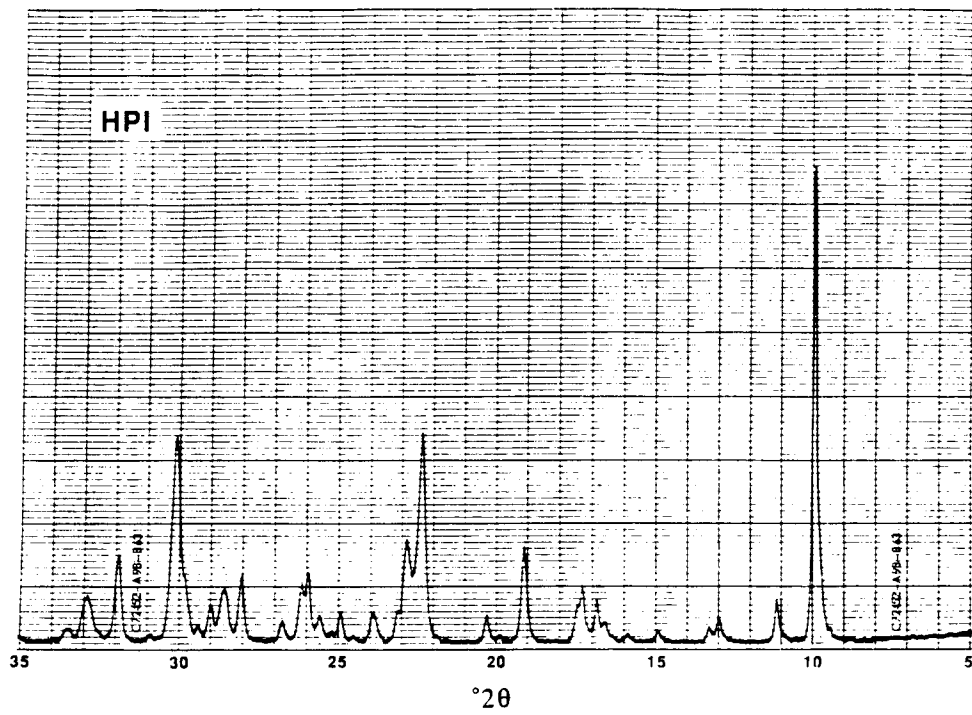


Figure 2-3. X-ray diffraction pattern of heulandite from Poona, Maharashtra State, India: (a) before and (b) after heating overnight at 450°C

### 2.1.3.2. *Preparation and Chemical Analysis of Clinoptilolite Material*

Powdered CDV material was prepared by first using a rock hammer to break the as-received samples (covered with a canvas bag) into pieces less than one-third of an inch in diameter. These small pieces were then ground in a Spex #8000 Mixer/Mill using a tungsten carbide vial. The CDV powders were sieved into five size ranges using a Ro-Tap sieve shaker and 8-inch-diameter stainless-steel sieves. The ranges were: (1) 35-100 mesh (500-150 microns), (2) 100-200 mesh (150-75 microns), (3) 200-325 mesh (75-45 microns), (4) 325-450 mesh (45-32 microns), and (5) <450 mesh (<32 microns). Sieving was repeated several times to minimize the retention of clinoptilolite grains of a particular size with grains in the larger size range.

Using the 100-200 mesh-size fraction, mineral impurities were separated from clinoptilolite by density separation using heavy liquid in 250-ml separatory funnels. The above size fraction was found to provide good separation between clinoptilolite and other solid phases. The heavy liquid was prepared by mixing tetrabromoethane (density = 2.9672 at 20°C) and NN-dimethyl formamide (density = 0.93445 at 20°C) (Hutchison, 1974). The separation was performed twice for each batch of clinoptilolite powder, initially using a heavy-liquid density of about 2.14 g/ml, and later using a density of about 2.08 g/ml. The tetrabromoethane and NN-dimethyl formamide were washed several times from the clinoptilolite with acetone. The tetrabromoethane was also recovered using liquid-liquid extraction for later reuse. To remove the acetone, the clinoptilolite powders were washed several times with deionized water in an ultrasonic bath and also soaked overnight in deionized water. The clinoptilolite was then dried for several hours at 80°C in a convection oven, and equilibrated with water vapor over a saturated NaCl solution inside a desiccator. When not being used in the experiments, the clinoptilolite was kept in the desiccator over saturated NaCl solution to maintain a constant (and equilibrium) water content in the crystal structure.

To check the efficiency of mineral separation using heavy liquids, the purified clinoptilolite (sample name CDV-P) and the heavy mineral separates (sample CDV-HS) were analyzed by XRD and optical microscopy. The XRD patterns of CDV-P and CDV-HS are shown in Figures 2-4(a) and 2-4(b), respectively. The approximate weight percent of the minerals present in the samples are given in Table 2-2. These results indicate that clinoptilolite is separated well from other minerals in the original material. Optical microscopy indicates that goethite remaining in CDV-P is intimately intergrown with clinoptilolite, and was not effectively removed by density separation.

Near homoionic Na-clinoptilolite was generated by treating 30 g of the CDV-P powder with 350-ml of 3-m sodium chloride solution at 70°C in a shaker water bath for about two weeks. The 3-m sodium chloride solution was replaced every two days, and the change in clinoptilolite composition to the more Na-rich variety was followed by taking aliquots of the solid being treated and analyzing their compositions by inductively coupled plasma-emission spectrometry (ICP) subsequent to lithium metaborate fusion and dissolution in an HCl/HNO<sub>3</sub> matrix. The samples thus treated were washed thoroughly with deionized water at

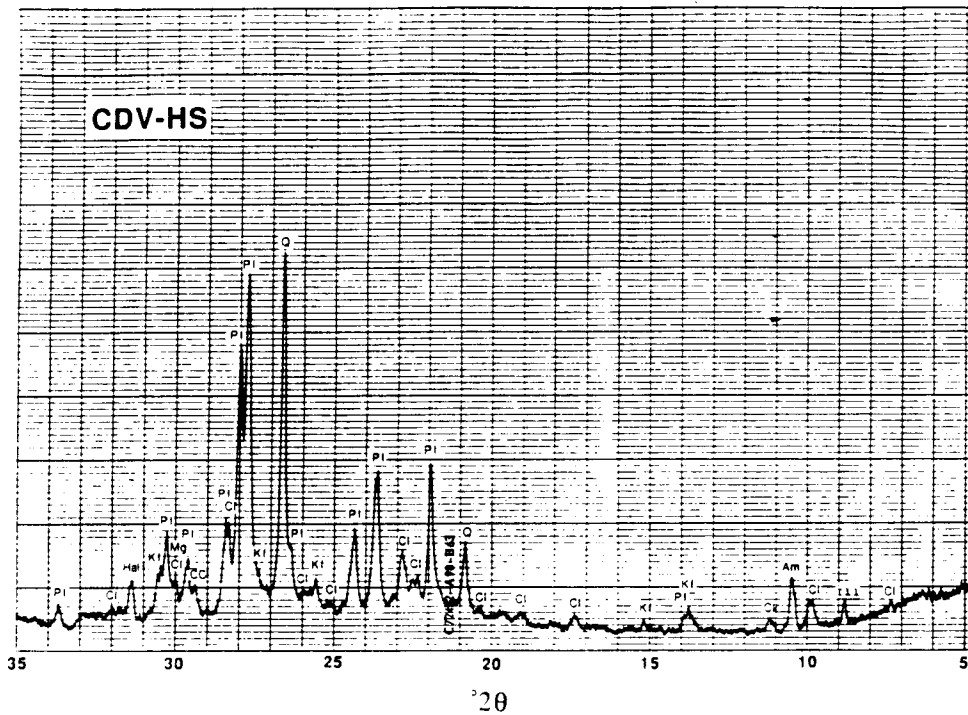
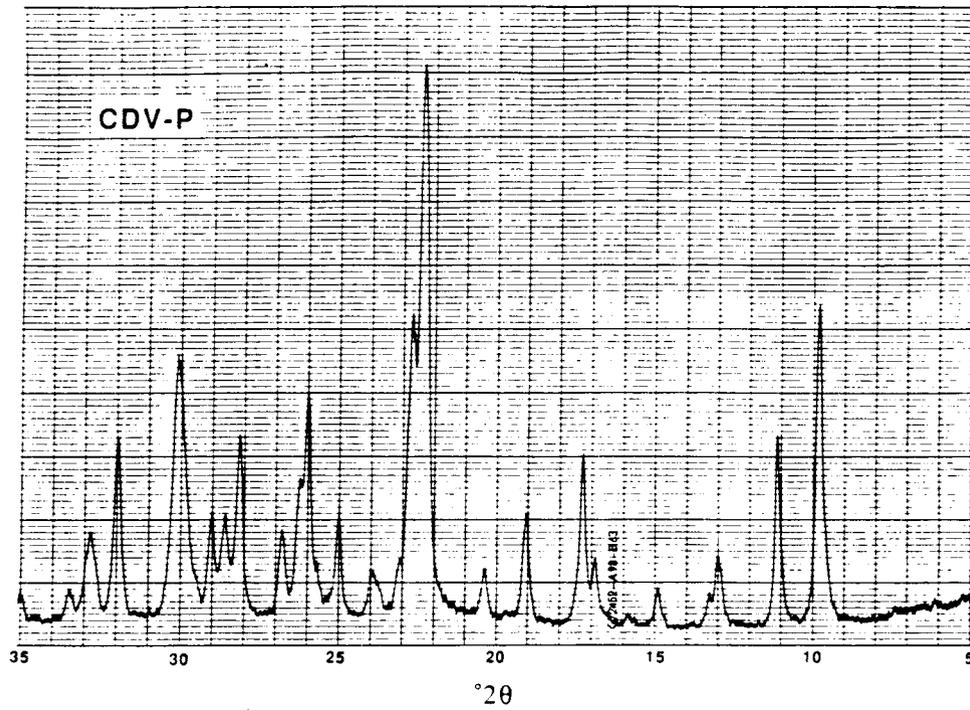


Figure 2-4. X-ray diffraction pattern of clinoptilolite-rich tuff from Death Valley Junction, California, after heavy-liquid deparation: (a) purified material and (b) heavy-mineral separate. Cl=clinoptilolite; Pl=plagioclase; CC=calcite; Q=quartz; Kf=K-feldspar; Ill=illite; Hal=halite; and Am=amphibole.

Table 2-2. MINERALOGIC COMPOSITION OF CLINOPTILOLITE SAMPLES

ZEOLITIZED TUFFS	MINERALOGY, APPROXIMATE WT. %													
	QUARTZ	PLAGIOCLASE	K-FELDSPAR	MAGNETITE	GOETHITE	CALCITE	HALITE	AMPHIBOLE	ILLITE (10A MICA)	SWECITE	CLINOPTILOTE	MORDENITE	AMORPHOUS/ BELOW DETECTION	
BULK XRD SAMPLE NO.														
CDV	1	1	1		TR			TR	TR	2	86	TR?	6	Based on XRD and petrographic analyses
CDV-P					2						98		-	Based on XRD and optical microscopy
CDV-HS	6	30	6	12	4	6	11?	2	3		20		-	Based on XRD only
TR = TRACE    ? = TENTATIVE IDENTIFICATION														

70°C to eliminate excess NaCl, dried in an oven at 80°C, and then equilibrated with water vapor over saturated sodium chloride solution at 25°C in a dessicator until constant weight was attained. This last step is necessary to provide a constant moisture content prior to chemical analysis and exchange experiments.

The compositions of the original and the near homoionic Na-form clinoptilolite samples were also determined by ICP. Analysis for Fe<sup>2+</sup> in these samples was performed by titration, and the water content of the sample was determined by measuring its weight before and after heating at 900°C for two hours. Results of the chemical analyses of the original material and the Na-exchanged clinoptilolite are given in Table 2-3.

The cation exchange capacity (CEC) of the Na-exchanged material used in the experiments was estimated to be 0.00217 equivalents/gram of zeolite, based on the aluminum content as found by chemical analysis. The sum of the equivalents of the exchangeable ions, that is, sodium, potassium, calcium, and magnesium (0.00227 equivs./gm), closely approximates the CEC. This suggests the possibility that magnesium and potassium in the Na-form remained as unexchanged cations in the clinoptilolite; however, their presence in residual solid impurities cannot be discounted.

### 2.1.3.3. *Ion Exchange Kinetic Experiments*

The rate of ion exchange between clinoptilolite and aqueous solutions was studied using the Na-enriched clinoptilolite prepared above. The aqueous solutions consisted of KCl, CaCl<sub>2</sub>, KCl+NaCl, and CaCl<sub>2</sub>+NaCl solutions, which were prepared from ACS grade reagents and deionized water (Barnstead Nanopure II system). The experiments were conducted as follows: 50 ml of the aqueous solution of known composition were added to weighed amounts (0.2-2.0 g) of Na-enriched clinoptilolite in 60-ml polyethylene bottles. The bottles were thermostatted at 25°C, and kept under agitation using a shaker water bath (Fisher Versabath 236) set at 80 rpm. Aliquots of the aqueous solutions were taken on a periodic basis for chemical

**Table 2-3. CLINOPTILOLITE CHEMICAL ANALYSES**

Component	Initial (Wt%)	Na-form (Wt%)
SiO <sub>2</sub>	67.51	68.59
Al <sub>2</sub> O <sub>3</sub>	11.01	11.07
TiO <sub>2</sub>	0.10	0.07
Fe <sub>2</sub> O <sub>3</sub>	0.83	0.52
FeO	0.00	0.00
MnO	0.03	0.01
MgO	0.35	0.22
CaO	0.70	0.00
Na <sub>2</sub> O	3.41	6.46
K <sub>2</sub> O	3.46	0.38
P <sub>2</sub> O <sub>5</sub>	0.01	0.005
H <sub>2</sub> O	14.50	14.35
<b>TOTAL</b>	<b>101.91</b>	<b>101.68</b>

analysis for potassium, calcium, and/or sodium using ICP spectrometry or using ion-selective electrodes (ISE). The amounts of solids used in the experiments and of aliquot volumes and dilution factors used in the sampling procedure were adjusted so that expected changes in aqueous solution concentrations could be resolved by ICP and ISE analyses. Samples of reference solutions were also taken to determine the actual initial concentration of the solutions, to monitor their stability with time, and to check the reproducibility of the chemical analyses. Samples for ICP analysis consisted of 2- or 5-ml aliquots, which were diluted to 50 or 100 ml with a 10 percent HCl + 2 percent HNO<sub>3</sub> matrix. ISE samples consisted of 1-ml aliquots, which were diluted to 10 ml with deionized water. ISE analyses utilized Orion ion-selective electrodes and an Orion EA 920 pH/mV/ISE/°C meter.

The experimental results are summarized in Figures 2-5 through 2-8. In these figures, the first column of symbols represents solution concentrations determined by ISE analysis; and the second column of symbols represents concentrations determined by ICP analysis. In general, the concentrations determined by the two methods agree within analytical uncertainty ( $\pm 10$  percent). Figures 2-5 and 2-7 show the decrease in concentrations of K<sup>+</sup> and Ca<sup>2+</sup> in solution, respectively, as a function of time. Figures 2-6 and 2-8 show the increase in Na<sup>+</sup> concentration in the aqueous phase with increasing time, as K<sup>+</sup> or Ca<sup>2+</sup> initially in solution exchanges for Na<sup>+</sup> initially in the zeolite phase.

Charge balance constraints for a binary-exchange reaction require that the number of equivalents of K<sup>+</sup> or Ca<sup>2+</sup> removed from solution equals the number of equivalents of Na<sup>+</sup> released from the zeolite. Table 2-4 compares the equivalents of K<sup>+</sup> or Ca<sup>2+</sup> removed from the aqueous phase with those of Na<sup>+</sup> released into solution. The value shown in Table 2-4 indicate that, except in two cases, the amount of Na<sup>+</sup> released into solution balances the amount of K<sup>+</sup> or Ca<sup>2+</sup> taken up by the solid phase within analytical uncertainty. The cause of the disagreement in two of the systems studied are not certain at this point, but may be a result of matrix effects in the analytical methods used. In general, it appears that the ion exchange is essentially binary and that H<sup>+</sup> in the aqueous phase does not significantly participate in the exchange process. The amount of exchangeable ions other than Na<sup>+</sup> that may have been present in the Na-enriched clinoptilolite or in mineral impurities appears to be negligible. The results of the preceding kinetic experiments indicate that ion-exchange equilibrium for the systems studied is closely approached in about two days. The results provide constraints on the minimum amount of time required for conducting the ion-exchange isotherm experiments. A minimum of four days was used in the isotherm experiments described below.

#### 2.1.3.4. *Ion-Exchange Isotherms*

Ion-exchange experiments for the binary systems K<sup>+</sup>-Na<sup>+</sup> and Ca<sup>2+</sup>-Na<sup>+</sup> were conducted at 25°C and at total solution concentrations of 0.05 and 0.50 N (equivalents/liter). The points on the isotherm were obtained by equilibrating accurately weighed amounts of the near homoionic Na-form of the clinoptilolite with a series of solutions containing the two competing cations in different concentration ratios, but at a constant normality. The 0.50 N aqueous mixtures were prepared by weight from reagent-grade chloride salts of the

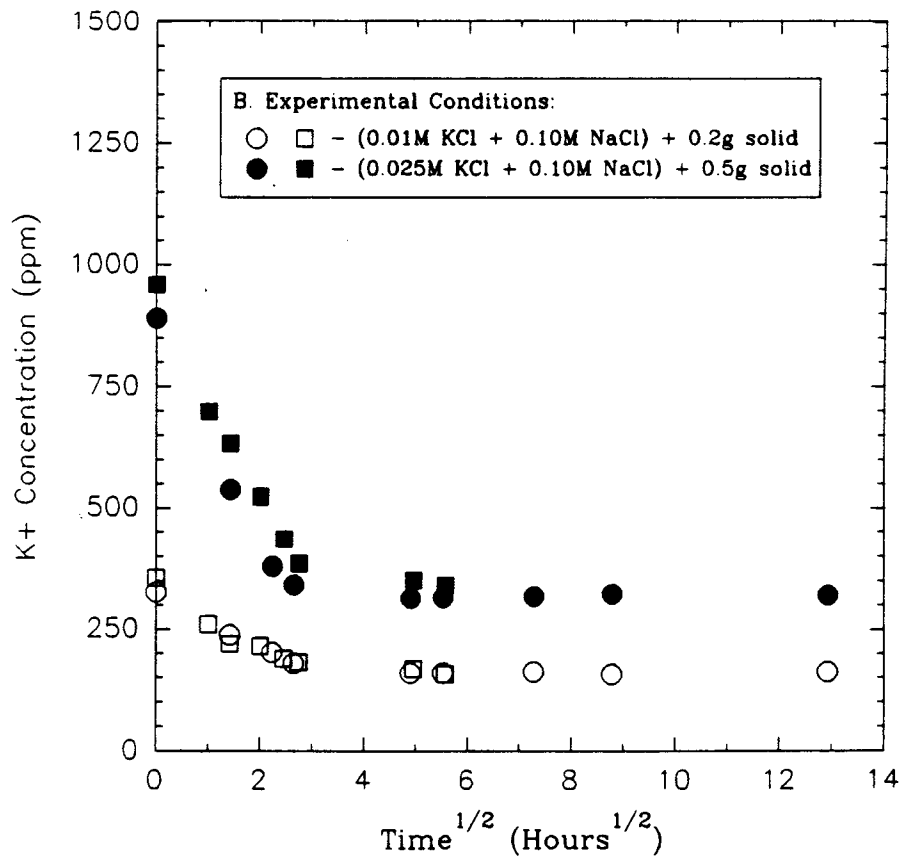
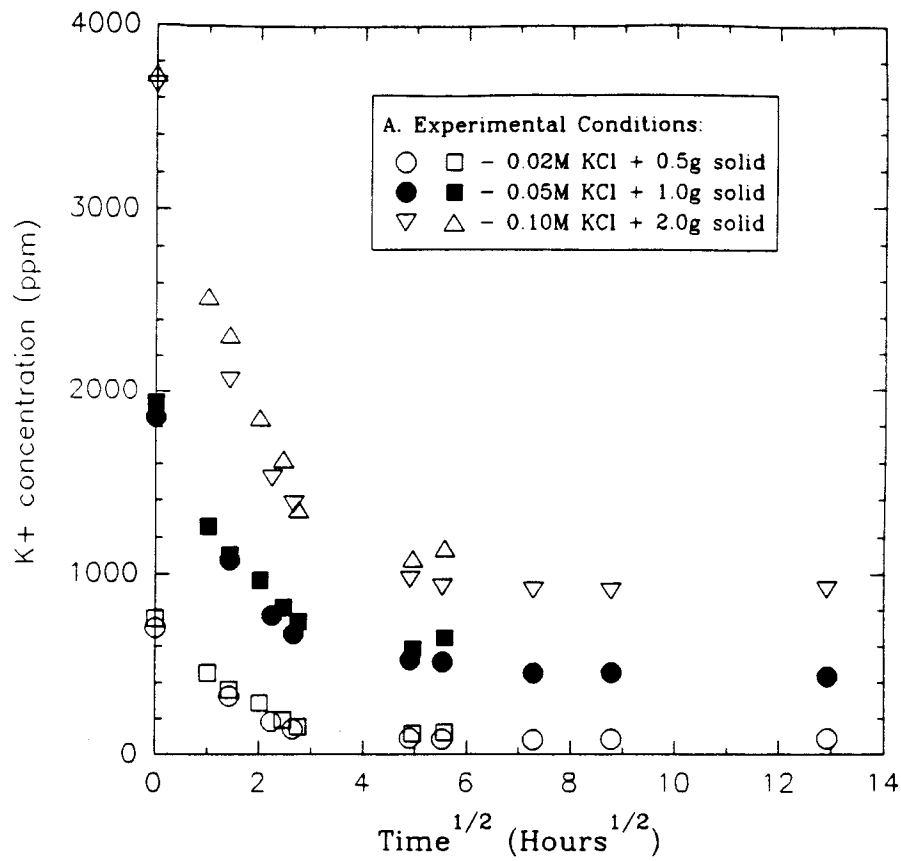


**Figure 2-5. Aqueous concentration as a function of time of K<sup>+</sup> in the KCl-NaCl solution equilibrating with initially homoionic Na-Clinoptilite**

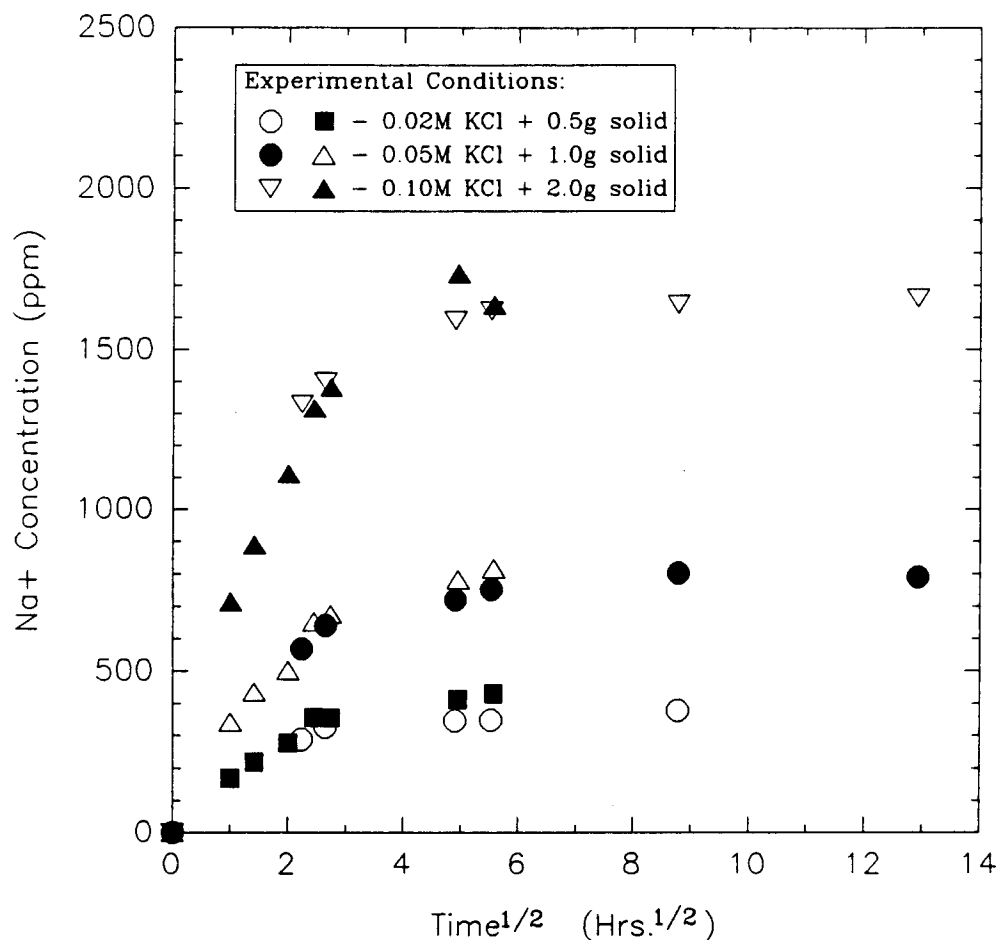


**Figure 2-6. Aqueous concentration as a function of time of Na<sup>+</sup> in the KCl-NaCl solution equilibrating with initially homoionic Na-Clinoptilolite.**

respective locations. The 0.05 N solutions were prepared by a ten-factor dilution of the 0.50 N mixtures. Weights of the clinoptilolite powder used in the experiments ranged from 0.05 to 1.0 gram, and solution volumes ranged from 5 to 100 ml. The ratios of zeolite-weight/solution-volume used in the experiments were estimated to yield significant differences in the initial and final concentrations of the cations in solution and a complete range of equilibrium exchange compositions. The clinoptilolite + solution mixtures were contained in 15-ml to 125-ml screw-cap plastic bottles. These were kept agitated in a shaker water bath thermostatted at

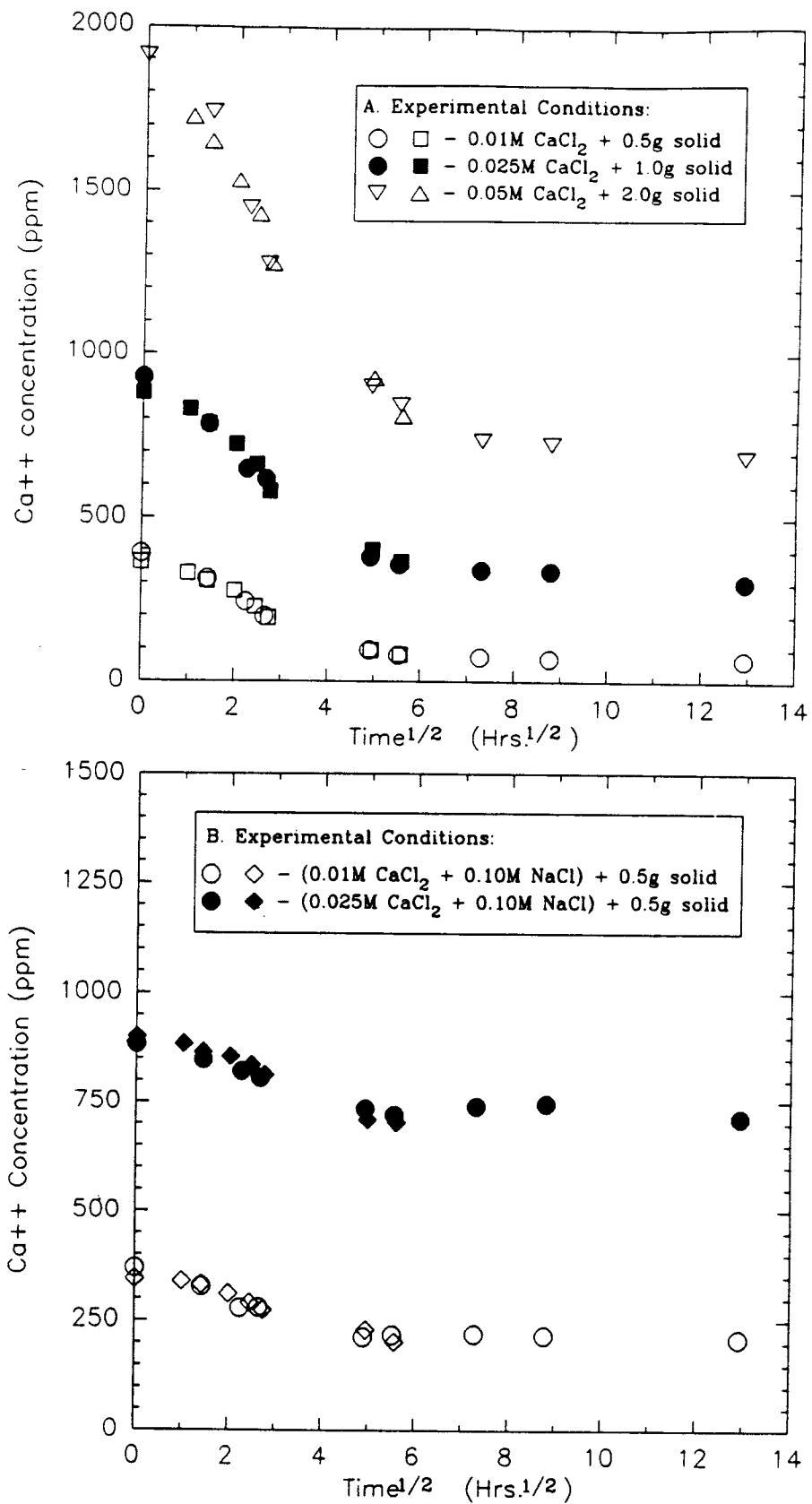


**Figure 2-7. Aqueous concentration as a function of time of Ca<sup>2+</sup> in the CaCl<sub>2</sub>-NaCl solution equilibrating with initially homoionic Na-Clinoptilolite**

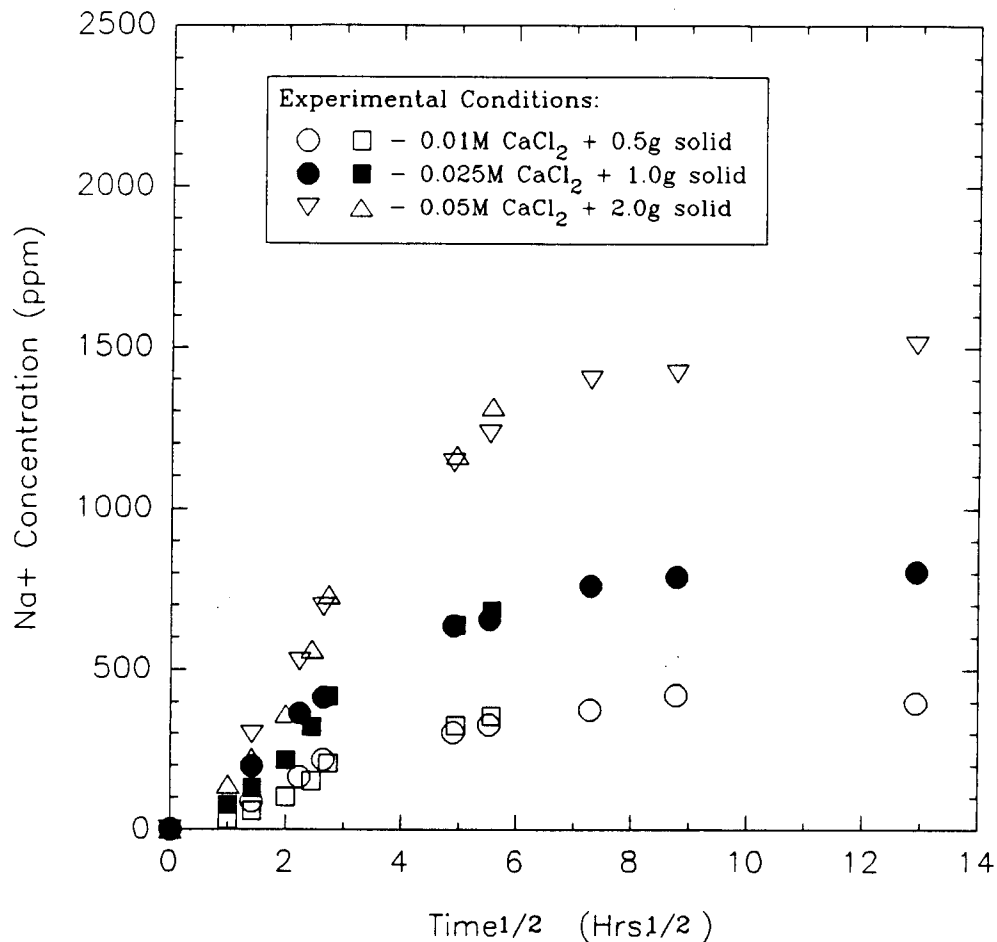


**Figure 2-8. Aqueous concentration as a function of time of Na<sup>+</sup> in the CaCl<sub>2</sub>-NaCl solution equilibrating with initially homoionic Na-Clinoptilolite**

25.0 ± 0.1°C for at least four days.

After equilibrium was established, aliquots of the aqueous solutions were taken and analyzed for the cations K<sup>+</sup> or Ca<sup>2+</sup>. For some solutions, Na<sup>+</sup> was also analyzed to check the stoichiometry of the exchange reactions by charge balance constraints. The solutions were analyzed using Orion ion-selective electrodes (ISE) and an Orion EA 920 pH/mV/ISE/°C meter. The exchange levels were calculated from the initial and final concentrations of the cation of interest, and from the weight of clinoptilolite powder and volume of solution used in the exchange experiments.

**Table 2-4. COMPARISON OF K<sup>+</sup> OR Ca<sup>2+</sup> EQUIVALENTS REMOVED FROM SOLUTION WITH NA<sup>+</sup> RELEASED INTO SOLUTION**

Initial Solution Composition	Equiv. K <sup>+</sup> removed	Equiv. Ca <sup>2+</sup> removed	Equiv. Na <sup>+</sup> released
0.02M KCl	0.0157		0.0156
0.05M KCl	0.036		0.034
0.10M KCl	0.070		0.071
0.01M KCl + 0.10M NaCl	0.0042		0.0085
0.025M KCl + 0.10M NaCl	0.015		0.016
0.01M CaCl <sub>2</sub>		0.016	0.017
0.025M CaCl <sub>2</sub>		0.030	0.034
0.05M CaCl <sub>2</sub>		0.079	0.072
0.01M CaCl <sub>2</sub> + 0.10M NaCl		0.008	0.012
0.025M CaCl <sub>2</sub> + 0.10M NaCl		0.011	0.012

#### 2.1.4. Results and Discussion

The ion-exchange data for the binary systems K<sup>+</sup>-Na<sup>+</sup> and Ca<sup>2+</sup>-Na<sup>+</sup> are plotted in Figures 2-9 and 2-10, respectively, in terms of the equivalent mole fraction of one cation in the solution phase versus the equivalent mole fraction of the same cation in the zeolite phase. Experimental data at a total solution concentration of 0.05 N are shown in Figures 2-9(a) and 2-10(a), while data at 0.50 N are shown in Figures 2-9(b) and 2-10(b). The results indicate a strong dependence of isotherm shape and zeolite selectivity on total solution concentration for the system Ca<sup>2+</sup>-Na<sup>+</sup>, which involves an exchange between monovalent and divalent cations. On the other hand, this dependence is small for K<sup>+</sup>-Na<sup>+</sup>, which involves both monovalent cations. This dependence results from the law of mass action for isotherms plotted in terms of equivalent mole fractions and is discussed in detail by Barrer and Klinowski (1974). Figures 2-10(a) and 2-10(b) illustrate that for more dilute solutions, clinoptilolite exhibits a higher selectivity for the cation of higher charge. This behavior, referred to as "concentration-valency effect," causes isotherms that become more rectangular and selective to the ion of higher valence with increasing dilution for exchange reactions where  $z_A \neq z_B$  (Barrer and Klinowski, 1974).

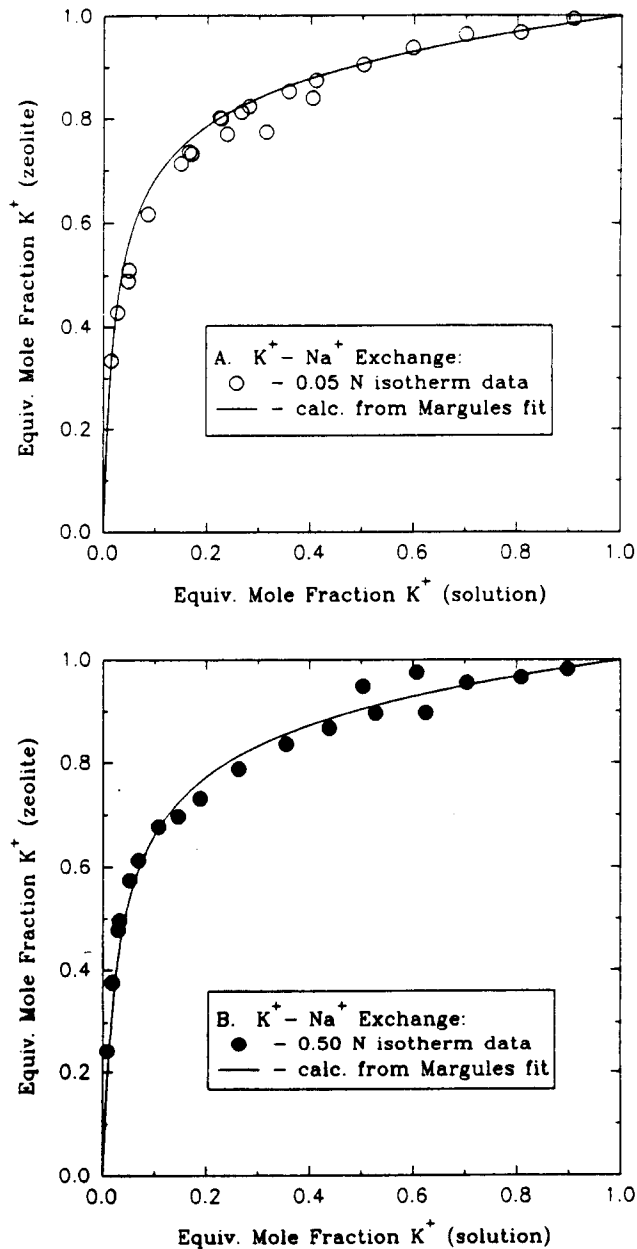
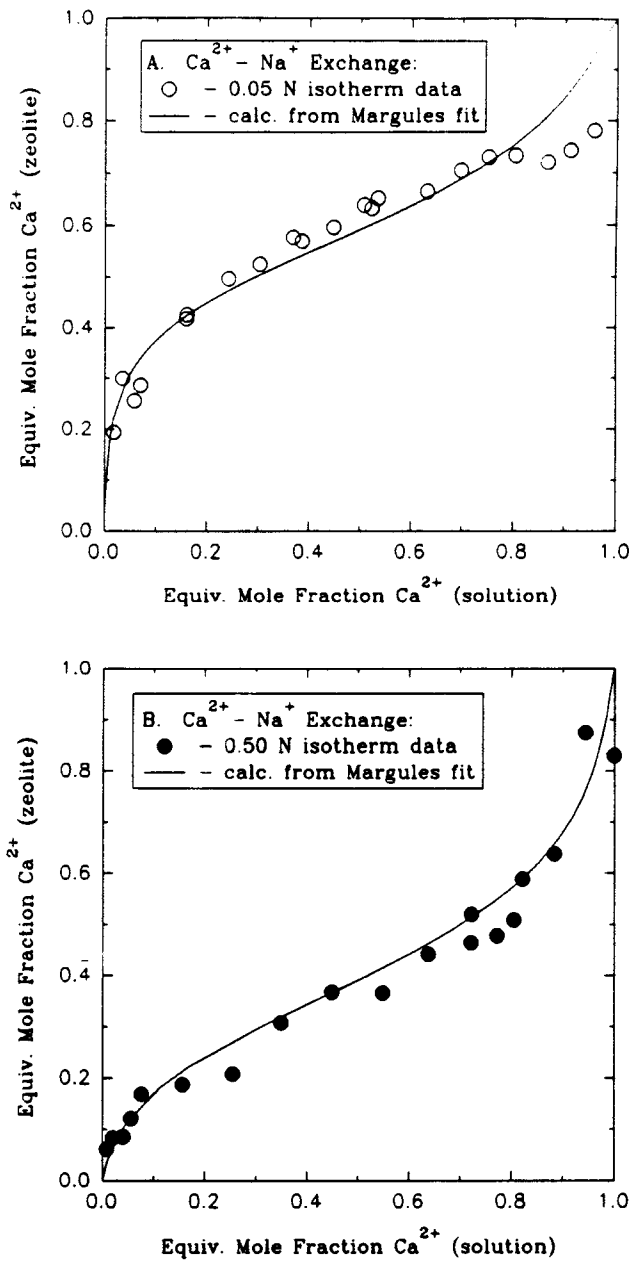


Figure 2-9. Isotherms at 25°C for the  $K^+ - Na^+$  binary system at total solution concentrations of (a) 0.05 N and (b) 0.50 N. The symbols are experimental data, and the solid curves represent values calculated using the Margules formulation for zeolite component activity coefficients and the Pitzer equations for aqueous solution activity coefficients.



**Figure 2-10. Isotherms at 25°C for the  $\text{Ca}^{2+}$ - $\text{Na}^{+}$  binary system at total solution concentrations of (a) 0.05 N and (b) 0.50 N. The symbols are experimental data, and the solid curves represent values calculated using the Margules formulation for zeolite component activity coefficients and the Pitzer equations for aqueous solution activity coefficients.**

The shifts in isotherm shapes as a function of total solution concentration based on a single measured isotherm can be predicted using Eqns. (4) and (15). This requires that activity coefficients for the zeolite and aqueous phases be known. In the binary systems studied here,  $K$ ,  $\ln f_A$  and  $\ln f_B$ , were determined using Eqns. (6) through (8) by integrating analytical functions fit to the 0.5 N isotherm data. Values of  $g^{ex}$  were calculated from  $\ln f_A$  and  $\ln f_B$  using Eqn. (12), which were then used to fit the Margules equation [Eqn. (13)]. For the binary system  $K^+$ - $Na^+$ , the derived Margules parameters  $W_K$  and  $W_{Na}$  have values of -0.11015 and -0.99043, respectively. For the system  $Ca^{2+}$ - $Na^+$ ,  $W_{Ca}$  and  $W_{Na}$  have values of -3.19315 and -1.20804, respectively. Values of  $g^{ex}$  derived initially from the 0.5 N isotherm data and those calculated from the Margules parameters are plotted in Figure 2-11, versus the cationic mole fraction of  $Na^+$ ,  $X_{Na}$ , in the clinoptilolite. This figure indicates that the Margules formulation describes adequately the nonideal behavior in the clinoptilolite phase. The dashed line in Figure 2-11 illustrates that, by definition,  $g^{ex}$  is zero over the whole composition range for an ideal solid solution.

Activity coefficients for the clinoptilolite phase can be calculated from the Margules parameters through Eqn. (14).  $K_v$  at a given  $X_A$  can be derived from Eqn. (15) using  $K$  values determined from the 0.5 N isotherm data, which are 17.2 and 0.193 for the  $K^+$ - $Na^+$  and  $Ca^{2+}$ - $Na^+$  systems, respectively. Equation (4) then yields values of aqueous solution compositions at a given  $X_A$ , based on the  $K_v$  values and aqueous activity coefficients calculated using the Pitzer equations. The solid curves in Figures 2-9 and 2-10 represent the isotherm values calculated accordingly for  $K^+$ - $Na^+$  and  $Ca^{2+}$ - $Na^+$ . Since only the 0.5 N data were used to generate  $K$ ,  $K_v$ ,  $\ln f_A$ ,  $\ln f_B$ , and  $g^{ex}$  initially, the solid curves in Figures 2-9(a) and 2-10(a) for ion exchange at 0.05 N concentration represent predicted values. As shown, the thermodynamic models discussed above can be used to predict reasonably well the isotherm shapes at other aqueous concentrations.

Equilibrium constants derived from this study are different from those determined by Ames (1964a,b), who gives  $K$  values of 12.7 and 0.851 for the  $K^+$ - $Na^+$  and  $Ca^{2+}$ - $Na^+$  systems, respectively, based on his experiments at a total solution concentration of 1.0 N. The differences are largely due to his use of a different activity coefficient model for the aqueous solution, and partly due to his use of a different clinoptilolite material. A reevaluation of his isotherm data using the Pitzer equations for aqueous activity coefficients yields  $K$ 's for  $K^+$ - $Na^+$  and  $Ca^{2+}$ - $Na^+$  equal to 20.8 and 0.184, respectively, which are close to values determined in this study.

### 2.1.5. Conclusions

Ion-exchange experiments conducted in this study indicate that thermodynamic models accounting for nonideal behavior in aqueous solutions and zeolite phases are useful in describing and predicting the solid solution and ion-exchange properties of the zeolite mineral clinoptilolite. These models provide a foundation for understanding ion exchange equilibria in multicomponent geochemical systems such as that expected at Yucca Mountain, Nevada.

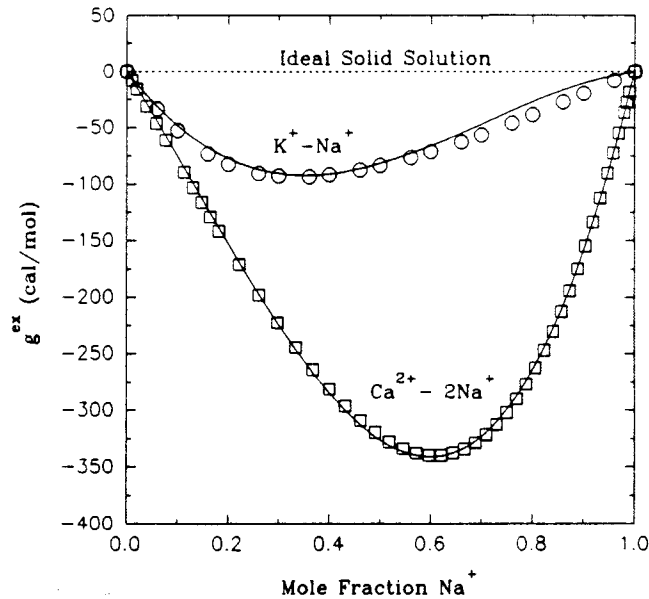


**Figure 2-11. Values of  $g^{ex}$  (cal/mol) vs. the cationic mole fraction of  $\text{Na}^+$ ,  $X_{\text{Na}}$ , in the zeolite for the  $\text{K}^+$ - $\text{Na}^+$  binary systems. Values derived initially from the 0.5 N isotherm data (see text) are indicated by symbols, while solid curves represent calculations from the Margules fit to those values. The dashed line represent  $g^{ex}$  values for an ideal solid solution.**

## 2.2. GEOCHEMICAL MODELING by William M. Murphy

### 2.2.1. Technical Objectives

The technical objective of the modeling task of the Geochemistry Research Project is to apply principles of thermodynamics, kinetics, and mass balance to the interpretation of natural and experimental systems pertinent to ambient and repository geochemical conditions at Yucca Mountain and to the prediction of the evolution of these systems.

### 2.2.2. Reaction-Path Modeling of Gas-Water-Rock Interactions

Reversible and irreversible reactions among minerals, aqueous solutions, and gases occur in response to changes in conditions, such as variations in temperature or the juxtaposition of mutually unstable materials. Reaction-path modeling comprises the calculation of these variations in phase chemistry using thermodynamic and kinetic principles and data. Four applications of reaction-path modeling relevant to the Yucca Mountain system are summarized

in the following sections. In the first, a conceptual model for the evolution of natural groundwaters in the Yucca Mountain environment is used to develop idealized initial conditions for the processes leading to the ambient gas-water-rock system. A partial equilibrium reaction-path model is then used to calculate the evolution of idealized water and mineral chemistries from the initial conditions. Comparisons between the calculations and geochemical data from Yucca Mountain permit an evaluation of the validity of the model. In the second application, results from the ambient system model are used in the definition of initial conditions for a simulation of nonisothermal perturbations to the geochemical system that may be representative of near-field repository conditions. This modeling includes treatment of nonisothermal kinetic dissolution and growth of mineral phases as well as equilibrium open-system gas fractionation processes. Results of these studies have been presented by Murphy (1990).

Two additional applications of reaction-path modeling are presented for experimental systems. In the first, a set of experiments is designed theoretically to determine the reversed phase equilibrium between analcime and Na-clinoptilolite in support of experimental studies in the Geochemistry Research Project. In the latter, a theoretical analysis is made of variations in the aqueous solution chemistry in localized corrosion experiments at elevated temperatures conducted as part of the Integrated Waste Package Experimentation Research Project.

Research reported here has employed computer programs and thermodynamic data in the 3245.R100 release version of the EQ3/6 geochemical modeling software package including the 3245.R45 data base (e.g., Wolery, 1983; Wolery et al., 1990). Programs and data have been modified subject to informal control to correct bugs, to enable nonisothermal kinetic and gas fractionation modeling, and to test the sensitivity of the model results to variations in the thermodynamic data. Kinetic data have been estimated from results reported in the literature as described below. Correct interpretation of the modeling results requires recognition of uncertainties and errors in the data as well as simplifications in the model system. For example, large uncertainties exist in the thermodynamic properties of zeolite minerals. Data for the solid solution properties of clinoptilolite used in the modeling exercises described below can be shown to be strictly incompatible with empirical results reported in Section 2.1 for the experimental task of the Geochemistry Research Project. In addition, estimations of reactive surface areas in natural systems, required in calculations of heterogeneous kinetics, are subject to large (e.g., order of magnitude) uncertainties, which are reflected by corresponding uncertainties in calculated times of reaction. While these issues are the subject of continuing research, insights to the evolution and controls on complex geochemical systems such as those relevant to the proposed Yucca Mountain repository can be obtained with exploratory calculations using these provisional modeling tools.

#### *2.2.2.1. Groundwater and Mineral Chemistry at Yucca Mountain*

**Conceptual Model and Initial Conditions.** The reaction-path simulation of the evolution of groundwater and mineral chemistry at Yucca Mountain requires a conceptual model for the initial water chemistry and the set of reactions affecting the system.

Previously reported conceptual and numerical models for groundwater and mineral chemistry at Yucca Mountain and similar environments (e.g., Benson, 1976; White et al., 1980; Kerrisk, 1983) have generally invoked dissolution of primary unstable solids such as volcanic glass, and growth of products such as smectite and zeolite as basic controls. This framework is adopted in the present study with the additional assumption that interactions between source water (i.e., rain) and caliche and/or dust containing calcite have an important effect. This aspect of the model is supported by geologic and geochemical data suggesting that calcium, bicarbonate, and possibly chloride in the Yucca Mountain groundwaters are derived partially or dominantly from sources other than the tuffs.

For example, unaltered Paintbrush Tuff from Yucca Mountain generally contains less than 1 percent CaO by weight, whereas rocks that have been partially altered to zeolites and/or clays typically contain CaO at three to four percent (Broxton et al., 1986). Although the altered rocks may have silica depletions of 10 to 20 percent and alumina enrichments up to 30 percent, suggesting some preferential leaching, the large increase in calcium concentrations indicates that it is added to the altered rocks from an external source. This is likely to be the prevalent near-surface caliche zone at Yucca Mountain, which is rich in calcite ( $\text{CaCO}_3$ ). A possible origin of the calcium near the surface is the widespread exposures of Paleozoic rocks in the region, some of which are dominantly or partially calcite and/or dolomite ( $\text{CaMg}(\text{CO}_3)_2$ ). These and other exposed rocks are subject to mechanical weathering by wind-blown particles leading to aeolian deposition of carbonate dust. Calcite in the soil zone, whether as dust or caliche, would rapidly dissolve in meteoric water, which is the likely source of groundwater recharge. Magnesium is also low in the unaltered tuffs of Yucca Mountain and enriched by several times in altered tuffs (Broxton et al., 1986), and may be similarly supplied by dissolution of dolomite deposited at the surface. The concept of recharge waters initially enriched with calcium and magnesium is supported by data showing that calcium and magnesium concentrations generally decrease with depth in waters extracted from core taken in the unsaturated zone at Rainier Mesa (White et al., 1980).

The chlorine content of the tuffaceous rocks at Yucca Mountain is low (approximately 500 ppm), and the molar fluorine to chlorine ratio in unaltered tuffs is approximately 10 (e.g., Warren and Broxton, 1986, cited in Kerrisk, 1987). In contrast, chloride is the second most abundant anion in groundwaters from the tuffaceous aquifer, where its molality usually exceeds the fluoride molality. This suggests an external source of chlorine, although it may also be due to preferential incorporation of fluoride in secondary minerals such as zeolites, clays, and apatite. An external source of chloride could be aerosol or dust halite or other salts derived from the numerous playas in the region and deposited at the surface of the mountain.

An important contribution to water chemistry at Yucca Mountain is  $\text{CO}_2$  derived primarily from soil-zone biological processes such as root respiration (e.g., Quade et al., 1989). Rainwater saturated with respect to atmospheric  $\text{CO}_2$  at a partial pressure of approximately  $10^{-3.5}$  bar has a bicarbonate content of approximately  $10^{-5}$  molal and a pH of approximately 5. In contrast, groundwaters from tuffaceous aquifers in the vicinity of Yucca Mountain have  $\text{CO}_2$  contents equivalent to  $10^{-2}$  to  $10^{-3}$  bar, which is significantly greater than the

atmospheric CO<sub>2</sub> pressure (e.g. Kerrisk, 1987). The vadose zone gases are primarily air with added CO<sub>2</sub> at approximately 0.1 to 0.13% in the upper 140 meters at Yucca Mountain (Thorstensen et al., 1990), which corresponds to approximately 10<sup>-2.9</sup> bar of CO<sub>2</sub> pressure. Somewhat higher CO<sub>2</sub> contents have been observed in gases very near the surface of Yucca Mountain (Yang, written communication, 1988; Thorstensen et al., 1990), which is consistent with soil-zone CO<sub>2</sub> generation. Consequently, CO<sub>2</sub> in the unsaturated zone gas and pore water may be derived in part by exsolution from the lower saturated zone waters and upward transport in the gas phase as well as downward migration from the soil zone.

Based on the conceptual model outlined above, the initial water for the reaction-path simulation of Yucca Mountain groundwaters is taken to be saturated with calcite. The pH is initially fixed at 7, which yields an equilibrium CO<sub>2</sub> pressure of 10<sup>-1.6</sup> bar and a bicarbonate concentration of approximately 4x10<sup>-3</sup> molal at 25°C. The initial solution in the model is set to contain 2x10<sup>-4</sup> m NaCl, a chloride content typical of saturated-zone tuffaceous groundwaters at Yucca Mountain (e.g., Kerrisk, 1987). For simplicity, only dominant elements and those required for dominant water-rock reactions are considered in the model (sodium, silicon, calcium, potassium, aluminum, carbon, chlorine, hydrogen, and oxygen). Magnesium, iron, manganese, fluorine, nitrogen, and other components are eliminated; and oxidation-reduction reactions are effectively omitted in the model by fixing the oxygen fugacity at 0.2 bar (e.g., atmospheric O<sub>2</sub>).

The major primary solid phases in tuffs at Yucca Mountain are alkali feldspar, cristobalite, quartz, tridymite, and glass (e.g., Bish and Chipera, 1989). The devitrified tuff at the proposed repository horizon is composed dominantly of alkali feldspar and cristobalite. The major element chemistry of cryptocrystalline Topopah Springs rhyolite is represented almost identically by alkali feldspar solid solution with minor calcium plus silica, [e.g., cristobalite (see Table 2-5)]. Because of this correspondence, the reaction-path simulations involving feldspar and silica should resemble reaction of primary glass. Yucca Mountain groundwaters, however, are strongly supersaturated with respect to quartz and other crystalline silica polymorphs (e.g., Kerrisk, 1987). Dissolution of feldspars coupled with equilibrium precipitation of clinoptilolite and approximate aluminum conservation can not generate these high silica concentrations. In contrast, the silicon:aluminum ratio in rhyolite glass (or bulk Topopah Spring Tuff) exceeds that in clinoptilolite. Alteration of glass is the most likely mechanism for generation of secondary clinoptilolite and elevated aqueous silica activities as asserted by other workers (e.g., White et al., 1980). This conclusion is supported by petrographic evidence indicating that clinoptilolite forms predominantly by alteration of rhyolitic glass at Yucca Mountain (e.g., Vaniman et al., 1984). To simulate a high silica aqueous environment, the reaction-path model for the ambient system incorporates aqueous SiO<sub>2</sub> buffering at 10<sup>-3.1</sup> molal, a value typical of saturated-zone waters at Yucca Mountain (e.g., Kerrisk, 1987).

The calculated reactions consist of irreversible dissolution of alkali feldspar solid solution in water with the initial composition described above, and of reversible growth of a secondary stable or metastable solid phase assemblage. Dominant secondary minerals in the upper sections of Yucca Mountain are clinoptilolite, mordenite, and smectite.

**Table 2-5. BULK COMPOSITION (WEIGHT PERCENT) OF TOPOPAH SPRINGS TUFF (TST) REPRESENTED AS FELDSPAR PLUS CRISTOBALITE, AND MODEL MINERAL CHEMISTRY**

<u>Oxide</u>	<u>TST*</u>	<u>Feldspar plus Cristobalite**</u>
SiO <sub>2</sub>	77	77.04
Al <sub>2</sub> O <sub>3</sub>	12.5	12.97
CaO	0.25	0.28
Na <sub>2</sub> O	3.5	3.48
K <sub>2</sub> O	6.5	6.23
<u>Model Minerals</u>	<u>Components</u>	
Cristobalite/Quartz	SiO <sub>2</sub>	
Feldspar	0.53 KAlSi <sub>3</sub> O <sub>8</sub> (sanidine) 0.45 NaAlSi <sub>3</sub> O <sub>8</sub> (high albite) 0.02 CaAl <sub>2</sub> Si <sub>2</sub> O <sub>8</sub> (anorthite)	
Calcite	CaCO <sub>3</sub>	
Clinoptilolite***	CaAl <sub>2</sub> Si <sub>10</sub> O <sub>24</sub> •8H <sub>2</sub> O Na <sub>2</sub> Al <sub>2</sub> Si <sub>10</sub> O <sub>24</sub> •8H <sub>2</sub> O K <sub>2</sub> Al <sub>2</sub> Si <sub>10</sub> O <sub>24</sub> •8H <sub>2</sub> O	
K-feldspar	KAlSi <sub>3</sub> O <sub>8</sub> (microcline)	

\*Typical values extracted from data reported by Byers (1985)

\*\*0.25 moles of feldspar with the composition given above plus 0.54 moles of cristobalite

\*\*\*Clinoptilolite was assumed to behave as an ideal solid solution of the listed components

In the lower sections, analcime and kaolinite occur instead of clinoptilolite and mordenite. Calcite and secondary quartz occur in many horizons, and authigenic K-feldspar is also present (e.g., Vaniman et al., 1984). For the ambient system model, a subset of these minerals is expected to form as secondary phases. Precipitation of quartz and other silica polymorphs has been suppressed in the model for the ambient system, representing kinetic inhibition of their formation, in order to maintain elevated aqueous silica concentrations comparable to observed values. Compositions of minerals occurring in the model are given in Table 2-5, and kinetic data are given in Table 2-6.

**Ambient-System Reaction-Path Calculation.** Two special attributes of the particular reaction-path model described here are the stability of the potassium clinoptilolite component and CO<sub>2</sub> volatilization. The dissolution reaction equilibrium constant for the K-clinoptilolite endmember estimated by Ogard and Kerrisk (1983) led to its apparent excessive stability in preliminary model results compared to observed clinoptilolite compositions (Broxton et al., 1986) and potassium concentrations in groundwaters (Kerrisk, 1987). For the models presented here, this equilibrium constant was therefore increased by a factor of ten to increase the solubility of K-clinoptilolite.

The distribution of CO<sub>2</sub> and CO<sub>2</sub> pressures at Yucca Mountain discussed above suggests that water either recharging in the vadose zone or flowing near the top of the saturated zone may be expected to lose CO<sub>2</sub> by volatilization to the gas phase. A variation of CO<sub>2</sub> pressure, introduced in the model by allowing CO<sub>2</sub> to volatilize slowly from the liquid, had a small effect in the model results.

The general features of the reaction-path simulation for the 25°C system are shown as solid curves in Figures 2-12 and 2-13. Dissolution of alkali feldspar leads to equilibrium growth of a clinoptilolite solid solution and calcite and to an increase in pH. Calcium in solution, which is initially high, decreases as it is incorporated in clinoptilolite, which is initially calcium-rich. The monotonic decrease of calcium serves as a monitor of reaction progress in Figures 2-12 and 2-13. As the calcium concentration in solution decreases, the clinoptilolite becomes progressively enriched in the potassium component; and eventually the potassium concentration in aqueous solution decreases as it is consumed by clinoptilolite growth. Sodium is not strongly incorporated in the zeolite, and its concentration in solution progressively increases due to feldspar dissolution. Although aqueous silica is buffered, the total silica concentration increases at the end of the simulation as a significant amount of H<sub>3</sub>SiO<sub>4</sub><sup>-</sup> forms at elevated pH. Bicarbonate concentrations drop initially and then vary only slightly over the more evolved portion of the reaction path.

**Comparison of Model Results and Data from Yucca Mountain.** The validity of the model can be evaluated by comparing the computed results with empirical data from Yucca Mountain, and by judging the reasonableness of variations and magnitudes of model-dependent variables. An examination of each component and phase reveals aspects of the model that correspond remarkably well to observations, and other aspects that are deficient. The absence of reliable water-chemistry data for the unsaturated zone at Yucca Mountain limits

Table 2-6. KINETIC DATA

**RATE EXPRESSIONS:**

$$\frac{d\xi}{dt} = k s a_{H^+}^n \left( 1 - \exp \left( \frac{-A}{R T} \right) \right)$$

$$k = \frac{T k^0}{T^0} \exp \left[ \frac{-\Delta H^\ddagger}{R} \left( \frac{1}{T} - \frac{1}{T^0} \right) \right]$$

- $\xi$ : reaction progress variable for the individual dissolution reaction  
 $t$ : time  
 $k; k^0$ : rate constant; rate constant at reference temperature  
 $s$ : surface area  
 $a_{H^+}$ : activity of the hydrogen ion  
 $n$ : order of the dissolution reaction with respect to the hydrogen ion  
 $A$ : chemical affinity for the dissolution reaction  
 $R$ : ideal gas constant  
 $T, T^0$ : temperature; reference temperature  
 $\Delta H^\ddagger$ : activation enthalpy

**DATA:**

reactant*	$s$ (cm <sup>2</sup> )	$k^0$ (25°) (moles/cm <sup>2</sup> /sec)	$\Delta H^\ddagger$ (kJ/mole)	$n$
feldspar	20000	3 X 10 <sup>-16</sup>	35.32	0
		2.5 X 10 <sup>-19</sup>	32.10	-0.4
cristobalite/ quartz	10000	1.6 X 10 <sup>-18</sup>	75.24	0
		5 X 10 <sup>-21</sup>	105.75	-0.5

\*There are two parallel reactions for each reactant. Feldspar rate parameters are based on data from Helgeson et al. (1984) for albite. Cristobalite and quartz rate parameters are based on data for quartz from Murphy and Helgeson (1989) and Knauss and Wolery (1988).

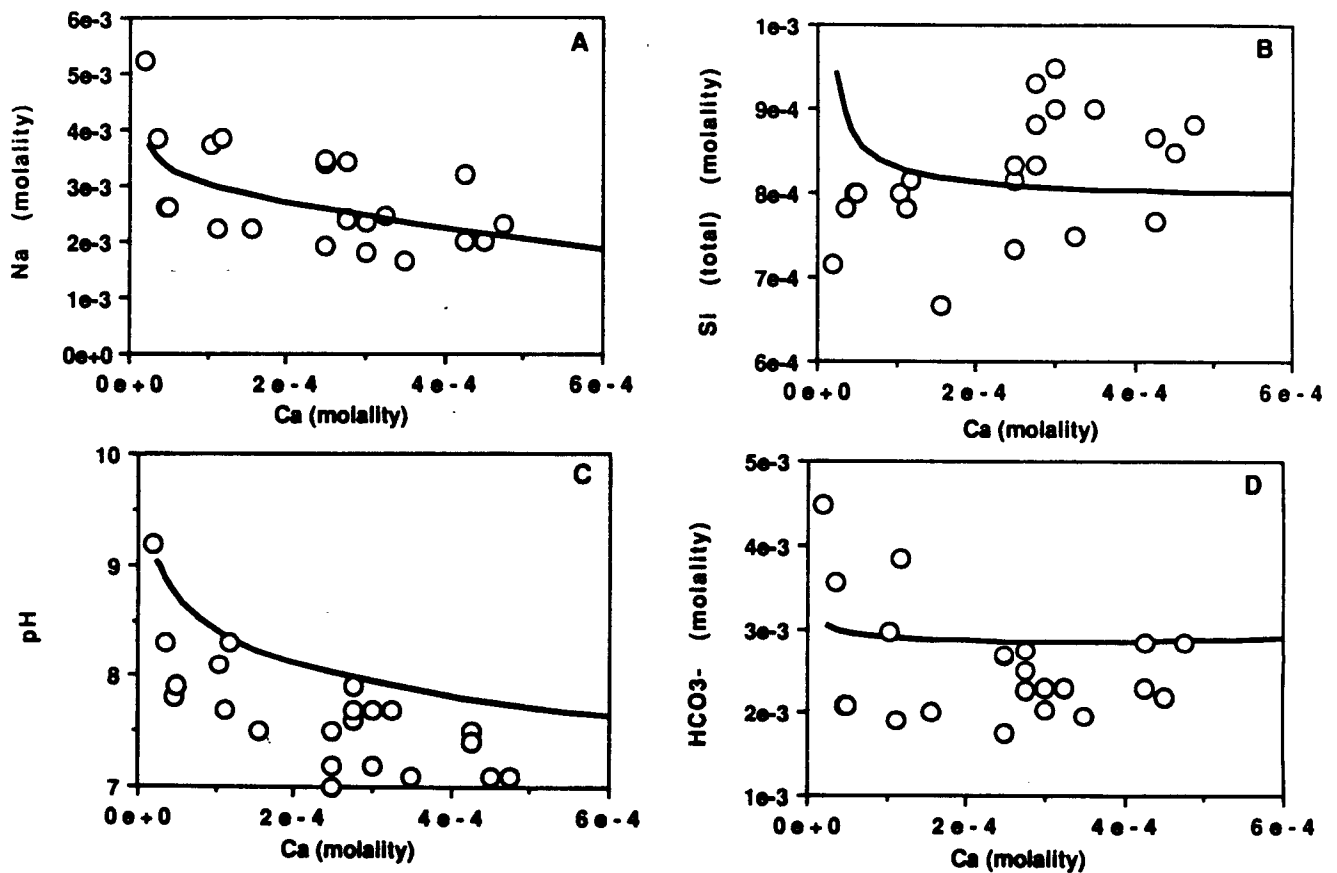


Figure 2-12. Comparison of aqueous solution compositions calculated in an isothermal (25°C) reaction-path model (curves) to measured water compositions from the tuffaceous aquifer at Yucca Mountain (open circles). The calcium concentration decreases with reaction progress in the model; therefore system evolution proceeds from right to left in the figures. See text for discussion of results.

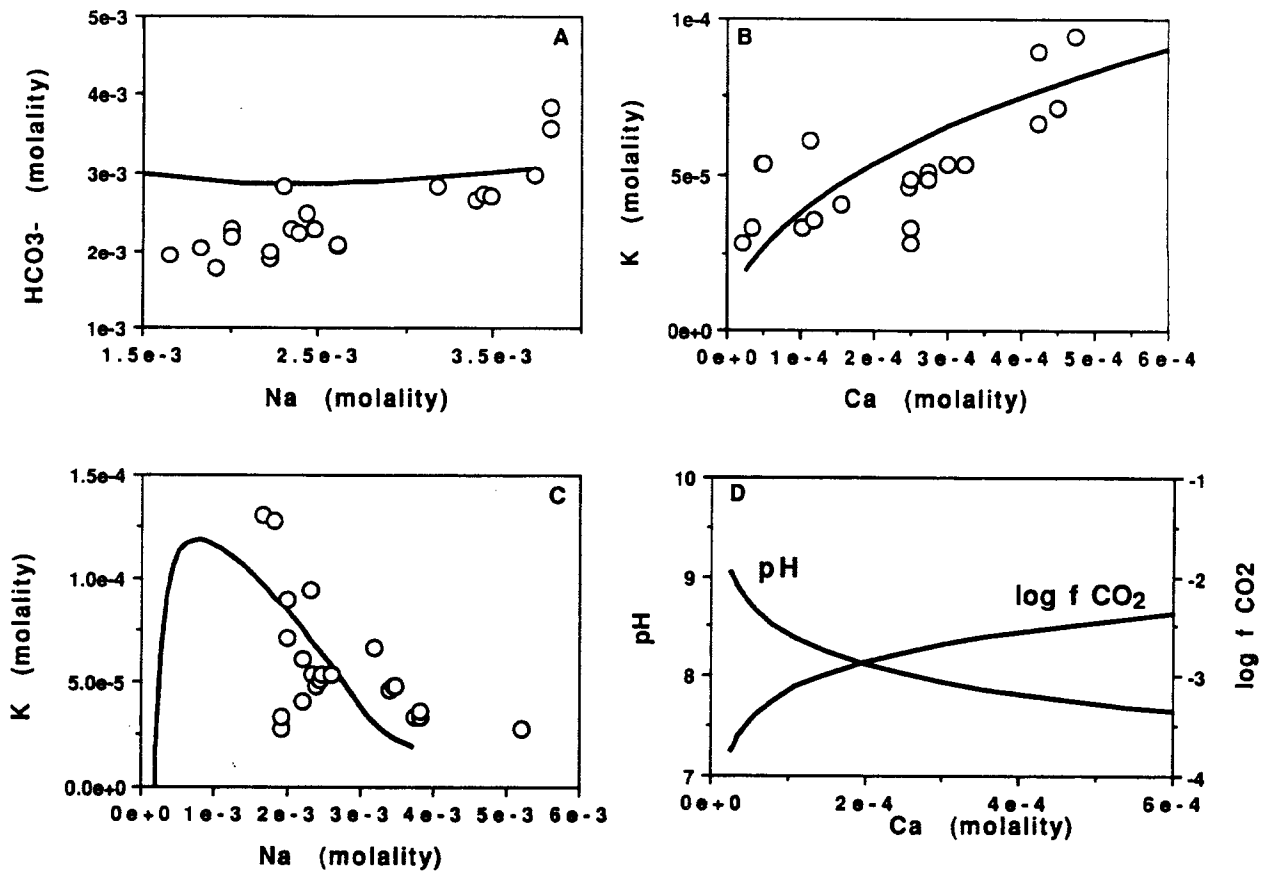


Figure 2-13. Comparison of aqueous solution compositions calculated in an isothermal (25°C) reaction-path model (curves) to measured water compositions from the tuffaceous aquifer at Yucca Mountain (open circles). See text for discussion of results.

comparisons to water compositions for the saturated zone. Data for waters taken from tuffaceous aquifers in the vicinity of Yucca Mountain compiled by Kerrisk (1987) (represented by open circles in Figures 2-12 and 2-13) have been used for this purpose. The early portion of the reaction-path simulation would not be expected to represent well the evolved waters taken from the saturated tuffaceous aquifer. Therefore, comparisons in Figures 2-12 and 2-13 focus primarily on the more advanced stages of reaction progress.

**Na<sup>+</sup>, Ca<sup>2+</sup>, and K<sup>+</sup>.** A dominant trend in the water chemistry calculated in the model is the progressive increase in Na<sup>+</sup> and decrease in Ca<sup>2+</sup>. Sodium increases because it is a major species released from the feldspar, its initial concentration is low, and the secondary phases are sodium-poor. Calcium decreases because it is initially at a high concentration in equilibrium with calcite at neutral pH, it is an important component of the secondary minerals clinoptilolite and calcite, and the dissolving rock is poor in calcium. This inverse relation between Na<sup>+</sup> and Ca<sup>2+</sup> is generally reflected in the data from Yucca Mountain vicinity groundwaters as illustrated in Figure 2-12a. The K<sup>+</sup> content of groundwater from the vicinity of Yucca Mountain ranges generally from  $3 \times 10^{-5}$  to  $1.4 \times 10^{-4}$  molal. In the model, the K<sup>+</sup> concentration increases to over  $1 \times 10^{-4}$  molal before potassium begins to be consumed in clinoptilolite growth (Figures 2-13b and 2-13c). The good correspondence in magnitude and trend between the groundwater data and model for these species is due in part to the adjustment of the properties of K-clinoptilolite and the CO<sub>2</sub> volatilization noted above.

**pH, CO<sub>2</sub>, and carbonate.** The modeled pH and logarithm of the CO<sub>2</sub> fugacity (Figure 2-13d) correspond well to measured pH and calculated fugacities for groundwaters at Yucca Mountain and vicinity reported by Kerrisk (1987). The modeled inverse relation between these variables matches almost identically the relation shown in Figure 8 of Kerrisk (1987) between empirical pH and calculated log fugacity. This match is achieved in part because Kerrisk calculated CO<sub>2</sub> fugacities using the same equilibria as in the model. CO<sub>2</sub> fugacity drops below the atmospheric level of  $10^{-3.5}$  bar at the end of the reaction-path simulation. This low CO<sub>2</sub> fugacity is unrealistic for the unsaturated zone at Yucca Mountain because air is expected to circulate in the mountain and because CO<sub>2</sub> gas concentrations measured in the unsaturated zone at Yucca Mountain do not fall below this level (Yang et al., written communication, 1988; Thorstensen et al., 1990). Nevertheless, Kerrisk (1987) reports a saturated-zone groundwater pH at 9.2 and calculates a corresponding CO<sub>2</sub> fugacity of  $10^{-3.8}$  bar for the USW H-3 well water at Yucca Mountain. These values correspond almost exactly to corresponding values from the termination of the model (Figure 2-12d). The modeled relation between pH and Ca in Figure 2-12c is controlled primarily by equilibrium between the water and calcite. Waters at Yucca Mountain are generally undersaturated or approach saturation with respect to calcite, which is reflected by the curve bounding the site data in this figure.

**Mineral chemistry.** The calculated Ca:K ratio for clinoptilolites is initially large and decreases to near 1.0. This corresponds well to measured values for the eastern calcic group and the calcium-rich subset of the transitional group of clinoptilolites at Yucca Mountain as given in Broxton et al. (1986). Clinoptilolites rich in Na, characteristic of the western alkalic and transitional groups, are not generated in the model.

The reaction-path model for the ambient water chemistry at Yucca Mountain summarized in this report is not definitive. Important components (e.g., magnesium and glass) have been omitted. Perfect partial equilibrium assumed with respect to secondary phases may be unrealistic, although it appears to be a reasonable approximation, particularly in the context of uncertainties in the thermodynamic data for clinoptilolite. The model solid-solution properties for clinoptilolite are approximations. Some important features of the Yucca Mountain environment are not well represented. For example, a clear correspondence between increasing sodium and bicarbonate concentrations in tuffaceous aquifer groundwaters is not well represented in the model (Figure 2-13a). Few data are available to judge the applicability of the water chemistry model to the unsaturated zone at Yucca Mountain. Nevertheless, informed assumptions concerning the origin and constraints on the water and mineral chemistry have permitted the generation of a model that reasonably represents many key features of the Yucca Mountain geochemical environment. Results of this model can be used to set initial conditions for reaction-path modeling of water- and mineral-chemistry variations resulting from repository-induced thermal perturbations as described in the following section.

#### *2.2.2.2. Near-field Modeling: Nonisothermal Kinetics and Gas Fractionation*

Temperature variations such as those anticipated in the near-field environment at Yucca Mountain would promote chemical reactions affecting water and mineral chemistry. The EQ6 reaction-path code can be used to model the nonisothermal geochemical evolution of this environment. Furthermore, the code (version 3245.R100) has been modified to permit simulations of two important processes relevant to temperature variations in a partially saturated medium. These processes are (1) nonisothermal, kinetic, irreversible dissolution and growth reactions and (2) open-system, equilibrium gas fractionation. Theory and practice of the modifications have been presented by Murphy (1986), Murphy (1989), and Arthur and Murphy (1989). Analogous modifications for nonisothermal kinetics have been incorporated by the geochemical modeling group at Lawrence Livermore National Laboratory in the recently released 3245.R119 version of EQ6 (Wolery et al., 1990). The results of two reaction-path simulations relevant to the near field at Yucca Mountain and employing these new modeling capabilities (Murphy, 1990) are summarized in this section.

Rates of rate-limiting irreversible reactions, such as feldspar dissolution and growth of secondary quartz, depend on temperature. The rates of these reactions relative to one another and to coupled processes, such as secondary growth of clinoptilolite and aqueous speciation, affect the evolution of water and mineral chemistry along a reaction path. Using coding in EQ6 for nonisothermal reaction-path calculations and isothermal kinetics, modifications permitting nonisothermal kinetics involve introduction of expressions and data for the temperature dependence of rate constants (Table 2-6).

The solubilities of volatile species in aqueous solution are also temperature dependent. Heating groundwater in contact with a gas phase will lead to fractionation of these species between liquid and gas phases as well as vaporization of the water.

A limiting model for this process is open-system, equilibrium gas fractionation analogous to Rayleigh distillation. In this process each infinitesimal increment of gas generated by vaporization of the liquid is assumed to be at thermodynamic equilibrium with the liquid, and is effectively removed from the system. By modifying coding in EQ6 for reaction kinetics as a function of solution composition, this process has been modeled by defining reactants with the compositions of volatile species (e.g., H<sub>2</sub>O and CO<sub>2</sub>), which can be removed (volatilized) from the aqueous phase (and the system) at rates proportional to their instantaneous equilibrium fugacities.

**Formulation of the Nonisothermal Kinetic Model.** The nonisothermal kinetic model is designed to approximate geochemistry such as that anticipated in the near-field environment at a Yucca Mountain repository during the period of heating. Temperature is calculated as a function of model time using a specified function. Although temperature would increase in the near field approximately in proportion to the logarithm of time (e.g., Pruess et al., 1990), a provisional linear time-temperature relation has been adopted:

$$T = T^0 + \tau t \quad (16)$$

where  $T$  represents temperature,  $T^0$  stands for the initial temperature,  $\tau$  stands for the time-temperature coefficient, and  $t$  denotes time. Time is calculated in EQ6 by solving integrated rate equations for rate-limiting irreversible reactions over increments of reaction progress. Equations and data defining the relations between time, rate constants, reactive surface area, and aqueous solution composition are specified in the model. Two examples of nonisothermal modeling presented here give alternate representations of the behavior of the system with respect to water-gas reactions. In the first example, volatilization or dissolution of CO<sub>2</sub> is controlled by maintaining a constant CO<sub>2</sub> fugacity independent of temperature, and the mass of H<sub>2</sub>O in the liquid phase is kept constant. In the second case, the rates of volatilization of H<sub>2</sub>O and CO<sub>2</sub> are assumed to be proportional to their equilibrium fugacities in the aqueous solution, calculated as a function of temperature and solution composition. The volatilization proportionality constant is the same for each species to properly account for equilibrium open-system vaporization, and is assumed to be independent of temperature.

The initial aqueous solution for the nonisothermal simulations has a composition generated in the isothermal model described above. The water chemistry represents an intermediate degree of reaction progress in the isothermal model corresponding to a calcium molality of  $3 \times 10^{-4}$ , and is therefore conditioned by extended reaction at 25°C with a solid phase assemblage consisting of alkali feldspar, silica phase(s), calcite, and clinoptilolite solid solution. It is at supersaturation with respect to several silica polymorphs, at equilibrium with calcite and clinoptilolite with Ca:K  $\approx$  1, and at pH  $\approx$  7.9 with a CO<sub>2</sub> fugacity of  $10^{-2.7}$  bar.

The solid phases of the 25°C model were also allowed to form in the simulation of the nonisothermal system. However, in contrast to the isothermal model, quartz and cristobalite were added to the primary reactant assemblage along with alkali feldspar. These silica polymorphs were permitted either to grow or to dissolve kinetically depending on solution

composition and temperature conditions. The high-silica metastability of natural groundwaters at Yucca Mountain, the strong temperature dependence of rates of growth and dissolution of silica minerals, and the apparent control on aspects of alteration mineralogy exerted by aqueous silica at Yucca Mountain suggest that temperature effects on silica concentrations may lead to important modifications of the near-field geochemical environment (e.g., Murphy, 1990). Aspects of this hypothesis are tested by the computations summarized below.

Rate expressions and parameters used in the modeling are summarized in Table 2-6. The time-temperature coefficient ( $\tau$ ) was set at  $10^{-5}$  °C/sec, which corresponds approximately to the average rate of increase to 100°C in the immediate near field computed by Pruess et al. (1990). Surface areas of the primary phases (i.e., feldspar, cristobalite, and quartz) total  $4 \times 10^4$  cm<sup>2</sup>/kg H<sub>2</sub>O and are assumed to be constant. This value corresponds to the surface area to water mass ratio for a water-filled, smooth-walled fissure approximately 0.5 mm thick at 25°C, if the primary phases are in contact with water on all of the fissure surface. Other materials (e.g., product phases) on the fissure surface, surface roughness, partial hydrologic saturation, detailed pore geometry, and other factors all complicate the interpretation of reactive surface areas in geologic media, which remains a major enigma in geochemical kinetic modeling. Despite the uncertainties in surface areas and other rate parameters, which are manifested in calculated times and complicate time-temperature correlations, kinetic modeling represents a major improvement over the use of arbitrary reaction rates because it allows the relative rates among numerous simultaneous dissolution and growth reactions to vary in a more realistic manner.

#### **Buffered Nonisothermal System Reaction-Path Calculation.**

Selected results from the CO<sub>2</sub>-buffered nonisothermal reaction-path model are shown in Figures 2-14 through 2-16, where temperature is used as the indicator of reaction progress and time. The temperature excursion above 100°C in the model involves an increase in the total pressure above 1 bar along the steam saturation curve, which may be unrealistic for the unsaturated Yucca Mountain environment. The elapsed time for the temperature increase from 25 to 120°C calculated in the model to be 110 days is obtained from Eqn. (16). The calculated sodium concentration in the solution continues to increase from its value generated in the isothermal model as feldspar continues to dissolve. Bicarbonate and total aqueous carbonate decrease in part because of precipitation of calcite, but primarily because of the decreasing solubility of CO<sub>2</sub> with increasing temperature (Figure 2-14a). The pH increases modestly from 7.95 to 8.45 between 25° and 120°C (Figure 2-15b). Calcium drops sharply as it is incorporated in secondary products. Potassium is approximately constant in time and temperature because of balanced production from feldspar dissolution and precipitation in clinoptilolite and secondary K-feldspar, which precipitates at temperatures above 55°C (Figure 2-16b).

With reaction progress and increasing temperature, the clinoptilolite composition evolves toward a more calcic composition at the expense of the potassium endmember (Figure 2-16a). In contrast, the Ca<sup>2+</sup> to K<sup>+</sup> ratio in the aqueous phase decreases strongly, primarily due to incorporation of calcium in secondary products. Mass balance relations are clearly reflected in the inverse variation of the Ca:K ratio between the solids and

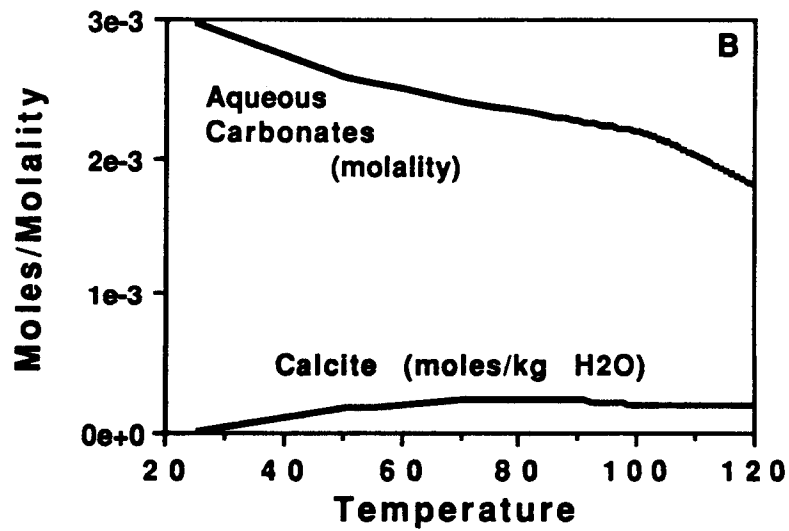
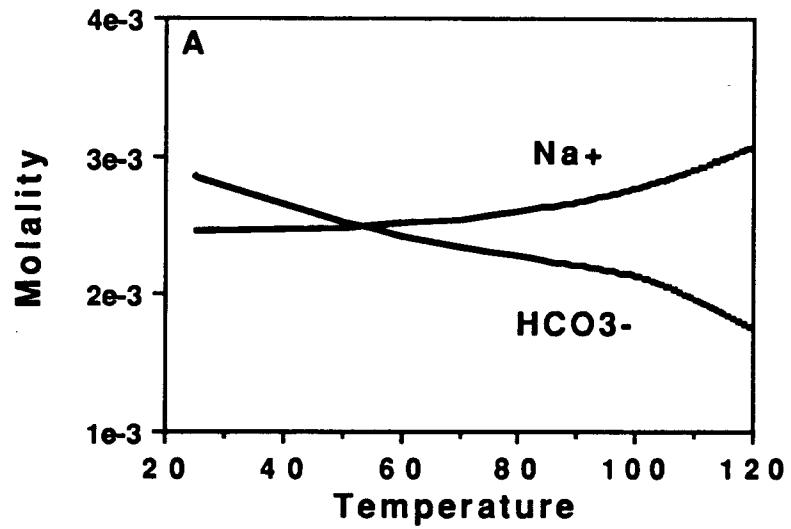


Figure 2-14. Changes in solution composition (A and B) and moles of calcite precipitated (B) as a function of temperature ( $^{\circ}\text{C}$ ) along a nonisothermal reaction path with buffered  $\text{CO}_2$ . See text for discussion of results.

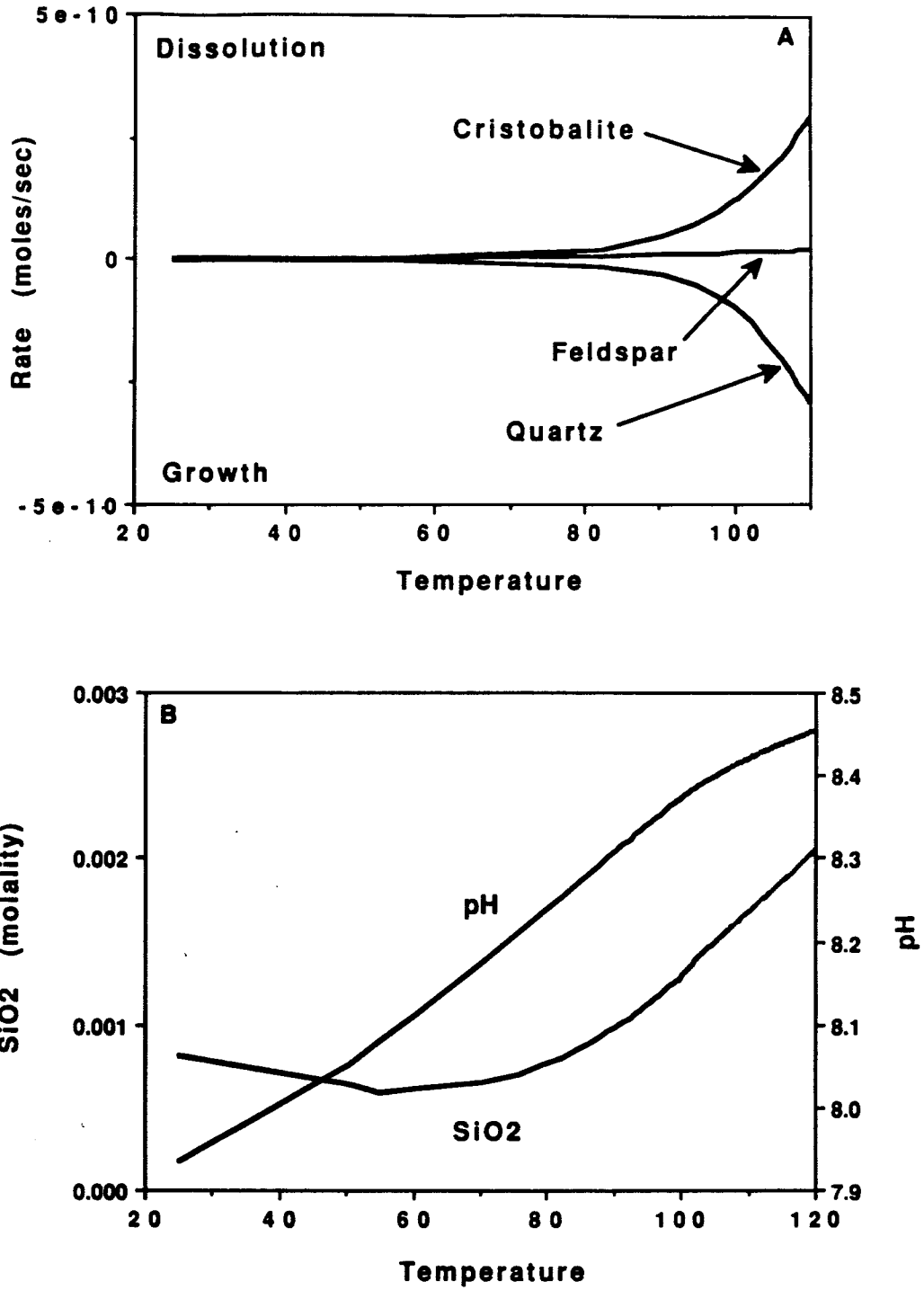


Figure 2-15. Rates of mineral dissolution and growth (A) and changes in solution compositions (B) as a function of temperature ( $^{\circ}\text{C}$ ) along a nonisothermal reaction path with buffered  $\text{CO}_2$ . See text for discussion of results.

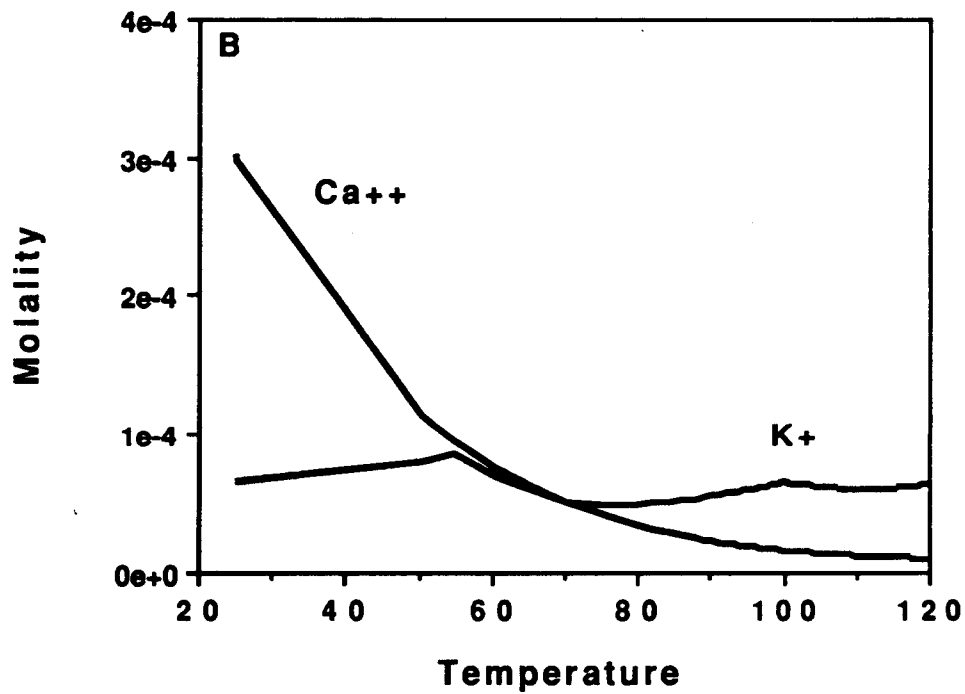
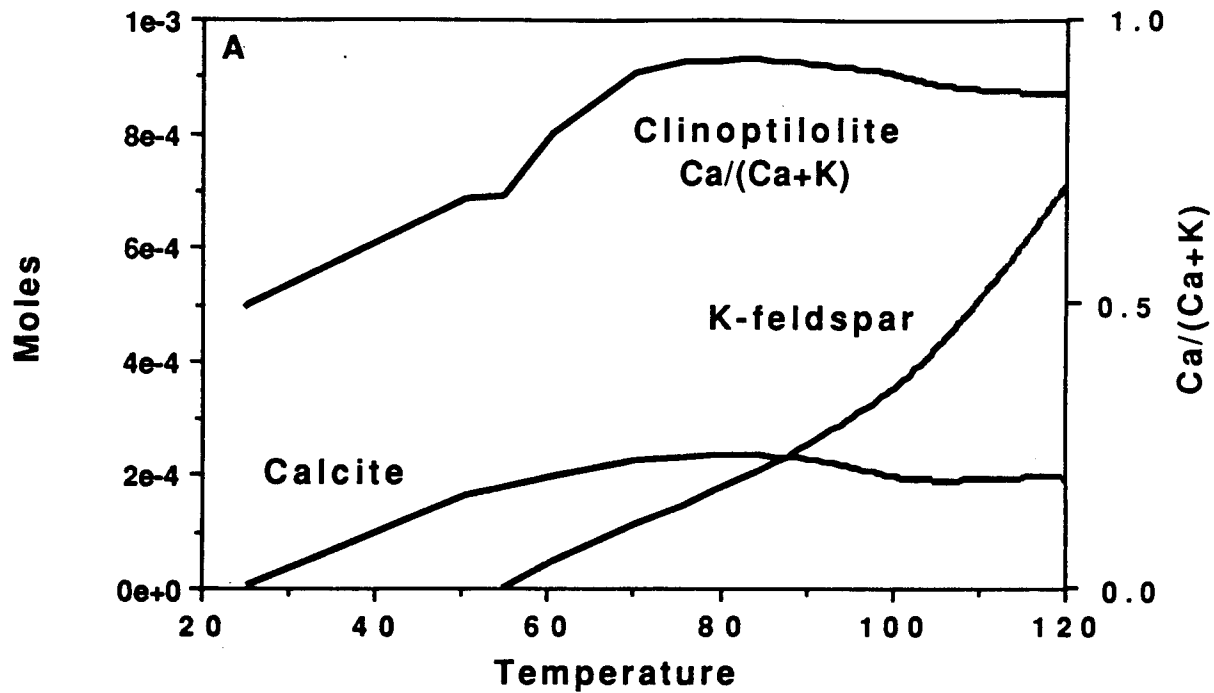
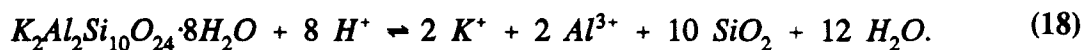
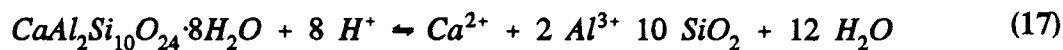


Figure 2-16. Variation of clinoptilolite composition (A), moles of calcite and K-feldspar precipitated (A) and changes in solution composition (B) as a function of temperature ( $^{\circ}\text{C}$ ) along a nonisothermal reaction path with buffered  $\text{CO}_2$ . See text for discussion of results.

aqueous solution. However, the pattern of increasing Ca:K ratio in the zeolite and decreasing Ca:K in the coexisting aqueous solution offers an apparent paradoxical relation with respect to equilibrium between these phases. This pattern is induced by the difference in the temperature dependence of the equilibrium constants for the Ca- and K-endmember clinoptilolite dissolution reactions:



The logarithm of the equilibrium constant for the former reaction decreases by 0.64 units between 25° and 100°C, whereas for the latter reaction its value increases by 0.62 units. Hence, the calcium endmember is greatly stabilized with respect to the potassium endmember with increasing temperature. The trend with depth of increasing Ca in clinoptilolite taken from fractures and decreasing dissolved Ca in water has been noted at Rainier Mesa (Benson, 1976; White et al., 1980), suggesting that local equilibria in even a slight geothermal gradient (as well as mass balance) may influence natural clinoptilolite compositional variations.

Aqueous silica concentrations in the model are influenced by kinetic dissolution and/or growth of primary feldspar, cristobalite, and quartz, and by equilibrium dissolution and/or growth of clinoptilolite and K-feldspar. Although rates for these reactions are low at low temperatures, the silica concentration decreases from the initially silica-rich solution as both quartz and cristobalite precipitate at temperatures below 50°C. At greater temperatures, the rate of quartz growth is roughly balanced by the rate of cristobalite dissolution. Silica concentrations increase markedly at temperatures above 70°C as the equilibrium solubilities of both quartz and cristobalite increase. Feldspar dissolution remains slow throughout the reaction, but increases slightly as temperature increases (Figure 2-15). Although the forward rate of feldspar dissolution increases strongly with temperature and increasing pH, changes in solution composition and equilibrium constants lead to a decrease in the affinity for feldspar dissolution along the reaction path, which moderates the overall reaction-rate increase.

**Nonisothermal Gas-Fractionation Reaction-Path Calculation.** In the gas-fractionation model both CO<sub>2</sub> and H<sub>2</sub>O vaporize at a rate of 10<sup>-5</sup> moles/second/bar times the equilibrium fugacity of the volatile species. Selected results from the nonisothermal reaction-path model with open-system gas fractionation are shown in Figure 2-17. Some variations are similar to the CO<sub>2</sub>-buffered nonisothermal system model, such as the increase in the aqueous sodium concentration, the initial precipitation and then dissolution of calcite, and the growth of secondary K-feldspar commencing at an elevated temperature (35°, versus 55°C in the buffered case). A dramatic difference is the rapid depletion of aqueous CO<sub>2</sub> from the system, resulting in a decrease in bicarbonate and a corresponding increase in pH. This leads to almost instantaneous growth of a large amount of calcite, which depletes the solution in calcium and causes the clinoptilolite to become enriched in potassium. Silica concentrations decrease initially

as in the buffered nonisothermal path. However, the additional increase in pH drives the reaction



to the right, leading to a greater reduction in the  $\text{SiO}_2(\text{aq})$  concentration. Precipitation of K-feldspar also contributes to this effect. As a consequence of lowered silica (and calcium) concentrations, the clinoptilolite originally in the system dissolves completely; and the solution becomes undersaturated with respect to this solid solution (shown by the break in Figure 2-17d). The period (and temperature) of solution undersaturation with respect to clinoptilolite corresponds to the minimum in the aqueous silica concentration. The effect is due in part to the kinetic treatment of quartz and cristobalite reactions in contrast to silica buffering employed in the isothermal model.

Following the initial purge of  $\text{CO}_2$  from the system, its rate of volatilization decreases; and the trend of the system evolution changes. The pH stabilizes at a value near 9.5, and then begins to decrease slightly at temperatures above  $50^\circ\text{C}$ . The aqueous silica concentration begins to increase above  $55^\circ\text{C}$ . The solution resaturates with respect to clinoptilolite, which begins again to precipitate in partial equilibrium at approximately  $45^\circ\text{C}$ . The second generation clinoptilolite is rich in calcium and poor in potassium. Calcium is effectively transferred from calcite to clinoptilolite with increasing temperature and reaction progress. Calcite begins to dissolve at  $50^\circ\text{C}$ , and dissolves completely at approximately  $100^\circ\text{C}$ . Cumulative volatilization up to  $100^\circ\text{C}$  removes approximately two percent of the initial  $\text{H}_2\text{O}$  and ninety percent of the initial  $\text{CO}_2$  from the aqueous system.

**Discussion of Nonisothermal Modeling Results.** The results of the nonisothermal modeling are subject to limitations and uncertainties that extend even beyond those discussed above in relation to the ambient system. The linear time-temperature relation does not represent well the predicted logarithmic heating rate of the near field. Local equilibrium with secondary K-feldspar is probably an unrealistic aspect of the particular models presented here. Extensive vaporization leading to concentrated solutions and drying has not been examined in these models. Fluid fluxes in the thermal gradients have not been considered in these examples. Nevertheless, the computations indicate that important mineral and solution chemistry variations are possible on predicted time scales that are short relative to the anticipated thermal period of the repository.

#### **2.2.2.3. *Reaction-Path Modeling for Analcime-Clinoptilolite Phase Equilibrium Experimental Design***

Experiments have been proposed in the Geochemistry Research Project to evaluate phase equilibria among clinoptilolite, analcime, and aqueous solutions. The objective of these studies is to investigate techniques to resolve the problem of uncertainties in the standard-state thermodynamic properties for clinoptilolite (Pabalan and Murphy, 1990). In this section a summary is given of the results of reaction-path models generated to assist in the

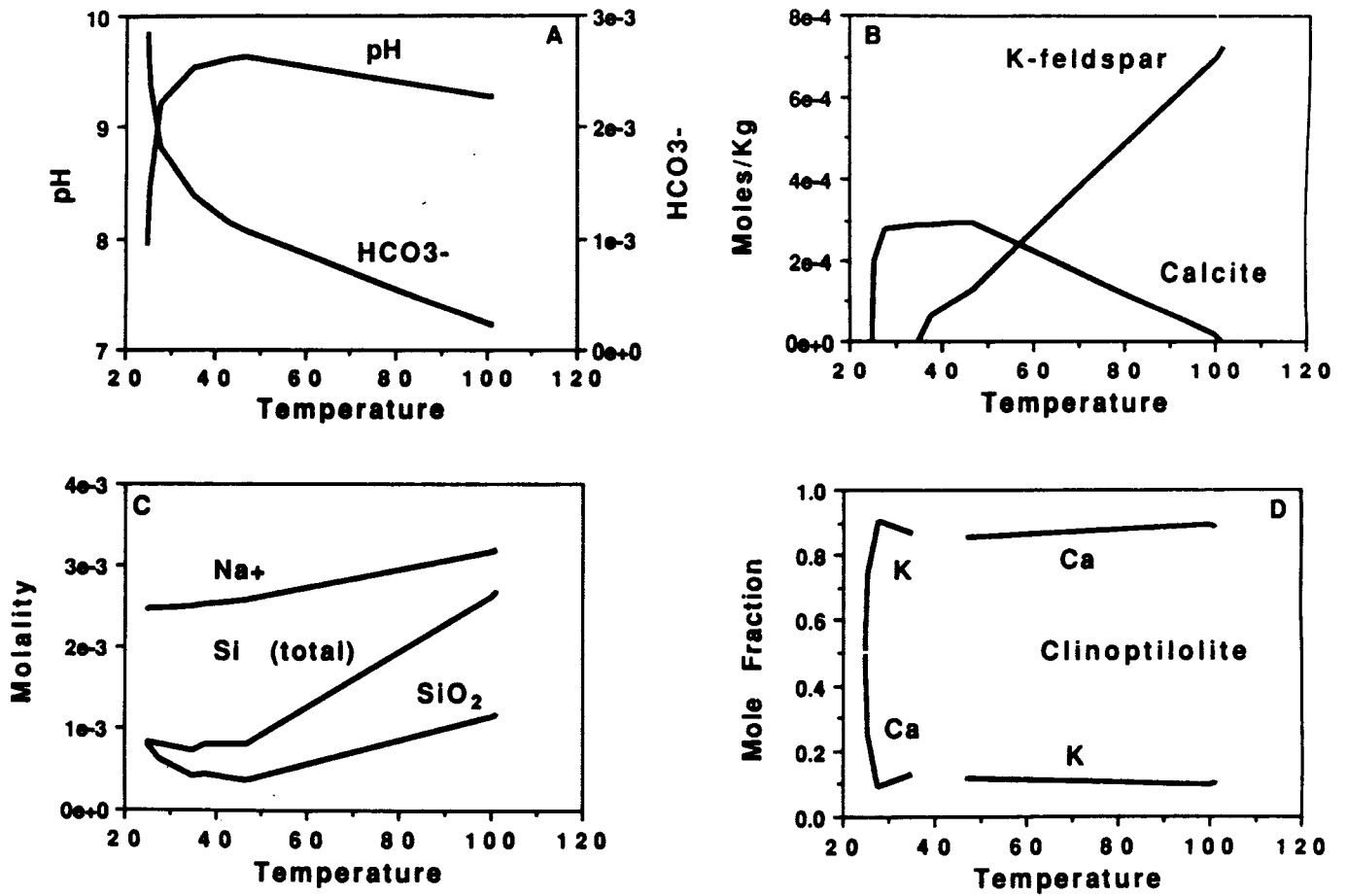
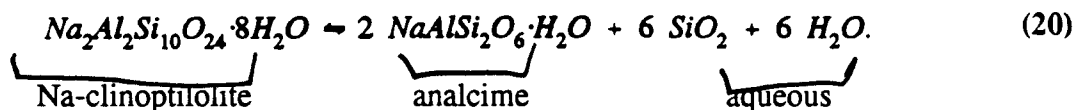


Figure 2-17. Changes in solution composition (A and C), moles of K-feldspar and calcite precipitated (B) and clinoptilolite compositions (D) as a function of temperature ( $^{\circ}\text{C}$ ) along a nonisothermal reaction-path with open-system  $\text{CO}_2$  volatilization. See text for discussion of results.

design of these experiments.

Although solubility studies can provide accurate determinations of the standard-state Gibbs free energies of minerals, experimental analyses of the solubilities of multicomponent solids are complicated by several factors. The studies generally require a detailed knowledge of numerous aqueous species, variations in the solid-phase compositions (e.g., solid solution), crystallinity of solid(s), and metastability of solid or aqueous phases. Furthermore, mineral dissolution is commonly incongruent and/or nonstoichiometric, and precipitation of secondary phases can complicate interpretation of the aqueous solution data. Reversals of phase-equilibrium determinations are generally required (i.e., equilibrium must be approached from undersaturation as well as oversaturation) to bracket the equilibrium state. Reaction-path modeling, theoretically accounting for these factors in simulations of the evolution of experimental systems, can be used to minimize ambiguities in the data interpretation and maximize the usefulness of the experimental results.

For the idealized mineral stoichiometries in the EQ3/6 database (3245.R45), aqueous silica activity alone controls equilibrium between the endmember sodium clinoptilolite and analcime in dilute solutions according to the following reaction:



Field relations at Yucca Mountain showing clinoptilolite associated with cristobalite, and analcime correlated with the absence of cristobalite support the role of aqueous silica in this transition (e.g., Kerrisk, 1983). These relations suggest an experimental design to equilibrate Na-clinoptilolite and analcime that focuses on aqueous silica concentration as a primary monitor of reaction progress and mass action. Although experiments should be designed to minimize ambiguities resulting from secondary-phase precipitation and variations in solution composition, metastability of a silica-rich aqueous solution with respect to quartz (and other silica polymorphs) is required for the equilibration of reaction.

Given the objectives outlined above, a set of reactions is proposed for initial experimental study. The initial aqueous solution is to be a  $10^{-1}$  molal NaCl plus  $10^{-2}$  molal NaHCO<sub>3</sub> solution equilibrated with atmospheric CO<sub>2</sub> at 25°C. Using EQ3 and the 3245.R45 database, the calculated pH of this initial solution is 9.08. This solution is to be reacted with powdered, physically purified analcime; and the dissolved CO<sub>2</sub> is to be buffered by equilibrium with air. The evolution of solution composition calculated with EQ6 is shown in Figure 2-18, also generated in accord with the 3245.R45 data. The solution is predicted to become saturated with respect to gibbsite after reaction progress representing  $6 \times 10^{-6}$  moles of analcime dissolution in 1 kilogram of H<sub>2</sub>O. Gibbsite is assumed in the model to precipitate at equilibrium with the solution as the reaction proceeds, and the evolution of the solution composition is plotted in the gibbsite field of Figure 2-18. The solution then equilibrates with analcime at reaction progress of  $3.27 \times 10^{-5}$  moles. The calculated pH of the solution remains nearly constant ending at 9.08.

The initial relatively high sodium concentration of  $1.1 \times 10^{-1}$  molal is almost unaffected by the analcime dissolution reaction. The total silica concentration increases from zero to  $6.53 \times 10^{-5}$  molal, providing a sensitive monitor of reaction progress and the kinetic approach to equilibrium. The final solution is predicted to be supersaturated with respect to paragonite (an uncommon low-temperature mineral), which is not expected to form because of kinetic nucleation inhibition. In contrast, the calculated solution remains undersaturated with respect to kaolinite, a common low-temperature alteration mineral.

Data for the kinetics of analcime dissolution will be available from this study, and their interpretation will be facilitated by careful characterization of the surface area of the reactant. The current absence of data for analcime dissolution rates precludes accurate predictions of the required duration of the experiments. Scoping kinetic studies will be necessary, and adjustments to the surface area to solution volume ratio and/or temperature can be made to optimize reaction times.

In the second phase of the experiment, powdered homoionic Na-clinoptilolite (see Section 2.1) is to be added to the solution previously equilibrated with analcime, retaining analcime in the system. EQ6 modeling of the consequent reactions indicates that the initially precipitated gibbsite dissolves and analcime precipitates. Assuming partial equilibrium with gibbsite and analcime, all gibbsite is consumed after dissolution of  $8.9 \times 10^{-6}$  moles of clinoptilolite (per kilogram  $H_2O$ ). Subsequent reaction progress is governed by clinoptilolite dissolution and coupled growth of analcime. The silica concentration, buffered at analcime-gibbsite equilibrium, resumes its increase after consumption of all gibbsite. The subsequent reaction path is plotted in the analcime field of Figure 2-18. Calculated equilibrium with Na-clinoptilolite plus analcime is achieved after dissolution of  $4.3 \times 10^{-5}$  moles of clinoptilolite and growth of  $1.2 \times 10^{-4}$  moles of analcime. The total silica concentration increases to  $2.6 \times 10^{-4}$  molal at analcime-clinoptilolite equilibrium. The pH remains closely buffered, achieving a final value of 9.075. The total sodium concentration is not strongly affected through the experiment, ending almost identically at its initial state. The solution is predicted to supersaturate with respect to albite and quartz, which are unlikely phases to crystallize in this low-temperature system, but paragonite supersaturation is eliminated because of a small decrease in the aluminum concentration.

Reversal of the equilibrium determination can be effected in conjunction with an additional analcime dissolution rate experiment in a high-silica solution. As before, the initial solution is a  $10^{-1}$  molal NaCl,  $10^{-2}$  molal  $NaHCO_3$  mixture equilibrated at  $25^\circ C$  with atmospheric  $CO_2$ . However, the initial total aqueous silica concentration is adjusted to  $10^{-3}$  molal. The pH is calculated to be 9.07 with EQ3. EQ6 calculations show that minor dissolution of Na-clinoptilolite in this solution brings it to equilibrium with the zeolite as indicated by the high silica end on the reaction-path curve in the clinoptilolite field in Figure 2-18. Subsequent addition of analcime to the clinoptilolite-equilibrated solution causes dissolution of analcime and growth of clinoptilolite. Assuming that clinoptilolite growth occurs in partial equilibrium with the solution, the solution composition calculated with EQ6 evolves in the clinoptilolite field as shown in Figure 2-18. Silica is the only aqueous species that changes appreciably along this

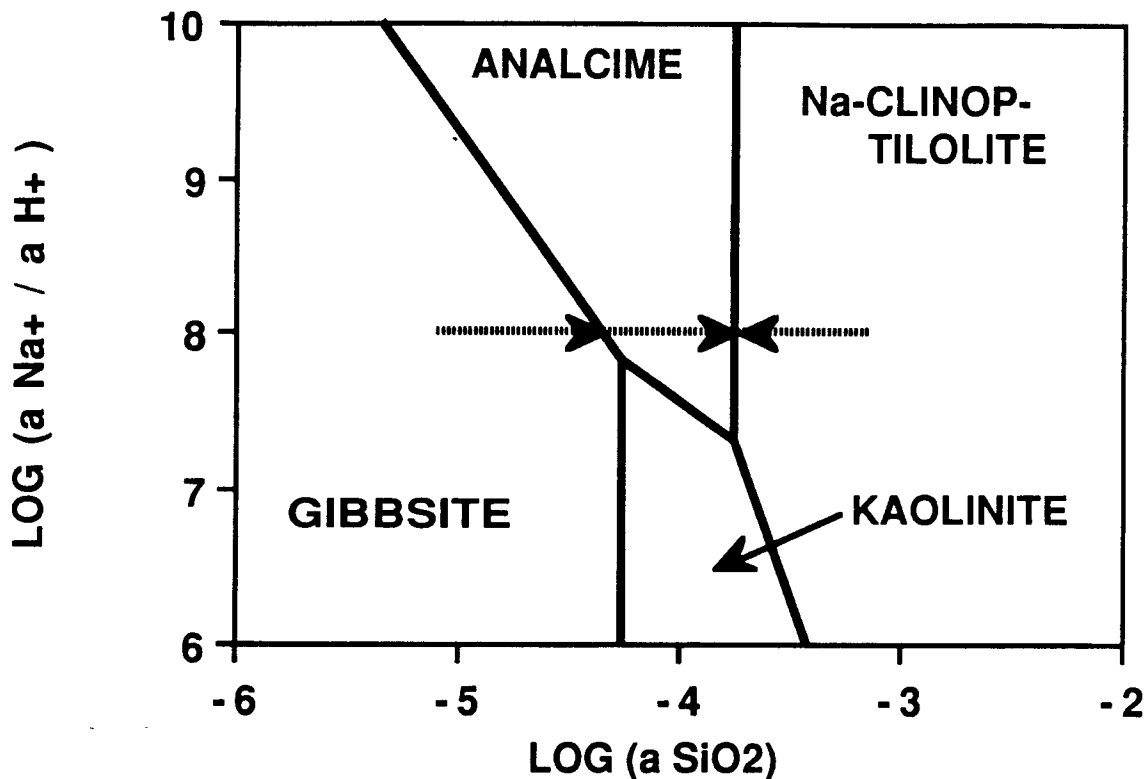


Figure 2-18. Reaction paths (represented by dashed arrows) for clinoptilolite-analcime equilibration studies, plotted in a thermodynamic activity diagram representing fields of mineral stability as a function of aqueous solution composition at 25°C. See text for discussion of results.

path, which terminates at clinoptilolite-analcime equilibrium approximately equivalent to the end point in the analcime-growth and clinoptilolite-dissolution study described previously.

Important differences are expected between the evolution of the experimental system and the computed simulation. Experimental reactants will not have ideal stoichiometries. Perfect partial equilibrium is not expected to occur between the solution and gibbsite, analcime, and/or clinoptilolite. The thermodynamic data on which the computations are based are uncertain. Adequate interpretation of the results will require complete chemical analyses of the aqueous solutions and solids from various points in the experiments. Nevertheless, aspects of the designed experiment should maximize the potential for obtaining accurate and interpretable results. In particular, the solution composition should be essentially constant except for aqueous silica, which will be the primary monitor of reaction progress and equilibrium. The elevated sodium concentrations and pH will minimize nonstoichiometric dissolution of the primary reactants, such as sodium depletion in the solids caused by ion

exchange. The computations indicate that complications due to secondary precipitation of clay minerals (affecting silica concentrations) will be minimized, and predicted metastabilities (supersaturations) are likely to be sustainable. Solution compositions will generally resemble natural solutions from Yucca Mountain, and the analcime-clinoptilolite relations controlled by aqueous silica concentrations appear to correspond to the natural controls based on Yucca Mountain field data. In the experimental studies, equilibrium, and therefore the ultimate determination of the standard-state thermodynamic properties of the reaction and of clinoptilolite, will be constrained reversibly by analcime-growth and clinoptilolite-dissolution in low-silica solutions, and by analcime dissolution and clinoptilolite growth at high-silica concentrations. Important new data on analcime dissolution and growth rates will be obtained. Refined modeling will be required to further design the tests and interpret the experimental results.

#### *2.2.2.4. Thermodynamic Analysis of Aqueous Solution Chemistry in Localized Corrosion Experiments*

The results of a thermodynamic and reaction-path analysis of the aqueous solution chemistry in experiments conducted as part of the Integrated Waste Package Experiments Research Project are presented in this section. An issue in the research is the control on the evolution of solution pH in corrosion experiments conducted at 95°C; the pH measured at room temperature after experimentation was significantly greater than the initial solution pH (Cragolino and Sridhar, 1991). In addition to pH, a detailed understanding of the aqueous speciation of the solutions at the elevated temperatures of the experiments may be useful for the interpretation of the localized-corrosion results. The EQ3/6 software package was used to address this problem, making use of the open-system, equilibrium gas-fractionation capabilities described above.

**Initial Solution Chemistry.** Initial solutions were prepared for localized corrosion experiments by dissolving sodium salts in water to obtain specific total anion concentrations. One relatively corrosive solution selected for the modeling study had total concentrations of anions and sodium as reported by Cragolino and Sridhar (1991) and given in Table 2-7. The measured pH of this solution at room temperature was reported to be 8.15.

The equilibrium aqueous speciation for the test solution was calculated for 25°C with the program EQ3. Concentrations of sodium salts were used as input mass constraints, and the pH was calculated by adjusting the H<sup>+</sup> (and OH<sup>-</sup>) species to obtain charge neutrality. An oxidation state was selected for all calculations for which aqueous species remained oxidized (e.g., the calculated equilibrium nitrite concentration was over twelve orders of magnitude lower than nitrate). Dominant calculated aqueous species in the 25°C test solution are reported in Table 2-7. The calculated pH was 8.137, in excellent agreement with the analytical result, which serves to validate the water-chemistry model. Notably, neutral NaHCO<sub>3</sub> accounts for over 4 percent of total carbonate, and NaSO<sub>4</sub><sup>-</sup> accounts for nearly 10 percent of total sulfate at 25°C. The calculated equilibrium CO<sub>2</sub> fugacity at 10<sup>-3.29</sup> bar, which is slightly greater than the atmospheric CO<sub>2</sub> fugacity of 10<sup>-3.5</sup> bar, indicates a small potential for CO<sub>2</sub> to exsolve from the solution as a gas at 25°C.

Table 2-7. COMPUTED WATER CHEMISTRY DATA FOR LOCALIZED-CORROSION STUDIES

SPECIES	INPUT mg/kg (A)	25°C EQUIL. molal (B)	95°C INITIAL molal (C)	95°C 0.36% VAPOR. molal (D)	95°C 1.8% VAPOR. molal (E)	25°C COOLED 0.36% VAP. molal (F)	25°C COOLED 1.8% VAP. molal (G)
Cl <sup>-</sup>	1000	2.82e-2	2.81e-2	2.82e-2	2.86e-2	2.83e-2	2.87e-2
SO <sub>4</sub> <sup>2-</sup>	1000	9.42e-3	9.16e-3	9.19e-3	9.31e-3	9.45e-3	9.58e-3
NaSO <sub>4</sub> <sup>-</sup>		9.93e-4	1.25e-3	1.26e-3	1.29e-3	9.98e-4	1.02e-3
NO <sub>3</sub> <sup>-</sup>	10	1.61e-4	1.61e-4	1.62e-4	1.64e-4	1.62e-4	1.64e-4
F <sup>-</sup>	2	1.05e-4	1.04e-4	1.04e-4	1.06e-4	1.05e-4	1.07e-4
NaF		4.53e-7	1.23e-6	1.24e-6	1.27e-6	4.56e-7	4.68e-7
HCO <sub>3</sub> <sup>-</sup>	85.5	1.31e-3	1.33e-3	1.08e-3	8.00e-4	8.86e-4	4.49e-4
NaHCO <sub>3</sub>		5.92e-5	1.66e-5	1.36e-5	1.01e-5	4.02e-5	2.06e-5
CO <sub>2</sub> (aq)		1.81e-5	4.60e-5	6.32e-6	2.15e-6	6.09e-7	8.46e-8
CO <sub>3</sub> <sup>2-</sup>		1.52e-5	9.00e-6	4.37e-5	6.98e-5	2.08e-4	3.86e-4
NaCO <sub>3</sub>		1.06e-6	8.31e-8	4.04e-7	6.52e-7	1.45e-5	2.72e-5
Na <sup>+</sup>	1165.466	4.96e-2	4.93e-2	4.95e-2	5.02e-2	4.98e-2	5.05e-2
pH	8.15	8.137	7.780	8.554	8.888	9.440	10.002
log fCO <sub>2</sub>		-3.29	-2.41	-3.28	-3.74	-4.76	-5.62

- Notes:
- (A) Reported total input concentrations for anions (Cragolino and Sridhar, 1991). Na<sup>+</sup> concentration calculated based on salt stoichiometry and atomic masses.
  - (B) Equilibrium aqueous speciation calculated with EQ3 at 25°C. pH calculated based on charge neutrality. Only major species of each component are reported.
  - (C) Equilibrium aqueous speciation calculated with EQ3 at 95°C. pH calculated based on charge neutrality. Only major species of each component are reported.
  - (D) Equilibrium aqueous speciation calculated with EQ6 at 95°C after 0.36 percent vaporization of water and equilibrium open-system fractionation of CO<sub>2</sub>. Only major species of each component are reported.
  - (E) Equilibrium aqueous speciation calculated with EQ6 at 95°C after 1.8 percent vaporization of water and equilibrium open-system fractionation of CO<sub>2</sub>. Only major species of each component are reported.
  - (F) Equilibrium aqueous speciation calculated with EQ3 at 25°C. Total concentrations of components are equivalent to the 95°C solution after 0.36 percent vaporization. pH calculated based on charge neutrality. Only major species of each component are reported.
  - (G) Equilibrium aqueous speciation calculated with EQ3 at 25°C. Total concentrations of components are equivalent to the 95°C solution after 1.8 percent vaporization. pH calculated based on charge neutrality. Only major species of each component are reported.

2-47

Drop notes to  
next page to  
make legible & increase  
size of table

**Initial Solution Chemistry at Elevated Temperature.** The mass constraints noted above were used in EQ3 to calculate the equilibrium aqueous solution composition at 95°C, the temperature of the localized-corrosion experiments. The temperature dependence of aqueous equilibria leads to modest changes in the solution (Table 2-7). The calculated pH under the experimental conditions is 7.78. Over 1 percent of the total carbonate exists as NaHCO<sub>3</sub>, and the NaSO<sub>4</sub><sup>-</sup> complex represents 12 percent of the sulfate and 2.5 percent of the sodium at 95°C. The most significant effect is from the change in carbonate speciation and decreasing solubility of CO<sub>2</sub> with increasing temperature. CO<sub>2</sub>(aq) (which includes all neutral carbonate species such as H<sub>2</sub>CO<sub>3</sub>) accounts for over 3 percent of the total carbonate at 95°C. The equilibrium CO<sub>2</sub> gas fugacity increases to 10<sup>-2.4</sup> bar at 95°C, which is over 10 times greater than the atmospheric CO<sub>2</sub> partial pressure. The water-vapor (steam) fugacity increases from 0.03 bar at 25°C to 0.82 bar at 95°C. At 95°C a significant potential exists for release of both H<sub>2</sub>O and CO<sub>2</sub> to the atmosphere.

**Equilibrium Open-System Volatilization at 95°C.** The program EQ6, modified to simulate equilibrium, open-system gas fractionation, was used to simulate the effects of vaporization of H<sub>2</sub>O and CO<sub>2</sub> from the corrosion test water at 95°C. The amount of volatilization of H<sub>2</sub>O and CO<sub>2</sub> in the experimental studies is unknown. Results of two sample calculations are reported here (Table 2-7), representing vaporization of 0.2 mole of H<sub>2</sub>O per kilogram (0.36 percent) and 1 mole of H<sub>2</sub>O per kilogram (1.8 percent). The pH of the 95°C solution increases markedly from the initial value of 7.78, and the carbonate speciation changes significantly because of CO<sub>2</sub> volatility associated with water vaporization. After 0.36 percent vaporization, the pH increases to 8.55 at 95°C, and HCO<sub>3</sub><sup>-</sup> decreases from 1.33x10<sup>-3</sup> molal to 1.08x10<sup>-3</sup> molal. After 1.8 percent vaporization, the pH increases to 8.89, and HCO<sub>3</sub><sup>-</sup> decreases to 7.86x10<sup>-4</sup> molal. The increase in pH leads to an increase of CO<sub>3</sub><sup>2-</sup> from 9.00x10<sup>-6</sup> to 6.86x10<sup>-5</sup> molal after 1.8 percent vaporization. The solution chemistry other than carbonate speciation and pH is not greatly affected.

**Cooling of Solutions to 25°C.** Total concentrations of sodium and anionic components in the partially vaporized 95°C solutions calculated using EQ6 (modified for open-system gas fractionation) were used as input constraints in EQ3 to calculate the pH at 25°C following cooling of the experimental solutions. The pH was calculated by adjusting the H<sup>+</sup> (and OH<sup>-</sup>) concentrations to obtain charge conservation in the equilibrium solutions. Results are shown in Table 2-7. For the model solution that sustained 0.36 percent vaporization, the calculated pH is 9.44 at 25°C. This calculation corresponds closely to the measured pH of 9.34 at room temperature (Cragolino and Sridhar, 1991). For the solution that sustained 1.8 percent vaporization the calculated pH is 10.00 at 25°C.

**Conclusions from Modeling Solutions in Localized Corrosion Experiments.** Thermodynamic analysis and mass-transfer modeling have provided an explanation for the observed difference between the initial low-temperature pH and pH measurements made in cooled solutions following corrosion experiments conducted at 95°C. An excellent correspondence was observed between the pH measured in the initial solution at

room temperature prior to heating and the calculated pH based on input concentrations of salts, charge neutrality, and equilibrium aqueous speciation. The correspondence lends credibility to the accuracy of the pH measurements and the calculations. The observed increases in pH were shown to be compatible with equilibrium, open-system CO<sub>2</sub> volatilization accompanying a small fraction of water vaporization. The calculations (1) identified significant variations in carbonate concentration and speciation as a consequence of heating and volatilization and (2) showed that NaSO<sub>4</sub><sup>-</sup> was a significant species at 95°C (12 percent of total sulfate).

### 2.2.3. Status of EQ3/6 Modeling and Capabilities

Progress has been made in the application of geochemical modeling to a variety of problems associated with the proposed Yucca Mountain repository site. The ambient system model presented in Section 2.2.2.1 represents well many of the key features of the Yucca Mountain geochemical environment. A number of important limitations exist, however, with respect to simplifications in the model system and uncertainties in the thermodynamic data. Validation of ambient system models using geochemical field data is a critical step to be taken prior to attempting predictions of repository-induced geochemical perturbations.

Capabilities for nonisothermal kinetic modeling and open-system gas fractionation have been introduced in the EQ6 code to permit modeling of important processes in the unsaturated near-field environment of the proposed repository. Preliminary results presented in Section 2.2.2.2 show that temperature variations and CO<sub>2</sub> volatilization can have important effects on water and mineral chemistry and masses on a short time scale. Further development of these models should involve more realistic representations of time-temperature relations, an improved kinetic approach to product mineral growth, and improved thermodynamic data for secondary solid phases.

Modeling of experimental systems presented in Sections 2.2.2.3 and 2.2.2.4 provides valuable experimental design constraints and data interpretations. Interactive modeling and experimentation should promote the most effective use of both.

### 2.3. REFERENCES

- Ames, L. L., Jr. 1964a. Some zeolite equilibria with alkali metal cations. *Amer. Mineral.* 49: 127-145.
- Ames, L. L., Jr. 1964b. Some zeolite equilibria with alkaline earth metal cations. *Amer. Mineral.* 49: 1099-1110.
- Argersinger, W. J., A.W. Davidson, and O.D. Bonner. 1950. Thermodynamics and ion exchange phenomena. *Trans. Kansas Acad. Sci.* 53: 404.
- Arthur, R. C., and W.M. Murphy. 1989. An analysis of gas-water-rock interactions during boiling in partially saturated tuff. *Sciences Geologiques Bull.* 42: 313-327.

- Barrer, R. M. 1978. Cation-exchange equilibria in zeolites and feldspathoids, *Natural Zeolites: Occurrence, Properties, Use*. L. B. Sand and F. A. Mumpton, eds. New York: Pergamon Press: 385-395.
- Barrer, R. M., and J. Klinowski. 1974. Ion exchange selectivity and electrolyte concentration. *J. Chem. Soc., Faraday Trans. 1*. 70: 2080-2091.
- Barrer, R. M., and A. J. Walker. 1964. Imbibition of electrolytes by porous crystals. *Trans. Faraday Soc.* 60: 171-184.
- Benson, L. V. 1976. *Mass Transport in Vitric Tuffs of Rainier Mesa, Nye County, Nevada*. Desert Research Institute NVO-1253-10, 38 pp. Reno, Nevada.
- Bish, D. L., and S. J. Chipera. 1989. *Revised Mineralogic Summary of Yucca Mountain, Nevada*. LA-11497-MS. Los Alamos, New Mexico: LANL.
- Bowers, T. S., and R. G. Burns. 1990. Activity diagrams for clinoptilolite: susceptibility of this zeolite to further diagenetic reactions. *Amer. Mineral.* 75: 601-619.
- Breck, D. W. 1976. *Zeolite Molecular Sieves*. New York: John Wiley.
- Broxton, D. E., R. G. Warren, R. C. Hagan, and G. Luedemann. 1986. *Chemistry of Diagenetically Altered Tuffs at a Potential Nuclear Waste Repository, Yucca Mountain, Nye County, Nevada*. LA-10802-MS. Los Alamos, New Mexico: LANL.
- Byers, F. M., Jr. 1985. *Petrochemical Variation of Topopah Spring Tuff Matrix with Depth (Stratigraphic Level), Drill Hole USW G-4, Yucca Mountain, Nevada*. LA-10561-MS. Los Alamos, New Mexico: LANL.
- Cheleshev, M. F., B.G. Berenschtein, T.A. Berenschtein, H.K. Grebanova, and H.C. Martinova. 1973. Ion exchange properties of clinoptilolite. *Dokl. Akad. Nauk SSSR*. 210: 1110-1112.
- Cragolino, G. A., and N. Sridhar. 1991. Localized corrosion of a candidate container material for high-level nuclear waste disposal. *Corrosion/91*. Paper 35, 21pp. Houston, Texas: National Association of Corrosion Engineers.
- Daniels, W. R., K. Wolfsberg, R. S. Rundberg, A. E. Ogard, J. F. Kerrisk, C. J. Duffy, T. W. Newton, S. D. Knight, F. O. Lawrence, V. L. Rundberg, M. Sykes, G. Thompson, B. Travis, E. Treher, R. Vidale, G. Walter, R. Aguilar, M. Cisneros, S. Maestas, A. Mitchell, P. Oliver, P. Oliver, N. Raybold, and P. Wanek. 1982. *Summary Report on the Geochemistry of Yucca Mountain and Environs*. LA-9328-MS. Los Alamos, New Mexico: LANL.

- Dyer, A., H. Enamy, and R. P. Townsend. 1981. The plotting and interpretation of ion-exchange isotherms in zeolite systems. *Sep. Sci. Technol.* 16: 173-183.
- Fletcher, P., and R. P. Townsend. 1985. Ion exchange in zeolites: the exchange of cadmium and calcium in sodium X using different anionic backgrounds. *J. Chem. Soc., Faraday Trans. 1.* 81: 1731-1744.
- Gaines, G. L., Jr., and H. C. Thomas. 1953. Adsorption studies on clay minerals: II. a formulation of the thermodynamics of exchange adsorption. *J. Phys. Chem.* 21: 714-718.
- Ganguly, J., and S.K. Saxena. 1987. *Mixtures and Mineral Reactions*. Berlin: Springer-Verlag: 14.
- Glueckauf, E. 1949. Activity coefficients in concentrated solutions containing several electrolytes. *Nature* 163: 414-415.
- Gottardi, G., and E. Galli. 1985. *Natural Zeolites*. New York: Springer-Verlag.
- Grant, S. A., and D.L. Sparks. 1989. Method for evaluating exchangeable-ion excess Gibbs energy models in systems with many species. *J. Phys. Chem.* 93: 6265-6267.
- Guggenheim, E. A. 1935. The specific thermodynamic properties of aqueous solutions of strong electrolytes. *Philos. Mag.* 19: 588.
- Helfferich, F. 1962. *Ion Exchange*. New York: McGraw-Hill.
- Helgeson, H. C., W. M. Murphy, and P. Aagaard. 1984. Thermodynamic and kinetic constraints on reaction rates among minerals and aqueous solutions: II. Rate constants, effective surface area, and the hydrolysis of feldspar. *Geochim. Cosmochim. Acta.* 48: 2405-2432.
- Hutchison, C. S. 1974. *Laboratory Handbook of Petrographic Techniques*. New York: John Wiley: 120-126.
- Jama, M. A., and H. Yucel. 1990. Equilibrium studies of sodium-ammonium, potassium-ammonium, and calcium-ammonium exchanges on clinoptilolite zeolite. *Sep. Sci. Technol.* 24: 1393-1416.
- Kerrisk, J. F. 1983. *Reaction-Path Calculations of Groundwater Chemistry and Mineral Formation at Rainier Mesa, Nevada*. LA-10560-MS. Los Alamos, New Mexico: LANL.

- Kerrisk, J. F. 1987. *Groundwater Chemistry at Yucca Mountain, Nevada, and Vicinity*. LA-10929-MS. Los Alamos, New Mexico: LANL.
- Knauss, K. G., and T. J. Wolery. 1988. The dissolution of quartz as a function of pH and time at 70°C. *Geochim. Cosmochim. Acta*. 52: 43-53.
- Meyer, R.E., W.D. Arnold, F.I. Case, G.D. O'Kelley, and J.F. Land. 1987. *Effects of Mineralogy on Sorption of Strontium and Cesium onto Calico Hills Tuff*. NUREG/CR-5463 ORNL-6589. Oak Ridge, Tennessee: Oak Ridge National Laboratory.
- Mumpton, F. A. 1960. Clinoptilolite redefined. *Amer. Mineral.* 45: 351-369.
- Murphy, W. M. 1986. Calculations of geochemical mass transfer as a function of temperature and time. *Proceedings of the Workshop on Geochemical Modeling*. K. J. Jackson and W. L. Bourcier, eds. Lawrence Livermore National Laboratory (LLNL) CONF-8609134: 27-33. Livermore, California: LLNL.
- Murphy, W. M. October 1989. Constraints on the chemistry of groundwater in the unsaturated zone at Yucca Mountain, Nevada, and in the proposed repository at that site. *Center for Nuclear Waste Regulatory Analyses Milestone Report*. San Antonio, Texas: CNWRA.
- Murphy, W. M. 1990. Reaction path models of gas-water-rock interactions in tuff (abstract). *Geological Society of America Abstracts with Programs*. 22(7): A158.
- Murphy, W. M., and H. C. Helgeson. 1989. Thermodynamic and kinetic constraints on reaction rates among minerals and aqueous solutions: IV. Retrieval of rate constants and activation parameters for the hydrolysis of pyroxene, wollastonite, olivine, andalusite, quartz, and nepheline. *Amer. Jour. Sci.* 289: 17-101.
- Ogard, A. E., and J. K. Kerrisk. 1983. *Groundwater Chemistry Along Flow Paths Between a Proposed Repository Site and the Accessible Environment*. LA-10188-MS. Los Alamos, New Mexico: LANL.
- Pabalan, R. T., and W. M. Murphy. 1990. *Progress in Experimental Studies on the Thermodynamic and Ion-Exchange Properties of Clinoptilolite*. CNWRA 89-006. San Antonio, Texas: CNWRA.
- Pitzer, K. S. 1973. Thermodynamics of electrolytes: theoretical basis and general equations. *J. Phys. Chem.* 77: 268-277.
- Pitzer, K. S. 1979. Theory: ion interaction approach. *Activity Coefficients in Electrolyte Solutions*. R. Pytkowicz, ed. Boca Raton, Florida: CRC Press: 157-208.

- Pitzer, K. S. 1987. A thermodynamic model for aqueous solutions of liquid-like density. *Reviews in Mineralogy* 17: 97-142.
- Pruess, K., J. S. Y. Wang, and Y. W. Tsang. 1990. On thermohydrologic conditions near high-level nuclear wastes emplaced in partially saturated fractured tuff 1. Simulation studies with explicit consideration of fracture effects. *Water Resour. Res.* 26: 1235-1248.
- Quade, J., T. E. Cerling, and J. R. Bowman. 1989. Systematic variations in the carbon and oxygen isotopic composition of pedogenic carbonate along elevation transects in the southern great basin, United States. *Geol. Soc. Amer. Bull.* 101: 464-475.
- Scatchard, G. 1968. The excess free energy and related properties of solutions containing electrolytes. *J. Amer. Chem. Soc.* 90: 3124-3127.
- Semmens, M. J., and M. Seyfarth. 1978. The selectivity of clinoptilolite for certain heavy metals. L. B. Sand and F. A. Mumpton, eds. *Natural Zeolites: Occurrence, Properties, Use*. New York: Pergamon: 517-526.
- Sposito, G. 1981. *The Thermodynamics of Soil Solutions*. New York: Oxford Univ. Press.
- Thorstensen, D. C., H. Haas, E. P. Weeks, and J. C. Woodward. 1990. Physical and chemical characteristics of topographically affected airflow in an open borehole at Yucca Mountain, Nevada. *American Nuclear Society Proceedings Nuclear Waste Isolation in the Unsaturated Zone Focus '89*: 256-270.
- Townsend, R. P. 1986. Ion exchange in zeolites: some recent developments in theory and practice. *Pure and Appl. Chem.* 58: 1359-1366.
- Townsend, R. P., P. Fletcher, and M. Loizidou. 1984. Studies on the prediction of multicomponent, ion-exchange equilibria in natural and synthetic zeolites. D. Olson and A. Bisio, eds. *Proceedings of the 6th International Zeolite Conf.* U.K.: Butterworths: 110-121.
- Townsend, R. P., and M. Loizidou. 1984. Ion exchange properties of natural clinoptilolite, ferrierite, and mordenite: 1. sodium-ammonium equilibria. *Zeolites* 4: 191-195.
- Vanselow, A. P. 1932. Equilibria of the base-exchange reactions of bentonites, permutites, soil colloids, and zeolites. *Soil Science* 33: 95-133.
- Vaniman, D., D. Bish, D. Broxton, F. Byers, G. Heiken, B. Carlos, E. Semarge, F. Caporuscio, and R. Gooley. 1984. *Variations in Authigenic Mineralogy and*

*Sorptive Zeolite Abundance at Yucca Mountain, Nevada, Based on Studies of Drill Cores USW GU-3 and G-3.* LA-9707-MS. Los Alamos, New Mexico: LANL.

White, A. F., H. C. Claassen, and L. V. Benson. 1980. *The Effect of Dissolution of Volcanic Glass on the Water Chemistry in a Tuffaceous Aquifer, Rainier Mesa, Nevada.* Geological Survey Water-Supply Paper 1535-A 34 pp.

Wolery, T. J. 1983. *EQ3NR, A Computer Program for Geochemical Aqueous Speciation-Solubility Calculations: User's Guide and Documentation.* UCRL-53414. Livermore, California: LLNL.

Wolery, T. J., K. J. Jackson, W. L. Bourcier, C. J. Bruton, B. E. Viani, K. G. Knauss, and J. M. Delany. 1990. Current status of the EQ3/6 software package for geochemical modeling. *Chemical Modeling of Aqueous Systems II.* D. C. Melchior and R. L. Bassett, eds. ACS Symposium Series 416. Washington, D.C.: American Chemical Society: 104-116.8.1.

### 3. THERMOHYDROLOGY

by Ronald T. Green and Franklin T. Dodge

*Investigators: Ronald T. Green (CNWRA), Franklin T. Dodge (SwRI),  
Steve J. Svedeman (SwRI), and Ronald H. Martin (CNWRA)*

#### 3.1. INTRODUCTION

Technical issues and uncertainties for the proposed Yucca Mountain HLW repository site require research on thermohydrological phenomena, i.e., phenomena associated with heat and fluid flow, to provide information for performance assessment and design criteria. Phenomena examined in the Thermohydrology Research Project are those driven by heat emanating from HLW emplaced in a geologic repository. The resultant information will be used to evaluate models of heat-driven flow processes used in performance assessments.

The understanding of coupled flow processes in the unsaturated (vadose) zone is in the developmental stage. Only in recent years has attention focused on unsaturated zones in consolidated geologic media. Of particular interest in the understanding of flow and transport in this zone is characterization of fracture/matrix interactions and the ability of a fracture to either impede or augment water movement through a medium, especially in the region close to heat-generating waste. This understanding is crucial because fractures may potentially impede flow and transport under one set of conditions but act as a conduit under different conditions.

There is limited understanding of the processes involved in the thermally driven formation of regions of saturation in otherwise partially saturated or unsaturated geologic media composed of fractures and matrix. In addition, mechanisms responsible for thermally driven, mass transport in the vicinity of a HLW repository are not clearly understood.

Transport of radionuclides from a HLW package is highly dependant on the temperature of heat-generating HLW. The heat-pipe phenomenon, potentially important mechanism in the region proximal to the waste, is not entirely understood. A heat-pipe, if present, can provide an efficient mechanism to remove heat by phase change of water (vaporization) near the heat source and transport of the vapor away from the source where it condenses at some distance at lower temperatures. Although the presence of a heat pipe proximal to heat-generating HLW has been, in theory, investigated and assessed, physical evidence on which to base predictions at the field scale is lacking.

A thorough understanding of the phenomena dependant upon the thermal regime associated with heat-generating HLW is required to provide information to predict flow and transport at a geologic repository and assist in its prudent design. The objective of the Thermohydrology Research Project is to investigate in detail the thermohydrologic-affected flow and transport phenomena both theoretically and through evaluation of laboratory-scale experiments and to extrapolate this information to repository-scale through use of dynamic

similarity principles. This report summarizes the progress of the Thermohydrology Research Project performed through 1990.

### 3.2. TECHNICAL OBJECTIVES

The specific objectives of the Thermohydrology Research Project are summarized as follows:

- Perform a critical assessment of the state-of-knowledge of thermohydrology for unsaturated fractured media, in the context of present NRC activities in the HLW geologic repository program. This assessment requires an in-depth review of existing literature and on-going programs. The assessment will focus on flow processes, heat transfer mechanisms, and state-of-the-knowledge experimental methods for porous media.
- Perform a detailed dynamic similarity or similitude analysis on the complete set of governing equations relevant to unsaturated flow and to determine the set of dimensionless parameters required to conduct appropriate laboratory simulations. In this analysis of modeling parameters, the range of parameter applicability and limitation on the magnitude of these parameters, as constrained by the principles of dynamic similarity, will be determined.
- Identify potential problems associated with the design and performance of laboratory simulations with scaled geometry, fluid, media, and other relevant properties subject to modeling distortion.
- Perform a series of separate effects experiments to identify and understand the role of each effect in the overall coupled processes involved in thermohydrologic phenomena.
- Design and perform comprehensive experiments whose results will continue to identify key dependent and independent parameters and their relationships to each other in the context of thermohydrologic issues.
- Develop the laboratory facilities, experimental methods, measurement techniques, and associated analytic skills to evaluate and validate other program results and to provide a high quality of technical assistance and research in support of NRC's licensing of a HLW repository.
- Examine and correlate laboratory results with field data in order to aid in the design of future field experiments.

Five tasks have been delineated for the purpose of accomplishing these objectives. Three of these were active during 1990 and are discussed in this section. They are: Task 1-Assessment of the State-of-Knowledge of Thermohydrology in Unsaturated Media; Task 2-Design and Execution of Preliminary Separate Effects Experiments; and Task 3-Design of Unsaturated Zone Thermohydrological Experiments.

### **3.3. ASSESSMENT OF THE STATE-OF-KNOWLEDGE OF THERMOHYDROLOGY IN UNSATURATED MEDIA**

An assessment of the state-of-knowledge of thermohydrology related to HLW has continued throughout the duration of the project. Additional efforts were expended this past year, including technical interchanges with DOE contractors.

Technical documents were summarized and are being incorporated into the Technical Document Index (TDI) maintained at the Center for Nuclear Waste Regulatory Analyses (CNWRA). These summaries will be available to the staff at both the NRC and CNWRA for future review and reference.

Unsaturated media pose significant challenges in modeling and phenomenological interpretations of their thermohydrologic behavior. While technology has been developed for saturated conditions, the knowledge base for unsaturated media is sparse. A key part of the strategy to develop the knowledge base has been participation in technical-exchange meetings and focused workshops. A series of technical interchanges involving CNWRA with NRC, representatives of the Department of Energy (DOE), and DOE contractors have occurred. The interchanges were with researchers at Lawrence Berkeley Laboratory on March 12, 1990; at Lawrence Livermore Laboratory on April 3, 1990; at Los Alamos National Laboratory on May 21, 1990; and at Sandia National Laboratory on May 22, 1990. Experiments with relevancy to thermohydrology were observed and discussed.

### **3.4. DESIGN AND EXECUTION OF PRELIMINARY SEPARATE-EFFECTS EXPERIMENTS**

Six separate-effects experiments were designed and performed to identify individually the key phenomena affecting the coupled and complex thermohydrological phenomena and to determine the magnitude of their influence for use in similarity studies and future experimental design. The effect of heat on the following processes has been investigated in these experiments:

- Liquid infiltration and distribution,
- Local heating of pore liquid,
- Gas and liquid convection,
- Matrix/fracture interaction,
- Transient heating, and
- Forced vs. free convection.

To investigate these phenomena, experiments were designed to measure a number of state variables within a test chamber such as temperature, suction pressure, and moisture content, using, respectively thermistors, tensiometers, and a gamma-ray densitometer. The flow of liquid water was monitored using colored dyes injected into the test chamber. The location of the dyes was recorded periodically with photographs.

The complexity of the early experiments was minimized but increased slightly in the later tests as basic relationships were investigated and as laboratory and measurement techniques improved. The first three experiments (Tests 1, 2, and 3) were conducted under isothermal conditions (more precisely, at the fluctuating ambient-temperature conditions) to investigate the processes affecting liquid infiltration and distribution. The latter tests (Tests 4, 5, and 6) were nonisothermal with a temperature gradient imposed across the test chambers for investigation of the thermal effect on liquid and gas flow. The media contained in the test chambers were comprised first of uniform beads (Tests 1 and 2); second of uniform bimodally sized beads (Tests 3 and 4); and third of uniform bimodally sized beads with a superimposed fracture simulated with uniformly sized beads (Tests 5 and 6).

### **3.4.1. Separate Effects Experimental Apparatus**

Experiments were performed using two basic sizes of test chambers. Experiments 1 through 4 were performed using the 60.5 x 66.0 x 7.6-cm test chamber (Figure 3-1). A test chamber of this comparatively large size was initially selected to provide an opportunity to inspect the processes of interest in detail (for example, flow patterns and drying fronts), but its size resulted in several technical difficulties. The large side walls exhibited significant levels of heat loss and temperature fluctuations, and the big interior caused difficulties in fabricating a uniform medium, and resulted in prohibitively long times for the processes under investigation to approach steady state.

To alleviate these difficulties, separate effects Tests 5 and 6 were performed using a smaller test chamber. The chamber for Test 5 measured 14.6 x 20.7 x 1.8 cm. Test 6 was conducted in a similarly sized chamber (15.2 x 20.3 x 5.3 cm); however, the thickness was increased to permit installation of monitoring instruments into the interior of the chamber and to provide a larger signal for the densitometer readings.

#### **3.4.1.1. Large Test-Chamber Construction**

The two side walls of the large chamber were constructed of a 1.9-cm thick clear acrylic plastic sheet. The four ends were constructed of anodized aluminum. The completed test chamber was sealed (with the exception of a small vent at the top of a side wall of the chamber to maintain atmospheric pressure) to prevent the loss of water or water vapor during the experiments. The small vent was presumed to not affect the balance of mass in light of the relatively short duration of these experiments.

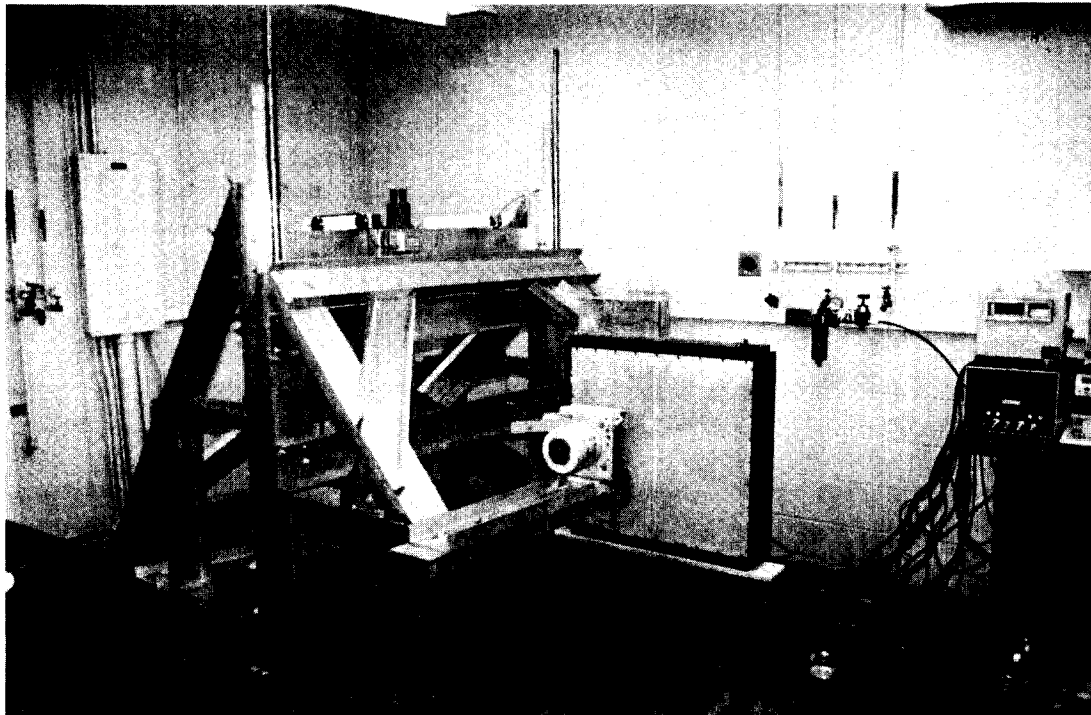


Figure 3-1. Test chamber - front view

The ends of the test chamber contained heat exchangers for maintaining those boundaries at constant temperatures. Although the first three experiments were conducted under approximately isothermal conditions, the heat exchangers permitted Test 4 to be performed under controlled, nonisothermal conditions.

A series of five tensiometers and seven thermistors was installed into the side of the larger test chamber for monitoring the suction pressure and temperature, respectively, during the experiment. The configuration of the sensor array is illustrated in Figure 3-2.

#### 3.4.1.2. *Small Test-Chamber Construction*

Tests 5 and 6 were performed using the smaller test chamber. The two side walls were constructed of 1.3-cm thick acrylic plastic for Test 5 and 1.9-cm acrylic plastic for Test 6. A 1.9-cm thick sheet of styrofoam insulation was applied to both side walls of the test chamber to reduce heat loss and inhibit thermal fluctuations. As in the larger test chamber, this smaller size test chamber was also fitted with heat exchangers but in the vertical not horizontal edges. Schematics in Figure 3-3 and 3-4 illustrate the design details of the smaller chambers.

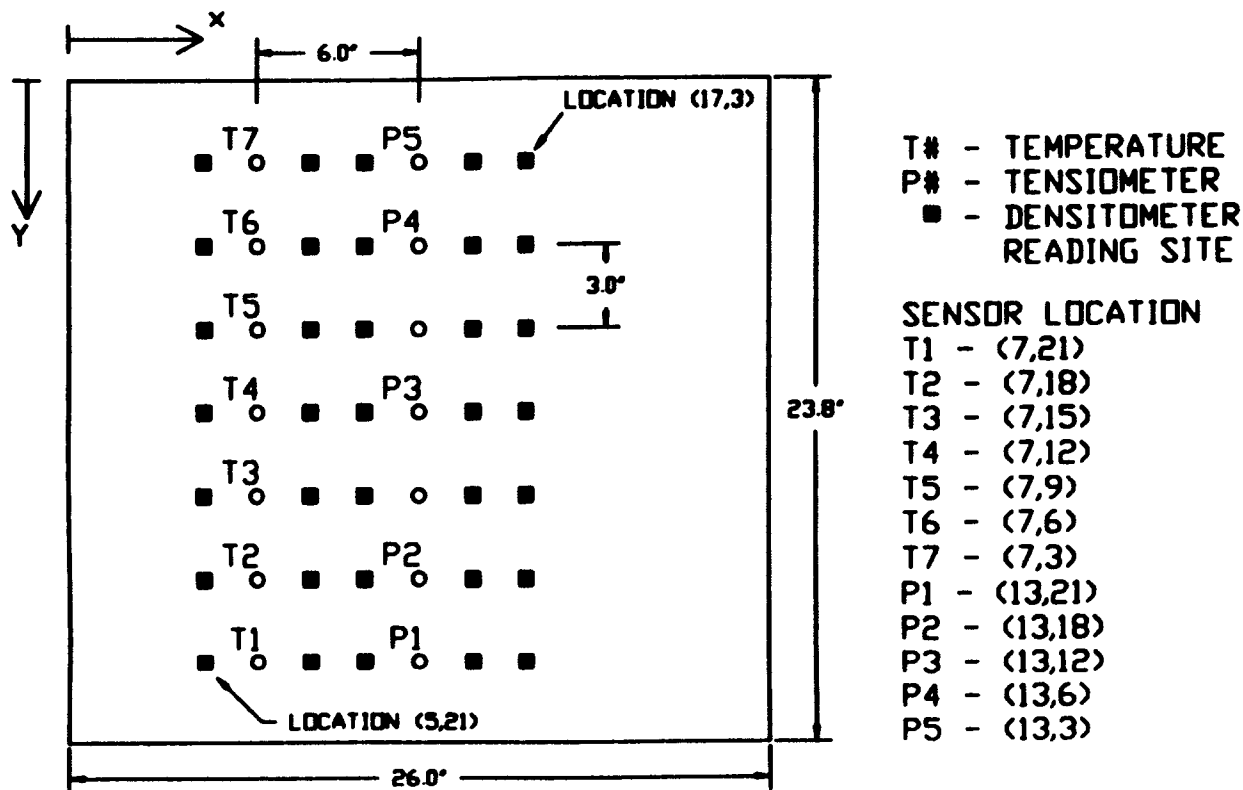


Figure 3-2. Configuration of sensors in the larger test chamber

Because of the smaller size of the test chamber used in Test 5, neither temperature probes nor tensiometers were installed in the side walls into the medium. However, a temperature probe was installed in the two heat exchangers. The greater thickness of Test 6 permitted the installation of two tensiometers into the interior of the chamber.

Two ports (one one-third of the distance up on the left and one one-third of the distance up on the right and both approximately 2.5 cm in from the heat exchangers) were installed in the side walls of the smaller test chambers to permit injection of colored dyes into the medium. The outer ends of the ports were sealed after injection to prevent water from moving into or out of the chamber. Additional access ports were installed into the top and bottom ends of the Test 6 chamber to allow full desaturation and saturation of the media in the chamber. This permitted baseline saturation measurements with the densitometer after the termination of the experiment.

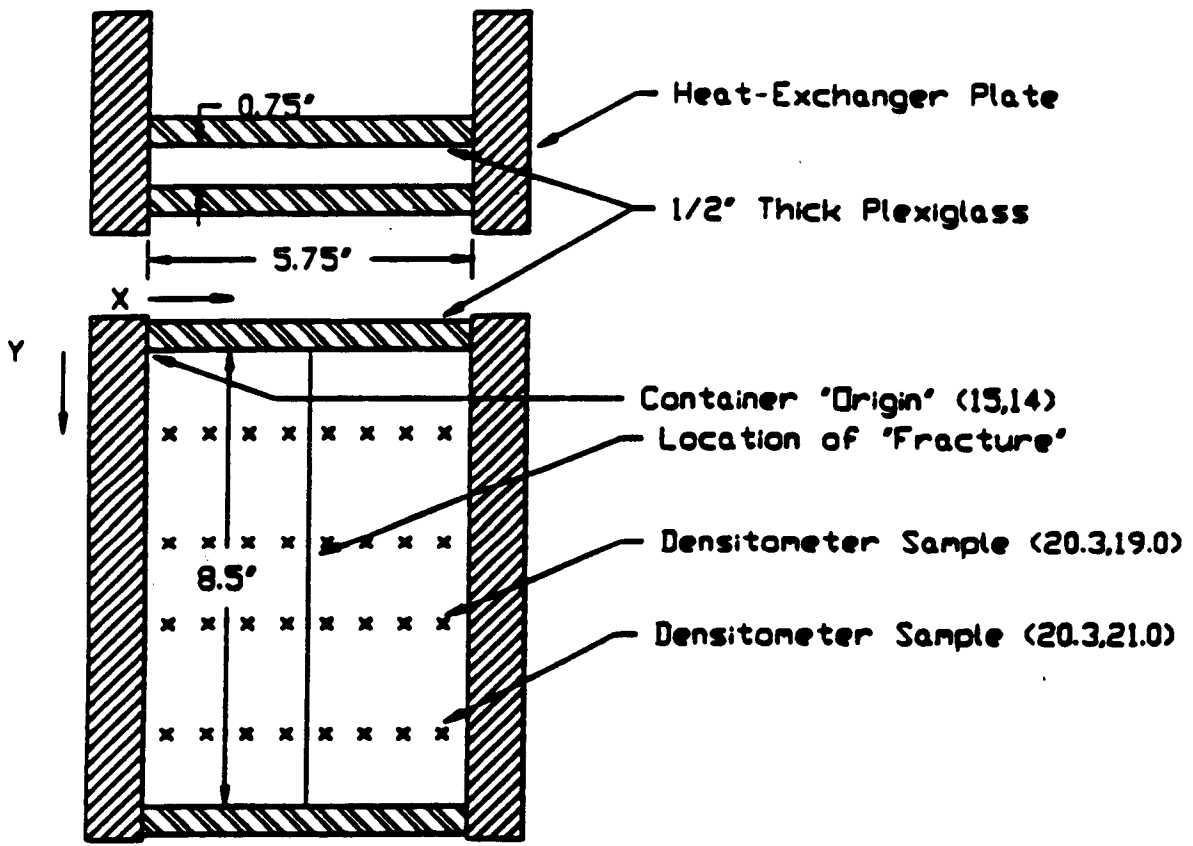


Figure 3-3. Design details of the smaller test chamber used in Test 5 with densitometer measurement locations

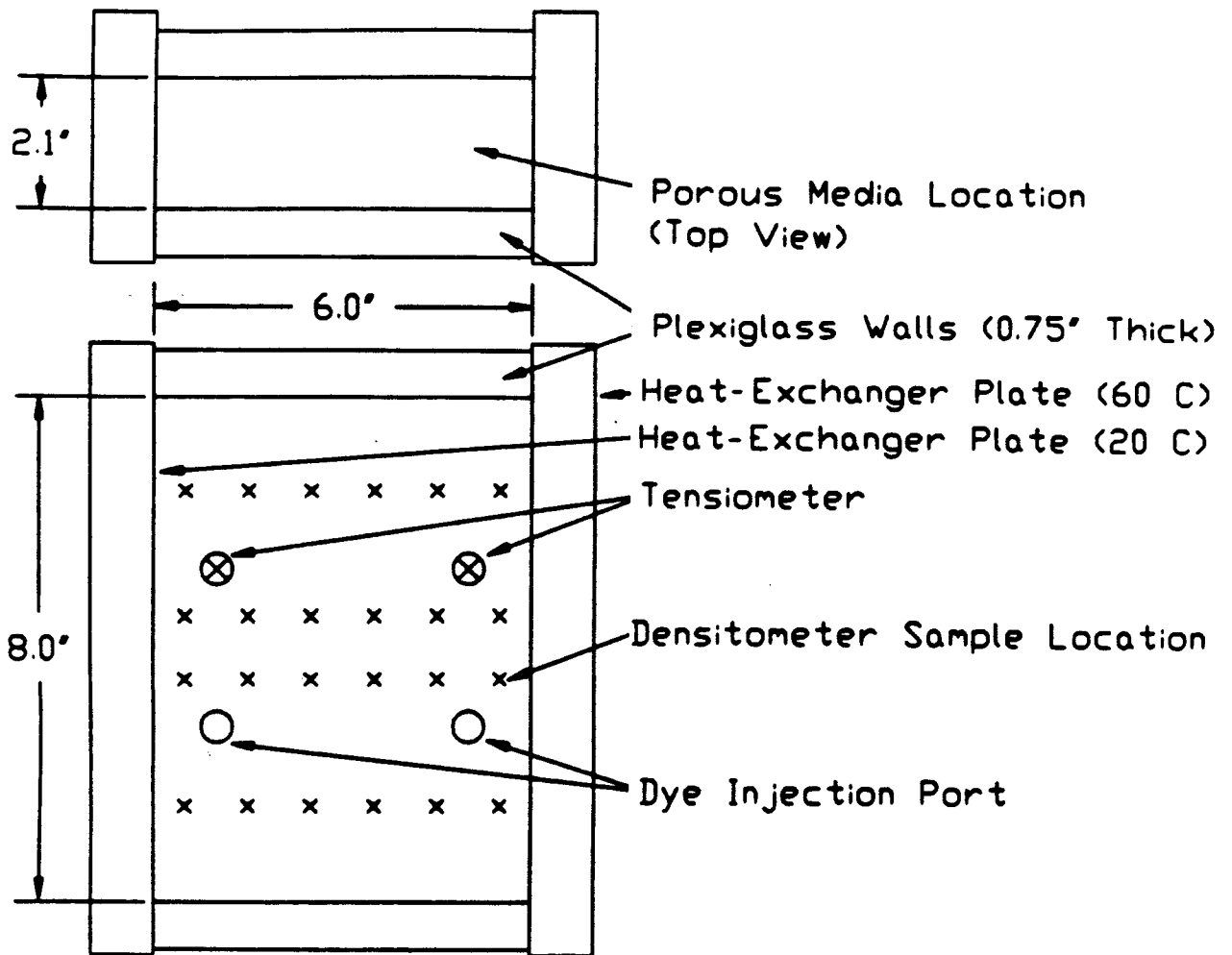


Figure 3-4. Design details of the smaller chamber used in Test 6 with tensiometer and densitometer measurement locations

### 3.4.2. Support Equipment

#### 3.4.2.1. Selection and Description

Selection of instrumentation used in the separate effects experiments was based upon applicability and usefulness of instruments for specific experiments. Suction pressure was measured during Tests 1 through 4 and 6 using tensiometers. The tensiometers were constructed of 0.95-cm ceramic porous cups connected to pressure sensors (designed for negative gauge pressures of 0 to 3.5 meters of water) using 0.95-cm outer diameter (OD) polyvinyl chloride (PVC) tubing (Figure 3-5). The 140PC Series pressure sensors, manufactured by Micro Switch, were equipped with an amplifier. The ceramic porous cups, manufactured by Soil Moisture Equipment Corporation, were one-bar high-flow cups. The ceramic porous cups are documented to have a pore size of 2.5 microns and a saturated hydraulic conductivity of  $8.6 \text{ E-6 cm/sec}$ .

The ambient temperature and the temperature within the test chambers were measured during the experiments using thermistors. The thermistors, manufactured by Yellow Spring Instruments, are in the 46000 Series manufactured by Yellow Spring Instruments and are specified to be accurate to within  $0.51^\circ\text{C}$  over the range of interest (0 to  $100^\circ\text{C}$ ).

A densitometer measured the moisture content in the separate-effects experiments. In Tests 1 through 4, a Texas Nuclear gamma-ray densitometer Model 9700D was used; the gamma-ray source was 500 millicuries of  $^{137}\text{Cs}$ . In Tests 5 and 6, a new  $^{241}\text{Am}$  stabilized NaI scintillation detector (Ludlum Measurement Model 44-14) equipped with a stabilized gamma counter/scaler single-channel analyzer (Model 2200-1), was used with the densitometer. Styrofoam insulation, added to the detector during Test 6 helped reduce densitometer fluctuations due to temperature variations. The gamma-ray densitometers were attached to a planar traversing table for scanning of the entire test chamber, thus leaving the test chamber stationary during the experiment. The traversing system had a location precision error of less than 0.4 mm in both the X and Z directions. The densitometer began and terminated each scanning sequence by recording the number of gamma-ray counts that penetrated through an aluminum mass located at the edge of the chamber. The detection counts recorded prior to and subsequent to each scanning sequence were compared to detect instrument drift that may have occurred during the course of the scanning sequence. The locations of the gamma-ray attenuation measurements used in Tests 5 and 6 are illustrated in Figure 3-3 and 3-4, respectively.

The data produced by the experiment were collected using a data acquisition system (DAS). Additional operational tasks conducted by the DAS included automatic data sampling, conversion of raw data to engineering units, control of the densitometer traversing system, data logging, data display and data plotting. The operation of the DAS was controlled by an IBM PS 2/80. Also included in the DAS were a multiplexer (HP3458A), a multimeter (HP3488A) and a traversing system controller (VELMEX 28351) to collect experimental data and operate the densitometer tracking and measurement system.

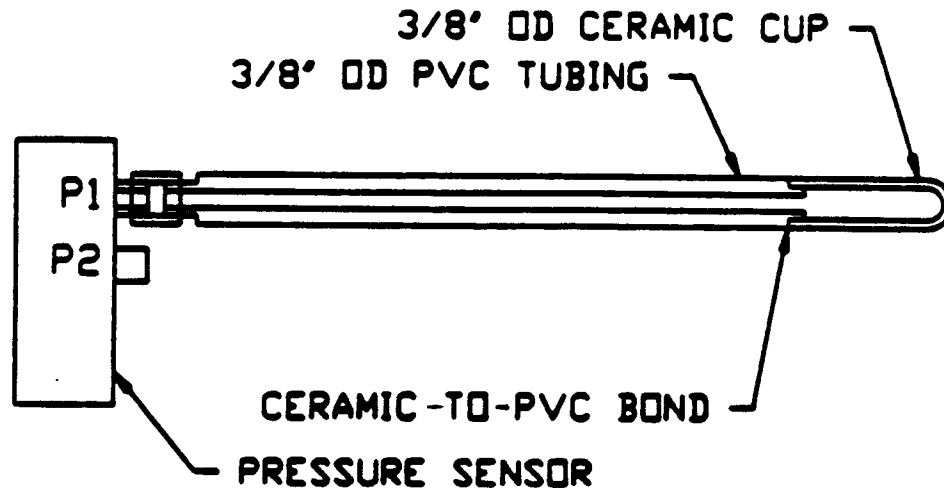


Figure 3-5. Schematic of the tensiometer

#### 3.4.2.2. Instrumentation Modifications

Several components of the densitometer were modified or altered through the course of the experiments. The densitometer was originally designed for pipeline applications. Accordingly, the 500 millicurie source of  $^{137}\text{Cs}$  had an incident source beamspread of 14 degrees from the principal direction. The incident gamma rays were collimated using 2.8-cm thick lead shielding with a 3.3 by 3.8-cm square aperture in the facing of the detector.

Incident gamma radiation from a  $^{137}\text{Cs}$  source is attenuated through a medium according to the following relationship,

$$I/I_0 = e^{-0.085\rho x} \quad (1)$$

where  $I_0$  is the incident radiation and  $I$  is the attenuated radiation. The coefficient, 0.085, is peculiar to  $^{137}\text{Cs}$ , which emits gamma radiation with an energy of 0.661 MeV. The symbol  $\rho$  denotes density, and  $x$  is the thickness of the medium through which the gamma rays are emitted. Therefore, the 2.8-cm thick sheet of lead shielding with density of 11.34 gm/cc absorbed approximately 93 percent of the incident gamma radiation everywhere except at the aperture.

Tests 1 through 4 were conducted using a test chamber with a cross-sectional width of 7.6 cm. The gain of the densitometer responses was adjusted relative to zero and 100 percent saturation. To ensure that all densitometer responses would be between the arbitrarily designated upper and lower limits, the full range for potential responses was set to slightly larger limits of 0 to 300 than the observed zero and 100 percent saturation readings of 60 and 260, respectively. Therefore, according to this arbitrary scaling scheme, a densitometer measurement of the medium at zero saturation gave a response of approximately 60 while full saturation gave a response of 260. Variations in the recorded responses of a fixed medium (aluminum blocks) were observed to be approximately 5 relative to the above described arbitrary scale. This translates to a variation of 2.5 percent of the total response associated with the maximum potential change. This variation is attributed to thermal drift in the densitometer, gamma-count probabilistic uncertainty, and other unidentified causes.

Some portion of the difference in count rates at various saturations may be attributed to the change in density of water resulting from temperature variations. The density of water is 0.9982 gm/cc at 20°C and 0.9832 at 60°C for a difference of 1.5 percent (*CRC Handbook of Physics and Chemistry*, 1982). The associated change in gamma-ray attenuation for water-density-induced changes in the 7.6-cm thick medium is calculated using Eqn. (1) to be 0.3 percent. Changes in gamma-ray attenuation attributed to thermally induced changes in water density are thereby not considered significant. Based on this analysis, limited quantitative use of the densitometer responses from Tests 1 through 4 is possible.

The densitometer detector was replaced prior to Test 5 to permit greater accuracy in gamma radiation measurements and to provide increased flexibility and ease in operation. Gamma radiation was recorded in terms of the more conventional counts per minute method with the new detector and not according to the arbitrary scaling scheme used in Test 1 through 4. In order to limit the solid angle of the incident gamma rays with the new detector, 5.1-cm thick lead shielding with a 0.6 by 0.6-cm square aperture was attached to the facing of the detector. The use of the smaller aperture as compared to the shielding aperture in Tests 1 through 4 was made possible by using the new detector. Additionally, the thicker lead shielding absorbed over 99 percent of the gamma radiation directed at the detector but not at the aperture.

The sensitivity of the densitometer to changes in moisture content in the Test 5 test container has been evaluated. (The thickness of the medium in Test 5 was 1.9 cm. Therefore, for a total porosity of 34.8 percent, the average cumulative thickness of pore space would be 0.66 cm.) The chamber was scanned with the medium at zero saturation with a response of approximately 130,000 counts per minute (cpm). At full (100 percent) saturation, the response was approximately 122,400 cpm for a difference of about 7,600 cpm between readings at zero and 100 percent saturation, which represents a total change of 5.8 percent. Similar counts for Test 6 will be made upon completion of the experiment.

Similar to Tests 1 through 4, a portion of the difference in count rates is attributed to the change in density of water resulting from temperature variations. The

associated change in gamma-ray attenuation is calculated using Eqn. (1) to be 0.1 percent. Changes in gamma-ray attenuation for Test 5 attributed to thermally induced changes in water density are not considered significant.

Variations in the recorded responses at fixed saturation levels were observed to be approximately 2,000 cpm. This variation is attributed to thermal drift in the densitometer, gamma-count probabilistic uncertainty, and other unidentified causes. Therefore, even though the variation in measurements is only 1.5 percent of the total count rate, the magnitude of the variation is roughly one-fourth of the total possible response attributed to changes in saturation. Based on this analysis, the use of densitometer responses to determine saturation levels quantitatively is not justified. The semi-quantitative analysis of densitometer measurements, however, does provide useful insight of Test 5.

### **3.4.3. Experimental Media Characteristics**

Industrial-grade, silica-glass beads were selected for use as the media in the preliminary separate effects experiments to avoid heterogeneity inherent to natural media and to have control over material properties. The values of media characteristics integral to this analysis were either calculated, when possible, or estimated for use in this investigation. The bead media were characterized according to size, porosity, and hydraulic properties, as described in this section, followed by descriptions of calculations and measurements of the characteristics evaluated during the execution of the five separate effects experiments.

#### **3.4.3.1. *Bead Size Calculations***

Three different bead sizes, factory designated as Nos. 812, 1420, and 2740, were used in Tests 1 through 6. The No. 812 size beads were factory-sieved between 125 and 177 microns; the No. 1420 size beads were sieved between 74 and 105 microns, and the No. 2740 size beads were factory-sieved between 28 and 53 microns. Population and volume grain-size distribution statistics were determined for the three different bead sizes. The grain-size distribution characteristics for the beads are summarized in Table 3-1.

#### **3.4.3.2. *Porosity Measurements***

Total porosity was measured for the various-sized glass-bead media employed in this investigation. The porosities of the bead media were primarily calculated from the volume and weight of the water content. Porosity was also checked during measurement of the media characteristics and during the execution of the separate effects experiments.

The porosities by volume and by weight are as follows. The No. 812 size beads had a volumetric porosity of 37.2 percent and a porosity by weight of 37.1 percent. The No. 1470 beads had a porosity by volume of 38.1 percent and a porosity by weight of 37.7 percent. The smallest sized beads, No. 2740 size, had a volumetric porosity of 37.6 percent and a porosity by weight of 37.8 percent.

**Table 3-1. GLASS-BEAD POPULATION AND VOLUME DISTRIBUTION STATISTICS**

Population Statistics						Volume Statistics			
Bead-Class No.	Sample #	Mean ( $\mu\text{m}$ )	Standard Deviation ( $\mu\text{m}$ )	Median ( $\mu\text{m}$ )	Coef. Variation %	Mean ( $\mu\text{m}$ )	Standard Deviation ( $\mu\text{m}$ )	Median ( $\mu\text{m}$ )	Coef. Variation %
812	160-1	130.27	1.46	140.09	1.12	159.54	1.40	162.61	0.88
1420	160-2	134.95	1.46	143.51	1.08	171.25	1.42	175.79	0.83
1420	80-1	82.24	1.46	88.19	1.77	106.59	1.41	108.60	1.33
1420	80-2	89.42	1.46	96.31	1.64	114.64	1.40	116.90	1.22
2790	40-1	58.84	1.43	62.81	2.44	78.90	1.51	78.45	1.91
2790	40-2	58.97	1.44	63.00	2.43	79.49	1.52	78.91	1.91

The porosity by volume of the No. 812 size beads was calculated during the moisture characteristic curve experiments to be 36.1 percent. Similarly, the porosity measurement for the No. 2740 size beads was 34.8 percent and for the Nos. 1420 and 2740 bead mix was 31.4 percent. The porosities by volume measurements made during the separate effects experiment Test 3 were 31.7 percent for the Nos. 1420 and 2740 bead mix.

#### **3.4.3.3. Hydraulic Conductivity Calculations**

The moisture characteristic curve was determined for the bead mix used in Tests 3 through 6 using the technique specified in ASTM D 2325 ("Capillary-Moisture Relationships for Coarse- and Medium-Textured Soils by Porous-Plate Apparatus," ASTM, 1977). A positive-pressure, porous-plate apparatus was used to incrementally increase pressure on the medium and measure the amount of water retained in the pores of the medium at those pressures. Consequently, only drying curves were determined using this procedure.

After the data for the capillary-moisture relationships were measured, the van Genuchten parameters were calculated by regressing a curve to the collected data and determining the parameters using the regressed line (van Genuchten, 1978). The unsaturated hydraulic conductivity for the bead media were then determined using the van Genuchten parameters. The Mualem-based restriction of  $m = 1 - 1/n$  was assumed in these calculations.

The capillary-moisture relationship for the Nos. 1420 and 2740 size bead mixture is illustrated as a water-retention curve in Figure 3-6. Measurement of pressures greater than 4.2 meters of water were attempted but were not successful because a pressure seal failed at the higher pressure. Also illustrated in this figure is a regression line that approximates the observed data. The van Genuchten parameters calculated from the regression line are a value for  $\alpha$  of 0.759, a value of  $n$  of 7.38, and a residual water content value of 0.341. These values for  $\alpha$ ,  $n$ , and the residual water content are incorporated as input for the numerical simulation (Section 3.6).

The unsaturated hydraulic conductivity was calculated using the closed-form solution of van Genuchten (1980) and the above mentioned values for  $\alpha$ ,  $n$  and the residual water content. These values are plotted for various values of negative pressure head in Figure 3-7.

#### **3.4.4. Separate Effects Experiments**

A total of six separate effects experiments was conducted as part of Task 2 of the Thermohydrology Research Project. The six experiments, referred to as tests, are described in this section and summarized in Table 3-2.

In Tests 1 and 2, the chamber was filled with single-sized glass beads. Test 1 was conducted using No. 812 size glass beads, and Test 2 used No. 2740 size beads. The medium in Test 3 and 4 was comprised of equal weights of Nos. 1420 and 2740 size glass beads.

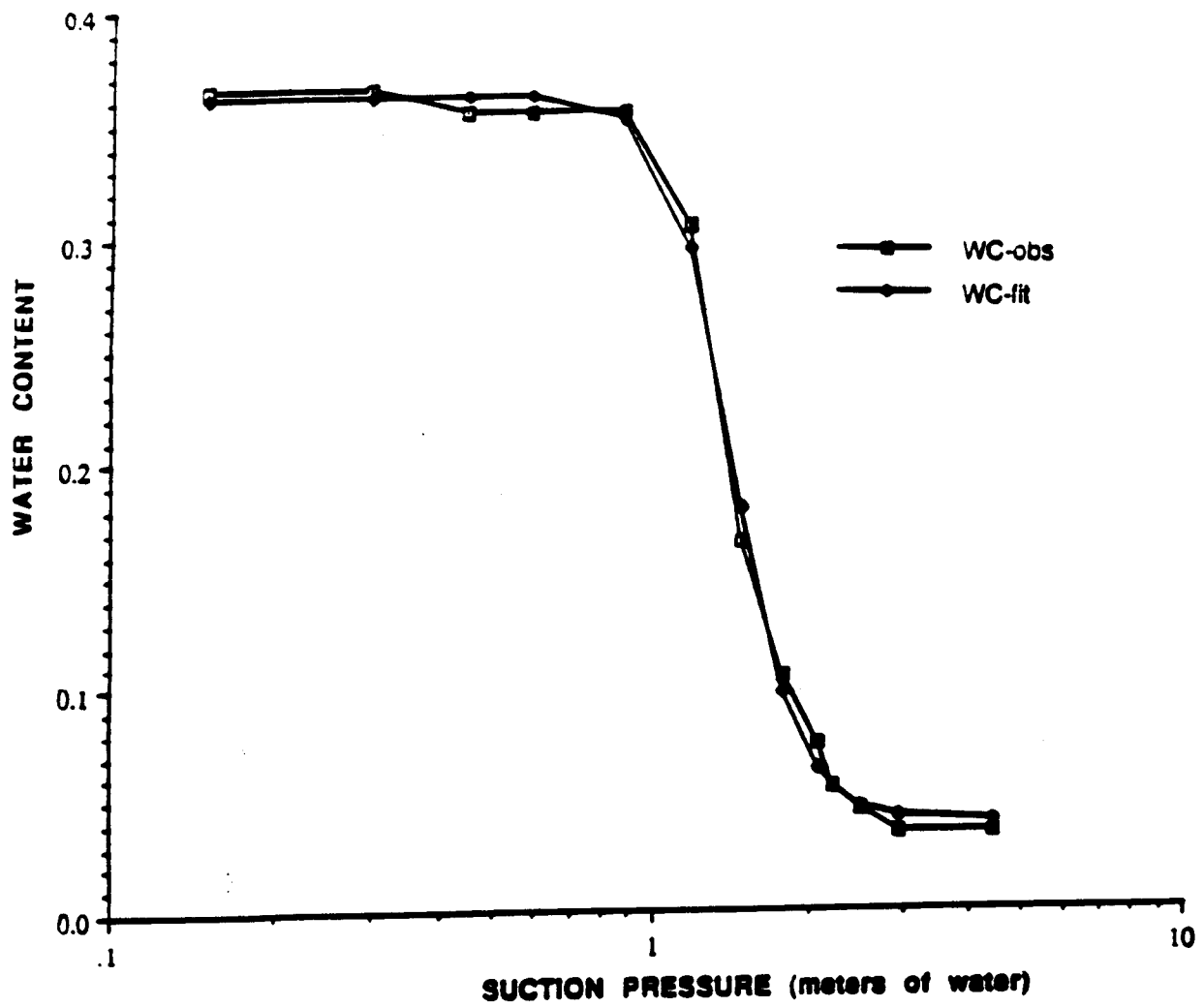


Figure 3-6. Moisture-release curve for No.s 1420 and 2740 glass-bead mixture

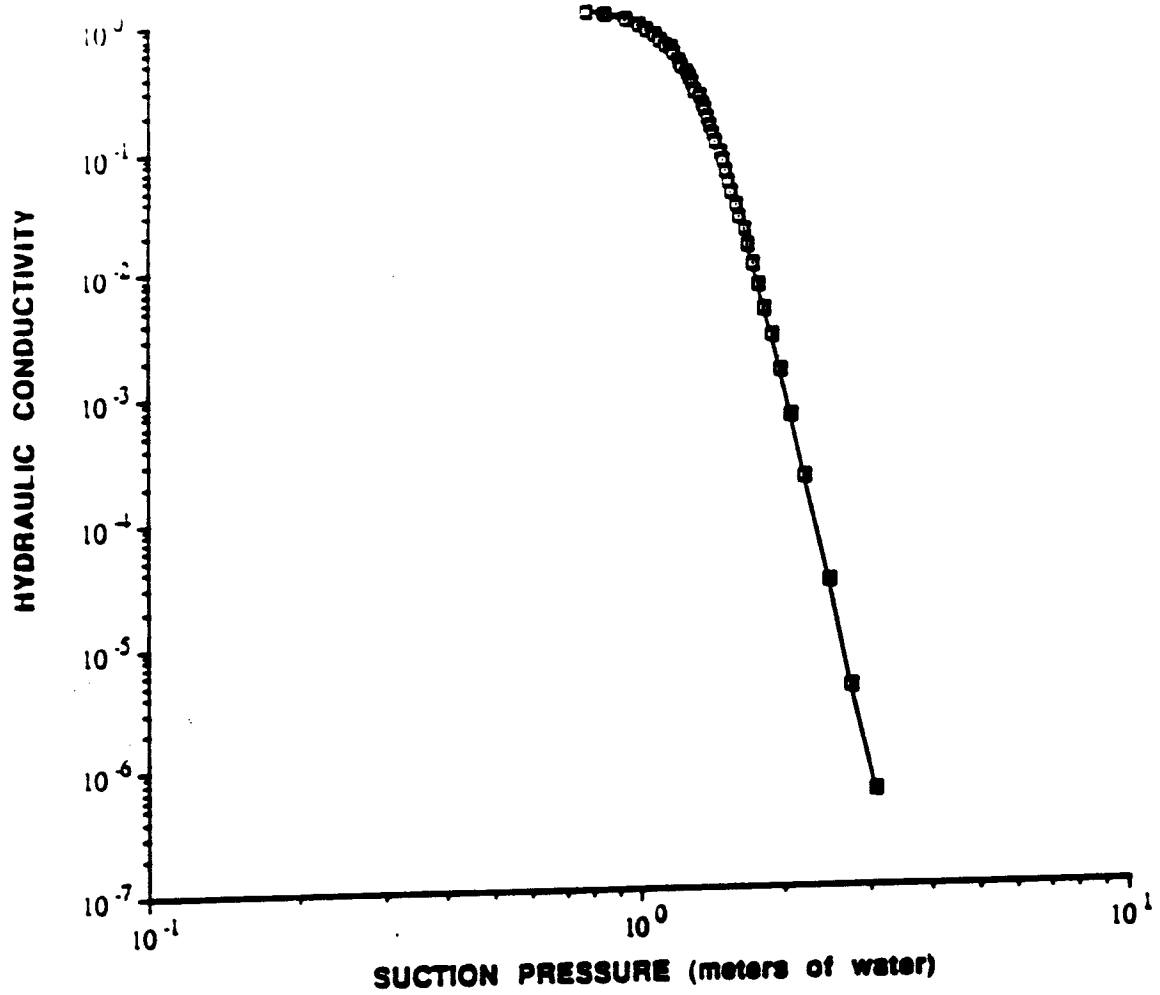


Figure 3-7. Calculated hydraulic conductivity curve for No.s 1420 and 2740 glass-bead mixture

Table 3-2. SUMMARY TO THE SEPARATE EFFECTS EXPERIMENTS

Test	Chamber Size (cm)	Thermal Boundary Conditions	Measurements		Saturation Measurements	Mediums
			Temperature Sensors	Pressure Sensors		
1	60.5 x 66.0 x 7.6	isothermal	7 internal 1 ambient	5 internal 1 ambient	7 rows of 5	uniform beads No. 812
2	60.5 x 66.0 x 7.6	isothermal	7 internal 1 ambient	5 internal 1 ambient	7 rows of 5	uniform beads No. 2740
3	60.5 x 66.0 x 7.6	isothermal	7 internal 1 ambient	5 internal 1 ambient	7 rows of 5	No.s 1420 and 2740 bead mix
4	60.5 x 66.0 x 7.6	rt & lf - adiabatic a) lower @ 20°C upper @ 60°C b) lower @ 80,95,105°C upper @ 20°C	7 internal 1 ambient	5 internal 1 ambient	7 rows of 5	No.s 1420 and 2790 bead mix
5	14.6 x 20.7 x 1.8	upper & lower - adiabatic a) rt at 20°C lf at 60°C b) rt at 60°C lf at 20°C	2 in heat exchanger 1 ambient	1 ambient	4 rows of 8	No.s 1420 and 2790 bead mix w/No. 812 fracture
6	15.2 x 20.3 x 5.3	upper & lower - adiabatic a) rt at 20°C lf at 60°C	2 in heat exchanger 3 on side wall 1 ambient	2 internal 1 ambient	4 rows of 6	No.s 1420 and 2790 bead mix w/No. 812 fracture

A medium with a simulated fracture was used in both Tests 5 and 6. The "matrix" medium was comprised of a mixture of equal parts of Nos. 1420 and 2740 size glass beads with a simulated "fracture" comprised of No. 812 size beads. The matrix mixture was pre-mixed with a pre-determined amount of water to provide a medium with an approximately uniform saturation content of 60 percent. The partially saturated bead mixture was placed in the upright chamber through the left side wall that had been removed. The moist mixture was periodically pressed into position during filling. After approximately half of the chamber was filled with the bead mixture, 2 ml of No. 812 size glass beads were evenly sprinkled over the exposed medium face. Since the area of the simulated fracture is 39.3 cm<sup>2</sup>, the average calculated thickness of the fracture was approximately 500 microns, or an average thickness of approximately three glass beads. The remainder of the chamber was then filled and compacted with the moist glass-bead mixture. After the final end plate of the chamber was secured in place, the chamber was rotated to its upright position so that the simulated fracture was vertically oriented and the heat exchangers were located on the right and left sides of the chamber.

#### **3.4.4.1. Experiment Test 1**

Test 1 was performed during an 11-day period to observe water movement through the No. 812 glass beads under near-isothermal conditions. A total of 3875 ml of deionized water was injected to fill 37 percent of the void space of the medium. After 8 days an additional 7600 ml of deionized water was added to the test chamber to bring the level of saturation to 100 percent. A vacuum pump was used to remove 3065 ml of water. Measured during this experiment were the ambient temperature and barometric pressure, temperature recorded by seven sensors within the test chamber, suction pressures measured relative to the barometric pressure using five tensiometers and moisture content measured with the densitometer (expressed in terms of relative counts).

#### **3.4.4.2. Experiment Test 2**

Test 2 was performed over a 13-day period to observe water movement through No. 2740 size glass beads under near-isothermal conditions. A total of 1100 ml of deionized water was initially injected to fill 11 percent of the void space of the medium. After 3 days, a total of 5870 ml of water was added to increase the average level of saturation to 68 percent. After 5.5 more days, deionized water was added to bring the level of saturation to 100 percent. A total of 220 ml of water was removed under a vacuum of 2.1 meters of water. The same parameters measured during Test 1 were measured throughout Test 2.

#### **3.4.4.3. Experiment Test 3**

Test 3 was performed over a 12-day period to observe water movement in a mixture of Nos. 1420 and 2740 beads under isothermal conditions. A total of 2000 ml of deionized water was injected to fill 21 percent of the void space. An additional 7610 ml of water were injected under a hydraulic head of 61 to 91 cm to saturate the medium. A

total of 1021 ml of water was extracted from the medium. The same parameters measured during Tests 1 and 2 were measured throughout Test 3.

#### **3.4.4.4. Experiment Test 4**

Test 4 was performed over a 23-day period to monitor water movement in a partially-saturated medium under nonisothermal conditions. The intact test chamber and medium remaining after the termination of Test 3 was used in Test 4. At commencement of the test, the temperature of the top heat exchanger was set at 60°C. The temperature of the lower heat exchanger was maintained at approximately 20°C imposing a temperature gradient of 0.66°C/cm for 3 days. The imposed vertical temperature gradient was reversed for the remainder of the experiment. At days 6, 8, and 9 of the experiment, the temperature of the lower heat exchanger was increased to 80°C, 95°C, and 105°C, respectively, while the top heat exchanger was maintained at 20°C. The temperature gradients for these three settings were 1.0°C/cm, 1.2°C/cm, and 1.4°C/cm, respectively. At day 9 and prior to setting the temperature to 105°C, approximately 20 ml of red dye was injected to help visualize the movement of water. At day 15, the constant temperature water bath was turned off but circulation of the fluid continued during the cool-down period. In addition to the parameters measured during Tests 1, 2, and 3, the movement of liquid was monitored using the injected dye.

#### **3.4.4.5. Experiment Test 5**

Test 5 was performed over a 40-day period to monitor water movement under nonisothermal conditions in a partially saturated medium with a simulated fracture. The heat exchangers on the right and left were initially held at 20°C and 60°C, respectively, thus imposing a temperature gradient of 2.7°C/cm. Approximately 2 ml of red dye and 2 ml of blue dye were injected with a syringe into the medium through the right and left ports, respectively. After 13 days, the temperatures of the right and left heat exchangers were reversed. As in the previous experiments, ambient temperature and barometric pressure, temperatures at the inlets of the two heat exchangers, and densitometer readings were measured through out the experiment. Because no tensiometers were installed in the medium during Test 5, suction pressures were not measured.

#### **3.4.4.6. Experiment Test 6**

Test 6 was initiated in late October 1990 and was ongoing as of the end of the year. The boundary conditions for Test 6 were the same as Test 5 with the exception that the temperatures maintained in the heat exchangers during Test 6 were held constant and not reversed as in Test 5. The protocol in Test 6 was designed to be similar to Test 5 with the anticipation that improvements in laboratory procedure and instrumentation measurement would provide more quantitatively significant results.

### 3.4.5. Separate Effects Experiments Results

The results of Tests 1 through 5 are presented in this section. For these preliminary tests, the experiments were conducted in a laboratory that does not have a controlled environment. Consequently the ambient temperature and barometric pressure fluctuated throughout the duration of the tests. A total ambient temperature fluctuation of 8°C and barometric pressure fluctuation of about 0.2 meters of water were recorded. The fluctuations in the ambient temperature were directly reflected in the temperatures recorded in the test chamber, although the temperatures recorded in the chamber relative to the ambient temperatures demonstrated slightly smaller fluctuations (approximately 5°C) during Tests 1, 2, and 3 and even less during the nonisothermal tests (Tests 4, 5 and 6).

#### 3.4.5.1. *Experiment Test 1*

During the initial water injection event, the injected water spread vertically in a circular pattern away from the point of injection until it reached a diameter of about 6 inches. The water then flowed downward until it reached the bottom of the test chamber where it started to spread laterally toward the edges of the test chamber. The water in the initial 6-inch diameter region visually appeared to become redistributed slightly over the next few days by migrating toward the bottom of the test chamber. These observations correlated positively with the measurements recorded with the densitometer.

During desaturation at day 10 in the test, the free surface of the water was observed to drop as the water was removed. Measurements made with the densitometer indicated that in regions above the observed free surface, the pore space in the medium was nearly unsaturated and the pores below the free surface were close to full saturation.

Tensiometers 4 and 5 dried out during the eighth day of the test and had to be refilled with water. Tensiometers 1, 2, and 3 were located in the saturated portion of the media and recorded suction pressures of about -0.35 meters of water. Tensiometers 4 and 5 were initially in the dry region, and suction pressures of -3.5 meters of water were recorded at both locations. Full scale for the sensors is -3.5 meters of water; therefore, negative pressures less than -3.5 meters of water may have been present but were not detected by these sensors.

The tensiometer readings reflected the vertical difference in their positions with an approximate 0.07 meters of water difference for each 7.6 cm change in elevation. Measurements from tensiometers 4 and 5 did not indicate that the pores in the upper portion of the test chamber became desaturated during the removal of water in day 10 of the experiment.

#### 3.4.5.2. *Experiment Test 2*

The initial injection of water was not readily accepted by the medium even though there was a positive head of 91 cm of water in the infiltration water column. This slow acceptance of water is attributed to the high air-entry pressure of the medium. The initial water injection uniformly infiltrated the medium in a radial pattern relative to the point of injection.

The second injection of water was more readily accepted by the medium. A downward component in water movement became apparent as the moisture content of the medium was increased. A slight settling of the medium, noticed during the second injection, was manifested as a vertically oriented, fault-like offset approximately 10 cm from the side of the chamber. The offset occurred in a region that had not yet been wetted by the infiltrating water. The offset acted as a barrier to water flow. Water did not infiltrate into media on the dry side of the offset, until the water had advanced to the lower plate, moved laterally past the offset and then moved upward into the dry portion.

When water was initially injected into the medium, the tensiometers were filled with water. The tensiometers that were located in the dry portions of the test chamber (tensiometers 4 and 5) remained at -3.5 meters of water (the full-scale negative output of the sensor) until the upper portion of the chamber became saturated, at which time the pressure increased to -1.4 meters of water. The response of a tensiometer in the bottom area was initially dry (suction pressure was -3.5 meters of water) but gradually increased to -2.1 meters of water as water infiltrated into this region. Tensiometers 2, 3, and 4 were initially located in a wet region with suction pressures of about -1.4 meters of water. After the medium was fully saturated on day 10, the suction pressure decreased at these three locations to a point that even positive pressures were recorded for a brief period. A slow leak in a thermistor connection allowed some water to escape with the result that pressure in the chamber decreased over the course of the day.

#### 3.4.5.3. *Experiment Test 3*

The movement of moisture responded to gravity during this isothermal experiment. The decrease in water content at the upper portion of the visible water pattern concurred with decreased densitometer readings; however, the densitometer measurements were not quantitatively significant.

#### 3.4.5.4. *Experiment Test 4*

Temperature and moisture content measurements collected during Test 4 concurred, in general, with the imposed boundary conditions. Temperature measurements were used to indicate that internal temperature fluctuations, and thermal losses through the side walls were excessive. The densitometer measurements indicated the trend of moisture contents; but the actual measurements, as in the earlier tests, were not quantitatively significant.

However, the general trend of the densitometer readings were sufficiently significant to indicate a change in moisture content in response to the changed temperatures at the boundaries.

#### **3.4.5.5. Experiment Test 5**

The movement of the colored dyes proved to be the most useful information collected during Test 5. Although general moisture-content trends can be made using the densitometer measurements, the resolution of the densitometer measurements was not sufficient to provide quantitatively significant data for evaluation purposes.

Shortcomings of the densitometer method used for Test 5 were the narrow depth of the test chamber, the effect of thermal and barometric fluctuations on the densitometer detector, and minor density differences in water that are attributable to temperature. The most significant of these shortcomings was the narrow depth (1.9 cm) of the test chamber. Since the porosity of the Nos. 1420 and 2740 glass-bead mix used in Test 5 was about 34.8 percent; at full saturation of the medium, water would only constitute about 0.6 cm of actual thickness. Therefore, the densitometer would be required to resolve minor quantities of total water for the water-content measurements to be significant. This proved to be beyond the capabilities of the densitometer used in this experiment.

Movement of the colored dyes visually displayed liquid-moisture movement within the medium. The movement of water vapor was not monitored in this experiment. As observed with the dye, the induced fracture had a pronounced effect upon the flow paths of water in the medium. In particular, liquid water had little movement across the fracture as evidenced by the dyes. Two flow cells were created whose boundaries were comprised of three sides of the test chamber and the induced fracture. Upon commencement of the experiment, the direction of the water flow was downward along the face of the heat exchanger until arriving at the lower end of the test chamber, then toward the interior of the chamber. This movement may have been due in part to gravity forces acting upon the localized higher moisture content at the point of injection.

Movement of water across the induced fracture was not noted until late in the test when the half of the medium near the higher temperature heat exchanger visibly began to dry and the medium on the other side became visibly wetter. Some movement of the red dye (and presumably some water) was observed crossing the fracture when the moisture content of the cooler half of the medium became high enough to wet the pores of the larger pored fracture. The movement of the dye is illustrated in photographs taken at 7, 14 and 23 days into the test (Figures 3-8 through 3-10).

### **3.5. DIMENSIONAL ANALYSIS OF THERMOHYDROLOGIC EQUATIONS FOR POROUS, VARIABLY SATURATED, FRACTURED MEDIA**

Multiphase flow in a porous, fractured, unsaturated, heated medium is a function of many parameters and physical phenomena. As yet, the physics of such a flow is not completely

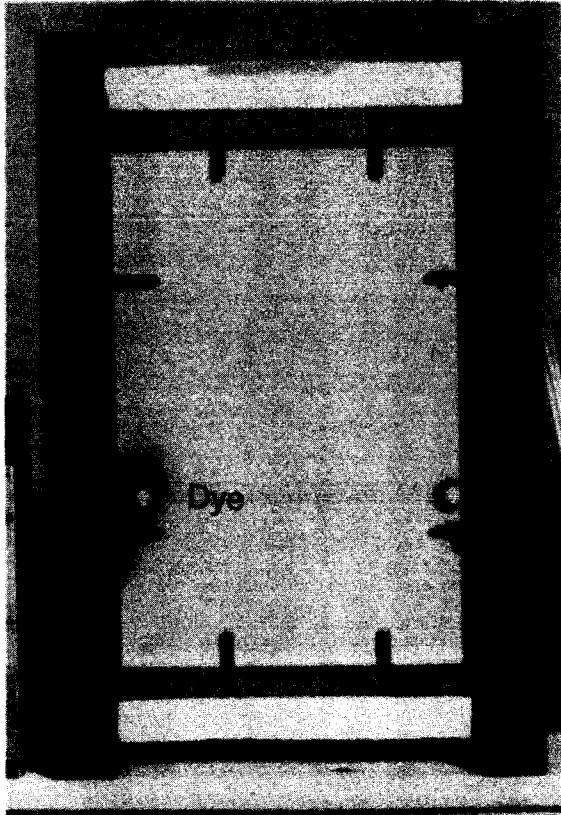


Figure 3-8. Photograph of test chamber at day 7 of Test 5

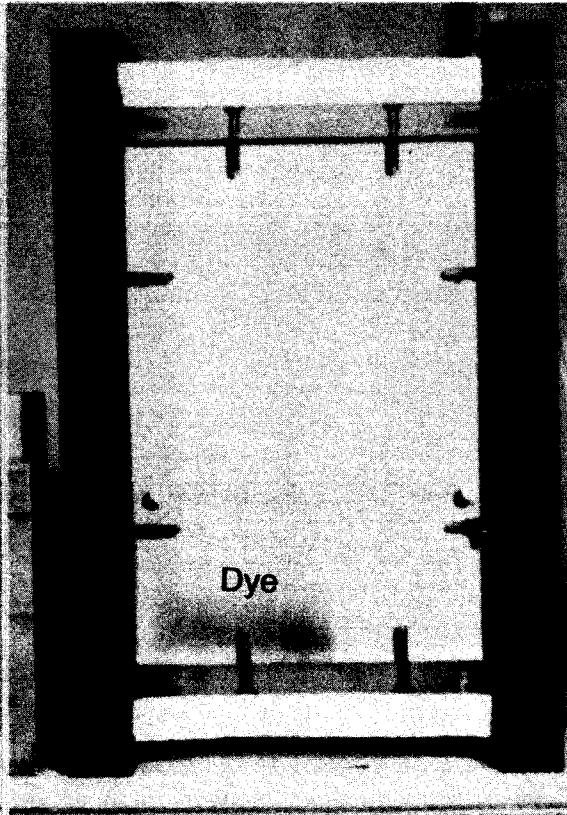


Figure 3-9. Photograph of test chamber at day 14 of Test 5

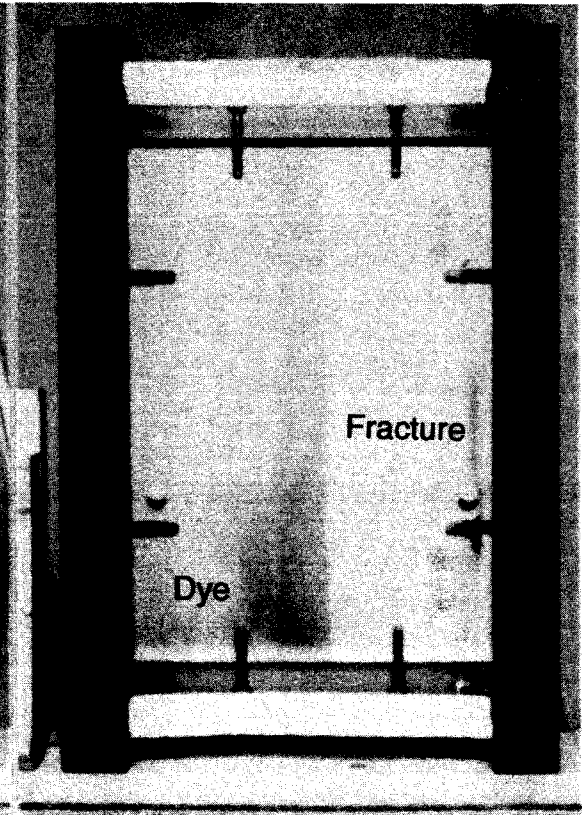


Figure 3-10. Photograph of test chamber at day 23 of Test 5

understood. A dimensional analysis of the flow and thermal response must therefore include all phenomena that might conceivably be important. Analytical or numerical analyses and separate small-scale tests are needed to interpret the dimensional analysis and to distinguish the important phenomena from the less important. From this information a feasible scale model can be formulated of an appropriate section of the repository based on the principles of dynamic similarity. The physical, geometric, property, response, and time-scaling parameters discussed in this section are suggested as being sufficient to characterize all the physics of the flow.

The following dimensional analysis is based on the equations in the TOUGH code (Pruess, 1987) that describe the transient thermohydraulic response of a variably saturated porous, fractured medium when heated by an embedded heat source or by a boundary whose temperature changes. These equations are modified, however, to include liquid transport between the porous matrix and the fractures, using the method given in the DCM-3D code (Updegraff and Lee, 1990, and Gureghian and Sagar, in this volume).

For convenience, the liquid phase of the fluid in the matrix-fracture volume is assumed to be water, and the gas phase is assumed to be a mixture of air and water vapor. Air is also assumed to be dissolved in the liquid phase. When the nondimensional equations are examined to determine their implications on scale modeling, the liquid and gas phases can be treated more generally.

The following general assumptions are made:

- (1) The matrix-fracture volume is analyzed by a dual porosity model.
- (2) Thermal equilibrium is instantaneous among all the fluid phases and the porous, fractured medium.
- (3) The mixture of air and water vapor is treated as an ideal gas.
- (4) Both the liquid and the gas are continuously distributed; that is, it is possible to reach any point, for example, in the liquid from any other point in the liquid by a path that lies completely within the liquid.
- (5) There are no sources or sinks of liquid or gas within the volume (i.e., additional liquid or gas must enter through the boundaries).
- (6) The amount of air dissolved in the water is small enough that the density of the liquid phase is equal to the density of the pure liquid.

Note that instantaneous pressure equilibrium between the matrix and the fractures is not necessarily assumed. Assumptions 1 to 4 are implied or stated in the TOUGH code development; the fifth and sixth assumptions represent the expected physical behavior of the scale model and the repository.

### 3.5.1. Conservation Equations, Constitutive Equations, and Boundary and Initial Conditions

The conservation equations are written for an elementary volume, which may contain both a porous matrix and a set of fractures, each with its own porosity. The flow of liquid between the matrix and the fractures is described by a transport term. No distinction in the equations between the matrix and the fractures is made, since the equations for either are of the same form. In the matrix-fracture transport term, however, subscripts  $i, j$  are used to indicate the direction of the flow (i.e.,  $i$  would represent the matrix and  $j$  the fractures when the matrix is considered, and vice versa when the fractures are considered).

#### 3.5.1.1. Conservation of Water

The general water-mass balance equation is

$$\frac{d}{dt} \iiint M_w dV = \iint \vec{F}_w \cdot \vec{n} dA - \iint \int \rho_w X_w \Gamma_{ij} dV. \quad (2)$$

The mass of water stored in the volume is

$$M_w = \phi(\rho_w X_w S_w + \rho_g Y_w S_g) = \phi[\rho_w X_w S_w + \rho_g Y_w (1 - S_w)] \quad (3)$$

where the last form follows from the relation that the sum of the liquid and gas saturations is one. The symbols are defined in Section 3.8.

The flux of water across the boundaries is the sum of the water transport in the liquid phase ( $l$ ) and in the gas phase ( $g$ ):

$$\vec{F}_w = \vec{F}_{wl} + \vec{F}_{wg}. \quad (4)$$

The gas phase transport is

$$\vec{F}_{wg} = -k \rho_g Y_w \left( \frac{k_{Rg}}{\mu_g} \right) [\nabla P_g - \rho_g \vec{g}] - D_{va} \rho_g \nabla Y_w. \quad (5)$$

To examine dimensional implications, the Boussinesq approximation is used to relate the gas density, pressure, and temperature:

$$\nabla P_g - \rho_g \vec{g} = -(\rho_g \beta_g g \Delta T) \vec{k} + \nabla P_{go} \quad (6)$$

where the final term represents a nonhydrostatic component of the gas pressure. For both the repository and the scale model, the gas motions are expected to be so slow that the pressure is

nearly hydrostatic (i.e., imposed by the boundaries and gravity); thus, the nonhydrostatic component in Eqn. (6) can be neglected.

The liquid phase transport is

$$\vec{F}_{wl} = -k\rho_w X_w \left( \frac{k_{Rw}}{\mu_w} \right) [\nabla P_w - \rho_w \vec{g}]. \quad (7)$$

The liquid pressure is also hydrostatically distributed:

$$P_w = -\int (\rho_w g) dz + P_{wo} \approx -\int (\rho_w g) dz. \quad (8)$$

But at any location where the liquid is in contact with the gas (i.e., where the liquid saturation level is less than one), the pressure is also related to the gas pressure and the capillary jump from the gas to the liquid:

$$P_w = P_g + P_{cap} + P_{wo} \approx P_g + P_{cap} = -\int (\rho_g g) dz - \left( \frac{\sigma}{d_o} \right) P_c. \quad (9)$$

Equations (8) and (9) relate the hydrostatic-pressure gradient to the capillary-pressure gradient.

Equation (9) implies that no buoyancy-driven liquid convection cells are the geometric size of the matrix-fracture volume because the liquid pressure is controlled by capillarity rather than by buoyancy. Cells driven by buoyancy can exist only on the scale of a water volume small enough not to be in contact with gas; that is, of the size of one or more pores completely filled with water. Circulation on the scale of the volume can certainly exist, but it is driven by pressure gradients. The apparent lack of natural convection in the liquid is completely different from what occurs when the medium is saturated.

The form of the matrix-fracture transfer term proposed in DCM-3D (Updegraff and Lee, 1990) is

$$\Gamma_{ij} = \gamma \sigma \left( \frac{k_{Rw}}{\mu_w} \right) \left[ \left( \frac{P_c}{d_o} \right)_i - \left( \frac{P_c}{d_o} \right)_j \right]. \quad (10)$$

Altogether, then, the equation representing conservation of water is

$$\begin{aligned}
& \frac{d}{dt} \iiint \phi [\rho_w X_w S_w + \rho_g Y_w (1 - S_w)] dV = \\
& \iint k \rho_w X_w \left( \frac{k_{Rw}}{\mu_w} \right) \left[ (\rho_w - \rho_g) g \vec{k} + \frac{\sigma}{d_o} \left( \frac{dP_c}{dS_w} \right) \nabla S_w + \frac{P_c}{d_o} \left( \frac{d\sigma}{dT} \right) \nabla T - \frac{\sigma P_c}{d_o^2} \nabla d_o \right] \cdot \vec{n} dA \\
& + \iint k Y_w \left( \frac{k_{Rg}}{\mu_g} \right) (\rho_g^2 \beta_g g \Delta T) \vec{k} \cdot \vec{n} dA - \iint D_{va} \rho_g \nabla Y_w \cdot \vec{n} dA \\
& - \iint \gamma \sigma \rho_w X_w \left( \frac{k_{Rw}}{\mu_w} \right) \left[ \left( \frac{P_c}{d_o} \right)_i - \left( \frac{P_c}{d_o} \right)_j \right] dV.
\end{aligned} \tag{11}$$

Note from Eqn. (11) that the capillary-induced pressure can vary from point to point by three different mechanisms: (1) liquid-saturation-level changes, (2) temperature and therefore surface-tension changes, and (3) pore-size changes. The isothermal equilibrium distribution of the liquid, from Eqn. (11), is given implicitly by the hydrostatic pressure balance:

$$\frac{\sigma}{d_o} \left( \frac{dP_c}{dS_w} \right) \nabla S_w - \frac{\sigma P_c}{d_o^2} \nabla d_o = -(\rho_w - \rho_g) g \vec{k}. \tag{12}$$

Since  $dP_c/dS_w$  is negative (i.e., capillarity decreases with increasing saturation), Eqn. (12) indicates that the equilibrium saturation level generally increases with depth (i.e.,  $\nabla S_w > 0$ ), as expected.

### 3.5.1.2. Conservation of Air

The general equation expressing the conservation of air is

$$\frac{d}{dt} \iiint M_a dV = \iint \vec{F}_a \cdot \vec{n} dA - \iiint \rho_w X_a \Gamma_{ij} dV. \tag{13}$$

The air stored in the volume is

$$M_a = \phi [\rho_w S_w X_a + \rho_g Y_a S_g] = \phi [\rho_w S_w (1 - X_w) + \rho_g (1 - S_w) (1 - Y_w)]. \tag{14}$$

The mass fluxes are evaluated similarly to those for water transport. The final form of the conservation equation is thus

$$\begin{aligned}
& \frac{d}{dt} \iiint \phi [\rho_w(1-X_w)S_w + \rho_g(1-Y_w)(1-S_w)] dV = \\
& \iint k \rho_w(1-X_w) \left( \frac{k_{Rw}}{\mu_w} \right) \left[ (\rho_w - \rho_g) g \vec{k} + \frac{\sigma}{d_o} \left( \frac{dP_c}{dS_w} \right) \nabla S_w + \frac{P_c}{d_o} \left( \frac{d\sigma}{dT} \right) \nabla T - \frac{\sigma P_c}{d_o^2} \nabla d_o \right] \cdot \vec{n} dA \\
& + \iint k(1-Y_w) \left( \frac{k_{Rg}}{\mu_g} \right) (\rho_g^2 \beta_g g \Delta T) \vec{k} \cdot \vec{n} dA + \iint D_{wa} \rho_g \nabla Y_w \cdot \vec{n} dA \\
& - \iiint \gamma \sigma \rho_w(1-X_w) \left( \frac{k_{Rw}}{\mu_w} \right) \left[ \left( \frac{P_c}{d_o} \right)_i - \left( \frac{P_c}{d_o} \right)_j \right] dV.
\end{aligned} \tag{15}$$

The diffusion term in this equation uses the relation that  $\nabla Y_a = -\nabla Y_w$ .

### 3.5.1.3. Conservation of Energy

The general form of conservation of energy is

$$\frac{d}{dt} \iiint E dV = \iint \vec{F}_e \cdot \vec{n} dA + \iiint \dot{q} dV - \iiint \rho_w (\Gamma_{ij})_e dV. \tag{16}$$

The energy stored in the volume is

$$E = (1-\phi) \rho_s u_s + \phi [\rho_w X_w S_w u_w + \rho_g Y_w S_g u_g + \rho_w X_a S_w u_a + \rho_g Y_a S_g u_a]. \tag{17}$$

Since the energy stored in the solid material can not be counted twice, Eqns. (16) and (17) must be used with care as a computing method. The energy stored in the solid material must be (1) either assigned to the matrix energy equation or to the fracture energy equation (but not to both) or (2) partitioned somehow between the two.

The various internal energy terms are expressed in terms of specific heats and temperature:

$$u_a = C_{va} \Delta T ; u_g = C_w \Delta T + u_{fg} ; u_s = C_s \Delta T ; u_w = C_w \Delta T. \tag{18}$$

The energy flux is expressed as

$$\vec{F}_e = -\kappa \nabla T + (C_w \Delta T) \vec{F}_{wl} + (C_w \Delta T + h_{fg}) \vec{F}_{wg} + (C_{Pa} \Delta T) (\vec{F}_{al} + \vec{F}_{ag}), \tag{19}$$

and the matrix-fracture transport term as

$$(\Gamma_{ij})_e = \gamma \sigma \left( \frac{k_{Rw}}{\mu_w} \right) [X_w C_w \Delta T + X_a C_{Pa} \Delta T]. \tag{20}$$

Altogether, conservation of energy is therefore expressed as

$$\begin{aligned}
& \frac{d}{dt} \iiint \{ (1-\phi) \rho_s C_s \Delta T + \phi [\rho_w X_w S_w + \rho_g Y_w S_g] C_w \Delta T + [\rho_w X_a S_w + \rho_g Y_a S_g] C_{va} \Delta T + \\
& \quad \phi \rho_g Y_w S_g \mu_{fg} \} dV = - \int \int \kappa \nabla T \cdot \vec{n} dA - \int \int (C_w \Delta T + h_{fg}) D_{va} \rho_g \nabla Y_w \cdot \vec{n} dA - \\
& \quad \int \int (C_{Pa} \Delta T) D_{va} \rho_g \nabla Y_a + \int \int (C_w \Delta T + h_{fg}) k Y_w \left( \frac{k_{Rg}}{\mu_g} \right) (\rho_g^2 \beta_g g \Delta T) \vec{k} \cdot \vec{n} dA + \\
& \quad \int \int C_w \Delta T k \rho_w X_w \left( \frac{k_{Rw}}{\mu_w} \right) \left[ (\rho_w - \rho_g) g \vec{k} + \frac{\sigma}{d_o} \left( \frac{dP_c}{dS_w} \right) \nabla T - \frac{\sigma P_c}{d_o^2} \nabla d_o \right] \cdot \vec{n} dA + \\
& \quad \int \int C_{Pa} \Delta T k \rho_w X_a \left( \frac{k_{Rw}}{\mu_w} \right) \left[ (\rho_w - \rho_g) g \vec{k} + \frac{\sigma}{d_o} \left( \frac{dP_c}{dS_w} \right) \nabla S_w + \frac{P_c}{d_o} \left( \frac{d\sigma}{dT} \right) \nabla T - \frac{\sigma P_c}{d_o^2} \nabla d_o \right] \cdot \vec{n} dA + \\
& \quad \int \int C_{Pa} \Delta T k Y_a \left( \frac{k_{Rg}}{\mu_g} \right) (\rho_g^2 \beta_g g \Delta T) \vec{k} \cdot \vec{n} dA + \int \int \int \dot{q} dV - \\
& \quad \int \int \int \gamma \sigma \left( \frac{k_{Rw}}{\mu_w} \right) \left[ \left( \frac{P_c}{d_o} \right)_i - \left( \frac{P_c}{d_o} \right)_j \right] (\rho_w X_w C_w \Delta T + \rho_w X_a C_{Pa} \Delta T) dV.
\end{aligned} \tag{21}$$

#### 3.5.1.4. Constitutive Equations and Initial and Boundary Conditions

The constitutive equations relating the various thermophysical properties to temperature, pressure, and saturation must also be specified. These relations are not expressed explicitly here but will be considered in analyzing similarity requirements from the nondimensional equations. It is worth noting, however, that (1) permeability depends on the size of the matrix pores (or fracture width), porosity, and connectivity of the pores and (2) relative permeabilities and capillary-pressure function are expressed as (empirical) functions of the reduced saturation.

The initial conditions specify the temperature and saturation distributions at the start of the simulation. The boundary conditions specify what the temperatures are at the boundaries for all time (e.g., insulated, isothermal, or convective) and whether water or gas infiltrates or escapes through the boundaries. A more complicated condition is the capillary pressure at the boundary. In the repository, the media are more or less infinite in extent, while for the scale model the media are either bounded by solid walls of some kind or terminate in contact with the air. For this analysis, the capillary condition is neglected by assuming that the scale-model boundaries are far away from the region of interest.

#### 3.5.2. Nondimensional Equations

The preceding equations are now made nondimensional. For this purpose, the volume and area are characterized by a significant length dimension of the problem, say the length  $L_H$  of the heater or of a heated boundary. The average or representative initial temperature  $T_o$  is used as a characteristic temperature. There are several characteristic time

scales; but diffusion time for heat conduction is one of the most important, so it is chosen:  $\rho_s C_s L_H^2 / \kappa$ . (If all the important phenomena are simulated "in scale" in the model, the other time scales will be simulated correctly.)

The nondimensional form of conservation of water mass is

$$\begin{aligned}
 & \frac{d}{d\tau} \iiint \left\{ \left( \frac{1}{Pr} \right) \phi [X_w S_w + \rho_{gw} Y_w (1 - S_w)] \right\} dV^* = \\
 & \iint \left\{ (Ca) k_{Rw} X_w \left[ Bo(1 - \rho_{gw}) \bar{k} + \left( \frac{dP_c}{dS_w} \right) \nabla^* S_w + Si \nabla^* \theta - \frac{1}{D_o} \right] \cdot \bar{n} \right\} dA^* + \\
 & \iint [\mu_{gw} k_{Rg} Y_w Gr_g \theta] \bar{k} \cdot \bar{n} dA^* - \iint \left[ \left( \frac{1}{Sc} \right) \nabla^* Y_w \right] \cdot \bar{n} dA^* - \\
 & \iint \left[ (Ca)_i \left( \frac{L_H^2}{k} \right) \gamma k_{Rw} X_w (1 - P_{cij}) \right] dV^*.
 \end{aligned} \tag{22}$$

Note that every term in Eqn. (22) is nondimensional; the nondimensional form of conservation of air mass is likewise:

$$\begin{aligned}
 & \frac{d}{d\tau} \iiint \left\{ \left( \frac{1}{Pr} \right) \phi [(1 - X_w) S_w + \rho_{gw} (1 - Y_w) (1 - S_w)] \right\} dV^* = \\
 & \iint \left\{ (Ca) k_{Rw} (1 - X_w) \left[ Bo(1 - \rho_{gw}) \bar{k} + \left( \frac{dP_c}{dS_w} \right) \nabla^* S_w + Si \nabla^* \theta - \frac{1}{D_o} \nabla^* D_o \right] \cdot \bar{n} \right\} dA^* + \\
 & \iint [\mu_{gw} k_{Rg} (1 - Y_w) Gr_g \theta] \bar{k} \cdot \bar{n} dA^* + \iint \left[ \left( \frac{1}{Sc} \right) \nabla^* Y_w \right] \cdot \bar{n} dA^* - \\
 & \iint \left[ (Ca)_i \left( \frac{L_H^2}{k} \right) \gamma k_{Rw} (1 - X_w) (1 - P_{cij}) \right] dV^*.
 \end{aligned} \tag{23}$$

The nondimensional form of conservation of energy is

$$\begin{aligned}
& \frac{d}{d\tau} \iiint \left[ \frac{(1-\phi)C_{sw}\rho_{sw}\theta}{Pr} \right] dV^* \\
& + \frac{d}{d\tau} \iiint \left[ \frac{\phi[X_w S_w + \rho_{gw} Y_w (1-S_w)]\theta + \phi \rho_{gw} Y_w (1-S_w) U}{Pr} \right] dV^* \\
& + \frac{d}{d\tau} \iiint \left[ \frac{\phi[(1-X_w)S_w + \rho_{gw}(1-Y_w)(1-S_w)]C_{vaw}\theta}{Pr} \right] dV^* \\
& = - \iint \left[ \left( \frac{C_{sw}}{Pr} \right) \nabla^* \theta \right] \cdot \vec{n} dA^* \\
& + \iint \left\{ (Ca)\theta k_{Rw} X_w \left[ Bo(1-\rho_{gw})\vec{k} + \left( \frac{dP_c}{dS_w} \right) \nabla^* S_w + S_i \nabla^* \theta - \frac{1}{D_o} \nabla^* D_o \right] \right\} \cdot \vec{n} dA^* \\
& + \iint \left\{ [(Ca)(\theta+H)k_{Rg} Y_g Gr_g \theta] \vec{k} \cdot \vec{n} dA^* - \iint \left[ \left( \frac{1}{Sc} \right) (\theta+H) \nabla^* Y_w \right] \cdot \vec{n} dA^* \right\} \\
& + \iint \left\{ (Ca)C_{Paw}\theta k_{Rw}(1-X_w) \left[ Bo(1-\rho_{gw})\vec{k} + \left( \frac{dP_c}{dS_w} \right) \nabla^* S_w + S_i \nabla^* \theta - \frac{1}{D_o} \nabla^* D_o \right] \right\} \cdot \vec{n} dA^* \\
& + \iint [C_{Paw}k_{Rg}(1-Y_w)\beta_g \theta^2] \vec{k} \cdot \vec{n} dA^* + \iint \left[ \left( \frac{C_{Paw}}{Sc} \right) \nabla^* Y_w \right] \cdot \vec{n} dA^* + \iiint \dot{Q} dV^* \\
& - \iint \left\{ (Ca_i) \left( \frac{L_H^2}{k} \right) k_{Rw} \theta (1-P_{cij}) [X_w + C_{Paw}(1-X_w)] \right\} dV^*.
\end{aligned} \tag{24}$$

### 3.5.3. Nondimensional Parameters

The nondimensional parameters that govern the response of the porous, variably saturated, fractured medium can be determined by inspection of Eqns. (22) and (24). They are written below in the common "pi" format.

Geometry:

$$\pi_1 = d_o/L_H \quad \pi_2 = k/L_H^2 \quad \pi_3 = \phi$$

Property ratios:

$$\begin{aligned}
\pi_4 &= \rho_{gw} = \rho_g/\rho_w & \pi_5 &= \rho_{sw} = \rho_s/\rho_w & \pi_6 &= \mu_{gw} = \mu_g/\mu_w \\
\pi_7 &= C_{sw} = C_s/C_w & \pi_8 &= C_{Paw} = C_{Pa}/C_w & \pi_9 &= C_{vaw} = C_{va}/C_w \\
\pi_{10} &= U = u_{fg}/C_w T_o & \pi_{11} &= H = h_{fg}/C_w T_o
\end{aligned}$$

Physical effects:



$$\begin{array}{lll}
\pi_{12} = k_{Rw} & \pi_{13} = k_{Rg} & \pi_{14} = Bo = \rho_w g L_H / (\sigma / d_o) \\
\pi_{15} = Ca = \sigma k \rho_w / d_o \mu_w^2 & \pi_{16} = Pr = (\rho_w / \rho_s) (C_s \mu_w / \kappa) & \pi_{17} = dP / dS_w \\
\pi_{18} = Si = (P_c T / \sigma) (d\sigma / dT) & \pi_{19} = Gr_g = \rho_g^2 k L_H g \beta_g T / \mu_g^2 & \pi_{20} = \gamma \\
\pi_{21} = Sc = \rho_g D_w / \mu_g & \pi_{22} = \dot{Q} = \dot{q} L_H^2 / \mu_w C_w T_o &
\end{array}$$

Response parameters and time scaling:

$$\begin{array}{lll}
\pi_{23} = \tau = \kappa t / \rho_s C_s L_H^2 & \pi_{24} = \theta = (T - T_o) / T_o & \pi_{25} = S_w \\
\pi_{26} = X_w & \pi_{27} = Y_w &
\end{array}$$

$P_{cij}$  is not included in this list as an independent term, since it can be formed from the combination of  $\pi_1$  and  $\pi_{18}$  for the matrix and the fractures. The pi terms for the initial and boundary conditions must be added to this list. For example, if an infiltration of water  $\dot{m}$  ( $\text{kg}/\text{m}^2\text{-sec}$ ) occurs at a boundary, an appropriate pi term is  $\dot{m}^2 d / \rho_w \sigma$ .

For exact similarity, each pi term has to have the same numerical magnitude for both the scale model and the prototype (i.e., the repository). This kind of similarity is unlikely. Instead, a more limited kind of similarity will be attempted. The important pi terms will only have roughly comparable magnitudes in the model and the prototype such that physical effects can be quantified and the validity of computer simulations can be examined.

#### 3.5.4. Discussion of the pi Terms

The relative importance of many of the pi terms has not yet been established. They probably are not all needed to ensure dynamic similarity between the scale model and the repository. With respect to scale-model geometry, all the actual fine details of repository almost surely cannot be duplicated exactly in a scale model because of the widely different size scale between pores and fractures. Analyses of representative simplified problems and TOUGH simulations for more complicated problems will be used to help establish the effects of this difference in sizes so that a representative scale model can be determined. The geometric design of the model (fractures, pore size, media material, etc.) is expected to be one of the most challenging parts of the scale-model formulation.

The pi terms that are ratios of fluid properties should not cause problems, since the model fluids will be similar to or the same as the repository fluids.

Regarding the pi terms that express the physics of the processes, each pi term in the scale model ideally should be equal in value to the corresponding term in the repository. In fact, the "scale" factors for the model are obtained by setting each model pi term equal to its repository pi term; this allows the relationship to be determined between each of the physical (i.e., dimensional) parameters in the model and the repository. The solution procedure usually,

however, results in contradictory relationships (e.g., the ratio of liquid viscosity in the model to that in the repository must have two or more different values in order to make two or more corresponding pi terms equal). If that occurs, physical reasoning, separate effects test results, and TOUGH simulations will be used to determine which of the conflicting scaling relationships are critical and which can be relaxed. Even so, it may be all the important effects cannot be simulated simultaneously in the model during any one test. If so, several tests must be conducted so that the effects can be varied systematically and the results parameterized.

### 3.6. SIMULATION ANALYSIS AND RESULTS

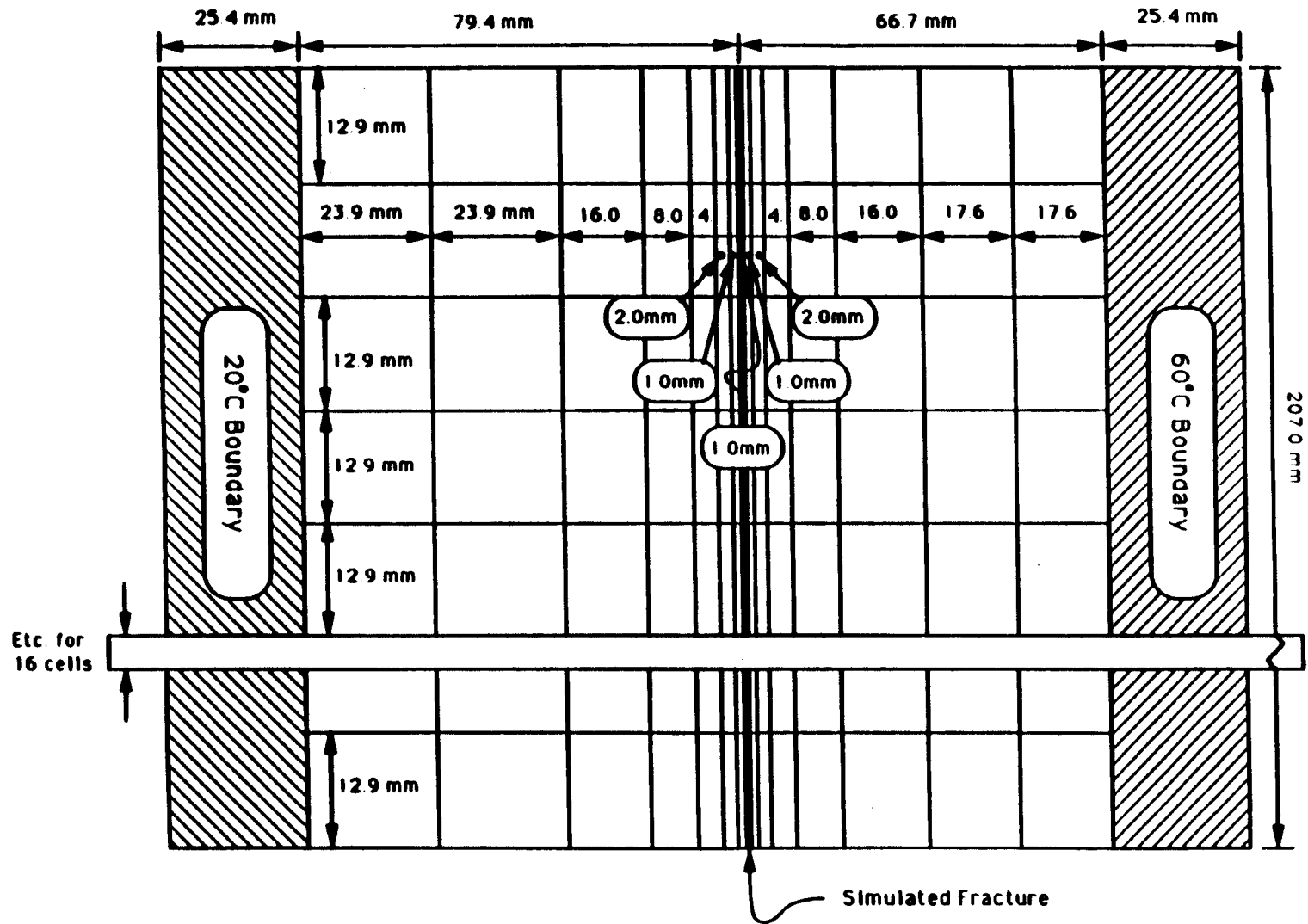
Parallel efforts have been conducted with regard to modeling the thermohydrological phenomena. The computer code TOUGH (Pruess, 1987) was acquired to assist in evaluating the separate-effects experiments (in particular, the nonisothermal, two-phase flow experiments to be completed as part of this task). The intention of performing the simulation is to assist in investigating the thermohydrologic processes and to evaluate the theory incorporated into the TOUGH code. The version of TOUGH modified by T. McCartin (NRC), called MCTUFF, has been adapted to run on a VAX 8700 at Southwest Research Institute (SwRI). TOUGH has been modified at the CNWRA to facilitate data entry and interpretation of the simulation results.

Specifically, the intention of these numerical exercises has been to evaluate the capabilities of TOUGH to simulate the two significant flow patterns observed in Test 5; that is, the apparent formation of a convection cell and the reluctance to flow across the simulated fracture under less-than-saturated conditions. Although the difficulty of simulating these complex processes have been documented (Runchal et al., 1985; Nitao and Buscheck, 1989; and Pruess et al., 1990), it is thought that such an assessment will provide valuable insight into the thermohydrological phenomena expected in the geologic medium near high-level waste.

The simulated medium was a vertically oriented, two-dimensional (20.7 by 14.6 cm) grid with variably sized elements that decreased in width proximal to the vertically oriented, simulated fracture (Figure 3-11). The two vertical edges of the container were simulated as constant-temperature (20 and 60°C), no-flow boundaries; and the two horizontal edges were treated as adiabatic no-flow boundaries. The simulated fracture was vertically located approximately half-way between the two vertical edges.

The hydrological characteristics of the matrix and the simulated fracture have been assigned values approximating those of the media in Tests 5 and 6. The matrix and fracture porosities were set at 35 percent. The intrinsic permeability of the matrix and fracture were  $1.2 \times 10^{-14} \text{ m}^2$  and  $1.2 \times 10^{-12} \text{ m}^2$ , respectively.

The van Genuchten parameters of the matrix were the same as those determined experimentally. Several different sets of van Genuchten parameters were assigned to the fracture in an attempt to accurately portray the physical nature of the fracture relative to the matrix. The van Genuchten parameters assigned to the matrix and fracture in these analyses are presented in Table 3-3 and illustrated in Figure 3-12. Set 1 of the parameters was calculated from the



3-34

Figure 3-11. Schematic of finite difference grid used in numerical simulations

laboratory-determined moisture-release curve for the matrix bead mix. Set 2 of the parameters was arbitrarily determined relative to the matrix parameters and assigned to the fracture. The van Genuchten parameters in Set 3 are particular to a fracture in a welded tuff and were determined by Peters et al. (1984).

The experiment was simulated using the TOUGH code for different sets of hydraulic properties assigned to the fracture. Parameters that proved to be difficult to determine were the van Genuchten parameters assigned to the fracture elements. Results of simulations using the Set 1 van Genuchten parameters assigned to the matrix and either Set 2 or Set 3 assigned to the fracture are presented here. The simulations were designed for a period of up to about 35 days, similar to the duration of the laboratory experiment Test 5.

The simulated values at 3,000,000 seconds (34.7 days) for temperature, capillary pressure, liquid-water saturation, and water-vapor saturation using the Set 1 and 2 parameters are presented in Figures 3-13 through 3-16, respectively. The simulated movement of water and water vapor in simulation 1 responded to the effect of the heated boundaries in a manner roughly similar to what was observed in the lab. As illustrated in Figures 3-15, liquid-water saturation levels decreased near the upper portion of the chamber, near the heated boundary. Likewise, water-vapor values decreased in the lower portion of the chamber proximal to the cool boundary. Some of this downward liquid movement was due in part to gravity drainage of the uniform initial saturation conditions. However, liquid-water and water-vapor movements were not adequately simulated in the region near the fracture. Close inspection of the fracture elements assigned to the arbitrarily determined van Genuchten parameters revealed that the simulated fracture had liquid-saturation levels greater than adjoining matrix elements. This is in contrast to what would be expected with respect to capillary forces and the relatively larger sized pores of the fracture.

The simulated fracture in a second set of simulations was assigned van Genuchten parameter values calculated for a fracture in welded tuff (Set 3 in Table 3-3) (Peters et al. 1984) (Figures 3-17 through 3-20). In these simulations, the fracture elements attained moisture contents that were lower than the adjoining matrix elements, as was observed in the laboratory experiments. Interestingly, liquid water appeared to dam up on the side of the fracture closest to the heated boundary. Additionally, the cool half of the simulated chamber did not display a significant response to the heated boundary nor to either the liquid water or the water vapor movement associated with the water movement in the heated half of the chamber. Water movement in response to gravity effects, however, was observed in the cool half. Unfortunately, these simulations were computationally intensive; only about one-half day of the experiment was simulated.

**Table 3-3. VAN GENUCHTEN PARAMETERS USED IN THE NUMERICAL SIMULATION ANALYSES**

Set No.	Title	Alpha	<i>n</i>	Residual Moisture	Reference
1	Bead Mix	0.759	7.38	0.03	lab results
2	Sim. Fracture	0.920	7.38	0.03	arbitrary
3	Fracture	1.285	4.23	2E-6	Peters et al. (1984)

### 3.7. SUMMARY AND DISCUSSION OF RESULTS

Insights gained from the laboratory portion of the research project at this intermediate point can be summarized in two categories, those that could help direct future efforts in the technical area of thermohydrology and recommendations for modifications in experimental procedures.

Sufficient resolution was not obtainable with either of the densitometer techniques under the applied conditions. Progress came with procurement of the more sensitive and more flexible detector, but measurements of moisture content were not sufficiently exact or repeatable to allow full quantitative analysis using the results. Future efforts with this instrumentation should provide results with a greater level of certainty, but the prospect of sound, quantitative moisture-content measurements using a densitometer is not ensured.

The effect of heterogeneities was demonstrated in Test 5 where a simulated fracture was observed to greatly affect the nature of water flow. Liquid water did not appear to flow across the fracture until the saturation level was sufficiently high and the suction pressure was sufficiently low to saturate the relatively larger sized pores in the fracture and to permit water flow into the less moist material. The phenomena observed in Test 2 with the accidentally induced offset were similar to the phenomena observed with the simulated fracture in Test 5.

Preliminary analyses using the numerical simulations provided results with potentially important implications. The hydrologic effect of fractures in a partially saturated, fractured medium is not entirely understood. Preliminary analyses of fractures investigated at a regional scale under isothermal conditions have indicated that partially saturated fractures will not act as impediments to flow of liquid water from matrix block to matrix block if there is even a low level of connectivity between the blocks (e.g., 10 percent) (Buscheck and Nitao, 1990).

Preliminary analysis of the numerical simulation of the Test 5 case provided results suggesting that fractures proximal to heat-generating waste may respond differently than those

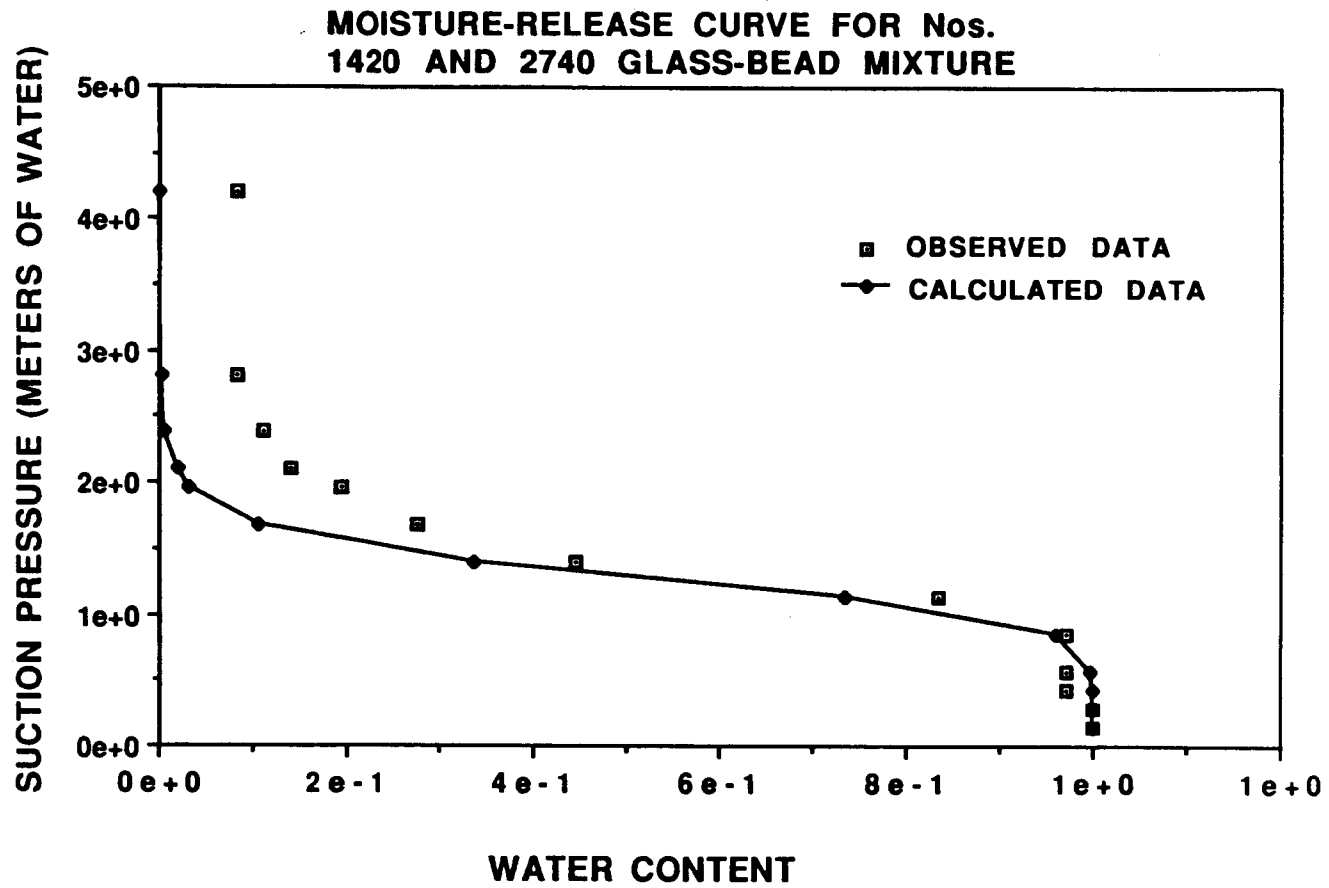
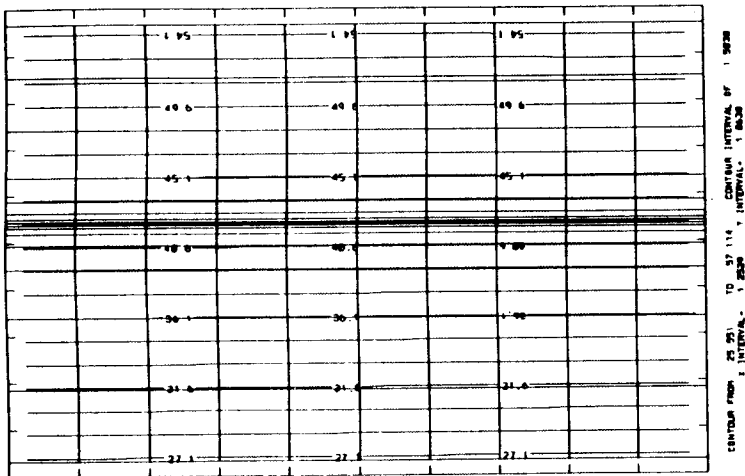


Figure 3-12. Moisture release curves for different sets of van Genuchten parameters

8E-C

Temp. Dist. at step: tstep.3000000

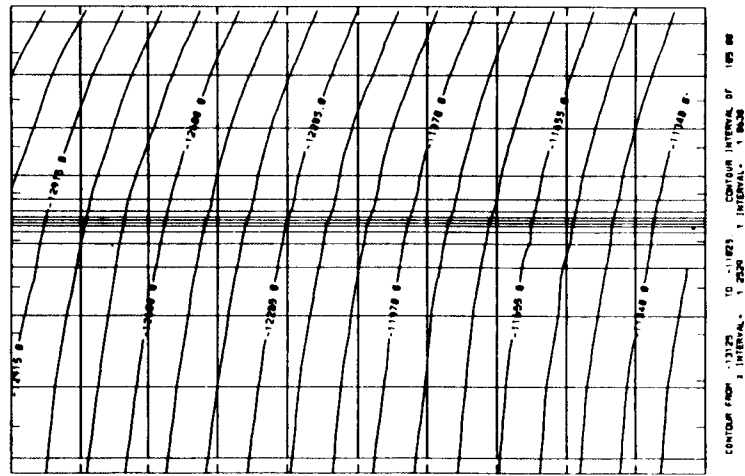


11-Apr-91 16:54:38  
Ronald H. Martin, DIV #20, SV Research Institute  
PO Drawer 28518, San Antonio, TX 78284 USA

Figure 3-13. Temperature distribution - simulation 1

Contour scale factor 1.0000E+00

Pressure Dist. at step: tstep.3000000

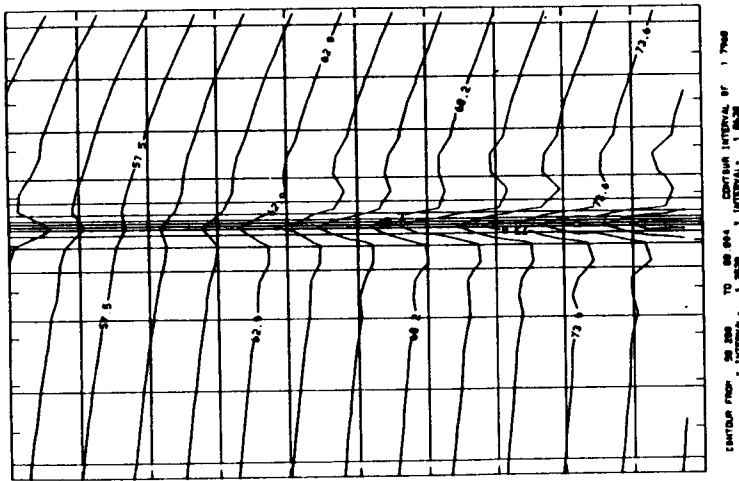


11-Apr-91 16:56:27  
Ronald H. Martin, DIV #20, SV Research Institute  
PO Drawer 28518, San Antonio, TX 78284 USA

Figure 3-14. Capillary pressure (Pascals) - simulation 1

3-39

Liquid Dist. at step. tstep.3000000

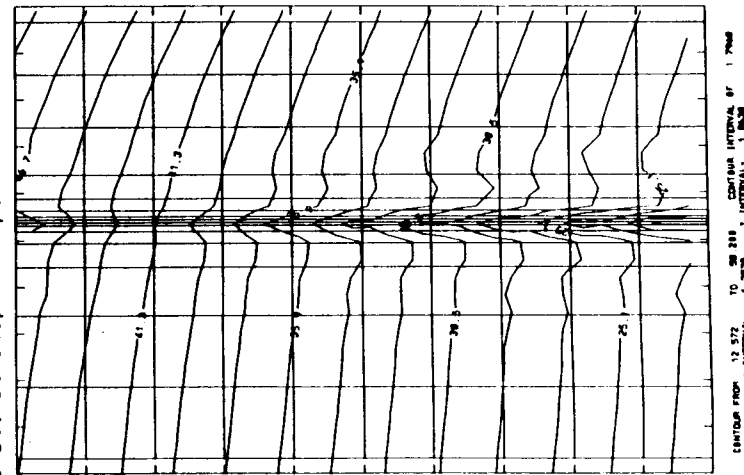


11-Apr-91 10:54:25  
 Ronald H. Martin, DIV #28, SV Research Institute  
 PO Drawer 28510, San Antonio TX 78204 USA



Contour scale factor 1.0000E-02

Gas Dist. at step. tstep.3000000



11-Apr-91 10:54:22  
 Ronald H. Martin, DIV #28, SV Research Institute  
 PO Drawer 28510, San Antonio TX 78204 USA

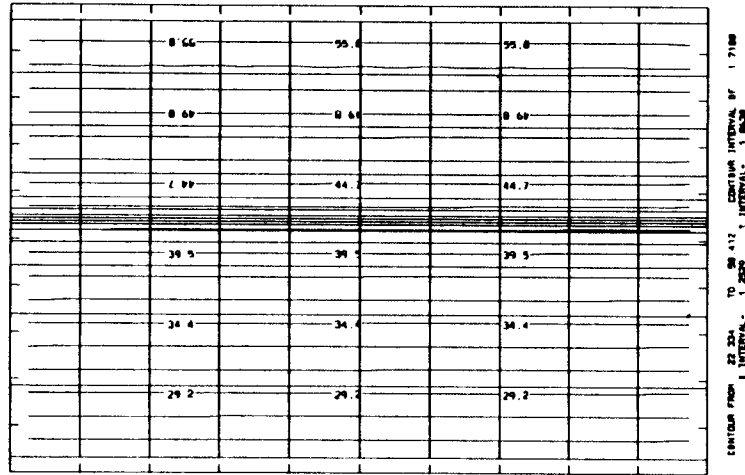


Figure 3-15. Liquid-saturation content - simulation 1

Figure 3-16. Gas-saturation content - simulation 1

3-40

Temp. Dist. at step: tstep.41447



Contour scale factor 1.0000E+00

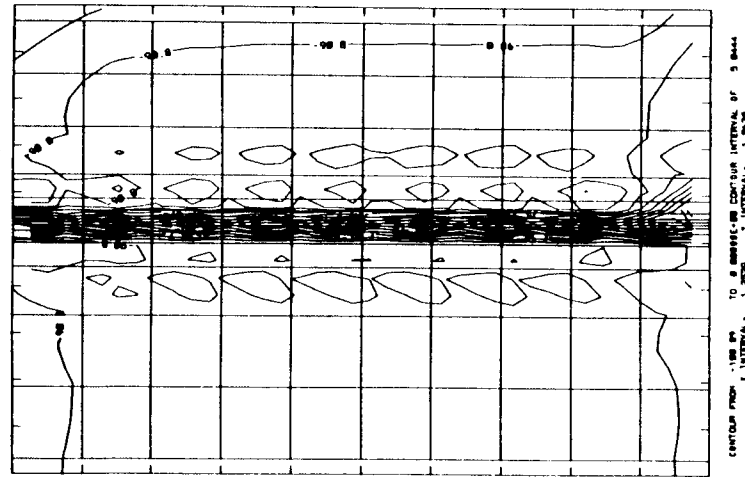
11-Apr-91 16:48:38  
Ronald H. Martin, DIV #28, SV Research Institute  
PO Drawer 28518, San Antonio, TX 78284 USA

Figure 3-17. Temperature distribution - simulation 2



Contour scale factor 1.0000E+00

Pressure Dist. at step: tstep.41447

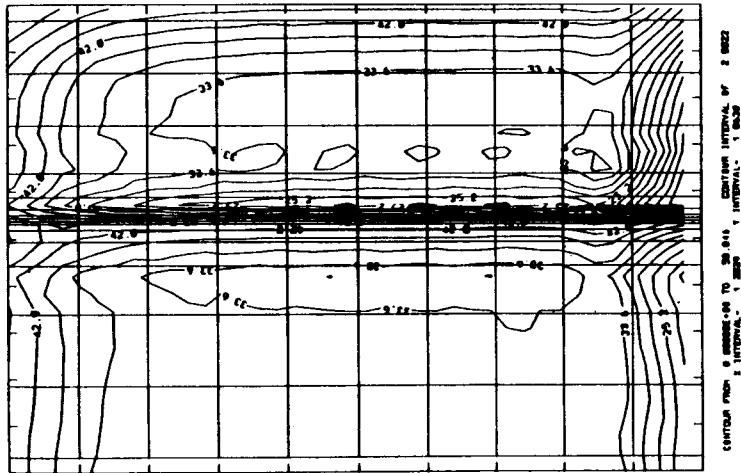


11-Apr-91 16:48:38  
Ronald H. Martin, DIV #28, SV Research Institute  
PO Drawer 28518, San Antonio, TX 78284 USA

Figure 3-18. Capillary pressure (Pascals) - simulation 2

3-41

Gas Dist. at step: tstep.41447



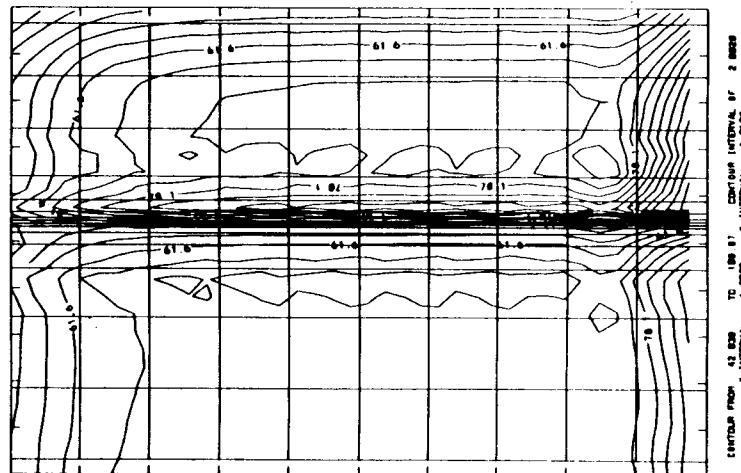
11-Apr-91 16:48:22  
Ronald H. Martin DIV #28 SV Research Institute  
PO Drawer 28518, San Antonio TX 78284 USA

Figure 3-19. Liquid-saturation content - simulation 2



Contour scale factor 1.0000E-02

Liquid Dist. at step: tstep.41447



11-Apr-91 16:48:25  
Ronald H. Martin DIV #28 SV Research Institute  
PO Drawer 28518, San Antonio TX 78284 USA

Figure 3-20. Gas-saturation content - simulation 2



Contour scale factor 1.0000E-02

in an isothermal medium. Because fractures have lower air-entry levels than pores in the matrix, they remained unsaturated for particular moisture contents when the adjoining matrix was essentially saturated. Consequently, as demonstrated in Test 5 and simulated with the TOUGH code, the movement of water vapor was not impeded by the presence of a fracture; however, the movement of liquid water was.

Based on these analyses and observations, the following preliminary interpretation was made. A heat-pipe process will occur only in the matrix block nearest the heat-generating source during the early stages after waste emplacement. Heat will be more efficiently removed from the heat source by phase change resulting from the water vaporization, thus maintaining the temperature near the heat source close to 100°C. As additional water is vaporized near the heat source and as the heat regime migrates into the medium, water vapor will be expected to move past the initial fracture and outward into the next matrix block. The matrix block nearest the heat source will become desaturated as the return flow of liquid water in the outer matrix block is arrested by the presence of the fracture. Liquid water will only cross the fracture when the moisture content of the matrix adjacent to the fracture is sufficiently high (and the suction pressure is sufficiently low) to cause the fracture to saturate. Prior to this, the matrix block on the heated side of the fracture will desaturate, thus denying to the heat-pipe process the return flow of liquid water necessary to continue.

Without the removal of heat by phase change, temperatures at the heat-source boundary will tend to increase. This same process was predicted by Pruess et al. (1985) in an investigation of the heat-pipe effect where liquid water was assumed to be immobile. The phenomenon of heat-pipe collapse with associated elevated temperatures could be expected to migrate outward if multiple vertical fractures are present near the heat source. This phenomenon has been investigated in only limited laboratory and numerical experiments and requires additional investigation to be verified.

The dimensional analyses have yielded a set of dimensionless equations and terms that may provide a means to apply dynamic similitude analysis to the problem of using laboratory-scale experiments to understand thermohydrologic phenomena at field-scale. The analyses can not be reasonably performed until the processes observed at the laboratory scale have been sufficiently understood. Foremost remaining in the characterization of the laboratory-scale experiments is the highly nonlinear fracture-matrix relationship.

### 3.8. SYMBOLS AND TYPICAL DIMENSIONAL UNITS

The following list contains the symbols and typical dimensional units used in the Thermohydrology Research Project.

$A$	cross-section area	$m^2$
$A^*$	nondimensional area, $A/L_H^2$	-
$Bo$	ratio of gravity pressure to capillary pressure (bond number), $\rho_w g L_H d_o / \sigma$	-

$Ca$	ratio of capillary pressure to viscous pressure (capillary number), $\sigma k \rho_w / d_o \mu_w^2$	-
$C_w$	specific heat of water	joule/kg-K
$C_{Pa}$	specific heat of air at constant pressure	joule/kg-K
$C_{Paw}$	ratio of energy stored in the air contained in the gas mixture to energy stored in the water, $C_{Pa}/C_w$	-
$C_s$	specific heat of matrix (solid)	joule/kg-K
$C_{sw}$	ratio of energy stored in matrix to energy stored in water, $C_s/C_w$	-
$C_{Va}$	specific heat of air at constant volume	joule/kg-K
$C_{Vaw}$	ratio of energy stored in the air dissolved in water to energy stored in the water, $C_{Va}/C_w$	-
$d_o$	typical dimension of matrix pore or fracture width	m
$D_o$	nondimensional pore or fracture size, $d_o/L_H$	-
$\underline{D}_{va}$	diffusion coefficient for air-vapor mixture	$m^2/sec$
$\underline{g}$	gravity vector, also $(-g)\bar{k}$	$m/sec^2$
$Gr_g$	ratio of gas-buoyancy force to viscous force (Grashof number), $\rho_g^2 k L_H \delta \theta_g T_o / \mu_g^2$	-
$h_a$	enthalpy of air	joule/kg
$h_g$	enthalpy of water vapor	joule/kg
$h_w$	enthalpy of water	joule/kg
$h_{fg}$	latent heat of vaporization (water)	joule/kg
$H$	ratio of latent heat to energy stored in water (enthalpy number), $h_{fg}/C_w T_o$	-
$k$	permeability of matrix or fracture	$m^2$
$k_{Rw}$	relative permeability function for water (empirical), $= f(S^\circ)$	-
$k_{Rg}$	relative permeability function for gas (empirical), $= f(S^\circ)$	-
$\underline{L}_H$	typical length of heater or heated boundary	-
$\underline{n}$	unit normal vector pointing out of area	-
$P_c$	capillary pressure function (empirical), $= f(S^\circ)$	-
$P_{cij}$	ratio of capillary pressure of $j$ -th medium to that of $i$ -th medium, $(P_c/d_o)_j / (P_c/d_o)_i$	-
$P_g$	gas pressure	newton/ $m^2$
$P_w$	liquid pressure	newton/ $m^2$
$Pr$	ratio of viscous diffusion to heat diffusion (modified Prandtl number), $(\rho_w/\rho_g)(C_s \mu_w/\kappa)$	-
$\dot{q}$	heat addition rate per unit volume	joule/ $sec \cdot m^3$
$\dot{Q}$	ratio of heat addition to viscous transport of stored energy (energy addition number), $\dot{q} L_H^2 / \mu_w C_w T_o$	-
$Sc$	ratio of mass diffusion to viscous diffusion	-

	(Schmidt number), $\rho_g D_{va}/\mu_g$	-
$S_g$	gas-saturation level	-
$S_i$	nondimensional change in capillary pressure with temperature, $(P_c T_o/\sigma)(d\sigma/dT)$	-
$S_w$	water saturation level	-
$S_r$	residual or irreducible saturation	-
$S^*$	reduced saturation, $(S_w - S_r)/(1 - S_r)$	-
$t$	time	sec
$T$	temperature	K
$T_o$	initial or reference temperature	K
$U$	ratio of liquid-to-vapor internal energy change to energy stored in water (internal energy number), $u_{fg}/C_w T_o$	-
$X_a$	mass fraction of air dissolved in water	-
$X_w$	mass fraction of liquid water in liquid	-
$u_a$	internal energy of air	joule/kg
$u_g$	internal energy of water vapor	joule/kg
$u_w$	internal energy of water	joule/kg
$u_{fg}$	latent internal energy of vaporization	joule/kg
$V$	volume	$m^3$
$V^*$	nondimensional volume, $V/L_H^3$	-
$Y_a$	mass fraction of air in gas mixture	-
$Y_w$	mass fraction of water vapor in gas mixture	-
$\beta_g$	thermal expansion coefficient of gas	1/K
$\gamma$	matrix-fracture interaction parameter	-
$\Gamma_{ij}$	liquid transport between material $i$ and $j$	1/sec
$\Delta T$	$T - T_o$	K
$\theta$	nondimensional temperature, $(T - T_o)/T_o$	-
$\kappa$	thermal conductivity of matrix-fluid mixture	joule/m-sec-K
$\mu_g$	viscosity of gas	newton/sec- $m^2$
$\mu_{gw}$	ratio of gas viscosity to water viscosity	-
$\mu_w$	viscosity of water	newton/sec- $m^2$
$\rho_g$	density of gas	kg/ $m^3$
$\rho_s$	density of matrix (solid)	kg/ $m^3$
$\rho_w$	density of water	kg/ $m^3$
$\rho_{gw}$	ratio of gas density to water density, $\rho_g/\rho_w$	-
$\rho_s/\rho_w$	ratio of matrix density to liquid density, $\rho_s/\rho_w$	-
$\sigma$	surface tension of water	newton/m
$\tau$	nondimensional time (Biot number), $\kappa t/\rho_s C_s L_H^2$	-
$\phi$	rock porosity	-
$\nabla$	vector derivative operator, $i\partial/\partial x + j\partial/\partial y + k\partial/\partial z$	1/m
$\nabla^*$	nondimensional vector derivative, $L_H \nabla$	-

### 3.9. REFERENCES

- Buscheck, T., and J. Nitao. Lawrence Livermore National Laboratory (LLNL). 1990. Personal Communication.
- Nitao, J. J., and T. A. Buscheck. 1989. *On the Movement of a Liquid Front in an Unsaturated, Fractured Porous Medium*. Lawrence Livermore National Laboratory (LLNL) UCID Report. NNA 891130.0051. Livermore, California: LLNL.
- Peters, R. R., E. A. Klavetter, I. J. Hall, S. C. Blair, P. R. Heller, and G. W. Gee. 1984. *Fracture and Matrix Hydrologic Characteristics of Tuffaceous Materials from Yucca Mountain, Nye County, Nevada*. Sandia National Laboratories (SNL) SAND84-1471. Albuquerque, New Mexico: SNL.
- Pruess, K., Y. W. Tsang, and J. S. Wang. 1985. Modeling of strongly heat driven flow in partially saturated fractured porous media. *Hydrogeology of Rocks of Low Permeability Memoirs*. Vol. XVII. International Association of Hydrologists: 486-497.
- Pruess, K. 1987. *TOUGH Users Guide*. NUREG/CR-4645, Berkeley, California: LBL.
- Pruess, K., J. S. Y. Wang, and Y. W. Tsang. 1990. On thermohydrologic conditions near high-level nuclear wastes emplaced in partially saturated fractured tuff, 1, simulation studies with explicit consideration of fracture effects. *Water Resources Research*. 26(6): 1235-1248.
- Runchal, A. K., B. Sagar, R. G. Baca, and N. W. Kline. 1985. *PORFLO-A Continuum Model for Fluid Flow, Heat Transfer, and Mass Transport in Porous Media: Model Theory, Numerical Methods and Computational Tests*. DE-AC06-77RL01030. Hanford, Washington: Rockwell International.
- Updegraff, D., and C. E. Lee. 1990. *Evaluation of DCM-3D - A Dual Continuum, 3-D Groundwater Flow Code for Unsaturated, Fractured, Porous Media*. NUREG/CR-5536-DRAFT. Washington, D.C.: Nuclear Regulatory Commission (NRC).
- van Genuchten, M. Th. 1978. *Calculating the Unsaturated Hydraulic Conductivity with a New, Closed-form Analytical Model*. Research Report 78-WR-08. Water Resources Program, Princeton, New Jersey.
- van Genuchten, M. Th. 1980. A Closed-form Equation for Predicting the Hydraulic Conductivity of Unsaturated Soils. *Soil Sci. Soc. Am. J.* 44: 892-898.

## 4. SEISMIC ROCK MECHANICS

by *Simon M. Hsiung and Asadul H. Chowdhury*

*Investigators: Mikko P. Ahola (CNWRA), Barry H. G. Brady (formerly at Itasca), Asadul H. Chowdhury (CNWRA), Jaak J. Daemen (consultant), Roger D. Hart (Itasca), Simon M. Hsiung (CNWRA), Daniel D. Kana (SwRI), and Steve D. McKinnon (Itasca)*

### 4.1. TECHNICAL OBJECTIVES

Six specific objectives have been identified for the Seismic Rock Mechanics Research Project. These are:

- (1) Develop a good understanding of the information currently available concerning seismic effects on underground structures.
- (2) Assess, by conceptual models and experimental studies, the capabilities and limitations of rock-joint models and computer codes currently in use.
- (3) Demonstrate, by laboratory model studies and instrumented field studies, the degree of accuracy (validation) for the rock-joint models and computer codes used for seismic analysis in a tuff medium.
- (4) Assess by instrumented field studies the significance of seismic pumping and to demonstrate the degree of validation for the rock-joint models and computer codes for simulation of seismic effects on groundwater hydrology.
- (5) Identify and assess the key seismic-related parameters that are applicable to the Yucca Mountain site.
- (6) Generate technical data for preparing licensing-related positions as they relate to the effect of seismic action on the underground repository in a tuff medium.

The objectives are to be addressed in the following eight tasks.

- (1) Task 1 - Focused Literature Search
- (2) Task 2 - Laboratory Characterization of Jointed Rock
- (3) Task 3 - Assessment of Analytical Models and Computer Codes
- (4) Task 4 - Rock Dynamics Laboratory and Field Studies and Code Validation
- (5) Task 5 - Groundwater Hydrology Field Studies and Code Validation

- (6) Task 6 - Yucca Mountain Scoping Analysis
- (7) Task 7 - Technical Report
- (8) Task 8 - Quarterly Research Report

The second, third, fourth, and fifth objectives are currently being worked on. Results to date are reported herein.

#### **4.2. EVALUATION OF ROCK-JOINT MODELS AND COMPUTER CODES**

The evaluation of rock-joint models and associated computer codes consists of two studies: qualification (Task 3) and validation (Tasks 4 and 5). At the present, the qualification studies are in progress, and they are reported in this section. The objective of Task 3 is to identify and qualify (against benchmark problems and laboratory test results) analytical models (rock joint) and associated computer codes which may be useful in explaining and understanding the behavior of excavations in brittle, jointed, and partially saturated rock when the host formations are subjected to displacements, velocities, and accelerations imparted by earthquake or ground-shock motions.

Several codes that may be applicable were identified as current candidates for assessment. These include the distinct element codes UDEC and 3DEC (Cundall, 1988), the discrete element code DECICE (Williams et al., 1985), the finite-element codes HONDO II and SPECTROM-331 (Key, 1986), and the boundary element code BEST3D (Banerjee et al., 1985). These codes may model the dynamic performance of jointed-rock masses. The particular feature of each code qualifying it for consideration in the qualification studies is the formulation of an interface element on which rigid-body slip or separation can occur under static or dynamic loading. Whether the interface meets the requirements for satisfactory simulation of discontinuous deformation of jointed rock is the concern of these studies.

Two types of qualification studies are being performed. The first is to confirm that a code can reproduce the response of four well-established conceptual models (benchmark analytical problems) of the performance of a jointed-rock mass. Codes with acceptable performance will be candidates for the second type of qualification studies on single rock joint performance. Each candidate code will be used in the second type of study to analyze the dynamic response of a well-designed and executed laboratory experiment on a single rock-joint. Assessment will be made of the ability of the rock-joint models to handle accumulation of permanent shear displacement induced by ground shocks and earthquakes.

Currently, qualification studies on the HONDO II and UDEC codes against the four benchmark analytical problems have been completed, and reports were prepared by Brady et al. (1990) and Brandshaug et al. (1990). A brief discussion on these two reports is presented in this report; for detailed technical results and discussions, readers should refer to those two

documents. Also completed were the qualification studies on the 3DEC code against three of the four benchmark analytical problems.

Figure 4-1 shows the four benchmark problems, which represent discontinuous rock masses considered in the current study. The first two problems are static, and the other two are dynamic. The Mohr-Coulomb joint model was used in the analysis of all four benchmark problems.

#### 4.2.1. Cyclic Loading of a Specimen With a Slipping Joint

An elastic block with an internal inclined closed joint is shown in Figure 4-1(a)i. When a constant axial displacement  $u_a$  is applied to one end of the block and the other end is fixed, the resulting load causes inelastic slip on the joint. If the sense of displacement on the end of the block is reversed, the original unloaded condition may be reestablished; the load-displacement paths for loading and unloading, however, are quite different. As shown by Olsson (1982), the stress-displacement relation for the loaded specimen illustrated in Figure 4-1(a)ii consists of three components. The subtle hysteresis response in a load-unload cycle is a result of joint slip and frictional locking at various stages of block deformation. A closed-form solution for the determination of the three slopes in Figure 4-1(a)ii were provided by Brady et al. (1985).

The results for the UDEC and 3DEC analyses with the standard Mohr-Coulomb rock joint for the stiffnesses (slopes) in loading and unloading were very close to the independent closed-form solution. Table 4-1 shows the results from the conceptual model, UDEC, and 3DEC in plane strain and plane stress.

It was observed that the results from both UDEC and 3DEC analyses agree less closely as the length of the slipping crack increases with respect to the width of the specimen. This observation is expected, as the conceptual model assumes uniform distribution of normal stress on the crack and the elastic extensions, while, in practice, stress concentrations become more significant as the length of the slipping crack increases.

The HONDO II analysis of a jointed block did not, however, reproduce the expected hysteric response. This suggested the joint formulation in HONDO II is not sufficiently rigorous to express the mechanics of joint deformation in terms of a Mohr-Coulomb joint. The source of the problem for inability to reproduce the expected response was not identified.

#### 4.2.2. Circular Excavation Intersected by a Joint

The circular excavation intersected by a joint presents a problem of joint slip in the zone of a relatively high-stress gradient generated near a circular excavation, as illustrated in Figure 4-1(b). Consideration of the state of stress on the plane of weakness shows that, at its intersection with the excavation, slip occurs when the angular coordinate of the joint intersection is greater than the angle of friction of the joint (Brady and Brown, 1985). Once slip occurs,

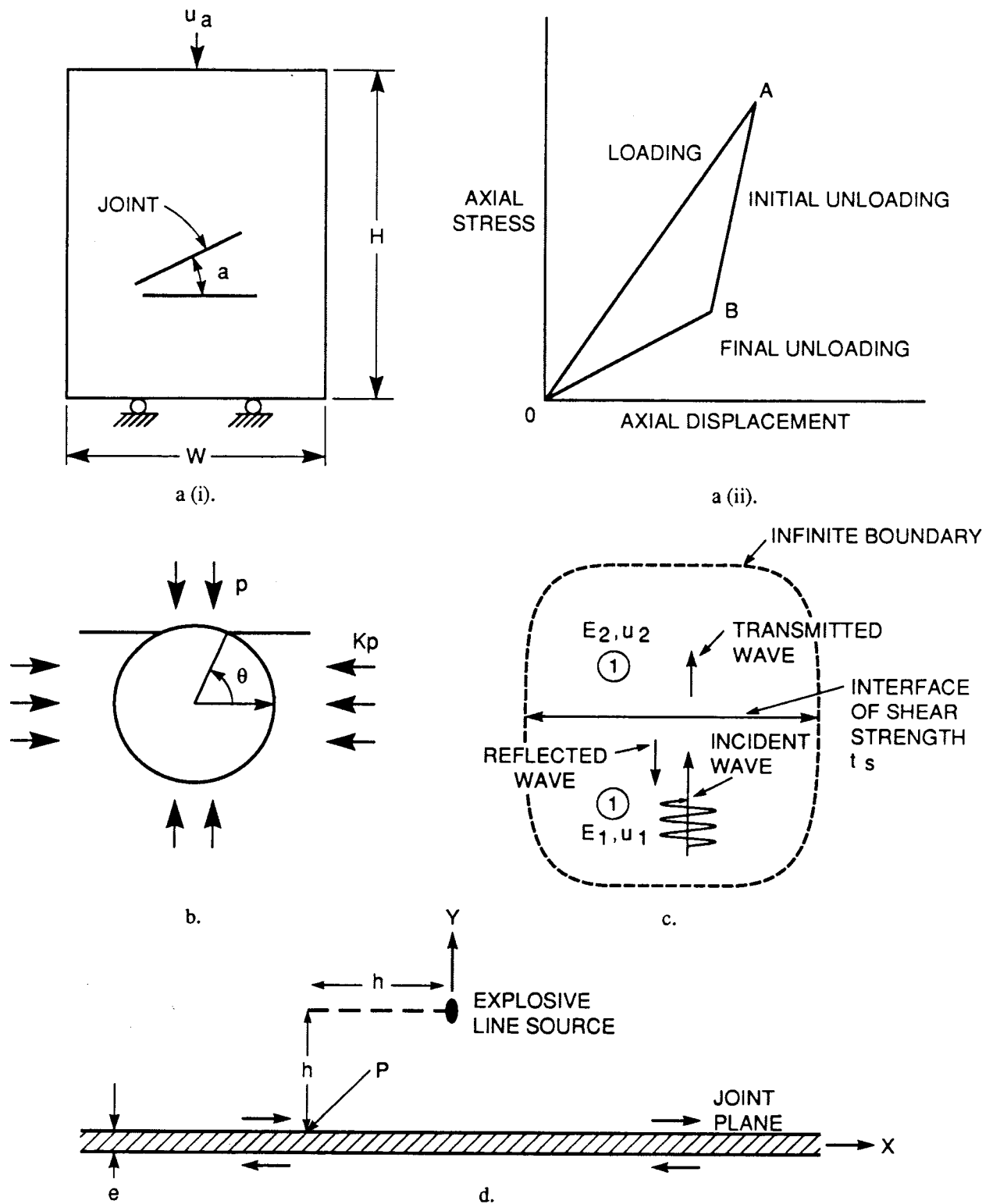


Figure 4-1. Four benchmark analytical problems: (a) cyclic loading of a specimen with a slopping joint, (b) joint intersecting a circular excavation, (c) slip in a jointed body induced by a harmonic shear wave, and (d) line source in an elastic medium with slip-prone joint

**Table 4-1. COMPARISON OF 3DEC RESULTS WITH CONCEPTUAL MODEL AND UDEC FOR A BLOCK WITH A SLIPPING CRACK UNDER CYCLIC LOADING**

Loading Segment	Conceptual Model	UDEC		3DEC Plane Strain		3DEC Plane Stress	
	Stiffness (GPa/m)	Stiffness (GPa/m)	Error (%)	Stiffness (GPa/m)	Error (%)	Stiffness (GPa/m)	Error (%)
Load (OA)	36.34	36.04	0.82	36.5	-0.44	36.8	-1.26
Unload (AB)	38.89	38.91	-0.05	38.83	0.15	38.33	1.43
Unload (BO)	34.52	34.14	1.10	35.27	-2.17	35.2	-1.96

static equilibrium can only be achieved when the tangential stress is zero at the boundary-joint intersection. This implies that substantial redistribution of stress may occur.

The results of the UDEC analysis indicated that, the stress magnitude calculated with UDEC converges on the results predicted analytically, despite the very high boundary stress gradient near the intersection of the joint and the excavation. Compared with the elastic solution, the boundary stress is reduced notably in the crown of the excavation and increased in the floor. These results are consistent with the discussion in the previous paragraph. The evaluation of HONDO II code was not performed against this benchmark problem, since it did not satisfy the previous simpler, static benchmark problem.

#### **4.2.3. Slip in a Jointed Body Induced by a Harmonic Shear Wave**

The dynamic behavior of a plane discontinuity loaded by a normally incident, plane harmonic shear wave presents a simple test of the dynamic performance of UDEC and 3DEC. The problem shown in Figure 4-1(c) consists of a normally incident, plane harmonic shear wave and a plane discontinuity with limited shear strength separating two homogeneous, isotropic, semi-infinite elastic bodies. If the transient shear stress exceeds the shear strength of the joint, slip will occur at the interface. As a result, energy is partitioned between reflected and transmitted waves and absorption at the interface. In an analysis of this problem by Miller (1978), closed-form solutions were derived for the transmission, reflection, and absorption

coefficients. Comparison of the acoustic coefficients for the wave propagation is conducted in terms of the dimensionless stress,  $\tau_d$ , of the incident wave, defined by:

$$\tau_d = (\rho G)^{1/2}(\omega U)/\tau_s \quad (1)$$

where  $\rho$  is mass density,  $G$  is shear modulus,  $U$  is displacement amplitude of incident wave,  $\tau_s$  is joint cohesion,  $\omega$  is frequency of incident wave, and  $(\rho G)^{1/2} = \gamma$ .

A special version of 3DEC (3DECSP) was used for analysis. This version has the capability to simulate nonzero cohesion and tension when discontinuity shear and/or tensile strength is exceeded.

Comparison of the acoustic coefficients for the wave propagation is conducted in terms of the dimensionless stress. Good correspondence is observed among the UDEC results, 3DEC results and closed-form solutions over a wide range of dimensionless stresses. Both UDEC and 3DEC analyses confirmed that when the joint has a limited shear strength or cohesion, the shear wave transmitted across the interface has the peak amplitude of shear stress.

The way in which boundary tractions can be specified in the HONDO II code prevented the comparison of acoustic coefficients at the interface for the HONDO II and closed-form solutions. The particular problem with HONDO II is that it is not possible to apply a static normal traction on one boundary and an independent, time-varying traction, either normal or shear, to another. This prevented application of a static normal stress to the joint, which is required to mobilize the joint shear strength and thus support wave propagation across it. The joint interface model incorporated in the HONDO II code does not include the component for cohesion. Examining the nature of the motion associated with shear-wave interaction with a joint of zero shear strength, the joint reflected the wave almost completely.

#### 4.2.4. Line Source in an Elastic Medium with a Slip-Prone Joint

The problem shown in Figure 4-1(d) consists of a plane joint of infinite lateral extent in an elastic medium and a dynamic load at some distance from the discontinuity. The closed-form solution to this problem was derived by Day (1985) as a special symmetric condition for the general problem of slip of an interface due to a dynamic point source (Salvado and Minster, 1980). The problem was solved in terms of the magnitude of slip induced on the joint by the explosive-induced local load.

The dimensionless slip at point P (Figure 4-1(d)) calculated using UDEC and 3DEC was plotted against the dimensionless time in Figure 4-2 and was compared with the analytical solution given by Day (1985). The result of the UDEC analysis provided satisfactory correspondence with the closed-form solution, confirming that the two-dimensional distinct-element scheme and the Mohr-Coulomb rock-joint model provided a coherent basis for dynamic analysis of jointed rock. This exercise and that involving harmonic loading of a jointed medium

as illustrated in Section 4.2.3 also confirmed the satisfactory performance of the viscous (nonreflecting) boundaries for the UDEC problem domain.

The result of the 3DEC analysis provided satisfactory correspondence with the closed-form solution until the dimensionless time of 1.49. After that, a considerable deviation was shown, which can be attributed to boundary iterations (reflection). The effects of boundary reflection on slip response may be reduced by adjusting the model size. The qualification study on HONDO II against the problem was not performed, since HONDO II did not satisfactorily reproduce the response of the previous simpler problem involving harmonic loading of a jointed medium.

#### **4.2.5. Summary of Results**

Performance of UDEC on the suite of benchmark problems indicates that the code is a valid simulation of jointed rock, to the extent that the mechanics of these media may be represented by the conceptual models expressed in the various problems. However, whether UDEC is a valid simulation of the engineering behavior of jointed rock requires laboratory studies to verify the Continuously-Yielding and Barton-Bandis joint formulations, and field studies to evaluate the behavior in a proper engineering setting.

In its current formulation, HONDO II is not capable of simulating the mechanics of jointed rock in a way suitable for repository design and performance assessment. Some of its deficiencies in this respect are related to the application of static and dynamic boundary loads in the analysis.

### **4.3. PRETEST ANALYSIS FOR THE ROCK-JOINT DYNAMIC SHEAR TEST**

The objective of this pretest analysis is to provide preliminary insight to assist in evaluating the effects of shear-test apparatus on dynamic response of the tuff-joint specimen. A series of numerical calculations were performed with the three-dimensional distinct element code, 3DEC, to simulate the shear-test apparatus and the dynamic shear test of a naturally jointed tuff specimen.

This analysis is considered the first step in the evaluation and development of an analytical model representation of a naturally jointed tuff specimen. The Coulomb and continuously yielding joint models are used in 3DEC to demonstrate the evaluation procedure. The Coulomb slip model is traditionally used in rock mechanics to describe primarily the static response of a rock joint. The continuously yielding model is a more complex algorithm that simulates continuous yielding, displacement-weakening, and hysteretic effects, and has greater potential to represent joint behavior associated with dynamic loading. These models are described in detail by Kana et al. (1989). The results of this analysis must be considered preliminary because actual test data from naturally jointed tuff specimens are not yet available. Nevertheless, these simulations serve as a starting point for correlation to laboratory test results once the experimental program has begun.

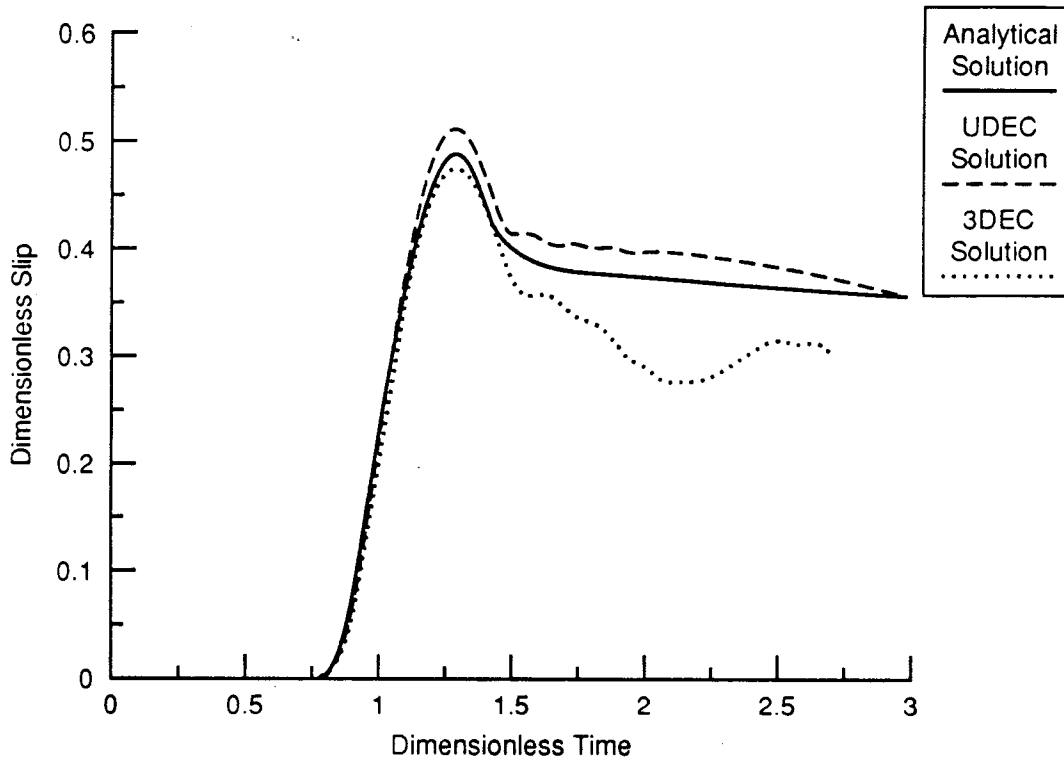


Figure 4-2. Comparison of dimensionless slip at point P with Coulomb joint-model dimensionless slip =  $(4 h p \beta^2 / m_0) \delta u$ , dimensionless time =  $t \beta / h$

#### 4.3.1. 3DEC Models of the Dynamic Shear Test

Two 3DEC models were used in the preliminary investigations: (1) a simple base model of a jointed-tuff specimen and (2) a full model consisting of a jointed-tuff specimen inside the shear box. The geometries of the two models are shown in Figures 4-3 and 4-4. The base model of the jointed-tuff specimen consists of two blocks and assumes uniform normal and shear stresses along the interface joint plane of these two blocks. The relative shear motion between the two blocks of the specimen is prescribed directly according to a given shear-displacement time history. Normal and shear stresses and normal displacements along the joint are calculated according to the prescribed Coulomb and continuously yielding joint models. This base 3DEC model is the primary tool for investigating the analytical representations for joint mechanical behavior.

The full model of the jointed specimen inside the shear box is a more elaborate representation of the shear-test condition, as described by Kana et al. (1990), and can be used to assess the influence of the actual experimental conditions on the dynamic response of the tuff-joint specimens.

#### 4.3.2. Simulation of the Demonstration Test on a Concrete-Joint Specimen

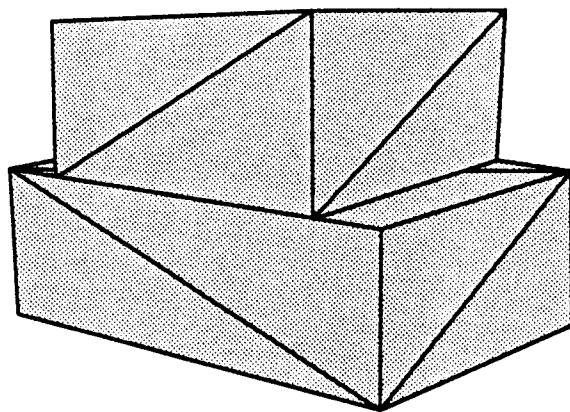


Figure 4-3. 3DEC simple base model of a jointed tuff specimen

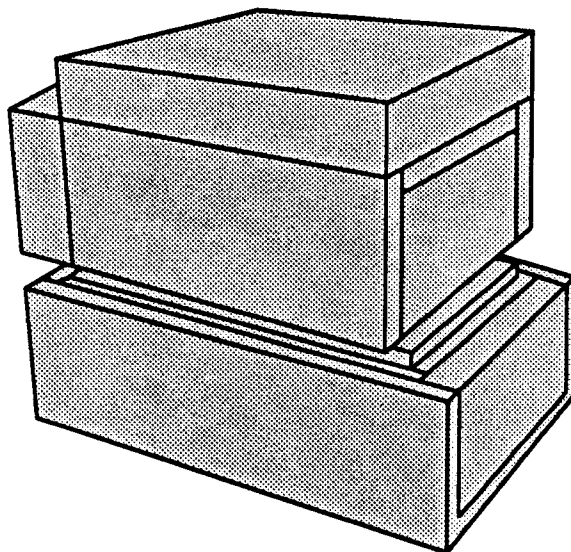


Figure 4-4. 3DEC full model consisting of a jointed tuff specimen inside the shear box

The application of the 3DEC base model is illustrated by simulating the pseudo-static demonstration test on a concrete-joint specimen, reported by Kana et al. (1990). The continuously yielding model is used for these simulations. Comparisons are illustrated below both for joint normal stress versus joint closure and for joint shear displacement versus joint shear stress.

In the continuously yielding model, the normal and shear stiffnesses for the joint are normal stress dependent and are given by

$$\begin{aligned} K_n &= a_n \sigma_n^{e_n} \\ K_s &= a_s \sigma_n^{e_s} \end{aligned} \quad (2)$$

where  $K_n$  is joint normal stiffness;  $K_s$  is joint shear stiffness; and  $a_n$ ,  $e_n$ ,  $a_s$ , and  $e_s$  are constants.

The joint normal-stress versus joint closure curve obtained from the 3DEC base model using the normal stiffness parameters derived from experimental results on a concrete-joint specimen (Kana et al., 1990) is compared to the experimental curve in Figure 4-5.

The best fit of the results from the continuously yielding model in 3DEC to the laboratory test results for joint shear stress versus joint shear displacement provides the following continuously yielding model parameters (Cundall and Lemos, 1988); and the best-fit curve is shown in Figure 4-6.

$\phi$	(intrinsic friction angle) = $37^\circ$
$\phi_{mo}$	(initial friction angle) = $85.9^\circ$
$R$	(joint roughness parameter) = 0.31 mm

#### 4.3.3. Preliminary Numerical Simulations of Tuff Joints

Joint and basic material properties for the jointed tuff specimens to be tested are not available. Therefore, "recommended" tuff-joint properties given in the *Site Characterization Plan Conceptual Design Report* (SCP-CDR) (MacDougall et al., 1987) were used to the extent possible to perform simulations for providing preliminary assessments of tuff-joint behavior based upon the different joint models. Since tuff properties for the continuously yielding model are not directly available from the SCP-CDR, two conditions of properties, one for a smooth joint and one for a rough joint, were investigated. The properties used in the joint models are listed in Table 4-2.

The 3DEC base model was used with an assumed constant normal stress of 5 MPa during shear testing. Joint responses to monotonic loading, load reversal, harmonic loading, and earthquake loading conditions were evaluated. The loading conditions were applied as displacement histories to the joint and inertial effects were neglected. Because neither the Coulomb nor the continuously yielding model are velocity dependent, the time scale does not influence the

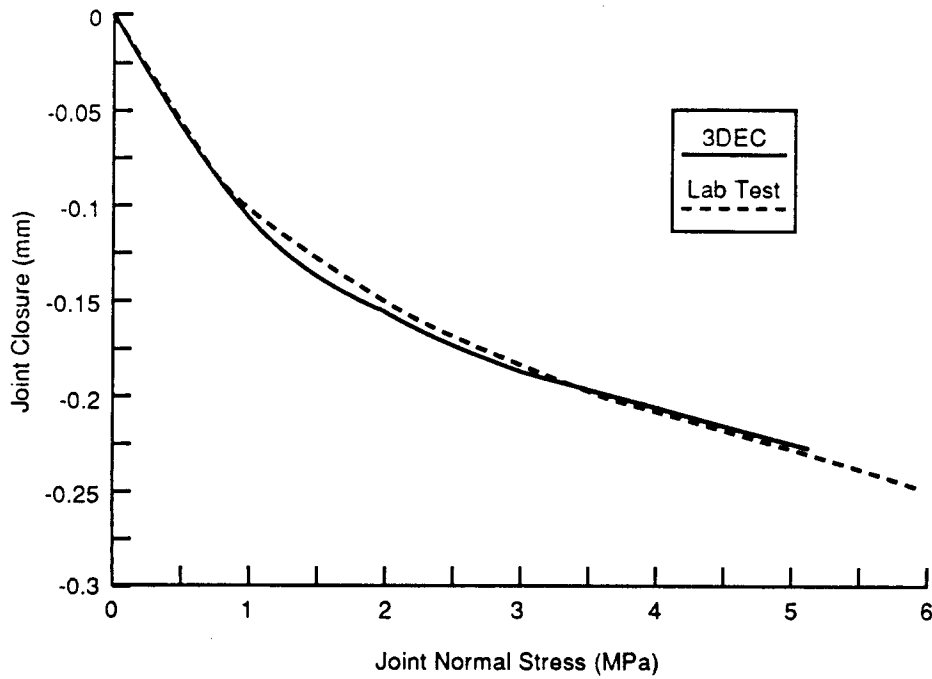


**Figure 4-5. Comparison of 3DEC model to laboratory test results for joint closure variation with pseudostatic normal stress**

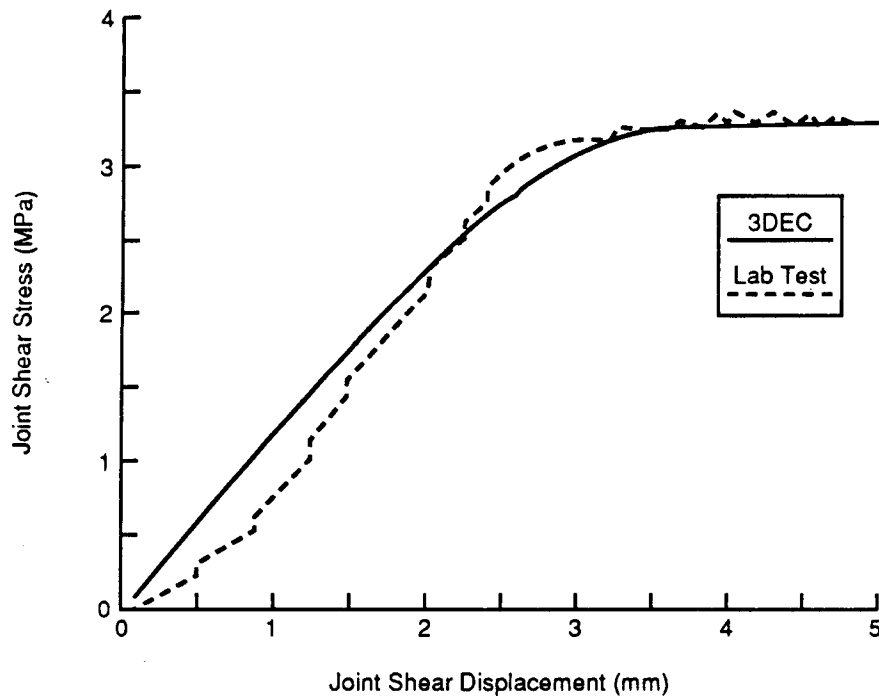


**Figure 4-6. Comparison of 3DEC model to laboratory results for joint stress variation with joint shear displacement at normal stress = 4.36 MPa**

**Table 4-2. ASSUMED TUFF-JOINT MODEL PROPERTIES**

Assumed Parameters	Coulomb Model	Continuously Yielding Model	
		Case 1	Case 2
Normal Stiffness (GPa/m)	100.0	100.0	100.0
Shear Stiffness (GPa/m)	10.0	10.0	10.0
Cohesion	0.0	0.0	0.0
Tensile Strength	0.0	0.0	0.0
Intrinsic Friction Angle	28.4	28.4°	28.4°
Initial Friction Angle	----	42.6°	56.7°
Roughness Parameter (mm)	----	0.1	0.1

→ shear stress-displacement results. /

#### **4.3.3.1. Monotonic Loading**

Figure 4-7 presents the resulting shear stress-displacement curves for the Coulomb model and continuously yielding model Cases 1 and 2. Both continuously yielding cases displayed yielding before the residual shear stress was reached. The properties assumed for Case 1 led to a curve without a peak, while Case 2 displayed a peak shear stress of 2.96 MPa, corresponding to a friction angle of 30.6 degrees. The maximum dilation angle calculated at the peak shear stress for the continuously yielding model Case 2 was 2.2 degrees. The Coulomb model and continuously yielding model Case 1 displayed no joint dilation.

#### **4.3.3.2. Load Reversal**

Reversal in shear loading was simulated by prescribing a shear displacement history as shown in Figure 4-8. The resulting shear stress-displacement curves are shown in Figures 4-9 and 4-10 for the Coulomb model and continuously yielding model Case 1, respectively.

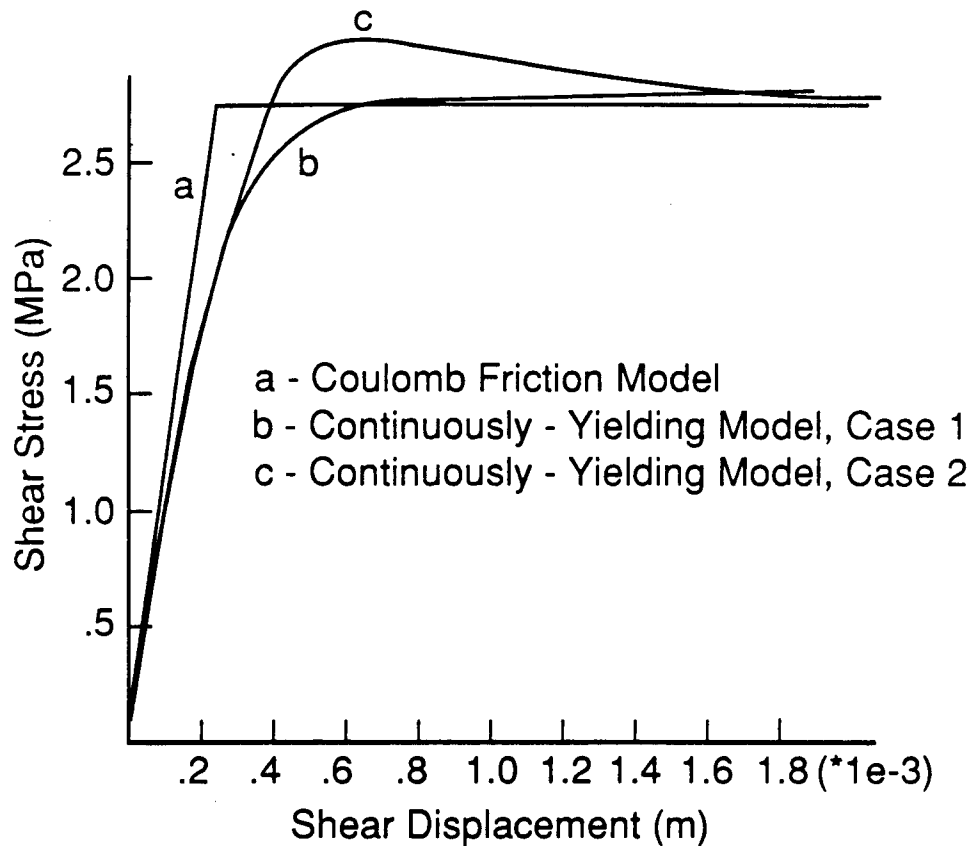


**Figure 4-7. Shear stress displacement curve for monotonic loading with Coulomb friction model and continuously yielding model cases 1 and 2**

**4.3.3.3. Harmonic Loading**

A sine-wave shear displacement was applied for the harmonic loading study. For both cases, the continuously yielding model displayed a loss in shear strength upon cyclic shearing (Figure 4-11) while the Coulomb model did not display shear strength loss.

**4.3.3.4. Earthquake Loading**

The shear stress-displacement curve for the Coulomb model based on a typical earthquake velocity drive is shown in Figure 4-12. Slip occurred at 2.7 MPa for this model. The curve for the continuously yielding model Case 2 is given in Figure 4-13.

**4.3.4. Influence of Test Conditions**

Preliminary calculations were made to study the influence of the shear-box test setup on joint response. The objective was to determine the influence of input frequency on joint motion, taking into account the stiffness of the grout, the shear box and the horizontal and vertical loading system. The full shear-box model, shown earlier in Figure 4-4, was used for the calculations.

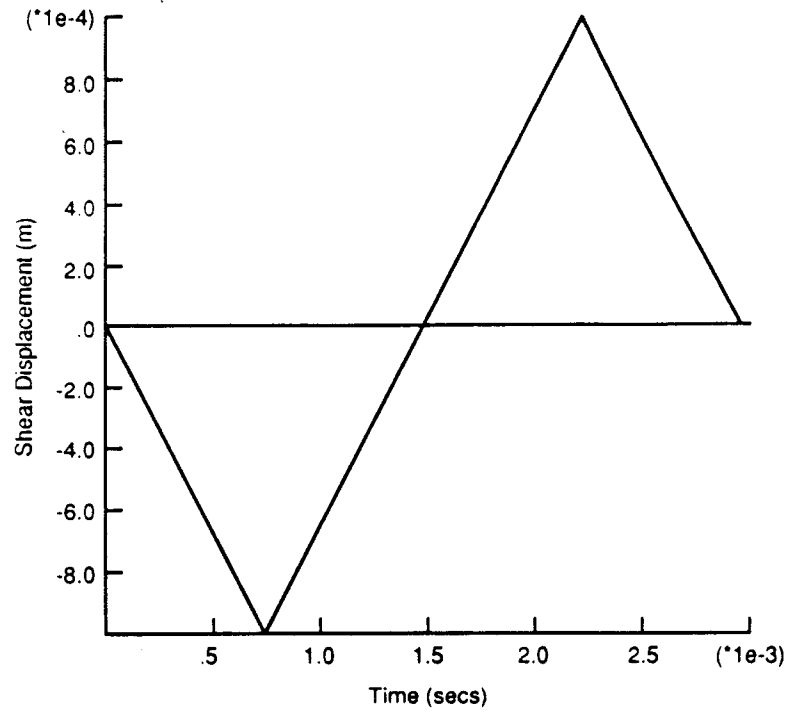


Figure 4-8. Shear displacement path for load reversal

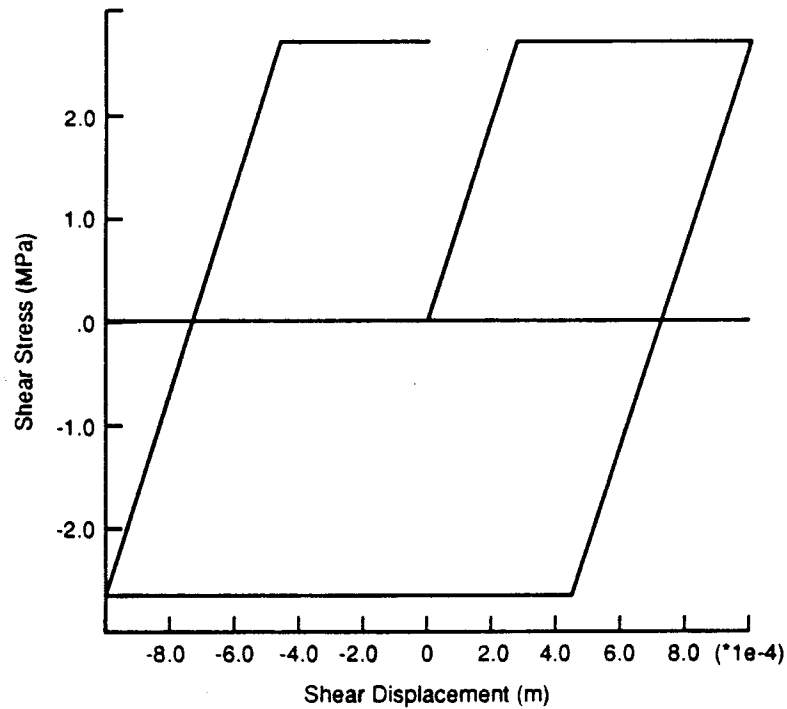


Figure 4-9. Shear stress displacement curve for load reversal with Coulomb friction model

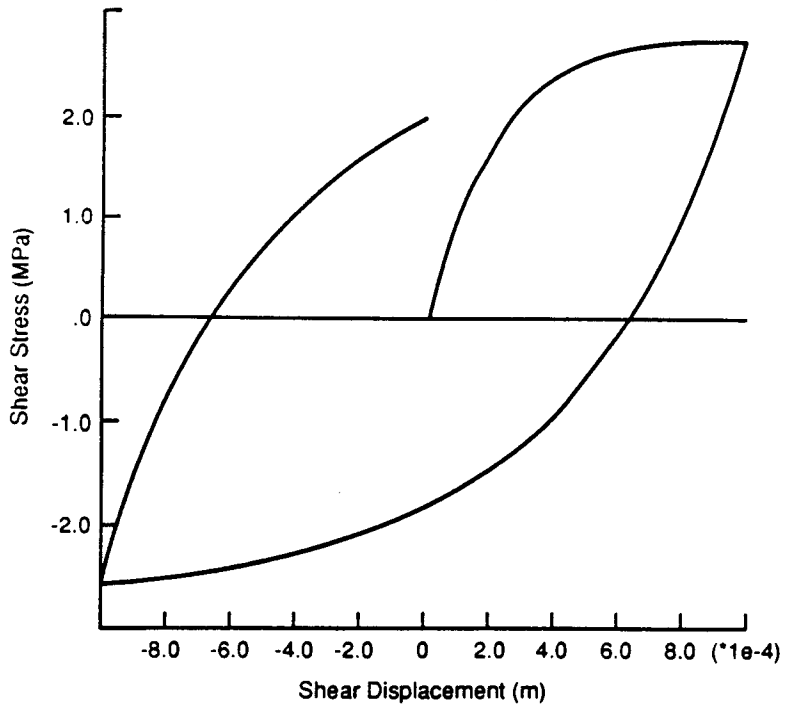


Figure 4-10. Shear stress displacement curve for load reversal with continuously yielding model, case 1

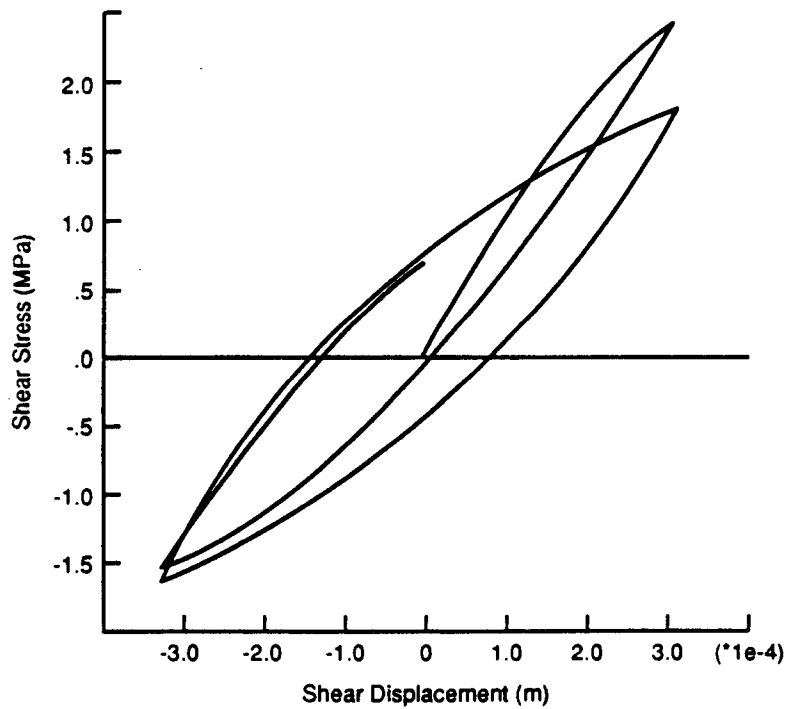
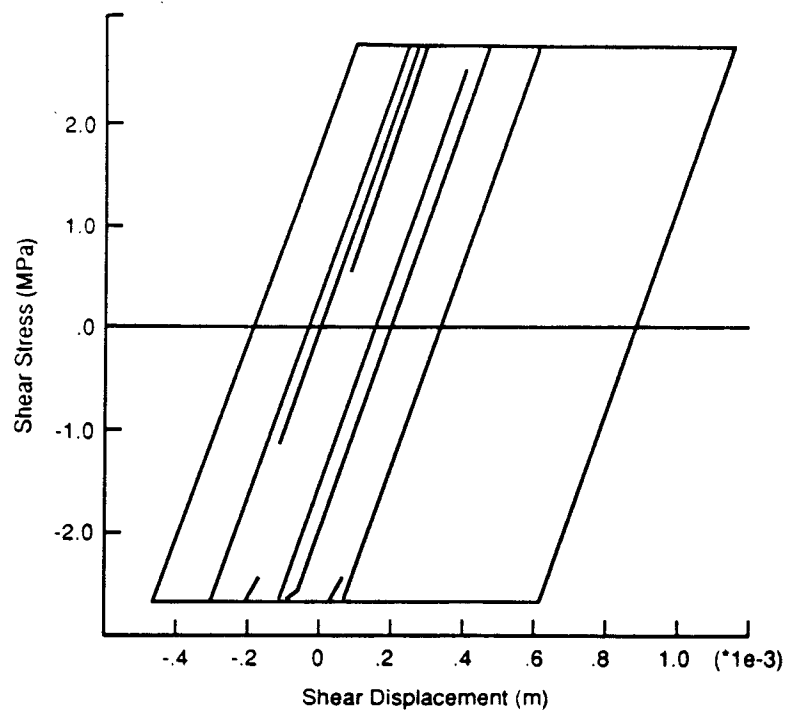
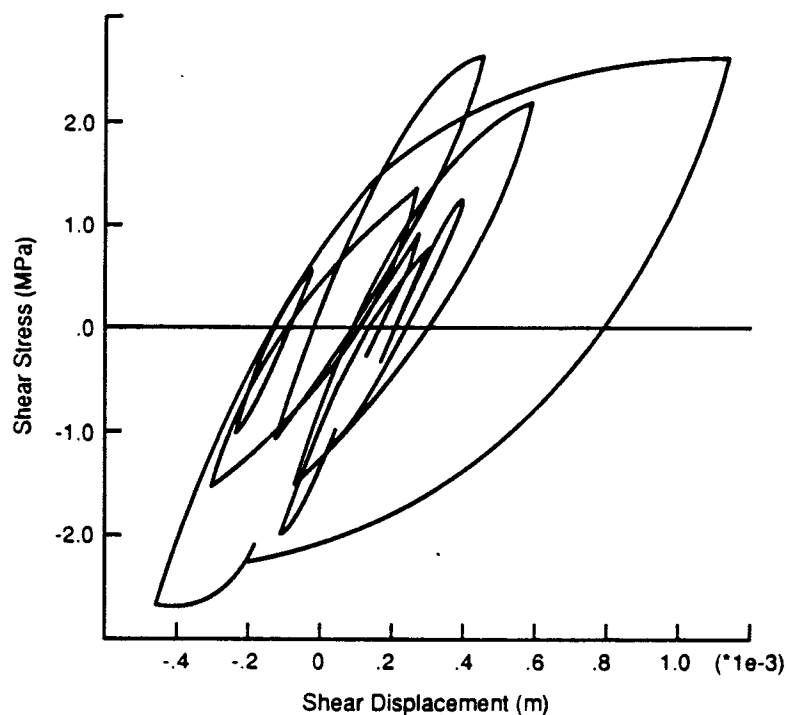


Figure 4-11. Shear stress displacement curve for harmonic loading with continuously yielding model, case 2



**Figure 4-12. Shear stress-displacement curve for earthquake loading with Coulomb friction model**



**Figure 4-13. Shear stress-displacement curve for earthquake loading with continuously yielding model, case 2**

#### 4.3.4.1. 3DEC Full-Shear Box Model

The 3DEC full-shear box model consists of blocks representing the tuff specimen with the same dimensions as the 3DEC base model. The full model, as shown in Figure 4-4, has a 1-inch thick grout layer, a 2-inch thick steel box, and horizontal and vertical loading blocks with stiffness approximating that of the load system. Figure 4-14 shows a vertical section through the 3DEC model and identifies the component materials. The bottom of the 3DEC model is fixed in all directions.

After a normal stress of 5 MPa is applied to the top loading block, the top block is fixed in the vertical direction during the dynamic shear-load phase. The dynamic load is applied as a horizontal velocity to the left loading block. Displacements and stresses are monitored during the simulations at five locations denoted on Figure 4-14. Point A corresponds to the left loading block; point B, to the top loading block; and points C, D, and E, to points along the tuff joint plane through the center of the model. The tuff joint is assumed to be elastic for the majority of the simulations. Table 4-3 presents the properties assumed for this analysis.

#### 4.3.4.2. Dynamic Analysis

A sine-wave drive signal was applied to the left loading block to study dynamic effects. Different frequency conditions were investigated. The peak velocity was varied for each frequency so that the peak displacements at point A for all cases were the same.

**Table 4-3. ASSUMED PROPERTIES FOR 3DEC FULL SHEAR BOX MODEL**

Model Materials	Young's Modulus (GPa)	Poisson's Ratio
Tuff Specimen	30.4	0.22
Grout	10.1	0.22
Steel	210.0	0.30
Left Loading Block	210.0	0.30
Top Loading Block*	210.0	0.30

\*For one run the Young's Modulus was 21 GPa to simulate a soft loading block.

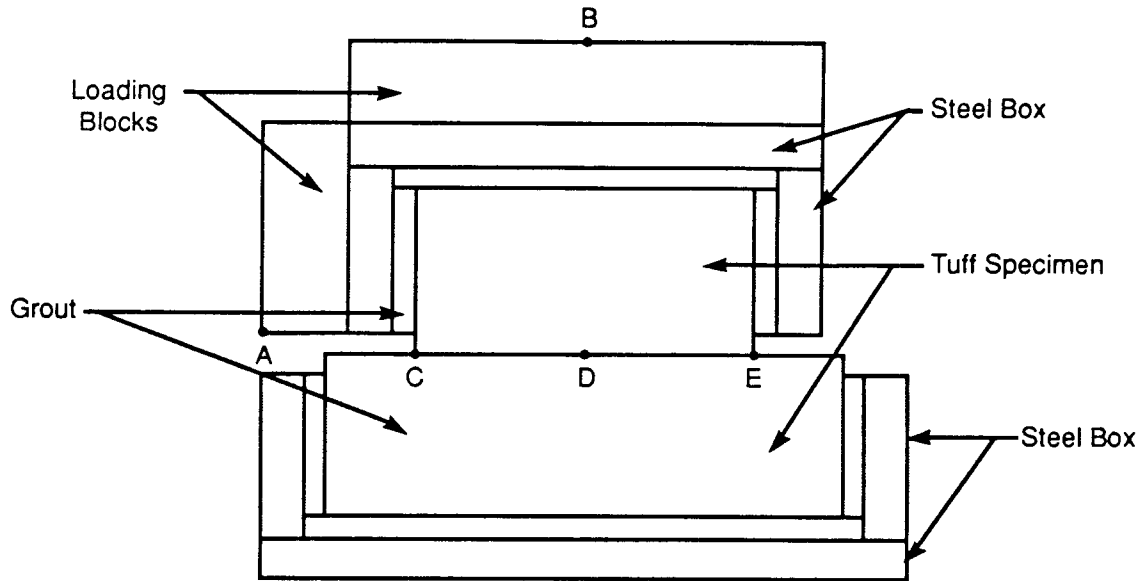


**Figure 4-14. Vertical section through 3DEC full shear box model**

The simulation results show an obvious deviation from the prescribed sine-wave input (Figure 4-15) as a consequence of the natural frequency of the model system. The influence of natural frequency decreases as input frequency decreases (compare Figures 4-15 and 4-16) and increases as the stiffness of the left loading block decreases. The normal stress across the joint was not uniform for these simulations. Normal stress at the center of the model was lower than that at the joint edges, and more slip was calculated at the center when the joint was allowed to slip.

#### **4.3.5. Summary and Recommendations**

The 3DEC base model can be used to investigate existing-joint constitutive relations and identify conditions when joint-model improvements are needed. As more information from the laboratory tests becomes available, the joint model can be improved or revised.

The 3DEC base model neglects inertial effects of joint behavior. Ascertaining the importance of velocity dependency on tuff-joint response by means of laboratory testing is important. If inertial effects are important, modification to the Coulomb model and continuously yielding model will be required.

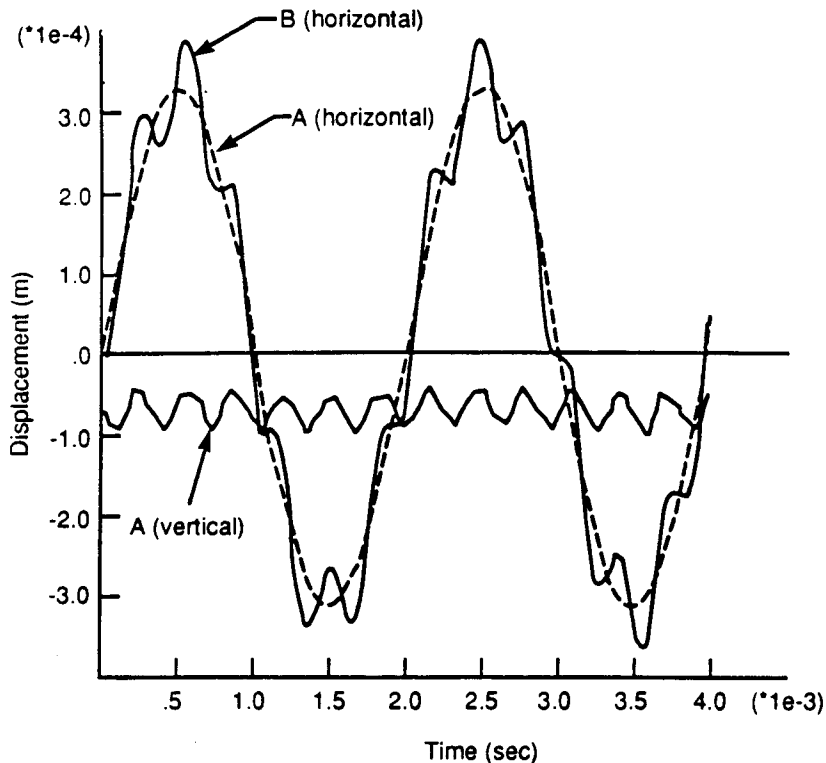


**Figure 4-15. Horizontal and vertical displacement histories for 500 Hz input frequency**

For the typical range of frequencies of earthquake loadings (i.e., less than 50 Hz), the response of the shear-test apparatus, given the assumed properties, did not influence joint response significantly. Information was not available, however, on the actual stiffness of components of the test apparatus. A new set of simulations with a more complete material characterization is required.

If explosive shock loading is simulated, the presence of high-frequency components in the input pulse may affect joint response. This phenomenon should also be investigated.

#### **4.4. LABORATORY INVESTIGATION OF ROCK-JOINT BEHAVIOR**

##### **4.4.1. Development of Laboratory Test Apparatus**

Task 2 of the Seismic Rock Mechanics Project includes various activities whose objective is the laboratory characterization of the static and dynamic behavior of jointed-rock specimens. Task 2 has two major preprogram activities: (1) design, development, installation, and operation of a rock-joint dynamic shear-test apparatus and (2) sample collection and preparation. The latter is discussed in the following subsection. The apparatus will be used to measure responses that will quantify the properties of rock joints when subject to various prescribed static and dynamic conditions. Both full-scale specimens extracted from field site and later scale-model specimens are to be accommodated by the apparatus. The development of the rock-joint, dynamic shear-test apparatus has been reported by Kana et al. (1990).

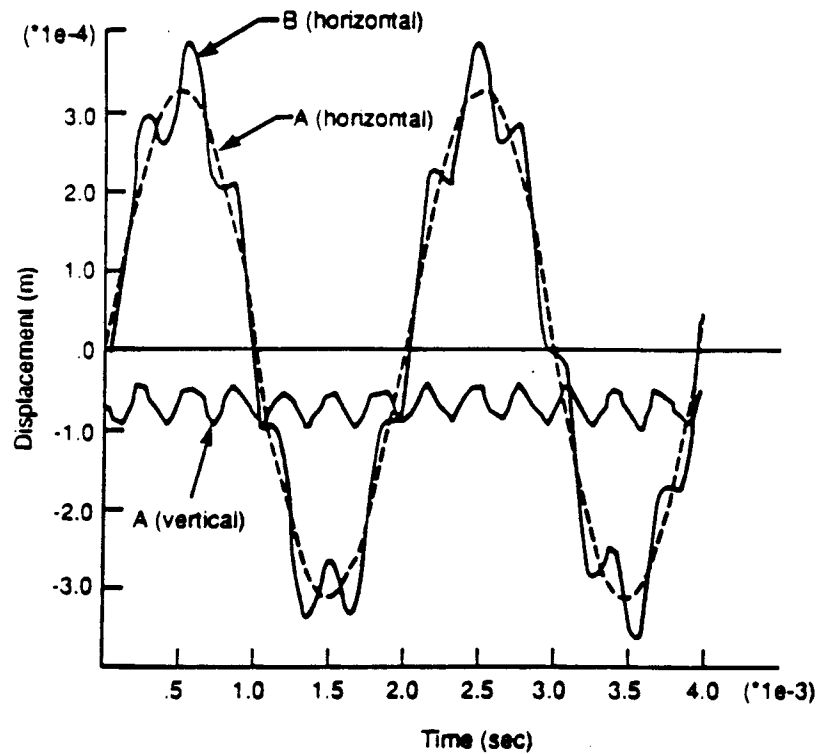
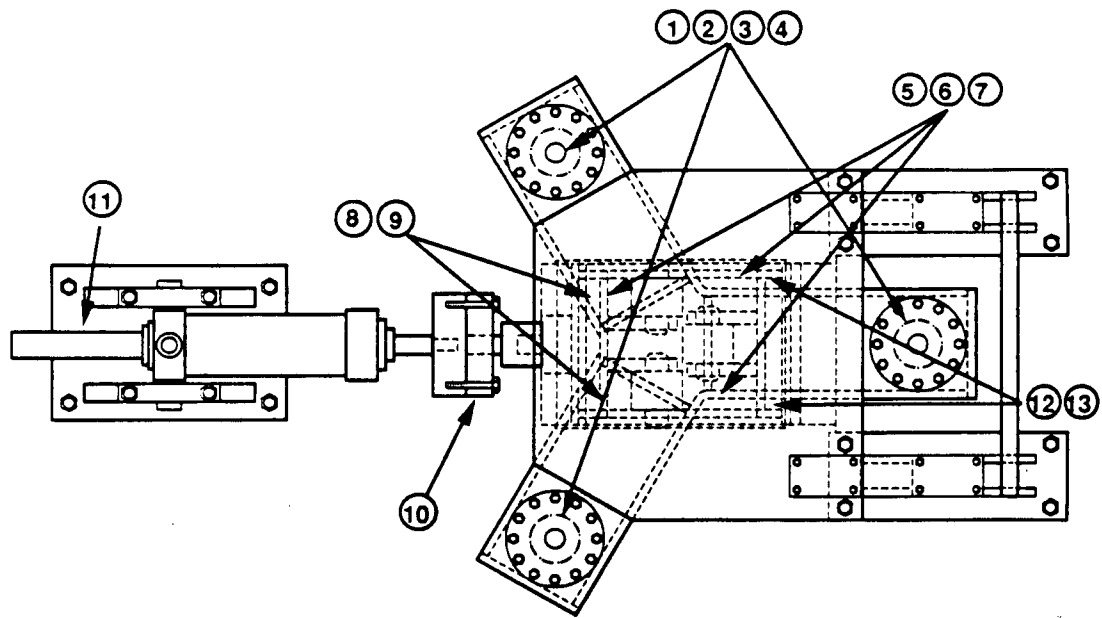


**Figure 4-16. Horizontal and vertical displacement histories for 50 Hz input frequency**

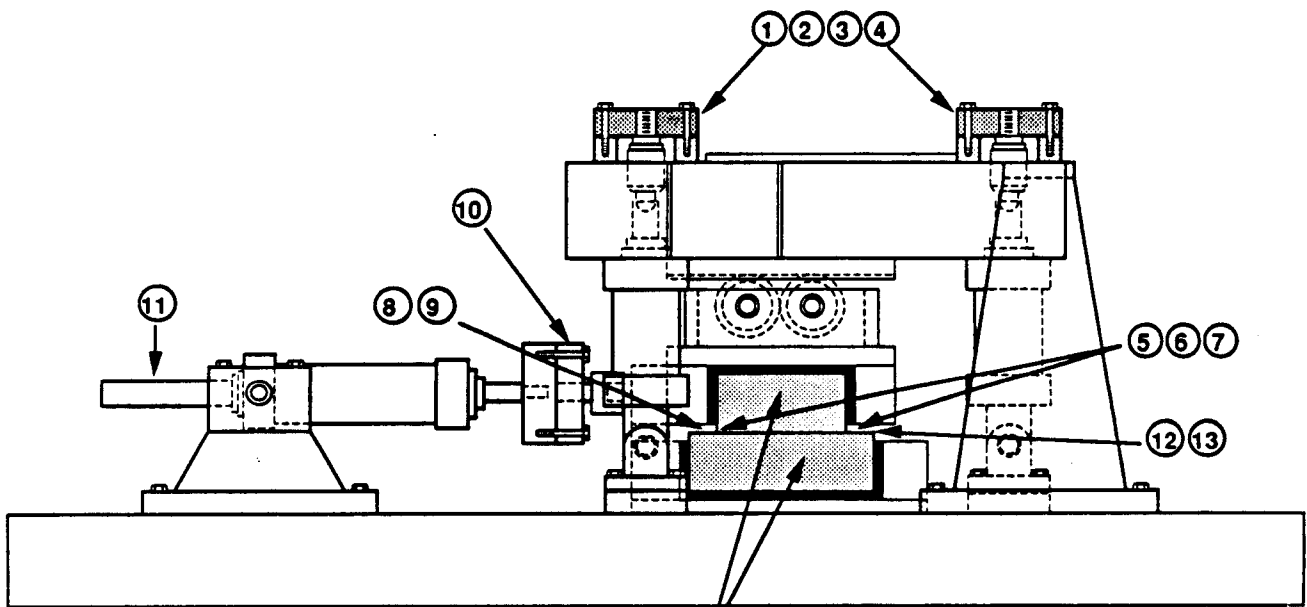
In order to perform direct dynamic shear tests for natural joints in tuff materials, a servocontrolled test apparatus with combined normal and direct shear capability was designed, fabricated, and assembled. The philosophy incorporated into the rock-joint, dynamic shear-test apparatus consists of providing a simulation of various dynamic motions of a natural rock joint and measuring of the reaction forces associated with each type of imposed motion. In effect, the apparatus is to simulate a single rock joint and to characterize its behavior under various types of static and dynamic loads. Thus, a jointed rock specimen is subjected to a static normal load representing the normal component of the in situ stress field. Then, a dynamic shear motion is applied, and the corresponding dynamic shear force is determined while the normal load is maintained and any normal motion is measured.

Figure 4-17 shows the assembly of the dynamic shear-test apparatus. The apparatus consists of vertical and horizontal servocontrolled loading actuators, reaction frames, and shear-box fixtures. The maximum loading capacity for each of the three vertical actuators is 30,000 lb (0.133 MN) and 50,000 lb (0.222 MN) for the horizontal actuator. Each vertical actuator is equipped with a 25,000-lb (0.1112 MN) capacity load cell for monitoring the applied forces. The instrumentation for monitoring the applied normal load is arranged to provide an analog output for the sum of the three load cells as well as for the individual signals. The horizontal actuator, equipped with a 50,000-lb (0.222 MN) load cell, can be operated in either load or displacement control modes. Several loading patterns such as harmonic load and displacement, ground shock, and earthquake time histories can be applied through the use of a function generator.



Note: Numbers refer to data channels identified in Table 4-4

TOP VIEW



TUFF SAMPLE

SIDE VIEW

Figure 4-17. Assembly and instrumentation diagram

The bottom shear box was designed to house a specimen with maximum dimensions of 12 x 8 x 4 inches (30.5 x 20.3 x 10.2 cm). The top shear box houses a specimen with maximum dimensions of 8 x 8 x 4 inches (20.3 x 20.3 x 10.2 cm). Both are grouted in their respective specimen boxes. A 1-inch (2.54-cm) gap between the top and bottom box edges of the assembled specimen unit is allowed. The bottom shear box and other fixed devices are bolted to a 4-foot x 7-foot x 6-inch (1.22-m x 2.13-m x 15.24-cm) thick steel base plate for rigidity. The horizontal translation of the top shear box along the direction of shearing is guided through three rollers between the top shear box and normal load frame and through side rollers not shown in Figure 4-17.

#### **4.4.1.1. Normal Load System**

Normal compression is applied to the specimen by three vertical actuators set at 120-degree angles about the specimen's vertical centerline. These actuators act through individual load cells whose output is summed and used as the control signal. The total normal load is controlled at a preselected static or slowly ramped value. This total resultant load is ultimately applied to the specimen via the normal load frame, which acts on the three normal load rollers (see top view of Figure 4-17), and thereby on the top specimen box. The line of action for this normal load is through the null position of the top specimen box. The normal load frame is constrained to three degrees of freedom: vertical translation, rotation about the horizontal axis in line with the shear, and rotation about the horizontal axis transverse to the shear. These constraints are assured by two double flexures connecting the normal load frame to a fixed reaction brace, and by the two side roller assemblies, which act on the top specimen box. Thus, the top specimen block is constrained to these same three degrees of freedom, plus a fourth, which is translation in the direction of shear.

#### **4.4.1.2. Horizontal Load System**

The horizontal actuator produces direct shear to the top specimen box via the horizontal load cell, which acts through a spherical coupling. This coupling accommodates slight misalignment in the horizontal shearing motion and allows for elevation changes of the top specimen due to vertical load, joint surface roughness, and progressive wear. Control of the horizontal actuator load is based on the horizontal, relative shear displacement, described in the next subsection.

#### **4.4.1.3. Instrumentation and Control**

Instrumentation channels are identified in Figure 4-17 and Table 4-4. All load cells are typical, commercial strain-gauge units with dominant sensitivity to tension and compression along one axis. Reaction to the applied static normal load is measured in terms of relative vertical displacements of the two blocks at three locations near the interface. The transducers used for measurements are a proximity (noncontacting) eddy-current sensing type, since horizontal movement of the two surfaces must be allowed, but only vertical displacement changes must be sensed.

The horizontal transducers, mounted by bonding onto the top specimen block, provide one measure of top-block relative motion at the near end of the block. All horizontal-displacement transducers are Linear Variable Differential Transformers (LVDTs), and any one of them can be used for horizontal-displacement control. One device is located on the horizontal actuator ram. However, to account for potential slack in the linkages and grout, two of the devices are located on the far side of the specimen blocks and are installed so as to measure horizontal displacement of the top block relative to the bottom block. An average of these two represents a measure of the fourth and final degree of freedom of the top block, and can be compared with a preselected input source, which depends on the dynamic motion desired. Thus, the affect of apparatus compliance is eliminated from the measurements.

#### **4.4.1.4. *Data Acquisition and Processing***

The 13 channels of data identified in Table 4-4 are sampled and recorded directly on the hard disk of a 640K memory personal computer with a 40-megabyte hard disk and diskette option. The computer also contains a special math coprocessor and high-speed card option. The software allows sampling of data at various preselected rates and times that are compatible with the various types of dynamic tests described above. Data are ultimately transferred to a diskette for further processing and plotting on other digital computers.

#### **4.4.1.5. *Pseudostatic Demonstration Tests***

A series of tests were conducted to demonstrate the capability of the apparatus. These tests vary from the relatively simple pseudostatic tests to the more complex earthquake simulations. In this section, preliminary evaluations of pseudostatic tests are discussed while those of seismic tests are discussed in the next section.

**Test Specimens.** For the pseudostatic tests, one artificial specimen and one natural-joint tuff specimen were used. The artificial specimen was cast from ordinary handyman rapid-set concrete mix. The components of the mix included portland cement, sand, lomard, and water. The grout was allowed to cure for at least 72 hours. A normal size 30.5 x 20.3 x 10.2-cm lower specimen was cast and mated with a 15.2 x 15.2 x 10.2-cm upper specimen. The natural joint specimen was prepared from Apache Leap welded tuff rock with a size of 30.5 x 20.3 x 10.2 cm for the bottom specimen and 20.3 x 20.3 x 10.2 cm for the upper specimen. It should be noted that the joint surface with the artificial specimen is representative of smooth joints while the natural joint of the tuff-rock specimen represents a joint with considerable roughness.

**Test Results.** The products of properly designed and executed direct shear tests are sets of data which permit characterization of deformations and strength properties. Data reduction results in determination of the parameters for various rock-joint models. For the pseudostatic direct shear tests conducted in the current demonstration exercise, the basic properties sought from the tests are the deformation characteristic under normal load, the shear deformation characteristic, and the limiting shear strength as a function of normal stress. Im-

**Table 4-4. INSTRUMENTATION CHANNEL IDENTIFICATION**

Channel No.	Measured Quantity
1	Vertical Load Cell No. 1
2	Vertical Load Cell No. 2
3	Vertical Load Cell No. 3
4	Analog Summation of Total Vertical Normal Load
5	Vertical Relative Speciman Displacement at Right of Bottom Speciman Block
6	Vertical Relative Speciman Displacement at Near Left of Bottom Speciman Block
7	Vertical Relative Speciman Displacement at Far Left of Bottom Speciman Block
8	Horizontal Acceleration at Near Left of Top Speciman Block
9	Horizontal Acceleration at Near Right of Top Speciman Block
10	Horizontal Load Cell
11	Horizontal Actuator Displacement

portant joint properties such as the dilatancy under shear deformation and the peak and residual strength characteristics are defined in terms of these components of a rock-joint model.

Data generated in the tests were reduced in a way consistent with that described by Goodman (1976). This methodology involved presentation of joint closure and shear resistance as a function of shear displacement for various values of applied normal stress, and identification of the corresponding values of the peak and residual shear strengths. The results could then be used to determine the relation between joint normal stress and shear strength.

In calculating the applied normal stress, the individual loads applied by the three vertical actuators were summed; and the surface area of the specimen was used to determine the average joint normal stress. No attempt was made to take account of any non-uniformity in the distribution of normal stress. Similarly, in determining the joint closure under applied normal stress and during joint shear, the average vertical compression (dilation) of the joint was calculated from the three measurements of vertical displacement. For testing of the natural joint specimen, only two measurements of vertical displacement were obtained.

The responses of the artificial and natural joints are presented in Figures 4-18 to 4-23. In Figures 4-18 and 4-19, joint closures are plotted against applied normal stress for loading to normal stress of 6 MPa for the artificial joint and 8 MPa for the natural joint, respectively. Closure for the artificial joint was approximated by measuring the relative vertical displacement between two points; one was located on the upper edge of the lower specimen box, and the other one was on the side of the upper specimen block, near the joint interface. For the natural rock joint, the two points taken for closure measurement were on the sides of specimen blocks. It is observed that complete closure for either joint is apparently not achieved. However, both plots suggest an asymptotic approach to a closure limit. A total of five loading and unloading cycles were performed on the natural joint, with results indicated that the jointing returned to undisturbed (in situ) level of consolidation as defined by Barton et al. (1985).

Plots of joint normal deformation during shear versus shear displacement for the artificial joint are presented in Figure 4-20. Two different styles of joint normal deformation are observed in the figure. For nominal applied normal stress of 0.5, 1.0, and 2.0 MPa, the slopes of the normal joint deformation versus shear displacement plots are relatively flat, while for the higher stress levels, significant joint closure develops during the applied shear displacement. A notable point concerning the normal displacement during shear is that closure continued to develop as shear displacement progressed. The just described phenomenon is different from the observation of the natural joint test, which tended to close at the beginning of shear and then was dilatant as shear displacement progressed further at the normal stress levels comparable to those for the artificial joint (Figure 4-21). The presence of greater roughness in the natural joint caused the difference. The rate of dilation with respect to shear displacement for the natural joint decreases at higher normal stress levels.

Figures 4-22 and 4-23 present shear stress versus shear displacement relations at the various applied stress levels for the artificial and natural joints, respectively. The shear response of the artificial joint does not show peak-residual behavior, while this behavior is observed for the natural joint at a normal stress of 0.5 MPa.

In Figure 4-24, the residual joint shear strengths at the various normal stress levels are plotted against the normal stresses for both artificial and natural joints. Both plots are linear with no or very small intercept on the shear stress axis and the calculated residual friction angles for both joints are about 37.5 degrees.

The general conclusion was that, with the unique capabilities of this machine, the results from the demonstration provided a basis for proceeding to determine the static and dynamic properties of natural joints in tuff.

*4.4.1.6. Preliminary Dynamic Tests for Earthquake Simulation with an Artificial Joint*

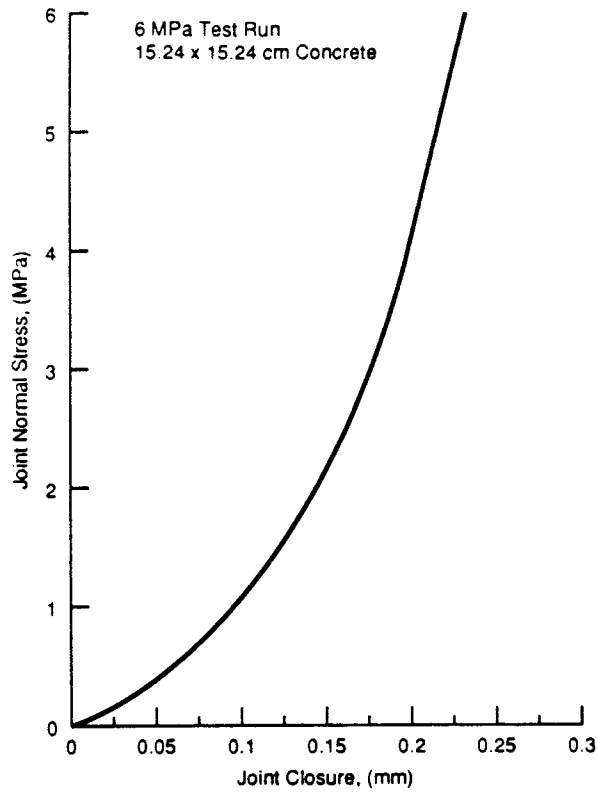


Figure 4-18. Joint closure variation with pseudostatic normal stress for the concrete joint

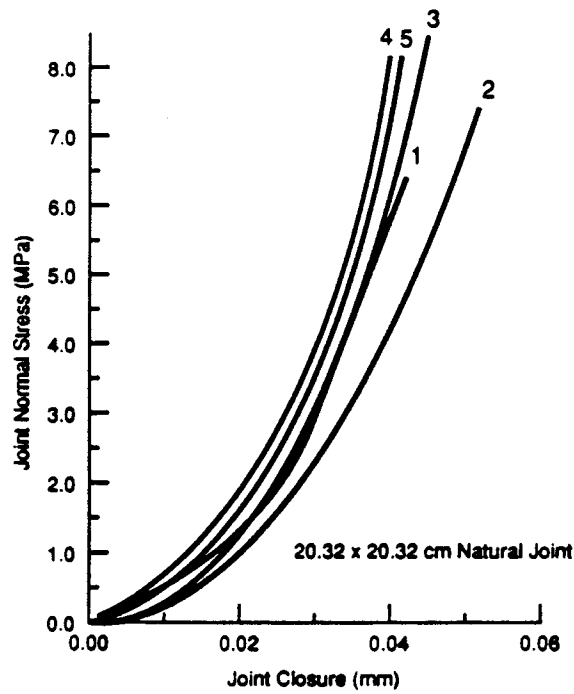


Figure 4-19. Joint closure variation with pseudostatic normal stress for the natural rock joint

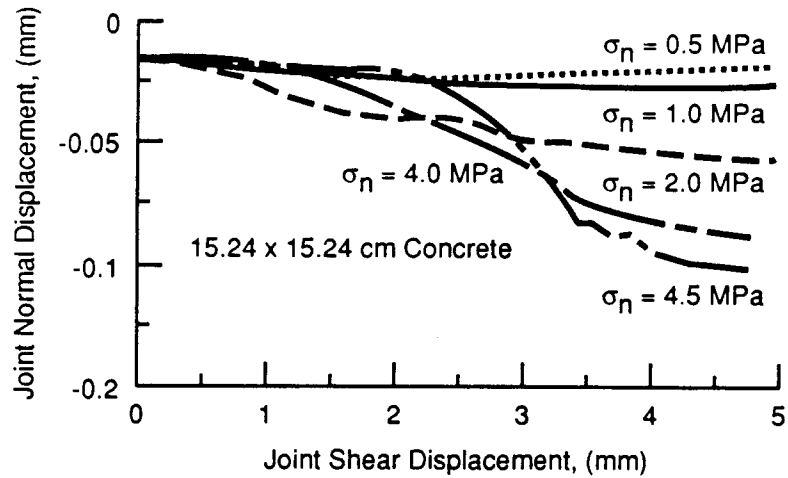


Figure 4-20. Influence of shear displacement on joint normal displacement for the concrete joint under combined pseudostatic load

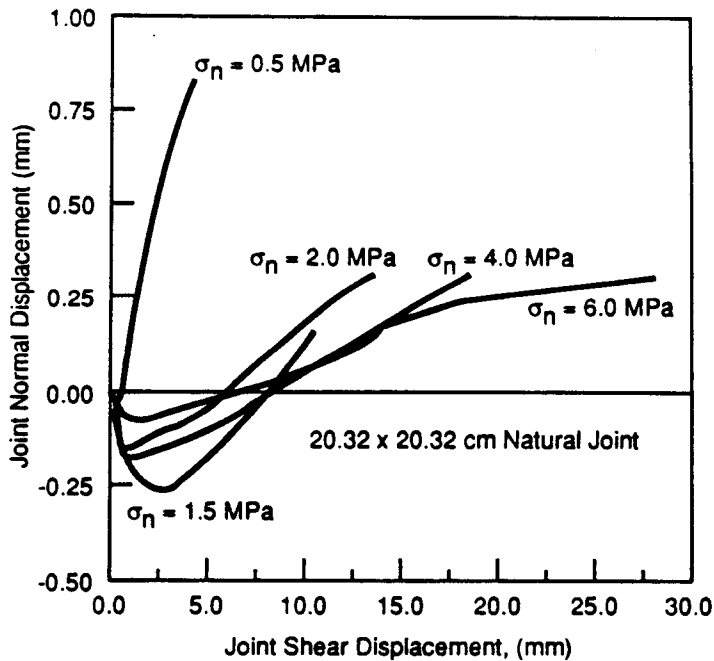


Figure 4-21. Influence of shear displacement on joint normal displacement for the natural rock joint under combined pseudostatic load

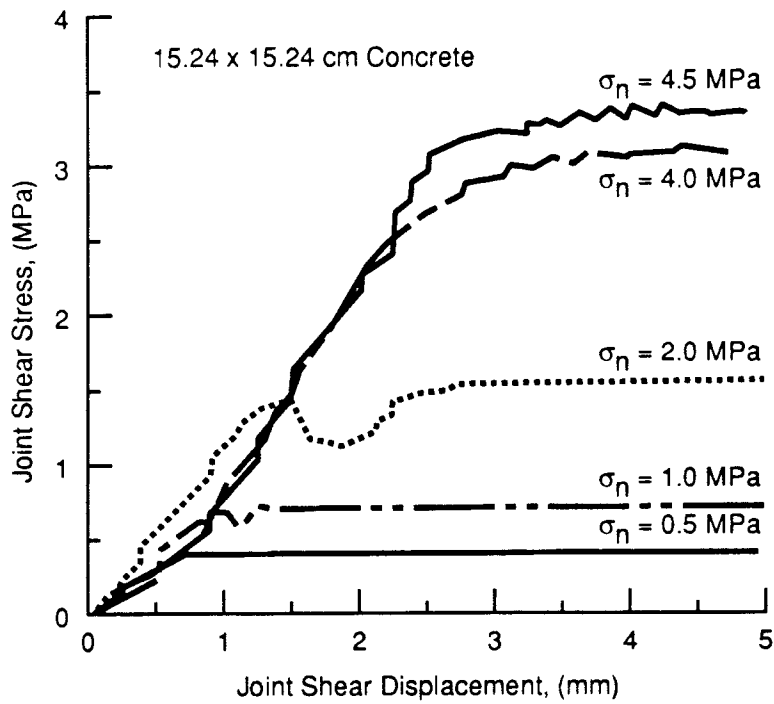


Figure 4-22. Shear stress versus shear displacement relationship for the concrete joint under combined pseudostatic load

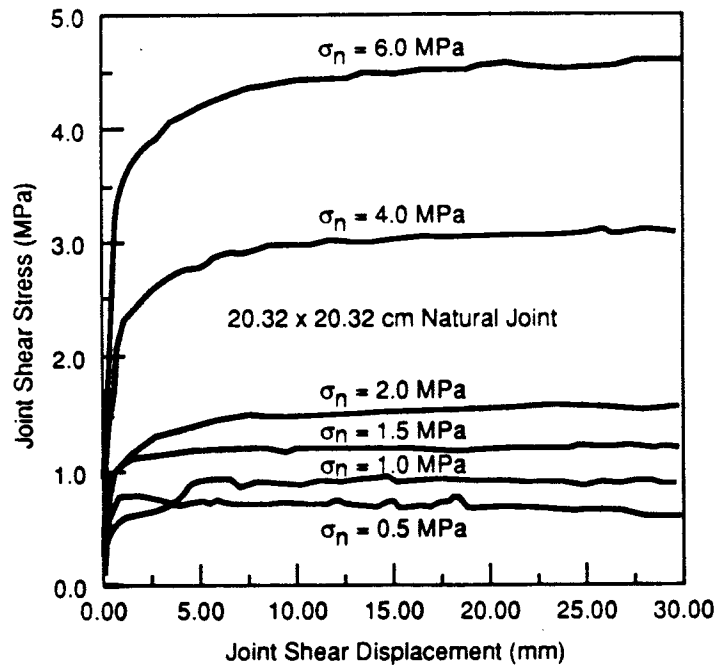


Figure 4-23. Shear stress versus shear displacement relationship for the natural rock joint under combined pseudostatic load

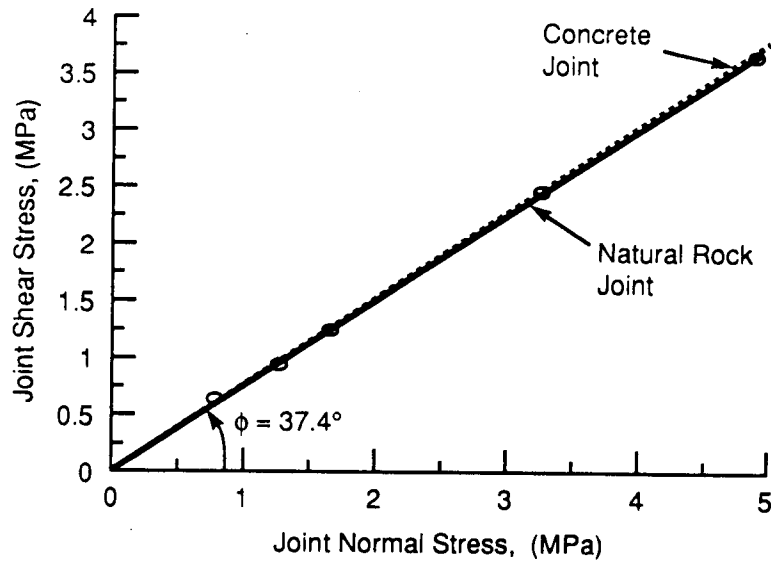


Figure 4-24. Frictional characteristics of both the concrete and natural rock joints under combined pseudostatic load

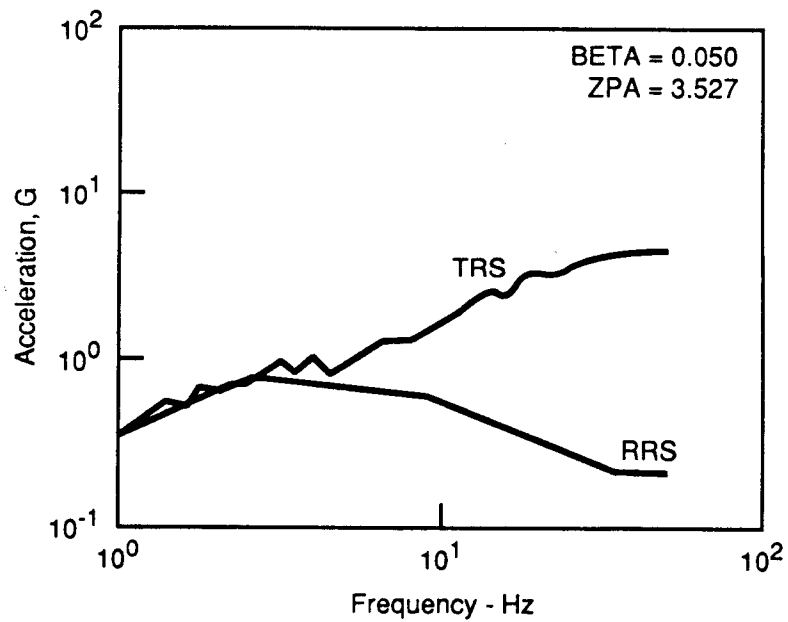


Figure 4-25. Unfiltered acceleration response spectrum at upper specimen block

Several types of dynamic shear tests will eventually be conducted with the apparatus. The most complex of these dynamic tests requires the matching of a test response spectrum to a specified response spectrum. The specified response spectrum used for demonstration of the capability of the apparatus was based on an NRC Regulatory Guide 1.60 earthquake ground-surface-response spectrum, which probably has wider frequency content than that of a subsurface spectrum. In general, time duration is longer than that for rockburst or explosive ground shock. It was felt that production of a representative earthquake time history with the apparatus was sufficient to demonstrate its capability, since all other types of dynamic tests are simpler.

Generation of a test time history whose response spectrum matches a specified response spectrum within given limits is a complex process that can be accomplished several different ways for laboratory simulations. It is complicated by the fact that a displacement-control drive signal must be generated for the horizontal actuator, which has itself an electrohydraulic transfer function that varies with frequency. The acceleration signal from the upper specimen block is normally used to compute the test response spectrum, which is then compared with the required spectrum; and this displacement drive signal must then be adjusted to provide any required correction. The synthesis process provided by Unruh (1982) is used for the calculation described above.

Figure 4-25 shows a test-response spectrum (TRS) computed from the direct measured acceleration compared with the required response spectrum (RRS), both for 5-percent damping. It can be seen that the test signal contains much more higher frequency content than does the RRS. This occurred even though zero input was used in those frequency bands. This energy, therefore, is generated by a nonlinear process, which was identified with the grinding of the rock interface during the motion.

The occurrence of the grinding process was expected, but the degree of its effect on the measured acceleration was more than anticipated. Some accounting is in order of this affect in matching of spectra based on motion measured at a distance from the source. In effect, the grinding process in the test apparatus is analogous to what occurs at the focus of an earthquake; but the higher frequencies generated are filtered as a function of measurement distance from the source.

A promising approach for matching of spectrum data is using a filter. For this demonstration test on the artificial joint, the measured acceleration signal was low-pass filtered below 10 Hz with a 24-db/octave slope. This cut-off frequency was chosen simply because no energy was input to the drive signal above that point. Figure 4-26 provides a comparison between the TRS and RRS. While this approach obviously will allow a match of the data, the exact cut-off frequency should be based on source proximity of the actual measured site data.

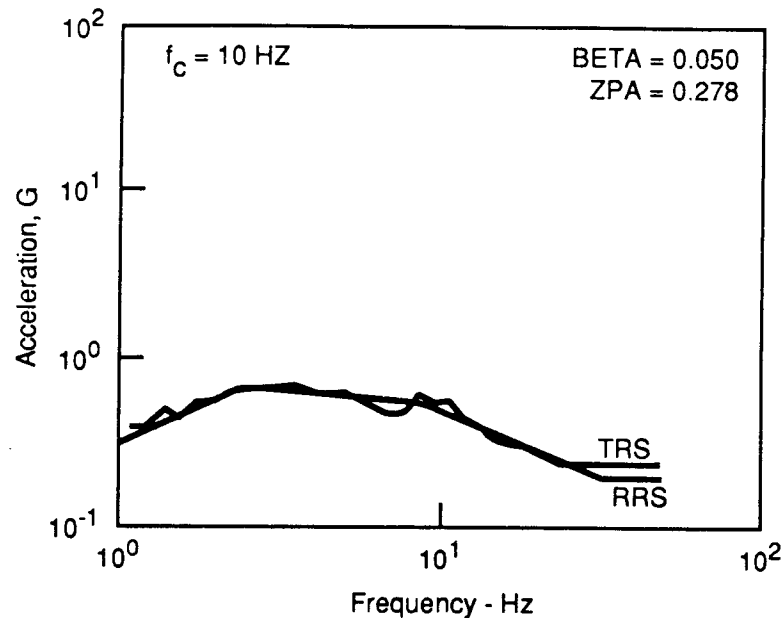


Figure 4-26. Filtered acceleration response spectrum at the upper specimen block

#### 4.4.1.7. Conclusions

The development of a dynamic, direct shear-test apparatus for the purpose of carrying out an extensive laboratory program for joint dynamic-behavior characterization was successful. This apparatus is capable of handling any kind of time history with reasonable complexity. The results of the demonstration tests provide a basis for proceeding to determine the static and dynamic behavior of natural joints in tuff.

The grinding action, which induces higher acceleration-frequency measurements than the required acceleration frequency during joint shear, will have a substantial impact on specifications for some of the dynamic tests required by the laboratory test program. Preliminary earthquake-type data indicate that matching a filtered acceleration-response spectrum will be required for a valid simulation. Procedures and hardware necessary for performing such tests have been shown to be adequate. The exact details will have to be adjusted somewhat, however, depending on the nature of site data from which a required response spectrum will be generated. In particular, a relationship between filter cut-off frequency and measured distance from a source must be established. Use of this filter process will probably be required on all dynamic tests to be conducted.

#### 4.4.2. Sample Collection and Preparation Activities

Task 2 includes a variety of testing activities for the determination of basic material properties of tuff, tuff-joint interface properties, and rock-joint responses under pseudo-static and various dynamic loading conditions with special interest in repeated dynamic loadings arising from earthquakes and ground shocks. To carry out the testing activities, a considerable number of specimens with a naturally occurring joint are needed; a current estimation suggested a minimum of 45 jointed tuff specimens. This number may vary as the experiments proceed and a better understanding on tuff joint behavior is obtained.

To acquire such a large number of jointed tuff specimens requires considerable effort. The following sections discuss some technical aspects regarding the activity for jointed tuff specimen collection.

##### 4.4.2.1. *Site Selection for Sample Collection*

One of the primary goals of the Seismic Rock Mechanics Project is to develop methodologies to evaluate, validate, and reduce uncertainties in the prediction models which eventually will be used to assess the effects of possible occurrences of earthquake as well as ground shock events on the short-term and long-term performance of a proposed underground repository at Yucca Mountain. The results of this study are expected to be used by the NRC staff and its contractors during the process of License Application as a basis to determine the adequacy of DOE's repository design relevant to seismic activities.

To better serve the purpose, one would expect that the rock specimens to be tested in the laboratory come directly from the site to be evaluated or studied; that is, from the proposed Yucca Mountain repository site. However, the collection of tuff rock-joint specimens from the Yucca Mountain site is not currently feasible because the site-characterization program proposed by the DOE has been delayed substantially. It is the understanding that the site-characterization program will not be started until the end of 1991, while Task 2 of the Seismic Rock Mechanics Project is to be completed in August 1991 to ensure that the overall objective of the project can be achieved in a timely fashion. In light of the complications, selection of an alternative site for sample collection to perform the studies proposed in Task 2 is justified.

Three criteria have been established to facilitate the process of site selection. The first is that the rock type at the site selected should be similar (e.g., welded and jointed) to the tuff material at the proposed repository horizon at the Yucca Mountain site so that the experimental results and the conclusions reached may be directly applicable. The second criterion is that the site to be selected should contain sufficient favorable locations for a collection of at least 50 rock-joint specimens. This criterion is important because of the relatively large dimension for the rock-joint specimens required to perform the proposed experiments in Task 2. The required dimension is 12 x 8 x 4 inches for the bottom portion and 8 x 8 x 4 inches for the top portion of a prepared rock-joint specimen, with a natural joint interface

between these two portions. The third criterion is that the site selected should be easily accessible. The activity for specimen collection involves not only collection itself but also transporting heavy equipment and specimens collected from the site.

Based on the three criteria, two alternative sites were evaluated, one in the southern part of Texas and the other at Apache Leap, Arizona. Field observation shows that the rock at the southern Texas site is a nonwelded tuff, which is different from that at the proposed repository horizon at Yucca Mountain. The southern Texas tuff also is considerably weaker. Thus, the tuff at the southern Texas site does not satisfy the first siting criterion, and so the site is not suitable for sample collection.

On the other hand, the Apache Leap site in Arizona is suitable for specimen collection. Its rock is a vitrified and densely welded tuff, which is similar to the tuff at the proposed repository horizon. Field observation indicates that Apache Leap tuff is moderately to heavily jointed. The tuff at the proposed repository horizon is also heavily jointed. While some differences in physical properties between the tuffs at these two sites do exist, these differences may be quantified so that validation of corresponding rock-joint models will still be achieved, provided that account is taken of differences in corresponding parameters.

The Apache Leap welded tuff has two predominant vertical joint sets, one minor subvertical joint set, and one horizontal joint set with joint spacing ranging from 2 inches to a few feet. The joint spacing is crucial to the success of the sample collection activity. For the purpose of this study, the joint spacing should be at least 4 inches to be collectable. However, field experience indicates that it will be much easier to collect specimens at areas with larger joint spacing. This restraint limits the usable areas for sample collection at the Apache Leap site. (Discussion for other restraints is provided in a later subsection.) The area of interest for sample collection at the Apache Leap site is located around an abandoned highway tunnel, so it is accessible in terms of transportation. A distinct advantage in selecting this area is that, since this section of the highway has been abandoned for quite some time, potential interference is minimized. This greatly facilitates the collection activity.

The Apache Leap site is a private property belonging to the Magma Mine Company. The Apache Leap Tuff Site Overview Committee (ALTSOC) is responsible for reviewing the application to access the Apache Leap site and making recommendations to the Magma Mine Company. Our request was approved in November 1989.

#### ***4.4.2.2. Important Considerations for Sample Collection***

Several important factors need to be considered regarding whether a local area at the site is suitable for sample collection and whether the rock-joints collected are acceptable for the project experiments. As stated previously, the objective of Task 2 is to determine tuff-joint behavior subjected to pseudostatic and dynamic loadings. The tuff at the proposed repository horizon at Yucca Mountain is about 800 feet below the surface, and the weathering condition on the tuff joints should be relatively minor. Therefore, collecting and

testing tuff joints that are highly weathered must be avoided. Because almost all the vertical joints seen on the ground at the site were believed to be highly weathered, they were not suitable for samples. This condition led to a decision to focus sample collection on the horizontal and vertical joints from inside the abandoned highway tunnel which is approximately 50 to 60 feet below the surface. This decision considerably reduced the potential area usable for sample collection at the selected site.

As discussed in Section 4.4.1, the rock-joint, dynamic shear-test apparatus was designed and fabricated to have a 1-inch gap between the top and bottom specimen-box edges of the assembled specimen unit. To prevent potential interference of the top box edge with the specimen joint interface of the bottom specimen half, not only must the specimen joint interface fall within the 1-inch gap, but also its apparent relief has to be smaller than 1/2 inch. This restraint was applied in the field to determine the acceptability of a collected joint interface.

#### 4.4.2.3. *Techniques for Sample Collection*

Several techniques are available for sample collection of rock-joints. Among them are chain saw, or wire saw cutting; high-pressure water-jet cutting; hydraulic fracturing; and large-diameter core drilling.

Considering the first three techniques, chain sawing has been used successfully in nonwelded tuff but not as successfully in welded tuff because of the frequent breakdown of the equipment. The high-pressure water-jet technique has demonstrated its effectiveness in cutting welded tuff; but this technique is still state-of-the-art and the cost for a high-pressure water jet is high. In addition, considerable amount of water would be required for the process of cutting; and the ability to maintain a constant water supply in the field is questionable and expensive. The third technique, hydraulic fracturing, requires considerable small-diameter drilling around the boundary of a rock block to be collected. This drilling serves two purposes: (1) it allows hydraulic pressure to be applied on the walls of the boreholes drilled, and (2) a preferential fracture path is created along the direction of the boreholes. However, because a considerable number of holes needs to be drilled for each sample to be collected, the process for collection is slow.

Another concern, and perhaps the most important one for the three techniques (chain saw, hydraulic fracturing, and high-pressure water jet), is that they can be used effectively only for shallow cutting. Difficulty arises as the cutting goes deeper. Given the large number of specimens needed for testing and relatively less amount of area usable for sample collection, obtaining an adequate number of specimens using these techniques would be difficult.

Large-diameter core drilling, on the other hand, is relatively favorable, it is reasonably fast and less expensive, and has less machine maintenance problems. Considerable experience has been accumulated over the years in core drilling in the welded tuff at

the Apache Leap site. To take advantage of this experience and also take into consideration favorable factors about large-diameter core drilling, the method was selected for the sample collection.

#### 4.4.2.4. *Discussion for Sample Collection*

Because of the large dimension needed for testing, it was determined that an 18-inch diameter core would be collected and that an 18-inch diameter, thin-wall core barrels would be used for the drilling.

When performing large-diameter core drilling, two basic methods for obtaining a rock-joint feature are used. One is drilling to intersect a joint feature, and the other is drilling parallel to the joint feature with the joint surface (interface) coinciding with the central plane of the core. The first method is preferred and usually allows sufficient dimension for joint-specimen preparation, but it often takes a longer time to obtain a rock joint than the second method does. This is especially true when the joint spacing is several feet wide. Although the second method has its advantages, it also has two problems. It is extremely difficult to (1) align the axis of drilling with the strike/dip of a joint interface and (2) make the joint interface to be collected coincide with the central plane of the core. Very often, under-sized core pieces are obtained, which are not suitable for rock-joint specimen preparation. The first method, therefore, was used for most of the drilling except for three holes, one vertical and two angled. Only one potentially useful joint specimen was obtained as a result of these three drillings.

Drilling for sample collection was performed by the Boyles Brothers Drilling Company. The company has a few thousand feet of drilling experience directly related to the Apache Leap site and of obtaining core samples with a diameter up to 6 inches. This experience was considered helpful to this project. Through the entire period of sample collection, a CNWRA representative was on site to provide technical decisions concerning location, direction (angle), and depth of drilling and to be responsible for technical aspects regarding packing and transporting core pieces collected. The entire activity for collecting tuff specimens was conducted following the CNWRA Technical Operating Procedure TOP-006, "Procedure for Obtaining Seismic Rock Mechanics Test Specimens from the Field." The drilling project was initiated on December 10, 1989, and completed on February 9, 1990. A Joy 22 drill rig (Figure 4-27) was used. A borehole was usually started using a 1.5- or 2.5-foot long core barrel (18 inches in diameter). If a joint interface were not intersected after a depth equal to the barrel length was drilled, this core barrel was replaced with a 4-foot long barrel for continuing drilling. A core breaker was used to break the core in the event that no joint was intersected after 4 feet of drilling.

A total of 29 boreholes was drilled. Figure 4-28 presents a schematic drawing showing the locations of the boreholes drilled for sample collection at the Apache Leap site. Of these, 8 were vertical holes, and 21 were angled or near-horizontal holes. Except for hole No. 14, all the angled holes were inside the highway tunnel, and most were on the north wall. The depth of drilling for the holes ranged from 5 to 11 feet. The hole numbers not

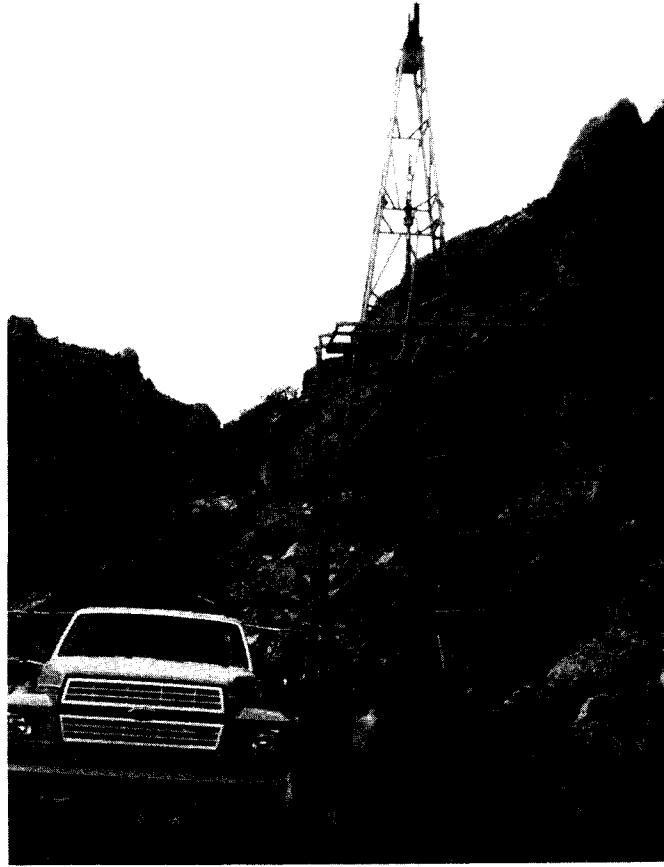


**Figure 4-27. Truck-mounted joy 22 drill rig**

indicated in the figure are those with drilled depths of less than 2 feet, and from which no potentially usable joint specimens were produced.

The vertical drilling produced only three potentially usable joint specimens. The reason is simply because most of the intersected horizontal-joint interfaces were too rough and their apparent relief exceeded the maximum 1-inch gap value set by the design of the test apparatus, as well as the 1/2-inch value for the purpose of avoiding interference. Even for those three joint specimens which were considered potentially usable, their joint interfaces barely satisfied the 1/2-inch requirement. This finding caused a major shift of drilling from the originally planned vertical direction to angle drilling. Although this shift substantially slowed down the drilling program, it was nevertheless necessary.

The program was also considerably impacted by two other problems. The first one was due to the abrasiveness of the Apache Leap welded tuff. The so-called

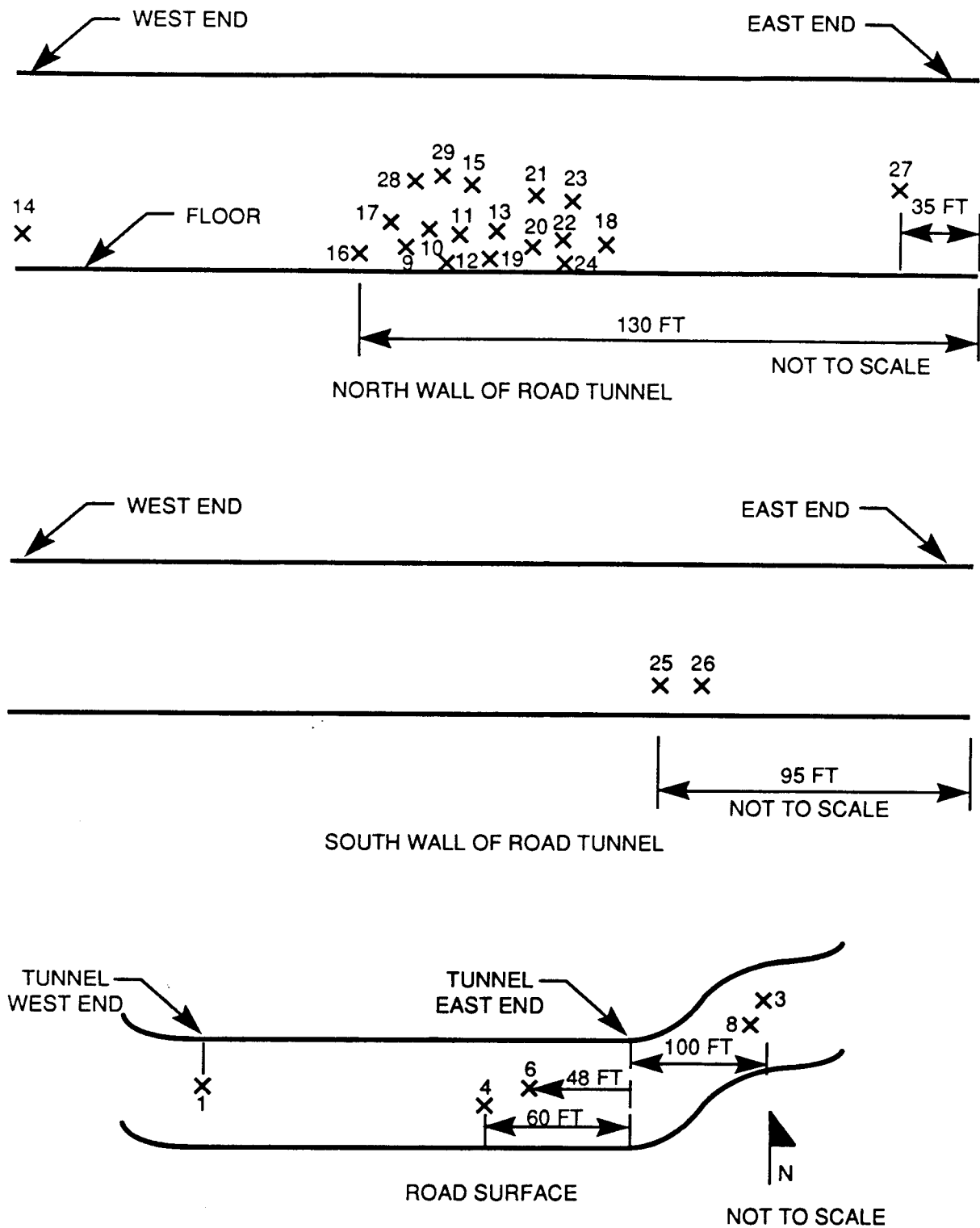


Figure 4-28. Location of drilled holes for sample collection at the Apache Leap site

diamond bits installed at the bottom end of a core barrel for cutting purpose consisted of industrial diamond particles in an alloy matrix. During cutting, the alloy matrix is supposed to be eroded to expose fresh diamond particles, and these diamonds cut the rock. If the rock is relatively soft, the diamonds will last a long time. Since the Apache Leap welded tuff is a hard rock, the diamonds wear out very quickly. However, cutting can still proceed smoothly if fresh diamonds can be exposed fairly quickly through erosion of the alloy matrix. The bits first selected for this sample-collection program had a matrix material that was very hard and difficult to erode away. As a result, drilling was slowed down substantially. This problem was mitigated by using diamond bits with relatively soft matrix material.

The second problem was associated with core breaking. The longest core barrel used in the program was 4 feet. If a joint interface were not intersected after 4 feet of drilling, the core needed to be broken and taken out of the hole for subsequent drilling; but breaking an 18-inch diameter core was difficult in the hard rock. A pair of wedges was used for this purpose at a shallow depth; at greater depths, a steel bar containing a wedge on one end was used. The force was applied by striking a 6- or 10-lb hammer to the end of the wedge. Experience indicated that 20 to 30 minutes were needed to break a shallow core loose; at relatively greater depths, even longer times and greater efforts were required. Sometimes severe damage to an otherwise perfect joint interface was incurred because of this breaking process.

At the completion of this collection activity, a total of 50 potentially usable joint specimens was obtained; 44 of them were from the central north wall of the abandoned highway tunnel and had relatively smooth joint interfaces. Figure 4-29 shows a typical 18-inch diameter core with a smooth joint interface. Several attempts were made to locate other favorable areas for drilling in light of potential safety concerns of a large number of boreholes in one small area, but these attempts failed.

#### 4.4.2.5. *Summary of Results*

The difficulties notwithstanding, the sample collection was a success. Fifty potentially usable joint specimens were obtained, which is 10 percent more than needed according to the current experimental plan. This surplus is necessary to ensure that an adequate number of joint specimens will survive the preparation procedure, or these additional specimens be used for other types of experiments, if required.

Drilling in welded tuff is a slow process. However, the rate of drilling may be improved by careful selection of matrix material used for diamond bits. Experience indicates that a relatively soft matrix material facilitates drilling in the tuff rock.

Breaking a large-diameter core (e.g., 18 inches in diameter) from a borehole is a difficult task. It was a constant problem during sample collection, and some potential specimens were lost because of it. A new design for a core breaker is required if a similar drilling activity is implemented. It was also found that drilling to intersect the joint has a better chance for obtaining usable jointed specimens than drilling parallel to the joint.



**Figure 4-29. 18-inch diameter core with a smooth joint interface**

#### **4.4.3. Specimen Preparation/Testing Activities**

The types of tests to be performed for jointed rock characterization include: (1) basic material properties tests, (2) jointed-tuff interface-characterization tests, (3) joint response for pseudostatic direct shear tests, (4) joint response for harmonic load tests, (5) joint response for ground-shock load tests, and (6) joint response for earthquake load tests. The first three types of tests are aimed at determining basic tuff matrix and joint properties, while the last three are performed for analyzing dynamic behavior of joints.

Direct shear test specimens are being prepared for dynamic shear testing. In addition, cylindrical specimens for mechanical characterization tests associated with the shear specimens, including uniaxial and triaxial compression and Brazilian disk tension tests, are being prepared. These mechanical characterization tests will be performed on cylindrical specimens collected from the same tuff rock cores from which the shear specimens are being prepared.

The shear specimens are prepared from 18-inch (457-mm) diameter core, which was drilled from the Superior, Arizona, site. Figure 4-30 shows a typical 18-inch (457-mm) diameter core collected from the field. The rock is a welded tuff of the Apache Leap formation. The top half of the shear specimen measures 8 x 8 x 4 inch (203 x 203 x 102 mm); the bottom

half, 12 x 8 x 4 inch (305 x 203 x 102 mm). The cores received from the field are cored in the laboratory to produce a 2 inch (50 mm) diameter. For uniaxial and triaxial compression testing, these are cut to a length of 5 inch (127 mm), and surface ground. For Brazilian disk tension testing, 2-inch (50-mm) diameter core is cut to a thickness of 0.5 inch (12 mm). Procedures for specimen preparation (both shear and mechanical characterization test specimens) were documented in the *Quality Assurance Program for Mechanical Characterization of Tuff, CNWRA*, by Daemen (1990).

#### **4.4.3.1. Direct Shear Specimen Preparation**

To date, 43 direct shear test specimens were prepared. Figure 4-31 shows a picture of a direct shear specimen in the cutting process using a slab saw. Figure 4-32 shows three prepared direct shear specimens. Progress in specimen preparation was slowed due to problems encountered in the cutting process. These problems are discussed briefly in Section 4.4.3.4.

#### **4.4.3.2. Uniaxial and Triaxial Compression Specimens**

Fifty-eight uniaxial specimens and twenty-five triaxial specimens have been tested. The test results for the uniaxial and triaxial compressive tests are listed in Table 4-5 and 4-6, respectively.

Statistical analysis gives a mean uniaxial compressive strength of 23,373 psi (with a standard deviation of 3,982 psi). The mean triaxial compressive strength is 29,225 psi (with a standard deviation of 2,957 psi) with 500-psi confining pressure, 34,944 psi (with a standard deviation of 3,122 psi) with 1,000-psi confining pressure, and 40,720 psi (with a standard deviation of 858 psi) with 1,500-psi confining pressure. Average values for Young's modulus and Poisson's ratio of the Apache Leap tuff are  $5.83 \times 10^6$  psi (with a standard deviation of  $0.51 \times 10^6$  psi) and 0.2 (with a standard deviation of 0.0032), respectively.

#### **4.4.3.3. Brazilian Disk Tension Specimens**

One to three disk specimens for each group of uniaxial and triaxial compression test specimens were cut to length from the 2-inch (50-mm) diameter cores. Figure 4-33 shows the core specimens after preparation for compression and Brazilian disk tension tests.

A total of 68 Brazilian disk tension specimens have been tested and the results are given in Table 4-7. The mean uniaxial tensile strength is 1,464 psi (with a standard deviation of 357 psi).

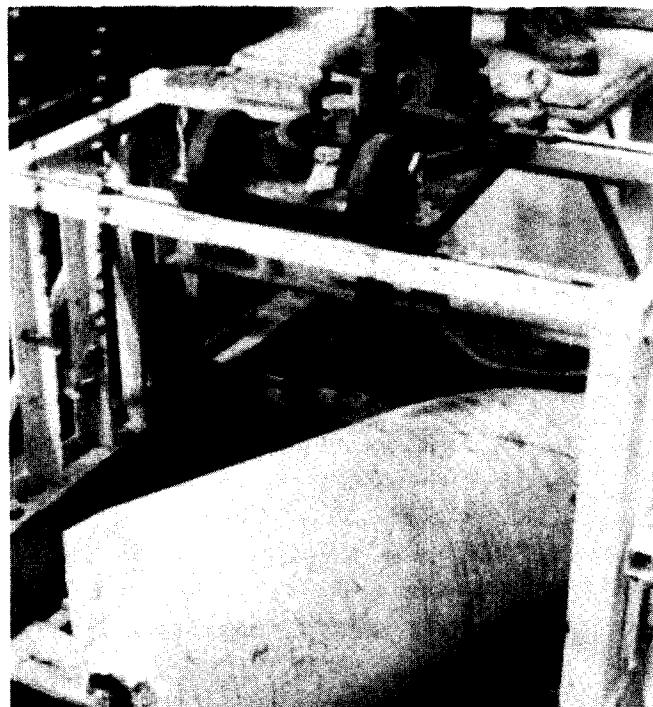


Figure 4-30. Core drilled at the field site shown set up for laboratory coring

#### *4.4.3.4. Problems for Direct Shear Specimen Preparation*

Several problems occurred in the preparation of direct shear specimens. One arose from using water as a cutting fluid to avoid the potential for altering fracture surface mechanical characteristics. This subjected unpainted metal parts of the saw mechanism to rapid rusting. The problem was partly solved by replacing threaded rod pieces with stainless steel. Also, the main carriage slide and another metal slide were cleaned frequently and given a protective coat of thick grease. This grease did not come in contact with the direct shear specimen. The use of water only, applied against the recommendations of the saw manufacturer, reduces cooling and cutting effectiveness and contributes to blade wear.

Some difficulty was encountered in clamping the large core pieces in the saw when the clamped rock surfaces were not flat. This resulted in the saw blade jamming in the sawcut. Because it was often necessary to back the blade off and reset the specimen, rougher or more uneven cuts resulted, which may be smoothed out by surface grinding.

#### *4.4.3.5. Development of Rock Profiler*

The parameters required for joint interface characterization for various analytical joint models are different, and the methodologies for acquiring them also vary. One important parameter for characterizing the Barton-Bandis joint model is joint-roughness coefficient (JRC). The determination of this parameter requires profile measurements of a rock-joint

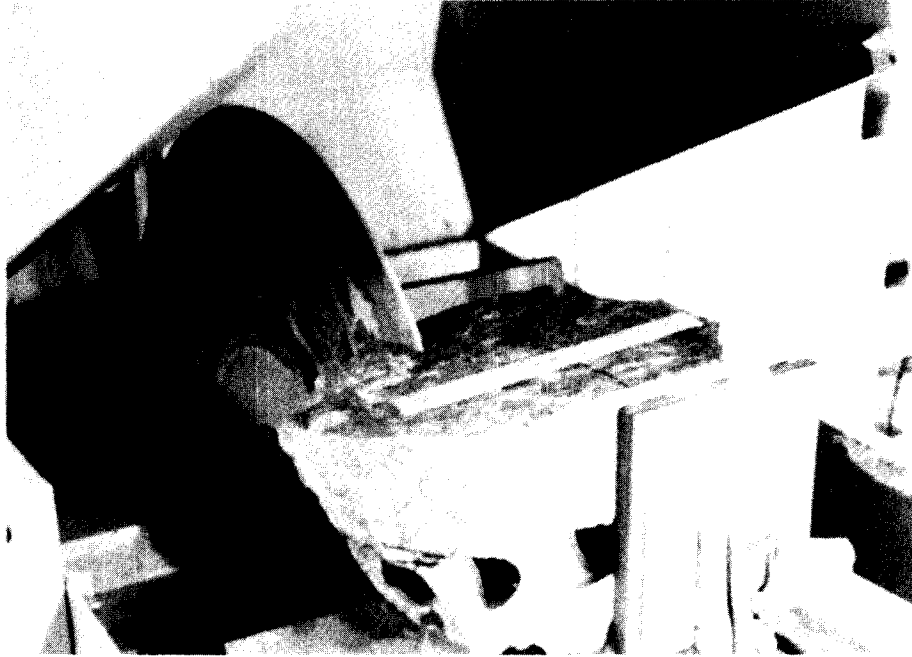


**Figure 4-31. Direct shear specimen shown in the cutting process using a slab saw**



**Figure 4-32. Three prepared direct shear specimens**

**Table 4-5. UNIAXIAL COMPRESSIVE STRENGTH, YOUNG'S MODULUS, AND POISSON'S RATIO OF APACHE LEAP TUFF**

Specimen No.	Failure Stress (psi)	Young's Modulus E (psi E6)	Poisson's Ratio $\nu$
SRM1.1.1-U-1	25,080	5.1	.19
SRM1.1.1-U-2	23,660	4.9	.19
SRM1.2.2-U-1	24,360	6.1	.23
SRM1.3.3-U-1	22,240	6.2	.23
SRM1.3.3-U-2	24,490	5.7	.17
SRM9.1.1-U-1	30,070	6.7	.19
SRM9.1.1-U-2	25,680	5.8	*.11
SRM9.3.4-U-2	11,000	--	--
SRM10.1.1-U-1	24,100	5.5	.18
SRM10.1.1-U-2	22,180	5.5	.17
SRM10.2.2-3-U-1	27,000	5.8	.23
SRM10.2.2-3-U-2	26,000	5.8	.24
SRM10.2.2-3-U-3	25,400	5.3	.16
SRM10.3.4-U-2	23,600	6.4	.28
SRM10.4.5-U-1	27,100	5.7	.21
SRM13.2.3-U-1	22,780	5.9	.19
SRM13.3.4-U-1	27,140	5.6	.23
SRM13.3.4-U-2	27,240	5.7	.25
SRM13.5.7-U-1	20,200	6.1	*.11
SRM13.5.7-U-2	27,200	6.0	*.12
SRM15.1.1-U-1	24,500	5.9	.20
SRM15.2.2-U-1	25,710	4.8	.18
SRM15.2.2-U-2	21,470	5.1	.23
SRM15.2.3-U-1	23,800	5.2	.19
SRM15.3.4-U-1	25,160	5.6	.29
SRM15.3.4-U-2	25,100	6.4	.17
SRM16.1.1-U-1	26,840	6.5	.19
SRM16.1.1-U-2	30,210	6.5	.19
SRM16.2.2-U-1	19,300	5.6	.18
SRM17.2.3-U-1	17,470	*19.3	.21

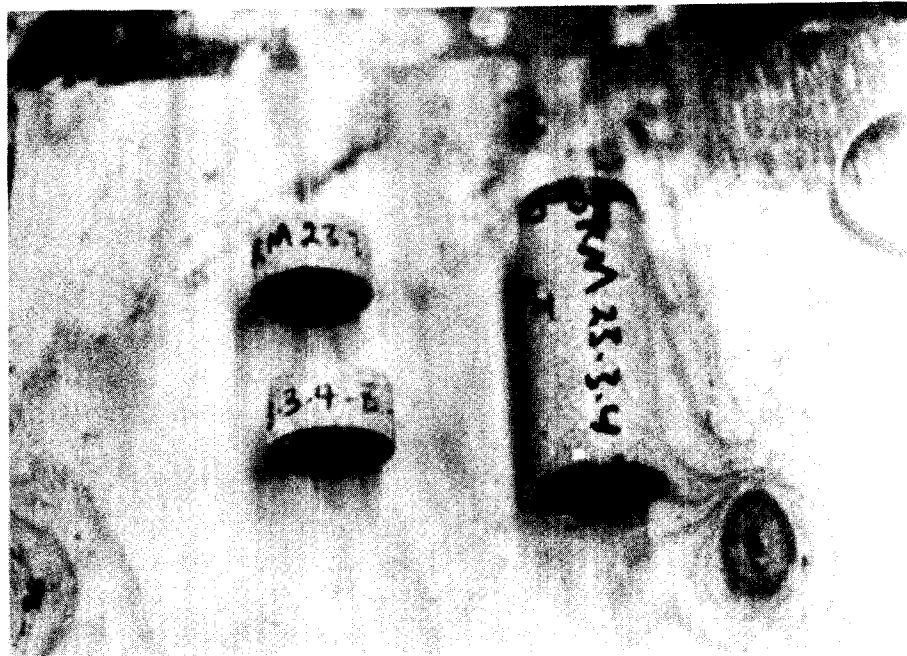
**Table 4-5. UNIAXIAL COMPRESSIVE STRENGTH, YOUNG'S MODULUS, AND POISSON'S RATIO OF APACHE LEAP TUFF (cont'd)**

Specimen No.	Failure Stress (psi)	Young's Modulus E (psi E6)	Poisson's Ratio $\nu$
SRM22.1.1-U-1	25,210	6.1	.20
SRM22.1.1-U-2	20,890	--	--
SRM22.4.4-U-1	22,990	5.5	*.11
SRM22.5.5-U-1	27,400	6.9	.20
SRM22.5.5-U-2	31,660	6.2	.16
SRM23.1.2-U-1	23,050	5.8	.20
SRM23.3.4-U-1	25,260	5.9	*.46
SRM23.3.4-U-2	20,180	5.9	.20
SRM25.1.1-U-1	16,280	*19.3	.17
SRM25.1.1-U-2	16,580	5.5	.25
SRM25.1.1-U-2	18,930	6.2	.22
SRM26.2.2-U-1	26,730	6.4	.17
SRM26.2.2-U-2	24,570	6.0	.24
SRM26.2.3-U-1	23,820	5.9	.21
SRM27.3.4-U-1	21,770	6.3	.20
SRM27.3.4-U-2	26,820	6.2	.20
SRM27.3.4-U-3	27,660	6.5	.21
SRM28.1.1-U-1	17,680	5.5	.17
SRM28.1.1-U-2	19,450	4.9	.17
SRM28.1.2-1-U-1	17,760	*16.5	.18
SRM28.2.3-U-1	25,700	6.5	.24
SRM28.2.3-U-2	23,790	6.6	.24
SRM28.3.4-U-1	16,430	*21.6	.17
SRM28.3.4-U-2	15,200	5.5	.25
SRM29.2.4-U-1	22,330	5.4	.20
SRM29.2.4-U-2	25,520	5.6	.18
SRM29.2.4-U-3	24,510	5.9	.17

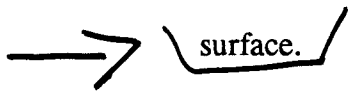
\* Further check required

Table 4-6. TRIAXIAL COMPRESSIVE STRENGTH FOR APACHE LEAP TUFF

Specimen No.	Failure Stress (psi)	Confining Pressure (psi)	Density (pcf)
SRM25.1.1-T-2	30,190	500	--
SRM17.2.3-T-1	24,780	500	151
SRM16.1.1-T-1	29,800	500	151
SRM23.3.4-T-1	31,600	500	--
SRM1.3.3-T-1	27,000	500	151
SRM1.1.1-T-1	28,900	500	149
SRM1.2.2-T-1	38,000	1,000	150
SRM9.1.1-T-1	40,200	1,500	150
SRM9.2.3-T-1	33,700	500	151
SRM9.3.4-T-1	29,800	1,000	151
SRM9.4.5-T-1	30,000	500	151
SRM9.4.5-T-2	40,700	1,500	151
SRM10.1.1-T-1	29,200	500	150
SRM10.1.1-T-2	30,700	1,000	150
SRM10.2.2-3-T-1	41,400	1,500	152
SRM10.2.2-3-T-2	35,900	1,000	150
SRM10.3.3-T-2	24,100	500	151
SRM10.3.4-T-1	32,200	500	151
SRM10.4.5-T-1	38,200	1,000	155
SRM10.4.5-T-2	39,600	1,500	151
SRM13.2.3-T-1	37,000	1,000	151
SRM13.3.4-T-1	41,700	1,500	151
SRM15.1.1-T-1	37,000	1,000	155
SRM15.2.2-T-1	35,000	1,000	151
SRM15.3.4-T-1	32,900	1,000	151



**Figure 4-33. Two Brazilian disk tension specimens and one compression specimen in the preparation process**



The "rock profiler" (Figure 4-34) is a noncontact, surface-height-gauging profilometer. It has been assembled primarily from off-the-shelf equipment, including an Asymtek A-102B benchtop gantry-type X-Y-Z positioner and a Keyence LC-2100/2320 laser displacement meter. An LC-2320 red-visible laser head, with specified displacement measurement resolution of about 0.5 micron, is attached to the Z-axis of the A-102B X-Y-Z gantry positioner.

A rock positioned beneath the A-102B is profiled by scanning the LC-2320 across the rock surface in the X- and Y-axis directions, in a raster scan pattern. The LC-2320 has a measurement window of about  $\pm 8$  mm from a standoff position of about 50mm. The LC-2100/2320 combination form the laser displacement meter that operates on a principle of triangulation; i.e., the apparent shift in the position of a laser light spot, as the laser head is raised or lowered, indicates displacement.

The rock-profiler movements are controlled by PC/AT commands to the A-102B X-Y-Z Table by way of a serial communications port. The A-102B Table has a built-in computer for interpreting high-level commands from the PC/AT and then executing the moves. A custom computer program written in Borland's TurboC, Version 2.0, is used to issue movement commands to the A-102B, to read the displacement measurement Z-axis movement from the LC-2100, and to format and store pertinent scanning and rock-profile displacement

**Table 4-7. RESULTS OF BRAZILIAN DISK TENSION TEST OF APACHE LEAP TUFF**

Specimen No.	Failure Stress (psi)	Specimen No.	Failure Stress (psi)
SRM9.2.3-B-1	1,900	SRM23.3.4-B-1	1,870
SRM9.2.3-B-2	1,910	SRM10.1.1-B-1	1,760
SRM9.3.4-B-1	990	SRM10.1.1-B-2	1,990
SRM9.4.5-B-1	1,610	SRM10.1.1-B-3	1,690
SRM9.4.5-B-2	1,930	SRM23.1.2-B-1	1,740
SRM10.2.2-1-B-1	1,560	SRM23.1.2-B-2	1,710
SRM10.2.2-2-B-1	1,200	SRM23.3.4-B-2	1,840
SRM10.2.2-2-B-2	1,080	SRM28.2.3-B-1	1,680
SRM10.2.2-2-B-3	1,150	SRM28.2.3-B-2	1,320
SRM10.3.3-B-1	1,100	SRM28.2.3-B-3	1,550
SRM10.3.4-B-1	1,480	SRM28.1.2-1-B-1	1,210
SRM10.4.5-B-1	1,370	SRM28.1.2-1-B-2	1,450
SRM10.4.5-B-2	1,500	SRM15.3.4-B-3	1,210
SRM13.2.3-B-1	920	SRM15.3.4-B-1	1,570
SRM13.2.3-B-2	1,040	SRM1.3.3-B-3	880
SRM13.3.4-B-1	1,500	SRM1.3.3-B-2	790
SRM13.3.4-B-2	1,510	SRM1.3.3-B-1	825
SRM13.3.4-B-3	1,210	SRM17.2.3-B-1	1,730
SRM15.1.1-B-1	1,040	SRM17.2.3-B-2	1,470
SRM15.1.1-B-2	1,460	SRM17.2.3-B-3	1,440
SRM15.2.2-B-2	1,220	SRM13.5.7-B-3	2,320
SRM15.2.3-B-1	1,080	SRM13.5.7-B-1	1,460
SRM16.2.2-B-2	1,700	SRM13.5.7-B-2	1,580
SRM16.2.2-B-2	1,170	SRM21.1.2-B-1	1,810
SRM22.5.5-B-1	1,600	SRM21.1.2-B-2	1,510
SRM22.5.5-B-2	2,170	SRM16.1.1-B-1	2,355
SRM25.1.1-B-2	1,110	SRM16.1.1-B-2	1,455
SRM25.1.1-B-3	1,680	SRM15.3.4-B-2	1,440
SRM26.2.3-B-1	920	SRM16.1.1-B-3	1,570
SRM27.3.4-B-1	1,380	SRM16.1.1-B-4	1,190
SRM27.3.4-B-2	1,320	SRM1.1.1-B-1	1,390
SRM28.3.4-B-1	850	SRM1.1.1-B-2	2,130
SRM29.2.4-B-1	1,380	SRM9.1.1-B-1	1,290
SRM29.2.4-B-2	1,430	SRM9.1.1-B-2	1,880

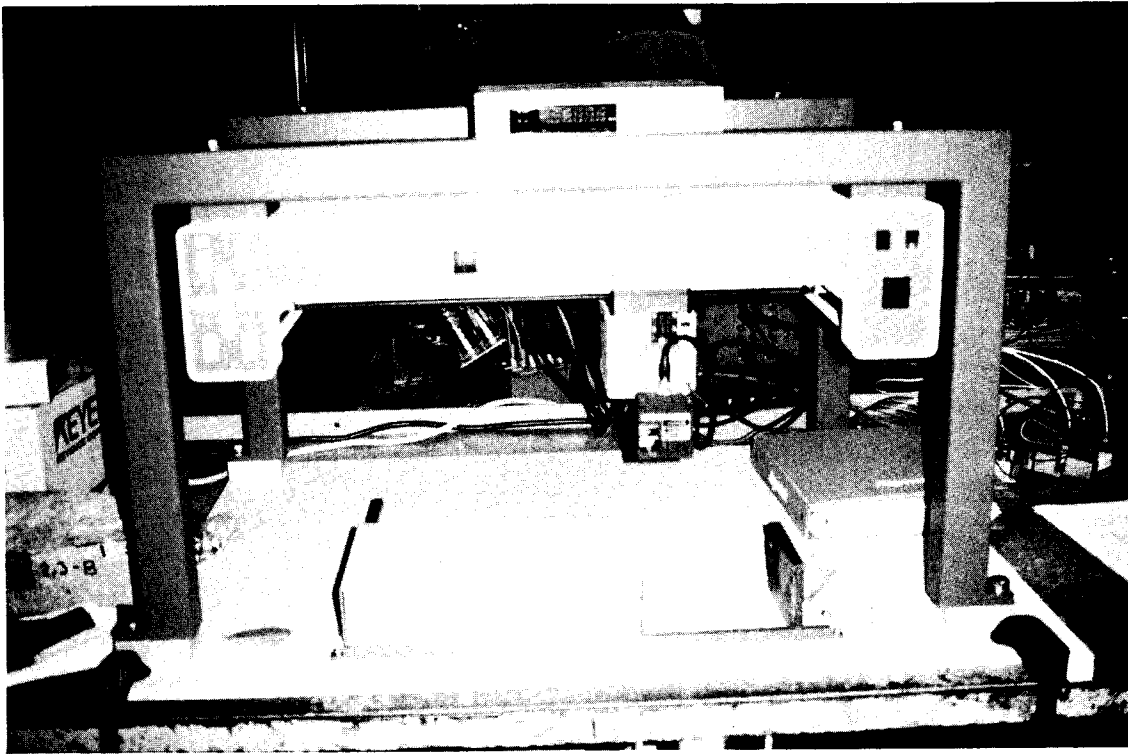


**Figure 4-34. Profilometer for joint surface profile measurement**

information to a PC/AT floppy or hard-disk data file. Additional software modifications were also made to further extend the rock-profiler measurement range from  $\pm 8$  mm to about  $\pm 25$  mm, as the rock surface variations exceeded the originally assumed range of  $\pm 8$  mm. The Z-axis of the A-102B is used to accomplish this greater range.

#### **4.5. NEVADA TEST SITE DATA COLLECTION ON GROUND-SHOCK EXCITATION**

Chapter 6 of the *Site Characterization Plan, Consultation Draft* (1988), contains a conceptual description of the Yucca Mountain repository system. Several components of this system will be subjected to seismic-design considerations. It is well accepted that the design of surface structures can be developed according to various well-known structural seismic standards and codes. However, the seismic behavior of underground structures is not well understood, and the seismic-design standards for underground facilities are not very well developed. Special efforts, therefore, must be made to understand the key parameters affecting the performance of underground structures and to ensure that analytical design models (e.g., computer codes) are capable of adequately simulating the observed seismic response of underground structures. Since ground shock due to underground explosion events is one source of seismic activities at the proposed Yucca Mountain site, data from field tests on ground-shock excitation are valuable for understanding the repository performance under ground shock and for validating the analytical design models.

The goal of this study is to assemble data sets on impulsive ground-shock field tests. These data will enable the CNWRA, and therefore the NRC, to develop methodologies to evaluate and reduce uncertainties in the analytical design models used in seismic assessment of a repository in tuff media. The objective is to quantify uncertainties in predicting the preclosure and postclosure seismic performance by understanding the capabilities and limitations of numerical modeling methods currently in use. A detailed report regarding the data collection on ground-shock excitation was prepared by Tinucci (1990).

Many types of nuclear-explosive (NE) and conventional high-explosive (HE) tests have been performed at the Nevada Test Site (NTS) and various sites for which block-motion information has been recorded. Important components of the block-motion information are the velocity and displacement data along major discontinuities forming geologic blocks. Tests have included surface bursts, shallow buried cratering, and deep underground vertical or horizontal line-of-sight events, of which the deep-underground NE and HE tests are of interest for this study.

From these tests, at least two types of motion data, driven and triggered, can be collected. Driven motion, of interest for this study, is dominated by the explosion-induced stress transients, whereas triggered motion is dominated by the partial seismic relief of pre-stress conditions. Driven-motion data can be further divided into very near-field motion in the collapse region and strong ground motion. It is the strong ground-motion data that are of interest because displacements are large enough to accurately measure differential displacements across geologic features without the rock mass being significantly damaged.

Data required to perform a complete block-motion analysis include the following (Bedsun et al., 1985).

- (1) **Site geology and geometry** of underground facilities. These descriptions include rock type and fault and bedding-plane characteristics in the field test.
- (2) **Block-motion observations** of velocity and displacement-time history records and final geologic block displacements after passage of the ground wave on opposing sides of a major structural feature.
- (3) **Ground motion**, which includes stress and particle velocity measurements. This motion can be accurately scaled to other locations by knowing the specified range (distance from the event) and without knowing the event yield.
- (4) **Material properties** for both effective rock-mass materials and discrete geologic features. These properties include rock index (e.g., density), wave speeds, strengths, and stiffnesses.
- (5) **Tectonic stress** magnitude and direction measurements of preblast in situ principal stresses.

A significant body of block-motion data, resulting from high-explosive, near-surface source events, was accumulated by the Air Force Weapons Laboratory (AFWL) during fielding of the High Explosive Simulation Technique (HEST) and the Direct Induced High Explosive

Simulation Technique (DIHEST) tests. These tests used high explosives buried in a geometric array to produce desired particle-velocity history at a given range from the array. A series of tests were carried out in three rock types--layered sedimentary, soft weathered tonalite or quartz diorite, and hard quartzite--in which block-motion data were recorded. Data from three of these tests (two in tonalite and the other in quartzite) were collected to become part of this block-motion database.

Block-motion data were also observed on contained underground tests (UGTs) at the NTS, including events within the Tunnel Beds Formation of Rainier Mesa which consists of partially saturated, zeolitized, bedded ashfall tuff. These tests used nuclear explosives buried in an underground tunnel or shaft to produce the shock wave. Data-collection efforts for nuclear tests where block motion was observed have concentrated on measuring the maximum extent, direction, and magnitude of relative displacements across geologic discontinuities. Among the tests, two have been selected as part of this block-motion database. The five cases being summarized are listed in Table 4-8.

During the late 1960s, AFWL was charged with the development of techniques using high explosives to simulate the airblast-induced and cratering-induced ground motions as part of the Hard Rock Silo nuclear design threat. HEST tests were used to simulate the airblast-induced ground motions, and DIHEST tests were used to simulate the cratering-induced motions.

HEST tests consisted of a cavity of uniform height bounded on the sides by a soil berm, above by a soil overburden of uniform thickness, and below by the test bed. Horizontal racks of high-explosive detonating cord were placed in the cavity and detonated at one end of the test bed. This detonation produced an explosive wave that propagated across the test bed, loading the earth with an overpressure pulse that decayed with time because of the compression and lifting of the overburden.

DIHEST tests consisted of a series of collinear boreholes with multiple high-explosive charges equally spaced through each hole. The detonation produced a rectangular-shaped planar wave that propagated horizontally across the test bed, and was intended to approximate an increment of the spherical direct-induced wave from a surface burst.

In the sequence of AFWL's test program, HANDEC II and ROCKTEST II tests were two of the latter tests and were conducted at the Cedar City, Utah, facilities. Both tests were combined HEST-DIHEST tests, which were to simulate a combined airblast overpressure and direct induced ground-shock pulse. The HANDEC II test was shot on August 14, 1969; and ROCKTEST II, being the larger of the two tests, was performed seven months later, on March 26, 1970. Test beds for the HANDEC II and ROCKTEST II were parallel to each other and spaced 55 feet apart, such that the centerline of the DIHEST array for HANDEC II test bed was located off the northwest corner of the ROCKTEST II test bed. Both test beds were located in a quartz diorite formation known as Cedar City tonalite. Tonalite is similar to quartz diorite, but contains over 10-percent quartz and no orthoclase or microcline feldspars (Saucier, 1969). It is 80-percent sodic plagioclase mineral of 3-mm average grain length.

The Structure And Rock Media Test (STARMET) event was the last test performed by AFWL under the Hard Rock Silo test program in which significant block-motion observations were made. STARMET was similar to the HANDEC II and ROCKTEST II tests except: (1)

**Table 4-8. FIELD TESTS FOR BLOCK MOTION DATABASE**

Event	Test Date	Rock Type	Number Observ.	Event Yield	Saturation	Test Type
HANDEC II	08/69	Tonalite	3	very small	unsat.	DIHEST
ROCKTEST II	03/70	Tonalite	3	small	unsat.	DIHEST
STARMET	11/70	Granite	4	very small	unsat.	DIHEST
MIGHTY EPIC	05/76	Tuff	18	moderate	part. sat.	UGT
DIABLO HAWK	09/78	Tuff	30	moderate	part. sat.	UGT

no HEST charges simulating an airblast were detonated, (2) the DIHEST array was about 100 times smaller, and (3) the rock type was a slightly metamorphosed, unweathered granite. The test-bed rock was quite strong, but was overlain about 50 percent by soil. Displacement occurred primarily along a single feature delimiting a large thrust block. The test was conducted on November 4, 1970, at the Pedernal Hills test site in central New Mexico. Details regarding joint patterns and discontinuities for the three sites are discussed in a separate report (Tinucci, 1990).

Block-motion problems associated with deep underground nuclear-explosion tests are much different from block-motion data recorded during DIHEST test events, which are near-surface events. MIGHTY EPIC and DIABLO HAWK tests were conducted by detonating underground nuclear explosions and recording ground and block motions at depths along major geologic features or faults. For the DIHEST tests, block motions were recorded primarily on major joints. The difference in the two types of driven block-motion events is the scale of geologic discontinuities, test configurations, tectonic stresses, induced stress waves, and magnitude of block motion.

Both MIGHTY EPIC and DIABLO HAWK events were designed under a "two-in-one concept" where the two events were detonated less than 500 feet apart in the same tunnel. Geologic formations and structures were reloaded. Material properties were assumed to be only slightly changed for the second event, DIABLO HAWK, because the magnitude of rock-mass deformations in the area of interest were not considered large enough to fail the rock, although seismic velocities in the rock mass were different afterwards. Both tests were sponsored by the Defence Nuclear Agency (DNA). The tests consisted of a nuclear explosive buried in a horizontal drift, called Horizontal Line of Sight (HLOS) configuration. The tests were conducted at the NTS, in the U12N.10 tunnel system beneath Rainier Mesa. Rainier Mesa is located 25 miles northeast of the proposed geologic repository site. Rainier Mesa generally consists of a rhyolitic welded ash flow tuff. The stratigraphic units at the test sites include Rainier Mesa, Paintbrush, Upper Tunnel Beds, Rubble, and Quartzite.

#### 4.5.1. Site Geometry

The HANDEC II test bed was a nominal 60 feet (down range from DIHEST event) and 90 feet wide. A HEST test event was performed to simulate the airblast-induced ground motion from a 1.5 megaton surface burst, which would generate a 3,000-psi overpressure that would decay to zero in about 0.3 sec (Cooper et al., 1971). A DIHEST test event, which simulated cratering-induced ground motion, was then performed 46 ms after the HEST test event. The centerline of the DIHEST array was located southwest of the test bed by 95 feet and was 200 feet in length. The DIHEST test consisted of 29 boreholes charged with a total of 46 tons of high explosives. The explosives in the boreholes were detonated simultaneously.

The ROCKTEST II test bed was more than 18 times larger than the HANDEC II test bed, with a down-range length of 250 feet and a width of 400 feet. The magnitude of the simulated airblast HEST event is classified, but can be assumed to be in the range between HANDEC I and HANDEC II events at 3,000- to 6,000-psi overpressure. The centerline of the DIHEST array was located northeast of the test bed by 75 feet and was 501.7 feet in length. The DIHEST array for ROCKTEST II consisted of 71 boreholes. The total 117 tons of high explosives were detonated simultaneously 45 ms after the HEST event.

The STARMET test bed was generally 120 feet down range from the DIHEST event to the west and 80 feet to the east. The DIHEST array was 100 feet wide and consisted of 11 boreholes. The DIHEST event was designed to simulate only a cratering-induced ground motion, using 4360 pounds of ammonium nitrate fuel oil explosives. The centerline of the DIHEST array was 20 feet southeast of the test bed.

The MIGHTY EPIC Horizontal Line of Sight (HLOS) event was conducted on May 12, 1976; and nearly two and one-half years later, on September 13, 1978, the DIABLO HAWK event was conducted in the same general vicinity. Part of the MIGHTY EPIC tunnel and support systems were designed to be reused by the DIABLO HAWK event. The concept afforded the DNA block-motion community the opportunity to study block-motion effects in previously loaded rocks. The N Tunnel system was driven nearly horizontally from the edge of the bluff back into the mesa, such that the MIGHTY EPIC working point (WP) was at a depth of 1,208 feet below the surface, and the water table was over 3000 ft below the surface. Faults were extensively mapped on the surface and at depth for which nine were considered throughgoing. Because of the depth of the test, in situ stresses were carefully measured in and around the test area. The announced yield of both MIGHTY EPIC and DIABLO HAWK test events was less than 20 KT. By comparison, the ROCKTEST II test was 0.117 KT of high explosive.

#### 4.5.2. Material Properties

The material properties for both test beds (HANDEC II and ROCKTEST II) are assumed to be the same because of close proximity. Tables 4-9 to 4-13 summarize the properties assumed representative of the HANDEC II/ROCKTEST II, STARMET, and MIGHTY EPIC/DIABLO HAWK sites. Extensive tests have been run on the tuff rocks at the MIGHTY EPIC/DIABLO HAWK sites; and, thus, intact material properties are considered to be well known. Fault and joint properties, on the other hand, have not been well characterized. The rock-strength properties listed in Table 4-12 are assumed intact rock-strength properties at the

MIGHTY EPIC and DIABLO HAWK sites. These properties can be assumed for the rock mass because of the massive nature of the stratigraphic units and lack of jointing. No site-specific published data were available for joint strengths. The properties listed in Table 4-13 are assumed values. They fall with the range of other similar rock types (Dietrich, 1981)

#### 4.5.3. Tectonic Stress

No site-specific stress measurements were found in the published literature for the HANDEC II, ROCKTEST II, and STARMET sites. However, estimates for the stress ratio ( $K_o$ ) of horizontal ( $\sigma_H$ ) to vertical stresses ( $\sigma_v$ ) based on the following equations are considered reasonable due to the near-surface stresses being much less than the induced pressure pulse.

$$\sigma_v = \gamma H$$

$$K_o = \sigma_H / \sigma_v = \frac{\tan^2(45 - \phi/2)}{\gamma m}$$

where  $H$  is the overburden depth and  $\gamma$  is the internal friction angle.

Tectonic stress distribution plays a much larger role for block motion in UGT tests such as MIGHTY EPIC and DIABLO HAWK than in near-surface tests such as DIHEST tests. This is because the orientation and magnitude of stresses may preferentially load faults or other geologic structures so that, with the added shock loading, the displacement field may be different. Tectonic stresses have been measured at several locations throughout Rainier Mesa by both overcoring and hydrofracturing techniques from surface boreholes and subsurface boreholes [Ellis, 1976 (not publicly available)]. Also, stresses were measured at two locations within the N.10 Tunnel complex: (1) near Fault 4 and (2) near Fault 5. Table 4-14 summarizes the tectonic stresses considered representative of the N Tunnel complex.

#### 4.5.4. Block Motion Data

Data from the HANDEC II and ROCKTEST II tests include displacing up to 2.6 feet of joints in silo walls, thrusting blocks 2 feet bound by distinct joints, heaving of silo closure units by 3 to 4 feet, opening and slipping of continuous cracks upward and up to 11 feet, and cratering near-explosive array areas. The block-motion data for the STARMET site can be best summarized by saying that largest displacements, approximately 5.6 feet in magnitude, occurred along a large block on the northwest side of the array. The block was bound by a 67 degrees dipping joint that intersected the line of structures parallel to the explosive array. Table 4-15 summarizes the data from these three tests that are considered useful for the purposes of the study.

Table 4-16 gives a summary of block-motion data recorded from the MIGHTY EPIC/DIABLO HAWK tests. The table also indicates fault structures for which no movement was recorded. The largest movement, about 5.5 feet in magnitude, for the MIGHTY EPIC event occurred along a fault about 240 feet from the working point; and it was about 10 feet at AB-1 station (the intersection of Fault 5 and AB drift) for the DIABLO HAWK event.

**Table 4-9. SUMMARY OF ROCK-MASS AND JOINT PROPERTIES FOR HANDEC II AND ROCKTEST II SITES**

Properties	Upper Layer	Lower Layer
<b><u>Rock Mass:</u></b>		
Depth Range (ft)	< 30.0	> 30.0
Density (pcf)	156.8	157.8
Deformation Modulus (ksi)	*1,790.0	*2,500.0
Poisson's Ratio	*0.14	*0.14
Unconfined Compressive Strength (ksi)	4.0	6.0
Tensile Strength (ksi)	1.0	0.5
Internal Friction Angle (deg)	25.0	29.0
Shear Strength Intercept (ksi)	0.3	0.6
<b><u>Joints:</u></b>		
Normal Stiffness (ksi/ft)	585.0	585.0
Shear Stiffness (ksi/ft)	275.0	175.0
Peak Friction Angle (deg)	29.0	29.0
Base Friction Angle (deg)	17.0	17.0
Cohesion (ksi)	0.0	0.0
Tensile Strength (ksi)	0.0	0.0

\*Adjustment is needed under different joint density

**Table 4-10. SUMMARY OF ROCK-MASS AND JOINT PROPERTIES FOR STARMET SITE**

Properties	Upper Layer	Lower Layer
<b><u>Rock Mass:</u></b>		
Depth Range (feet)	< 20.0	> 20.0
Density (pcf)	63.0	164.0
Deformation Modulus (ksi)	4,200.0	5,000.0
Poisson's Ratio	0.12	0.13
Unconfined Compressive Strength (ksi)	1.0	2.0
Tensile Strength (ksi)	0.04	0.05
Internal Friction Angle (deg)	26.0	29.0
Shear Strength Intercept (ksi)	2.8	2.8
<b><u>Joints:</u></b>		
Normal Stiffness (ksi/feet)	17,500.0	17,500.00
Shear Stiffness (ksi/feet)	8,700.0	8,770.0
Peak Friction Angles (deg)	35.0	35.0
Base Friction Angle (deg)	26.0	26.0
Cohesion (ksi)	0.0	0.0
Tensile Strength (ksi)	0.0	0.0

**Table 4-11. ROCK-MASS DEFORMATION PROPERTIES FOR STRATIGRAPHIC UNITS AT MIGHTY EPIC/DIABLO HAWK SITE**

Stratigraphic Unit	Young's Modulus (ksi)	Poisson's Ratio
Rainier Mesa	3,410	0.25
Paintbrush	550	0.26
Upper Tunnel Beds	650	0.25
Test Location Beds:		
MIGHTY EPIC	1,810	0.18
DIABLO HAWK	1,790	0.17
Rubble	1,550	0.28
Quartzite	6,800	0.30

**Table 4-12. SUMMARY OF ASSUMED INTACT ROCK-STRENGTH PROPERTIES FOR STRATIGRAPHIC UNITS AT MIGHTY EPIC/DIABLO HAWK SITE .**

Stratigraphic Units	Uniaxial Compressive Strength (ksi)	Tensile Strength (ksi)	Average Internal Friction Angle (deg)	Average Shear Strength Intercept (ksi)
Rainier Mesa	18	2.9	40	34.8
Paintbrush	4.0	1.0	10	1.7
Upper Tunnel Beds	43	0.29	10	1.45
Test Beds	2.83	0.36	8	1.26
Rubble	--	0	25	0
Quartzite	8.0	0.32	28	2.4

**Table 4-13. SUMMARY OF ASSUMED JOINT-STRENGTH PROPERTIES FOR MIGHTY EPIC/DIABLO HAWK SITE**

Properties	Intra-Bed Fractures	Faults	Bedding Planes
Peak Friction Angle (deg)	32	14	7
Base Friction Angle (deg)	26	11	6
Cohesion (ksi)	0.3	0.5	0.5
Tensile Strength (ksi)	0	0	0

**Table 4-14. SUMMARY OF TECTONIC STRESS DATA FOR MIGHTY EPIC/DIABLO HAWK SITE**

Stress Component	Magnitude (ksi)	Orientation	
		Plunge (deg)	Bearing (deg)
General:			
$\sigma_1 = \sigma_{H1}$	1.01	0	N34E
$\sigma_2 = \sigma_v$	0.92	90	
$\sigma_3 = \sigma_{H2}$	0.48	0	N56W
Near Fault 4:			
$\sigma_1 = \sigma_{H1}$	1.24	17	N83E
$\sigma_2 = \sigma_v$	0.82	50	N59W
$\sigma_3 = \sigma_{H2}$	0.89	34	N25W
Near Fault 5:			
$\sigma_3$ (22)*	0.20		
$\sigma_3$ (38)	0.38		
$\sigma_3$ (63)	0.63		

\*distance in feet from Fault 5



Table 4-15. HANDEC II, ROCKTEST II AND STARMET DATA SUMMARY

Item	Radial Range (ft)	Strike	Dip	Total	Component of Displ. (ft)	Comments
<u>HANDEC II</u>						
Average Test Bed	125	N13E	29E	1.5	1.3 RL,SS 0.73 R,DS	
Silo S-2	95	N11E	65E	2.1	LL,SS	Movement along preexisting jt.
SW corner	120	NS	30W	2.62	NA	Testbed movement along low-angle jt.
Silo S-11	105	N72W	26NE	0.32	R,DS	Shear surface in structure
<u>ROCKTEST II</u>						
Joint	200	N10W	20	11.7	R,DS	Clay filled and/or iron stained
Silo S-05	125	N53W	Vert	>0	LL,SS	Joint in silo, clay filled
Joint B	130	N38W	28NE	0.58	R,DS	Not mapped pretest
<u>STARMET</u>						
Thrust block	55	N30E	67NW	5.6	2.5 RL,SS 5 R,DS	NW quadrant of testbed, avg. displ.
Silo W-5	35	N35E	67NW	5.4	R,SS	Joint iron-stained testbed ctr. line
Silo W-6	36	N35E	67NW	3.7	R,SS	Same as W-5, 10ft S testbed ctr. line
Silo W-7	45	N35E	67NW	2.3	R,SS	Same as W-5, 29ft S testbed ctr. line

LL=left lateral; SS=strike slip; R=reverse; DS=dip slip; Vert=vertical

4-58

Table 4-16 . MIGHTY EPIC AND DIABLO HAWK DATA SUMMARY

Item	Radial			Component		Comments
	Range (ft)	Strike (deg)	Dip (deg)	Total (ft)	of Displ. (ft)	
<u>MIGHTY EPIC</u>						
Fault 5 bypass	332	NS	60E	2.2	1.6 R,DS 1.5 LL,DS	Damp gouge in fault 0.25 in. thick
Fault 5 B drift	407	N5W	70E	1.5	0.8 R,DS 1.3 LL,SS	Damp gouge in fault 0.25 in. thick
Tt3BC/3D A drift	290	N85W	15S	>3	R,DS	Damp clay layer on contact 0.25 in. thick
Fault A drift	290	N30E	72W	>0	R,DS,LL,SS	Fault through SRI structure
Fault LOS drift	243	NS	55W	>5.5	R,DS	Fault near #6 in the LOS drift
Fault	383	N35E	68NW	2.9	1.5 NS,DS 2.5 LL,SS	Fault in interface drift
Fault 7 A drift	293	N15W	60SW	0	0	Tight and dry
Fault 8 A drift	295	N45W	68SW	0	0	Two planes tight and dry
Fault 7 B drift	404	N15W	70SE	0	0	Tight and dry

Vert=vertical; NA=not measured; LL=left lateral; LOS=line of sight; SS=strike slip; R=reverse; DS=dip slip; N=north; E=east; S=south; W=west; ?=unknown; NS=normal slip; Horiz=horizontal

Table 4-16. MIGHTY EPIC AND DIABLO HAWK DATA SUMMARY (Cont'd)

Item	Radial			Component		Comments
	Range (ft)	Strike (deg)	Dip (deg)	Total (ft)	of Displ. (ft)	
Fault 8 B drift	404	N40W	70SW	0	0	Two planes tight and dry
Fault 4 bypass	521	N15W	86W	0	0	Tight
Fault 3 bypass	710	N70E	80SW	0	0	Tight and dry
Fault 2 bypass	1091	N20W	67SW	0	0	Tight and dry
Fault 4 C drift	950	N15E	90W	0	0	Tight
Borehole MH-1	239			4.35	4 north 1.7 up	Water-saturated zone in tuff
Borehole MH-1	250	N90E	25S	1.72	1.4 north 1.0 east	At tuff paleo-colluvium interface
Borehole MH-2	310	N90E	25S	4.3	3.9 north 1.4 east	1.3 vert. at tuff paleo-colluvium contact
Borehole MH-2	403	N90E	25S	2.6	2.4 north 0.4 east	0.8 vert. at tuff paleo-colluvium contact

Vert=vertical; NA=not measured; LL=left lateral; LOS=line of sight; SS=strike slip; R=reverse; DS=dip slip; N=north; E=east; S=south; W=west; ?=unknown; NS=normal slip; Horiz=horizontal

Table 4-16. MIGHTY EPIC AND DIABLO HAWK DATA SUMMARY (Cont'd)

Item	Radial			Component		Comments
	Range (ft)	Strike (deg)	Dip (deg)	Total (ft)	of Displ. (ft)	
<b>DIABLO HAWK</b>						
Surface fracture	485	N15W	vert.	1.7	NA	Fracture was open at surface 0.1-6.0 in.
Fault 3BP	730	N35W	85W	0	NA	Tight and dry
Fault LOS	630	N25W	80W	0	NA	Tight and dry
LOS-1	530	N17E	65W	0.5	0.4 LL,SS 0.3 R,DS	Pin measurement
LOS-2	443	N47E	82SE	> 1.0	> 1.0 R,DS	Pin measurement, LOS pipe damage
CB-1	190	N21E	68NW	> 1.7	> 1.7 R,DS	Pin measurement
AB-1	255	N2E	66E	10.2	10 RL,SS 1.5-2 R,DS	Pin measurement
3BC/3D AB drift	165	N75E	18S	5 to 10	NA	Bedding plane in AB drift
3BC/3D Q AX-2	305	N85E	15S	> 0	NA	Damaged structure

Vert=vertical; NA=not measured; LL=left lateral; LOS=line of sight; SS=strike slip; R=reverse; DS=dip slip; N=north; E=east; S=south; W=west; ?=unknown; NS=normal slip; Horiz=horizontal

Table 4-16. MIGHTY EPIC AND DIABLO HAWK DATA SUMMARY (Cont'd)

Item	Radial			Total	Component	
	Range	Strike	Dip		of Displ.	
	(ft)	(deg)	(deg)	(ft)	(ft)	Comments
Fault in AX-4	330	N26E	70W	5.2	NA	Damaged structure
Fault Q CS 2+80	350	N20E	70W	1.5 to 10	NA	Damage in AB drift
Fault in CY-23	438	N10E	70W	0 to 1.0	NA	Damaged structure and cables
Fault 5 B drift	304	N5E	66E	> 1.9	NA	Filled with damp gouge
Fault C drift	348	N30W	66NE	> 0	NA	Fault severed TRW short cables
C1 bulkhead	223	N85E	17S	2.0 to 3.5	NA	Bedding planes in Tt4B formation
Fault D drift	290	N25W	75SW	2.0	NA	Secondary fault water tank structure
Fault D1 drift	320	N35W	75SW	1.7	NA	Secondary fault D1 ministructure
Fault Q AZ5&AZ6	350	N35W	75SW	1.1	NA	Movement between structures
Fault 4 Q CZ1	282	N15E	80E	0.1 to 1.0	NA	Structure damaged tight and dry

Vert=vertical; NA=not measured; LL=left lateral; LOS=line of sight; SS=strike slip; R=reverse; DS=dip slip; N=north; E=east; S=south; W=west; ?=unknown; NS=normal slip; Horiz=horizontal

Table 4-16. MIGHTY EPIC AND DIABLO HAWK DATA SUMMARY (Cont'd)

Item	Radial			Component		Comments
	Range (ft)	Strike (deg)	Dip (deg)	Total (ft)	of Displ. (ft)	
Fault 4 E drift	410	N29E	80E	0.4	NA	E drift offset by tight and dry
Fault Q Sta. CB1	315	N20E	75W	> 1.7	NA	Fault in main reentry drift near sta. CB1
LOS-3	390	N25E	65E	0	NA	No LOS pipe damage pin measurement
BP-1	940	N25E	60E	0	NA	Pin measurement
CB-4	485	N35E	76SE	0	NA	Pin measurement
CB-5	496	N25W	66SW	0	NA	Pin measurement
CB-6	500	Due N	70W	0	NA	Pin measurement
AB-2	420	N30W	65SW	0	NA	Pin measurement
AB-3	434	N30W	68SW	0	NA	Pin measurement tunnel linear undamaged
AB-4	461	N25W	75SW	0	NA	Pin measurement tunnel linear undamaged

Vert=vertical; NA=not measured; LL=left lateral; LOS=line of sight; SS=strike slip; R=reverse; DS=dip slip; N=north; E=east; S=south; W=west; ?=unknown; NS=normal slip; Horiz=horizontal

Table 4-16. MIGHTY EPIC AND DIABLO HAWK DATA SUMMARY (Cont'd)

Item	Radial		Component			Comments
	Range (ft)	Strike (deg)	Dip (deg)	Total (ft)	of Displ. (ft)	
AB-5	589	N25W	85NE	0	NA	Pin measurement
AB-6	604	N15W	75NE	0	NA	Pin measurement
LOS-4	280	N40W	85NE	NA	MA	Inaccessible
BP-2	840	N10W	75E	NA	NA	Inaccessible
BP-3	793	Due N	65W	NA	NA	Inaccessible
BP-4	643	N35W	85NE	NA	NA	Inaccessible
Fault 2 BP-5	590	N35W	77W	NA	NA	Tight and dry inaccessible
Fault 2R BP-6	542	N10E	7SE	NA	NA	Tight and dry inaccessible
BP-7	395	N45E	80SE	NA	NA	Inaccessible
BP-8	380	N15E	70E	NA	NA	Inaccessible

Vert=vertical; NA=not measured; LL=left lateral; LOS=line of sight; SS=strike slip; R=reverse; DS=dip slip; N=north; E=east; S=south; W=west; ?=unknown; NS=normal slip; Horiz=horizontal

Table 4-16. MIGHTY EPIC AND DIABLO HAWK DATA SUMMARY (Cont'd)

Item	Radial			Component		Comments
	Range (ft)	Strike (deg)	Dip (deg)	Total (ft)	of Displ. (ft)	
BP-8A	377	NA	NA	NA	NA	Inaccessible
Fault 3 BP-9	218	N35W	90SW	NA	NA	Tight and dry inaccessible
Fault 5 BP-10	203	N15E	76E	NA	MA	Damp gouge inaccessible
Fault 4 CB-2	220	N5E	80W	NA	NA	Tight inaccessible
CB-3	395	N10W	82E	NA	NA	Inaccessible
Fault 6 RE-1	258	N35E	88SE	NA	NA	Tight and dry inaccessible

Vert=vertical; NA=not measured; LL=left lateral; LOS=line of sight; SS=strike slip; R=reverse; DS=dip slip; N=north; E=east; S=south; W=west; ?=unknown; NS=normal slip; Horiz=horizontal

#### 4.6. FIELD SITE INVESTIGATION

At the proposed waste emplacement horizon of Yucca Mountain, the geomechanical conditions are understood to be a competent rock material, prominent vertical and sub-vertical jointing, and faults which transgress the site environs. Also, at this horizon, the rock mass is unsaturated, with the watertable 200 to 400 m below the emplacement horizon. An important phenomenon that could affect both short- and long-term performance of a repository is repeated ground motions due to seismic activities (Kana et al., 1989). Conceivably, ground motions from earthquakes could cause relative displacements along discontinuities on the canister, room, and repository scales, any or all of which could jeopardize the performance of an underground HLW repository.

Rock-mass hydraulic response due to seismic events can be expressed through a variety of phenomena, including fluctuations in water-well levels; flooding of mines and other underground excavations; appearance of new springs, streams, and sandboils; or localized soil liquefaction. Two time scales are involved in these phenomena. Immediate response involves groundwater changes attending passage of the ground wave, and is represented by effects such as short-term water-well fluctuations. Pseudo-static response reflects permanent changes in rock mass conditions such as fracture permeability or watertable, and in groundwater flow under these changed conditions. Both short- and long-term groundwater response to repeated seismic loadings may have significant implications for the performance of an underground nuclear waste repository. One concept involves "seismic pumping," which purportedly may drive groundwater of an aquifer below an initially unsaturated repository horizon to the host horizon. In case of long-term response, permanent elevation of the watertable may be hypothesized, resulting in flooding of the repository horizon.

All these effects may be analyzed if techniques are established for simulation of rock mass and groundwater changes accompanying passage of a seismic wave. The needs are (1) to determine how significant are the geomechanical response and the local geohydrologic changes attending seismic events, (2) to establish a reliable set of field data reflecting the relation between geomechanical responses/geohydrologic changes and seismic events in a properly characterized rock mass, and (3) to determine if currently available analytical methods can adequately describe seismically induced changes in geomechanical responses/groundwater conditions.

The exploratory Seismic Rock Mechanics research program was intended to study repository response due to repetitive dynamic loadings. This research project has the twin focus of understanding the key parameters affecting repository performance under repeated seismic loadings and evaluating current capability for calculating such effects. As a part of this research, an extensive instrumentation program has been undertaken. Its aim is to generate a reliable data set of a particular site for evaluating analytical methods for simulation of the effects of seismic activities.

Since there appears to be little data available on subsurface-motion generation from natural earthquakes for the study of rock structural responses and geohydrologic changes, nor will these data be accumulated quantitatively in the near future, the study of mine seismic events offers an attractive alternative. Seismic events in mines are by far the most prolific source of information on the response of underground excavations to seismic loading. It is notable that

no systematic differences have been observed between these mine seismic events and natural earthquakes (McGarr, 1984). This is extremely important in that observed underground mine responses (geomechanical and geohydrologic) may be applied to predicting repository response to natural earthquakes.

#### 4.6.1. Field Site Evaluation and Selection

As discussed earlier, the seismic studies performed to date on underground structures and associated geohydrologic response have not been subject to an adequate level of experimental and field investigations. Field data collections and evaluations are especially inadequate for application to the proposed repository in the jointed and fractured tuff at Yucca Mountain. At the same time, it is necessary to understand the key parameters affecting the repository under repeated seismic loadings in order to support the requirements in 10 CFR Part 60 for repository design, safe operations, waste retrievability, integrity of the engineered barriers, and post-closure repository performance. Thus, the results of the proposed field investigations are extremely important. The data generated in the field investigations will (1) clarify and quantify the relation among seismically induced ground motion and mechanical response and changes in groundwater conditions (2) evaluate the performance of several commercially available computer codes in simulating the seismic effects on excavation and host-rock deformation and on groundwater hydrology, taking into account rock structure, site conditions, joint properties, and recorded histories of seismic loading.

To achieve these results, three important factors govern the selection of a mine site for the study of seismic events. The first is that the host rock mass should be well characterized geologically and structurally. Naturally jointed rock mass is a must. The second is that the recurrence time for seismic events and/or rockbursts needs to be small. These conditions provide the capacity to: (1) measure, over a reasonable time span, deformation of excavations and groundwater responses in jointed rock subject to repetitive seismic loadings and (2) relate the observations to the rock-mass structural conditions. The third is that mechanical response and groundwater hydrology studies should be performed at the same mine.

Among the potential sites located in the U. S. and Canada, the Lucky Friday Mine satisfies all the three governing factors for site selection. This mine is in the Coeur d'Alene region, Mullan, Idaho, and has been well-characterized geologically. Extensive publications concerning geology in the region are readily available (White and Winston, 1977). In addition, this mine is among several other mines in the region which has had extensive rock mechanics studies in the past. A substantial database presently exists on the rock mechanics of the Lucky Friday Mine.

The mine experiences a significant problem in mining-induced seismicity. The seismicity is the result of either violent failure of the intact rock through propagation of new shear fractures, or slip on existing fault or bedding surfaces. These events can be quite large in magnitude, with the largest measured to date at 4.0 Richter scale. The mine experiences over 50 greater than 1.0 Richter events per year, and on the order of 10 to 20 events with magnitudes greater than 2.0 Richter scale.

#### **4.6.2. General Description and Site Geology**

The Lucky Friday Mine is located in the Coeur d'Alene Mining District in Idaho's panhandle region. It is one of the deepest working mines in the western hemisphere, with maximum mining depth approximately 5,300 feet below ground surface. The rock formations in the Coeur d'Alene district consist of mainly the St. Regis member (the upper formation) and Revett member (the lower formation). The St. Regis formation is predominantly purple argillite; and the Revett formation is composed of interbedded units of vitreous quartzite, sericitic quartzite, and greenish siltite-argillite. The Revett formation contains well-defined lower, middle, and upper members. The rock formations are folded with the syncline dipping a few degrees eastward. Revett formation at the mine horizon reaches ground surface in the west of the structure. The ore-bearing stratum, which strikes east-west direction and is nearly vertical with almost 1,500 feet of minable strike length, lies primarily within the Revett formation and is located at the north side of the syncline. The stratum is bounded on its north and south extent by faults, and is cut by several major fault structures (Figure 4-35). The primary minerals produced are silver, lead, and zinc. The bedding planes can be continuous, rather-planar surfaces, which often show evidence of past shearing. The beds dip approximately 70 degrees from horizontal, and strike conformally with the ore-bearing stratum, at least in the southern sections of the mine.

The permeability of the Revett formation is very low. Water is found within the Osburn fault, Whiteledge fault, fracture zones near the faults, ore-bearing stratum, and several fault structures between the Osburn and Whiteledge faults.

Districtwide in situ measurements indicate that the maximum horizontal stress is about 1.35 times the minimum horizontal and vertical stresses. The maximum horizontal stress around the Lucky Friday Mine is in the direction of N45°W.

#### **4.6.3. Mine-wide Seismic Activity Monitoring System**

The mine has performed extensive studies into the location, nature, and causes of the seismic events. Currently a micro-seismic system with more than 30 channels is installed that continuously monitors the microevents and locates the coordinates of the events. The microseismic monitoring system is designed to monitor acoustic emissions having frequencies of 10 to 5,000 Hz (Jenkins et al., 1990). Historical data are available from this system dating back to the early 1970s. Also in operation is a macroseismic monitoring system for mine-wide monitoring. This macroseismic system was installed by the U. S. Bureau of Mines and is designed to provide the ability for full waveform analysis for larger seismic events that normally cause damage to a mine. Events of Richter magnitude greater than 0.5 are the primary target. The data-storage system includes time-of-arrival and frequency-duration data. Data can be analyzed to determine parameters, including source location, time, magnitude, and amplitude of waveforms. This macronetwork provides essential information for evaluating analytical methods for simulation of the effects of seismic activities.

#### **4.6.4. Instrumentation**

The instruments were installed at the Lucky Friday Mine to monitor: (1) the short- and long-term responses of excavations and their supports to repeated seismic events and (2) the

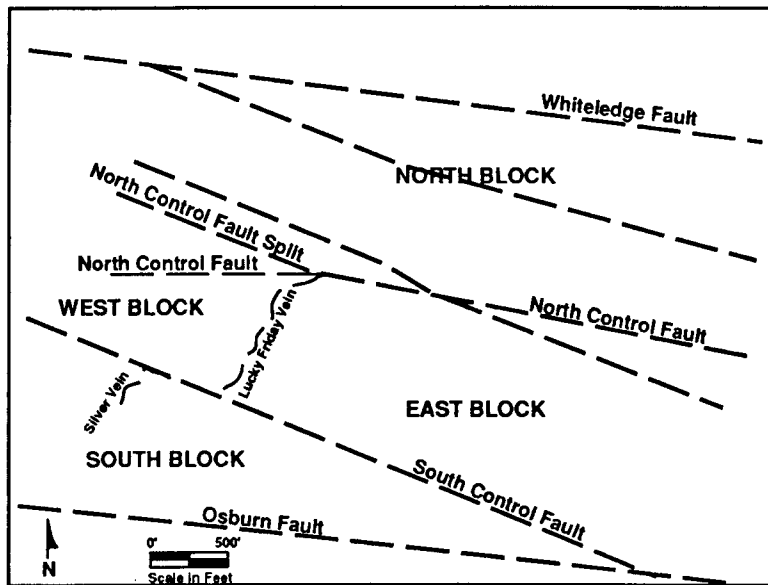


Figure 4-35. Plan view of the Lucky Friday orebody showing fault structures

change in water pressure in faults or other structures in the rock mass as a result of seismic loading.

#### 4.6.4.1. Excavation Response

The transient and long-term displacement response of excavations will be monitored in close proximity to seismic events greater than 1 Richter magnitude. The objective in this study is to monitor the effects of dynamically induced stress (and failure) states. This is accomplished at the Lucky Friday Mine by instrumenting tunnels in the footwall ramp system below the present mining. The mine uses underhand cut-and-fill mining method for stoping the orebody. The general advance of the mining is downward. Four stopes are used on each level, which advances downward in a series of 10-foot high cuts. The haulage development for each stope is a spiralling ramp in the footwall of the orebody. Almost all the seismic activities in the mine occurred in the footwall where bedding planes dip toward the orebody. When mining proceeds downward, the states of stresses near the mining area are modified to such a condition that the normal stress on the bedding plane decreases, while the shear stress on the bedding planes increases. These states of stresses provide a favorable condition for slip to occur along the bedding planes that causes seismic activity and or rockburst. While in the hanging wall, the bedding planes are dipping away from the orebody. The modified stress conditions are such that high normal stress and relatively low shear stress are on the bedding planes. Therefore, they do not provide a favorable condition for slip.

Two sites were selected near the bottom of the present ramp under development for instrumentation to monitor mechanical responses of underground openings under repeated seismic events. Because these excavations are below the stope, they are relatively undisturbed by the stoping. These two sites are about 1,588 m (5210 feet) below the ground level. Figure 4-36 shows a portion of the ramp system at the 5210 level where the two instrumentation sites are located. One site (LFM95-C2) is about 30.5 m (100 feet) from the orebody to be mined, and the other one (LFM95-C1) is about 76.2 m (250 feet) away. The two sites are located on the opposite side of a syncline as shown in the figure. The bedding planes intersect the instrumentation cross section of LFM95-C1 site at an approximate 50-degree angle and at a 15-degree angle for the LFM95-C2 site. Both instrumentation sites have a 3.05-m (10-foot) square cross section, and are supported by 1.8-m (6-foot), resin-grouted rebar, 5.1- x 5.1-cm (2- x 2-inches) chain-link mesh. A support with 3.81- to 5.1-cm (1.5- to 2-inch) fiber-reinforced shotcrete is also used at the LFM95-C2 site.

Three basic types of instruments were used for this study: (1) extensometers to monitor long-term displacement changes around excavations, (2) triaxial velocity gauges to determine the transient response of the rock at excavation surfaces, and (3) closure points to monitor opening closure. Calibration of the instruments used at the Lucky Friday Mine is discussed in a separate section.

Figure 4-37 shows a cross section of the tunnel and location of the instruments for both sites. These cross sections were taken when facing the orebody. Five 5-anchor rod extensometers were installed per site. The deep anchor is at approximately 7.9 m (26 feet) down hole, with anchors at roughly 1.5-m (5-foot) intervals. Hydraulically inflated anchors were used to ensure a nonslipping grip. The rod displacement is sensed by linear potentiometers in the extensometer head, which has a range of 5 cm (2 inches). The linear potentiometers are read by a data acquisition system described later.

The layouts for the extensometers are essentially the same except for the extensometer hole No. 5 at the LFM95-C2 site. This hole was drilled 15-degrees downward from the horizontal axis to avoid a potential interference with an up-ramp tunnel nearby (refer to Figure 4-36). All extensometer boreholes were diamond drilled with a diameter of approximately 7.6 cm (3 inches), and the NX-sized cores were recovered from these boreholes for rock basic-material and joint-properties characterization.

The extensometer boreholes were scoped using a TV borehole camera before the installation of extensometers. Viewing of the boreholes was performed with the camera in a side-view arrangement. The camera was held with a special tool at a constant distance to the borehole surface to allow measuring the observed features such as fractures. Measurements of fracture sizes and angles were taken from a TV monitor where the picture was magnified five to one. Figure 4-38 shows typical scoping results for the horizontal borehole No. LFM95-C1 site. A highly fractured zone, about 1 m (3.3 feet) wide, was identified approximately 1 m from the tunnel surface. This information is going to facilitate the interpretation of rock displacement data since one hydraulically inflated anchor of an extensometer may be located in this fracture zone. Downholes at both cross-sections were not scoped to protect the camera from water damage. Two additional boreholes were also drilled at the LFM95-C2 site for scoping purposes to provide necessary information for the construction of a three-dimensional geologic structure plot around the tunnel. One borehole was drilled perpendicular to the projected

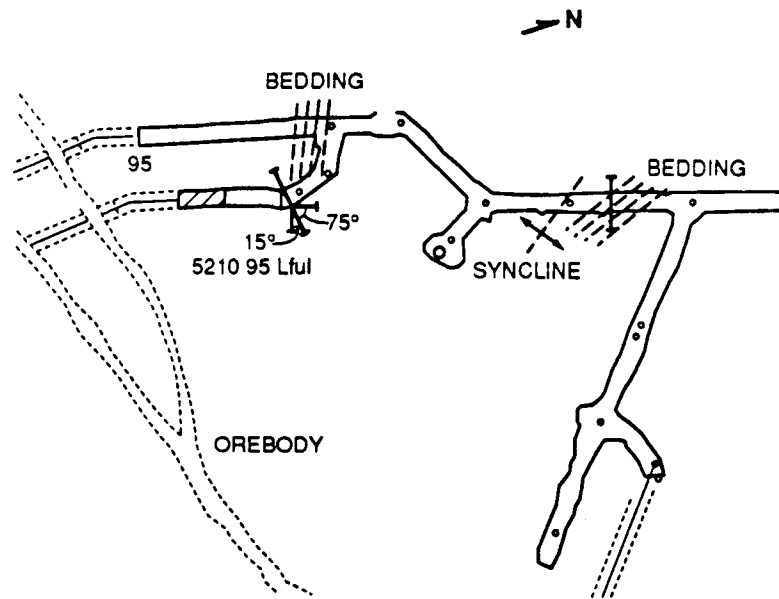


**Figure 4-36. Ramp system at the 5210 level at the Lucky Friday mine**

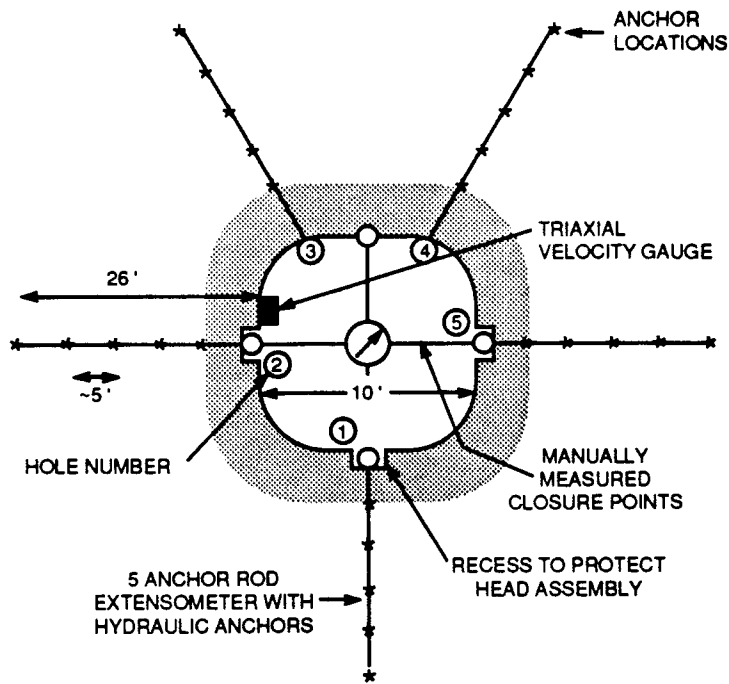
bedding planes, with the other one parallel to the bedding planes (No.s 6 and 7 holes in Figure 4-36). The construction of a three-dimensional structural geology is necessary to assist evaluating models of rock joint deformation and computer codes for simulation of the effect of seismic activities.

Long-term closures will be measured by a tape extensometer for at least two opening cross-sections at each site.

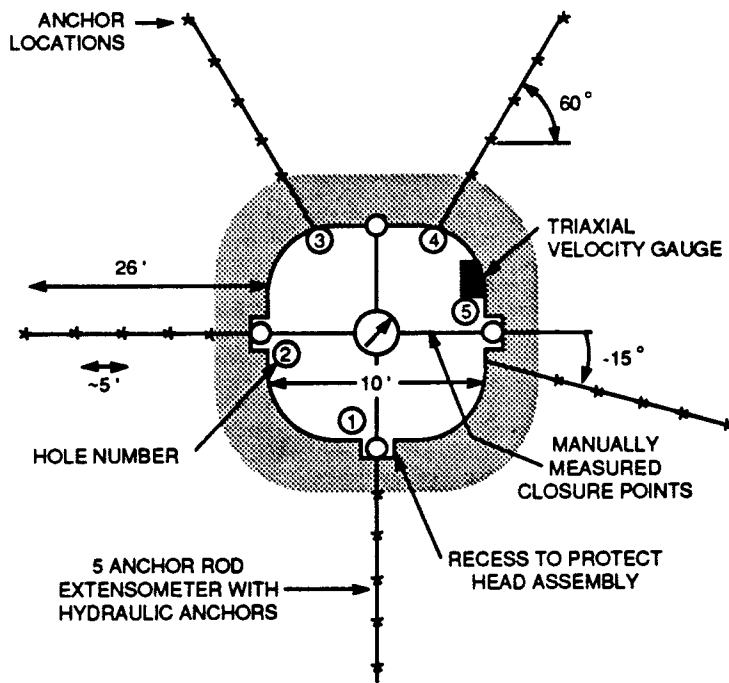
The magnitude of the ground shock must be measured at the instrumentation site. A triaxial velocity gauge is installed at each site for the monitoring function. The readouts from these velocity gauges, in conjunction with the U.S. Bureau of Mines' mine-wide macro-seismic monitoring system, provide sufficient rockburst events information.

#### **4.6.4.2. Pore Water-Pressure Measurement**

To study the changes in water pressure in faults and other structural features in the rock mass as a result of seismic loading, these fault structures should be in close proximity to the seismicity and be fully saturated with water. Therefore, the zones in which the fracture are sampled must be below the present workings, which provide a draw-down to the surrounding groundwater. The faults must be pierced and packed off, with pressure measurements taken in the packed-off regions. One site at the 5700-level station, which is about 152



(a) LFM95-C1 Site



(b) LFM95-C2 Site

Figure 4-37. Instrumentation array for cross sections of the 5210 level

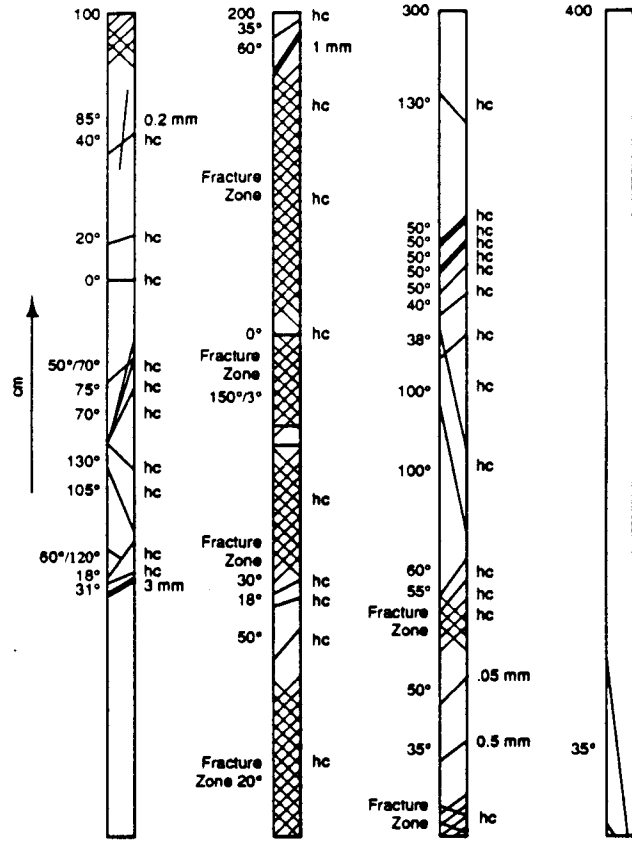


Figure 4-38. Geologic mapping of extenzometer hole No. 5 at LFM95-C1 site

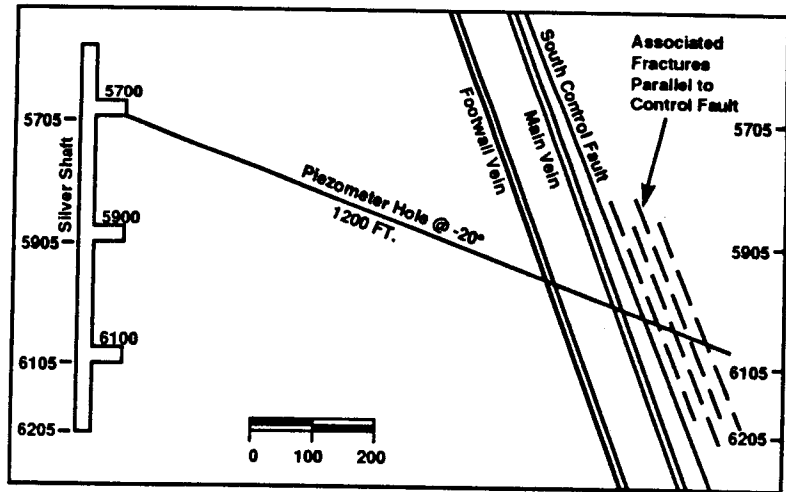


Figure 4-39. Lucky Friday silver shaft cross section of the drill hole for piezometer installation (view looking N74°E)

m (500 feet) below the two mechanical response instrumentation sites, was found suitable for the purpose of monitoring transient pore-water pressure change along several fault structures.

An NQ size hole (7.6 cm in diameter) is being drilled at approximately 20 degrees downward in a southerly direction from the 5700-level station (Figure 4-39). The hole is directed toward an intersection with the main and footwall split fault structures as well as with the South Control fault. These structures should be intersected within about 365 m (1200 feet), some 122 m (400 feet) below the 5700 level. Approximately four zones will be selected for pore-water pressure monitoring.

The faults are packed off using inflatable straddle packers (Figure 4-40). The straddle-packer sections are separated by pipe, and stiff pipe sections are used to push the packers into position using the feed of a diamond drill. A vibrating-wire pressure transducer is installed in the interval between each straddle packer and in at least one nonfault zone between the packed regions. A backup pressure-measurement capability is provided using a set of secondary access tubes to the packed intervals. The packers are inflated with water via inflation lines. The magnitude of the ground shock at the pore-water pressure-measurement site will be measured by a hydrophone, as well as by the Bureau of Mines' macroseismic system.

#### **4.6.5. Data Acquisition**

The extensometer and piezometer data acquisition system consists of two primary components: two underground dataloggers and a surface personal computer. A conceptual schematic diagram for data acquisition for extensometer and piezometer readouts is provided in Figure 4-41. A 32-channel datalogger with power supply is located at the LFM95-C1 site within the 5210 ramp and the other datalogger is at the 5700-level station. Multiplexer boards are located at each extensometer installation site to sample the extensometers and send the readings to the datalogger. The data obtained are converted to engineering unit and temporarily stored in the memory of the datalogger. Four piezometers are connected through a multiplexer to the datalogger at the 5700-level station. The data collected are engineering values. A backup transfer-tube gauge for each piezometer is available in the event of loss of piezometers. The two dataloggers are networked via a coaxial cable. Communication from the surface computer is made to all instruments via the datalogger at the 5700 level.

The seismic data acquisition system is shown in Figure 4-42. The magnitude of ground shock monitored by the triaxial velocity gauges at the excavation response measurement sites and the hydrophone at the pore-water pressure-measurement site is amplified at gauge locations by signal amplifiers, and analog signals are sent to the ground surface via twisted pairs and filtered to remove any frequency higher than 500 Hz. using an Anti-Aliasing Filter.

#### **4.6.6. Instrument Calibration**

##### **4.6.6.1. Five-Anchor Extensometer Calibration**

The five-anchor extensometers selected for the field study are Geokon Model A-6G, which consists of three basic components: hydraulic borehole anchors, 1/4-inch diameter glass-fiber measurement rods with 1/2-inch protective plastic tubes, and the hydraulically anchored head-assembly. The relative displacement between an anchor and the head-

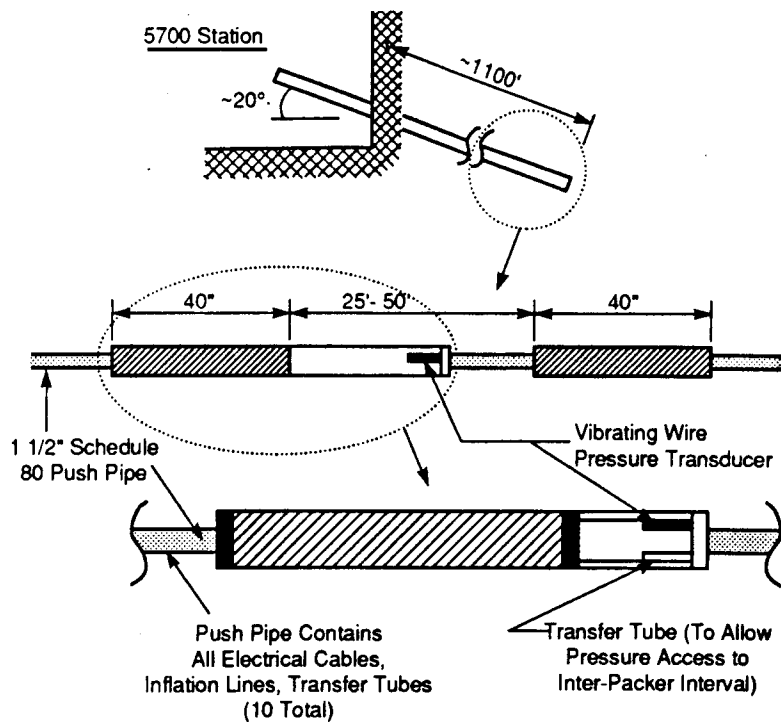


Figure 4-40. Schematic drawing of piezometer installation showing straddle packers

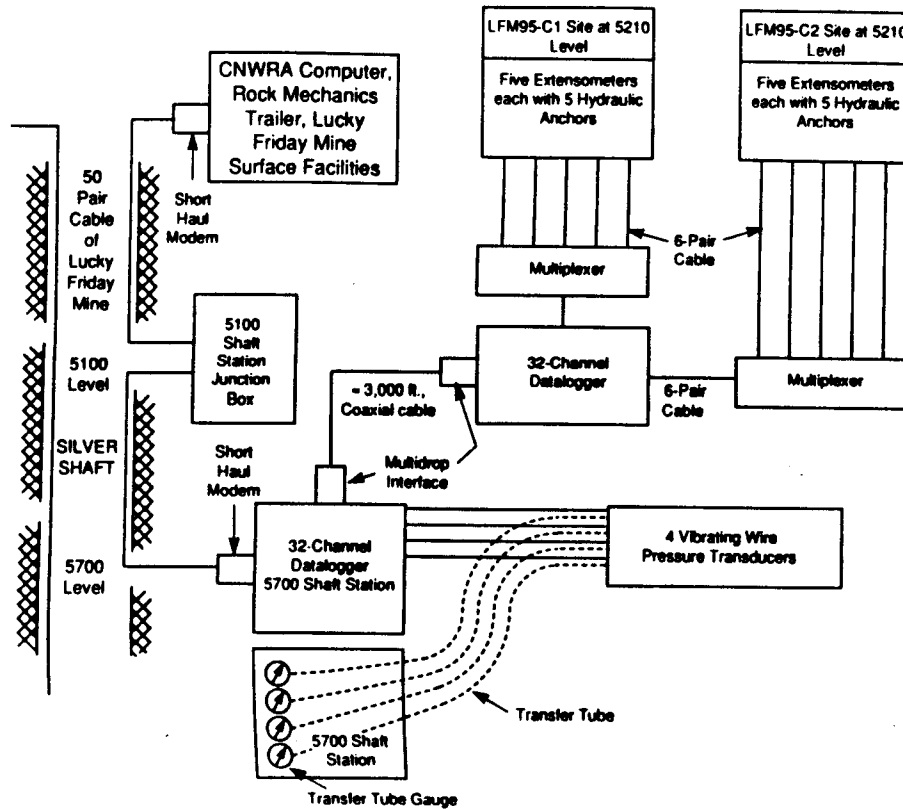
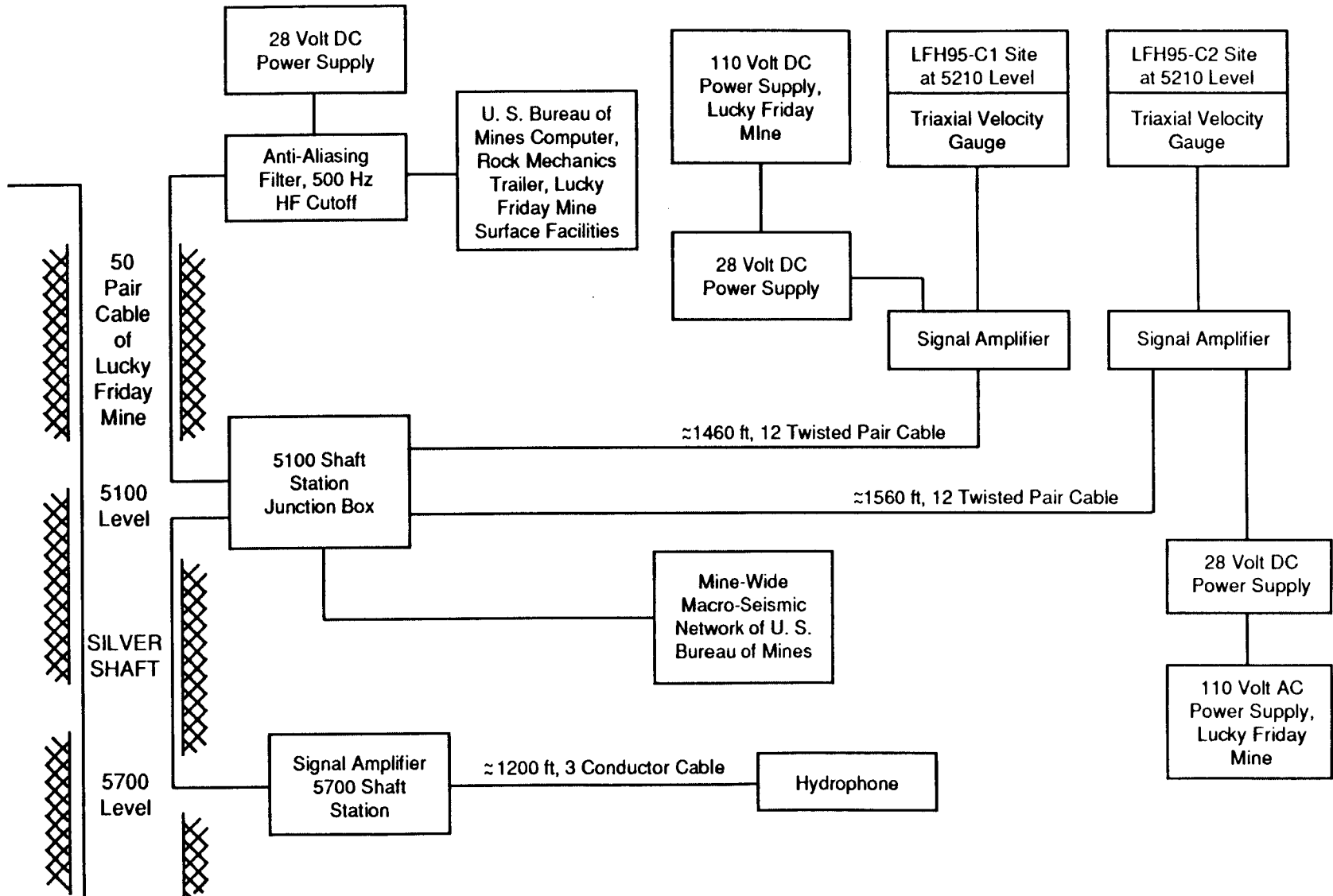


Figure 4-41. Schematic diagram of extensometer and piezometer data acquisition system

Figure 4-42. Schematic of seismic data acquisition system



assembly anchor is measured using a linear potentiometer with a maximum range of 2 inches. These extensometers provide measurements of relative movements along the borehole axis at approximately 5-foot intervals. Figure 4-43 presents one of the five-anchor extensometers.

Ten extensometers were calibrated one at a time through a data acquisition system to be used in the field (as shown schematically in Figure 4-41). Figure 4-44 displays the equipment used for data acquisition and extensometer calibration. The calibration was performed using a National Institute of Standards and Technology (NIST) traceable Do All Gage Block Set to provide known displacements. The glass-fiber measurement rods of an extensometer were released (disconnected) from the anchors and rigidly clamped into a circular plate at the head assembly end so that the five measurement rods could be calibrated as a unit through the programmed scanning of the datalogger. Gauge blocks with specified thickness were placed between the extensometer assembly head and the plate clamping device used to move the five measurement rods in unison. A total of ten measurements for each measurement rod were taken over a range of relative displacement of approximately 1.6 inches. The calibration was designed in such a way that measurements were taken in both directions with respect to the corresponding linear potentiometers.

After the calibration, data obtained for both gauge block and measurement rods were entered into a Lotus spreadsheet database and normalized against their initial readings. Linear regression analysis was then performed between the normalized gauge block and each measurement-rod data set. Table 4-17 presents the calibration data and regression results for a typical 5-anchor extensometer. These results indicated that, within the range of interest, all 50 linear potentiometers (five for each extensometer) show linear response with respect to rod displacement. The R-squared values are very close to 1.0 for all potentiometers, while the corresponding estimated intercepts (listed as "Constant" in the table) are very small for all potentiometers and, therefore, may be negligible. In general, the tangent of the slope (listed as "X coefficient" in the table) for all linear potentiometers ranges from 0.956 to 0.996. These X coefficients will be used as correction factors during actual data collection in the field. Figure 4-45 shows a typical calibration-curve plot.

#### **4.6.6.2. *Triaxial Velocity-Gauge Calibration***

The objective of the velocity-gauge calibration process was to define the voltage output of the velocity transducers in a defined frequency range for a known velocity input. The results of the calibration process were summarized as plots, and a table of the voltage level for the primary and cross-axis terms at defined frequencies were normalized to an input of 1.0 in./sec velocity.

The equipment used in the calibration process can be divided into several basic groups. The first consists of the electrodynamic shaker, associated power amplifier, and servo controller. The electrodynamic shaker has the capability of both vertical and horizontal excitation with a slip table. In this way, the orientation of the test item could be maintained with respect to installation in the field. The servo controller and amplifier are utilized to provide input to the shaker for the closed-loop control process. The servo controller provides the logarithmic swept sinusoidal signal to drive the shaker.

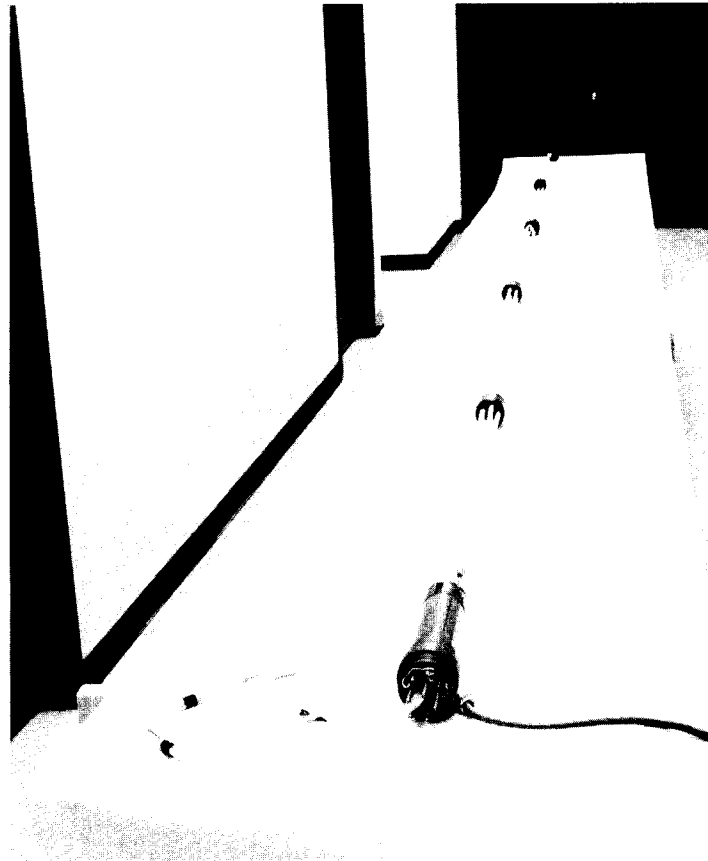


**Figure 4-43. Five-anchor extensometer**

The motion of the shaker was monitored using an accelerometer mounted in close proximity to the test item. For this testing, two accelerometers and associated amplifiers were used. The first was a reference standard accelerometer that is traceable to NIST. A second accelerometer was also used with extended low frequency and low-acceleration capabilities. This second accelerometer was first calibrated with respect to the standard accelerometer. Within the frequency and amplitude range of overlap of these two accelerometers, the resulting controls of velocity were identical.

Two triaxial velocity transducers, Electrolab Model 1130GS, were calibrated in the system, each with a matched amplifier as schematically shown in Figure 4-46. Cabling was set up to provide a gain of 10dB on the amplifier. The velocity transducer was attached to the shaker through an interface plate, V-blocks, and clamps. The orientation of the velocity transducer was set to match required installation procedures.

The final set of instrumentation was associated with data acquisition, analysis, and display (ZONIC 6088 FFT analyzer with display and printer). The frequency range of the analyzer was set to match the sweep range. The full-scale range and the engineering units per volt for each channel were set as required. The data type was set to "periodic"

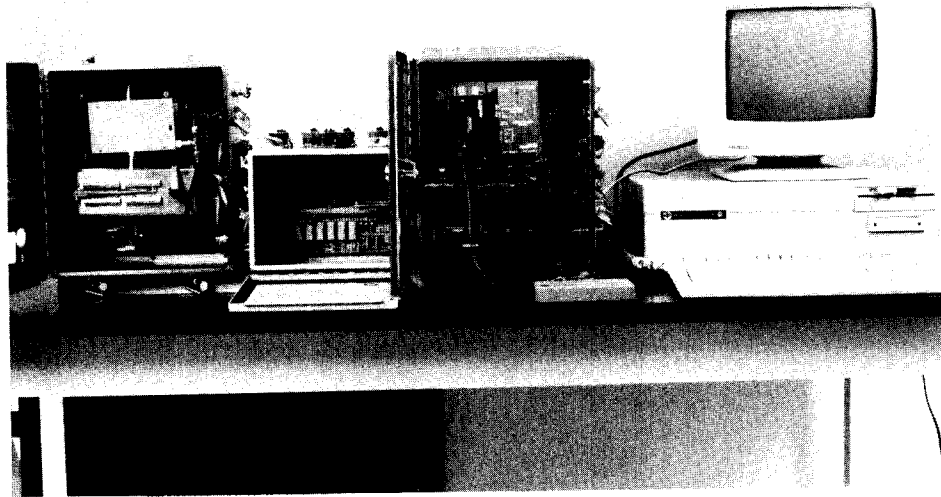


**Figure 4-44. Field data acquisition system**

with continuous sampling and no data overlap. The number of samples for a given test was a function of the sweep time and the cutoff frequency range of the analyzer.

The majority of the data is presented in the frequency domain, i.e., amplitude as a function of frequency. The frequency-domain data are presented in terms of a transfer function relating the output voltage to a constant-amplitude sine-wave signal. For a logarithmic swept signal, a transfer function must be used to obtain a flat output for a constant-level input because of the number of samples in each frequency interval. The level of the constant-amplitude sine-wave was set such that the transfer function gave results in terms of volts for a velocity level of 1 inch per second.

Plots were obtained for the voltage output of the velocity transducer in the direction of excitation and the two cross-axis terms (Figure 4-47). In addition, tables were obtained for the voltage levels for primary axis as a function of frequency. Limited time-history output was provided to obtain some indication of the shape of the voltage output of the velocity transducer in relation to the input acceleration.

**Table 4-17. EXTENSOMETER CALIBRATION DATA CHART FOR MPBX No. B**  
(all units are in inches)

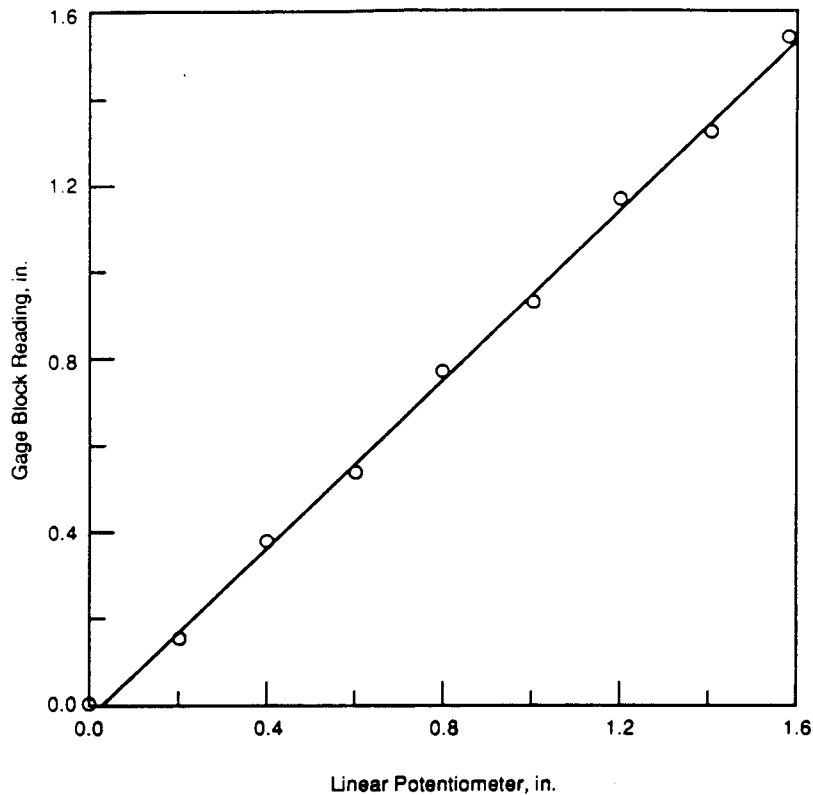
Gauge Block	Pos#1		Pos#2		Pos#3		Pos#4		Pos#5		
	Readout	Norm									
2.385	0.000	0.21	0.000	0.185	0.000	0.183	0.000	0.172	0.000	0.192	0.00
2	0.385	0.589	0.379	0.562	0.377	0.561	0.378	0.549	0.377	0.569	0.377
1.6	0.785	0.985	0.775	0.957	0.772	0.959	0.776	0.943	0.771	0.963	0.771
1.2	1.185	1.37	1.16	1.34	1.155	1.34	1.157	1.33	1.158	1.35	1.158
0.8	1.585	1.76	1.55	1.73	1.545	1.74	1.557	1.72	1.548	1.74	1.548
1	1.385	1.57	1.36	1.54	1.355	1.54	1.357	1.53	1.358	1.55	1.358
1.4	0.985	1.18	0.97	1.15	0.965	1.15	0.967	1.14	0.968	1.16	0.968
1.8	0.385	0.796	0.586	0.768	0.583	0.77	0.587	0.753	0.581	0.773	0.581
2.2	0.185	0.389	0.179	0.362	0.177	0.361	0.178	0.349	0.177	0.370	0.178
2.385	0.00	0.21	0.00	0.185	0.00	0.181	-0.002	0.171	-0.001	0.191	-0.001

<u>Regression Output for Pos#1</u>		<u>Regression Output for Pos#2</u>		<u>Regression Output for Pos#3</u>	
Constant	0.003108	Constant	0.002208	Constant	0.001958
Std Err of Y Est	0.005267	Std Err of Y Est	0.00512	Std Err of Y Est	0.005863
R Squared	0.999915	R Squared	0.999919	R Squared	0.999895
# of Observations	9	# of Observations	9	# of Observations	9
Degrees of Freedom	7	Degrees of Freedom	7	Degrees of Freedom	7
X Coefficient(s)	0.978959	X Coefficient(s)	0.975866	X Coefficient(s)	0.980138
Std Err of Coef.	0.003417	Std Err of Coef.	0.003321	Std Err of Coef.	0.003804

<u>Regression Output for Pos#4</u>		<u>Regression Output for Pos#5</u>	
Constant	0.001094	Constant	0.001404
Std Err of Y Est	0.004184	Std Err of Y Est	0.004018
R Squared	0.999946	R Squared	0.999995
# of Observations	9	# of Observations	9
Degrees of Freedom	7	Degrees of Freedom	7
X Coefficient(s)	0.978553	X Coefficient(s)	0.978299
Std Err of Coef.	0.002714	Std Err of Coef.	0.002607



**Figure 4-45. Extensometer calibration curve for MPBX No. B, position 3**

The final calibration gave similar results for the primary sensitivity axis for each transducer. The voltage output is not constant for a constant velocity input throughout the entire frequency range, nominally 2 to 500 Hz (Figure 4-47). Because of the design of the transducer, a low frequency roll-off occurs below 20 Hz. In the high-frequency range, roll-off caused by the filters is evident. Between the high- and low-frequency roll-off points, the output voltage is fairly constant.

The transducer has a cross-axis response; but in most cases, it is an order of magnitude below the primary axis response and can be ignored.

#### **4.6.6.3. Vibrating-Wire Piezometer Calibration**

Four Geokon Model 4500H vibrating-wire transducers were calibrated using an NIST-traceable Ashcraft Dead Weight Tester. A Geokon GK-401 readout box was used to provide the excitation to vibrate the wire in the piezometer and readout display. The displaced value is in the unit of  $f^2 \times 10^{-3}$  where  $f$  is frequency. Each piezometer was calibrated individually, with the pressure being increased from zero to 500 psi at a 100-psi interval and then decreased in similar fashion to zero. The cycle was repeated twice for each piezometer.

Calibration data were recorded and entered into a Lotus spreadsheet. The changes for the piezometer readings with respect to the initial reading for each piezometer were calculated and listed under the column "Norm" in Table 4-18. A linear-regression analysis was performed for the applied pressure and normalized piezometer readout. The regression

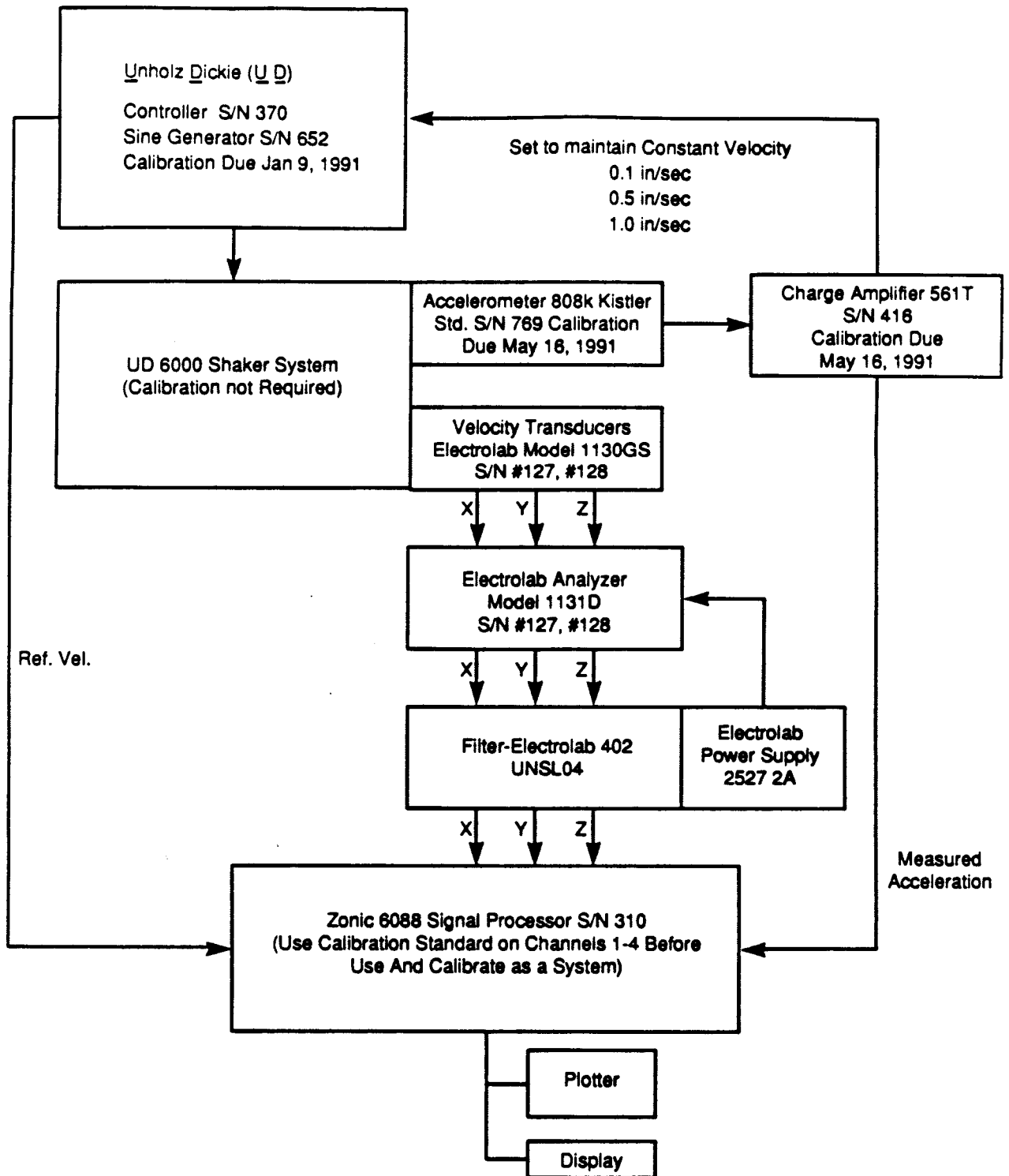


Figure 4-46. Calibration of electrolab triaxial velocity transducers

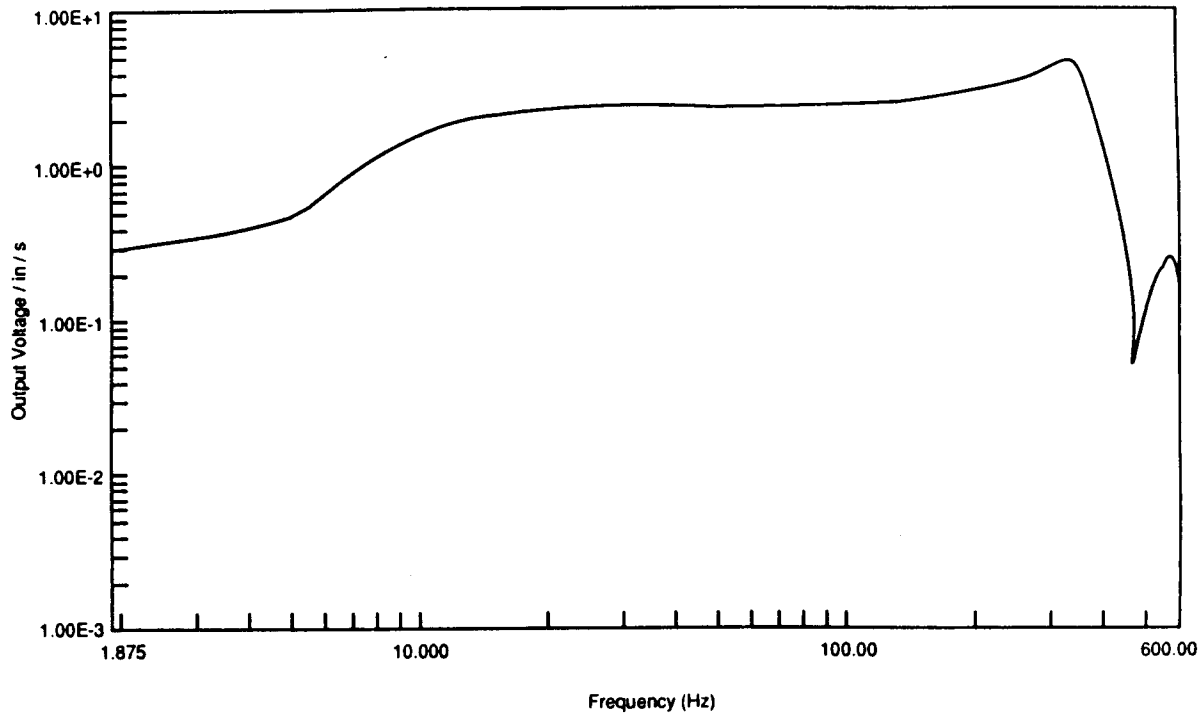


Figure 4-47. Output voltage in the principal excitation direction (X-axis for this plot) vs. frequency

results of all four piezometers indicated that they all behaved linearly (with  $R^2$  value practically equal to one) to pressure changes in the range of interest, that is from 0 to 500 psi. The estimated y-intercepts are small and negligible. Table 4-18 presents regression results for Piezometer Serial No. 12785. The regression results are in close agreement with manufacturer-provided results. The calibration factors (X coefficient as shown in Table 4-18) for all piezometers and those provided by the manufacturer are listed and compared (Table 4-19).

The calibration factors from the regression analysis will be used for hydrologic pressure determination in the field study.

#### 4.6.7. Discussion and Summary

Little data has been found available on subsurface motion generated from natural earthquakes for the study of rock mechanical and geohydrologic responses. Quantitative accumulation of these types of data is not likely in the foreseeable future, since occurrence of earthquakes is not yet predictable. In order to obtain a better understanding of the dynamic responses of underground structure and associated geohydrology, study of mining-induced seismic activities offers an attractive alternative.

**Table 4-18. TRANSDUCER SERIAL  
NO. 12785 READING CHART**

Applied Pressure	Piezometer	
	Readings	Norm
0	9468	0
100	8669	799
200	7835	1633
300	7013	2455
400	6189	3279
500	5336	4132
400	6174	3294
300	7000	2468
200	7820	1648
100	8635	833
0	9437	31
100	8637	831
200	7823	1645
300	7002	2466
400	6177	3291
500	5337	4131
400	6175	3293
300	6999	2469
200	7820	1648
100	8636	832
0	9439	29
Regression Output:		
Constant		-0.79433
Std Err of Y Est		1.635372
R Squared		0.9999
No of		21.0
Observations		
Degrees of		19.0
Freedom		
X Coefficient(s)		0.121743
Std Err of Coef		0.000279

**Table 4-19. COMPARISON OF CALIBRATION FACTORS**

Piezometer No.	Calibration Factors*		
	Regression Results	Manufacturer Supply	Difference (%)
12783	0.12543	0.12564	0.17
12784	0.12317	0.12331	0.11
12785	0.12174	0.12212	0.31
12786	0.12795	0.12779	0.13

\* Unit for the calibration factors is psi/digit

The ultimate objective of this field study program is to obtain a complete data set for evaluating the performance of computer codes in simulating seismic activities. The information needed in this data set include mine-wide geologic structure, rock-mass and joint properties, mining history, source location and velocity spectra of relevant seismic events, and the corresponding structural and hydrologic responses.

The Lucky Friday Mine was selected for the field investigation because the region is geologically well characterized, the mine is seismically active often with large magnitude events, and a mine-wide macroseismic monitoring system is in operation.

The field instrumentation implemented in the mine includes two sites for excavation response monitoring and one site for hydrologic response monitoring. They are all located below the current workings. Sufficient information should be able to be gathered as the mining proceeds toward and eventually passes by the instrumentation sites. The installation of instruments for the study of mechanical response was completed, and data collection has started.

#### **4.7. SUMMARY**

Activities carried out for the Seismic Rock Mechanics Project during this year included computer-code qualification studies, pretest analysis for rock-joint dynamic test, laboratory test-apparatus development, sample collection and preparation, pseudostatic rock-joint shear tests, testing of cylindrical specimens for tuff material characterization, development of rock-joint profile-measurement capability, Nevada Test Site (NTS) data collection on ground-shock excitation, calibration of field instruments used at the Lucky Friday Mine, and instrumented field studies.

Among the six identified computer codes, qualification studies on the UDEC and HONDO II codes against four benchmark analytical problems were exercised. Results indicate

that UDEC performs valid simulations of jointed rock, to the extent that the mechanics of these media may be represented by the conceptual models expressed in the problems, while HONDO II has a limited capability.

Three of the four benchmark analytical problems were analyzed for the qualification study on the 3DEC computer code. Results indicate that 3DEC provides satisfactory correspondence with the conceptual models expressed in the three benchmark problems. The results also indicate that the effect of the nonreflecting boundary condition as implemented in the 3DEC for dynamic analysis depends on the size of the domain used in the analysis. Qualification study on the 3DEC against the fourth benchmark problem is near completion.

Pretest analysis was performed to provide guidance to assist in evaluating the effects of shear test apparatus on dynamic response of the tuff-joint specimen. A series of numerical calculations were performed with the 3DEC code to simulate the shear-test apparatus and the dynamic shear test of a naturally jointed tuff specimen. The results of the calculations for the typical range of frequencies of earthquake loadings (i.e., less than 50 Hz) showed that the response of the shear-test apparatus, given the assumed properties, did not influence joint response significantly.

A dynamic direct shear-test apparatus was developed, which includes a 90,000-lb vertical and 50,000-lb horizontal loading capacity and is designed to house a specimen with maximum size of 12 x 8 x 4 inches for the lower specimen and 8 x 8 x 4 inches for the upper specimen. Demonstration tests of the apparatus indicates that it is capable of accomplishing the objectives of the Seismic Rock Mechanics Project.

Sample collection at the Apache Leap site in Arizona was successfully performed. A total of 50 potentially usable joint specimens were collected. Forty-three direct shear joint specimens were prepared during this year. Tests were conducted on 45 uniaxial compression specimens, 25 triaxial compression specimens, and 68 Brazilian disk tension specimens. The average uniaxial compressive strength was found to be 23,255 psi. The average triaxial compressive strengths are 29,225 psi with a confining pressure of 500 psi, 34,944 psi with a confining pressure of 1,000 psi, and 40,720 psi with a confining pressure of 1,500 psi. Typical values for Young's modulus and Poisson's ratio of the Apache Leap tuff are  $5.4 \times 10^6$  psi and 0.2, respectively.

Development and assemblage were completed of a rock profilometer for measurement of rock-joint surfaces. The measured profile data will be processed to calculate the corresponding joint-roughness coefficient to be used for analyzing the Barton-Bandis rock-joint model.

Vast amounts of data on ground motion under impulsive loading have been generated in the course of underground nuclear explosions at the NTS and during other field tests related to weapons performance. Five field test cases for which some of the most complete data sets have been collected were selected, and data were summarized. A database has been constructed that contains test information and results regarding the five tests. A separate report regarding this topic was prepared.

The Lucky Friday Mine at Mullan, Idaho, was selected for the instrumented field studies on mechanical and geohydrologic responses to seismic activities. Installation of a field instrumentation network to monitor the short- and long-term response of excavations to repeated seismic events as a result of seismic loading was completed. Data collection is underway. This instrumentation network is coupled with the mine-wide, macroseismic network of the U.S. Bureau of Mines. Drilling of an NQ borehole for the study of water-pressure change as a result of rockburst is near completion. Installation of packers and piezometers will begin early next year.

#### 4.8. REFERENCES

- Banerjee, P. K., and S. Ahmad. 1985. Advanced three-dimensional dynamic analysis by boundary element methods. *Advanced Topics in Boundary Element Analysis*. Cruse, T. A., et al., eds. New York: American Society of Mechanical Engineers (ASME) 72:65-81.
- Barton, N., S. Bandis, and K. Bakhtar. 1985. Strength, deformation and conductivity coupling of rock-joints. *Int. J. Rock Mech. Min. & Geomech. Abstr.* 22: 121-140.
- Bedsun, D.A., B.L. Ristvet, and E.L. Tremba. 1985. *Summary and Evaluation of Techniques to Predict Driven and Triggered Block Motion: A State -of-the-Art Assessment*. S-Cubed Final Report to DNA, S-Cubed 850-7135, DNA Contract 001-84-C-0126.
- Bedsun, D.A., B.L. Ristvet, and E.L. Tremba. 1987. *A Summary of Observations of Block Motion for Explosive Events in Rock*, S-Cubed Technical Report to Defense Nuclear Agency (DNA), DNA-TR-87-227. Washington, D.C.: DNA.
- Brown, E.T., and J.A. Hudson. 1974. Fatigue failure characteristics of some models of jointed rock. *Earthquake Eng. and Struct. Dyn.* 2: 379-386.
- Brady, B. H. G., and E. T. Brown. 1985. *Rock Mechanics for Underground Mining*. London: George Allen and Unwin:527.
- Brady, B. H. G., M. L. Cramer, and R. D. Hart. 1985. Preliminary analysis of a loading test on a large basalt block. Technical Note. *Int. J. Rock Mech. Min. Sci. & Geomech. Abstr.* 22:345-348.
- Brady, B. H. G., S. M. Hsiung, and A. H. Chowdhury. 1990. *Qualification Studies on the Distinct Element Code UDEC Against Some Benchmark Analytical Problems*. NRC Contract NRC-02-88-005. CNWRA 90-004. San Antonio, Texas: Center for Nuclear Waste Regulatory Analyses (CNWRA):1-148.
- Brandshaug, T., B. Dasgupta, B. H. G. Brady, S. M. Hsiung, and A. H. Chowdhury. 1990. *Qualification Studies on the Finite Element Code HONDO II Against Some Benchmark Analytical Problems*. NRC Contract NRC-02-88-005. CNWRA 90-006. San Antonio, Texas: CNWRA:1-39.

- Cooper, H. F. Jr., F. Henry, and S.E. Blouin. 1971. Dynamic in situ rock properties from buried high explosive arrays. *Proceedings 12th Sym. on Rock Mechanics*. Rolla, Missouri: University of Missouri, Rolla: 45-70.
- Cundall, P. A. 1988. Formulation of a three-dimensional distinct element model: Part I - A scheme to detect and represent contacts in a system composed of many polyhedral blocks. *Int. J. Rock Mech. Min. Sci. & Geomech. Abst.* 25(3): 107-116.
- Cundall, P. A., and J. V. Lemos. 1988. Numerical simulation of fault instabilities with the continuously-yielding joint model. *Proceedings 2nd International Symposium on Rockbursts and Seismicity in Mines*. Mineapolis, Minnesota: University of Minnesota.
- Daemen, J. J. K. 1990. *Quality Assurance Program for Mechanical Characterization of Tuff, the CNWRA*. Tucson, Arizona: Department of Mining and Geological Engineering, University of Arizona.
- Day, S. M. 1985. Test problem for plane strain block motion code. S-Cubed, Inc., Memorandum to Itasca, Inc., Minneapolis, Minnesota.
- Dietrich, J. H. 1981. *Constitutive Properties of Faults with Simulated Gouge*.
- DOE. 1988. *Site Characterization Plan, Consultation Draft*. Vol III DOE/RW-0160. Washington, D.C.: DOE.
- Ellis, W.L., and J.E. Magner. 1980. *Compilation of Results of Three-Dimensional Stress Determinations Made in Rainier and Aqueduct Mesas, Nevada Test Site, Nevada*. U. S. G. S., USGS Open-File Report 80-1098. Reston, Virginia: Geological Survey.
- Goodman, R.E. 1976. *Methods of Geological Engineering in Discontinuous Rock*. St. Paul, Minnesota: West Publishing.
- Jenkins, F. M., T. J. Williams, and C. J. Wideman. 1990. Rock burst mechanism studies at the Lucky Friday Mine. *Proc. of the 31st U.S. Symp.* Golden, Colorado: Colorado School of Mines: 955-962.
- Kana, D. D., B. H. G. Brady, B. W. Vanzant, and P. K. Nair. 1989. *Critical Assessment of Seismic and Geomechanics Literature Related to a High-Level Nuclear Waste Underground Repository*. CNWRA 90-001:150. San Antonio, Texas: CNWRA.
- Kana, D. D., D. C. Scheidt, B. H. G. Brady, A. H. Chowdhury, S. M. Hsiung, and B. W. Vanzant. 1990. *Development of a Rock-Joint Dynamic Shear Test Apparatus*. NRC Contract NRC-02-88-005. CNWRA 90-005. San Antonio, Texas: CNWRA:1-27.

- Key, S. W. 1986. A data structure for three-dimensional sliding interface. Sponsored by the International Society for Computational Methods on Boundary Elements. Held in Tokyo, Japan: 1-29.
- MacDougall, H. R., L. W. Scully, and J. R. Tillerson (compilers). 1987. *Site Characterization Plan Conceptual Design Report*. Sandia National Laboratories (SAND). SAND 84-2641. Albuquerque, New Mexico: SAND.
- McGarr, A. 1984. Scaling of ground motion parameters, state of stress, and total depth. *J. Geophys. Res.* 89(B8):6969-6979.
- Miller, P. K. 1978. The effects of boundary friction on the propagation of elastic waves. *Bull. Seis. Soc. America* 68:987-998.
- Olsson, W. A. 1982. Experiments on a slipping crack. *Geophys. Res. Letters* 9(8):797-800.
- Salvado, C., and J. B. Minster. 1980. Slipping interfaces: A possible source of radiation from explosive sources. *Bull. Seis. Soc. America* 70:659-670.
- Saucier, K.L. 1969. Properties of Cedar City tonalite. *U.W. Army Engineer Waterways Experiment Station, Corps of Engineers (USCE), Miscellaneous Paper C-69-9*. Washington, D. C.: USCE.
- Tinucci, J.P. 1990. *Field Test Database on Ground Shock Excitation*. Draft Report Prepared for CNWRA. San Antonio, Texas: CNWRA.
- Unruh, J.F. 1982. *Digital Control of a Shaker to a Specified Shock Spectrum*. 52nd Shock and Vibration Bulletin. Part 3. Washington, D. C.: Naval Research Laboratory: 1-9.
- Williams, J. R., G. Hocking, and G. G. W. Mustoe. 1985. The theoretical basis of the discrete element method. *Proceedings of the International Conference on Advances in the Numerical Mathematics in Engineering*. United Kingdom: University of Swansea:897-906.
- White, B. G., and D. Winston. 1977. The Revett-St. Regis "transition zone" near the Bunker Hill Mine, Coeur d'Alene District, Idaho. *Soc. of Economic Geologists' Coeur d'Alene Field Conference*. Golden, Colorado: Society of Economic Geologists pp. 25-30.

## 5. INTEGRATED WASTE PACKAGE EXPERIMENTS

*by Gustavo Cragnolino and Narasi Sridhar*

*Investigators: Gustavo Cragnolino (CNWRA) and Narasi Sridhar (CNWRA)*

### 5.1 TECHNICAL OBJECTIVES

The overall technical objectives of the Integrated Waste Package Experiments (IWPE) Project are to:

- (1) Develop a good understanding of the information currently available on metal corrosion and on other metal degradation processes.
- (2) Assess the current status of Yucca Mountain Project (YMP) Waste Package Programs.
- (3) Conduct waste package experiments to scope and study the key parameters affecting long-term material performance.
- (4) Assess experimentally YMP selected waste package materials and designs and provide independent evaluation for reasonable assurance of long-term performance.
- (5) Facilitate a continuous technical integration support to NRC and the Center for Nuclear Waste Regulatory Analyses (CNWRA) in the area of waste-package performance.

The objectives of the IWPE are planned to be accomplished under the following tasks which are consistent with Revision 2 of the program plan:

- (1) Task 1 - Corrosion, including Localized Corrosion, Uniform Corrosion, and Internal Corrosion
- (2) Task 2 - Stress Corrosion Cracking
- (3) Task 3 - Materials Stability
- (4) Task 4 - Microbiologically Influenced Corrosion
- (5) Task 5 - Other Degradation Modes
- (6) Task 6 - Periodic Reporting

The current report follows the task classification just given with a focus on Task 1. Literature reviews have been performed in Tasks 2, 3, and 4. Experimental programs will be initiated in Tasks 2 and 3 during the next reporting period. Studies on hydrogen absorption and embrittlement, conducted under Task 5, are ongoing at The Ohio State University and will be the subject of a topical report to be issued in FY91. The information contained in this report is essentially a summary of previous quarterly research reports which, however, followed the task classification adopted in Revision 1 of the IWPE Project Plan. During the periods covered by these quarterly reports, Revision 2 of the IWPE Plan was submitted to the NRC and was approved in October 1990. Revision 3 of the Plan, which incorporates the suggestions of NRC staff, was submitted to the NRC in December 1990 and currently is being reviewed.

## **5.2 CORROSION OF CONTAINER MATERIALS**

The activities and salient results in four subtasks within Task 1 are described in this report. These subtasks are:

- Task 1.1.1: Review of experimental results from other programs related to localized corrosion
- Task 1.1.2: Characterization of materials in the initial condition
- Task 1.1.3a: Pitting variability studies
- Task 1.1.3b: Full factorial tests

### **5.2.1 Review of Experimental Results Related to Localized Corrosion**

During this reporting period, a critical review of the experimental results obtained by other laboratories involved in the study of HLW container materials was initiated. The emphasis was placed on the candidate Fe-Cr-Ni alloys, since our own experimental program on Cu-based alloys has not yet been initiated.

Electrochemical studies of localized corrosion reported by Lawrence Livermore National Laboratory (LLNL) were conducted by Glass et al. (1984) and reviewed recently by McCright et al. (1987). Potentiodynamic polarization curves were obtained at a potential sweep rate of 1 mV/s to study the anodic behavior of AISI 304L and 316L stainless steels and Alloy 825 in tuff-conditioned J-13 well water (Table 5-1) at temperatures ranging from 50 to 90°C. For the three alloys, relatively high pitting-potential values were reported ( $> 700$  millivolts vs. Saturated Calomel Electrode [ $mV_{SCE}$ ]); and no significant hysteresis was noted in the reverse potential scan, resulting in very small differences between pitting and repassivation potentials. In addition, a very slight dependence of the pitting and repassivation potentials with temperature was noted for the three alloys within the 50 to 90°C range. All these observations indicate that the breakdown observed in the potential-current density curves at high anodic potentials was the result of oxygen evolution, and it cannot be attributed to pit initiation. Corrosion potentials

ranging from -200 to -100 mV<sub>SCE</sub> were measured on the three alloys in air-saturated J-13 well water. No noticeable effect of temperature on the corrosion potentials was observed.

Of the three Fe-Cr-Ni alloys, AISI 304L stainless steel was the single material in which the effect of higher chloride concentrations was studied (Glass, 1984). A significant decrease in the pitting potential ( $E_p$ ) was observed when NaCl at concentrations higher than 25 ppm was added to tuff-conditioned J-13 well water (which already had about 6 ppm chloride) at 90°C. For example, by increasing the added NaCl concentration from 25 to 50 ppm, the pitting potential decreased from 730 to 220 mV<sub>SCE</sub>. At even higher concentrations (10,000 and 30,000 ppm),  $E_p$  decreased to values that were very close to the corrosion potential (-100 to -200 mV<sub>SCE</sub>), confirming the occurrence of pitting corrosion at high chloride concentrations. However, no significant effect of temperature on  $E_p$  was noted within the 50 to 90°C range, even in the presence of 1000 ppm NaCl, conditions in which  $E_p$  values around 150 mV<sub>SCE</sub> were measured. Within that temperature range, the repassivation potential ( $E_{rp}$ ) decreased from -140 to -220 mV<sub>SCE</sub> with increasing temperature. The corrosion potentials were found to be very close to the  $E_{rp}$  values at temperatures equal to and greater than 70°C. No visual observation of pitting corrosion was reported; but it is apparent that in J-13 well water containing NaCl at concentrations greater than 50 ppm, pitting corrosion occurred as indicated by the measurement of relatively low pitting potentials. As noted above, no data were reported for the other candidate alloys at chloride concentrations higher than those present in the J-13 well water.

It should be emphasized that an adequate characterization of the environment expected at the tuff repository and, in particular, of its evolution with time, does not exist. A complete description of the environment, in terms of such variables as water chemistry, pH,  $E_h$ , and trapped and dissolved gases, is not yet available. Most of the corrosion studies have been carried out using natural or simulated J-13 well water, solutions concentrated by evaporation from J-13 well water, or solutions based on J-13 water containing increasing concentrations of aggressive species (e.g., 1000X in Cl<sup>-</sup> concentration). It should be noted that J-13 is a well in the proximity of the proposed Yucca Mountain repository site, but by no means can it be conceived that the chemical composition of its water is representative of the unsaturated zone in the planned repository. In addition, no consideration was given in the LLNL work to possible alterations of the water chemistry as noted above.

The experimental work conducted by Cortest Columbus Technologies under NRC sponsorship has been published in six reports (Beavers, 1988a, 1988b, 1989a, 1989b, 1990a, 1990b). In addition to these reports, Cortest prepared a review of the literature relevant to the tuff repository (Beavers, 1990c). The initial experimental results from this project have also been published as a paper (Beavers, 1990d).

The purpose of the Cortest experimental work on cyclic potentiodynamic polarization (CPP) was to examine the effects of environmental and metallurgical variables on the electrochemical behavior of candidate container materials. Using this method, the pitting and repassivation potentials as well as the corrosion and passive currents were determined. The corrosion potential was measured initially, before the potential scan was started and after the

**Table 5-1. CHEMICAL COMPOSITION RANGES OF J-13  
WELLWATER (GLASSLEY, 1990)**

Species	mmoles/liter	mg/liter
Li <sup>+</sup>	0.006 - 0.024	0.04 - 0.17
Na <sup>+</sup>	1.83 - 2.17	42 - 50
K <sup>+</sup>	0.10 - 0.17	3.7 - 6.6
Mg <sup>2+</sup>	0.07 - 0.10	1.7 - 2.5
Ca <sup>2+</sup>	0.29 - 0.37	11.5 - 15
Sr <sup>2+</sup>	0.0002 - 0.001	0.02 - 0.1
Fe <sup>3+</sup>	<0.0002 - 0.003	<0.01 - 0.16
Al <sup>3+</sup>	0.0003 - 0.004	0.008 - 0.11
Si(SiO <sub>2</sub> )	0.95 - 1.14	26.6 - 31.9
NO <sub>3</sub> <sup>-</sup>	0.113 - 0.168	6.8 - 10.1
F	0.029 - 0.135	1.7 - 2.7
Cl <sup>-</sup>	0.178 - 0.237	6.3 - 8.4
HCO <sub>3</sub>	1.93 - 2.34	118 - 143
SO <sub>4</sub> <sup>2-</sup>	0.177 - 0.219	17 - 21
pH		6.8 - 8.3

specimen was exposed to the solution overnight. A fractional factorial experimental matrix was used for the evaluation of the effect of many environmental variables including pH and temperature. This methodology was previously used for corrosion studies of various alloy/environment systems encountered in different industrial applications in which several dissolved species were known to affect the resistance to localized corrosion (Koch, 1988). It was also used to study the corrosion behavior of carbon steels in high-temperature groundwater for HLW packaging within the scope of the Basalt Waste Isolation Project (Thompson, 1990).

Four of the six materials initially selected by the Department of Energy (DOE) as candidate alloys for the YMP were used by Cortest. They were: AISI 304L stainless steel, Alloy 825, CDA 102 (Oxygen-Free Copper) and CDA 715 (Cu-30Ni).

The valuable aspect of the approach adopted by Cortest for the statistically designed experiment is the attempt to identify the role of the different anionic and cationic species that may accelerate or inhibit localized corrosion. However, the success of the approach depends heavily on the criteria used in the selection of the independent variables of interest and the dependent variables. Fifteen variables were chosen by selecting the concentration of thirteen different species in addition to pH and temperature. Nine of these species are present in J-13 well water; three species ( $\text{NO}_2^-$ ,  $\text{H}_2\text{O}_2$ , and oxalic acid) are considered to be formed by radiolysis, and the remaining one ( $\text{O}_2$ ) is present in the unsaturated zone from air and also is formed by radiolysis of water.

Several problems arise from this particular selection of species and concentration values studied. They are as follows:

- (1) The concentration of  $\text{HCO}_3^-$  is dependent on pH. This means, for example, that for an initial concentration of  $\text{HCO}_3^-$  equal to 2000 mg/l or 32 mmoles/l, the actual concentration will be significantly lower at pH 5 than at pH 10 since at the lowest pH,  $\text{HCO}_3^-$  has been mostly transformed in  $\text{CO}_2$  which has evolved from the solution. Therefore, the effect of  $\text{HCO}_3^-$  concentration on the dependent parameters cannot be assessed independently of the effect of pH.
- (2) The concentrations of Si and Al in solution are dependent on the concentration of  $\text{F}^-$ , which acts as a complexing agent. In the case of Al, which is added to the solution as Sulfate, the stable complex is  $\text{AlF}_6^-$ . The formation of this complex reduces the concentration of  $\text{Al}^{3+}$  well below the initial concentration, mainly when the  $\text{F}^-$  concentration is 200 mg/l, equivalent to 10.5 mmoles/l, and represents a concentration that is more than 10 times higher than the highest  $\text{Al}^{3+}$  concentration used in the test matrix [20 mg/l or 0.74 mmoles/l]. Si is added in the form of  $\text{SiO}_2 \cdot x\text{H}_2\text{O}$ , which is a relatively insoluble compound, but it can be converted to  $\text{SiF}_6^-$ . This is particularly true at the lowest concentration included in the test matrix, which is 0.035 mmoles/l. Even at the highest initial concentration, 3.5 mmoles/l, the concentration of noncomplexed Si is significantly reduced, making invalid the adoption of the initial concentration as representative of the particular environment.
- (3) Several species were included in the test matrix because they may be generated in the repository environment as a result of radiolysis. These species are  $\text{NO}_2^-$ ,  $\text{H}_2\text{O}_2$ ,  $\text{H}_2\text{C}_2\text{O}_4$  (oxalic acid), and also  $\text{O}_2$ , although  $\text{O}_2$  was also included as a consequence of the aerobic nature of the repository. The reasons for the inclusion of oxalic acid in favor of other organic species is not clear. Although it can be argued that, in the repository, the presence of organic compounds can be expected, by no means can it be assumed that oxalic acid is the prevailing species. Acetic acid is stable up

to 300°C, while oxalic decomposes above 150 to 170°C. The additional fact that oxalic acid is a good complexing agent for iron may complicate even further the interpretation of the results. Regarding the reducible/oxidizable species, these species interfere with the measurement of the true anodic behavior of the material because the current associated with their reduction or oxidation cannot be distinguished from that corresponding to metal dissolution or passivation. The ideal situation is to remove all the electrochemically active species that may participate in charge-transfer reactions at the metal surface (i.e., species such as oxygen and H<sub>2</sub>O<sub>2</sub>) and study the anodic behavior of such a surface by applying controlled potentials. The role of the radiolytically generated species should be studied under open-circuit conditions to interpret their effect on the redox potential of the environment and the corrosion potential of the metal. The role of anionic species, which are able to act as reducible species as well as inhibitors such as nitrate and nitrite, can be studied using potentiodynamic/potentiostatic methods. At neutral or slightly alkaline pH, the kinetics of their reduction is sufficiently slow; and, as a consequence, they do not interfere with the anodic response of the metallic electrode. Under such conditions, their behavior as inhibitors tends to predominate.

From the statistical analysis of the data, conducted with the Statistical Analysis System program (SAS Institute Cary, N.C.), the magnitude of the beneficial and detrimental effect of the environmental variables on the different electrochemical parameters was assessed in quantitative terms. It was found that for AISI 304L stainless steel, chloride promotes a significant decrease of pitting and repassivation potentials, whereas nitrate increases the value of both parameters. No other variable was found to have an effect on the repassivation potential. The pitting potential increases with pH and HCO<sub>3</sub><sup>-</sup> and decreases with temperature. However, as noted above, pH and HCO<sub>3</sub><sup>-</sup> are not independent variables. Nevertheless, all these observations are in qualitative agreement with the expected behavior of AISI 304 and 304L stainless steels on the basis of experimental results in less complex environments (Szklańska-Smiałowska, 1986; Sedriks, 1979). From a quantitative point of view, the correlations are relatively poor, since the adjusted R<sup>2</sup> values for E<sub>p</sub> and E<sub>rp</sub> were found to be 0.32 and 0.55, respectively.

For Alloy 825, the results are not easily explainable, since no anion including chloride was found to have a detrimental effect on pitting potential. In contrast, F<sup>-</sup> exhibited a beneficial effect by increasing that potential. Both Mg<sup>2+</sup> and H<sub>2</sub>O<sub>2</sub> decrease E<sub>p</sub> and E<sub>rp</sub>. E<sub>rp</sub> also decreases with pH and chloride concentration and increases with NO<sub>3</sub><sup>-</sup> and oxalic acid. From a quantitative point of view, the correlations are also relatively poor for Alloy 825, since the adjusted R<sup>2</sup> values for E<sub>p</sub> and E<sub>rp</sub> were found to be 0.19 and 0.47, respectively. As recognized by the authors (Beavers, 1990d), the very low R<sup>2</sup> value for E<sub>p</sub> seems to reflect the fact that the potentials measured, in this case, are not true pitting potentials but potentials corresponding to the oxidation of water to oxygen in agreement with the relatively high E<sub>p</sub> values.

The corrosion potential is the third parameter of interest to evaluate the tendency to localized corrosion of a given alloy in a particular environment. If the corrosion potential ( $E_c$ ) is higher than the pitting potential, the alloy is susceptible to pitting corrosion; and if it is lower than the pitting potential but higher than the repassivation potential, propagation of localized corrosion (crevice and/or pitting corrosion) may occur. For AISI 304L, it was found (Beavers et al., 1990a) that  $H_2O_2$ ,  $Ca^{2+}$ , and pH increase the corrosion potential, whereas Si,  $HCO_3^-$ ,  $F^-$ ,  $Cl^-$ ,  $Al^{3+}$ ,  $O_2$  and temperature decreased it. Although the effect of  $H_2O_2$  is understandable, the observation that  $O_2$  has the opposite effect is questionable. In the case of Alloy 825, the results seem to be more consistent with previous observations, since pH,  $H_2O_2$ , and  $O_2$  increase the corrosion potential and  $HCO_3^-$ ,  $F^-$ , and temperature decrease it. Also, the adjusted  $R^2$  values exhibited a better correlation for the corrosion potential than for the other electrochemical parameters. Values of 0.57 and 0.66 were calculated for AISI 304L stainless steel and Alloy 825, respectively.

Some of the problems and limitations associated with the lack of independence of some variables were recognized by the authors in a previous publication (Thompson, 1990). Despite the above mentioned criticisms, the approach used by Beavers and Thompson is an important attempt at defining the quantitative effects of relevant environmental variables on localized corrosion. By conducting studies in solutions containing anionic and cationic species found in J-13 well water, but covering a wide range of concentrations, they were able to identify regions of the environmental space where additional research is needed.

### **5.2.2 Characterization of Container Materials in the Initial Condition**

As a requirement for most of the tasks in the IWPE project, it is essential that the initial condition of the candidate container materials be characterized fully. This characterization will (1) result in a better understanding of differences in corrosion data among various laboratories, (2) ensure that testing is performed on sound materials, and (3) enable quantification of any microstructural changes due to long-time exposure to temperatures in the range of 200 - 300°C. The material-characterization project consists of optical metallography, SEM-EDX analysis of various microstructural features, and corrosion studies in standard solutions designed to test the intergranular corrosion susceptibility.

The chemical compositions of the specific heats of materials examined in this report are given in Table 5-2. These materials were obtained as 12.7 mm (0.5") plates and tested in the as-received conditions, that is, without any further thermomechanical treatments.

#### **5.2.2.1 Metallography**

The cross-sections of the plates were examined via optical metallography. The details of the microstructures were given in a previous report (CNWRA, 1990a). The principal findings are summarized as follows:

**Table 5-2. HEAT NUMBERS AND CHEMICAL COMPOSITIONS OF THE CANDIDATE  
CONTAINER MATERIALS IN THE IWPE PROGRAM**

Alloy	Heat No.	Composition (wt. percent)							
		Ni	Fe	Cr	Mo	W	Cu	Al	OtherC - 0.022
304L	T0954	9.14	Bal.	18.3	-	-	-	-	C - 0.01
316L	P80746	10.04	Bal.	16.4	2.1	-	0.3	-	C - 0.01
Incoloy <sup>(a)</sup> alloy	HH4371FC	41.1	30.4	22.1	3.2	-	1.8	-	Ti - 0.82
Hastelloy <sup>(b)</sup> alloy	8-3175	Bal.	3.8	21.4	13.6	3.0	-	-	C - 0.004
CDA - 102	6681	-	-	-	-	-	99.95	-	-
CDA - 613	M5459	-	2.5	-	-	-	90.54	6.65	-
CDA - 715	7037/6132a	29.6	0.5	-	-	-	69.1	-	C - 0.13

<sup>(a)</sup> - Incoloy is a registered trademark of Inco Alloys International

<sup>(b)</sup> - Hastelloy is a registered trademark of Haynes International, Inc.

- (1) The microstructures of AISI 304L and 316L stainless steels and Hastelloy alloy C-22 exhibited an equiaxed grain microstructure typical of solution annealed materials. Alloy 825 exhibited dual grain sizes with large grains surrounded by small grains. However, no grain-boundary precipitates were observed in this material.
- (2) The microstructures of the Cu-Ni alloy (CDA 715) and Cu-Al alloy (CDA 613) showed numerous dark particles within the matrix and a grain morphology typical of hot-worked material. The dark particles are iron-rich particles, since iron, which has a low solubility in copper, is an intentional alloying addition to these alloys. This was verified for CDA 613 by SEM-EDX analysis of the particles. An example of such an analysis is shown in Figure 5-1. Such inhomogeneities in chemical composition in these alloys may have an impact on localized corrosion. The microstructure of copper (CDA 102) appeared fully annealed. The microstructure of CDA 715 needs further analysis.

#### ***5.2.2.2 SEM-EDX Analysis of Surfaces and Bulk***

SEM-EDX analysis was performed specifically to identify compositional differences between the bulk and surface of Cr-containing materials. The analyses were performed on the mill-surface (as-descaled surface) and mid-section of the plates. The results of the complete analyses were given in a previous report (CNWRA, 1990a). The Cr analyses for surface and bulk are shown in Figure 5-2. Significant surface depletion of Cr can be seen for alloys 825 and C-22, but not for 304L and 316L stainless steels.

The origin of the depletion is speculative at this time. It is hypothesized that chromium depletion occurs during the annealing stage when the surface chromium is converted to an oxide resulting in Cr depletion below the surface. During the descaling operation (also called pickling operation) in the mill, the surface oxides are removed along with some of the Cr-depleted layer underneath (Covino, 1987). However, the extent of dissolution of the Cr-depleted layer will depend on the corrosion resistance of the particular alloy. In alloys 825 and C-22, containing high Cr and Mo, the depleted layer is not dissolved completely, resulting in a residual depleted layer in the final product. In AISI 304L and 316L stainless steels, the dissolution rate of the depleted layer is fast enough so that no vestige of this layer is present in the final product.

#### ***5.2.2.3 Corrosion Tests in Standard Solutions***

Corrosion tests in standard solutions were conducted: (1) to ensure that the starting conditions of the materials were appropriate, that is, the materials as-supplied were not sensitized, and (2) to determine if the variations in surface composition or microstructure

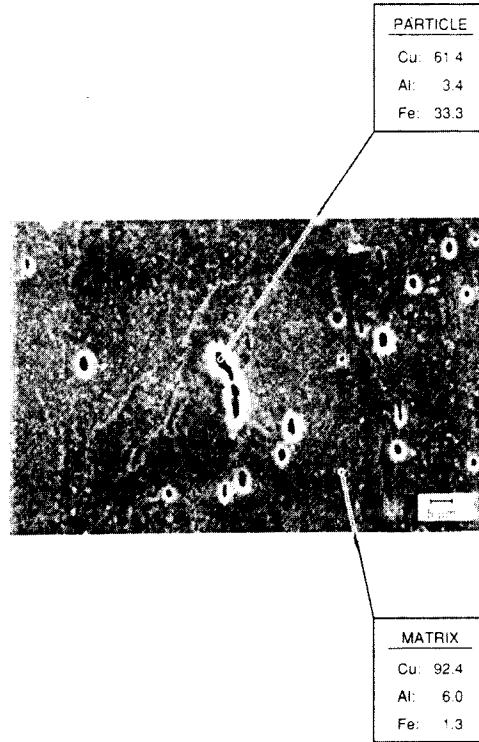


**Figure 5-1. SEM-EDX analysis of polished and etched CDA-613 alloy**

affected performance in standard tests. The test method chosen was ASTM A-262, Practice B for the stainless steels and ASTM G-28, Practice A for the Ni-base alloys (Alloys 825 and C-22). Both these tests involve immersing the samples in a boiling solution of 50-percent (wt.) sulfuric acid + 42 g/l ferric sulfate. The corrosion rate in this environment increases with a decrease in chromium content, so the test is sensitive to chromium depletion. In the case of AISI 304L and 316L stainless steels and Alloy 825, the immersion time was 120 hours. Alloy C-22 was tested for 24 hours. Weight-loss determinations were made at the end of the immersion period; and from the weight-loss values and measured sample areas, equivalent corrosion rates were determined. Duplicate samples were tested for each condition, and average corrosion rates are plotted in Figure 5-2. The corrosion rates of polished samples (which is the recommended method of testing in the ASTM standards) of all the alloys except Alloy 825 agree quite closely with published values in the literature (Streicher, 1958; Craig, 1989). The measured values for Alloy 825 are considerably lower than that of published values (Brown, 1969). This difference can be explained by the fact that the alloy's composition has been modified since 1969 and is currently melted with higher chromium and lower carbon than before. Since the ASTM G-28A test involves an oxidizing environment, the higher chromium content in the current alloy can be expected to result in lower corrosion rates.

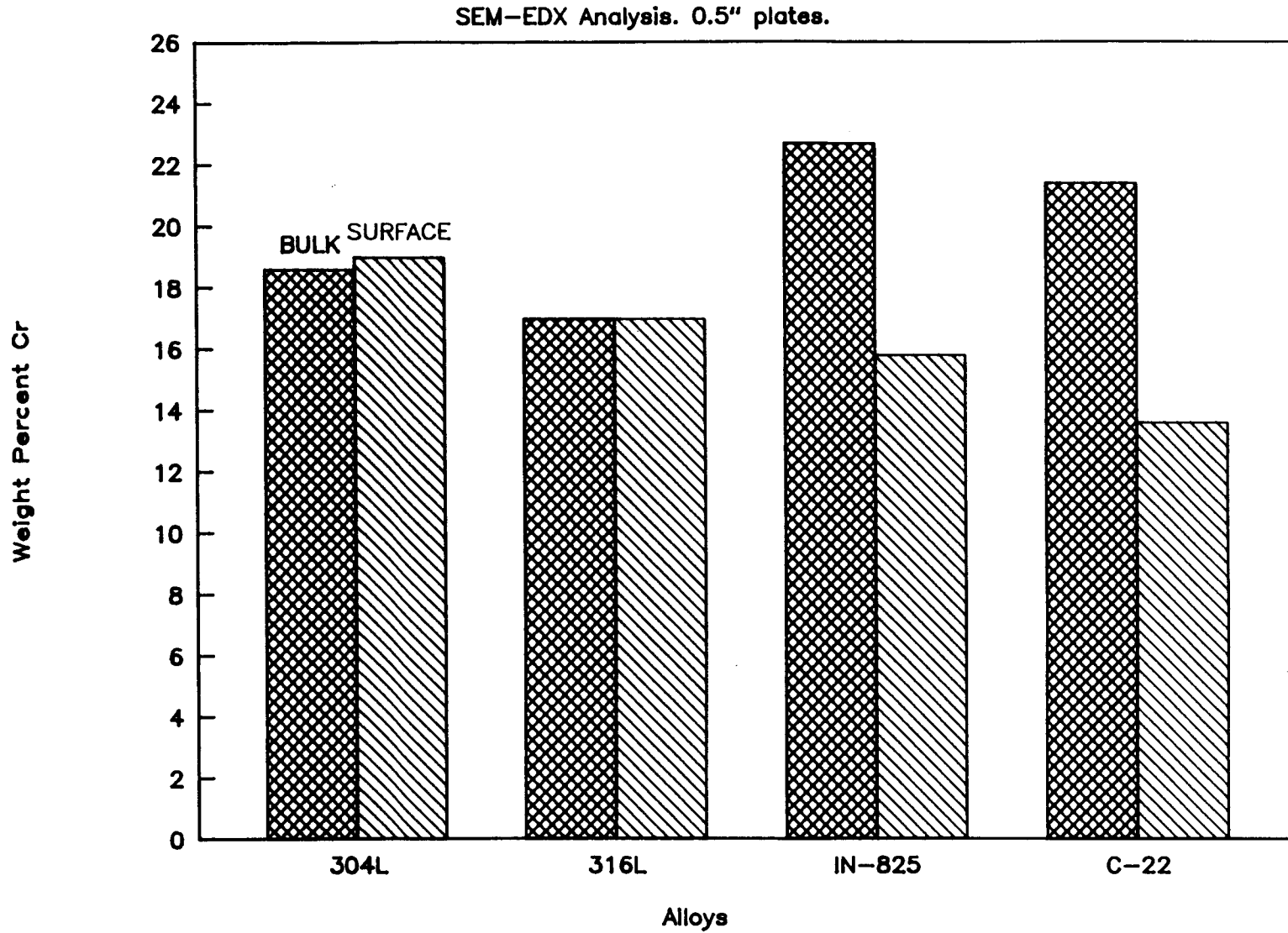


Figure 5-2. Surface Cr depletion

Figures 5-2 and 5-3 indicate that the samples of Alloys 825 and C-22 in the as-received surface condition exhibited higher corrosion rates than those with polished surfaces. These results corroborate the observed chromium depletion in the case of these two alloys (Figure 5-3). The differences between the two surface conditions for AISI 304L and 316L stainless steels are not as large, again in agreement with the lack of significant chromium depletion in these alloys. Polishing (to 120-grit finish) removes the depleted layer substantially and, hence, decreases the corrosion rate.

The significance of the surface Cr depletion may be in the comparison of laboratory test results with field test/performance results. In laboratory tests, the surface layer is machined off, so chromium depletion is generally not of concern. The surface composition is important in the actual field performance of the container material where the surface is not machined. This factor will be considered in future long-term localized corrosion and stress corrosion cracking studies. The current results may be used as the basis for future quality-control specifications.

### 5.2.3 Pitting Variability Tests on Alloy 825

Much of the testing reported in the literature concerning the localized corrosion behavior of this Alloy 825 in simulated J-13 water has been performed at two chloride levels, 6 and 1000 ppm. The response curve of this alloy, however, with respect to chloride concentration can only be deduced by performing tests at intermediate chloride levels. Additionally, since pitting is a stochastic process, it was of interest to determine the variability of the process at each chloride concentration. Cyclic, potentiodynamic polarization tests, therefore, were carried out on multiple samples of Alloy 825 in simulated J-13 water with a chloride level of 6 ppm and the same solution augmented in a chloride level to 20, 100, 200, 300, and 1000 ppm. The 6 ppm solution represents the chloride content of the natural J-13 water. The 20 ppm chloride solution represents the chloride content of the simulated J-13 solution prepared by the Battelle procedure. The chloride content of the pore water from unsaturated tuff has been shown to range from 34 to 105 ppm (Glassley, 1990). The CNWRA Technical Operating Procedure TOP-010 (CNWRA, 1990b) was used in the preparation of the solutions. Potassium chloride was used to enhance the chloride concentration where necessary.

**Test Techniques.** The specimen and cell configurations were similar to those described in ASTM G-5. Platinum gauze was used as the counter electrode. Saturated Calomel Electrode (SCE) was used as the reference electrode, along with a long salt-bridge with a Vycor tip so that the reference electrode was at ambient temperature. All potentials in this report will be referred to the SCE at room temperature. The correction for thermal liquid junction potential is estimated to be about 20 mV at 95°C and is not considered here. All tests were conducted using either a PAR 173/276 or a PAR 273 potentiostat with a PAR 342C software. In very low chloride environments, especially with the use of the PAR 273 potentiostat, a severe noise problem was encountered with the use of a salt bridge solution of the same composition as the test solution. In these cases, a higher concentration solution,

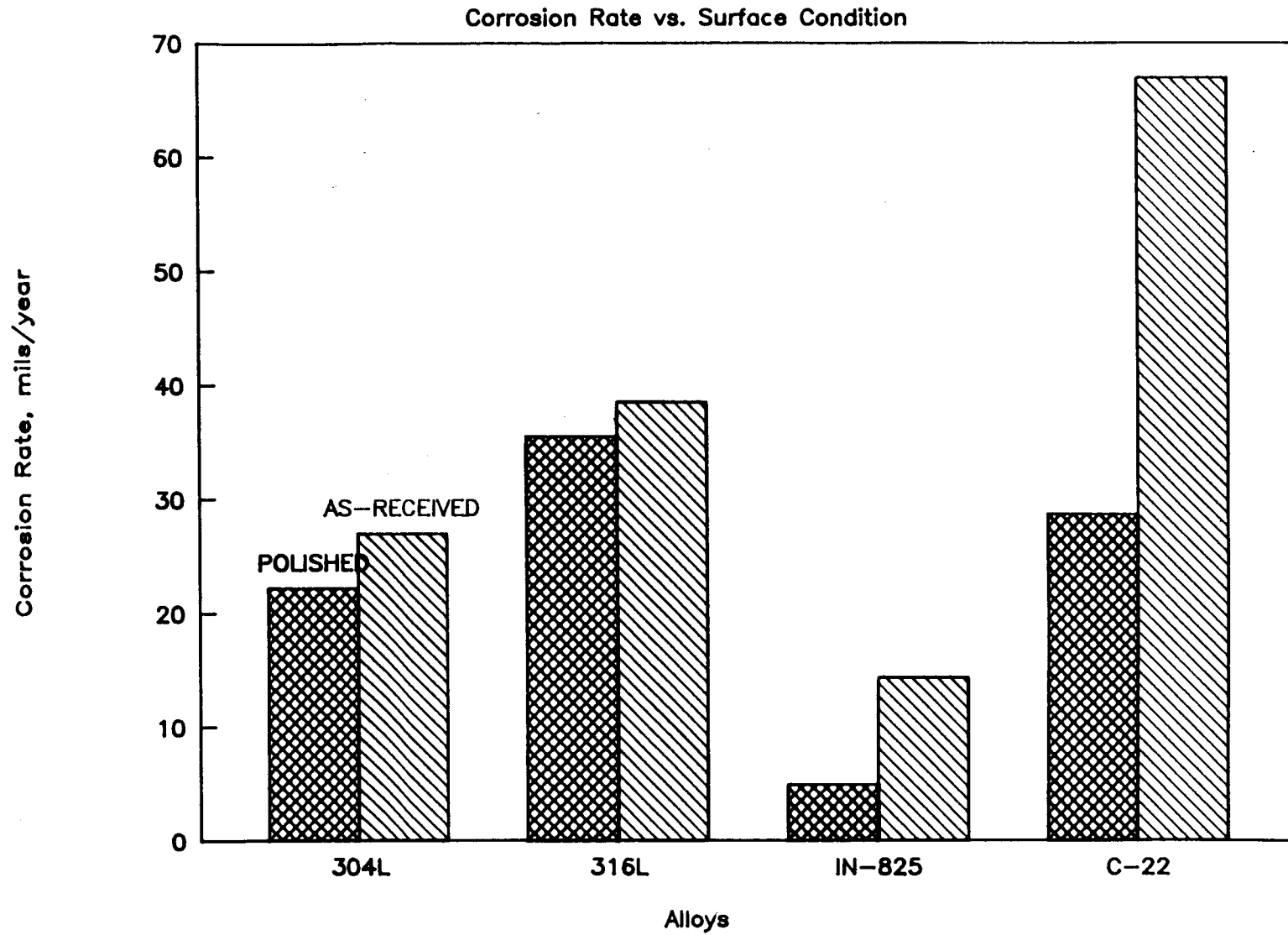


Figure 5-3. ASTM A-262 B test results

usually a 0.5N KCl solution, was employed to mitigate the noise. Following the test, the chloride content of the test solution was measured using an ion-selective electrode; and no change in chloride concentration was noted. An Allihn condenser with drip tip and an outlet trap helped minimize evaporative losses. The CNWRA's Technical Operating Procedure TOP-003 (CNWRA, 1989) was followed for preparing the samples, and TOP-008 (CNWRA, 1990c) was used for conducting the polarization tests. The procedure for conducting the cyclic polarization tests was similar to that given in ASTM G-61.

The results of cyclic polarization tests are shown in Table 5-3. An example of a polarization curve is shown in Figure 5-4. Several features are worthy of note in this figure. The corrosion potential is relatively low, which is indicative of deaerated conditions. The average value of the corrosion potential was  $-573 \text{ mV}_{\text{SCE}}$  with a standard deviation of 48.6 mV. The initial room-temperature pH was also quite reproducible with an average value of 8.24 and a standard deviation of 0.1. Following the initial passive region, a secondary anodic peak was observed at approximately 277 to 382  $\text{mV}_{\text{SCE}}$ . The peak potential was a function of ionic content (conductivity) but not a function of chloride level, since the peak was present even in a nonchloride environment. The peak has been observed in the case of Hastelloy alloy C-22 and AISI 304L and 316L stainless steels. Although various speculations exist regarding the cause of this peak, no particular mechanism has been established clearly. Because the common feature among all these alloys is the chromium content, the peak may be related to the oxidation of  $\text{Cr}^{3+}$  ( $\text{Cr}(\text{OH})_3 \cdot n\text{H}_2\text{O}$ ) to  $\text{Cr}^{6+}$  ( $\text{CrO}_4^{2-}$ ).

Following the peak, a rapid increase in current density was noted above a potential termed as pitting potential ( $E_p$ ). The term pitting potential can be misleading in some cases, as no pitting was observed in some environments when the sample was examined visually (at 40X magnification) after the test. In the cases where no pitting was observed, this potential must be considered to be only that due to oxygen-evolution. In other cases, pitting was observed at the end of the test, but the potential at which increase in current density was observed was close to the oxygen-evolution potential. Both processes, in these cases, took place simultaneously. In addition, crevice corrosion also occurred in borderline cases.

On reversing the direction of scan of the potential, the return curve exhibited varying degrees of hysteresis. In tests with pitting or crevice corrosion, the hysteresis was significant. In others, not significant hysteresis was observed. However, this has not always been the case. In other test programs currently underway at the CNWRA, considerable hysteresis has been present without any localized corrosion. The point of intersection of the reverse curve with the forward curve is called the protection or repassivation potential ( $E_r$ ) or protection potential ( $E_{\text{prod}}$ ). It has been argued, based on short-term test results, that below this potential any pit already nucleated will repassivate; and, hence, the alloy will be protected from localized corrosion. As mentioned in the IWPE Program Plan, the validity of argument will be evaluated for long-term exposure.

The data generated are presented in Figure 5-5. Samples where pitting or crevice corrosion were observed at 40X magnification are shown in the figure. In the simulated

**Table 5-3. RESULTS OF CYCLIC POLARIZATION TESTS ON INCOLOY  
ALLOY 825 IN SIMULATED J-13 SOLUTIONS MODIFIED TO  
VARIOUS CHLORIDE LEVELS**

Test No.	Chloride (ppm)	$E_p$ (mV <sub>SCE</sub> )	$E_{peak}$ (mV <sub>SCE</sub> )	$E_{rp}$ (mV <sub>SCE</sub> )	$E_{corr}$ (mV <sub>SCE</sub> )	$(E_p - E_{rp})$ (mV)	Initial pH	Final pH
34	0	783	382	741	-579	42	8.31	9.73
27	6	767	377	717	-480	50	8.23	9.78
30	6	768	355	706	-522	62	8.31	9.69
32	6	760	351	698	-534	62	8.30	9.76
33	6	743	322	685	-547	58	8.21	9.85
29	6	769	356	705	-557	64	8.30	9.61
31	6	747	322	681	-527	66	8.32	9.89
24	20	736	327	675	-570	61	8.31	9.86
8	20	773	380	707	-565	66	8.28	9.61
14	20	735	339	687	-470	48	8.30	9.85
22	20	739	335	683	-506	56	8.34	9.72
21	20	738	349	682	-588	56	8.28	9.56
23	20	761	352	697	-573	64	8.29	9.50
12	20	646	374	121	-543	525	8.27	9.48
16	100	740	323	366	-542	374	8.30	9.65
19	100	729	316	669	-637	60	8.25	9.72
9	100	754	361	688	-576	66	8.05	9.59
18	100	742	341	656	-592	86	8.32	9.64
17	100	726	329	672	-520	54	8.23	9.71
15	100	739	350	417	-563	322	8.30	9.66
20	100	739	334	309	-571	430	8.26	9.56
26	200	728	315	415	-526	313	8.40	9.85
10	200	746	353	152	-600	594	8.05	9.52
13	200	723	334	377	-579	346	8.27	9.67
25	200	740	335	335	-546	405	8.28	9.70
11	300	579	347	34	-566	545	8.05	9.52
47	300	628	316	103	-589	525	8.32	9.52
48	300	729	320	51	-585	678	8.38	9.41
5	1000	691	282	-35	-655	726	8.08	-
3	1000	699	294	-46	-647	745	8.12	9.50
4	1000	679	298	-63	-631	742	8.11	9.49
6	1000	467	291	-26	-610	493	8.10	9.48
2	1000	669	284	135	-657	534	8.09	9.71
1	1000	682	277	-48	-668	730	8.14	9.66
7	1000	699	306	-42	-643	741	8.11	9.65

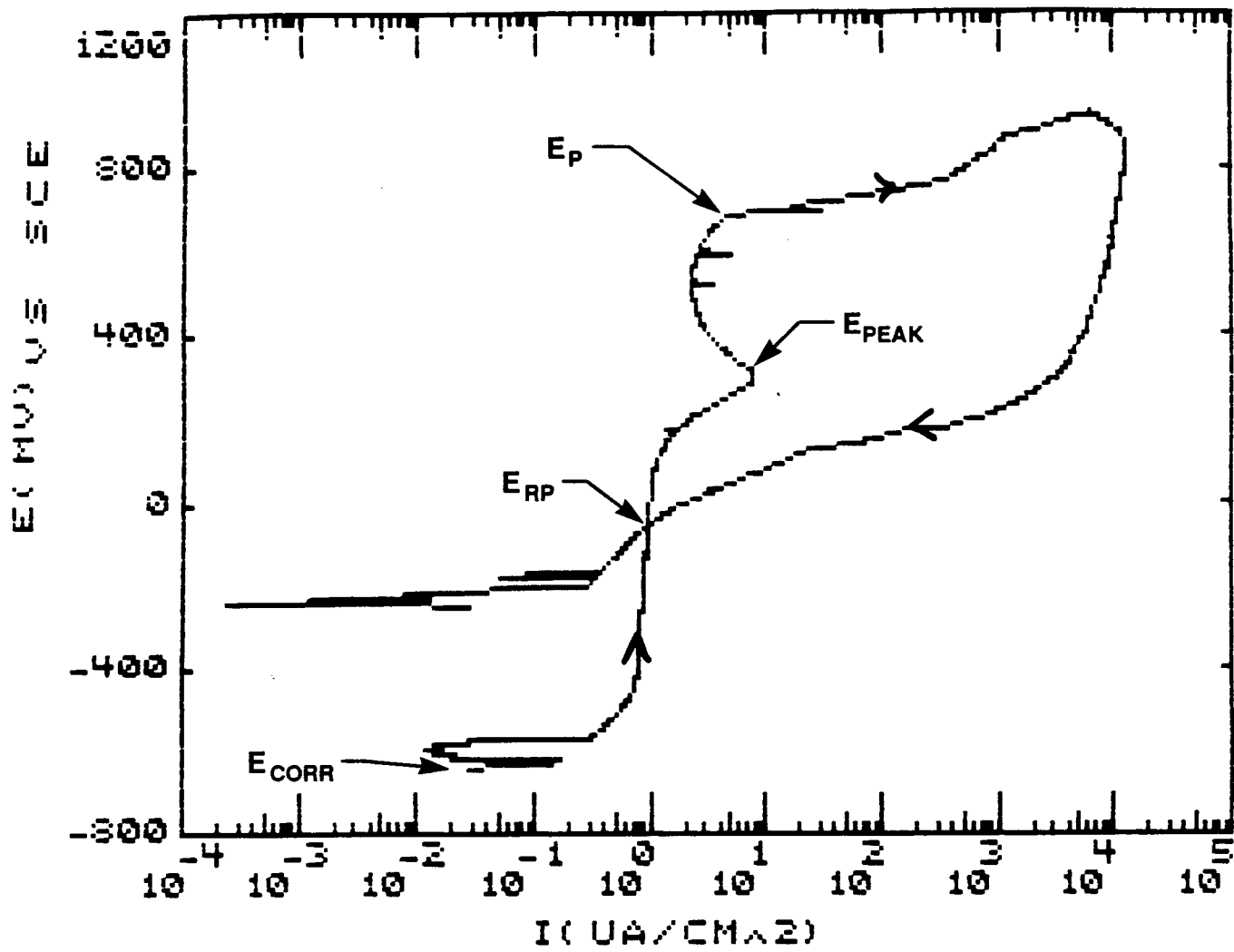


Figure 5-4. Sample curve from a cyclic polarization test

J-13 water containing 6 ppm chloride, which resembles the natural environment the closest, none of the seven samples tested showed pitting or crevice corrosion. This finding is similar to those of others and the results from previous tests at the CNWRA (Sridhar, 1990). In the simulated J-13 water augmented with chloride to 1000 ppm, all the samples that were tested pitted, again confirming previous results. In the solutions with 20 to 300 ppm chloride, pitting and crevice corrosion occurred on varying proportions of the samples. In the 20 ppm chloride solution, crevice corrosion occurred only on one of seven samples tested. In the 100 ppm solution, more samples showed crevice corrosion. Both pitting and crevice corrosion were observed in the higher chloride solutions. This environmental response can be compared to that of AISI 304L stainless steel which is shown in Figure 5-6. These data are a collection of previously reported data (Sridhar, 1990). More samples of 304L stainless steel, pitted in the 20 ppm solution. The 304L samples showed much lower pitting potentials in the high chloride solution than alloy 825.

#### **5.2.4 Effect of Environmental Variables on Localized Corrosion of Alloy 825 Factorial Experiments**

Cyclic polarization tests were performed in accordance with CNWRA Technical Operating Procedure CNWRA TOP-008. The solutions for the factorial experiments were prepared in accordance with the CNWRA's procedure CNWRA TOP-010. All salts were added as sodium salts to eliminate interference with other cations. The anions that were varied were chloride (6 and 1000 ppm), sulfate (20 and 1000 ppm), nitrate (10 and 1000 ppm), and fluoride (2 and 200 ppm). The lower levels of these anions correspond to the concentrations present in natural J-13 water. Bicarbonate was added to all these solutions to a level of 85.5 ppm. The initial pH at room temperature averaged 8.15 with a standard deviation of 0.08. The final pH at room temperature was 9.34 with a standard deviation of 0.27. As discussed by Murphy (CNWRA, 1990d), these values are in reasonably good agreement with the calculated values. The increase in pH results from ex-solution of CO<sub>2</sub> due to the combined effects of temperature and deaeration of the solution with Argon.

##### **5.2.4.1 Factorial Design**

A two-level, full factorial design was adopted using five factors: Cl<sup>-</sup>, SO<sub>4</sub><sup>-</sup>, NO<sub>3</sub><sup>-</sup>, F<sup>-</sup>, and temperature (T). The test trial order was randomized before testing. The five-factor interaction was used to block the experiments in terms of a block of experiments using the PAR 173/276 potentiostat and the other using the PAR 273 potentiostat. This approach speeded up the experimentation and, at the same time, enabled any systematic differences in the instrumental effects to be detected. In the eventual analysis, however, the instrumental differences were considered to be minimal; and four- and five-factor interactions were used to determine pooled variance. Variances were also calculated independently from replicate tests. A description of the factorial design can be found in Mason et al. (1989).

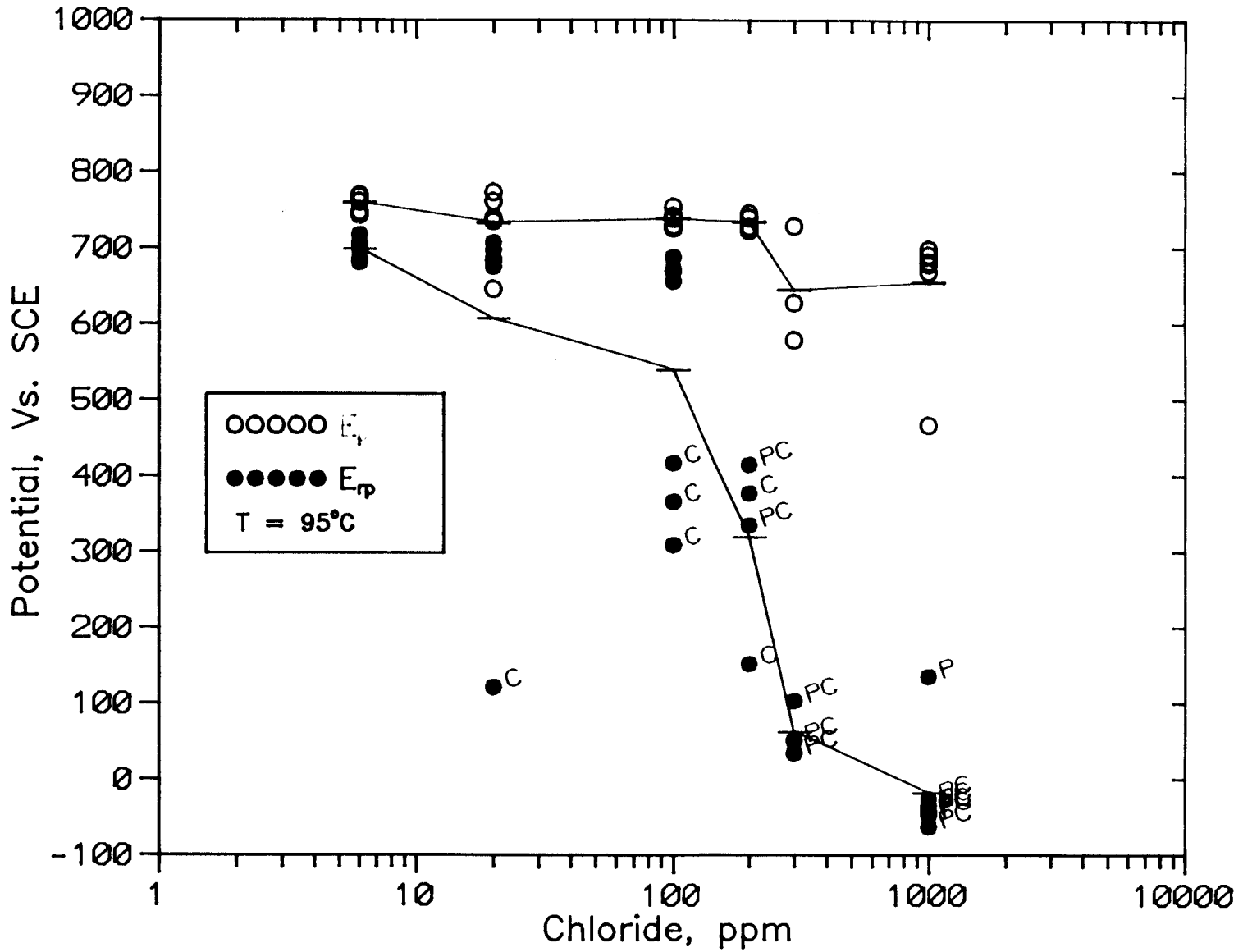


Figure 5-5. Effect of chloride in simulated J-13 water on pitting of alloy 825 P=pit, C=crevice attack

5-19

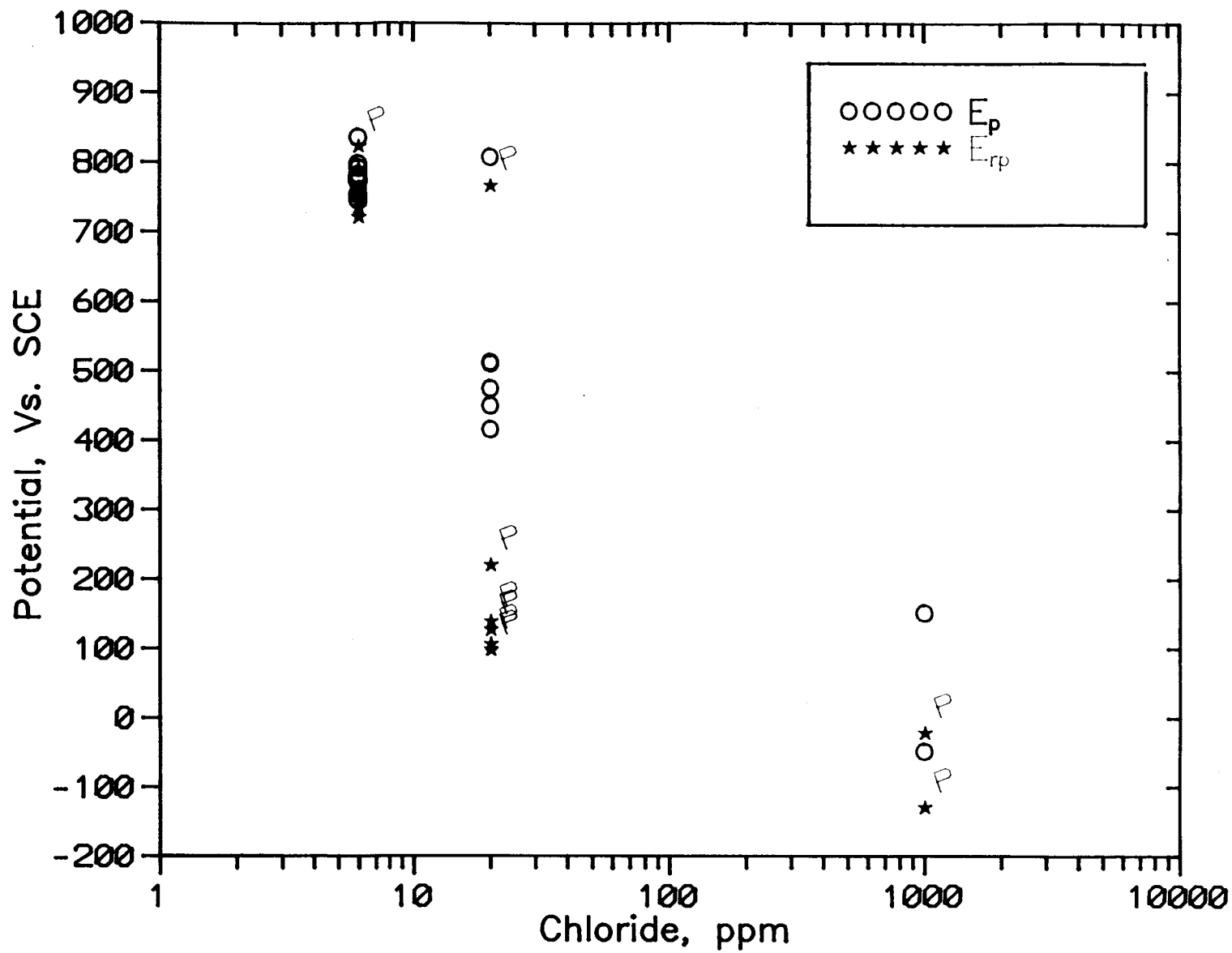


Figure 5-6. Effect of chloride in simulated J-13 water on pitting of 304L stainless steel P=pits

#### 5.2.4.2 Electrochemical Observations

Selected polarization curves are shown in Figures 5-7 and 5-8 to illustrate the anodic behavior observed in these tests. As shown in Figure 5-7, nitrate had a major inhibitive effect on pitting in the high chloride environment, since practically no hysteresis was present in the 1000 ppm nitrate solution and the specimen exhibited no pitting. It was also clear from many of the tests that there was a poor correlation between the parameters of the polarization curves and the visual evidence of pitting. This was especially true at low chloride contents and low temperatures. For example, as shown in Figure 5-8, the specimen tested in a solution containing 6 ppm chloride and 2 ppm fluoride showed a smaller hysteresis than another tested in a solution containing 6 ppm chloride plus 200 ppm fluoride. However, the former pitted while no pitting was found in the latter; so statistical analysis using just the electrochemical parameters will result in misleading interpretation of environmental effects on pitting.

#### 5.2.4.3 Visual and SEM Examination

Specimens were examined after the test under a low-power microscope (70X magnification). In selected cases, scanning electron microscopy (SEM) of the specimens was conducted. Five broad classifications were created as shown in Table 5-4. Details of the SEM examination were reposted previously (CNWRA, 1990e). While these ratings have a certain element of subjectivity, it should be noted that a rating based only on the number of pits per unit area is insufficient to characterize the behavior because both the depth of pits and type of corrosion products associated with the pits varied. The most severe cases (Rating = 4) had not only deep pits but also crevice corrosion. No thick corrosion products were deposited on the pits. Specimens of Rating = 3 also exhibited deep pits of a similar kind but did not show extensive crevice corrosion. The pits were found to have considerable undermining beneath the surface. In some specimens, the pits were quite numerous but shallow and covered with a brown deposit. No crevice corrosion was observed in these specimens, which were given a rating of 2. Finally, in one specimen, the pits were found to be flat depressions surrounded by a brown corrosion product. This specimen was given a rating of 1 to distinguish it from the shallow but narrow pits of Rating 2. In the case of specimens exposed to high fluoride environments, a loosely adherent, yellowish film was found to have formed uniformly over the entire surface.

#### 5.2.4.4 Localized Corrosion Index (LCI)

In the literature on localized corrosion, the hysteresis in the polarization curve reflected by  $E_p - E_{rp}$  is often considered to be a measure of the extent of localized corrosion. In the present investigation, however, this correlation was not always observed. This is illustrated in Figure 5-9 where the visual rating is plotted against the hysteresis,  $E_p - E_{rp}$ . A lack of correlation between these two parameters is evident especially at intermediate and low values of hysteresis. Since both the electrochemical parameter, ( $E_p - E_{rp}$ ) and the visual rating carry part of the information required to characterize the localized corrosion behavior, an index

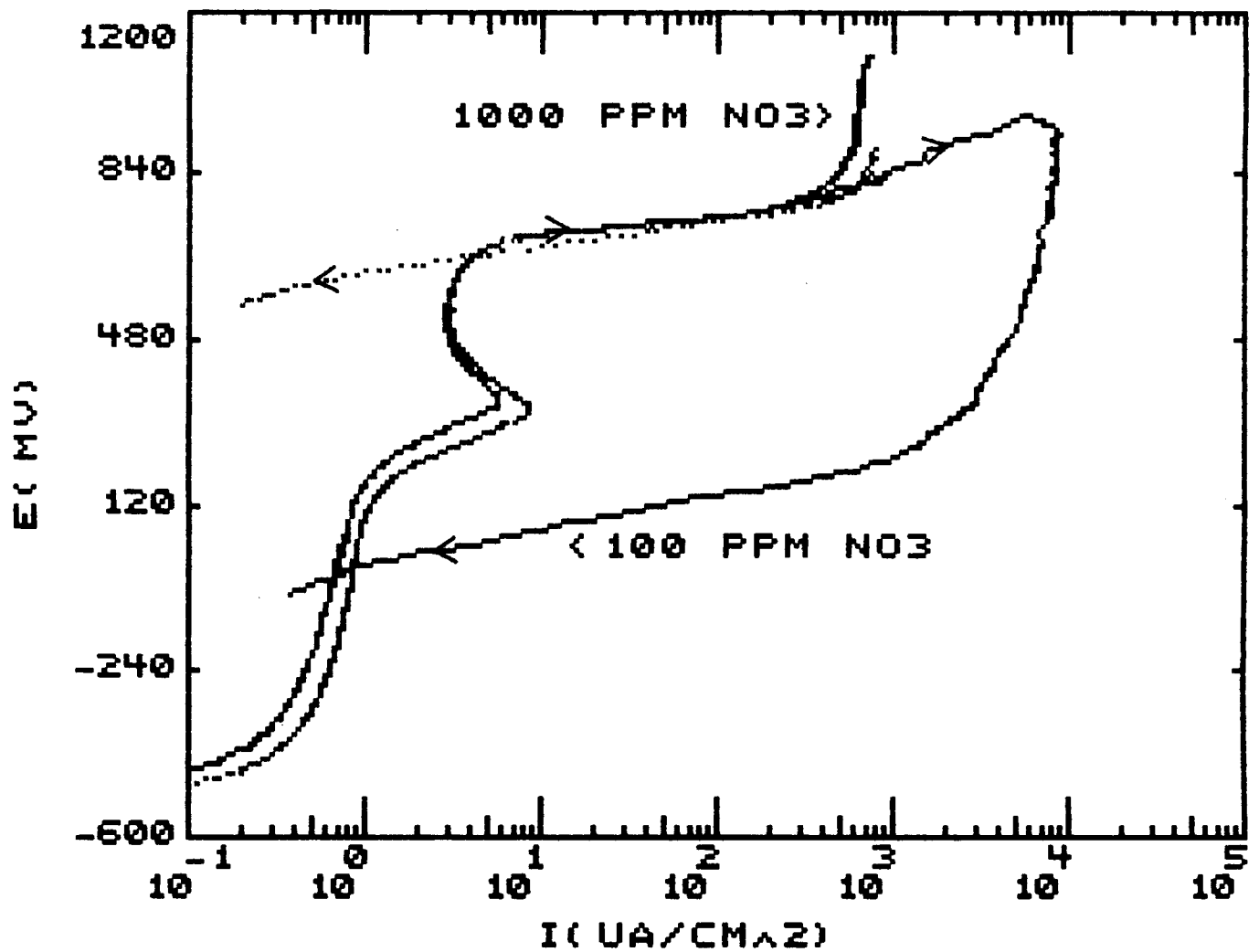


Figure 5-7. Typical cyclic polarization curves for alloy 825 at 95°C indicating the effect of nitrate at a chloride concentration of 1000 ppm

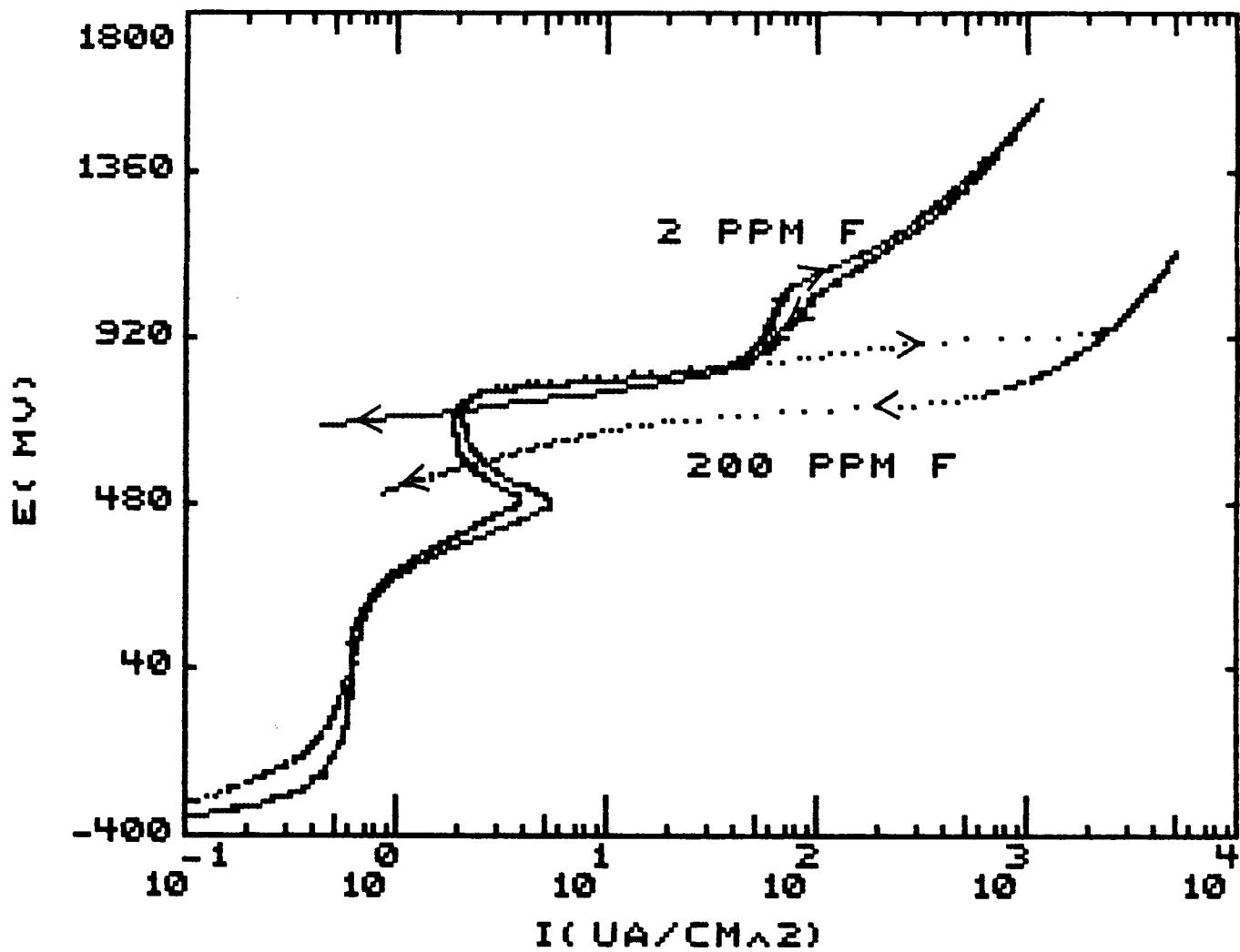


Figure 5-8. Typical cyclic polarization curves for alloy 825 at 60°C indication the effect of fluoride at a chloride concentration of 6 ppm

**Table 5-4. RATING OF LOCALIZED CORROSION BY VISUAL AND SEM-EDX EXAMINATION**

Rating	Description	Corrosion Product
4	Severe pitting, crevice corrosion	Rich in Cr, Mo
3	Less severe pitting, no crevice	Rich in Cr, Mo
2	Numerous shallow pits	Rich in Fe
1	Shallow, flat areas of corrosion	Rich in Fe
0	No localized corrosion	

called the Localized Corrosion Index (LCI) was introduced as shown in Eqn. (1).

$$LCI = (E_p - E_{rp}) * \text{Visual Rating} \quad (1)$$

This index is zero in cases where no pitting was observed even if there is a sizable hysteresis. It also differentiates cases where similar hysteresis is observed with widely varying severity of localized corrosion. The LCI was then used as the measured parameter for statistical analysis. The results of the tests, along with the computed LCI, were listed in a previous report (CNWRA, 1990e).

**Statistical Analysis of Results.** While the approach is capable of yielding up to four-factor interactions, the initial approach was to consider only the main effects of the five variables and the two factor interactions. The higher factor interactions were then pooled to calculate the variance in the results and to construct the 95-percent confidence intervals for the factor coefficients. Another approach was to consider not only the main effects and two-factor interactions, but also the three-factor interactions. Again, higher order interactions were used for pooled error calculations. Upon inspection of the second analysis, it was evident that the three-factor interactions, with the possible exception of the temperature-chloride-sulfate interaction term, were not significant. The three-way interaction of temperature, chloride, and sulfate was dominated by the adverse effect of chloride. Additionally, it was concluded that the statistical model with three-factor interactions is more complicated than warranted by the test technique. Since the potentiodynamic test approach was expected to yield only trends in the behavior of the material and not lifetime predictions, use of more complicated models is of

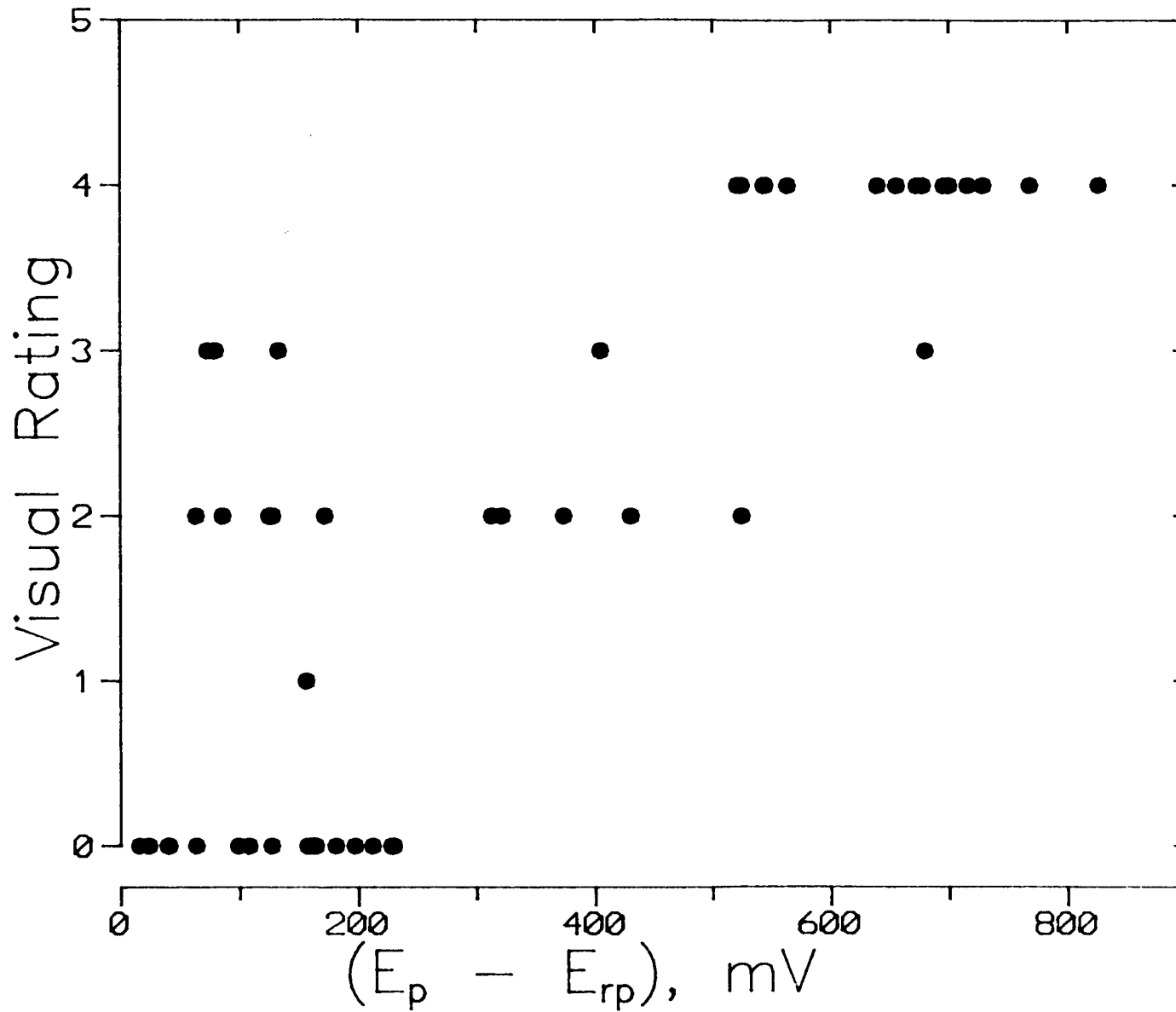


Figure 5-9.  $E_p - E_{rp}$  vs. visual rating of alloy 825 specimens indicating a lack of correlation between these two parameters

marginal benefit. The pooled variance associated with the three-factor model was used, nevertheless, in analyzing the results. The residuals from the model and actual measurements exhibited a normal distribution. The resulting equation for localized corrosion is shown in Eqn. (2):

$$\begin{aligned}
 LCI = & 660 + 591(X_{Cl}) - 23(X_T) - 76(X_F) - 587(X_{NO_3}) + 51(X_{SO_4}) \\
 & + 8(X_{Cl}X_T) - 26(X_{Cl}X_F) - 589(X_{Cl}X_{NO_3}) + 49(X_{Cl}X_{SO_4}) \\
 & + 64(X_TX_F) - 32(X_TX_{NO_3}) + 41(X_TX_{SO_4}) + 3(X_FX_{NO_3}) \\
 & + 17(X_FX_{SO_4}) - 72(X_{NO_3}X_{SO_4})
 \end{aligned} \tag{2}$$

$LCI = (E_p - E_{rp}) * \text{Visual Rating}$  and has the units of millivolts. Note that the parameters  $X_{Cl}$ , etc. refer to the coded values and not the actual values of these variables and thus are dimensionless. For example, when the chloride concentration is at the lowest level used in the test matrix,  $X_{Cl}$  is -1; and at the highest chloride concentration, it is +1. To convert any concentration of a species A to its coded value, the following equation should be used:

$$X_A = \frac{2(A - A_{avg})}{(A_{max} - A_{min})} \tag{3}$$

where A is the actual concentration of species A.  $A_{max}$ ,  $A_{min}$ , and  $A_{avg}$  are the maximum, minimum, and average concentrations respectively, of species A in the experimental matrix. The  $R^2$  value for the statistical model shown in Eqn. (2) was 0.993.

Not all the factors in Eqn. (2) are of significance, however. Analysis of Variance (ANOVA) must be performed on the coefficients in Eqn. (2) (Mason, 1989) to determine the statistical significance of the various factor effects. In performing this analysis, the confidence interval so determined is dependent on the standard deviation of the observed electrochemical parameters. This standard deviation can be determined either by repeated tests using a single combination of environmental factors or by assuming that all the higher order interactions involving three or more factors are really due to random errors in the experiments. In the current set of experiments, these two measures of error are approximately equal, so the latter was used for estimation of confidence intervals. Figure 5-10 shows a plot of the coefficients of all the factors listed in Eqn. (2) with their 95-percent confidence intervals. For the terms T, Cl\*T, Cl\*F, T\*NO<sub>3</sub>, T\*SO<sub>4</sub>, F\*NO<sub>3</sub>, and F\*SO<sub>4</sub>, the 95-percent confidence intervals of the coefficients straddle zero, indicating that these factors may not be important. On the other hand, Cl, NO<sub>3</sub>, Cl\*NO<sub>3</sub>, T\*F, and NO<sub>3</sub>\*SO<sub>4</sub> are clearly important because their confidence intervals are clearly displaced from zero. The terms F, SO<sub>4</sub> and Cl\*SO<sub>4</sub> are

borderline cases and may be included in a more detailed model. Based on the above analysis, a simplified equation for LCI can be expressed as

$$LCI'' = 660 + 591(X_{Cl}) - 587(X_{NO_3}) - 589(X_{Cl}X_{NO_3}) - 72(X_{NO_3}X_{SO_4}) + 64(X_T X_F) \quad (4)$$

where LCI'' has the same meaning as LCI, but the value computed from Eqn. (4) will differ from that calculated from Eqn. (2). It must be emphasized that the approach used here is not a least squares fit where dropping of terms will be reflected in a change in the coefficients of the remaining terms. The design of the experiment implies orthogonality of all factors, so dropping any factor will not affect the coefficients of the remaining terms. Dropping of terms will affect, however, the degree of fit of the statistical model to experimental data as reflected by the R<sup>2</sup> value. Thus, the R<sup>2</sup> value for Eqn. (4) is 0.979, which is still considered to be good. These equations are valid only within the experimental range of the five factors considered.

The experimental design used above can only result in a linear relationship. The predictions from Eqn. (2) agree reasonably well with the measured values when the variables are at the extremes of the matrix. However, the deviation from linearity can be visualized by comparing predicted and measured values of LCI at intermediate values of some of the variables using eqns. (2) and (3):

- Case 1:      Cl: 300 ppm, T: 95 C, NO<sub>3</sub><sup>-</sup>: 10 ppm, F: 2 ppm, SO<sub>4</sub><sup>2-</sup>: 1000 ppm  
 Predicted LCI = 901; Measured LCI = 2692
- Case 2:      Cl: 1000 ppm, T: 80 C, NO<sub>3</sub><sup>-</sup>: 10 ppm, F: 2 ppm, SO<sub>4</sub><sup>2-</sup>: 20 ppm  
 Predicted LCI = 2364; Measured LCI = 2784
- Case 3:      Cl: 1000 ppm, T: 95 C, NO<sub>3</sub><sup>-</sup>: 10 ppm, F: 2 ppm, SO<sub>4</sub><sup>2-</sup>: 200 ppm  
 Predicted LCI = 2361; Measured LCI = 3072
- Case 4:      Cl: 1000 ppm, T: 95 C, NO<sub>3</sub><sup>-</sup>: 100 ppm, F: 2 ppm, SO<sub>4</sub><sup>2-</sup>: 20 ppm  
 Predicted LCI = 2082; Measured LCI = 2916
- Case 5:      Cl: 1000 ppm, T: 95 C, NO<sub>3</sub><sup>-</sup>: 10 ppm, F: 100 ppm, SO<sub>4</sub><sup>2-</sup>: 20 ppm  
 Predicted LCI = 2232; Measured LCI = 3304

It can be seen (Case 1) that the variation of localized corrosion with chloride concentration is far from linear, since the predicted value was much lower than the observed value of LCI. This is discussed further in the next section. Because temperature did not have a significant effect, the predicted LCI at intermediate values of T (Case 2) agrees

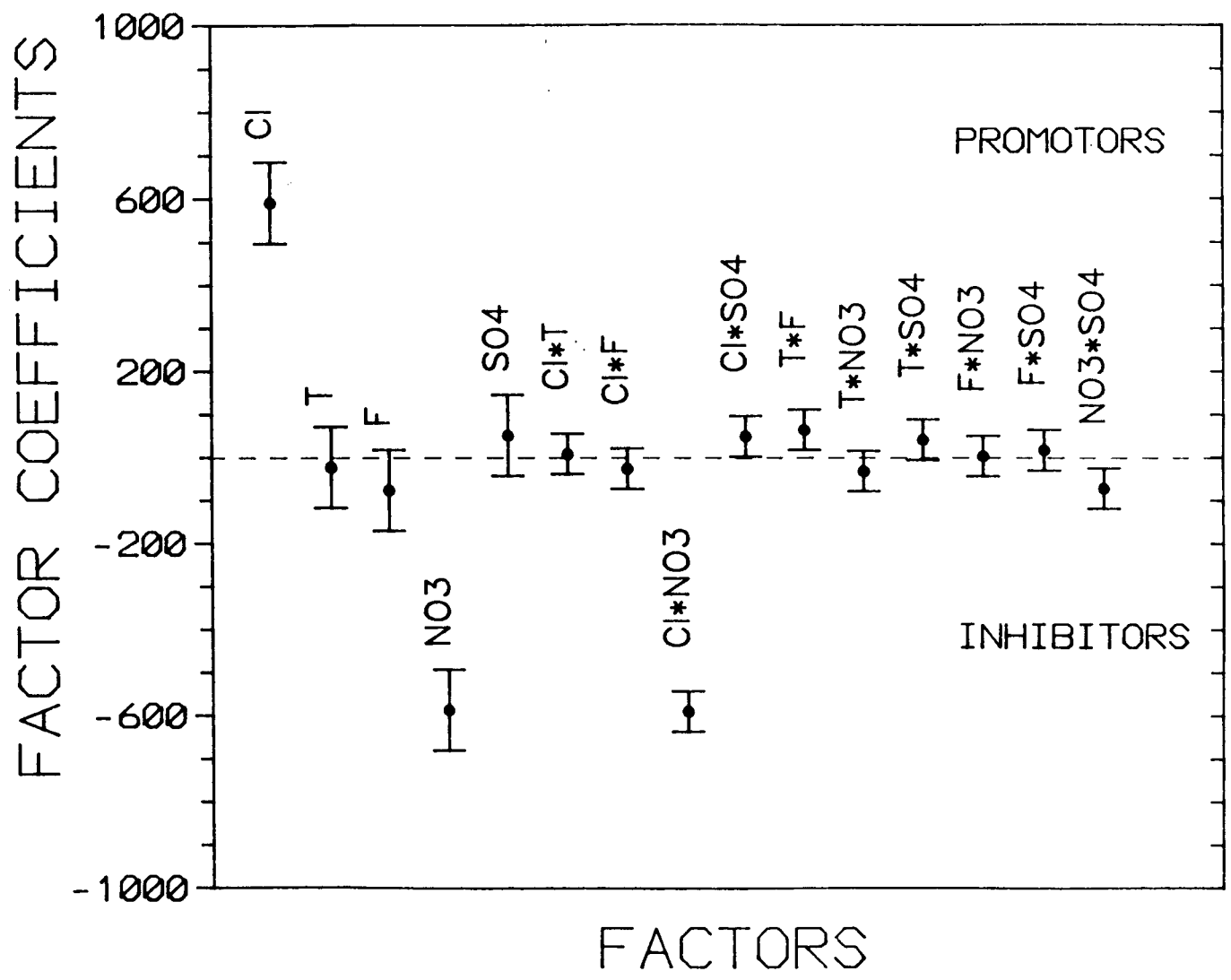


Figure 5-10. The coefficients in eqn. (2) plotted for various factors along with their 95 percent confidence intervals

reasonably well with observed values. For the cases of sulfate, nitrate, and fluoride, the deviation from linearity is smaller than observed for chloride (Cases 3-5).

The results of the factorial experiments clearly illustrate the importance of environmental variables in the development of localized corrosion. The main effect of chloride was similar to that found in the experiments with simulated J-13 water shown in Figure 5-5. The experiments did reveal lack of a direct correlation between electrochemical parameters, such as pitting potential, repassivation potential and the difference between them, and the visual evidence of pitting. This is particularly true at low chloride concentrations, as shown in Figure 5-9. Specimens without any sign of localized corrosion showed hysteresis values ( $E_p - E_{rp}$ ) as great as 200 mV. On the other hand, specimens exhibiting a severe attack, as indicated by a rating value of 2, gave rise to polarization curves with relatively low hysteresis values (<100 mV). Although it may be questionable to generalize these observations to other alloy/environment systems, it appears that for environments containing low chloride concentrations or certain combination of other anionic species, the simple approach of using electrochemical parameters for quantitative assessment of localized corrosion could be inappropriate. The introduction of the combined index, termed LCI, allows one to overcome that limitation and to establish an unambiguous, albeit subjective, rating for the statistical evaluation of the environmental effects. The use of another form of this index may be more appropriate for another alloy. For example, the current form of LCI cannot distinguish between materials that may have differing pitting and repassivation potentials but the same hysteresis and localized corrosion appearance. In such cases, the LCI may have to be modified, such as shown below

$$MOD\ LCI = \frac{(E_p - E_{rp})}{E_p} * \text{Visual Rating.} \quad (5)$$

As indicated by Eqn. (1) and shown graphically in Figure 5-10, chloride and nitrate are the two dominant anionic species in terms of their effect on localized corrosion of Alloy 825, chloride being a promoter and nitrate an inhibitor. This is similar to their effect on austenitic stainless steels (Szkłarska-Smiałowska, 1986). In the 6 ppm chloride solution, nitrate does not appear to act as an inhibitor; but the pitting was shallow and of a different type (Rating 2) from the pitting in the high chloride solutions. It must be emphasized here that pitting in these solutions occurred at very high anodic potentials in the transpassive region. Indeed, in experiments with zero ppm chloride solutions at 60°C, a similar type of pitting was found. The mechanism for this type of pitting is not yet clear; possibly pitting, which occurs at high potentials in these types of environments, is a form of selective dissolution associated with the transpassive dissolution of Cr.

Equation (4), a simplified form of Eqn. (2), shows coefficients affecting the predominant environmental factors. Besides the anionic species discussed above, it is seen that fluoride has a slight inhibiting effect, whereas nitrate interacts with sulfate to suppress its weak action as a promoter, as illustrated in Figure 5-9. The inhibiting effect of fluoride was

found mainly in the low-chloride solutions (Table 5-2). In all the solutions containing fluoride, a loose layer of corrosion product was observed. It is possible that fluoride, acting as a strong complexing agent, promotes uniform rather than localized corrosion. Sulfate was found to be a weak promotor of localized corrosion (Figure 5-10), mainly in high-chloride concentrations (Table 5-2). The effect of sulfate found in this investigation is in contrast to the beneficial effect of sulfate found by Leckie and Uhlig (1966) for 18Cr-8Ni stainless steel.

### 5.2.5 Effect of Temperature on Localized Corrosion of Alloy 825

The effect of temperature on the anodic behavior of Alloy 825 was studied in simulated J-13 water in which the chloride content was 6 ppm. The potentiodynamic polarization curves were similar, with the corrosion potential and the transpassive anodic peak displaced to lower potentials with increasing temperature. At potentials above the regime of oxygen-evolution reaction, a quasi-limiting current density appeared, followed by a region of increasing current (CNWRA, 1990e). The value of the quasi-limiting current density increased with increasing temperature, but at 95°C this distinctive behavior is no longer observed. The presence of pits was detected in the specimens tested at temperatures extending from 30 to 80°C, and no pitting was observed at 95°C. The pits were quite shallow and covered by brown corrosion products enriched in iron. Intergranular attack was clearly noticeable at the bottom of the pits. According to observations reported previously, this type of pitting is within the Rating 2. The occurrence of this type of pitting is not related to a characteristic or critical potential as it is for the pitting observed in more concentrated chloride solutions (> 100 ppm). It seems to occur at potentials above that corresponding to the oxygen evolution reaction, precisely within the potential range in which the quasi-limiting current density was observed. Since this shallow form of pitting was observed, even in the absence of chloride, in a solution similar to simulated J-13 water in which chloride was replaced by sulfate for adequate conductivity, it seems to be related to selective and localized transpassive dissolution at very high potentials rather than to localized breakdown of the passive film by the chloride anion. Thus, this phenomenon is not realistic in practical terms because such high potentials are not attainable in natural environments even under highly oxidizing conditions.

The weak effect of temperature on the susceptibility to localized corrosion of Alloy 825 within the 60 to 95°C range, as evaluated through the factorial experiments, seems surprising, but appears to be related to the relatively high pitting potentials exhibited by this alloy in all the solutions tested. It is well known (Szkłarska-Smiałowska, 1986; Cragolino, 1987) that many metals and alloys exhibit a strong dependence of the pitting potential on temperature ranging from 25 to 150°C. The pitting potential decreases with temperature, reaching an almost constant value at even higher temperatures. The temperature range in which the pitting potential is a strong function of temperature is displaced to higher temperatures with increasing alloy resistance to pitting corrosion (Brigham, 1973). On the other hand, for a given alloy, it is displaced to lower temperatures with increasing aggressiveness of the environment as characterized, for example, by the increase in the chloride concentration. An alloy extremely resistant to pitting in a given solution exhibits a high pitting potential, in some cases, unattainable within the range of stability of water as a solvent. For these highly resistant alloys,

an increase in temperature or in the concentration of the aggressive species is required to promote the occurrence of pitting within the range of corrosion potentials prevailing in natural environments.

Since only a weak dependence of the pitting potential on temperature was observed in the solution containing 1000 ppm chloride, additional cyclic polarization curves were obtained in a 10,000 ppm chloride solution over the temperature range that extends from 30 to 95°C. For this purpose, solutions containing 1000 and 10,000 ppm Cl<sup>-</sup> with the addition of 20 ppm SO<sub>4</sub><sup>2-</sup>, 10 ppm NO<sub>3</sub><sup>-</sup>, 2 ppm F<sup>-</sup>, 88 ppm HCO<sub>3</sub><sup>-</sup> and Na<sup>+</sup> as a single cation were used to study the effect of temperature on the pitting and repassivation potentials. The results are summarized in Figure 5-11, where  $E_p$  and  $E_{rp}$  are plotted as a function of temperature for both chloride concentrations. The lines in the figure are linear regression fits. As shown, both  $E_p$  and  $E_{rp}$  decrease with temperature with approximately the same slope for the 10,000 ppm chloride solution. The extremely weak dependence of  $E_p$  with temperature was confirmed for the 1000 ppm chloride solution. However,  $E_{rp}$  in this solution also decreases with temperature but with a less pronounced slope than in the more concentrated chloride solution.

From this analysis, it can be deduced that Alloy 825 in the 1000 ppm chloride solution is in the upper plateau region of the pitting potential vs. temperature curve, showing a behavior characteristic of a material with a relatively high resistance to pitting corrosion (Brigham, 1973). This may also explain the lack of temperature dependence observed by other authors (Glass, 1984; Beavers, 1990a) in solutions containing low chloride concentrations. In a more aggressive solution, such as that containing 10,000 ppm chloride, the pitting potential lies in the transition region where the dependence on temperature becomes dominant. However, the repassivation potentials are quite low despite the relatively high pitting potentials measured at 95°C, even in the solution containing 1000 ppm chloride. The repassivation potential in the 10,000 ppm chloride solution at 95° was -343 mV<sub>SCE</sub>, which was close to the open-circuit potential measured in the deaerated solution. These results indicate that further studies are needed to evaluate the susceptibility to localized corrosion under potentiostatic conditions over the potential range extending from  $E_{rp}$  to  $E_p$ . Results of these studies will be compared to those obtained under free corroding conditions that may be present in the repository environment.

#### 5.2.6 Effect of Si on Localized Corrosion of Alloy 825

The natural J-13 water has Si as one of the major components. In the past formulations of simulated J-13 water, Si has been added as SiO<sub>2</sub>·nH<sub>2</sub>O. However, because of its low solubility, unknown water of hydration, and slow dissolution rate, addition of silicic acid results in time-varying concentration of Si in the solution (Pabalan, 1989). Because of this, Si was excluded from the factorial experiments. Subsequently the effect of dissolved Si on localized corrosion was studied subsequently by adding sodium metasilicate to simulated J-13 solutions of different chloride concentrations. The simulated J-13 solutions were prepared as described in section 5.2.3. Two chloride concentrations were examined: 6 ppm and 300 ppm. To each of these solutions, 0.0232 g/l of sodium metasilicate was added. Duplicate cyclic polarization tests were conducted on alloy 825. The results are shown in Table 5-4.

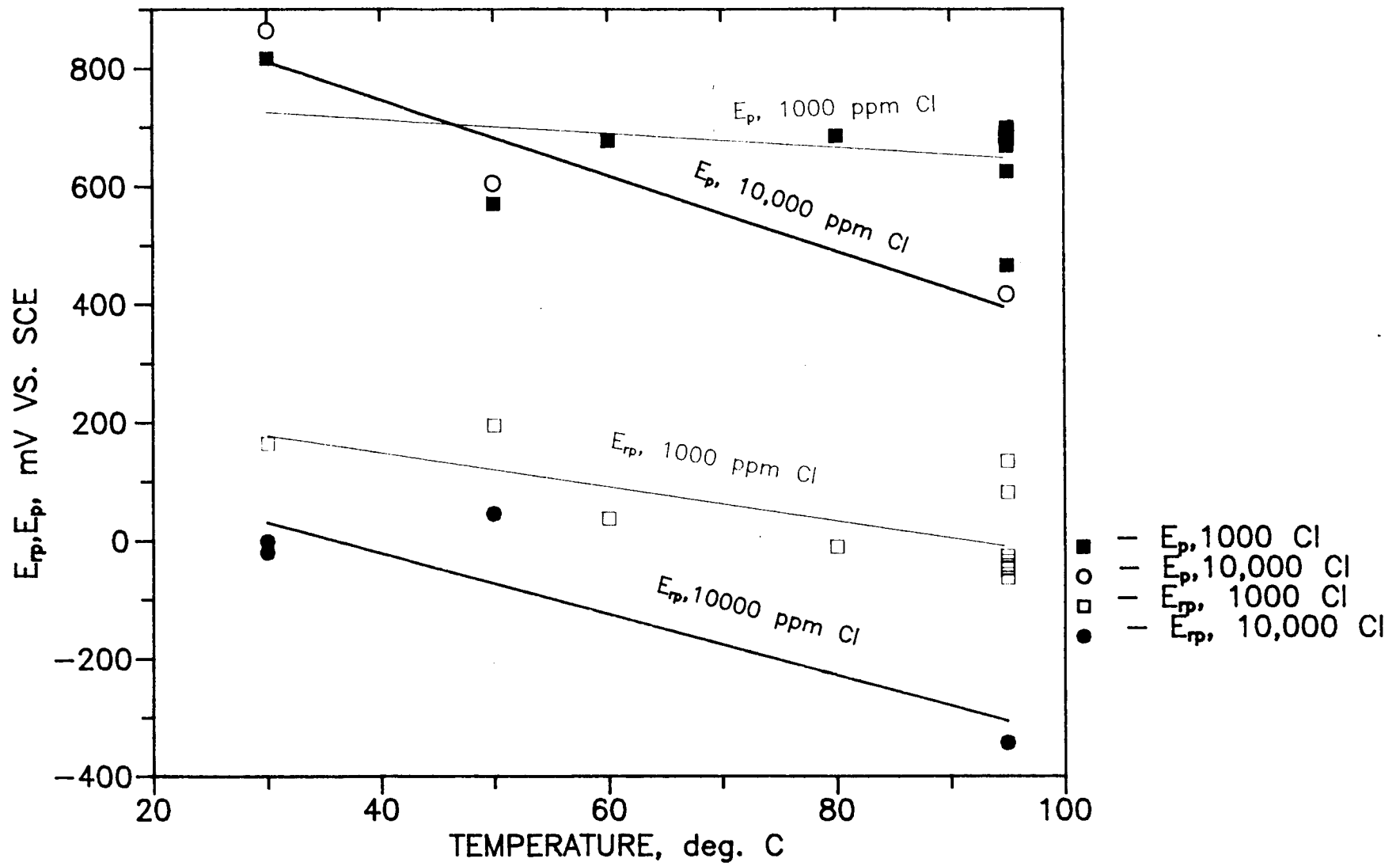


Figure 5-11. Effect of temperature and chloride concentration on  $E_p$  and  $E_{rp}$  of alloy 825

As seen in Table 5-5, Si, added as metasilicate, does not have a significant effect on localized corrosion of Alloy 825 in simulated J-13 well water containing 6 and 300 ppm chloride.

#### 5.2.7 Effect of $Mg^{2+}$ on Localized Corrosion

Since the natural J-13 water has significant concentrations of Mg and this cation has been found by Beavers et al. (1990a) to be one of the important species promoting localized corrosion, its effect was studied by adding  $MgCl_2 \cdot 6H_2O$  to a 1000 ppm Cl solution instead of NaCl (0.347g/l Mg). The results, given in Table 5-6, show that addition of 348 ppm  $Mg^{2+}$  lowered the final pH due to hydrolysis. Addition of  $MgCl_2$  lowered the pitting potential slightly (20 - 80 mV) and the repassivation potential by a greater extent (86 - 157 mV). These results are in contrast with the results of Beavers et al. (1990a), who found that addition of 20 mg/l Mg resulted in a decrease of both pitting and repassivation potentials by about 175 mV. According to Beaver's analysis, Mg is the most dominant ionic species affecting localized corrosion of Alloy 825 since its coefficient is higher than that of any other ionic species including chloride. Because of these differences, further experiments on the role of Mg, especially in low chloride concentrations, may be necessary.

#### 5.2.8 Effect of Nitrite

Nitrite has been determined to be one of the radiolysis products in a moist air environment (Van Konynenburg, 1986). Most of the experimental program has concentrated on quantifying the effects of nitrate. It was believed that the effect of nitrite will be equivalent to that of nitrate. This was verified by separate experiments where 1000 ppm nitrite (as  $NaNO_2$ ) was added to a solution containing 1000 ppm chloride. As shown in Table 5-7, nitrite had the same inhibitory action as nitrate in that no pitting of Alloy 825 was observed in this solution.

#### 5.2.9 Effect of Aeration and $H_2O_2$

In previous experiments, the response of Alloy 825 to applied anodic potentials under a variety of environmental conditions was examined. In a separate set of experiments, open-circuit potentials were measured on Alloy 825 and Pt immersed in simulated J-13 water containing 6 ppm and 1000 ppm chloride at 95°C. The purpose of these tests was to determine the effect of redox species such as of oxygen present in the natural environment and  $H_2O_2$  created as a result of radiolysis. The solutions were aerated using bottled air.  $H_2O_2$  was added such that the concentration in the solution increased in steps of 0.1 mM.

The summary of results are shown in Table 5-8. The open-circuit potentials of both Alloy 825 and Pt in aerated solution containing 1000 ppm chloride attained steady values of -280 mV and +140 mV, respectively. Although the value observed for Pt is well below the equilibrium value, the potential measured on Alloy 825 is even more irreversible.

**Table 5-5. EFFECT OF SI ON LOCALIZED CORROSION OF ALLOY 825 IN A CYCLIC POLARIZATION TEST**

Parameters	6 ppm Chloride		300 ppm Chloride	
	0 Na <sub>2</sub> SiO <sub>3</sub>	0.023g/l Na <sub>2</sub> SiO <sub>3</sub>	0 Na <sub>2</sub> SiO <sub>3</sub>	0.023g/l Na <sub>2</sub> SiO <sub>3</sub>
E <sub>corr</sub> (mV <sub>SCE</sub> )	-480 to -557	-555, -565	-566 to -589	-545, -518
E <sub>p</sub> (mV <sub>SCE</sub> )	+743 to +769	+773, +763	+579 to +729	+713, +731
E <sub>tp</sub> (mV <sub>SCE</sub> )	+681 to +716	+729, +719	+34 to +103	+40, +31
Initial pH	8.21 to 8.32	8.91, 8.82	8.05 to 8.38	8.87, 8.85
Final pH	9.61 to 9.89	9.94, 9.90	9.41 to 9.52	9.75, 9.82
Localized corrosion observed?	None	None	Yes	Yes

**Table 5-6. EFFECT OF MG<sup>2+</sup> ON LOCALIZED CORROSION OF ALLOY 825**

Parameters	Concentration of Mg <sup>2+</sup> in 1000 ppm Cl <sup>-</sup> Solutions		
	0 ppm	1.7 ppm	348 ppm
E <sub>corr</sub> (mV <sub>SCE</sub> )	-555	-610 to -668	-644 to -659
E <sub>p</sub> (mV <sub>SCE</sub> )	+626	+467 to +699	+546 to +605
E <sub>tp</sub> (mV <sub>SCE</sub> )	+ 82	-63 to +135	-75 to -4
Initial pH	8.12	8.08 to 8.14	8.08
Final pH	9.37	9.48 to 9.71	8.05 to 8.30
Localized corrosion observed?	Yes	Yes	Yes

**Table 5-7. EFFECT OF NO<sub>2</sub><sup>-</sup> ON LOCALIZED CORROSION OF ALLOY 825**

Environment	Parameters			
	E <sub>CORR</sub>	E <sub>p</sub>	E <sub>rp</sub>	Localized
	mV <sub>SCE</sub>	mV <sub>SCE</sub>	mV <sub>SCE</sub>	Corrosion Observed?
1000 ppm Cl <sup>-</sup>	-555	+626	+82	Yes
1000 ppm Cl <sup>-</sup> + 1000 ppm NO <sub>3</sub> <sup>-</sup>	-509	+712	+672	No
1000 ppm Cl <sup>-</sup> + 1000 ppm NO <sub>2</sub> <sup>-</sup>	-432	+577	+577	No

**Table 5-8. EFFECT OF AERATION OF H<sub>2</sub>O<sub>2</sub> ADDITION ON OPEN-CIRCUIT POTENTIALS (mV VS. SCE) OF ALLOY 825 AND PT SIMULATED J-13 SOLUTIONS AT 95°C**

Condition	Alloy 825		Platinum	
	6 ppm Cl	1000 ppm Cl	6 ppm Cl	1000 ppm Cl
Deaerated, Argon	-545	-525	-478	-448
Argon + 0.5 mM H <sub>2</sub> O <sub>2</sub>	+118	+108	+73	+59
Aerated	-298	-280	+170	+140
Aerated + 0.5 mM H <sub>2</sub> O <sub>2</sub>	+132	+106	+79	+53

These open-circuit measurements are governed not only by charge-transfer conditions but also by transport limiting processes. Hence, the measurements deviate considerably from the thermodynamically expected values. In the case of deaerated environments, the potentials of both Alloy 825 and Pt increased with the addition of peroxide, although the increase was more pronounced for Alloy 825 than Pt (Table 5-6). The value of the potential for Alloy 825 and Pt in the 0.5 mM  $H_2O_2$  solution is almost independent of the presence of dissolved oxygen, indicating that the reduction of  $H_2O_2$  is the controlling cathodic reduction on both metals.

Regarding the performance of Alloy 825 in the natural environment, the  $E_p$  and  $E_{rp}$  values measured in deaerated environments (Figure 5-5) must be compared to the corrosion potentials measured with aeration and peroxide. The corrosion potentials in solutions with the addition of 0.5 mM peroxide are higher than the repassivation potential above a chloride concentration of about 300 ppm. Since the potentiodynamic tests which yielded the  $E_{rp}$  values are short-term tests and the corrosion potentials were measured under static conditions, localized corrosion may occur at chloride concentrations even lower than 300 ppm chloride in the natural environment over long periods of time.

### 5.3 SUMMARY OF RESULTS

The findings from preliminary microstructural and surface characterization of the candidate waste container materials are presented as well as results of localized short-term corrosion tests on Alloy 825. This part of the investigation emphasized the development of a systematic understanding, based on short-term tests, of the effects of various environmental species that may be present in the repository after emplacement of the waste packages on the corrosion of a waste package material. The current state of understanding can be summarized as follows:

- (1) The presence of iron-rich particles in CDA-613 may lead to preferential corrosion due to the electrochemical dissimilarity of these particles and the copper-rich matrix. Future investigations of this alloy should consider this aspect in greater detail.
- (2) Chromium depletion at the surface of the nickel-based, chromium-containing alloys led to increased corrosion in a standard oxidizing environment. Hence, the effect of the depletion on the container performance should be considered for general and localized corrosion processes as well as stress corrosion cracking.
- (3) The threshold chloride level for localized corrosion of Alloy 825 in oxidizing, aqueous environments is quite low (20 - 100 ppm).
- (4) Crevice corrosion occurred prior to pitting in many samples of Alloy 825 exposed to chloride solutions. Crevice corrosion is an important failure mode and should be examined more systematically.

- (5) Near the threshold chloride levels when localized corrosion initiates, considerable scatter in data was observed. The statistical distribution of the electrochemical parameters,  $E_p$  and  $E_{rp}$ , is not the same throughout the environmental space.
- (6) In the factorial experiments, especially in low chloride solutions, no correlation occurred between the electrochemical parameters and visual evidence of localized corrosion. Since using only the electrochemical parameters will result in a statistical analysis that is physically meaningless, a Localized Corrosion Index (LCI) = Visual Rating \* ( $E_p - E_{rp}$ ) was used to analyze the results. With this approach, a good fit between the experimentally observed values and those predicted by the statistical model was obtained ( $R^2 = 0.993$ ).
- (7) The analysis of the factorial experiments indicated that chloride is a promoter of localized corrosion; nitrate is an inhibitor of localized corrosion; and chloride and nitrate have a major interaction, that is, nitrate is an effective inhibitor when the chloride level is high. The inhibitive effect of nitrate was found only above a concentration of 100 ppm. Fluoride was found to be an inhibitor of localized corrosion, its effect being evident mainly in the low chloride environment. Sulfate was found to be a mild promoter of localized corrosion. Temperature was found to have no significant effect within the range of temperatures studied.
- (8) In solutions with chloride concentrations  $\leq 1000$  ppm, both the pitting and repassivation potentials were relatively independent of temperature in the range of 50 to 95°C. In the 10,000 ppm chloride solution, both these potentials decreased with temperature. In the 6 ppm chloride solution, a small inverse temperature effect (greater localized corrosion with a decrease in temperature) was noted. In this latter case, localized corrosion occurred at high anodic potentials and, so it may not be relevant to repository conditions.
- (9) Considerable nonlinearity in the functional dependence of LCI on chloride was noted. The observed values of LCI at intermediate chloride concentrations were higher than predicted by the linear regression equation.
- (10) Nitrite was found to have the same inhibitory role as nitrate. Silicon added as metasilicate did not have any significant effect on localized corrosion. Replacement of  $K^+$  or  $Na^+$  by  $Mg^{2+}$  resulted in a slight decrease in the final pH of the solution. The effect of up to 348 ppm  $Mg^{2+}$  on localized corrosion also was not significant, especially compared to that published before.
- (11) Presence of dissolved oxygen and hydrogen peroxide increased the corrosion potential of Alloy 825 by 245 and 630 mV, respectively. The corrosion potential in the presence of 0.5 mM hydrogen peroxide was above the repassivation potential in the 300 ppm chloride solution, indicating a possibility of localized corrosion in this environment under long-term exposure.

#### 5.4 REFERENCES

- Beavers, J. A., and N. G. Thompson. 1988a. *Container Corrosion in High Level Nuclear Waste Repositories*. NRC Contract No. NRC-04-87-009. Year 1, First Semi-Annual Report. Columbus, Ohio: Cortest Columbus, Inc.
- Beavers, J. A., and N. G. Thompson. 1988b. *Container Corrosion in High Level Nuclear Waste Repositories*. NRC Contract No. NRC-04-87-009. Year 1, Second Semi-Annual Report. Columbus, Ohio: Cortest Columbus, Inc.
- Beavers, J. A., and N. G. Thompson. 1989a. *Container Corrosion in High Level Nuclear Waste Repositories*. NRC Contract No. NRC-04-87-009. Year 2, First Semi-Annual Report. Columbus, Ohio: Cortest Columbus, Inc.
- Beavers, J. A., and N. G. Thompson. 1989b. *Container Corrosion in High Level Nuclear Waste Repositories*. NRC Contract No. NRC-04-87-009. Year 2, Second Semi-Annual Report. Columbus, Ohio: Cortest Columbus, Inc.
- Beavers, J. A., and C. L. Durr. 1990a. *Container Corrosion in High Level Nuclear Waste Repositories*. NRC Contract No. NRC-04-87-009. Year 3, First Semi-Annual Report. Columbus, Ohio: Cortest Columbus, Inc.
- Beavers, J. A., and C. L. Durr. 1990b. *Container Corrosion in High Level Nuclear Waste Repositories*. NRC Contract No. NRC-04-87-009. Year 3, Second Semi-Annual Report. Columbus, Ohio: Cortest Columbus, Inc.
- Beavers, J. A., and N. G. Thompson. 1990c. *Environmental Effects on Corrosion in the Tuff Repository*. NUREG/CR-5435. Washington, D.C.: NRC.
- Beavers, J. A., N. G. Thompson, and W. V. Harper. 1990d. Potentiodynamic polarization studies of candidate container materials in simulated tuff repository environments. *Mat. Res. Soc. Symp. Proc.* 176: 533.
- Brigham, R. J. and E. W. Tozer. 1973. Temperature as a pitting criterion. *Corrosion*. 29(1): 33.
- Brown, M. H. 1969. The relationship of heat treatment to the corrosion resistance of stainless alloys. *Corrosion*. 25(10): 438.
- CNWRA. 1989. *Technical Operating Procedure for Preparing Electrochemical/Corrosion Test Specimens*. CNWRA TOP-003-01. San Antonio, Texas: CNWRA.

- CNWRA. 1990a. *Integrated waste package experiments*. Report on Research Activities for the Quarter April 1 through June 30, 1990. CNWRA 90-02Q. San Antonio, Texas: CNWRA: 5-1.
- CNWRA. 1990b. *Technical Operating Procedure for Preparing Simulated J-13 water and Its Modifications*. CNWRA Technical Operating Procedure TOP-010. San Antonio, Texas: CNWRA.
- CNWRA. 1990c. *Technical Operating Procedure for Conducting and Verifying Cyclic Polarization Tests*. CNWRA TOP-008. San Antonio, Texas: CNWRA.
- CNWRA. 1990d. *Unsaturated Mass Transport (Geochemistry)*. Report on Research Activities for the Quarter July 1 through September 30, 1990. CNWRA 90-03Q. San Antonio, Texas: CNWRA: 2-2.
- CNWRA. 1990e. *Integrated Waste Package Experiments*. Report on Research Activities for the Quarter July 1 through September 30, 1990. CNWRA 90-03Q. San Antonio, Texas: CNWRA: 5-2.
- Covino, B. S. 1987. *Fundamentals of Stainless Steel Acid Pickling Processes*. Bureau of Mines Information Circular 9195. New Steelmaking Technology from Bureau of Mines. Chicago, IL: United State Department of the Interior.
- Cragolino, G. A. 1987. Review of pitting corrosion in high temperature aqueous solutions. *Second International Conference on Localized Corrosion*. Houston, Texas. National Association of Corrosion Engineers (NACE), to be published.
- Craig, B., ed. 1989. *Handbook of Corrosion Data*. Materials Park, Ohio: ASM International: 605.
- Glass, R. S., G. E. Overturf, R. E. Garrison, and R. D. McCright. 1984. *Electrochemical Determination of the Corrosion Behavior of Candidate Alloys Proposed for Containment of High-Level Nuclear Waste in Tuff*. UCID-20174. Livermore, California: LLNL.
- Glassley, W. E. 1990. *Geochemical Interactions*. Presentation to the Nuclear Waste Technical Review Board. January 18-19. Pleasanton, California. Livermore, California: Lawrence Livermore National Laboratory (LLNL).
- Koch, G. H., J. M. Spangler, and N. G. Thompson. 1988. *Corrosion Studies in Complex Environments*. ASTM STP 970. Philadelphia, PA: American Society for Testing and Materials (ASTM).

- Leckie, H. P. and H. H. Uhlig. 1966. Environmental factors affecting the critical potential for pitting in 18-8 stainless steel. *J. of Electrochemical Society*. 113(12): 1262.
- Mason, R. L., R. F. Gunst, and J. L. Hess. 1989. *Statistical Design & Analysis of Experiments*. New York, NY: John Wiley & Sons.
- McCright, R. D., W. G. Halsey, and R. A. Van Konynenburg. December 1987. *Progress Report on the Results of Testing Advanced Conceptual Design Metal Barrier Materials under Relevant Environmental Conditions for a Tuff Repository*. UCID-21044, Livermore, CA: LLNL.
- Pabalan, R. 1989. *Test of Technical Procedure for Preparing Simulated and Modified J-13 Well Water*. Internal CNWRA Memorandum, August 10. San Antonio, Texas: CNWRA.
- Sedriks, A. J. 1979. *Corrosion of Stainless Steels*. New York, NY: John Wiley & Sons.
- Sridhar, N., G. Cragolino, and F. F. Lyle. 1990. *Progress Report of Activities and Recommendations in the Integrated Waste Package Experimental Program*. May 1988 through April 1990. CNWRA Intermediate Milestone Report 20-3704-042-005-900. NRC Contract No. NRC-02-88-005. San Antonio, Texas: CNWRA.
- Streicher, M. A. 1958. *Intergranular Corrosion Resistance of Austenitic Stainless Steels*. ASTM Bulletin. 229: 77. Philadelphia, PA: ASTM.
- Szklarska-Smialowska, Z. 1986. *Pitting Corrosion of Metals*. Houston, Texas: NACE.
- Thompson, N. G. and J. A. Beavers. 1990. *Effect of Ground-Water Composition on the Electrochemical Behavior of Carbon Steel: A Statistical Experimental Study*. ASTM STP 1086. Philadelphia, PA: ASTM.
- Van Konynenburg, R. A. 1986. *Radiation Chemical Effects in Experiments to Study Reaction of Glass in an Environment of Gamma-irradiated Air Groundwater and Tuff*. Livermore, CA: LLNL.

## 6. STOCHASTIC ANALYSIS OF UNSATURATED FLOW AND TRANSPORT

*by Rachid Ababou*

*Investigators: Rachid Ababou (CNWRA), Ronald Martin (CNWRA), and Michael Muller (SwRI)*

### 6.1 INTRODUCTION

A quantitative characterization of large-scale flow and radionuclide transport through the heterogeneous unsaturated, fractured rock of Yucca Mountain will be necessary to evaluate compliance with the siting criteria and performance objectives associated with the proposed HLW repository (10 CFR 60.112 and 60.113). The technical issues concerning radionuclide migration at Yucca Mountain must be understood so as to demonstrate that the hydrogeologic conditions at the repository site strongly inhibit radionuclide transport to the accessible environment and meet performance criteria. In particular, realistic modeling of the complex, heterogeneous flow and transport processes at Yucca Mountain requires incorporating the effects of relatively small-scale variability in modeling large-scale unsaturated flow and radionuclide transport. Examples of geologic features that can have significant overall effect on flow and transport are: discontinuities such as faults and fractures, finer fissures, and stratification of the porous matrix. Most of these features lead to anisotropic behavior.

The objectives of the Stochastic Analysis of Unsaturated Flow and Transport Project are as follows:

- To perform a review of the literature on field-scale flow-transport in the presence of heterogeneities, and assess available models and data relevant to the subject site;
- To select a global modeling approach to large-scale unsaturated flow and transport in heterogeneous, stratified, and fractured rock;
- To develop auxiliary models and numerical algorithms for incorporation into the global model; and
- To perform large-scale simulations and participate in the validation of flow and transport models for the Yucca Mountain repository.

The project is divided in three tasks to accomplish the objectives.

- (1) Task 1 - Review, Analysis, and Initial Development of Modeling Approach
- (2) Task 2 - Stochastic Submodel Development, Auxiliary Analyses, and Implementation of Related Numerical Algorithms

(3) Task 3 - Large-Scale Flow/Transport Simulation and Input/Output Data Analyses

The effective starting date of the project was February 2, 1990. The complete results of literature review, initial data assessment, model selection, and first stages of model development will be presented in the final Technical Report for Task 1, due May 1, 1991.

## 6.2 IDENTIFICATION OF SITE-SPECIFIC HYDROGEOLOGIC ISSUES

### 6.2.1 Regulatory Background

The basic objectives of the project will be better understood through a review of pertinent technical issues concerning radionuclide migration at Yucca Mountain. The NRC regulations in 10 CFR Part 60 require in particular that the geologic setting for a HLW repository exhibit a combination of conditions that provide reasonable assurance of waste isolation. It must be demonstrated that the hydrogeologic conditions at the repository site strongly inhibit radionuclide transport to the accessible environment. This requirement has been codified by NRC in terms of groundwater travel time [10 CFR 60.113(a2)]:

The geologic repository shall be located so that pre-waste-emplacment groundwater travel time along the fastest path of likely radionuclide travel from the disturbed zone to the accessible environment shall be at least 1,000 years or such other travel time as may be approved or specified by the Commission.

Following NRC's definition, the term groundwater is understood here to include all water below land surface. The accessible environment includes both the geosphere (atmosphere, land surface, oceans, etc.) and the portion of the lithosphere inside a controlled area. The latter extends laterally at most 10 kilometers away from the boundary of the underground facility in all horizontal directions (10 CFR 60.2). But, if radionuclides reach the water table through the unsaturated zone, subsequent transport through the saturated zone may possibly constitute a relatively faster route to the accessible environment. Accordingly, it is assumed in this project that the water table is equivalent to the accessible environment, an assumption which can be discarded later for purposes of global performance assessment.

Future modification of the 1,000 year rule for travel time was not ruled out by NRC (10 CFR 60.113.b). The travel-time rule quoted above makes implicit use of probabilistic ("likely") terminology. This interpretation of the rule raises a question directly relevant to this project: how "likely" should the fastest path of radionuclide travel time be for the performance criteria to be met?

Another related question concerns the fastest radionuclide travel pathway. Compliance with the standards promulgated by the Environmental Protection Agency (EPA) may possibly require a different formulation of the problem; that is, characterization of the whole distribution

of travel pathways and of the total mass of radionuclides that will be transported per unit time through each given class or group of pathways. Therefore, in addition to the distribution of travel times, the distribution of radionuclide mass flux densities (mass per unit time crossing a unit area) may also be viewed as a meaningful performance criterion. Furthermore, due to the presence of heterogeneities at many different scales at the site, travel times and other observables need to be characterized unambiguously for prescribed scales of averaging in space and time. The modeling approach should be selected with these requirements in mind.

### 6.2.2 Specific Technical Issues

In the case of the Yucca Mountain site, the questions raised above are complicated by the highly heterogeneous and nonlinear nature of the subsurface flow processes. It will be useful to briefly describe some aspects of the hydrogeologic conditions prevailing at the site before presenting the general approach used in this research.

The design repository zone as envisioned by the Department of Energy (DOE) is intended to be situated deep in relatively dry unsaturated tuffs, about 300 meters below land surface and 250 meters above the water table (Site Characterization Plan, 1988: Sections 3.9.1, 3.9.2, 3.9.3, and references therein). The hydrogeologic environment at the repository site is illustrated in Figure 6-1, from DOE's Site Characterization Plan (1988, Figure 3.40), and in Figure 6-2, from Peters and Klavetter (1988, Figure 1). The flow pathways marked by arrows in both figures are hypothetical.

In addition to the presence of markedly distinct geologic units and tectonic faults, the geologic units are themselves variously fractured. The Topopah Spring unit (TSn) where the repository is located is a low-porosity welded tuff believed to be "densely fractured," while the underlying Calico Hill unit (CHn) is a higher porosity nonwelded tuff with seemingly much lower fracture density (Site characterization Plan, 1988). Finally, the net annual infiltration from rainfall and surface water over Yucca Mountain is believed to be on the order of 0.1-1.0 mm/year in the mean, from a mean annual rainfall of about 150 mm/year. Without going into much detail, these mean values do not take into account the more extreme rainfall rates that may occur due to interannual fluctuations, interseasonal fluctuations, and individual storms. In addition, they only reflect contemporary rainfall and infiltration conditions.

Under the ambient conditions just described, any radionuclides hypothetically released from the repository zone probably will be transported predominantly in the unsaturated flow regime. Locally saturated flow conditions and perched water tables may also occur in the vadose zone, possibly due to short and intense rainfalls or extreme climatic fluctuations on larger time scales. Therefore, in this project, the term "unsaturated" will include partially saturated as well as unsaturated conditions unless stated otherwise. In addition, this project will fully investigate three-dimensional groundwater flow systems with horizontal and vertical flow paths, since both types of pathways may eventually carry radionuclides to the "accessible environment"; that is, to lateral compliance boundaries (through horizontal pathways), to the ground surface (vertically upwards), and to the water table (vertically downwards). Since this investigation is

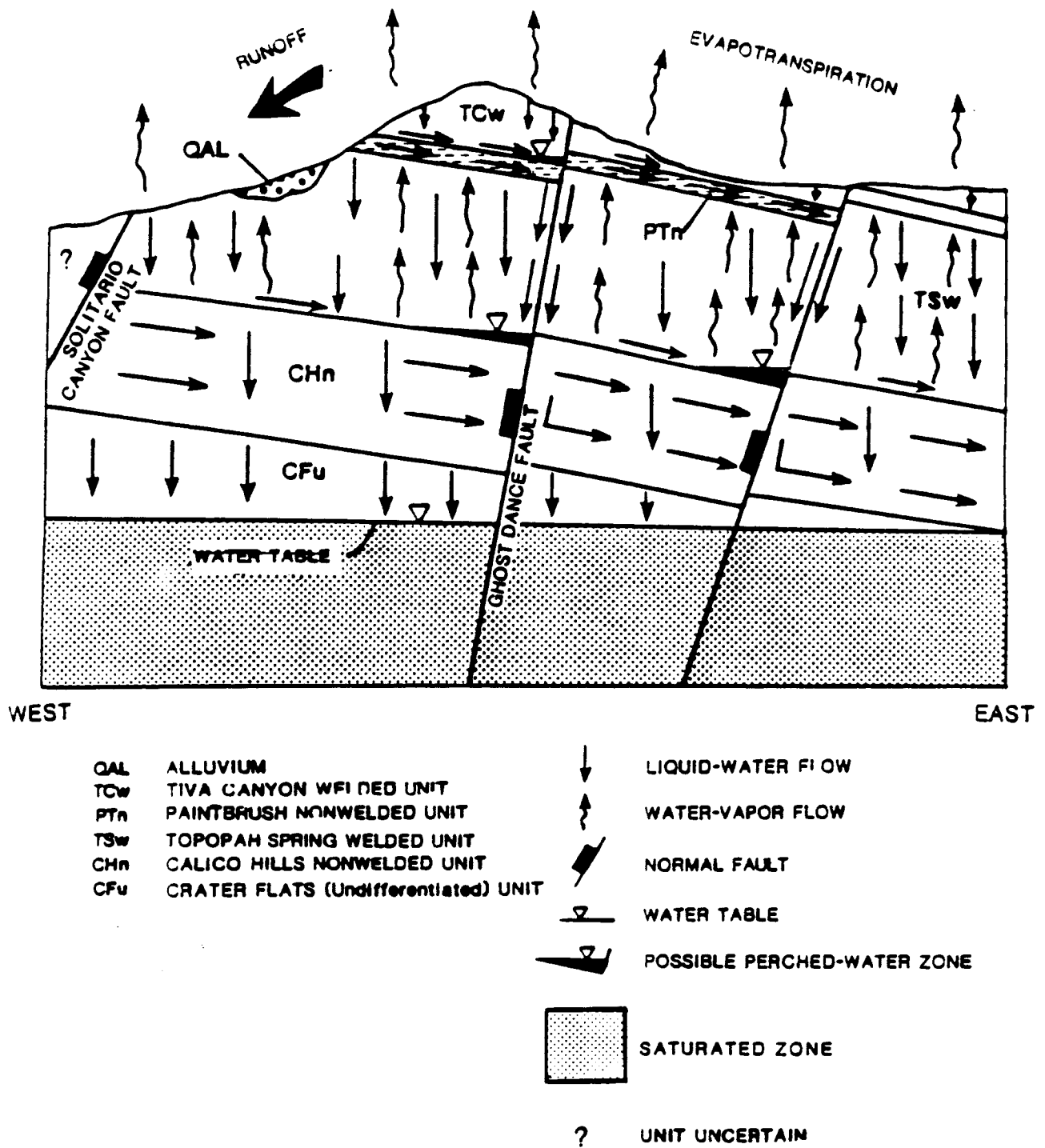


Figure 6-1. Idealized moisture flow system through the east-west section at Yucca Mountain (modified from Montazer and Wilson, 1986, and DOE Site Characterization Plan, 1988)

PETERS AND KLAVETTER: MODEL FOR WATER MOVEMENT

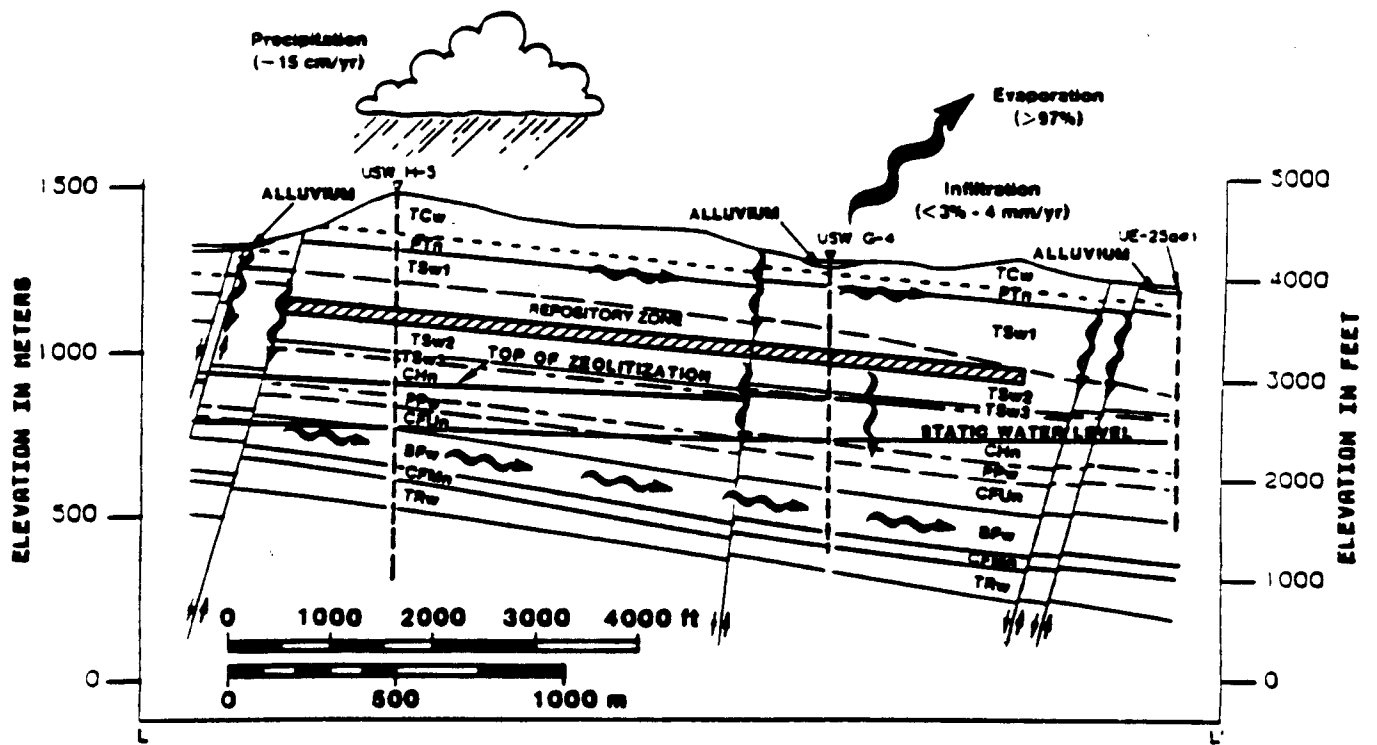


Figure 6-2. Idealized moisture flow system through the east-west section at Yucca Mountain (from Peters and Klavetter, 1988)

limited to the case of single-phase water flow, the possible upwards flow of water vapor will not be modeled (only upwards liquid flow). For all practical purposes, the concern here will be mostly with the horizontal and downward liquid movements in a variably saturated or unsaturated environment.

Furthermore, because of the natural heterogeneity, stratification, and fracturing of the porous rock, significant variability of flow and radionuclide pathways and travel times is expected to occur at Yucca Mountain. Formation heterogeneities could span a wide range of scales from submeter scale up. This is to be contrasted with the global length scales of interest: typically hundreds of meters vertically and around 1 to 10 kilometers horizontally. Theoretical and experimental research conducted in the last decade has shown that formation heterogeneity enhances the large-scale dispersion of tracer particles transported by water. The presence of near-horizontal strata and fractures can also increase the lateral spreading of radionuclides, much more so than would occur in isotropic porous media. The presence of vertical fractures may lead to contrary effects, depending on the flow regime and ambient moisture conditions.

Finally, the occurrence of high-intensity rainfall events, arriving erratically in time, may drastically modify the subsurface flow regime from what would be inferred using an average infiltration rate model. Perhaps the shortest significant time scale of climatic inputs to the system may be taken to be storm duration, typically on the order of hours or even less. This is indeed much smaller than the global time scale of interest for contaminant migration, say on the order of  $10^3$ - $10^4$  years or more.

In summary, realistic modeling of the complex, heterogeneous flow and transport processes at Yucca Mountain will require incorporating the effects of relatively small-scale space-time variability over fairly large space-time scales of simulation. In this project, a stochastic approach will be used to account for the effects of space-time variability in modeling large-scale unsaturated flow and radionuclide transport under the hydrogeologic conditions just described. As presently envisioned, this conceptual approach will be enriched by auxiliary models (submodels) to represent separate or sub-scale processes, and will be implemented numerically.

### 6.3 CONCEPTUAL APPROACHES TO FIELD-SCALE FLOW MODELING

Here, the focus is on the flow problem as a prerequisite to radionuclide transport modeling. In particular, accurate modeling of flow and transport over large space-time scales depends heavily on an adequate representation of a hierarchy of natural heterogeneities and/or fractures of many sizes and shapes. [See, for instance, Cushman (1990) for a recent collection of works in this area and Ababou and Gelhar (1990) for a fractal approach to aquifer flow heterogeneity.] One of the main difficulties in large-scale, subsurface flow-transport modeling is the representation of such three-dimensional heterogeneities and discontinuities. Moreover, in the case of unsaturated flow, the spatial features of geologic media must be represented through nonlinear matrix/fracture hydrodynamic properties. The difficulty in modeling heterogeneous flow processes, therefore, is compounded in the case of partially saturated or

unsaturated flow by the nonlinear nature of the governing equations because of the nonlinear pressure-dependence of water retention and hydraulic conductivity.

Based on the project's ongoing literature review, scientific approaches to field-scale flow modeling can be broadly classified in two types. The first is essentially a direct simulation of the detailed hydrodynamics based on classical Darcy-Richards equations. This requires an explicit representation of fine-scale heterogeneities, stratification, and/or fracturation of the geologic medium (e.g., based on a combination of geostatistical models and hydrogeologic data). The second approach, coarse-scale or effective modeling makes use of auxiliary sub-scale models, more or less physically-based, for describing in a simplified way the detailed hydrodynamics processes not explicitly accounted for in the coarse-scale simulation model. Combinations of these two approaches are conceivable (e.g., explicit representation of major fracture networks combined with implicit representation of remaining fractures and porous matrix heterogeneity).

A clear advantage of the direct simulation approach is that, in principle, it requires only basic phenomenological equations to model the flow system, such as the classical Darcy-type equations, and additional constitutive relations for fractures, if any. However, while fine-scale spatial variations of groundwater velocity are known to play a significant role in radionuclide transport and dispersion (Gelhar and Axness, 1983; Winter et al, 1984; Dagan, 1987), there are obvious limits to how extensively and explicitly the broad spectrum of geologic heterogeneities can be represented in a flow model. In the first place, site-specific data are not likely to be available with the required degree of detail, so that much work must be put in auxiliary analyses (statistical interpolation and conditioning; use of soft information; statistical continuum models of heterogeneous, porous media; random fracture network models; and so on). Secondly, the computational demands are likely to be high, which requires an informed evaluation of computational feasibility and a careful selection of advanced solution methods and supercomputer resources. The computational demands in the case of fractured porous media, with both continuum and discontinuum-type heterogeneity, are likely to be even higher owing to the extreme disparity of active fluctuation scales -- from fracture aperture up to the largest identifiable geologic features.

The alternative approach to field-scale modeling based on auxiliary hydrodynamic models may alleviate part of the above-mentioned demands. The main idea behind this second type of approach is to simplify the overall flow model by subsuming certain spatial features and processes in simplified black-box models. For instance, only meso-scale to macro-scale features would be explicitly represented, while micro-scale to meso-scale heterogeneities and fractures would be subsumed in various submodels. The simplest types of submodels serve to express effective constitutive relationships, matrix/fracture transfer relationships, and so forth in a quasi-analytical fashion. As mentioned earlier, this type of approach can be used in combination with explicit modeling of certain types of heterogeneities, major geologic features, and so on, while other aspects are treated implicitly. Part of the modeling effort is thus transferred from the global model to the submodel(s). However, many questions regarding the conceptual/empirical basis of the submodels, their consistency with the global model, their intrinsic range of validity,

and the identifiability of their internal parameters must be fully answered before such submodels can be used with confidence.

Based on these considerations from the ongoing literature review, the following areas of research have been initially pursued towards the development of a large-scale flow model for Yucca Mountain:

- Analyses of numerical algorithms and computational feasibility
- Direct simulation, visualization, and interpretation of generic three-dimensional unsaturated flow systems
- Hydrodynamic sub-models for heterogeneous, stratified, composite, and/or fractured porous media.

The initial research accomplishments in these three areas are reported below.

## **6.4 NUMERICAL HYDRODYNAMICS**

### **6.4.1 Numerical Analysis of Nonlinear Unsaturated Flow**

In an initial effort to evaluate certain aspects of the unsaturated flow-modeling problem from a numerical viewpoint, a study was recently developed to examine the effects of nonlinearity on the stability and accuracy of numerical solutions, the interplay between capillary-driven and gravity-driven flow, and the convergence of nonlinear solution schemes in the case of homogeneous media (Ababou, 1990). The findings of this study outline the role of gravitational flow, which is expressed through a dimensionless Peclet number ( $Pe = \alpha \Delta z$ ) proportional to the slope  $\alpha$  of the log-conductivity/pressure curve. The parameter  $\lambda_c = 1/\alpha$  is essentially a capillary diffusivity length scale. The mesh size of a numerical flow model should be no larger than  $\lambda_c$ , which typically lies in the range 10 to 100 cm for sandy to clayey soils, but could be smaller for a fractured rock mass and larger for the tight porous matrix of intact rock.

Consider now the case where the numerical model explicitly incorporates the detailed three-dimensional features of the heterogeneous geologic medium. In the case of a continuum porous matrix with random heterogeneity, previous theoretical analyses and high-resolution numerical experiments (Ababou, 1988; Ababou and Gelhar, 1988), indicate that the effects of nonlinearity and heterogeneity are inextricably intertwined. This makes it difficult to analyze not only the simulation results, but also the numerical solution schemes themselves. Nevertheless, the accuracy of solutions can be evaluated ex-post using mass balance checks. The large datasets generated by the detailed numerical model also can be processed graphically and compared to other information from field observations and/or theoretical studies. A specific example along these lines is presented below (Section 6.5).

## 6.4.2 Algebraic System Solvers

In the type of numerical flow model envisioned here, the solution of large sparse algebraic systems constitutes the computationally intensive part (computational kernel) of the numerical code. In the case of three-dimensional, high-resolution field-scale models of unsaturated flow, the systems to be solved will be large, nonlinear, and poorly conditioned due to high-conductivity contrasts.

Although the final solution algorithms have not been selected yet, the development of a series of iterative, sparse matrix solvers (modules) that exploit the particular diagonal data structure of the discretized, three-dimensional unsaturated flow equations has been pursued. The initial focus was on symmetric matrix solvers, based on the observation that unlike Newton methods, Picard-type linearization schemes generate sequences of symmetric matrix systems (Ababou, 1988). The new preconditioned iterative solvers are based on SIP (Strongly Implicit Procedure) and Conjugate Gradients iterations with various types of preconditioning. Their efficiency will be tested in Task 2.

## 6.5 DIRECT HIGH-RESOLUTION SIMULATIONS

### 6.5.1 Background

As mentioned above, one possible modeling approach is to take into account the detailed geologic features, explicitly and directly, in the governing flow equations. These must then be solved numerically. A direct numerical simulation approach based on a continuum random-field representation of heterogeneity was previously developed for saturated groundwater flow and transport (Ababou, et al., 1989; Tompson and Gelhar, 1990), and for unsaturated flow systems as well (Ababou, 1988). Even in the absence of explicit fractures, the numerical model of spatially random *unsaturated* flow attains a high level of complexity. The simulation results require a good deal of auxiliary analysis, both experimental and theoretical, in order to be properly understood and interpreted (Ababou, 1988; Ababou and Gelhar, 1988). If more complex types of processes were included (e.g., multiphase and coupled hydro-thermo-mechanical processes) the overall model could become even more intricate. Although this project is concerned only with the case of partially saturated flow the latter can be viewed as a special case of immiscible two-phase flow (water, plus a passive air phase). The results obtained so far without fractures are discussed below. Fractures will be introduced in Tasks 2 and 3 of the project.

### 6.5.2 Simulation Results and Analysis

A high-resolution, three-dimensional finite-difference model based on a mixed variable formulation of partially saturated/unsaturated flow has been previously used to model strip-source infiltration and drainage in a randomly heterogeneous and imperfectly stratified soil (Ababou, 1988; Ababou and Gelhar, 1988). The flow regime, soil properties, and boundary

conditions were selected to mimic (albeit with some differences) the first Las Cruces strip source experiment, one of the test cases of INTRAVAL (INTRAVAL, 1991). The nonlinear behavior and statistical properties of the soil were inferred, in part, from preliminary hydrodynamic data collected at the trench site. The 15 x 15 x 5 m computational domain was discretized into 300,000 cells, each with its own distinct unsaturated conductivity curve.

As part of our involvement in the validation exercise of INTRAVAL, the transient moisture-plume simulation data were processed and visualized on an IRIS 4D workstation at the CNWRA, with the aid of three-dimensional isosurface and volumetric color graphics software (Figures 6-3 and 6-4). This approach provided direct evidence of moisture-dependent horizontal spreading, which lends credence to a previous theoretical finding based on linearized spectral perturbation solutions of stochastic unsaturated flow Mantoglou and Gelhar, (1987). Thus, it can be seen from the color pictures of Figures 6-3 and 6-4 that the marginally wet outer shell of the plume (blue) exhibits more horizontal spreading than the wet core of the plume (purple). In the case at-hand, moisture-dependent anisotropy due to the imperfect, random layering of hydraulic soil properties. Such imperfect stratification is a pervasive feature of both consolidated and unconsolidated geologic media, including the tuff formations of Yucca Mountain.

## 6.6 EFFECTIVE AND SUB-SCALE HYDRODYNAMIC MODELS

As explained earlier (Section 6.3), auxiliary submodels may be needed to achieve full-scale simulations of unsaturated flow in complex environments like Yucca Mountain. A continuum submodel for the effective hydrodynamic properties of heterogeneous unsaturated media with anisotropic and/or fracture-like features is being developed. Briefly, the submodel is based on a general two-parameter random-field model of unsaturated conductivity. Besides anisotropy due to stratification and/or preferred fracture orientation, the model also takes into account statistical cross-correlation between saturated conductivity and capillary diffusivity ( $\lambda_c$  - defined earlier as the inverse slope of log-conductivity versus pressure). The statistical properties of the resulting family of unsaturated curves are investigated analytically. The preliminary analysis of conductivity curves reveals the existence of an upper envelope and a dense crossing point. The latter occurs at a certain critical pressure which corresponds, roughly, to a local minimum of the effective conductivity anisotropy ratio as a function of pressure. Both the upper envelope and the crossing point of unsaturated conductivities appear to depend significantly on the cross-correlation coefficient.

These findings need to be further confirmed using direct simulations and field-data analyses. In addition, related results on the effective conductivity tensor of randomly stratified, saturated media could also be exploited (Ababou, 1990). Refinements of these and other similar concepts will be explored, with a view to modeling unsaturated flow in highly heterogeneous fractured and porous rocks (Task 2).

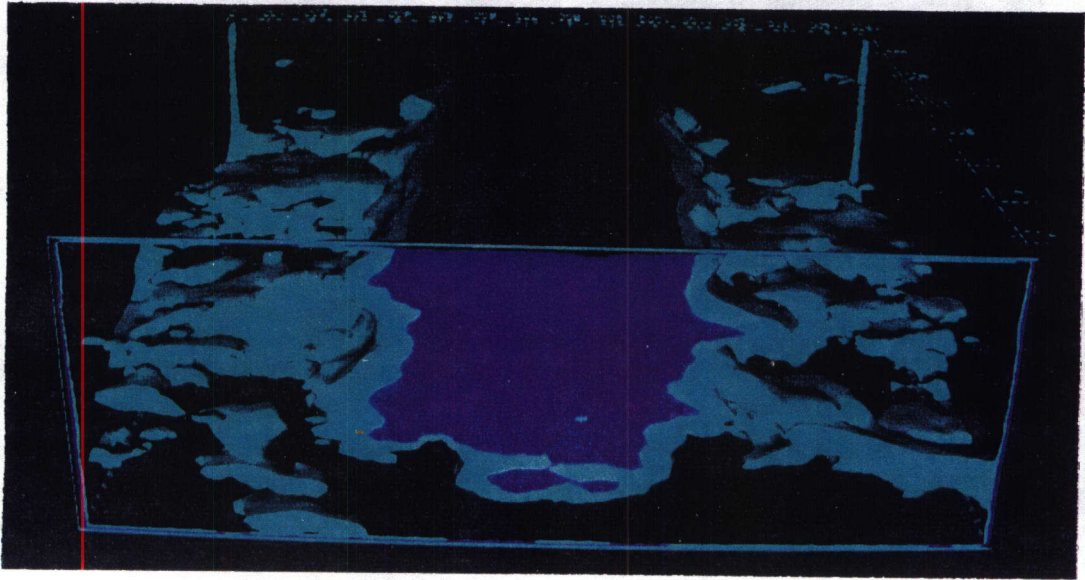


**Figure 6-3. Front view of a peeled-off three-dimensional moisture plume from stochastic flow simulations**

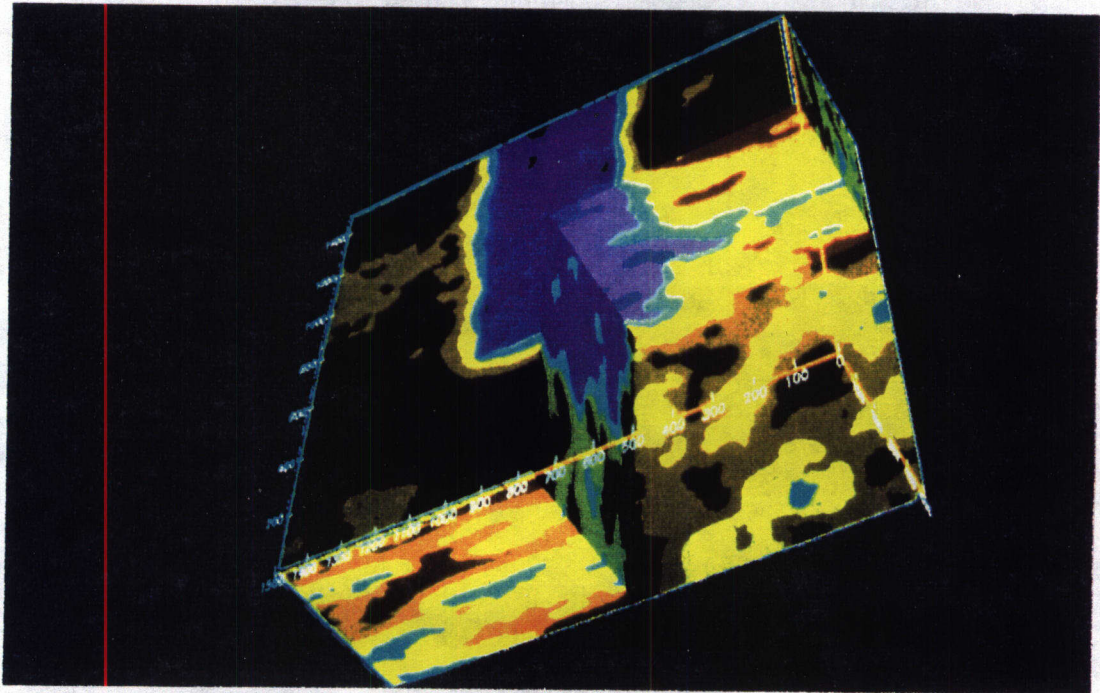


**Figure 6-4. Back view of a three-dimensional moisture pattern from stochastic flow simulations; the cut-off moisture plume is visible in purple and blue**

## 6.7 SUMMARY

The work accomplished so far has produced preliminary results in several areas and indicated future research towards the simulation of realistic, heterogenous unsaturated flow and contaminant systems at Yucca Mountain. The site-specific and regulatory issues pertinent to the subject site were analyzed in Section 6.2. In this report, the primary focus was on unsaturated groundwater flow modeling in highly heterogeneous geologic formations. While the unknown effects of hydrogeologic variability in both space and time need to be investigated, the problems addressed here relate essentially to spatial heterogeneity, with a view to producing realistic groundwater velocities for field-scale radionuclide transport simulations.

Based on the project's ongoing literature review, two broad types of conceptual modeling approaches were identified and discussed in Section 6.3: direct high-resolution simulation with explicit representation of heterogeneities, and coarser-scale simulation with auxiliary models for separate effects and sub-scale flow processes. Numerical analyses and algorithms relevant to both types of models were developed (Section 6.4); that is, (1) numerical analyses on the effects of nonlinearity and of the gravitational components of flow with regard to accuracy, stability, and convergence of nonlinear iterations and (2) development of specialized sparse, iterative matrix solvers. In addition, progress was made in the area of direct high-resolution flow simulation as part of an involvement in the model-validation exercise of INTRAVAL. Building on previous simulation works, large three-dimensional datasets were visualized and interpreted, notably in terms of the relation between soil stratification and horizontal water movement (Section 6.5). Finally, a new sub-scale model of hydrodynamic properties is being developed with a view to modeling large-scale unsaturated flow in stratified and fractured rock formations (Section 6.6).

## 6.8 REFERENCES

- Ababou, R. 1988. *Three-Dimensional Flow in Random Porous Media*. Ph.D thesis. Dept. of Civil Engineering, Massachusetts Institute of Technology (MIT). 2 vols. Cambridge, Massachusetts MIT: 833.
- Ababou, R., and L. W. Gelhar. 1988. A high-resolution finite difference simulator for 3D unsaturated flow in heterogeneous media. *Proceedings of VIIth Conference on Computational Methods in Water Resources*. New York: Elsevier & Computational Mechanics Publications: 1: 173-178.
- Ababou, R., D. McLaughlin, L. W. Gelhar, and A. F. Tompson. 1989. Numerical Simulation of Three Dimensional Saturated Flow in Randomly Heterogeneous Porous Media, *Transport in Porous Media*, 4: 549-565.

- Ababou, R. 1990. Identification of effective conductivity tensor in randomly heterogeneous and stratified aquifers. *Fifth Canadian American Conference on Hydrogeology: Parameter Identification and Estimation for Aquifers and Reservoirs*. Calgary Alberta, Canada. Dublin, Ohio: Water Well Journal Publishing Company, National Water Well Association (to be published).
- Ababou, R. 1990. Numerical analysis of unsaturated flow equations. *Proceedings VIIIth Conference on Computational Methods in Water Resources*. G. Gambolati et al., eds. Venice, Italy: Computational Mechanics Publications and Springer-Verlag: A:151-160.
- Ababou, R., and L. W. Gelhar. 1990. Self-similar randomness and spectral conditioning: analysis of scale effects in subsurface hydrology. *Dynamics of Fluids in Hierarchical Porous Media*. Chapter XIV. J. Cushman, ed. New York: Academic Press: 393-428.
- Cushman, J. 1990. *Dynamics of Fluids in Hierarchical Porous Media*. J. Cushman, ed. New York: Academic Press: 505.
- Dagan, G. 1987. Theory of solute transport by groundwater. *Ann. Rev. Fluid Mech.* 19: 183-215.
- DOE. December 1988. Site hydrogeologic system. *Site Characterization Plan Vol. II, Part A, Chap. 3.9.*, Nuclear Waste Policy Act, Section 113. DOE/RW-0199. Washington, D.C.: DOE.
- Gelhar, L. W., and C. L. Axness. 1983. Three-dimensional stochastic analysis of macrodispersion in aquifers. *Water Resources Research*. 19: 161-180.
- INTRAVAL. 1991. An International Project to Study Validation of Geosphere Transport Models. Unsaturated Zone Test Cases, Appendix C: Las Cruces Trench Site, in Phase I Final Report, to be published by Swedish Nuclear Power Inspectorate, Box 27106, S-102, 52, Stockholm, Sweden.
- Mantoglou, A., and L. W. Gelhar. 1987. Effective hydraulic conductivities of transient unsaturated flow in stratified soils. *Water Resources Research*. 23(1): 57-67.
- Peters, R. R., and E. A. Klavetter. 1988. A continuum model for water movement in an unsaturated fractured rock mass. *Water Resources Research*. 24(3): 416-430.
- Tompson, A. F. B. and L. W. Gelhar. 1990. Numerical simulation of solute transport in three-dimensional, randomly heterogeneous porous media. *Water Resources Research*. 26(10): 2541-2562.

Winter, C. L., C. M. Newman, and S. P. Neuman. 1984. A perturbation expansion for diffusion in a random velocity field. *SIAM J. Appl. Math.* 24: 411-424.

## 7. GEOCHEMICAL NATURAL ANALOGS

by English C. Percy and William M. Murphy

*Investigators: English C. Percy (CNWRA) and William M. Murphy (CNWRA)*

### 7.1 TECHNICAL OBJECTIVES

The Geochemical Analog Project is designed to provide knowledge of the state of the art in natural analog studies applied to contaminant transport and to conduct investigations at a specific site or sites. Task 1 of the project, "Literature Review," was completed with the submission of the report entitled *Geochemical Natural Analog Literature Review* (Percy and Murphy, 1990, CNWRA 90-008). Task 2, "Identification of Site and Development of Workplan" began late in 1990 and is underway at present. Objectives of Task 1 included: compilation and evaluation of research conducted on natural analogs relevant to contaminant transport at the candidate HLW repository at Yucca Mountain; review of literature on potential sites for a natural analog study or studies to be undertaken; and evaluation of these sites with respect to the (1) degree of relevance to understanding contaminant transport at Yucca Mountain, (2) possibility of constraining initial and boundary conditions, (3) feasibility of research at the sites, and (4) potential usefulness for validation of the unsaturated-zone contaminant-transport model.

### 7.2 RESEARCH RESULTS FROM TASK 1

Natural analogs are occurrences of a material or process in nature that may be viewed as comparable to some aspect of a system of interest. In this case, the system of interest is a HLW repository. Natural materials approximating components of a repository may be studied to gain a better understanding of the expected behavior from the repository material. Similarly, a process that occurs (or has occurred) in nature and that may be significant to the performance of a repository may be investigated to learn of possible effects on a repository system.

Natural analog studies have been conducted for many years, and geologists have always been limited in their investigative approaches by the physical and temporal scales of many aspects of their subject. Mountains do not fit into a laboratory, and the time and forces involved in building them are not available for experiments. In many cases, therefore, the only test of a geologic hypothesis is how well it fits with observations of nature's experiments. Consequently, it is often difficult to prove a geologic hypothesis in the same sense that hypotheses in other disciplines can be proven through rigorous duplication of experiments by many investigators. Geologists rely instead on generalizations inferred from numerous observations of analogous rocks to test their ideas; that is, they use natural analogs.

### **7.2.1 Limitations of Natural Analog Studies**

Though natural analog studies extend the sort of investigations possible in the laboratory, they have a variety of inherent limitations. Chief among these is the incompleteness of the geologic record, at any geologic analog site, of all of the processes and events important (or potentially important) to the development of the analog. Furthermore, the record that exists may be uninterpretable. Erosion, metamorphism, hydrothermal or meteoric alteration, and structural disruption are all processes commonly responsible for erasing portions of the geologic record. Even if a given portion of the geologic record is not erased by a later event, the overlapping effects of subsequent phenomena may make it difficult or impossible to sort out the detailed history of geologic events and processes which occurred in an area. Consequently, it is generally difficult to adequately constrain the initial and boundary conditions for specific processes within natural geologic systems. Temperatures, pressures, fluid compositions, timing of process onset, and duration are all examples of factors that may only be indirectly estimable. Of course, limits may always be placed, but they may be broad. Quantification of effects to the degree desired is often difficult.

There are no natural analogs of an entire repository system. A given site will only be analogous to some portion of a repository or to a subset of the processes that will occur in a repository. Furthermore, additional processes will have occurred that are not characteristic of the repository. Therefore, choices must be made as to the processes of greatest relevance and the ability to isolate them for study.

The elements and materials involved in an analog study are, by definition, approximations of the materials and elements to be placed in a repository. The approximations may be quite close; for example, uraninite is a good analog to the bulk composition and crystal form of spent fuel (Finch and Ewing, 1989); basaltic and rhyolitic glasses hydrate similarly to vitrified HLW (Arai et al., 1988). However, there is almost always some deviation; for example, uraninite does not contain the internal phase segregations present in spent fuel; borosilicate nuclear waste forms have compositions substantially different from basaltic or rhyolitic glass. Some technological materials (e.g., cast steel) are particularly difficult to approximate with natural materials.

The 10,000 year period required for HLW isolation is a difficult period to approximate with natural analogs. Most ore deposits are much older ( $10^6$  to  $10^9$  years), and most anthropogenic sites are much younger (0 to  $10^3$  years). To make the best use of an analog study, the process(es) studied should have occurred over an interval of  $10^3$  to  $10^4$  years.

### **7.2.2 Contributions of Natural Analog Studies**

The above limitations notwithstanding, critical contributions can be made by natural analog studies. Only through the use of natural analogs can we identify and confirm that a process occurs in nature as well as in a laboratory or in theory. Natural analogs allow testing of the pertinence of individual processes over geologic time and the assessment of the relative

importance of various processes as they interact in nature. Through analog investigations we may determine the conditions under which the processes occur and the effects of the processes as well as the magnitude and duration of the phenomena.

Mathematical models of natural phenomena are developed through a process of iterative interaction with natural analogs and laboratory and field experiments. Long-term predictions of models can in no way be directly validated via laboratory or field experiments; and given the uncertainties involved in analog studies, it may be that a given model cannot be validated (in a strict sense) through the use of natural analogs. However, natural analogs provide the only means of testing the models of long-term processes for relevance. The International Atomic Energy Agency (IAEA) definition of validation of a model is:

A conceptual model and the computer code derived from it are 'validated' when it is confirmed that the conceptual model and the derived computer code provide a good representation of the actual processes occurring in the real system. Validation is thus carried out by comparison of calculations with field observations and experimental measurements. (IAEA, 1982)

The results of short-term, small-scale laboratory experiments and of the long-term predictions of models based on the laboratory experiments may be compared to observations of natural systems which have operated for long periods at large scales (i.e., natural analogs). This process of testing by comparison constitutes validation of the model. The limitations of validation by comparison, however, must be clearly understood. The comparisons are not expected to be exact; in fact, because performance-assessment models are typically conservative in their predictions, they will deliberately differ from reality. Comparison of model predictions with the results of natural analog investigations therefore will generally only permit confirmation that the model takes into account the appropriate processes in appropriate ways. Validation of a predictive model by such comparison results in reasonable assurance that the model accurately reflects future behaviors. This is the level of confidence required by 10 CFR Part 60 section 60.101(a)(2), which reads in part:

Proof of the future performance of [a HLW repository] over time periods of many hundreds or many thousands of years is not to be had in the ordinary sense of the word. For such long-term objectives and criteria, what is required is reasonable assurance . . . .

### 7.2.3 Natural Analog Studies

A wide variety of geologic sites have been studied as natural analogs, including: ore deposits, igneous contact zones, natural glasses, nuclear explosion sites, uraniferous nodules, sediment contacts, hydrothermal systems, mine tailings, rock alteration, archaeological sites, and uraniferous veins. A complete listing and description of the sites identified is found in the Task 1 milestone report CNWRA 90-008 (Pearcy and Murphy, 1990).

#### **7.2.4 Processes and Events Likely to Control Contaminant Transport at Yucca Mountain**

Processes and events that are likely to control contaminant transport at Yucca Mountain fall into two groups:

- (1) Those likely to be important at any geologic HLW repository
- (2) Those peculiar to Yucca Mountain.

##### ***7.2.4.1 Processes Important to Contaminant Transport at any Geologic HLW Repository***

Processes likely to be important in general to contaminant transport at geologic HLW repositories include:

Mineral/container/waste form dissolution and/or precipitation

Aqueous speciation of repository fluids (including organic complexing and radioelement speciation)

Colloid transport and/or retardation of waste elements  
microbial activity (redox controls, mineral precipitation/dissolution, and formation of organic colloids)

Matrix and intra-crystalline diffusion of elements

Fracture flow of fluids and gases

Matrix flow of fluids and gases

Changes in permeability due to thermal, chemical, or physical effects

Redox equilibration (kinetics) and redox front migration

Chemical species and mineral phase stability, solubility and metastability

Radiolysis

Thermally driven elemental diffusion

Convective (buoyancy driven) fluid movement

Alpha recoil effects

Adsorption

Ion exchange

Coprecipitation

Dispersion

#### ***7.2.4.2 Processes and Events Peculiar to Contaminant Transport at Yucca Mountain***

A number of processes important to contaminant transport result from (1) the occurrence of the proposed repository at Yucca Mountain in tuffaceous host rock, (2) the chemically oxidizing environment of the site, and (3) the partial hydrologic saturation of the proposed repository horizon. The host tuffs contain large amounts of glass fragments which interact readily with groundwater. This interaction may take the form of elemental exchange, dissolution of the glass, or alteration of the glass or its components to new minerals. Large volumes of the tuffs underlying the repository horizon have been altered so that they contain abundant zeolites; sorption onto these zeolites is likely to impede radionuclide transport. The response of these tuffs to thermal and hydrothermal alteration may change their sorptive capacity. Mineralogic alteration of the tuffaceous host rocks may also result in volume change which, could open fractures, therefore enhancing fluid flow and contaminant transport. The oxidizing environment at the site will (1) increase the potential for the waste forms and waste containers to degrade by oxidation, (2) determine the oxidation state of the radioelements and the phases that control their solubilities and concentrations, and (3) increase mobility of contaminant species that are more soluble in an oxidized state. The lack of hydrologic saturation at the repository level means that unsaturated fluid flow will control contaminant transport (as long as undersaturation is maintained), including vapor-phase transport. Undersaturation also means that the hydrostatic pressure will be low, increasing the tendency for water vaporization in the presence of a thermal pulse from the waste.

#### **7.2.5 Geochemical Processes Amenable to Natural Analog Study**

All of the processes listed above are potentially amenable to analog study. Choices among them therefore depend on which processes are considered to be the most important to contaminant transport at the proposed repository at Yucca Mountain, and which are well exhibited at identified natural analog sites.

### 7.2.6 Criteria for the Successful Use of Natural Analogs

Chapman et al. (1984) presented the following criteria for selecting analogs:

- (1) The process involved should be clear-cut. Other processes that may have been involved in the geochemical system should be identifiable and amenable to quantitative assessment as well so that their effects can be 'subtracted.'
- (2) The chemical analogy should be good. It is not always possible to study the behavior of a mineral system, chemical element, or isotope identical to that whose behavior requires assessing. The limitations of this should be fully understood.
- (3) The magnitude of the various physico-chemical parameters involved (such as pressure, temperature, pH, Eh, and concentrations) should be determinable, preferably by independent means and should not differ greatly from those envisaged in the disposal system.
- (4) The boundaries of the system should be identifiable (whether it is open or closed and, consequently, how much material has been involved in the process being studied).
- (5) The time scale of the process must be measurable, since this factor is of the greatest significance (the *raison d'etre*) for a natural analog.

Airey and Ivanovich (1985) added a requirement for transport analogs:

- (1) A contaminant transport analog requires a spatial discontinuity across which to observe transport.

In addition to the above criteria:

- (2) The source term (e.g., the original distribution of the elements of interest) must be well constrained.
- (3) The environmental analog must be close. The argument that an analog has suffered more extreme conditions than the system of comparison and therefore provides a conservative example is inappropriate. *More extreme* conditions are *different* conditions than those present in the system of comparison; such different conditions may include different processes or different combinations of processes than at the site of interest.

It must be understood that it is highly unlikely that any one site can fully meet all of these desirable conditions. Realistically, these criteria will be approached rather than achieved. It is important, therefore, to identify the analog aspects of greatest interest when evaluating a site for possible study.

#### **7.2.7 Potential Sites for a Natural Analog Study**

The uranium ore deposits at Peña Blanca, Mexico, and McDermitt Caldera, Nevada-Oregon, and the archaeological site at Santorini, Greece, have been identified as potential sites for natural analog studies. These sites were described in the quarterly report for April 1 - June 30, 1990 (CNWRA 90-02Q).

Briefly, sites at Peña Blanca, McDermitt, and Santorini occur in the hydrologically unsaturated zone of siliceous tuff sequences, and the sites have climates similar to that of southern Nevada. The past and present oxidation of uraninite at Peña Blanca and McDermitt constitutes an analog for the alteration of spent nuclear fuel. The processes of migration of uranium and other elements from sites of initial mineralization under unsaturated, oxidizing conditions at Peña Blanca and McDermitt are analogous to those that would occur in the Yucca Mountain repository. Studies using buried artifacts at the Santorini archaeological site as analogs of contaminant sources would permit analyses of the rates and mechanisms of trace-elemental migration in a geologic setting analogous to Yucca Mountain. The initial and boundary conditions at Santorini could be especially well defined, and the time period since burial of the artifacts (3600 years) is comparable to the period of interest in radioactive waste management.

#### **7.2.8 Conclusions**

Task 1 resulted in the identification of a wide variety of material occurrences and processes that have been studied as natural analogs. Broadly speaking, many sites could be considered as comparable to some aspect of a HLW repository. It is necessary, though, to select sites for analog study which most closely match the important characteristics of the system of interest while bearing in mind the limitations inherent in such studies. These limitations include the incompleteness of the geologic record, difficulty of quantifying important effects, presence at a given site of only a subset of the processes which will occur in a repository, and existence at natural sites of materials that are only approximations of the materials to be used in a repository. These limitations notwithstanding, only through the use of natural analogs can we identify and confirm that a process occurs in nature as well as in a laboratory or in theory. Natural analogs allow testing of the pertinence of individual processes over geologic time, assessment of the relative importance of various processes, and the effects of the coupling of processes. Through analog investigations we may determine the conditions under which the processes occur and the effects of the processes as well as the magnitude and duration of the phenomena.

Validation of numerical models is the reason most often cited for conducting natural analog studies. At the same time, the likelihood that a study will produce results useful for validation and for the nature of the validation which may reasonably be expected from analog studies must be clearly understood. Because of the uncertainties, it may be that a given model cannot be validated (in a strict sense) through the use of natural analogs. Nevertheless, natural analogs provide the only means of testing models of long-term processes for pertinence. The results of short-term, small-scale laboratory experiments and the long-term predictions of models based on the laboratory experiments may be compared to observations of natural systems which have operated for long periods at large scales (i.e., natural analogs). This process of testing by comparison can contribute to validation of the model. Validation of a predictive model by such comparison provides a measure of assurance that the model accurately reflects future behaviors.

Uranium deposits at Peña Blanca, Mexico, and McDermitt caldera, Nevada-Oregon, and archaeological sites at Santorini, Greece, offer good analogs of processes expected to occur in the geologic setting of the proposed HLW repository at Yucca Mountain, Nevada. However, there are no perfect analogs. The source term and boundary conditions at Peña Blanca and McDermitt may be difficult to constrain closely because of the complexity of the original hydrothermal systems and subsequent alteration. Conversely, at Santorini (where the source term and boundary conditions are relatively well known) the material and elemental sources are not necessarily close analogs to spent fuel or vitrified waste forms. Nevertheless, the physical similarities between these sites and Yucca Mountain could permit identification and characterization of relevant waste form degradation and contaminant migration phenomena, and could aid in the development and validation of predictive models for performance assessments.

### 7.3 REFERENCES

- Airey, P. L., and M. Ivanovich. 1985. Geochemical analogs of high level radioactive waste repositories. B. Come and N. Chapman, eds. *Commission of the European Communities Natural Analog Working Group, First Meeting*. Brussels:CEC.
- Arai, T., Y. Yusa, N. Sasaki, N. Tsunoda, and H. Takano. 1988. Natural analogue study of volcanic glass - a case study of basaltic glasses in pyroclastic fall deposits of Fuji Volcano, Japan. *Scientific Basis for Nuclear Waste Management XII - Materials Research Society Symposium Proceedings*. Pittsburgh: Materials Research Society: 73-80.
- Chapman, N. A., I. G. McKinley, and J. A. T. Smellie. 1984. The potential of natural analogues in assessing systems for deep disposal of high-level radioactive waste. Swedish Nuclear Fuel and Waste Management Co. (SKB) and the Swiss Radioactive Waste Cooperative (NAGRA). NTB 84-41. KBS 84-16. Eir Ber 545.
- CNWRA 1990. *Report on Research Activities for the Quarter April 1 through June 30, 1990*. CNWRA 90-02Q. San Antonio, Texas: CNWRA.

Finch, R. J., and R. C. Ewing. 1989. Alteration of natural  $UO_2$  under oxidizing conditions from Shinkolobwe, Katanga, Zaire: A natural analogue for the corrosion of spent fuel. Swedish Nuclear Fuel and Waste Management Company (SKB). Technical Report 89-37.

International Atomic Energy Agency (IAEA) 1982. *Radioactive Waste Management Glossary*. IAEA Report IAEA-TECDOC-264. Vienna, Austria: IAEA.

Pearcy, E.C., and W. M. Murphy. 1990. Geochemical natural analogs literature review. CNWRA 90-008. San Antonio, Texas: CNWRA.

## 8. PERFORMANCE ASSESSMENT RESEARCH

*by Budhi Sagar and A. Berge Gureghian*

*Investigators: Budhi Sagar (CNWRA) and A. Berge Gureghian (CNWRA)*

### 8.1. REVIEW OF EQUATIONS FOR MULTIPHASE, MULTISPECIES FLOW AND TRANSPORT IN FRACTURED POROUS MEDIA by Budhi Sagar

#### 8.1.1. Task Objectives

The objective of Task 2 is to modify the PORFLO-3 computer code to include liquid-vapor phase change under nonisothermal conditions.

#### 8.1.2. Introduction

The primary motivation for this review of equations for multiphase, multispecies flow and transport in fractured porous media is to formulate equations for incorporation in an existing unsaturated flow and transport computer code. The existing code, PORFLO-3<sup>1</sup> (Runchal and Sagar, 1989; Sagar and Runchal, 1990), simulates flow, heat transfer, and mass transport in variably saturated, fractured porous media. However, it makes the customary assumption that the gas phase is single component (air only) and that this phase is stationary. Thus the unsaturated nature of the flow system is accounted for by relating the liquid saturation and hydraulic conductivity to capillary pressures, and the motion of air is not explicitly modeled. In order to study the flow system close to the waste packages, the mobility of the gas phase needs to be considered. In addition, because of the considerable amount of thermal energy transmitted by the waste packages, the gas phase must be treated as at least a mixture of air and water vapor. This necessitates inclusion of phase change (from liquid to gas and vice versa) considerations in the formulation of equations. Also, to include in the study is the migration of additional gas components that may be generated because of the presence of volatile substances in the waste form. Such components of immediate importance are oxides of <sup>129</sup>I and <sup>14</sup>C. Thus, the desire is to have the gas mixture consist of three components - air, water vapor, and at least one other gas such as CO<sub>2</sub>.

As stated above, this review was undertaken with very specific objectives, so its scope is limited. A comprehensive review of all aspects of the multiphase, multispecies flow and transport problems in fractured porous media would include discussions of many fundamental problems such as methods of space and time averaging for arriving at the

---

<sup>1</sup> The PORFLO-3 code was originally developed by ACRI (Los Angeles) for Westinghouse Hanford Company with funding from the defense waste program of the U.S. Department of Energy (DOE). The DOE has granted a copyright to the ACRI on this software. The copyright permits the use of the software for the purposes of the U. S. Government without any fees, but the software cannot be freely distributed. Dr. A. K. Runchal of ACRI has been retained as a consultant to make needed modification to the code.

differential equations, phase discontinuities in multiphase systems, and use of nonequilibrium thermodynamic relations. Such a comprehensive review will also require far larger resources than expended on this review and was not attempted.

### 8.1.3. Conceptual Framework

A conceptual picture (cross-section) of multiphase flow through a fractured porous medium is shown in Figure 8-1. Four distinct phases are represented: solid, water, a liquid that is immiscible in water (e.g., hydrocarbons), and gas. Each phase maintains its own characteristics or properties. Water may have any number of dissolved constituents (e.g., radionuclides), and the solid phase may be made up of many minerals. Similarly, the gas phase may be made up of a number of constituents (e.g., air, water vapor, and  $\text{CO}_2$ ). The assumptions are that each phase is a continuum and that distinct boundaries separate these phases. However, mass and energy transfer may occur across phase boundaries. For example, water may evaporate to add to the gas phase, and air may dissolve in water to add to the water phase. Fractures are also shown in Figure 8-1. Fractures may contain all the phases contained in the rest of the matrix except that they represent a space-scale vastly different from the adjoining matrix. Because of their comparatively smaller width, fractures are usually treated as porous media of reduced dimensionality. That is, the fractures are two-dimensional in three-dimensional domains. The flow and transport properties of fractures can, however, be different from those of the matrix by orders of magnitude.

The primary conceptual assumption in the equations discussed in the following is that each of the phases is a continuum; that is, for the solids, liquids, and gases under consideration, the density, temperature, velocity, and so forth are all smooth, continuous point functions. This type of overlapping continuum is also called a mixture. The governing equations for such mixtures can be obtained by first writing microscopic balance equations and then averaging them over appropriate volumes. The averaging techniques are discussed by Hassanizadeh and Gray (1979a,b) and Abriola (1984). Alternatively, one can write the macroscopic (or global) balance equations directly (e.g., Whitaker, 1976) and derive the local differential equations from them. The situations in which the continuum assumption breaks down, such as inclusion of gas bubbles in water, are far more complex and are not discussed here.

### 8.1.4. Balance Laws of Continuum Mechanics

#### 8.1.4.1. Balance Laws For a Simple Continuum

In contrast to a mixture, simple continuum is made up of only one phase. A macroscopic balance law for a simple continuum can be written by considering a volume,  $V$  at time  $t = 0$  containing material points from the continuum under consideration. This control volume is shown in Figure 8-2. At  $t > 0$ , the same material points occupy a volume  $V(t)$ . The boundary of  $V$  is  $\partial V$  with outward unit normal,  $n$ . Let the mass density of the material inside  $V$  be  $\rho(X,t)$ , where  $X \in V$ . The general form of the macroscopic balance

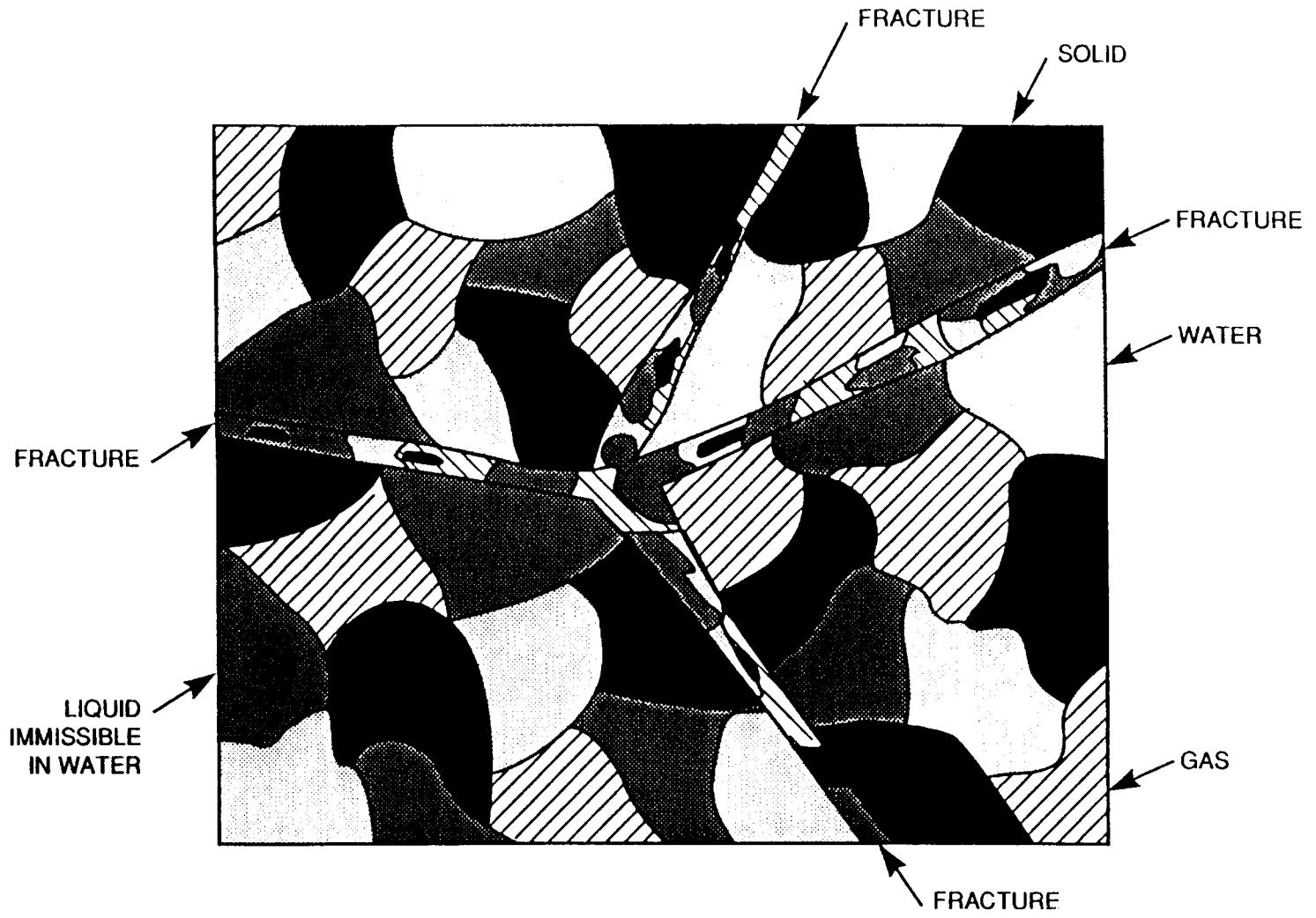


Figure 8-1. Conceptual picture of multiphase flow through fractured porous media

law over  $V$  for the material under consideration is

$$\frac{d}{dt} \int_V \rho \Psi dx - \oint_{\partial V} \tau \cdot n da - \int_V \rho w dx = 0 \quad (1)$$

where  $\Psi$  is a generic conserved quantity defined per unit mass,  $\tau$  is the flux of this quantity across surfaces in three-dimensional space, and  $w$  denotes external supplies of the conserved quantity.

If we let  $\Psi = 1$  and  $\tau = V$  (velocity) in Eqn. (1), we get an equation for mass balance as

$$\frac{d}{dt} \int_V \rho dx - \oint_{\partial V} \rho V \cdot n da - \int_V \rho w dx = 0. \quad (2)$$

→  $\bar{T}$  For the momentum balance equation,  $\rho =$  mass density;  $\Psi = V$ ;  $\bar{T}$  the stress tensor (which is the momentum flux per unit mass); and  $w = b$ , the body force per unit mass that is the external source of momentum. With these substitutions, the momentum balance equation becomes

$$\frac{d}{dt} \int_V \rho V dx - \oint_{\partial V} \bar{T} \cdot n da - \int_V \rho b dx = 0. \quad (3)$$

An equation for energy balance is obtained by putting  $\rho =$  mass density;  $\Psi = E + 1/2 V \cdot V$  (internal energy plus kinetic energy per unit mass);  $\tau = -q + \bar{T} \cdot V$  ( $q$  is the heat flux and  $\bar{T} \cdot V$  is the mechanical work done by stress); and  $w = h + b \cdot V$  ( $h$  is the rate of external heating and  $b \cdot V$  is the work done by body forces). Thus, the energy balance equation becomes

$$\frac{d}{dt} \int_V (E + \frac{1}{2} V \cdot V) dx + \oint_{\partial V} (q - \bar{T} \cdot V) \cdot n da - \int_V (h + b \cdot V) dx = 0. \quad (4)$$

From Eqns. (2) to (4), governing differential equations can be obtained in three steps. The contour integral in these equations can be changed into a volume integral by using the Divergence theorem (Williamson et al., 1972), that is,

$$\oint_{\partial V} f \cdot n da = \int_V \nabla \cdot f dx. \quad (5)$$

The next step is to apply the Reynolds transport theorem (White, 1984) to the time derivative

$$\frac{d}{dt} \int_V f dx = \int_V \left[ \frac{\partial f}{\partial t} + \nabla \cdot (Vf) \right] dx. \quad (6)$$

The final step is to use the duBois-Reymond lemma (Allen et al., 1988) to remove the integrals from the equation. This lemma asserts that in a region containing  $V$  and  $\partial V$ , if

$$\int_V f dx = 0 \quad \forall V \subset V, \quad (7)$$

then  $f$  vanishes identically on  $V$ . Applying these three steps to Eqn. (1) and assuming no singular surfaces (e.g. separating phases) will lead to

$$\frac{\partial}{\partial t} (\rho \Psi) + \nabla \cdot (V \rho \Psi) - \nabla \cdot \tau - \rho w = 0. \quad (8)$$

Thus Eqns. (1) and (8) are equivalent.

#### 8.1.4.2. Balance Equations For Mixtures

In the case of mixtures, the solid, liquid, and gas phases may exchange mass, momentum, and energy at their boundaries. Each phase itself may be made up of a number of constituents or species. Thus the gas phase may have three species: air, water vapor, and  $\text{CO}_2$ . The primary differentiation between species and phases is that of scale. Those constituents that can be differentiated only at the molecular scale are called species, while those that can be differentiated at the microscopic (e.g., pore) or larger scales are phases. The implicit assumption here is that in the gas phase, air and water vapor can be distinguished at the molecular scale; but at the scale of a pore or larger, these two species are so well mixed that they behave as a single entity (or phase). At a macroscopic scale (i.e., a control volume such as Figure 8-2), the phases seem to overlap or occupy the same space in an average sense. These considerations make the derivation of balance equations for mixtures more difficult. In fact, a number of unresolved questions remain (Truesdell, 1984) related to the precise thermodynamics of mixtures. The thermodynamics of a nonreacting multispecies mixture has been described by Muller (1968) where the fluids in the mixture are treated as linearly viscous with a single temperature. This treatment resulted in a generalized Fick's law of diffusion. The case of a binary reactive fluid system has been investigated by Huang (1973). In his work, Huang develops constitutive equations based on thermodynamic theory and certain invariance principles. In the following, because of the limited objective stated in Section 8.1.1, a much simpler view of mixtures is taken.

In the discussion below,  $\alpha$  and  $\beta$  are used as either superscripts or subscripts to represent phases and species respectively; and  $\alpha = s$  is solid;  $\alpha = \ell$  is liquid (when water is the only liquid phase,  $\ell = w$  in some equations); and  $\alpha = g$  is gas. The immiscible liquid of Figure 8-1 is not considered any further since its inclusion will be similar

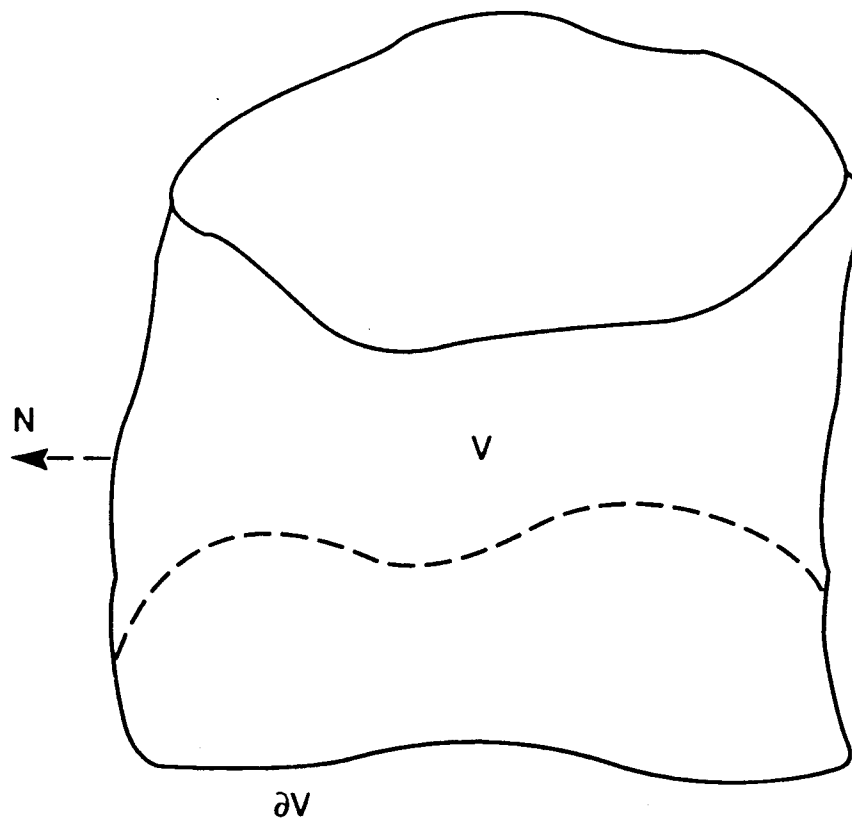


Figure 8-2. Macroscopic control volume for continuum balance equations

to the other phases. Similarly,  $\beta = a$  is air;  $\beta = w$  is water vapor (note that  $w$  is also used for liquid water when appropriate); and  $\beta = c$  is carbon dioxide. Some of the physical quantities such as the mass density are definable for both the species and phases. Thus  $\rho^\alpha$  is the mass of phase  $\alpha$  per unit volume of  $\alpha$  while  $\rho^\beta$  is the mass of species  $\beta$  per unit volume of  $\beta$ . On the other hand, some variables will be defined only for the phases. An example is the velocity,  $V^\alpha$ , which is defined only for the phases. Thus different species in the gas mixture (or the dissolved radionuclides in water) have a single velocity associated with them. Other symbols used and some obvious relations are:

$\phi^\alpha$  = volume fraction of phase  $\alpha$  [volume of  $\alpha$ /total volume]

$$\sum_{\alpha} \phi^\alpha = 1, \quad \text{also} \tag{9}$$

$$1 - \phi^s = \text{porosity} = \phi$$

$S^\alpha$  = saturation of phase  $\alpha$  [volume of  $\alpha$ /pore volume]

$\rho_g$  = mass density of gas =  $\sum \rho^\beta$ ,  $\beta$  = gas species [*a*, *w*, and *c*] [ $\text{ML}^{-3}$ ]

$m^\alpha$  = mass fraction of phase  $\alpha$  [mass of  $\alpha$ /total mass of mixture]

$m_\beta^\alpha$  = mass fraction of species  $\beta$  in phase  $\alpha$  [mass of  $\beta$ /mass of  $\alpha$ ]

$$\sum_\beta m_\beta^\alpha = 1 \quad \forall \alpha \quad (10)$$

$M^\alpha$  = molar density of phase  $\alpha$  [ $\text{Mo L}^{-3}$ ]

$W_\beta$  = molecular weight of species  $\beta$

$P$  = pressure [ $\text{M L}^{-1} \text{T}^{-2}$ ]

$T$  = temperature [ $\Theta$ ]

$K$  = intrinsic permeability [ $\text{L}^2$ ]

$K_r^\alpha$  = relative permeability of phase  $\alpha$

$\mu_\alpha$  = dynamic viscosity of phase  $\alpha$  [ $\text{ML}^{-1} \text{T}^{-1}$ ]

$E_\alpha$  = internal energy of phase  $\alpha$  [ $\text{HM}^{-1}$ ]

$H_\beta^\alpha$  = enthalpy of species  $\beta$  in phase  $\alpha$  [ $\text{HM}^{-1}$ ]

$H_g$  = enthalpy of gas phase [ $\text{HM}^{-1}$ ]

$$H_\alpha = \sum_\beta H_\beta^\alpha \quad (11)$$

$s_\beta^\alpha$  = external source of species  $\beta$  in phase  $\alpha$  [ $\text{T}^{-1}$ ]

$g$  = acceleration due to gravity [ $\text{LT}^{-2}$ ]

$d$  = depth [ $\text{L}$ ]

$\lambda$  = composite thermal conductivity [ $\text{HL}^{-1} \text{T}^{-1} \Theta^{-1}$ ]

$D_g$  = gas phase diffusivity [ $\text{L}^2 \text{T}^{-1}$ ]

$J_\alpha$  = flux vector for phase  $\alpha$  [ $ML^{-2}T^{-1}$ ]

$w_\beta^\alpha$  = external supply of species  $\beta$  in phase  $\alpha$  [ $T^{-1}$ ]

Initially, the existence of fractures in the control volume will be neglected. In a porous medium, the general balance law of continuum mechanics for mixtures analogous to Eqn. (1) applicable to species  $\beta$  can be written as

$$\sum_\alpha \left[ \frac{d}{dt} \int_V \phi^\alpha \rho^\alpha \Psi_\beta^\alpha dx - \oint_{\partial V} \tau_\beta^\alpha \cdot n da - \int_V \phi^\alpha \rho^\alpha w_\beta^\alpha dx \right] = 0. \quad (12)$$

Equation (12) represents conservation of a quantity  $\Psi_\beta^\alpha$  associated with species  $\beta$  in phase  $\alpha$ . The mass conservation equation for species  $\beta$  can be obtained by substituting  $m_\beta^\alpha$  for  $\Psi_\beta^\alpha$ ;  $(\phi^\alpha \rho^\alpha m_\beta^\alpha \mathbf{V}^\alpha + J_{\beta\alpha})$  for  $\tau_\beta^\alpha$  and  $s_\beta^\alpha$  for  $w_\beta^\alpha$  in Eqn. (12). Replacing  $\rho^\alpha$  with  $M^\alpha$ , the mass conservation equation can be written in terms of moles of  $\beta$ . Note that the flux of  $\Psi$  out of the control volume for a mixture is made up of advective (represented by velocity  $\mathbf{V}$ ) and nonadvective (e.g., diffusive), which is represented by  $J_\beta^\alpha$ . Following the three steps [i.e., Eqns. (5) to (7)], mass conservation equations for the various species may be written in the differential equation form. Some examples are provided below.

**Mass Conservation for Solids.** From Eqn. (12), the following equation for conservation of solids is obtained.

$$\frac{\partial}{\partial t} (\phi^s \rho^s m_s^s) + \nabla \cdot (\phi^s \rho^s m_s^s \mathbf{V}^s) - \nabla \cdot \mathbf{J}^s - \phi^s \rho^s w_s^s = 0. \quad (13)$$

The quantities sub- or super-scripted with  $s$  all pertain to the solid phase. Considering that some of the species in mixture are chemically reactive, some exchange of mass will occur at the solid-fluid interfaces. However, the change in mass of the solid phase is assumed to be so small that this change can be neglected. Note that such a change will generally not be negligible for the species in the fluid phases. This approximation means that  $m_s^s \approx 1$ . It is also assumed that there is no external source for the solid phase, i.e.,  $w_s^s = 0$ . Also solid-solid diffusion can be neglected, so that  $\mathbf{J}^s = 0$ . These assumptions reduce Eqn. (13) to

$$\frac{\partial}{\partial t} (\phi^s \rho^s) + \nabla \cdot (\phi^s \rho^s \mathbf{V}^s) = 0. \quad (14)$$

Equation (14) can be simplified further by assuming that while the solid matrix deforms, the solid particles themselves are rigid and incompressible. With this assumption and some algebraic manipulations, Eqn. (14) reduces to

$$\frac{\partial \phi^s}{\partial t} = -\nabla \cdot \phi^s \mathbf{V}^s. \quad (15)$$

Further development of Eqn. (15) requires that the velocity vector  $\mathbf{V}^s$  be further defined. This definition would obviously require consideration of constitutive (stress-strain) relations describing mechanical properties of the solids (see Ertekin and Ali (1979) for such equations for nonisothermal conditions and Valliappan and Khalili-Naghadeh (1990) for fractured media). Since the solid equation will not be included in PORFLO-3, this equation will not be developed any further; however, investigation of the potential role of lithostatic pressure upon those in fissures should be addressed in the future.

**Mass Conservation of Water.** Water exists in liquid and gas phases in the mixture. Liquid water also has species dissolved in it. The dissolved species are assumed to be in small concentrations, so these do not alter the mass density of liquid-phase water. In order to write the mass balance equation for water, summation over liquid and gas phases must be carried out. Thus,

$$\frac{\partial}{\partial t} (\phi [S^l \rho^l m_w^l + S^g \rho^g m_w^g]) = -\nabla \cdot (\phi [S^l \rho^l m_w^l \mathbf{V}^l + S^g \rho^g m_w^g \mathbf{V}^g]) + \nabla \cdot \mathbf{J}_w^g + \phi^w \rho^w m_w^l. \quad (16)$$

Note that in Eqn. (16), the external supply of water is assumed to be only in the liquid phase. The diffusional mass transfer term  $\mathbf{J}_w^g$  accounts for diffusion of water vapor within the gas phase and is written as

$$\mathbf{J}_w^g = -D_g \rho^g \nabla m_w^g. \quad (17)$$

Later in Section 8.1.8, an alternate form of Eqn. (16) is shown as possible. That is, two separate mass-conservation equations may be written, one each for liquid water and water vapor. In such a formulation, the formation and condensation of water vapor appears as a source/sink term in the conservation equations.

**Mass Conservation of Air.** The equation for conservation of air is very similar to Eqn. (16). While air has no phase change, some air is assumed to be dissolved in water. The equation is

$$\frac{\partial}{\partial t} (\phi [S^l \rho^l m_a^l + S^g \rho^g m_a^g]) = -\nabla \cdot (\phi^g \rho^g m_a^g \mathbf{V}^g + \phi^l \rho^l m_a^l \mathbf{V}^l) + \nabla \cdot \mathbf{J}_a^g + \phi^g \rho^g m_a^g. \quad (18)$$

The expression for  $\mathbf{J}_a^g$  is similar to Eqn. (17).

**Mass Conservation for CO<sub>2</sub> or Another Gas.** There is no phase change for this gas species also. However, this gas (e.g., CO<sub>2</sub>) may be reactive, i.e., it may

sorb on solids as well as react with dissolved constituents in water. Such reactions should be accounted for by writing additional terms.

$$\frac{\partial}{\partial t}(\phi[S^l \rho^l m_c^l + S^s \rho^s m_c^s]) = -\nabla \cdot (\phi^s \rho^s m_c^s \mathbf{V}^s + \phi^l \rho^l m_c^l \mathbf{V}^l) + \nabla \cdot \mathbf{J}_c^s + \phi^s \rho^s w_c^s - I_c^l - I_c^s \quad (19)$$

where  $I_c^l$  and  $I_c^s$  are mass exchange terms with liquid and solid respectively. The units of these terms are  $ML^{-3}t^{-1}$ . The expressions for  $I_c^l$  and  $I_c^s$  will depend upon the mineral phases present in liquid and solid with which  $CO_2$  reacts as well as on temperature and pressure.

**Mass Conservation for Species Dissolved in Liquid.** Mass conservation for species dissolved in water can similarly be written as follows:

$$\frac{\partial}{\partial t}(\phi^l \rho^l m_n^l + \phi^s \rho^s m_n^s) = -\nabla \cdot (\phi^l \rho^l m_n^l \mathbf{V}^l) + \nabla \cdot \mathbf{J}_n^l + w_n - I_n - R_c(\phi^l \rho^l m_n^l + \phi^s \rho^s m_n^s). \quad (20)$$

The subscript  $n$  denotes the dissolved species which may be radionuclides. The  $R_c$  (units  $t^{-1}$ ) is the decay rate constant of the radioactive species. Other reactions or precipitation phenomena are lumped in the  $I$  term.

### 8.1.5. Momentum Equation

The momentum equation for mixtures [analogous to Eqn. (3)] is extremely complex since the nature of the stress tensor in each phase must be investigated. Even for two phases, solid and water (e.g., saturated porous medium), the momentum equation based on Eqn. (3) leads to the Navier-Stokes equation at the pore scale, which is seldom used in the current state-of-the-art modeling of flow through porous media. Darcy's equation is typically used instead. Originally, Darcy's equation was derived from experimental data, but more recently it has been derived from the basic momentum equation [Eqn. (3)] by neglecting inertia terms (Hassanizadeh, 1986a, b). This more current derivation of Darcy's equation is valid only for single fluids flowing in the laminar range (Reynolds number  $< 1$  where the Reynolds's number is based on the particle size). For more discussion of applicability of Darcy's equation, see Cheng (1978).

The generalized form of the Darcy equation is

$$\mathbf{V}^\alpha = \frac{-\tilde{K} k_{r\alpha}}{\mu_\alpha} \cdot (\nabla P^\alpha - \rho^\alpha g \nabla D) \quad (21)$$

where  $\tilde{K}$  is the intrinsic permeability tensor (units of  $L^2$ );  $k_{r\alpha}$  is the relative permeability (unitless),  $0 \leq k_{r\alpha} \leq 1$ ;  $D$  is the depth and  $\mu_\alpha$  is the dynamic viscosity (units of  $ML^{-1}T^{-1}$ ).  $\mathbf{V}^\alpha$  is really the average flux of phase  $\alpha$ . The phase velocity can be approximated by dividing  $\mathbf{V}^\alpha$  by  $\phi^\alpha$ . It is noted that applicability of Eqn. (21) to potential high-velocity gas flow through fractures would require investigation in the future.

### 8.1.6. Energy Equation

In writing the energy equation for the mixtures, the kinetic energy term  $\left[\frac{1}{2} V \cdot V \text{ in Eqn. (4)}\right]$  is assumed to be negligible. This assumption implies that the fluids move slowly, which is also the assumption for the Darcy equation (see Section 8.1.5) to be valid. Another assumption is that at a point in space, all phases reach thermal equilibrium instantaneously. Thus, all the phases present at a given point have the same temperature. Based on these assumptions, the energy equation can be written as follows:

$$\frac{\partial}{\partial t} [\phi \{S^l \rho^l E^l + S^g \rho^g E^g\} + \phi^s \rho^s E^s] = \quad (22)$$

$$-\nabla \cdot (H^l \rho^l V^l + H^g \rho^g V^g) - \nabla \cdot (J_w^g + J_a^g) - \nabla \cdot (K_{teq} \nabla T) + \rho^g H^g w_g + \rho^l H^l w_l$$

where the velocities  $V^l$  and  $V^g$  are given by the Darcy equation discussed in Section 8.1.5.  $K_{teq}$  is the composite thermal conductivity of the solid-liquid-gas phase system. The  $J_w^g$  and  $J_a^g$  are diffusive flux terms and are given by

$$J_w^g = D_g \rho^g H_w^g \nabla m_w^g \quad (23)$$

and

$$J_a^g = D_g \rho^g H_a^g \nabla m_a^g. \quad (24)$$

Heat transfer by radiation is not included in Eqn. (22) but should be considered in the future. The conservation equations (including the Darcy equation) are to be supplemented by constitutive equations before these are solved. The constitutive equations provide thermodynamic relationships based on equilibrium between gas and liquid phases and also on other relations such as between capillary pressure and saturation. Some of these constitutive equations are discussed in Section 8.1.8 where existing computer codes are reviewed. Fourier law for heat conduction is already used in the deviation of Eqn. (22).

### 8.1.7. Treatment of Fractures

Geologic features such as fractures, fault zones, and small-sized clastic dikes may present a special problem in modeling multiphase flow. These features are distinguished from the neighboring rock by two attributes: (1) their characteristic dimensions differ greatly from those of the adjoining rock and (2) their characteristic flow and transport properties are different from the adjoining rock. Thus, fracture apertures may vary from less than a micron to a few millimeters. Such fractures may be embedded in rock whose characteristic dimension may be tens or hundreds of meters. Therefore, the length scale for these features may be smaller by orders of magnitude from the length scale of the rock. On the other hand, the hydraulic properties (e.g., saturated hydraulic conductivity) of fractures may be orders of magnitude larger than that of the rock. Fracture flow modeling in the context of evaluating the DCM3D code has been reviewed in Section 8.2 in this volume (Gureghian and Sagar).

From the theoretical view point, the simplest treatment of fractures is to treat them as ordinary heterogeneities in multidimensional domain. In such a treatment, these features are treated as separate computational elements with their special dimensions and their own flow and transport properties. Generally, these features are assumed to be porous media themselves, so that their characterization is similar to that of the rock. In the case where the fractures are open and the flow through them rapid (this assumption needs to be checked for gas flow), the governing momentum equation may have to be different from the Darcy equation. Also, any single fracture may be heterogeneous in itself, causing preferential flow channels to form. However, in most investigations of practical interest, the fracture characteristics are never known at a scale to find these channels deterministically. The main difficulty with this straight-forward approach is that the vastly disparate dimensions of computational elements give rise to numerical inefficiencies and instabilities. The main advantage is that no special constitutive equation for interaction between the rock and fractures is required. Most codes such as the TOUGH and PORFLO3 are capable of this approach.

At least four other are recognized approaches (see Gureghian and Sagar, this volume) for modeling flow and transport through fractures. The one intended to be followed in PORFLO3 assumes that the fractures would indeed behave like porous media even though their characteristic dimensions and properties are vastly different from those of the rock. One further assumption however, will be made. The conditions under which average pressures and gradients of average pressures are equal across fracture-rock interfaces under fully saturated conditions have been investigated by O'Neill (1978). We shall assume that a space-scale can be defined below which the pressures, temperatures, and concentrations will attain equilibrium between the fracture and matrix. It is at this scale that a control volume for writing of the governing equations will be defined. These assumptions allow writing the mixture balance equations in a natural way. As an example, consider the equivalent of Eqn. (12) for the case in which there are  $N$  fractures. The balance equation can now be written as

$$\sum_{\alpha} \left[ \frac{d}{dt} \left( \int_{V_m} \phi^{\alpha} \rho^{\alpha} \Psi_{\beta}^{\alpha} dx + \sum_{f=1}^{f=N} \int_{V_f} \phi^{\alpha} \rho^{\alpha} \Psi_{\beta}^{\alpha} dx \right) - \sum_{\alpha} \left[ \left( \oint_{\partial V_m} \bar{\tau}_{\beta}^{\alpha} \cdot n dx + \sum_{f=1}^{f=N} \oint_{\partial V_f} \bar{\tau}_{\beta}^{\alpha} \cdot n dx \right) - \int_{V_m} \phi^{\alpha} \rho^{\alpha} w_{\beta}^{\alpha} dx \right] \right] = 0 . \quad (25)$$

The only difference between Eqns. (12) and (25) lies in the additional fracture terms in Eqn. (25). Obviously, this formulation is possible only when within the control volume, the dependent variable (i.e., pressure, temperature, and concentration) is the same in the rock and fracture. Fluxes between rock matrix and fractures, however, can not be obtained explicitly in this approach.

### 8.1.8. Review of Existing Multiphase Codes used in the HLW Program

A review of existing nonisothermal multiphase computer codes currently under use in the HLW program was done by Updegraff (1988). He identified four codes: TOUGH (Pruess, 1987), NORIA (Bixler, 1985), PETROS (Hadley, 1985), and WAFE (authored by Travis, cited by Oster (1982), documentation unavailable). A search of literature revealed one other code (unnamed) by Forsyth (1989). A brief review of these codes is provided below.

#### 8.1.8.1. TOUGH Computer Code

Out of the codes listed above, perhaps the best known and most used is the TOUGH code developed by K. Pruess of the Lawrence Berkeley Laboratory primarily for geothermal applications. Three nonlinear partial differential equations representing conservation of air, water, and heat are solved in three-dimensional space simultaneously in TOUGH. Air can occur in the liquid phase as a dissolved constituent of liquid water. Henry's law as stated below is used to determine the mass fraction of air in liquid water.

$$m_a^w = \frac{P_a}{K_h} \cdot \frac{W_a}{W_w} \quad (26)$$

where  $W$  is the molecular weight,  $P_a$  is the partial air pressure, and  $K_h$  is the Henry's constant. Water can occur either as liquid or as vapor. Thermodynamic equilibrium is assumed between liquid water and its vapor, and International Formulation Committee's (1967) steam tables are used to obtain vapor pressure at a given temperature. In the gas phase made up of air and water vapor, mass transfer by molecular diffusion is accounted for. This binary diffusion coefficient in TOUGH is taken to be a function of temperature and pressure, i.e.,

$$D_{wa}^o = \tau \phi S^\alpha \frac{D_{wa}^o}{P_g} \left[ \frac{T-273.15}{273.15} \right]^\eta \quad (27)$$

where  $P_g = P_a + P_w$  is the gas phase pressure,  $\tau$  is the tortuosity factor (a property of the porous medium), and  $\eta = 1.80$  for air-water vapor mixture (Vargaftik, 1975). The value of  $D_{wa}^o$  at standard conditions ( $P_g = 1$  bar,  $T = 0^\circ$  C) is  $2.13 \times 10^{-5}$  m<sup>2</sup>/s.

The heat conservation equation is written in terms of enthalpy. The air, water, and solid phases are assumed to be at thermal equilibrium at all times. In calculating the equivalent thermal conductivity of the solid-fluid matrix, conductivity of the air phase is neglected. The equivalent thermal conductivity is allowed to be saturation dependent through either of the following equations.

$$\begin{aligned} K &= K_{dry} + \sqrt{S_w} (K_{wet} - K_{dry}) \\ K &= K_{dry} + S_w (K_{wet} - K_{dry}) \end{aligned} \quad (28)$$

The governing equations in TOUGH are discretized using the integrated finite difference technique and linearized through the Newton-Raphson method. Various shaped discrete elements can be used. However, element volumes, interfacial areas, and distances between grid blocks are required as input. The bandwidth of the matrix, therefore depends on the element shapes. The algebraic equations are solved using the Harwell matrix solver. Liquid and gas saturations are related to capillary pressure ( $P_c = P_g - P_l$ ) and so are the relative conductivities through seven alternate functions, which include the popular van Genuchten (1980) relations. The boundary conditions handled in TOUGH are somewhat limited. Grid block edges not connected to other blocks are assigned zero-flux conditions for both fluid and heat. Boundary grid blocks assigned large volumes fix the pressure and temperature values at those initially specified. It is difficult to specify zero flux for water and fixed temperature at the same boundary. Boundary conditions with nonzero fluxes have to be specified as sources and sinks. Time-varying boundary conditions have to use the restart feature. No special provision is made in TOUGH for fractures. Fractures can be included in TOUGH as computational elements on the same basis as rock elements.

The currently available version of the TOUGH code does not include other constituents in air (e.g., CO<sub>2</sub>) or dissolved components (e.g., radionuclides) in water. An updated version called TOUGH-2 is expected to be available (Pruess - personal communication) in the near future which may rectify these deficiencies.

#### 8.1.8.2. NORIA Computer Code

The NORIA code was developed by Bixler (1985) at the Sandia National Laboratory. Like TOUGH, it is designed to simulate the transport of water, air, and heat through porous media. However, the governing equation set contains four equations. Three equations represent mass conservation of liquid water, water vapor, and air. The fourth equation represents the conservation of energy. In the conservation equation for liquid water, evaporation/condensation is used as a separate term,  $F_v$ ; that is,

$$\rho^l \frac{\partial \phi^l}{\partial t} = -\nabla \cdot J_l - F_v \quad (29)$$

where  $J_l$  is the liquid mass flux vector given by a combination of the Darcy equation and Boussinesq approximation for natural convection; that is,

$$J_l = -\rho^l \frac{\bar{K} k_{rl}}{\mu_l} \cdot \nabla (P_l^* - \rho^l g B z \Delta T) \quad (30)$$

where  $B$  is the liquid volumetric expansion coefficient,  $z$  is the vertical coordinate, and  $\Delta T$  is the difference between a reference temperature and local temperature.  $P_l$ , the liquid head, includes elevation; that is,

$$P^* = P_l + \rho^l g z. \quad (31)$$

Nonequilibrium thermodynamic relations are used for the  $F_v$  term, with the default being

$$F_v = C \frac{(\phi^l - \phi_r^l)}{(P_v^* - P_v)} \quad (32)$$

in which  $\phi_r^l$  is the residual liquid content,  $P_v^*$  is the equilibrium vapor pressure of water as a function of temperature, and  $C$  is constant. The vapor conservation equation will also have the  $F_v$  term in it as follows:

$$\frac{\partial(\rho^g m_w^g)}{\partial t} = -\nabla J_v + F_v \quad (33)$$

The gas pressure  $P_g$  (and the vapor pressure  $P_w$ ) follows the ideal gas law of

$$\rho_g = \frac{P_g}{R_g T} \quad (34)$$

where  $R_g$  is the gas constant divided by the molecular weight. The  $J_v$  term for vapor flux includes four mechanisms - flux due to pressure and temperature gradients, Knudsen diffusion, and binary diffusion. The form of equation for  $J_v$  is

$$J_v = -\rho_v \frac{\bar{K}k_{rg}}{\mu_g} \cdot \nabla P_g^* - \rho_g m_w^g \nabla P_g^* \left( \frac{D_{kv} D_{ka}}{A} - \frac{(P_g/P_w) D_{kv} D_b}{A} \right) + \rho_g m_w^g \nabla T \left( \frac{R_a D_{kv} D_t}{A} \right) \quad (35)$$

where  $A = (P_g D_b + P_v D_{ka} + P_a D_{kv})$ ;  $P_g^* = P_g + \rho_g g z$ ;  $D_{kv}$  and  $D_{ka}$  are the vapor and air Knudsen-diffusion coefficients; and  $D_b$  and  $D_t$  are the binary and thermal diffusion coefficients, respectively. A similar set of equations are also written for air except that no vaporization term appears in this equation.

Thermal equilibrium among all phases is also assumed in NORIA. Heat transfer by radiation is not included. Terms for conduction, convection, heat loss (gain) by vaporization (condensation), and external source (sink) terms are considered. The energy conservation equation is written in terms of temperature (rather than enthalpy as in TOUGH):

$$[\rho c]_{eq} \frac{\partial T}{\partial t} = -(c_l J_l + c_v J_v + c_a J_a) \cdot \nabla T + \nabla \cdot (\bar{K}_{t,eq} \cdot \nabla T) - F_v L + Q \quad (36)$$

where the equivalent heat capacity term is given by

$$[\rho c]_{eq} = \phi^s \rho^s c_s + \phi^l \rho^l c_l + \phi^g (\rho_v c_v + \rho_a c_a). \quad (37)$$

A similar expression for the equivalent thermal conductivity  $K_{t,eq}$  can also be written.

The governing equations are solved by the Galerkin finite element method using quadratic-basis functions over isoparametric elements. A predictor-corrector method is employed for time stepping. Newton-Raphson method is used to linearize the equations. No special provision is made for fractures.

#### 8.1.8.3. *PETROS Computer Code*

The PETROS computer code (Hadley, 1985) is restricted to solving one-dimensional equations. In addition, in PETROS, the mass conservation equation is written in terms of the saturation (rather than pressure as in TOUGH and NORIA). This further limits the application of PETROS to situations in which no saturated regions occur. The basic equations are the same as described above for NORIA. Because of its limited applicability, this code is not discussed further.

#### 8.1.8.4. *Model by Forsyth*

Forsyth (1989) has recently published some papers on application of non-isothermal multiphase flow with respect to its applications to HLW repositories. Forsyth's governing equations are similar to the equations of TOUGH and have already been described in the main body of the text. That is, there are three governing equations - one each for conservation of water and air respectively and one for energy conservation in terms of enthalpy.

Forsyth's formulation however, has one major difference: It provides for inclusion of random fractures by the dual porosity approximation. In this approach, the rock matrix and fractures are treated as separate continua throughout the region of interest; so every point contains fracture and matrix variables. The two continua are connected by fluid and heat exchange terms (Dean and Lo, 1988; Gilman and Kazemi, 1983; Pruess and Narasimhan, 1985).

The governing equations are discretized by integrated finite differences. Called the finite volume approach in Forsyth's papers, this term is actually more descriptive for the integrated finite-difference technique. In a domain with  $N$  finite volumes, in dual porosity continua, there are  $2N$  nodes ( $N$  for rock and  $N$  for fractures) solved by a LU factorization iterative solver with orthomin acceleration (Forsyth and Sammon, 1986). In an article included in this volume as Section 8.2, Gureghian and Sagar have discussed the merits of the dual-porosity approach.

Equations for variation of fluid properties and some other correlations used by Forsyth (1989) are described below. The molar density of water is taken to be function of pressure and temperature,

$$M_w = M_{wr} [1 + \alpha_w (P_l - P_r) - \beta_w (T - T_r)] \quad (38)$$

where

$$M_{wr} = \text{reference molar density} = 5.55 \times 10^4 \text{ moles/m}^3$$

$$\begin{aligned}\alpha_w &= 4.3 \times 10^{-6} \text{ (Kpa)}^{-1} \\ \beta_w &= 2.1 \times 10^{-4} \text{ (}^\circ\text{K)} \\ T_r &= \text{reference temperature} = 273 \text{ }^\circ\text{K} \\ P_r &= \text{reference pressure} = 10^5 \text{ Pa}\end{aligned}$$

The gas is assumed to behave ideally; and its molar density is given by

$$Mg = \frac{P_g}{R_g T} \quad (39)$$

where  $R_g = 8.314 \times 10^{-5} \text{ Pa}\cdot\text{m}^3/(\text{mole}\cdot^\circ\text{K})$ . The mass densities of liquid and gas phases are calculated as follows.

$$\rho_l = \rho_w m_w^l + \rho_a m_a^l \quad (40)$$

and

$$\rho_g = \rho_w m_w^g + \rho_a m_a^g \quad (41)$$

where,  $\rho_w = 10^3 \text{ Kg/m}^3$  ( $18.02 \times 10^{-3} \text{ Kg/mole}$ ) and  $\rho_a = 28.97 \times 10^{-3} \text{ Kg/mole}$ . The equilibrium ratios for various species are empirically determined by the following relations.

$$m_a^g = Z_a m_a^l \quad ; \quad m_w^g = Z_w m_w^l \quad (42)$$

where  $Z_a$  and  $Z_w$  are taken to be

$$Z_a = \frac{1 \times 10^9}{(7.6 P_g \gamma)} \quad ; \quad Z_w = \exp\left[-P_{cg} \frac{S_l}{M_l RT}\right] Z_w^s \quad (43)$$

where  $\gamma$  is dependent on temperature - ( $T = 273^\circ\text{K}$ ,  $\gamma = 30.5$ ); ( $T = 293^\circ\text{K}$ ,  $\gamma = 19.8$ ); and ( $T = 323^\circ\text{K}$ ,  $\gamma = 13.9$ ).  $P_{cg}$  is the capillary pressure and

$$Z_w^s = \frac{0.8777 \times 10^{-8} (T-243)^{4.76}}{P_g} \quad (44)$$

Equation (44) indicates a lowering of vapor pressure due to the capillary effects (Pollock, 1986; Tsang and Pruess, 1988).

The enthalpies are calculated as follows. For liquid,

$$H_l = C_w (T - T_r) m_w^l + C_a (T - T_r) m_a^l \quad (45)$$

where  $C_w = 75.4 \text{ J}/(\text{mole}\cdot^\circ\text{K})$ ;  $C_a = 29.2 \text{ J}/(\text{mole}\cdot^\circ\text{K})$ ; and  $T_r = 273^\circ\text{K}$ . For air, the enthalpy is

$$H_a^s = C_a(T-T_r); \quad (46)$$

and for water vapor, it is

$$H_w^s = C_w(T-T_s) + L + 30.5(T-T_s) \quad (47)$$

where  $T_s = T$ , if  $S_t > 0$ ; otherwise  $T_s$  is the solution of the equation  $m_w^s - Z_w(T_s) = 0$ .  $L$  is the latent heat,  $L = 0$  if  $T_s > T_c$  where  $T_c = 647^\circ\text{K}$ . For  $T_s < T_c$ ,  $L = 4.814 \times 10^3 (T_c - T_s)^{.38}$  (J/mole). The enthalpy of gas phase is obtained as the sum of its constituent species weighted by their respective enthalpies.

In calculating internal energies, the small amount of dissolved air is neglected and

$$E_w = H_w - \frac{P_w^6}{M_w} \quad ; \quad E_g = H_g - \frac{P_g^6}{M_g} \quad (48)$$

in which  $P_w$  and  $P_g$  is in Pa. The viscosities of water and gas are treated as (empirical) functions of temperature as follows,

$$\mu_w = \frac{10^{-6}}{\{12.1 + 2.88(T-273) + 7.78 \times 10^{-4}(T-273)^2\}} \quad (49)$$

and

$$\mu_g = 10^{-10} \{1.574 + .0044(T-273)\}. \quad (50)$$

The units of viscosities in the above equations are Pa-day. Finally, the gas phase diffusivity is taken as

$$D_g = \frac{D_g^o \phi S_g (T/273)^{2.334}}{(P_g/100)} \quad (51)$$

Other functions are being reviewed before selection for inclusion in PORFLO-3.

### 8.1.9. Summary and Conclusions

A brief review of the equations for modeling of nonisothermal multiphase, multicomponent flow and transport is presented. The basic equations can be classified into balance and constitutive. The balance equations are based on laws of continuum mechanics. These can be written either very broadly over a finite-control volume or locally on a point. In this review, the averaging techniques required to give a firm theoretical basis to these equations. In effect, the concept of the 'representative elementary volume' was accepted without defining it in any great detail. Within such a representative volume, the assumption was that the various properties of the phases and species under consideration can be specified as some average (therefore constant) values. Ultimately these equations are intended to be solved numerically.

This would require discretization of the equations on a finite-sized discrete mesh. Each element of such a mesh would then constitute a representative elementary volume. However, in most instances of practical importance, the mesh construction is based not only on the considerations of representative elementary volumes but also on such other factors as size of computer memory, computational time, and distribution of data. This assumption, therefore is mostly an abstract idea.

The momentum equation in these discussions is replaced by the Darcy equation modified for multiphase flow. This requires the important assumption that inertia forces are negligible; that is, the fluid velocities are small. This is generally true for liquid flow but is suspect for gas flow, especially under large pressure gradients. Such large pressure gradients may occur where sources of gas are present in the domain. In this review, however, the non-Darcian flow was not considered. The primary reason for this is that flow laws in porous medium are not yet established. While one may borrow from turbulent fluid mechanics, such laws would have to be established through experimentation. Also, the non-Darcian flow assumptions will add to the nonlinearity of the problem, making it even more difficult to solve than with the Darcian assumption.

Many of the constitutive equations for multiphase, multispecies flow and transport modeling are of empirical nature; that is, these represent correlations obtained experimentally. Thus application of such equations is limited to the ranges of temperature and pressure and other conditions under which these were derived. The primary constitutive equations are those that define the dependence of fluid mobility on saturation, provide ratios of various species in different phases, and define the dependence of thermal and mass transport properties on temperature and pressure. In this review, some examples of these equations used by previous investigators have been presented. In general, the choice is between using these correlations in either a tabular or functional form.

In the documentation of PORFLO-3, the actual equations used will be discussed, and details of the numerical schemes will be provided.

---

**ACKNOWLEDGEMENTS:** The author is grateful to Dr. A. K. Runchal (ACRI, Los Angeles) for numerous discussion on the topic of this paper. Technical comments from Dr. R. Green (CNWRA), Dr. T. Margulies (NRC), and Dr. J. Randall (NRC) resulted in significant improvements. Dr. W. Patrick provided programmatic review and helped improve the readability of the paper. The author acknowledges with sincere thanks the help rendered by all these reviewers.

## **8.2. EVALUATION OF DCM3D - A DUAL CONTINUUM, 3-D GROUNDWATER FLOW CODE FOR UNSATURATED, FRACTURED, POROUS MEDIA<sup>2</sup> by A. Berge Gureghian and Budhi Sagar**

### **8.2.1. Technical Objectives of Task**

The technical objective of Task 3 of the PA Research Project is to evaluate the performance assessment technology developed by the Sandia National Laboratory (SNL) for the U. S. Nuclear Regulatory Commission (NRC) from the mid-seventies to 1990. The technology will be evaluated for its application to the partially saturated tuff medium - currently the only medium under investigation for a high-level nuclear waste repository in the United States. As studies progress, appropriate modifications to the SNL technology will be made or new technology appropriate to the site and engineered system developed.

A computer code called DCM3D was recently developed by SNL for use in performance assessment of the tuff site. This code is limited to the simulation of water flow in variably saturated fractured porous media. This computer code is being evaluated to meet the objective of Task 3 of Performance Assessment Research at the CNWRA. Another SNL code currently being evaluated is the transport code NEFTRAN.

### **8.2.2. Introduction**

Because of the large space-time scales involved, mathematical modeling appears to be the only viable method that is currently available in assessing the performance of the potential geologic high-level nuclear waste repository, . A fractured geologic medium is currently being considered by the U. S. Department of Energy (DOE) as a potential HLW repository candidate site. In order to demonstrate compliance with the NRC's quantitative performance requirements such as groundwater travel time (10 CFR 60.113) and the total system performance (10 CFR 60.112 or EPA's 40 CFR 191), mathematical investigations using site specific data must be performed. The subject of this paper is focused primarily on the review of existing concepts for modeling of water through fractured geologic media under isothermal conditions. We expect that this review of the background material will put the theory of the DCM3D code in perspective.

---

<sup>2</sup>The DCM-3D computer code was developed by C. David Updegraff (GRAM, Inc.) and Clarence E. Lee (Applied Physics, Inc.) at the Sandia National Laboratory (SNL) for the NRC. As part of the NRC contract transfer for research and assistance in performance assessment from SNL to CNWRA, this was one of the SNL developed computer codes provided to the CNWRA. The latest version of DCM-3D, obtained at the CNWRA in December, 1991, has been made operational on the SwRI's VAX 8700 computer.

Documentation on the code is scheduled to be published by the authors as NUREG/CR-5536. This present review is based on an advanced copy of the draft documentation and a very brief experience of implementing the code.

As stated above, the objective of this review is limited to obtaining sufficient background understanding for the evaluation of the DCM3D computer code. As such, this review is not designed to be comprehensive. We shall choose topics for review that fulfill the stated objective and omit others not directly related.

### **8.2.3. Approaches for Modeling Flow in Fractured Geologic Media**

#### **8.2.3.1. Analysis Needs**

The ultimate objective of groundwater flow codes is to estimate the velocity field. This velocity field can then be used to determine the trajectory of water particles and their travel time from the repository horizon to the biosphere as well as fluxes of water crossing boundaries of interest. The velocity field is also needed to determine the transport of constituents dissolved in water. Field measurement of groundwater flux and travel time is unrealistic because of the large spatial extent and natural heterogeneity of the hydrogeologic system that must be investigated. Moreover, the large travel times required by the NRC and EPA regulations regarding future predictions of groundwater flow conditions can be accomplished only with the use of mathematical models. Thus the hydrologist is required to address the following important modeling issues (this list is by no means exhaustive):

- the formulation of a conceptual model of groundwater flow for the hydrogeologic system being studied;
- the selection of the appropriate mathematical model and computer code;
- the assumptions under which the model simulates the behavior of the repository system and its limitations;
- the verification of the computer code and validation of the mathematical model;
- the acquisition of the required data to implement the chosen model.

The above steps are interdependent. The conceptual model of the various physicochemical processes provides the basis for the development and selection of the appropriate mathematical model. On the other hand, the mathematical modeling is fundamental to the understanding of the transient and spatially varying flow processes. At the same time, without verifying the computer code and validating the mathematical models the modeler's perception of groundwater flow in real hydrogeologic system may be incorrect. In addition, feedback has to exist between data acquisition and the conceptual and mathematical model formulation. Site investigations have to provide the data required by the models on the one

hand, but on the other hand the conceptual mathematical models have to reflect the limitations in data acquisition and be appropriate for the intended uses of the analyses.

Presently, the understanding of the hydrologic characterization of fractured unsaturated fractured rock is still in an embryonic stage. Therefore modeling concepts reviewed here may undergo significant changes in the future.

#### 8.2.3.2. *Modeling Approaches*

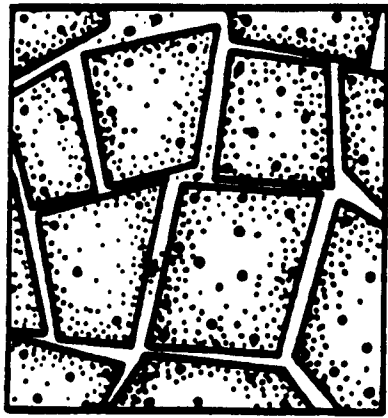
Five candidate conceptual modeling approaches for predicting flow in fractured geologic media for use in performance assessment of HLW repositories are currently available:

- the equivalent continuous porous medium model (ECPM);
- the double porosity model (DPM);
- the discrete fracture network model (DFNM);
- the discrete fracture equilibrium model (DFEM);
- the discrete fracture non-equilibrium model (DFNEM).

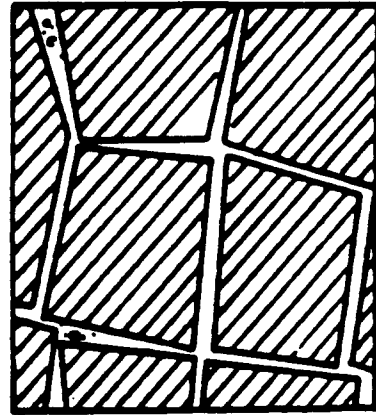
A brief description of these approaches is provided below.

**The Equivalent Continuous Porous Medium Model (ECPM).** In the equivalent continuous porous medium model [Figure 8-3(a)], the hydrogeological system which includes fractures and porous rocks is represented by a continuum (Hubbert, 1956), where the REV (representative elementary volume) concept (Bear, 1972) is supposed to prevail. The REV of a medium corresponds to the volume above which continuum parameters e.g., porosity and permeability, cease to vary. Figure 8-4 illustrates the statistical definition of representative elementary volume in the context of permeability. Note that the concept of REV in fractured media is not unique as shown by Snow (1969), who pointed out that permeability of fractured rock may increase with increasing tested volume, whereas, Freeze (1975), Smith (1978), Smith and Freeze (1979) have concluded that it may not always be possible to define equivalent homogeneous properties for naturally heterogeneous systems.

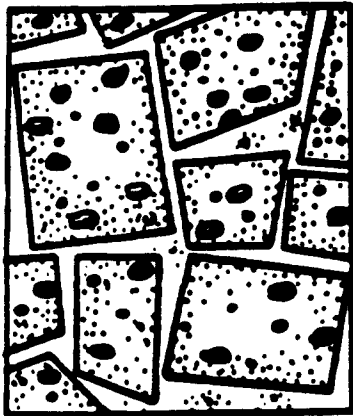
An additional requirement in support of the ECPM concept is the volume of fractured rock tested at random, which must behave as an equivalent volume of homogeneous anisotropic porous material. In other words, such a volume must display the salient feature of a symmetric permeability tensor. This physical characteristic of the rock sample is investigated by means of hydrologic experiments (ideally large scale pumping tests, e.g., Hsieh, 1983) designed to measure its permeability in the direction of the imposed gradient or the flux. For a symmetric tensor, polar plots of the inverse square root of permeability



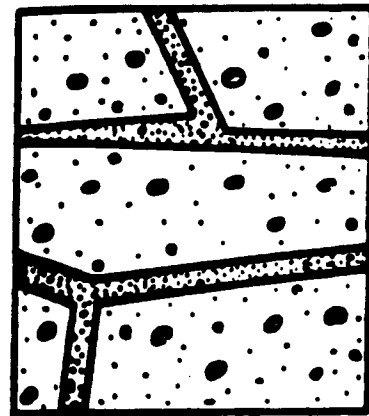
(a)



(b)



(c)



(d)

Figure 8-3. Schematic representation of: (a) fractured medium, (b) double-porosity medium, (c) discrete-fractured medium, (d) heterogeneous medium (Streltsova, 1976)

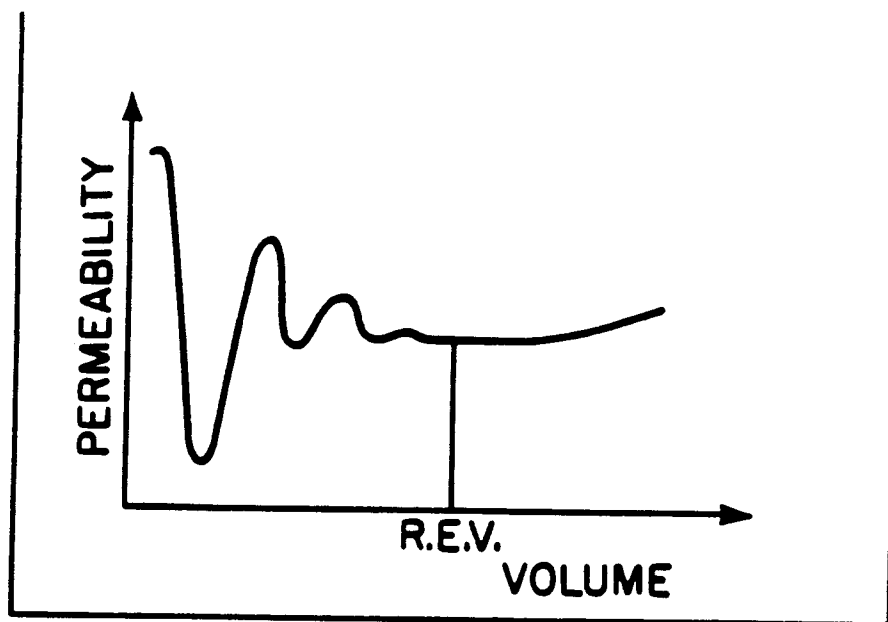


**Figure 8-4. Statistical definition of permeability and representative elementary volume (REV)**

versus the direction of measurement (or angle) must correspond to either an ellipse or an ellipsoid (Long, 1983), all of which depend on whether these tests are performed in a two- or three-dimensional domain. With these requirements in place, classical equivalent porous-media mathematical models may then be suited to investigate such fractured hydrologic system.

The equivalent continuum porous-medium concept related to flow through fractures rocks was first proposed by Snow (1965). Snow (1969) assumed an independence of flow at the intersection of the joints and derived the permeability tensor of a network of parallel fractures by adding the contribution from each one of these. The determination of the permeability tensor of an equivalent anisotropic media based on well tests was presented by Rocha and Franciss (1977). The validity of this approach, which provides a correction factor to the theoretical tensor obtained by Snow's method, seems to be restricted to radial flow systems. Long et al. (1982), using a finite-element program developed by Wilson (1970), have investigated the impact of various parameters such as fracture density, aperture, and orientation on the overall permeability of the media, assuming that the rock matrix is impermeable. Long's (1983) results revealed that the ECPM becomes applicable when "the fracture density is increased, apertures are constant rather than distributed, orientations rather constant, and larger sample sizes tested." This last point suggests that the scale factor closely

related to the theory of Fractals (Mandelbrot, 1977) plays an intimate role in the viability of the ECPM approach.

Klavetter and Peters (1986) have proposed an equivalent porous-medium model for partially saturated flow. In their case, typical composite characteristic curves are developed embodying the saturated-unsaturated properties of the fracture and matrix respectively (see examples in Figure 8-5). The physical justification of this model is based on calculations reported by Wang and Narasimhan (1985) dealing with a drainage situation in an unsaturated, fractured rock where pressure heads were almost identical measured along a direction normal to the flow in both fracture and matrix.

The ECPM approach could be easily implemented by standard numerical models based on either finite-element, boundary-element or finite-difference methods of solution designed to investigate groundwater flow in porous media. This approach does have, however, some additional drawbacks noted as follows.

- Difficulty is encountered in the extrapolation of the medium properties usually extracted through a limited number of experimental boreholes to an entire pluton.
- Even when the ECPM is valid, the size of the REV may be very large with respect to the scale of the problem. Therefore hydrological predictions which might be true at the repository scale might not be true at other scales.

**Double Porosity Model (DPM).** Within the category of equivalent continuous, porous media models, a second, more complex formulation for fractured porous media exists that is called the double-porosity flow models [see Figure 8-3(b)]. Note that DCM3D adopts this theoretical concept.

According to this concept, porosity in reservoir rocks may be assigned to two porous-media regimes; primary and secondary, defined as follows.

- Primary porosity is that made up of the void spaces between mineral grains of the reservoir-rock solid framework. In this type of porosity, a definite relationship occurs generally between porosity and absolute permeability as given by Kozeny-Carman's (Carman, 1956) equation (see also Pirson, 1953). This is synonymous with the matrix rock, whose properties are controlled by sedimentation, cementation, and lithification of the original deposits.

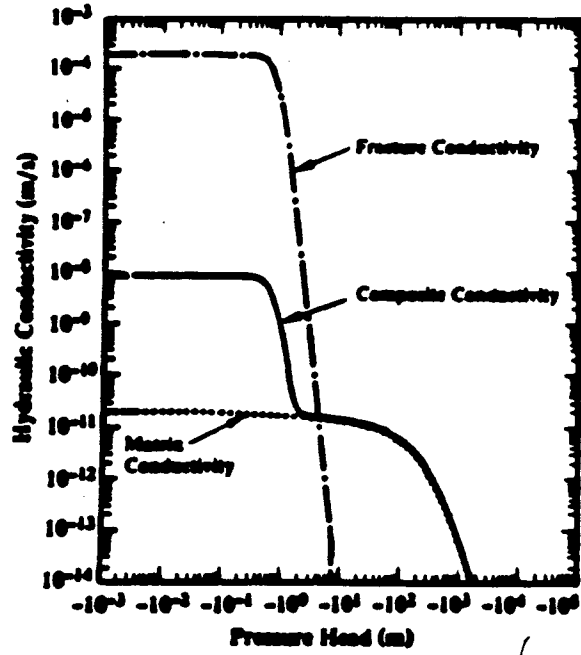
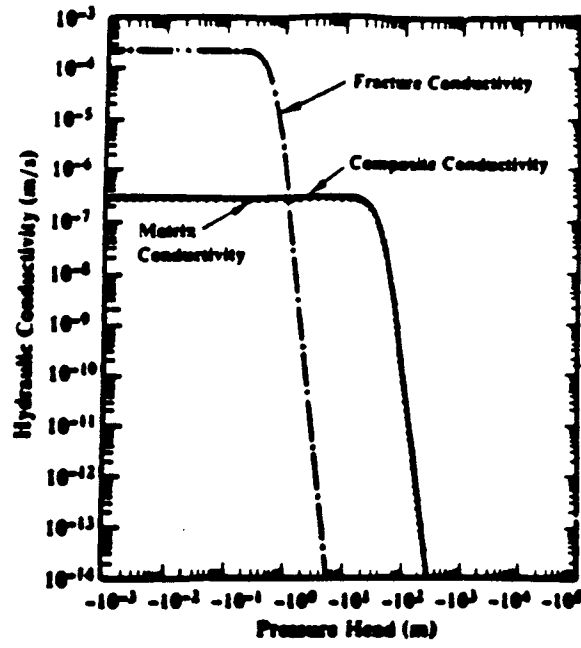


Figure 8-5. Conductivity curve for unit CHnz (Klavetter and Peters, 1986)

- Secondary porosity, also known as fracture porosity, is controlled by fracturing, jointing, and infilling as a result of precipitation. It is not highly interconnected and usually cannot be correlated with permeability. This is synonymous to fracture network.

The modeling of flow of a single-phase, slightly compressible fluid using the double-porosity approach was originally proposed by Barenblatt et al. (1960). This approach consists of (1) looking at a fractured block as one containing two media or two superimposed ECPMs where the first includes the fractures and the second the rock matrix and (2) allowing these two media to interact hydraulically. Barenblatt et al. (1960) argue that the characteristic property of flow in fractured rocks appears to be that intensive exchange of liquid takes place between the two media. This concept introduces the assumption of two liquid pressures at each point in space: one pertaining to the liquid in the fissures and the other pertaining to the average pressure of the liquid in the pores, thus giving way to a liquid-exchange process between the two media.

In double porosity media, the ratio of the permeability of the first medium to the second may vary by several orders of magnitude. The same is not true, however, for media porosity and compressibility. Thus, high permeability is associated with low fluid-storage capacity in the case of the fracture and low permeability, and high fluid-storage capacity is associated with the rock matrix.

In order to develop equations that describe fluid flow in naturally fractured reservoirs, idealizations are necessary to obtain a mathematically tractable model. With the dual-porosity idealization, the governing equations are described by a pair of mass conservation equations, one for each aforementioned regime. These equations are coupled by way of source function corresponding to the transfer of fluid between fracture and rock matrix. This source function itself is a function of the prevailing pressure gradient at the interface of fracture and matrix.

Streltsova-Adams (1978), who presented a thorough discussion of fluid flow in fractured reservoirs, classifies the double-porosity model as one in which the storage volumes of the primary and secondary regions are of the same order of magnitude, while the transmissivity is a result of the fracture system. Evans (1983) describes the double-porosity approach as a mathematical approximation and its physics to be ill defined. In support of his statement, Evans (1983) points out the difficulty relating computed pressures pertaining to fracture and matrix at every point in the system to the ones obtained through physical measurements.

Several other double-porosity related models designed to handle natural fractured reservoirs used by the petroleum industry have been reported by Gilman and Kazemi (1983), Kazemi (1969), and Warren and Root (1963) and others. Typically an idealized model composed of rectangular parallelepipeds, where the block represented the matrix and the

space between them represented the fractures, was introduced by Warren and Root (1963) [see Figure 8-6(a)]. In this case, flow can occur between fracture and rock matrix; however, flow between individual matrix blocks cannot occur. Kazemi (1969) presented a study concerning the transient pressure behavior of naturally fractured reservoirs using a model consisting of a finite circular reservoir with a well located at its center where all the fractures were assumed to be horizontal [see Figure 8-6(b)].

**Discrete-Fracture Network Model (DFNM).** The discrete-fracture network model [Figure 8-3(c)] envisions a system whose matrix permeability and porosity are negligible. In this case, the storativity and transmissivity of the reservoir would be due exclusively to the fracture network; and the geometry of each individual fracture is assumed to be known including its orientation, length, and hydraulic or effective aperture. Moreover hydraulic head is calculated at the fracture intersections assuming the network to be rigid. Modeling of groundwater flow in a discretely fractured rock system can be achieved using either a deterministic or stochastic approach.

In the deterministic approach, the flow is simulated in all significant, conductive, individual fractures; and from field measurements for specific hydrogeologic systems the geometric and hydrologic characteristics of all individual fractures are required as input. In general, data collection on a large scale and in such detail is quite unrealistic. Nevertheless, the deterministic models play a significant role for studying the mechanism of flow in fractured media, for setting defensible criteria for equivalent porous-media approximations, and for deriving equivalent porous-media characteristics.

In the stochastic approach (Robinson, 1982; Schwartz et al., 1982; Long, 1983), the geometry of the fractures is described as a random process. Interconnected networks of discrete fractures are generated using appropriate probability distribution functions. Fractures are simulated as line segments in two dimensions (see Figure 8-7) and as disk-shaped elements in three dimensions (Huang and Evans, 1984; Long et al., 1985; Dershowitz et al., 1985) (see Figure 8-8).

Flow through individual fractures is idealized as one between two smooth parallel plates [Poiseuille's (1846) type of flow]. This has been shown to be proportional to the cube of the fracture aperture (i.e., cubic law). In addition to a prevailing laminar flow regime, no head loss is assumed at each fracture intersection. The cubic law has been validated for a variety of geometry and for a wide range of geometries and stress conditions (Tsang and Witherspoon, 1981; Neuzil and Tracy, 1981).

The disadvantage of this modeling concept is inherent to the amount of geometric details that it entails. The computational complexity of the DFNM also seems to be far beyond the capacity of present-day computers, not to mention the availability of field data on fracture distributions, which for their physical interpretation rely strongly on statistics and probability.

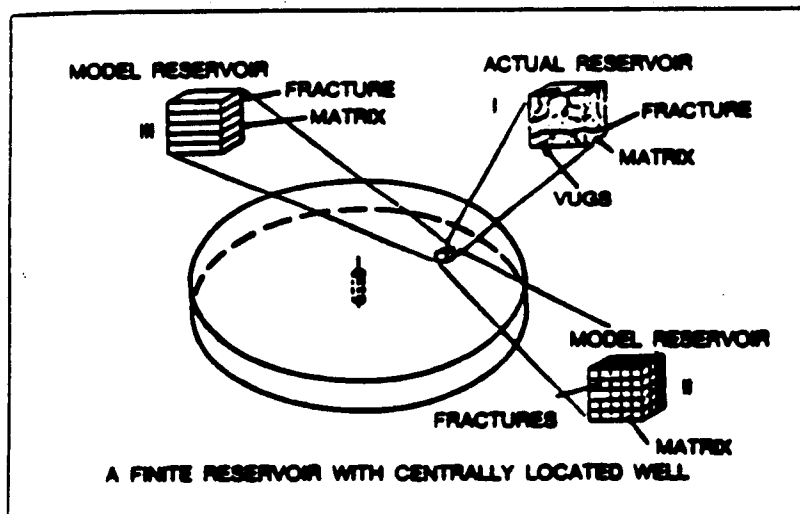
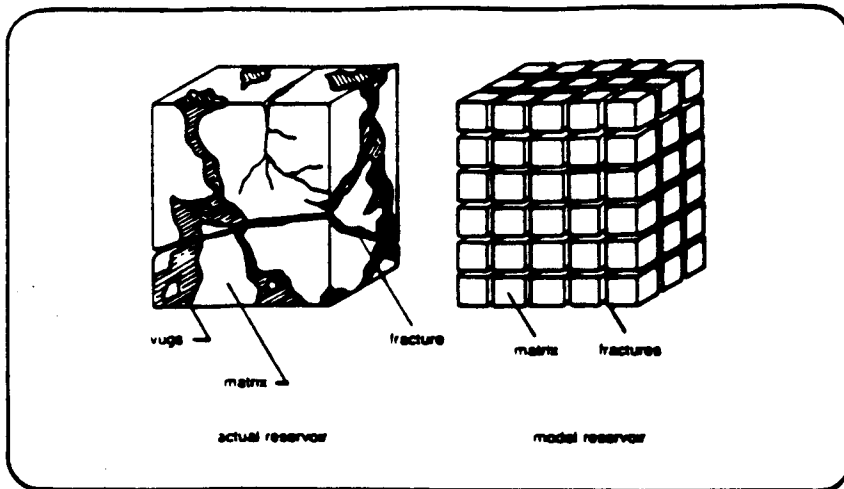


Figure 8-6. Idealization of naturally fractured porous medium. II is the Warren-Root model and III is the Kazemi model

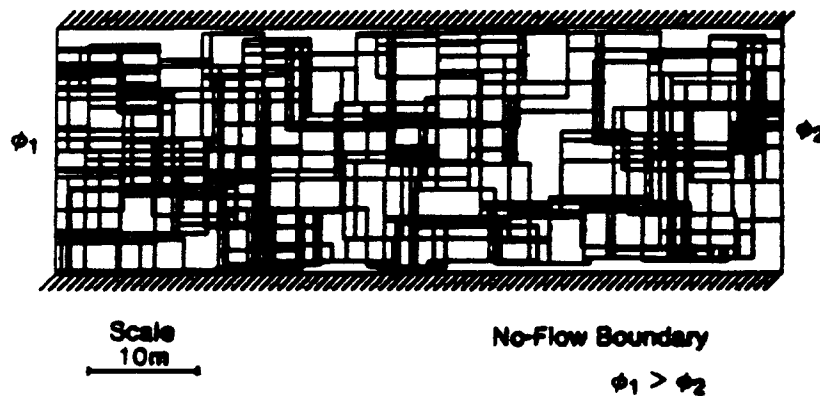
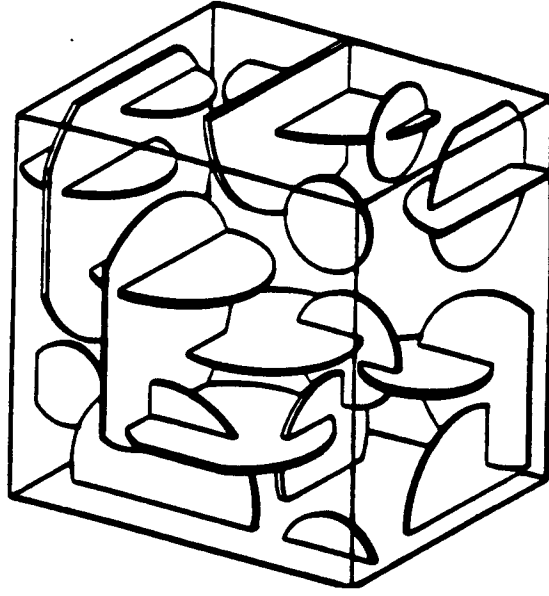


Figure 8-7. Example of a discrete-fracture network generated with two orthogonal fracture sets (Schwartz and Smith, 1985)

**Discrete Fracture Equilibrium Model (DFEM).** In the discrete-fracture equilibrium model, in addition to considering the geometry of the fracture system explicitly (as in network models described above), flow through the rock matrix is also accounted for. This formulation is closely tied to finite-difference and finite-element methods of obtaining numerical solution to governing equations.

This approach proposed first by Gureghian (1971, 1975) for steady-state flow assumes that pressure equilibrium prevails at the interface of fractures and porous rock. Explicit inclusion of such fractures is ideally suited to finite-element codes where fractures in a two-dimensional flow domain are simulated either by line elements or by planes in a three-dimensional one. In the first instance, simulated fractures are collinear with the sides or in the second instance coplanar with the faces of the elements. This modeling approach has gained



**Figure 8-8. Example of (a) a three-dimensional fracture network of disk shaped orthogonal fractures and (b) cubic region isolated from the network shown in (a)**

wide acceptance; its use becomes quite cumbersome, however, when the fracture density exceeds a certain threshold.

The main assumption of the DFEM approach is that at some (finite) scale of discretization of the rock-fracture system, the fluid pressure in the fracture is the same as that in the adjoining rock. Thus, within an element of a numerical grid, pressure is a single value in contrast to two values of DPM models. However, the flow through the element is calculated by summing it over the matrix surface and the cross-sectional area of the fractures. An example of this type of formulation in fractured media is found in Sagar and Runchal (1990).

The advantage of the DFEM approach is that the geometry as well as the hydraulic properties of the fractures is directly used in the model and the interaction between the fractures and the rock matrix is considered at a scale larger than the scale of discretization. While the computational effort required in DFEM is less than that required in the double-porosity formulation (because only one equation per node is to be solved rather than two), at the same time the amount of input data required is much greater.

The main disadvantage of the DFEM approach is that fracture-matrix interaction occurs only at scales larger than the scale of the calculational element. Thus the pressure distribution very close to the fracture is not accurately obtained.

**Discrete Fracture Nonequilibrium Model (DFNEM).** In the discrete-fracture nonequilibrium model approach, no assumption regarding fracture-matrix interaction is made. In this approach, fractures are treated as flow media embedded in the rock. In obtaining numerical solutions to flow problems in this approach, the fractures are treated as elements of distinct properties. Full geometry and hydraulic characteristics of the fractures are required to as input. In such models, channeling of flow within individual fractures can also be treated.

Because no assumption regarding flow interaction between the fractures and rock matrix is made, this formulation has the potential of producing the best results. It is, however, encumbered by large computational effort, numerical instabilities, and huge data input requirements. The great advantage is that almost any model designed to model flow through porous medium can be adapted for this approach.

#### **8.2.3.3. *Fluid Motion in Geologic Media***

Some background information on mathematics of fluid motion in porous media will be highlighted, which may be of help in appreciating the assessment of the model under review.

**Saturated Flow in Rock Matrix.** The groundwater-flow regime in saturated porous rock is assumed to be laminar (see Bear, 1972), justifying the legitimacy of

Darcy's law. This specifies a linear relationship between specific discharge and the hydraulic gradient  $J$  (boldface is used to represent vectors and tensors) written as

$$\mathbf{q} = \bar{K}J = -\bar{K}\nabla\Phi \quad (52)$$

where the constant of proportionality  $\bar{K}$  (L/T) in a three-dimensional, anisotropic medium corresponds to the saturated hydraulic conductivity tensor (Ferrandon, 1948). This tensor is defined as

$$\bar{K} = \bar{K}(x,y,z) = \bar{k}_s \frac{\rho g}{\mu} \quad (53)$$

where

$\nabla$  = is the gradient operator =  $\partial/\partial x, \partial/\partial y, \partial/\partial z$  ( $L^{-1}$ )

$\bar{k}_s$  = the saturated intrinsic permeability tensor ( $L^2$ )

$\rho$  = fluid density ( $ML^{-3}$ )

$\mu$  = dynamic fluid viscosity ( $ML^{-1}t^{-1}$ )

$g$  = the acceleration of gravity ( $Lt^{-2}$ ).

The total hydraulic head  $\Phi$  in Eqn. (53) is defined as

$$\Phi = h+z \quad (54)$$

where

$h$  = pressure head defined as  $p/\rho g$  (L)

$p$  = hydrostatic pressure ( $ML^{-1}t^{-2}$ )

$z$  = elevation from datum (L).

With the fluid assumed to be slightly compressible and to be under nonisothermal conditions, the equation of state of the fluid density restricted to the first term of a Taylor series expansion may be written as

$$\rho = \rho_0[1 + \alpha(p - p_0) - \beta(T - T_0)]$$

where

$\alpha$  = coefficient of compressibility of fluid ( $M^{-1} Lt^2$ )

$\beta$  = thermal coefficient of volume expansion ( $T^{-1}$ )

with subscript 0 denoting the reference value of the variable. Similarly, if the fluid viscosity is assumed to be temperature dependent  $\mu = \mu(T)$ , then this may be represented by a functional relationship (see for example Bingham, 1922).

**Saturated Flow in an Idealized Fissure.** Steady-state laminar flow in idealized fissures, whether of cylindrical or rectangular shape, is governed by the cubic law, which is the solution of Navier-Stokes equation for flow in such solid structures.

*Plane Laminar Crack.* The flow rate of a liquid in a plane, laminar crack simulating an idealized fracture with constant aperture  $b$  and width  $d$  (see Childs, 1971) and transecting a rock mass is referred as the cubic law and is written as

$$Q = -\frac{\rho g}{\mu} \left( \frac{b^3}{12} \right) \nabla \Phi \quad (56)$$

with an intrinsic permeability corresponding to

$$k = \frac{b^2}{12} \quad (57)$$

and  $\nabla \Phi$  refers to the potential gradient prevailing across ends of the fracture.

*Cylindrical Fissure.* The flow rate of a liquid in a cylindrical tube simulating an idealized fissure with constant diameter  $D$  is given by

$$Q = -\frac{\rho g}{\mu} \left( \frac{\pi D^4}{128} \right) \nabla \Phi \quad (58)$$

with an intrinsic permeability corresponding to

$$k = \frac{\pi d^2}{32} \quad (59)$$

**Unsaturated Flow.** Buckingham's (1907) theory of "capillary potential" which is equivalent to assuming the suitability of Darcy's equation for partially saturated porous flow was validated experimentally by Richards (1931). Childs and Collis - George (1950) were the first to propose an equation reasonably effective to predict the hydraulic conductivity of unsaturated soils bases on their soil water characteristic curve. Experimentally determined relationships between moisture content (or degree of saturation) and capillary pressure [see Figure 8-9(a)] on the one hand and hydraulic conductivity (or relative permeability and capillary pressure [see Figure 8-9(b)] of the porous medium on the other thus become prerequisites for an accurate prediction of the pressure and specific discharge at a required point in space and time in the unsaturated flow domain of interest. In this case, Eqn. (53) becomes

$$\tilde{K} = \tilde{k}_r k_r(\theta) \frac{\rho g}{\mu} \quad (60)$$

where

$k_r$  = relative intrinsic permeability ( $L^2$ )

$\theta$  = volumetric soil-water content (nS)

$S$  = degree of water saturation, ( $0 \leq S \leq 1$ )

$n$  = porosity.

The relative permeability  $k_r$ ,  $0 \leq k_r \leq 1$  depends upon the water saturation. This functional relationship between  $k_r$  and  $S$  is determined experimentally. In mathematical modeling of partially saturated groundwater-flow problems current practice is to adopt algebraic functions for simulating experimental data of the unsaturated properties of porous media, as reported in Figure 8-9(a) and (b). The coefficients of the selected functions are determined through standard nonlinear optimization techniques (see Gureghian et al., 1982). Following Klavetter and Peters's (1986) selection of a satisfactory model for characteristic curves, Updegraff and Lee (1990) adopted the van Genuchten (1989) model to represent the saturation and relative permeability characteristic curves.

The first van Genuchten expression describing the relation between effective degree of saturation  $S_e$  and capillary pressure based on the Burdine model is given by

$$S_e = \left[ \frac{1}{1 + (\alpha p)^\gamma} \right]^\lambda \quad (61)$$

with

$$S_e = \frac{S - S_r}{1 - S_r} \quad (62)$$

where  $S_r$  corresponds to the residual degree of saturation. The constants  $\alpha$ ,  $\gamma$  and  $\lambda$  are to be determined.

The second van Genuchten expression describing the relationship between relative intrinsic conductivity and effective degree of saturation based on Mualem's method (1976) is given by

$$k_r = (S_e)^2 \left[ 1 - \left[ 1 - (s_e)^{\frac{1}{\lambda}} \right]^\lambda \right]^2 \quad (63)$$

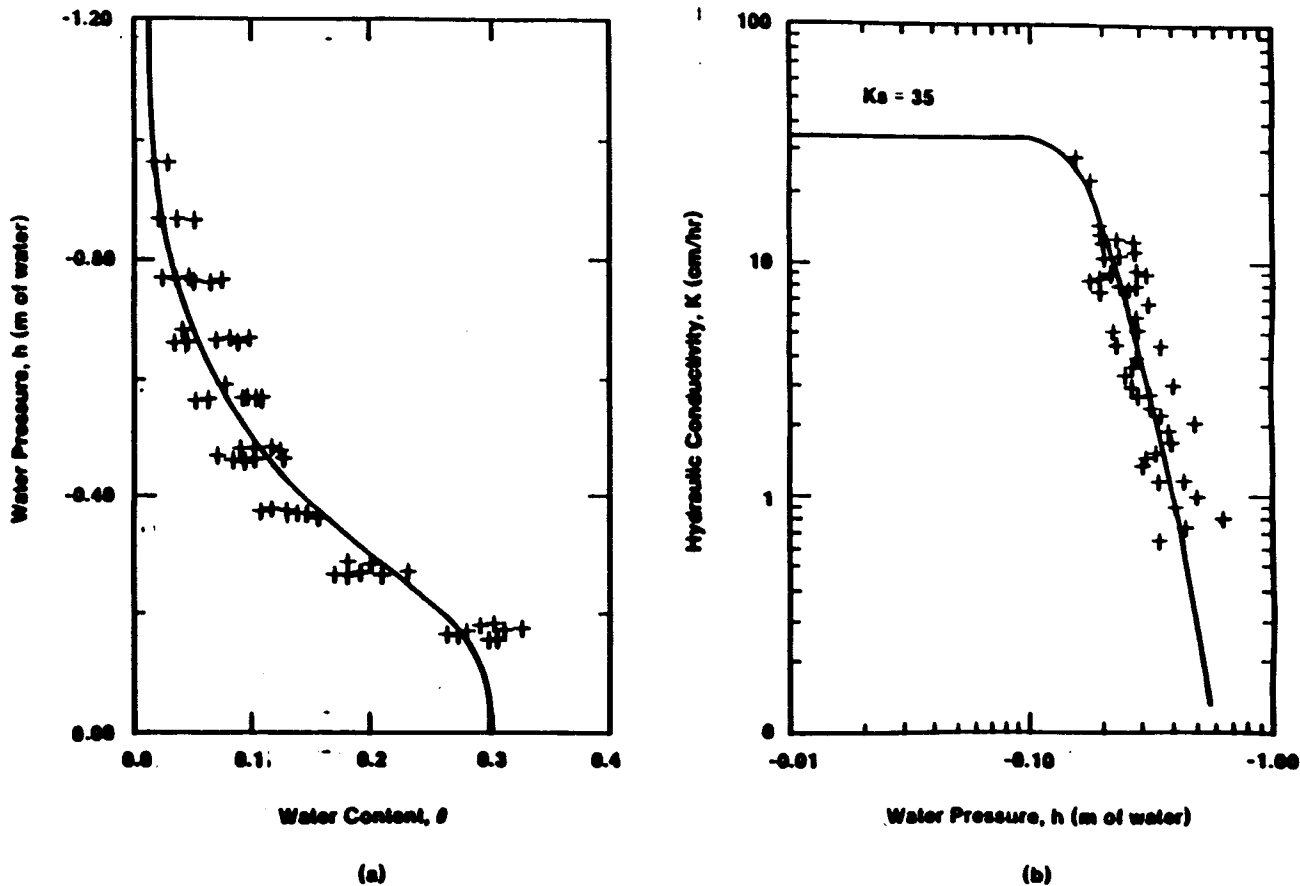


Figure 8-9. Soil characteristic curves (Updegraff and Lee, 1990)

Many other algebraic expressions of this nature are available in soil physics literature. Note that these are valid both for the matrix and fracture continuum.

**Governing Flow Equations in the Double-Porosity Model.** The governing equations simulating single-phase flow in a dual-porosity continuum under saturated-unsaturated and isothermal conditions (Barenblatt et al., 1960) may be written as follows for fracture [Eqn. (64)] and for porous rock [Eqn. (65)]:

$$\frac{\partial}{\partial t}(\rho n^f S^f) = -\nabla \cdot (\rho q^f) + \rho \Gamma + \rho Q^f \quad (64)$$

→ and ↘

$$\frac{\partial}{\partial t}(\rho n^m S^m) = -\nabla \cdot (\rho q^m) - \rho \Gamma + \rho Q^m \quad (65)$$

where

$\nabla \cdot$  = is the divergence operator =  $\partial/\partial x + \partial/\partial y + \partial/\partial z$  ( $L^{-1}$ )

$Q$  = strength of volumetric source or sink term ( $t^{-1}$ )

$\Gamma$  = strength of volumetric transfer term between matrix and fractures ( $T^{-1}$ )

$t$  = time.

Subscripts  $f$  and  $m$  refer to fracture and matrix, respectively.

The volumetric transfer term which determines the rate of water exchange between the matrix and the fractures, is given by

$$\Gamma = \frac{a \tilde{k}_s^m k_r^m}{\mu} (p^m - p^f) \quad (66)$$

where  $a$  has the dimensions of reciprocal area ( $1/L^2$ ). This is a shape factor that reflects, on the one hand, the geometry of the matrix and on the other hand, controls the fluid transfer between the two media. The definition of the shape factor as reported by Updegraff and Lee (1990) is given by

(67)

$$a = \frac{A_s}{l}$$

where

$A_s$  = the specific area of the fracture per unit volume ( $L^{-1}$ )

$l$  = a length parameter ( $L$ ).

Such a definition of the shape factor may be seen to be realistic only when the double-porosity model is in line with the conceptual idealization of fractured rocks as proposed by Warren and Root (1963) or Kazemi (1969), in which case well-defined geometries of the fractured block may conveniently be adopted.

Equations (64) and (65) represent a system of coupled nonlinear partial differential equations, which may have a closed-form solution under very restrictive assumptions (see e.g., Barenblatt et al., 1960; Warren and Root, 1963; Streltsova, 1976). Their

solution requires: a knowledge of the imposed boundary conditions, a mathematical description of the saturated and unsaturated material properties of the components of the fractured media, and a deterministic or stochastic computer code based on a finite-difference or finite-element solution method suited to handle such physical and mathematical nonlinearities.

#### **8.2.3.4. Review of DCM3D**

The mathematical model implemented in the DCM3D computer code (draft NUREG/CR-5536) is based on the dual-porosity approach that has been adapted for application to variably saturated media. As explained above, this approach assumes that the flow field is covered by two overlapping fields the matrix and the fissures. A particular feature of this model is the existence of two simultaneous pressure gradients at each point. Fluid exchange between fissures and matrix caused by pressure differences is represented by a source function in the equations of mass conservation. The constitutive relationship of this mass exchange term [Eqn. (66)] in this document is a composite of Eqns. (2-1) and (2-19)) in NUREG/CR-5536 and is the subject of ongoing debate. Nevertheless, the authors have adopted the definitions of the transfer coefficient reported in the literature by Streltsova (1976) and van Golf-Racht (1982) for a saturated medium and extended this to an unsaturated one. Given the fact that the double-continuum model has been used in reservoir modeling work of oil and gas reservoirs under saturated conditions (e.g., Warren and Root, 1963), the extension of this concept to a similar flow system under partially saturated conditions looks quite legitimate. Although the authors of DCM3D seem to have overlooked the difficult task of characterizing the components of the transfer coefficient, it would have been desirable if they had reported an illustrative problem displaying all the characteristic features of the theory adopted in their work.

Four illustrative problems, or test cases, demonstrating the operation of DCM3D were reported by the authors. We have revisited these four test cases using the latest version of DCM3D transmitted by SANDIA on February 21, 1991. A summary of our investigations is given as follows.

**One-Dimensional Horizontal Infiltration.** This test case deals with a one-dimensional semi-infinite horizontal-infiltration problem in a partially saturated homogenous soil. The tube of soil that displays a uniform residual-moisture content is held at a constant value of moisture content at one end; and, as time progresses, the moisture front is diffused into the porous matrix. The moisture in the tube begins to increase with respect to distance and time. The purpose of this problem is to test the DCM3D's ability to simulate transient unsaturated flow in a porous medium.

Inconsistency was noted between the saturation vs. soil-water pressure curve as shown on p.89 and the data reported on page 92 (i.e., FUNCTION SREL) used in this particular computer run. Model results compare favorably with Philip's (1955) analytical solution; hence the verification of the adopted numerical solution seems to have met its preset objective. It would have been desirable to witness a similar investigation for the case of vertical infiltration, which would have provided a check of the numerical solution in the presence of the

gravity component. We were able to reproduce exactly the results of this problem on Southwest Research Institute's (SwRI) VAX 8700.

#### **One-Dimensional, Horizontal Saturated Matrix/Fracture Flow.**

This test case solves the one-dimensional, horizontal saturated matrix flow problem and compares it to an analytic solution to Eqns. (64) and (65) of this document. The analytical solutions to these equations reported in Appendix B of NUREG/CR-5536 have been reviewed, and they appear to be correct. This problem was run as a dimensionless one. Reported results of the pressure heads in both migration zones (i.e., fracture and rock matrix) and for a wide range of the dimensionless time steps indicate that for values of this parameter greater than a threshold value, the two solutions schemes are in excellent agreement. We were able to reproduce exactly the results of this problem on SwRI's VAX 8700.

**Flow to a Well in a Fractured Porous Media.** This test case solves the two-dimensional, axi-symmetric case of the flow to a well in fractured (in this instance, the matrix permeability is assumed negligible) and un-fractured porous media. The fractured well flow problem is described in Ross et al. (1982) and was originally solved by Streltsova-Adams (1978). The purpose of this problem is twofold: test the transfer term between the matrix and the fractures and test the code ability to solve multidimensional problems. A comparison of the predicted drawdowns with well-established analytical solutions indicates that the agreement is excellent in both cases with the exception of the solutions associated with small values of the dimensionless time. We were able to reproduce exactly the results of this problem on SwRI's VAX 8700. Note that in this instance the geometry of the flow domain was simulated by a quadrant and the solution obtained in cartesian coordinates.

**Two-Dimensional Recharge.** This test case deals with the two-dimensional recharge problem in an experiment performed and modeled by Vauclin et al. (1979). The purpose of this problem is to test if the governing equations implemented in the DCM3D are capable of solving unsaturated flow problems. The model consists of a 2-m- high by 3-m-long vertical slab of homogeneous soil, recharged at a constant infiltration rate of  $4.111 \times 10^{-5}$  m/s applied over a 0.5-m long region at the top left corner of the slab. The watertable is initially set at 0.65 m. The upstream boundary of the slab including its base are impermeable. The downstream boundary includes: a portion extending from the slab base to the watertable height where constant values of pressure heads are assigned; the remaining portion corresponding to the seepage face is made subject to a zero flux boundary condition. As infiltration progresses in time, the watertable gradually rises with a decreasing slope in the direction of the outflow boundary.

Numerical results from DCM3D indicate significant discrepancies with these experimental results, particularly at large simulation times. The authors have attributed these anomalies to the existence of some soil heterogeneities. However, the seepage-face boundary condition was not implemented in DCM3D; instead, a no-flow boundary was assigned along the seepage face. The impact of this assumption was that the infiltration rate on the

watertable fluctuations was negligible. Interestingly, in this case, the impact is known a priori, so such an assumption may be acceptable. But in the likely event where the fluctuations of the watertable at the outflow face may be appreciable, the current version of DCM3D may not perform well. We were able to reproduce exactly the results of this problem on SwRI's VAX 8700.

#### 8.2.3.5. *Preliminary Conclusions*

If the purpose of the DCM3D computer code is "to possess the ability to predict velocity fields, pressures, and moisture content" in unsaturated, fractured rock, the test cases reported under their model-verification scheme may be deemed necessary, but not sufficient to assure the reader that this objective has been adequately met. It may also be noted that numerical models based on the double-continuum approach reported in the literature, implicitly assume an ordered pattern of fractures and porous blocks of equal dimensions [e.g., orthogonal fracture network, spherical blocks (i.e., Leibniz packing)] or parallel fracture-prismatic block. It would be of interest to the reader to know whether the authors want to restrict the application of their model to the aforementioned types of fracture configuration or apply it in an abstract fashion to a randomly distributed system of microfractures as long as the "scales of the pores and the fracture are nearly equivalent." The subject dealing with the direction, length, connectivity, and orientation of fractures which may be in conformity to their premise is not discussed. The authors should provide some lead to the investigator as to how the transfer coefficient is to be determined. The validation of such a model is deemed mandatory in order to reduce the degree of uncertainty inherent to the transfer coefficient. The need is therefore, to develop additional test cases involving synthetic experiments performed by means of porous-media codes designed to simulate well-ordered fracture networks under saturated, steady- and transient-state flow conditions.

To make the code and its documentation more useful for the users of the code, the following suggestions are made:

- Each one of the three convergence criteria appears to be problem dependent. Guidance on selecting the values of these criteria should be provided in the code documentation.
- The method for creating the input file is too rigid due to the adoption of a fixed-format input. Modifications such that at least comments can be included will be helpful.
- The dimensioning of the variable arrays that must be adjusted to fit the size of a problem should be discussed in the documentation.

- Standard soil-moisture curves should be included as options that can be specified from the input file. This should be in addition to the present option where the user can substitute the user's own module for the evaluation of these properties.

We are in the process of developing a test problem independently of the four test problems discussed by the authors. This test problem will investigate the (1) ease with which a fracture flow problem can be set up for DCM3D, (2) way an estimate of the volumetric transfer term can be made, and (3) efficiency of the code. The investigation will be accomplished by developing a fracture flow problem that can be solved by codes other than DCM3D (e.g., TOUGH) and comparing these solutions in terms of accuracy and computational efficiency.

### 8.3. REFERENCES

- Abriola, L. M. 1984. *Multiphase Migration of Organic Compounds in a Porous Medium: A Mathematical Model, Lecture Notes in Engineering*. C. A. Brebbia and S. A. Orszag, eds. New York, New York: Springer-Verlag.
- Allen M. B. III, G. A. Behie, and J. A. Trangenstein. 1988. *Multiphase Flow in Porous Media, Lecture Notes in Engineering*. C. A. Brebbia and S. A. Orszag, eds. New York, New York: Springer-Verlag.
- Barenblatt, G. E., Iu. P. Zheltov, and I. N. Kochina. 1960. Basic concepts in the theory of homogeneous liquids in fissured rocks. *J. Appl. Math. Mech. Eng. Transl.*, 24(5): 1286-1303.
- Bear, J. 1972. *Dynamics of Fluids in Porous Media*. New York, New York: Elsevier Publishing Company.
- Bixler, N. E. 1985. *NORIA - A Finite Element Computer Program for Analyzing Water, Vapor, and Energy Transport in Porous Media*. Sandia National Laboratories SAND84-2057. Albuquerque, New Mexico: SAND: 115.
- Buckingham, E. 1907. Studies in the movement of soil moisture. *U.S. Dept. Agric. Bur. Soils Bull.* Washington, D.C.: U. S. Dept. of Agriculture 38: 29-61.
- Carman, P. C. 1956. *Flow of Gases through Porous Media*. New York, New York: Academic Press: 192.
- Cheng, P. 1978. Heat transfer in geothermal systems. *Advances in Heat Transfer*. Vol. 14. New York, New York: Academic Press: 1-105.
- Childs, E. C. 1969. *The Physical Basis of Soil Water Phenomena*. London: John Wiley & Sons Ltd: 493.

- Childs, E. C., and N. Collis-George. 1950. The permeability of porous materials. *Proc. R. Soc. Ser A*. 201 London: Royal Society: 392-405.
- Dershowitz, W. S., B. M. Gordon, J. C. Kafritaas and H. Herda. 1985. A New Three-Dimensional Model for Flow in Fractured Rock in *Memoires of Hydrogeology of Rocks of Low Permeability*. Vol. XVII. *Inter. Assoc. of Hydrologists Symposium on the Hydrology of Rocks of Low Permeability*. Hanover, Germany: Verlag Heinz Heise: 441-448.
- Duguid, J. O., and P. C. Y. Lee. 1977. Flow in fractured porous media. *Water Resour. Res.* 13: 558-566.
- Ertekin, T., and S. M. Farouq Ali. 1979. *Numerical Simulation of the Compaction-Subsidence Phenomena in a Reservoir for Two-phase Nonisothermal Flow Conditions*. Third International Conference on Numerical Methods in Geomechanics, Aachen. 2-6 April.
- Ferrandon, J. 1948. *Les lois de l'ecoulement de filtration*. *Genie Civil* 125: 24-28.
- Forsyth, P. A. 1989. *Radioactive Waste Disposal Heating Effects in Unsaturated Fractured Rock*. Faculty of Mathematics. Ontario, Canada: University of Waterloo.
- Forsyth, P. A., and P. H. Sammon. 1986. Practical considerations for adoptive implicit methods in reservoir simulation. *J. Comp. Phys.* 62: 265-281.
- Freeze, R. A. 1975. A stochastic-conceptual analysis of one-dimensional groundwater flow in nonuniform homogeneous media. *Water Resour. Res.* 11(5): 725-741.
- Gilman, J. R., and H. Kazemi. 1983. Improvements in simulation of naturally fractured reservoirs. *Soc. Pet. Eng. J.*: 695-707.
- Gureghian, A. B., and B. Sagar. 1990. Evaluation of DCM3D: A dual-continuum, 3-D groundwater flow code for unsaturated fractured porous media. *Research Program Annual Report for the calendar year 1990 (January 1 through December 31, 1990)*. CNWRA 90-01A. San Antonio, Texas. CNWRA.
- Gureghian, A. B. 1971. *Influence of Fissures in Porous Media*. M.Sc Dissertation. Dundee, Scotland: University of Dundee.
- Gureghian, A. B. 1975. A study by the finite-element method of the influence of fractures in confined aquifers. *Soc. Pet. Eng. J.*: 451-463.

- Gureghian, A. B., B. R. Stitt, and L. P. Sanathanan. 1982. *Calculation of Unsaturated Hydraulic Conductivity*. ANL/EIS-14. Argonne, Illinois: Argonne National Laboratory (ANL).
- Hadley, G. R. 1985. *PETROS - A Program for Calculating Transport of Heat, Water, Water Vapor, and Air Through a Porous Material*. SAND84-0878. Albuquerque, New Mexico: SAND: 67.
- Hassanizadeh, M., and W. G. Gray. 1979a. General conservation equations for multiphase systems: 1. averaging procedures. *Adv. in Water Res.* 2: 131-144.
- Hassanizadeh, M., and W. G. Gray. 1979b. General conservation equations for multiphase systems: 2. mass, momenta, energy, and entropy equations. *Adv. in Water Res.* 2: 191-203.
- Hsieh, P. A. 1983. *Theoretical and Field Studies of Fluid Flow in Fractured Rocks*. Ph.D. dissertation. Tucson, Arizona: University of Arizona 200.
- Huang, M. 1973. Ph.D. Thesis. Baltimore, Maryland: The John Hopkins University.
- Hubbert, M. K. 1956. Darcy's law and the field equations of the flow of underground fluids. *Petroleum Transactions*. New York, New York: American Institute of Mining, Metallurgical, and Petroleum Engineers (AIME) 207: 222-239.
- International Formulation Committee (IFC). 1967. *A Formulation of the Thermodynamic Properties of Ordinary Water Substance*. IFC Secretariat. Dusseldorf, Germany: IFC.
- Kazemi, H. 1969. Pressure transient analysis of naturally fractured reservoirs with uniform fracture distribution. *Soc. Pet. Eng. J.*: 451-462.
- Klavetter, E. A., and R. R. Peters. 1986. *Estimation of Hydrologic Properties of An Unsaturated, Fracture Rock Mass*. SAND84-2641. Albuquerque, New Mexico: SAND.
- Long J. C. S. 1983. *Investigation of Equivalent Porous Medium Permeability in Networks of Discontinuous Fractures*. Ph.D. Thesis, Earth Sciences Division. Lawrence Berkeley Laboratory. Berkeley, California: University of California: 277.
- Long, J. C. S., J. S. Remer, C. R. Wilson, and P. A. Witherspoon. 1982. Porous media equivalents for networks of discontinuous fractures. *Water Resou. Res.* 19(3): 645-658.

- Long, J. C. S., P. Gilmour, and P. A. Witherspoon. 1985. A model for steady fluid flow in random three-dimensional networks of disc shaped fracture. *Water Resour. Res.* 19(3): 645-658.
- Mandelbrot, B. B. 1977. *Fractals, Form, Chance and Dimension*. San Francisco: W. H. Freeman.
- Marsily, G. de. 1985. Flow and Transport in Fractured Rocks: Connectivity and Scale Effects. *Inter. Assoc. of Hydrologists Symposium on the Hydrogeology of Rocks of Low Permeability*. Vol. XVII. Hanover, Germany: Verlag Heing Heise.
- Muller, I. 1968. A thermodynamic theory of mixtures of fluids, *Arch. Rep. Mech. Anal*, Vol. 28: 1-39.
- Neuzil, C. E., and J. V. Tracy. 1981. Flow through fractures. *Water Resour. Res.* 17(1): 191-199.
- O'Neill, L. 1978. The transient three-dimensional transport of liquid & heat in fractured, porous Media. Ph.D. Thesis. Princeton, New Jersey: Princeton University.
- Oster, C. A. 1982. *Review of Ground-Water Flow and Transport Models in the Unsaturated Zone*. NUREG/CR-2917, PNL-4427. Washington, DC: NRC.
- Philip, J. R. 1957. Numerical solution of equations of the diffusive type with diffusivity concentration-dependent. *Trans. Faraday Society* 51: 885-892.
- Pirson, S. J. 1953. Performance of fractured oil reservoirs. *Bulletin of the American Association of Petroleum Geologists (AAPG)*. 37(2). Tulsa, Oklahoma: AAPG: 232-244.
- Poiseuille, J. 1842. *Recherches experimentales sur le mouvement des liquides dans les tubes de tres petites diametres*. *Comptes Rendus* 11: 961-967, 1041-1048.
- Pollock, D. W. 1986. Simulation of fluid flow and energy transport processes associated with high-level radioactive water disposal in unsaturated alluvium. *Water Resour. Res.* 22: 765-775.
- Pruess, K. 1987. *TOUGH User's Guide*. NUREG/CR-4645. Berkeley, California: Livermore Berkeley Laboratory (LBL).
- Robinson, P. C. 1982. *Connectivity of Fracture Systems - A Percolation Theory Approach*. Theoretical Physics Div, AERE- TP.918. Harwell, England: Atomic Energy Research Established.

- Rocha, M., and F. Franciss. 1977. Determination of permeability in anisotropic rock masses from integral samples. *Structural and Geotechnical Mechanics*, W. J. Hall, ed. New York, New York: Prentice-Hall: 178-202.
- Runchal, A. K., and B. Sagar. 1989. *PORFLO-3: A Mathematical Model for Fluid Flow, Heat, and Mass Transport in Variably Saturated Geologic Media: Users manual Version 1.0*. WHC-EP-0041. Richland, Washington: Westinghouse Hanford Company (WHC).
- Sagar, B., and A. K. Runchal. 1990. *PORFLO-3: A Mathematical Model for Fluid Flow, Heat, and Mass Transport in Variably Saturated Geologic Media: Theory and Numerical Methods Version 1.0*. WHC-EP-0042. Richland, Washington: WHC.
- Sagar, B., and A. K. Runchal. 1990. *PORFLO-3: A Mathematical Model for Fluid Flow, Heat, and Mass Transport in Variably Saturated Geologic Media, Theory and Numerical Methods*. Richland, Washington: WHC.
- Schwartz, F. W., L. Smith, and A. S. Crowe. 1982. Stochastic analysis of groundwater flow and contaminant transport in a fractures rock system. *The Scientific Basis for Nuclear Waste Management*, Stephen V. Topp, ed. 457-463.
- Schwartz, F. W., and L. Smith. 1985. A new continuum approach for modeling dispersion in fractured media. *Inter. Assoc. of Hydrologists Symposium on the Hydrogeology of Rocks of Low Permeability*. Hanover, Germany: Verlag Heinz Heise.
- Smith, L. 1978. *Stochastic Analysis of Steady-State Groundwater Flow in a Bounded Domain*. Ph.D., Thesis, University of British Columbia, Vancouver, Canada.
- Smith, L., and R. A. Freeze. 1979a. Stochastic analysis of steady-state groundwater flow in a bounded domain. 1: one-dimensional simulations. *Water Resour. Res.* 15(3): 521-528.
- Smith, L., and R. A. Freeze. 1979b. Stochastic analysis of steady-state groundwater flow in a bounded domain. 2: two-dimensional simulations. *Water Resour. Res.* 15(6): 1543-1559.
- Snow, D. T. 1965. *A Parallel Plate Model of Fractured Permeable Media*. Ph.D. Thesis. Berkeley, California: University of California 351.
- Snow, D. T. 1969. Anisotropic permeability of fractured media. *Water Resour. Res.* 5(6): 1273-1289.

- Streltsova, T. D. 1976. Hydrodynamics of groundwater flow in a fractured formation. *Water Resour. Res.* 12(3): 405-414.
- Truesdell, C. A. 1984. *Rational Thermodynamics*. New York, New York: Springer-Verlag.
- Tsang, Y., and K. Pruess. 1988. A study of thermally induced convection near a high level nuclear waste repository in a partially fractured tuff. *Water Resour. Res.* 23: 1958-1966.
- Tsang, Y. W., and P. A. Witherspoon. 1981. Hydromechanical behavior of a deformable rock fracture subject to normal stress. *J. Geophys. Res.* 86(B10): 9287-9298.
- Updegraff, C. D. 1988. *Comparison of Strongly Heat-Driven Flow Codes for Unsaturated Media*. SAND. NUREG/CR 5367. Washington, DC: NRC.
- Valliappan, S., and N. Khalili-Naghadeh. 1990. Flow through fissured porous media with deformable matrix. *Int. J. Num. Met. in Eng.* 29: 1079-1094.
- van Genuchten, M. Th. A closed form equation for predicting the hydraulic conductivity of unsaturated soils. *Soil Science* 44(5): 892-898.
- van Golf-Racht, T. D. 1982. *Fundamentals of Fractured Reservoir Engineering*. New York, NY: Elsevier/North Holland Inc.
- Vargaftik, N. B. 1975. *Tables on the Thermophysical Properties of Liquids and Gases*. New York, NY: John Wiley & Sons.
- Vauclin, M., D. Khanji, and G. Vachaud. 1979. Experimental and numerical of a transient two-dimensional unsaturated-saturated water table recharge problem. *Water Resour. Res.* 15(5): 1089-1101.
- Wang, J. S. Y., and T. N. Narasimhan. 1985. Hydrologic mechanisms governing fluid flow in a partially saturated, fractured porous medium. *Water Resour. Res.* 21(12): 1861-1874.
- Warren, J. E., and P. J. Root. 1963. The behavior of naturally fractured reservoirs. *Soc. Pet. Eng. Jour.* 245-255.
- Whitaker, S. 1976. *Elementary Heat Transfer Analysis*. New York, New York: Pergamon Press.

- White, F. M. 1974. *Viscous Fluid Flow*. New York, New York: McGraw-Hill Book Company.
- Williamson, R. E., R. H. Crowell, and H. F. Trotter. 1972. *Calculus of Vector Functions*. Englewood Cliffs, New Jersey: Prentice-Hall.
- Wilson, C. R. 1970. *An Investigation of Laminar Flow in Fractured Porous Rocks*. Ph.D. Thesis. Berkeley, California: University of California: 178.
- 10 CFR Part 60. 1986. *Disposal of High-Level Radioactive Waste in Geologic Repositories*. Washington, DC: NRC.
- 40 CFR Part 191. 1985. *Environmental Standards for the Management and Disposal of Spent Nuclear Fuel, High Level and Transuranic Radioactive Wastes; Final Rule*. Washington, DC: U.S. Environmental Protection Agency.

**BIBLIOGRAPHIC DATA SHEET**

(See instructions on the reverse)

1. REPORT NUMBER  
(Assigned by NRC. Add Vol., Supp., Rev.,  
and Addendum Numbers, if any.)

2. TITLE AND SUBTITLE

Report on Research Activities for Calendar Year 1990

3. DATE REPORT PUBLISHED  
MONTH | YEAR

4. FIN OR GRANT NUMBER

5. AUTHOR(S)

Rachid Ababou, Asadul H. Chowdhury, Gustavo Cragnolino, Franklin T. Dodge,  
Ronald T. Green, A. Berge Gureghian, Simon M. Hsiung, William M. Murphy,  
Roberto T. Pabalan, English C. Pearch, Budhi Sagar and Narasi Sridhar

6. TYPE OF REPORT

Technical

7. PERIOD COVERED (Inclusive Dates)

8. PERFORMING ORGANIZATION - NAME AND ADDRESS (If NRC, provide Division, Office or Region, U.S. Nuclear Regulatory Commission, and mailing address; if contractor, provide name and mailing address.)

Center for Nuclear Waste Regulatory Analyses  
Southwest Research Institute  
6220 Culebra Road  
San Antonio, TX 78228

9. SPONSORING ORGANIZATION - NAME AND ADDRESS (If NRC, type "Same as above"; if contractor, provide NRC Division, Office or Region, U.S. Nuclear Regulatory Commission, and mailing address.)

Division of Engineering  
Office of Nuclear Regulatory Research  
U.S. Nuclear Regulatory Commission  
Washington, D.C. 20555

10. SUPPLEMENTARY NOTES

None

11. ABSTRACT (200 words or less)

This is an annual status report on the results of research conducted on behalf of the NRC by the Center for Nuclear Waste Regulatory Analyses in support of activities under the Nuclear Waste Policy Act, as Amended. Eight specific projects are underway. The Geochemistry project is using laboratory methods and computer calculations to assess key geochemical constraints and to evaluate sorptive properties of zeolite present at the proposed repository site. The Thermohydrology project has as its focus improved understanding of heat and fluid flow in unsaturated media. Laboratory, field, and calculational studies are combined in the Seismic Rock Mechanics project to examine the effects of repeated seismic loadings on the rock-mechanical and hydrological responses of rock masses. The Integrated Waste Package Experiments have been initiated to evaluate degradation modes of candidate waste container alloys. Three-dimensional computer analysis techniques are being used to investigate spatial variability of flow and transport in variably saturated fractured porous media in the Stochastic Flow and Transport project. The recently initiated Geochemical Analogs project seeks to investigate the role of such analogs in the licensing process, and is currently focused on locating and evaluating a potential site for investigation. The Performance Assessment project is directed toward developing and evaluating methodologies for evaluation of the long-term performance of the proposed repository.

12. KEY WORDS/DESCR:PTORS (List words or phrases that will assist researchers in locating the report.)

geochemistry; zeolites; sorption; hydrogeology; thermohydraulics; thermodynamics;  
physical models; flow; fractured media; porous media; transport; unsaturated zone;  
rock mechanics; shear; fracture; seismic response; hydromechanical response; coupled  
processes; natural analogs; waste package; corrosion; container; degradation; failure;  
material properties; performance assessment

13. AVAILABILITY STATEMENT

Export Controlled

14. SECURITY CLASSIFICATION

(This Page)

Unclassified

(This Report)

Export Controlled

15. NUMBER OF PAGES

16. PRICE

## DO NOT PRINT THESE INSTRUCTIONS AS A PAGE IN THE NUREG REPORT

### INSTRUCTIONS

NRC FORM 335, BIBLIOGRAPHIC DATA SHEET, IS BASED ON GUIDELINES FOR FORMAT AND PRODUCTION OF SCIENTIFIC AND TECHNICAL REPORTS, ANSI Z39.18-1987 AVAILABLE FROM AMERICAN NATIONAL STANDARDS INSTITUTE, 1430 BROADWAY, NEW YORK, NY 10018. EACH SEPARATELY BOUND REPORT—FOR EXAMPLE, EACH VOLUME IN A MULTIVOLUME SET—SHALL HAVE ITS UNIQUE BIBLIOGRAPHIC DATA SHEET.

- 1. REPORT NUMBER.** Each individually bound report must carry a unique alphanumeric designation (NUREG) assigned by the Regulatory Publications Branch, Division of Freedom of Information and Publications Services, in accordance with American National Standard ANSI Z39.23-1983, Standard Technical Report Number (STRN). Use uppercase letters, Arabic numerals, slashes, and hyphens only, as in the following examples: NUREG-0100, NUREG/CP-0010, NUREG/CR-0100, and NUREG/BR-0010. For reports in a series add Vol., Supp., Rev., and Addendum, when necessary. Add contractor cross-reference identification number (if any) below NUREG-series number, e.g., PNL-XXXX, SANDXX-XXXX, SAI-XXXX.
- 2. TITLE AND SUBTITLE.** Title should indicate clearly and briefly the subject (coverage) of the report; including any subtitle to the main title. When a report is prepared in more than one volume, repeat the primary title, add volume number and include subtitle for the specific volume. Use upper and lower case letters, but capitalize computer code names. Do not use acronyms and initialisms in titles; may be added in parenthesis.
- 3. DATE REPORT PUBLISHED.** Each report must carry a date indicating month and year published.
- 4. FIN OR GRANT NUMBER.** Insert the FIN or grant number under which report was prepared.
- 5. AUTHOR(S).** Give name(s) in conventional order (e.g., John R. Doe, J. Robert Doe). List author's affiliation if it is different from the performing organization.
- 6. TYPE OF REPORT.** State draft, final, preliminary, topical, technical, regulatory, annual, quarterly, etc.
- 7. PERIOD COVERED.** Add inclusive dates.
- 8. PERFORMING ORGANIZATION NAME AND MAILING ADDRESS.** Give name, street, city, state, and ZIP code. List no more than two levels of an organizational hierarchy. Display the name of the organization exactly as follows: Division, Office, Organization or Government agency, and address.
- 9. SPONSORING ORGANIZATION.** If NRC, type "Same as above"; if contractor, provide NRC Division, Office or Region, U.S. Nuclear Regulatory Commission, and mailing address.
- 10. SUPPLEMENTARY NOTES.** Enter information not included elsewhere but useful, such as: Prepared in cooperation with ... Presented at conference of ... To be published ... Docket No. ... When a report is revised, indicate whether the new report supersedes or supplements the older report.
- 11. ABSTRACT.** Include a brief (200 words or less) factual summary of the most significant information contained in the report. If the report contains a significant bibliography or literature survey or multiple volumes, mention it here. Abstract is to be prepared by author or project manager.
- 12. KEY WORDS/DESCRIPTORS.** Select from the Energy Data Base Subject Thesaurus, DOE/TIC-700R R-5, the proper authorized terms that identify the major concept of the research and are sufficiently specific and precise to be used as index entries for cataloging.
- 13. AVAILABILITY STATEMENT.** Denote public releasability, for example "unlimited", or limitation for reasons other than security.
- 14. SECURITY CLASSIFICATION.** Enter U.S. Security Classification in accordance with U.S. Security Regulations (i.e., unclassified).
- 15. NUMBER OF PAGES.** Leave blank. (Added by NTIS)
- 16. PRICE.** Leave blank. (Added by NTIS)